

NASA CR-162,051

NASA CONTRACTOR
REPORT

XV
XXI

NASA CR-162051

FOR REFERENCE

NOT TO BE TAKEN FROM THIS ROOM

1982 NASA/ASEE SUMMER FACULTY FELLOWSHIP PROGRAM

Edited by

Dr. B. F. Barfield
Professor of Mechanical Engineering
The University of Alabama
Tuscaloosa, AL

Mr. Marion I. Kent
Office of University Affairs
Marshall Space Flight Center, AL

Dr. James Dozier
Director, Research and Technology Office
Marshall Space Flight Center, AL

Dr. Gerald Karr
Professor of Mechanical Engineering
The University of Alabama in Huntsville
Huntsville, AL

LIBRARY COPY

MAY 11 1983

LIBRARY, NASA
MARSHALL SPACE FLIGHT CENTER

August 1982

Prepared for

NASA - Marshall Space Flight Center
Marshall Space Flight Center, Alabama 35812

1. REPORT NO. NASA CR-162051	2. GOVERNMENT ACCESSION NO.	3. RECIPIENT'S CATALOG NO.	
4. TITLE AND SUBTITLE 1982 NASA/ASEE Summer Faculty Fellowship Program		5. REPORT DATE December 1982	6. PERFORMING ORGANIZATION CODE
		8. PERFORMING ORGANIZATION REPORT #	
7. AUTHOR(S) Editors: B. Barfield, M. Kent, J. Dozier, and G. Karr		10. WORK UNIT NO.	
9. PERFORMING ORGANIZATION NAME AND ADDRESS The University of Alabama Tuscaloosa, Alabama and The University of Alabama in Huntsville		11. CONTRACT OR GRANT NO. NGT-01-002-099	13. TYPE OF REPORT & PERIOD COVERED Contractor Report
		14. SPONSORING AGENCY CODE	
12. SPONSORING AGENCY NAME AND ADDRESS National Aeronautics and Space Administration Washington, DC 20546		15. SUPPLEMENTARY NOTES	
16. ABSTRACT <p>For the eighteenth consecutive year, a NASA/ASEE Summer Faculty Fellowship Research Program was conducted at the Marshall Space Flight Center (MSFC). The program was conducted by the University of Alabama and MSFC during the period June 1, 1982 through August 6, 1982. Operated under the auspices of the American Society for Engineering, the MSFC program, as well as those at five other NASA Centers, was sponsored by the Office of University Affairs, NASA Headquarters, Washington, DC. The basic objectives of the programs, which are in the nineteenth year of operation nationally, are (1) to further the professional knowledge of qualified engineering and science faculty members; (2) to stimulate an exchange of ideas between participants and NASA; (3) to enrich and refresh the research and teaching activities of participants' institutions; and (4) to contribute to the research objectives of the NASA Centers.</p> <p>The Faculty Fellows spent ten weeks at MSFC engaged in a research project commensurate with their interests and background and worked in collaboration with a NASA/MSFC colleague. This document is a compilation of Fellows' reports on their research during the summer of 1982. University of Alabama Report No. BER-289-94 presents the Co-Directors' report on the administrative operations of the Research Fellowship Program. Further information can be obtained by contacting any of the editors.</p>			
17. KEY WORDS		18. DISTRIBUTION STATEMENT Unclassified-Unlimited N83-17359 # +TRW # N83-17402	
19. SECURITY CLASSIF. (of this report) Unclassified	20. SECURITY CLASSIF. (of this page) Unclassified	21. NO. OF PAGES 855	22. PRICE NTIS

RESEARCH REPORTS

1982 NASA/ASEE SUMMER FACULTY FELLOWSHIP PROGRAM

George C. Marshall Space Flight Center
The University of Alabama
and
The University of Alabama in Huntsville

EDITORS:

Dr. B. F. Barfield, Professor of Mechanical Engineering
The University of Alabama

Mr. Marion I. Kent, Office of University Affairs
Marshall Space Flight Center

Dr. James Dozier, Director, Research and Technology Office
Marshall Space Flight Center

Dr. Gerald Karr, Professor of Mechanical Engineering
University of Alabama in Huntsville

NASA CR - 162051

PREFACE

For the eighteenth consecutive year, a NASA/ASEE Summer Faculty Fellowship Research Program was conducted at the Marshall Space Flight Center (MSFC). The program was conducted by The University of Alabama and MSFC during the period June 1, 1982 through August 6, 1982. The program was operated under the auspices of the American Society for Engineering Education (ASEE). The program at MSFC, as well as those at five other NASA Centers, was sponsored and funded by the Office of University Affairs, NASA Headquarters, Washington, D.C. The basic objectives of the programs, which are in the nineteenth year of operation nationally, are:

- a. To further the professional knowledge of qualified engineering and science faculty members;
- b. To stimulate an exchange of ideas between participants and NASA;
- c. To enrich and refresh the research and teaching activities of participants' institutions; and,
- d. To contribute to the research objectives of the NASA Centers.

The Faculty Fellows spent ten weeks at MSFC engaged in a research project commensurate with their interests and background and worked in collaboration with a NASA/MSFC Colleague. This document is a compilation of Fellow's reports on their research during the Summer of 1982. University of Alabama Report No. BER-289-94 presents the Co-Directors' report on the administrative operations of the Research Fellowship Program. Further information can be obtained by contacting any of the editors.

TABLE OF CONTENTS

- I. Agarwal, R. K.: "Electrically Reconfigurable Logic Array"
- II. Ainsworth, O. R.: "Control Pole Placement Relationships"
- III. Allen, Vernon R.: "Development of Test Methodology for Dynamic Mechanical Analysis Instrumentation"
- IV. Antar, Basil N.: "Instability of a Solidifying Binary Mixture"
- V. Askew, Raymond F.: "Plasma Ignition for Laser Propulsion"
- VI. Barnes, Grover D.: "A Preliminary Study of Environmental Parameters Associated with the Feasibility of a Poly-generation Plant at Kennedy Space Center"
- VII. Bayuzick, Robert J.: "Containerless Processing of Nb-Ge Alloys in A Long Drop Tube"
- VIII. Beil, Robert J.: "Theoretical Model of the Effect of Crack Tip Blunting on the Ultimate Tensile Strength of Welds in 2219-T87 Aluminum"
- IX. Brown, Robert A.: "Reflectance Measurements"
- X. Brundidge, Kenneth C.: "Investigation of Mesoscale Meteorological Phenomena as Observed by Geostationary Satellite"
- XI. Carter, Thomas E.: "Fuel Optimal Maneuvers of Spacecraft"
- XII. Chang, Kichoon.: "Solidification Studies of Monotectic Systems"
- XIII. Davenport, John W.: "A Recursive Algorithm for Zernlike Polynomials"
- XIV. Davis, Jack H.: "Chromium Ion Plating"
- XV. Dearth, John J., Jr.: "Origin and Control of Instability in SCR/TRIAC Three-phase Motor Controllers"
- XVI. Grone, Bob: "A Scheduling Algorithm for Spacelab Telescope Observations"
- ✓ XVII. Hagan, Martin T.: "Shape Control of Large Space Structures"
- XVIII. Hall, William B.: "Structural Application of High Strength, High Temperature Ceramics"
- XIX. Hardee, Philip: "Orbital Precession, Precessing Accretion Disks and Pulse Timing Residuals in Binary Systems with Mass Transfer and Hydrodynamic Stability of Jets Produced by Mass Accreting Systems"

- XX. Hutton, David V.: "Finite Element Analysis of a Deployable Space Structure"
- XXI. Jalali, Fereydoun.: "Detection and Analysis of Radio Frequency Lightning Emissions"
- ✓ XXII. Kadaba, Prasanna V.: "Thermal Radiation Viewfactor Methods, Accuracy and Computer-Aided Procedures"
- XXIII. Laird, C. E.: "Studies of Neutron and Proton Nuclear Activation in Low-Earth Orbit"
- XXIV. Leighly, H. P., Jr.: "The Determination of the Stacking Fault Energy in Copper-Nickel Alloys"
- XXV. Ludwick, Larry M.: "Ultrahigh Molecular Weight Aromatic Siloxane Polymers"
- XXVI. Marshall, Thomas C.: "In Situ Measurements of Thunderstorm Electrical Properties"
- XXVII. McCord, Richard L.: "Population Control of Self-Replicating Systems"
- XXVIII. McDonald, Malcolm W.: "Study of and Proposals for the Correction of Errors on a FMCW Radar Ranging Device Designed to Facilitate Docking of a Teleoperator Maneuvering System"
- XXIX. McManus, Samuel P.: "Production of Metal Particles and Clusters"
- XXX. Moore, James T.: "Ageostrophic Winds in the Severe Storm Environment"
- XXXI. Payne, James E.: "Fabrication Techniques for Superconducting Readout Loops"
- XXXII. Payne, Linda L.: "Optical Contacting of Quartz"
- XXXIII. Pujol, Alfonso, Jr.: "The Application of Digital Signal Processing Techniques to a Teleoperator Radar System"
- XXXIV. Ray, John R.: "Spin and Gravitation"
- XXXV. Rogers, Jon G.: "Autonomous Onboard Crew Operations: A Review and Developmental Approach"
- XXXVI. Rush, J. E.: "Experimental Study of Time-Dependent Flows in Laboratory Atmospheric Flow Models"
- XXXVII. Siegrist, Kyle: "A Markov Chain Model for Reliability Growth and Decay"
- XXXVIII. Six, N. Frank: "Magnetospheric Ray Tracing Studies"

- XXXIX. Smith, David R.: "Modification and Evaluation of a Barnes-Type Objective Analysis Scheme for Surface Meteorological Data"
- XL. Turner, J. B., Jr.: "An Analysis of Nickel Cadmium Batteries"
- XLI. Wang, Jai-Ching: "Investigation of Compositional Segregation during Unidirectional Solidification of Solid Solution Semiconducting Alloys"
- XLII. Williams, A.: "The Study of X-Ray Scattering to Determine Surface Topography of Smooth Surfaces"
- XLIII. Williams, George, Jr.: "Studies with Sample Conductivity, Insertion Rates, and Particle Deflection in a Continuous Flow Electrophoresis System"

1982

NASA/ASEE SUMMER FACULTY RESEARCH FELLOWSHIP PROGRAM

MARSHALL SPACE FLIGHT CENTER

The University of Alabama

Electrically Reconfigurable Logic Array

Prepared By: R. K. Agarwal
Academic Rank: Assistant Professor
University & Department: AL A&M University - Dept. of Eng. Technology

NASA/MSFC:
Laboratory: Information & Electronics Systems Lab.
Division: Electronics Development Division
Branch: Design Techniques Branch

MSFC Counterpart: John M. Gould
Teddy Edge
Date: July 23, 1982

Contract #: NASA-NGT-01-002-099
(University of Alabama)

ELECTRICALLY RECONFIGURABLE LOGIC ARRAY

by

R. K. Agarwal

Assistant Professor of Electrical Engineering Tech.
Alabama A&M University
Huntsville, AL

ABSTRACT

The VLSI technology has been exploited to build more complication and special purpose devices. Some of these devices tailored to certain complex algorithm, systolic array processors, combinational logic, programmable logic array and graphic display. The use of microcircuit is due to its leverage in high integration and uniformity for mass production of simple logic or circuit elements in the algorithm.

How does one compose the complicated systems using algorithmically specialized logic circuits or processors. One solution is to perform relational computations such as union, division and intersection directly on hardware. These relations can be poplined efficiently on network of processor having array configuration. These processors can be designed and implemented with few simple cells.

In order to determine the state-of-the-art in Electrically Reconfigurable Logic Array (ERLA), a survey of the available programmable logic array (PLA) and the logic circuit elements used in such arrays was conducted. Based on this survey some recommendations are made for ERLA devices.

LIST OF FIGURES

<u>Figure #</u>	<u>Title</u>	<u>Page</u>
1	Microprocessor CPU	I-11
2	Programmable Logic Array	I-11
3	Schematic Representation of Dynamic	I-12
4	Two Examples of Lattice Structure	I-12
5(a)	Block diagram of the R-PLA	I-13
5(b)	Detail Diagram of the R-PLA	I-13
6	Basic Electrically Erasable Nonvolatile Memory Element	I-14
7	Cell with Access Transistor and Voltage Variable Bootstrap Capacitor	I-14
8	Circuit Diagram of 1024-Bit Buried Gate Electrically Erasable ROM	I-15

INTRODUCTION

For the last 20 to 25 years, the semiconductor industry has been in the turmoil of innovative changes and has been the prime example of innovative excellence in the U.S.A. Similar innovation going in the NASA programs as well as in the electronic laboratory of the Marshall Space Flight Center. With the innovation of integrated circuit and now with very large integrated logic array (circuit in the range 100,000 to 1,000,000 on a single chip), new approaches have to be invented as how to interconnect such logic array. In the order to keep the manufacturing cost have the logic arrays are fabricated with the standard logic circuits. Using the computer aided mask design. These arrays can be connected to the desired configuration. With the invention of Programmable logic array, it is deasible to see if these logic arrays can be reprogrammed or its configuration changed electrical signed in the field. The first objective of this investigation is to find on-going work in the areas of electrically reconfigurable logic arrays (ERLA). Also study different circuit configurations and fabrication microelectronic techniques with are presently used in programmable logic arrays, and investigate if any of the current fabrication technique may be suitable for 'ERLA' design.

CONCLUSIONS AND RECOMMENDATIONS

The Electronically Reconfigurable Logic Arrays (ERLA) is a processed array of microelectronic devices whose configuration (and/or connection) can be changed by external stimuli. There are two approaches to the design of such a system. System one where the system is partitioned into number of small processor elements (PE) also known as bit slice microprocessors whose word length could vary by external stimuli. These PE's (or MPU's) connects through microprocessor control units (MUC) as shown in fig. 1.

The other approach is the Arrays Logic MACROS. The type of logic array considered is the dual or folded array configuration where first one array is made up of programmable decoders whose putput selects words in the second array. The programmable decode array which performs the product function known as AND array, the second array which performs the sum function called OR array, as shown in figure 2.

It seems simple to use any of these two approaches to make ERLA but in practice designs engineer is faced with numbers of basis problems. One of the two main problems are how to interconnect each cross point cell in the associative (AND) logic array and the second problem is having to change the basic function of 0, 2, do't care condition at the cross points as shown in figure 2. The following is the summary of what is available in terms of reprogrammable logic array or ERLA and also which logic circuit configuration and fabrication technique is candidates for ERLA at the present time.

The Restructurable VLSI is another name given to ERLA. The Lincoln Laboratory of Massachusetts Institute of Technology has been working on RVLSI. The Lincoln Laboratory is using dynamic bonding in the Multi Project Chip (MPC) Style of fabricating experimental NMOS integrated circuits. Many unrelated designs are placed on a single die, having each with its own I/O pads. The MPC implementation technique tends to minimize mask and wafer fabrication cost per design but not without some disadvantages. A scheme for the dynamic bonding of experimental NMOS test projects has been implemented by Lincoln Laboratory as shown in fig. 3 in this scheme, all projects of a multi project die are interfaced to the same set of physical I/O pads. The power is turned on for the selected project only. Dynamic bonding would make it feasible to test projects at the wafer level, simplify the packaging procedure, and allow all projects on a die to be tested after packaging.

Redundancy is necessary in very large integrated circuits since processing these circuits are not perfect and some of the circuitry will not function. The Lincoln Laboratory is using an approach to partition the total circuit into pieces which can be individually tested after fabrication. These pieces are interconnected using X-Y grid of conductors and primary interest centers on the device placed at crossing. The Lincoln Laboratory is using lasers zappable links. The zappable links built at Lincoln Laboratory use metal-metal structures. Data gathered at the laboratory showed that these failure modes involving metal-poly and metal-substrate shorts in various test structures. The possibility are that these mechanisms could be exploited to form useful links in MOSIS. Attempts were made to use laser zapping the links but it appeared that three times the amount of beam intensity was required to cut through poly as through metal, indicating that it is possible to make a metal-poly link without shorting through to the substrate.

Some of the future VLSI systems will rely on the use of Programmable Building Blocks. Each building block consists of a set of cell design together with rules for combining the cells into larger circuits, thus using these circuits in larger systems. In the programmable logic array, programmable building blocks are frequently used to implement logic design. These building blocks can be made to change these logical functional output using electrical stimuli. These building blocks can be personalized to obtain various functions. Forter and Kung introduces a new programmable building block for recognition of regular languages. The building block can be programmed for any regular expression using a syntax directed construction method which also allows easy and mechanical verification of circuit properties. The recognizers made using these building blocks are efficient pipeline circuits that have constant response time and avoid broadcast. The Programmable recognizes array (PRA) provide compact reconfigurable layouts, requiring only $n \log n$ area for the regular expression of length n . (5)

Another candidate for ERLA is parallel computer. One such computer architecture research is going on at Purdue University called the Configurable, Highly Parallel (Chip) computers. A Chip computer is composed of a set of homogeneous micro-processor elements connected at regular intervals to the switches connected by data paths to each other or to the PE's. The switch lattice is a regular structure formed from programmable switches connected by data paths. The PE's are connected to the switch lattice at regular intervals rather than being directly connected to each other. External storage devices connects to the lattice at the perimeter switches. (7) Figure 4 shows examples of switch lattices. The PE's are shown as squares, the switches as circles and the data path as lines. The switches are circuits rather than packet switches. Each switch contains sufficient local memory to store several interconnecting configuration settings. A particular setting enables the switch to establish a direct, static connection between two or more of its incident data paths. The design of the PE's determines the degrees to which Chip computer is a general purpose computer, hence influenced by the intended applications. A parallel program is considered as the composition of several parallel algorithms each with its own processor interconnection pattern. (7)

A programmable logic array has been recognized as an AND plane forming product terms, followed by an OR plane combining product terms to give required output. In other words these devices realize combinational and sequential logic. In order to make this reconfigurable logic array, AND and OR planes must have the

programming links at each cross point replaced by a link controlled from the memory element or any other external stimuli. The memory element at the crosspoint of each AND and OR grid must also have a means of altering their information content according to some external input.⁽⁸⁾ Figure 5(a) and 5(b) shows diagram of a general rewritable-programmable logic array (R-PLA, another name for ERLA) using conventional current mode logic (CML) memory element as proposed by Tanka, Ozawa and Mori.⁽⁹⁾ The ERLA can be constructed by splitting a conventional random access memory into two sections. Hence each cell structure of the ERLA (R-PLA) is thought as the conventional RAM, differing from the complicated cell structure is proposed in (10). Figure 5(a) and 5(b) shows logically as well as electrically that Search and Read parts of R-PLA can perform logic-in-memory without the use of special AND gates in each cell in the Read mode and can enter a Write data from a word direction in the Write mode. In this R-PLA, bit personalities can be easily loaded and dynamically changed word by word to achieve specific logic function during processing.

As mentioned earlier, there is not much thought given to electrically Reconfigurable Logic Arrays, but an extensive literature is available in Alterable or Rewritable Read-Only-Memories (ROM) or electrically reprogrammable ROM (REPROM). The semiconductor fabricated technique most promises for REPROM or ERLA is MNOS. The devices consists of N-channel or P-channel memory transistors with floating (buried) gate, non-volatile memory transistor, which enables reprogramming operation as proposed in (11). The memory is programmed by electron injection by junction avalanche. An internal voltage multiplication scheme using varactor boot strapping is used. Erasure takes place by modified Poole-Frenkel conduction in a Si_3N_4 of 700-Å thickness which overlays the buried (floating) gate. In this example, standard silicon gate P-MOS processing is used (12). Bit retention is very good even at 150°C.

The buried gate memory element, as explained in (12), after writing consists of an "ON" P-MOS transistor with a conducting channel. After erasing, the floating gate holds practically no negative charge, leaving the transistor in the "OFF" state. A single transistor and an erase gate is shown in figure 6⁽¹²⁾ in its simplest form. The floating gate is charged after the write pulse, resulting in an output voltage. An erase pulse at terminal E reduces the storage charge on the floating gate below the transistor threshold voltage. Fig. 7 shows a better form of buried-gate cell involves the addition of a boot strap variable capacitor which is inserted between the access transistor and the floating gate. This provide lower writing voltage by multiplying the voltage of the internal mode.

Fig. 8 shows a 1024 bit erasable buried gate ROM chip. To write, a bit is selected by coincident addressing with V_{DD} and P-terminal at -23V. Reading is done by addressing the same way as writing except that V_{DD} and E-terminal are at -15V. It appears at this time that the techniques presented represents a reasonable approach to construct Electronically Reconfigurable logic array. The buried (floating) gate transistor have highest promise for Electrically Reconfigurable logic array. The transistor memory cell can be used in an AND, OR plane. The logic functions can be changed by altering cross point storage in the matrix AND plane as shown in Fig.1. Same type logic or (memory) cell can be used in PE's for the modulator approach in ERLA.

It is recommended that future work should be directed toward MNOS buried (floating) gate transistor element. Also the use of cellular logic in designing specific logic function should be implemented. The buried (floating) gate (shown in fig. 7) can be used as an element for AND and OR plane of macro logic array. (Shown in fig. 1). It only need five metal lines (two for x and y input. one for erase, one to write and one to read) to interconnect entire AND plane. The read output of the buried gate has to be connected as wired 'OR' on the AND plane before it connects to OR plane. Further study is needed to implement buried MNOS gate in the Programmable Logic Array (PLA) macro so that the PLA can be programmed electrically in the field or run as parallel computers. It is further recommended that an experimental ERLA system should be designed, built and tested as a feasibility study.

REFERENCES

1. Scott, M.A., and Smith, K.C., "A Dynamically Reconfigurable Microprocessor Architecture" IEEE Trans. on Computer, Vol. 5.
2. Jones, J.W., "Array Logic Macros" IBM J. Res. Development, March 1975, pp. 120-126.
3. Anderson, Alen H. "Restructurable VLSI Program Semi-annual Summary Report, Lincoln Laboratory, Mass. Inst. of Tech. April 1979-March 1980, ADA09075.
4. Anderson, Alen H., "Restructurable VLSI Program" Semi-annual Tech, Summary Report, Lincoln Laboratory MIT, April-September 1981 issue Jan. 1982.
5. Forter, J.J., and Kung, H.T., "Recognize Regular Languages with Programmable Building Blocks" Interim Report Dept. of Computer Science, Carnegie-Mellon University, June 19, 1981-AD-A104874
6. Snyder, Lawrence, "Overview of the CHIP Computer "VLSI 81-Book, Edited by John P. Gray, Academic Press, pp. 237-246.
7. Snyder, Lawrence, "Programming Processor Interconnection Structures" Dept. of Computer Science, Purdue University, Oct 1981, AD-A109294.
8. Kinniment, D.J., "Regular Programmable Control Structures "VLSI 1981, edited by John P. Gray, Academic Press. pp.191-202.
9. Tanaka, Mamoru; Ozawa, Shinju, and Mori, Shinsaku, "Rewritable Programmable Logic Array of Current Mode Logic IEEE Trans. on computers Vol. C-30 No. 3 March 1981 pp. 229-234.
10. Fleisher, J., and Maissel, L.I. "An Introduction to Array Logic" IBM J. of Res & Dev. March 1975, pp. 98-109.
11. WADA, Toshi, "Electrically Reprogrammable ROM Using N-channel Memory Transistors with Floating Gate" Solid State Electronics, Vol. 20 1977 pp. 623-627.
12. Newgebauer, Constantine A.; Burgess, James G. and Stein, L "Electrically Erasable Buried-Gate Nonvolatile Read-only Memory" IEEE Trans. on Elec. Devices. Vol. ED-24 No. 5 May 1977 pp. 612-618.
13. Rossler, Bernard, "Electrically Erasable and Reprogrammable Read only Memory using the N-channel SIMOS one-transistor cell "IEEE Trans on Elec. Devices, ED-24 No. 5 May 1977, pp. 606-613.
14. Brewer, Joe E., "MNOS Density Parameters" IEEE Trans. on Elec. Devices, ED-24 No. 5 May 1977, pp. 618-625.
15. Wagner, Richard H. A. "The Gated-Access MNOS Memory Transistor" IEEE Trans. on Elec. Devices. Vol. ED-27, No. 1 Jan. 1980, pp. 226-276.
16. Lonky, M.L.; Fagan J.L.; & Victorey J.P. "VINRAM-AN MDS/MNOS RAM" NAECON 1977, pp. 628-632.

17. LODI, Robert J. Browvicka, M.B.; Kosicki, B.B.; Pogemiller, T.A.; and Eklund, M.V. "MNOS BORAM Memory Characteristics" IEEE Journal of Solid State Circuits Vol. SC-11 No. 5, Oct. 1976, pp. 622-630.
18. Sakural, Junji, "An Experimental Study of the BO-Mos Dynamic RAM Cell" IEEE Trans. of Electron Devices, Vol. ED-28, No. 10, Oct. 1981.
19. Greenwood, Ed, "VLSI Array Processor" R&D Status Report, Jan. 11, 1982, AD-A 111986.
20. Wood, Roy A., "A High Density Programmable Logic Array Chip" IEEE Trans. on Computers, Vol. C-28, No. 9, Sept. 1979, pp. 602-607.
21. Smith, Kent F.; Carter, Tony M. and Hunt, Charles E. "Structured Logic Design of Integrated Circuits Using the Storage/Logic Array (SLA)", IEEE J. of Solid State Circuits, Vol. SC-17, No. 2, April 1982. pp. 395-406.
22. Logue, J.C.; Brickman, N.F.; Howley, F.; Jones, J.W. and Wu, W.W. "Hardware Implementation of a Small System in Programmable Logic Array" IBM J. of Res. and Development, March 1975, pp. 110-119.
23. Patil, Suhas S. and Welch, Terry A. "A Programmable Logic Approach for VLSI" IEEE Trans. on Computer, Vol. C-28, No. 9 Sept. 1979, pp. 594-601.
24. Mukhopadhyay, Amar "Hardware Algorithms for String Processing: IEEE. Trans of Computer, May 1980, pp. 508-511.
25. Kambayashi, Yahuko "logic Design of Programmable Logic Arrays." IEEE Trans of Computers. Vol. 28, No. 9, Sept. 1979, pp. 609-617.
26. Golden, R.L.; Latus, P.A.; and Lowy, P. "Design Automation and Programmable Logic Array Macro". IBM J. Res. Development, Vol. 24 No.1, Jan. 1980 pp. 23-31
27. Mudge, Craig, J. "VLSI Chip Design at the Crossroads." VLSI 81, Academic Press. John P. Gray, editor pp. 205-215.
28. Marques, Alves J. "MOSAIC: A Modular Architecture for VLSI System Circuits" VLSI 81, Academic Press, John P. Gray, editor, pp. 53-61.
29. Kautz, William H., "Programmable Cellur Logic" Recent Developments in Switchup Theory, Book-Amar Murkhopadhyay, editor, Academic Press, 1971. Chapter IX, pp. 369-421.
30. Goates, Gary B.; Waldron, Harvey M.; Patil, Suhar S.; Smith, Kent F. and Tatman, Joseph A., "Storage/Logic Arrays for VHSIC." Proceedings of Semi-Custom Integrated Circuit Technology Symposium, May 26-27, 1981 Glen W. Preston, editor, pp. 191-207.
31. Siskind, Jeffery Mark; Southerland, Jay Roger and Gouch, Kenneth Walter "Generating Custom High Performance VLSI Designs from Succint Algorithmic Descriptions" MIT Lincoln Laboratory, Lexington, MA, Dec. 1981.
32. Brewer, J.E., "MNDS-BORAM Manufacturing Methods and Technology Project" Research and Development Technical Report, DELET-TR-80-0259, Jan. 1982 Westinghouse Electric Corp. Baltimore, MD.

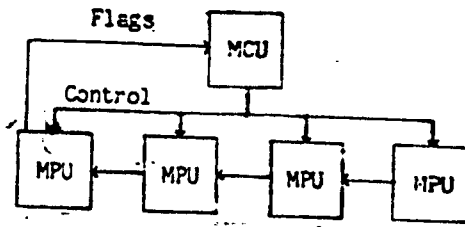


Fig. 1

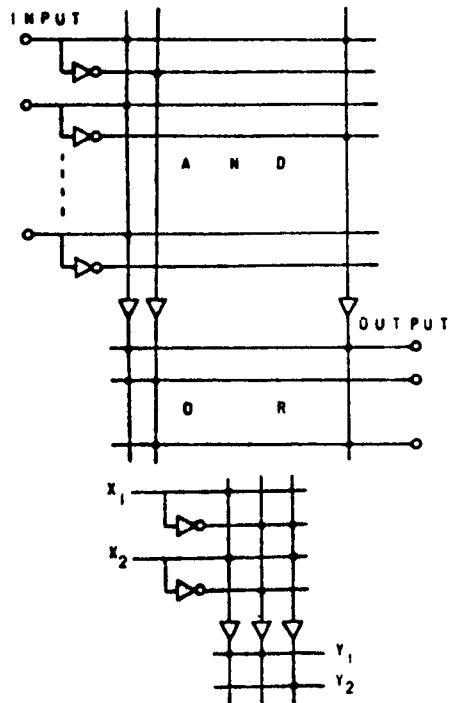


Fig. 2

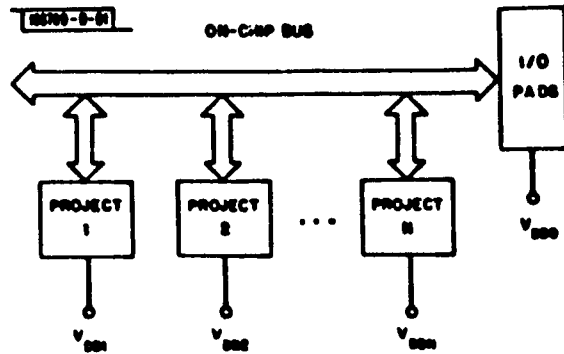


Fig. 3

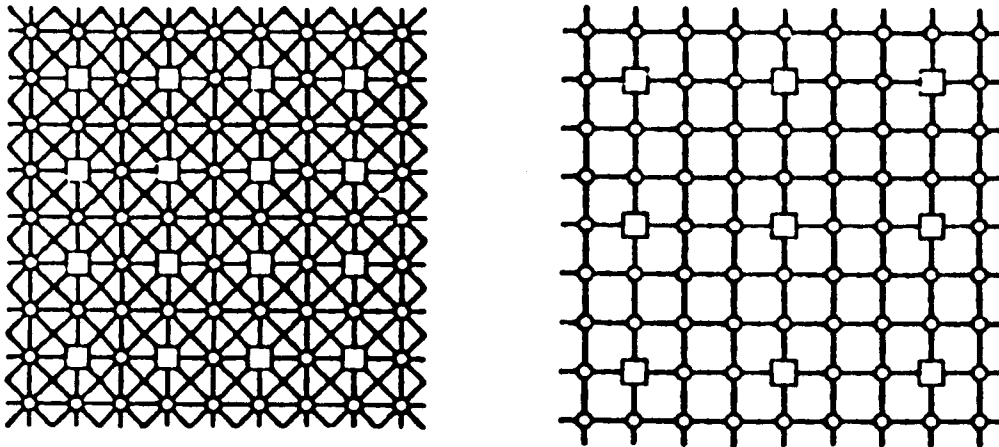


Fig. 4

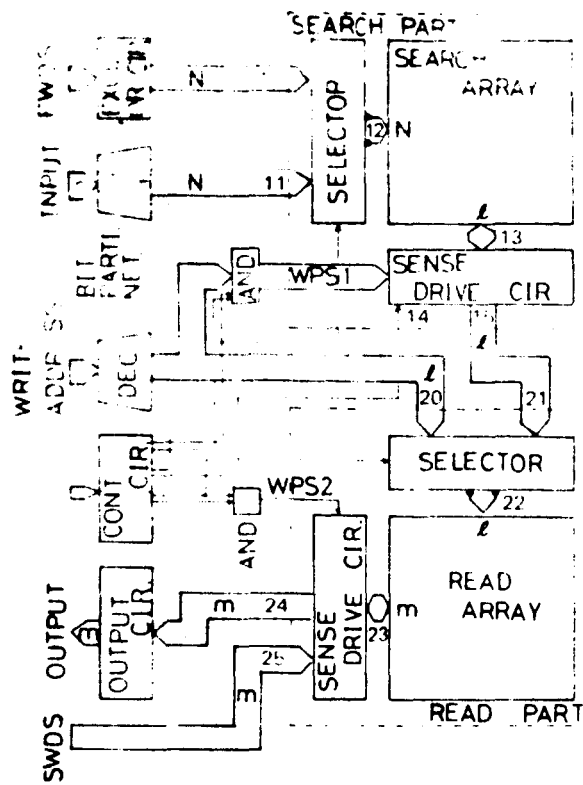


Fig. 5(a)

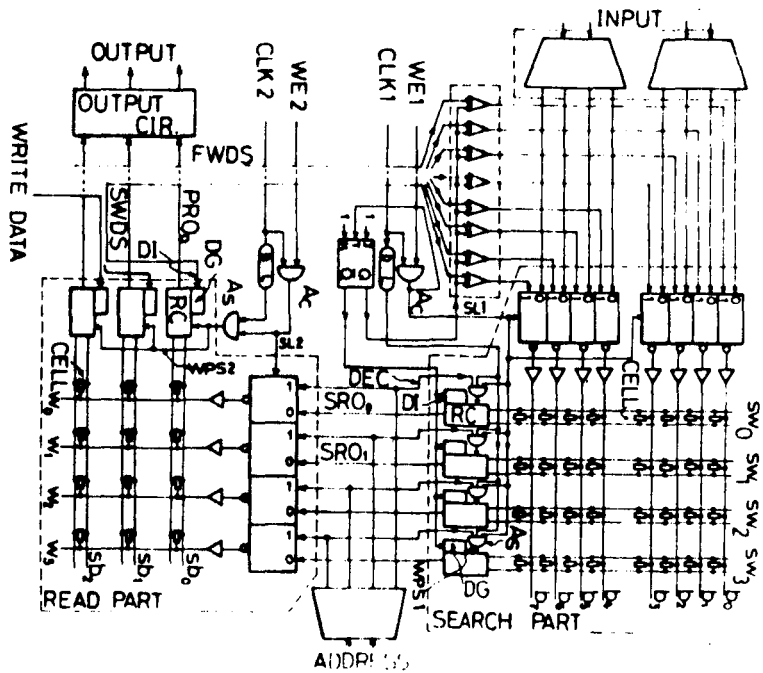


Fig. 5(b)

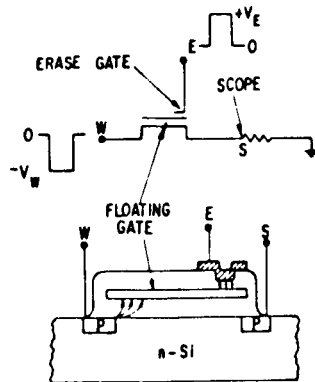


Fig. 6

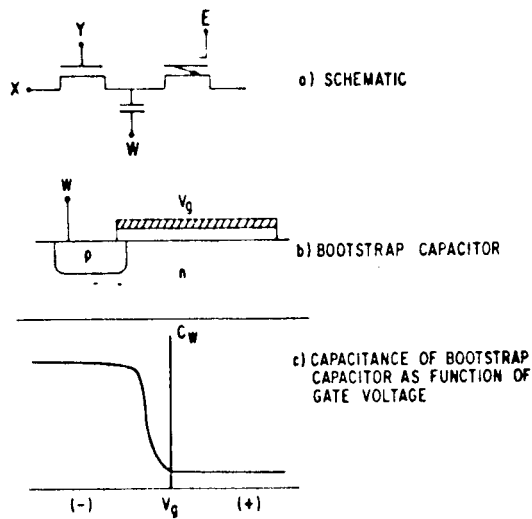
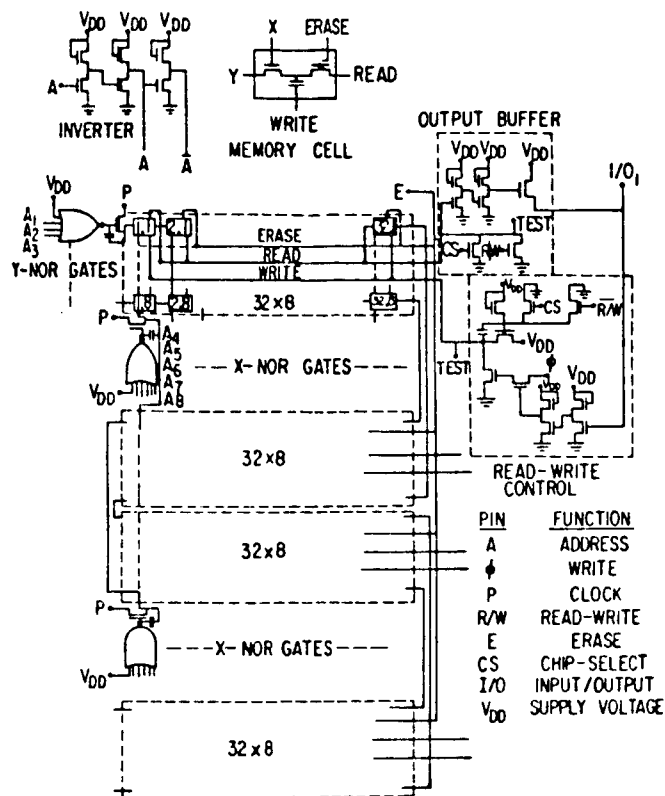


Fig. 7



PIN	FUNCTION
A	ADDRESS
φ	WRITE
P	CLOCK
R/W	READ-WRITE
E	ERASE
CS	CHIP-SELECT
I/O	INPUT/OUTPUT
VDD	SUPPLY VOLTAGE

Fig. 8

1982

NASA/ASEE SUMMER FACULTY RESEARCH FELLOWSHIP PROGRAM

**MARSHALL SPACE FLIGHT CENTER
THE UNIVERSITY OF ALABAMA**

CONTROL POLE PLACEMENT RELATIONSHIPS

Prepared By: O. Richard Ainsworth, Ph.D.
Academic Rank: Professor
University and Department: The University of Alabama
Department of Mathematics
NASA/MSFC:
Laboratory: Systems Dynamics
Division: Control Systems
Branch: Pointing Control Systems
NASA Counterpart: Henry B. Waites
Date: August 6, 1982
Contract No.: NASA-NGT-01-002-099
(The University of Alabama)

CONTROL POLE PLACEMENT RELATIONSHIPS

By

O. R. Ainsworth, Ph.D.
Professor of Mathematics
University of Alabama
University, Alabama

ABSTRACT

A Closed Form Pole Placement Scheme (CFPPS) is currently being used to synthesize control systems for the Large Space Structure (LSS) ground test, which is located at MSFC, and the Solar Array Flight Experiment II (SAFE II), which will be flown in 1987. Since most LSS possess a very low frequency fundamental and a dense modal pattern, designing a LSS control system without modal interaction is extremely difficult. The CFPPS is a very efficient control design tool relative to LSS modal constraints, but the migration of the unconstrained poles is an enigma.

Using a simplified LSS model, a technique has been developed which gives algebraic relationships for the unconstrained poles. The relationships, which were obtained by this technique, are functions of the structural characteristics and the control gains. Extremely interesting relationships evolve for the case when the structural damping is zero. If the damping is zero, the constrained poles are uncoupled from the structural mode shapes. These relationships, which are derived for structural damping and without structural damping, provide new insight into the migration of the unconstrained poles for the CFPPS.

INTRODUCTION

The CFPPS uses techniques from both the frequency domain and the state space analysis to synthesize control systems. An experienced control engineer can take advantage of the frequency design methods and place the appropriate poles of an open loop system such that the closed loop system has the desired performance goals. In using the state space techniques, the CFPPS masks off the migration of the system poles which are not placed. Herein lies the research objectives which are to determine the migration characteristics of these free poles by algebraic relationships which involve the system structural model data.

THE CLOSED FORM POLE PLACEMENT SCHEME (CFPPS)

The system description used to derive the pole placement scheme is

$$\dot{x} = Ax + Bu, \quad (1)$$

$$y = Cx, \quad (2)$$

$$\dot{z} = Dz + Ey, \text{ and} \quad (3)$$

$$u = Fz \quad (4)$$

where

x : $n \times 1$ plant state vector,

u : $r \times 1$ control state vector,

z : $p \times 1$ filter states,

y : $m \times 1$ measurement vector,

D : $p \times p$ specified filter matrix, and

E : $p \times m$ specified matrix.

After some algebraic matrix manipulations⁽¹⁾, the pole placement constraint relationships are

$$Q = | I_p - P(\lambda_i)F |_{j^*} = 0 \quad (5)$$

where

F : $r \times p$ unknown control gain matrix,

$$P(\lambda) = (\lambda I_p - D)^{-1} E C (\lambda I_n - A)^{-1} B,$$

λ_i : placed characteristic root, and

j^* : the j^{th} row of (5).

This procedure yields at least p independent relationships ⁽²⁾, so p poles of the system described by (1) - (4) can be arbitrarily placed.

LARGE SPACE STRUCTURE MODAL DESCRIPTION

Almost all vibrational data for a Large Space Structure is given in modal coordinate form. For a scalar input, a proportional-derivative (PD) controller and no filter, the modal coordinate representation for (1) - (4) is

$$A = \begin{bmatrix} A_1 & 0_1 & \dots & 0_1 \\ 0_1 & A_2 & \dots & 0_1 \\ \vdots & \vdots & \dots & \vdots \\ \vdots & \vdots & \dots & \vdots \\ 0_1 & 0_1 & \dots & A_n \end{bmatrix}$$

$$B^t = \begin{bmatrix} 0 & s_1 & 0 & s_2 & \dots & 0 & s_n \end{bmatrix}$$

$$C = \begin{bmatrix} t_1 & 0 & \dots & t_n & 0 \\ 0 & v_1 & \dots & 0 & v_n \end{bmatrix}$$

where $0_1 = \begin{bmatrix} 0 & 0 \\ 0 & 0 \end{bmatrix}$,

$$A_1 = \begin{bmatrix} 0 & 1 \\ 0 & 0 \end{bmatrix},$$

$$A_i = \begin{bmatrix} 0 & 1 \\ -\omega_i^2 & -\lambda \zeta_i \omega_i \end{bmatrix},$$

ω_i is the frequency of i^{th} mode in rad/sec,

ζ_i is the damping of i^{th} mode,

s_i is the i^{th} modal slope at the control effector,

t_i is the i^{th} modal slope at the attitude sensor,

and

v_i is the i^{th} modal slope at the attitude rate sensor.

The system model used for this study is a two mode case and the A, B, and C system matrices are shown in table 1. The simplification to the two mode case allows insight to be gained into the pole migration without the burden of undue complications that a higher order system possesses. The pole migrations for the two mode case are shown in tables 1-3. As the rigid body poles are placed on the 45° axis lines in the complex plane, the bending mode poles migrate in a circular arc until they reach the real axis, then they move along the real axis. How and why these poles migrate as they do is a function of the modal data and this functional relationship is developed in the next section.

ALGEBRAIC CONSTRAINT RELATIONSHIPS

Given the system

$$\dot{x} = Ax + Bu \tag{6}$$

$$y = Cx \tag{7}$$

$$u = Fy \tag{8}$$

where

$$A = \begin{bmatrix} 0 & 1 & 0 & 0 \\ 0 & 0 & 0 & 0 \\ 0 & 0 & 0 & 1 \\ 0 & 0 & -.394 & -.00628 \end{bmatrix}$$

$$B^t = \begin{bmatrix} 0 & a & 0 & b \end{bmatrix},$$

$$C = \begin{bmatrix} a & 0 & b & 0 \\ 0 & a & 0 & b \end{bmatrix}, \text{ and}$$

$$F = \begin{bmatrix} p & q \end{bmatrix},$$

the open loop characteristic polynomial is

$$|\lambda I_4 - A| = \lambda^2 \Delta$$

where

$$\Delta = (\lambda^2 + .00628\lambda + .394).$$

The control equation constraint (see equation 5) for this system is

$$Q_1 = \lambda^4 + A_1\lambda^3 + B_1\lambda^2 + C_1\lambda + D_1 \quad (9)$$

where

$$A_1 = .00628 + b^2q + a^2p, \quad (10)$$

$$B_1 = a^2p + a^2(.00628)q - b^2p + .394, \quad (11)$$

$$C_1 = (.394)a^2q + (.00628)pa^2, \text{ and} \quad (12)$$

$$D_1 = (.394)a^2p. \quad (13)$$

Now if the roots of (9) are to be

$$r_{1,2} = \alpha \pm i\alpha \text{ and} \quad (14)$$

$$r_{3,4} = \beta \pm i\gamma \quad (15)$$

where $(\alpha, \beta < 0)$,

then the characteristic polynomial is

$$\begin{aligned} Q_z = & \lambda^4 + \lambda^3(-2\alpha - 2\beta) + \lambda^2(2\alpha^2 + \gamma^2 + \beta^2 + 4\alpha\beta) \\ & + \lambda(-2\alpha\gamma^2 - 2\alpha\beta^2 - 4\beta\alpha^2) + 2(\alpha\gamma)^2 + 2(\alpha\beta)^2 = 0 \end{aligned} \quad (16)$$

Equating the coefficients of Q_1 and Q_2 leads to the equations

$$-2(\alpha + \beta) = A_1, \quad (17)$$

$$\beta^2 + 2\alpha^2 + \gamma^2 + 4\alpha\beta = B_1, \quad (18)$$

$$-2\alpha(\beta^2 + \gamma^2 + 2\alpha\beta) = C_1, \text{ and} \quad (19)$$

$$2\alpha^2(\gamma^2 + \beta^2) = D_1. \quad (20)$$

Equations (17-20) yield 3 unknowns (α, β, γ) on the left hand side and 4 on the right hand side (A_1, B_1, C_1, D_1), so that placing a pair of roots on the 45° line gives a relationship between A_1, B_1, C_1 , and D_1 - but it will be fourth order. This is not very tractable, so we impose a constraint that we want simple relationships. This can be done by fixing α and asking what a, b, p, q can produce this α , and, if so, are they a feasible set.

So let

$$C_1 = -2\alpha C_2, \quad (21)$$

$$D_1 = 2\alpha D_2, \quad (22)$$

$$A_1 = -2A_2, \text{ and} \quad (23)$$

$$B_1 = B_2, \quad (24)$$

and we arrive at the relationships

$$\alpha + \beta = A_2, \quad (25)$$

$$\beta^2 + \gamma^2 + 2\alpha^2 + 4\alpha\beta = B_2, \quad (26)$$

$$\beta^2 + \gamma^2 + 2\alpha\beta = C_2, \text{ and} \quad (27)$$

$$\gamma^2 + \beta^2 = D_2. \quad (28)$$

which eliminate the third and fourth degree equations. So for a pair of roots to lie on the 45° axis in the left half side of the complex plane and for the absolute value of that root to equal $|\alpha|$, the set (A_2, B_2, C_2, D_2) must satisfy

$$2\alpha^2 = D_2 - 2C_2 + B_2 \text{ and} \quad (29)$$

$$B_2 - D_2 = 2\alpha^2. \quad (30)$$

If (a, b, p, q) exists so that (29) and (30) are satisfied and if they also belong to an attainable set, then we have conditions for placing the root at a desired location. We can treat α as a parameter and get a set of solutions in terms of α , and observe what effect increasing or decreasing α has upon the set (a, b, p, q) .

Substituting for (a, b, p, q) in (29) and (30) when the damping is zero yields generic equations of the form

$$-b^2p = f_1(\alpha, a, p, q) \text{ and} \quad (31)$$

$$2a^2 = f_2(\alpha, a, p, q) - b^2p. \quad (32)$$

Equations (31) and (32) show that

$$2a^2 = f_3(\alpha, a, p, q) \quad (33)$$

which decouples α from the flexible mode's shape.

CONCLUSIONS AND RECOMMENDATIONS

Algebraic constraint relationships are developed which can be used to predict the unplaced pole migrations of a fourth order system in terms of the structural characteristics. These constraint relationships add insight in the control synthesis technique used by the CFPPS. These relationships will be implemented on a computer and the results of the study will be published.

It is recommended that the system be generalized to n modes to see if tractable results can be obtained. If so, the results would be of great value in the synthesis of control systems for Large Space Structures.

REFERENCES

1. Waites, H. B., "Control Pole Placement Methods," NASA Memorandum ED12-81-1, dated March 2, 1981.
2. Davison, E. J. and Wang, S. H., "On Pole Assignment in Linear Multivariable Systems Using Output Feedback," IEEE Transactions and Automatic Control, Vol. AC-20, No. 4, August 1975, pp 516-518.

A	B	C	D
0	1	0	0
0	0	0	0
0	0	-0.394	-0.00620
0	0	0	0
P			
0	0	0	0
0.1	0	0	0
0	0	0	0
0	0	0	0
C			
0.1	0	1	0
0	0.1	0	1
NFDRIVER 1	-.00001	.00001	
-1.00E-5	-1.00E-5		
-1.00E-3	-1.00E-3		
-4.14E-3	-6.20E-1		
-4.14E-3	-6.20E-1		
GAINS			
-2.00E-8	-2.00E-3		
NFDRIVER 1	-.0001	.0001	
-0.0001	-0.0001		
-0.0001	-0.0001		
-0.0131	0.620		
-0.0131	0.620		
GAINS			
-2.00E-6	-2.00E-2		
NFDRIVER 1	-.001	.001	
-0.001	-0.001		
-0.001	-0.001		
-0.103	-0.619		
-0.103	-0.619		
GAINS			
-0.0002	-0.2		
NFDRIVER 1	-.004	.004	
-0.004	-0.004		
-0.004	-0.004		
-0.403	-0.470		
-0.403	-0.470		
GAINS			
-0.00317	-0.0		
NFDRIVER 1	-.005	.005	
-0.005	-0.005		
-0.005	-0.005		
-0.503	-0.369		
-0.503	-0.369		
GAINS			
-0.00494	-1		
NFDRIVER 1	-.006	.006	
-0.006	-0.006		
-0.006	-0.006		
-0.603	-0.153		
-0.603	-0.153		
GAINS			
-0.00707	-1.2		
NFDRIVER 1	-.007	.007	
-0.007	-0.007		
-0.007	-0.007		
-0.372	0		
-1.03	0		
GAINS			
-0.00955	-1.4		
NFDRIVER 1	-.000	.000	
-0.000	0.000		

-0.000	-0.000
-0.29	0
1.31	0
GAINS	
-0.0124	-1.5
NFDRIVER 1	-.01 .01
-0.01	-0.01
-0.01	-0.01
-0.200	0
-1.79	0
GAINS	
-0.0109	-1.92
NFDRIVER 1	-.02 .02
-0.02	-0.02
-0.02	-0.02
-0.0002	0
-3.77	0
GAINS	
-0.0612	-3.04
NFDRIVER 1	-.03 .03
-0.0361	0
-0.03	-0.03
-0.03	-0.03
-4.92	0
GAINS	
-0.001	-4.96
NFDRIVER 1	-.035 .035
-0.0216	0
-0.035	-0.035
-0.035	-0.035
-0.01	0
GAINS	
-0.0672	-5.04
NFDRIVER 1	-.030 .030
-0.0142	0
-0.030	-0.030
-0.030	-0.030
-4.9	0
GAINS	
-0.0500	-4.94
NFDRIVER 1	-.04 .04
-0.00989	0
-0.04	-0.04
-0.04	-0.04
-4.70	0
GAINS	
-0.0372	-4.82
NFDRIVER 1	-.042 .042
-0.00520	0
-0.042	-0.042
-0.042	-0.042
-4.62	0
GAINS	
-0.0210	-4.66
NFDRIVER 1	-.05 .05
-0.00997	0
-0.05	-0.05
-0.05	-0.05
-3.8	0
GAINS	
-0.040	-3.85

LEGEND:
 NFDRIVER a b c
 a implies multiplicity of complex root b±jc.
 Outputs after NFDRIVER are the closed loop characteristic roots.

TABLE 1. MODEL DESCRIPTION AND POLE PLACEMENT


```

NFDRIVER 1 -.06 .06
-0.0239 0
-0.06 -0.06
-0.06 -0.06
2.75 0
GAINS
0.13 -2.01
NFDRIVER 1 .07 .07
-0.0394 0
-0.07 -0.07
-0.07 -0.07
1.96 0
GAINS
0.192 -2.03
NFDRIVER 1 .08 .08
-0.051 0
-0.08 -0.08
-0.08 -0.08
1.41 0
GAINS
0.234 -1.5
NFDRIVER 1 .09 .09
-0.0608 0
-0.09 -0.09
-0.09 -0.09
1.05 0
GAINS
0.262 -1.15
NFDRIVER 1 .1 .1
-0.0609 0
-0.1 -0.1
-0.1 -0.1
0.002 0
GAINS
0.28 -0.217
NFDRIVER 1 .2 .2
-0.0809 0
-0.175 0
-0.2 -0.2
-0.2 -0.2
GAINS
0.288 -0.483
NFDRIVER 1 .3 .3
-0.0537 0
-0.0817 0
-0.3 -0.3
-0.3 -0.3
GAINS
0.2 -0.616
NFDRIVER 1 .4 .4
-0.023 0
-0.0349 0
-0.4 -0.4
-0.4 -0.4
GAINS
0.0651 -0.728
NFDRIVER 1 .42 .423
-0.0141 0
-0.0242 0
-0.42 -0.423
-0.42 -0.423
GAINS
0.0397 -0.835

```

```

NFDRIVER 1 -.44 .44
-0.000727 0
-0.00016 0
-0.44 -0.44
0.44 -0.44
GAINS
-0.000802 -0.074
NFDRIVER 1 -.48 .48
-0.00418 -0.0126
-0.00418 -0.0126
-0.48 -0.48
-0.48 -0.48
GAINS
-0.018 -0.093
NFDRIVER 1 .5 .5
-0.00383 -0.0298
-0.00383 -0.0298
-0.5 -0.5
-0.5 -0.5
GAINS
0.111 -0.29
NFDRIVER 1 .8 .8
-0.000757 -0.0521
-0.000757 -0.0521
-0.8 -0.8
-0.8 -0.8
GAINS
0.002 -1.38
NFDRIVER 1 1 1
-0.0004 -0.0561
-0.0004 -0.0561
-1 -1
-1 -1
GAINS
1.59 -1.97
NFDRIVER 1 1.5 1.5
-0.000139 -0.0597
-0.000139 -0.0597
-1.5 -1.5
-1.5 -1.5
GAINS
4.87 -2.96
NFDRIVER 1 -2 2
-7.57E-5 -6.09E-2
-7.57E-5 -6.09E-2
-2.00E0 -2.00E0
-2.00E0 -2.00E0
GAINS
-7.63 -3.95
NFDRIVER 1 -5 5
-3.37E-6 -6.22E-2
-3.37E-6 -6.22E-2
-5.00E0 -5.00E0
-5.00E0 -5.00E0
GAINS
-49.1 -9.09
NFDRIVER 1 -10 10
-3.13E-6 -6.24E-2
-3.13E-6 -6.24E-2
-1.00E1 -1.00E1
-1.00E1 -1.00E1
GAINS
-198 -19.8

```

TABLE 2. POLE PLACEMENT FOR TWO MODE MODEL

```

NFDRIVER 1 -100 100
-3.11E-5 -6.25E-2
-3.11E-5 -6.25E-2
-1.00E2 -1.00E2
1.00E2 1.00E2
NFDRIVER 1 -200 200
-3.11E-5 -6.25E-2
-3.11E-5 -6.25E-2
-2.00E2 -2.00E2
2.00E2 2.00E2
NFDRIVER 1 .4 .4
-0.023 0
-0.0349 0
-0.4 -0.4
0.4 0.4
NFDRIVER 1 -.42 .42
-0.0146 0
-0.025 0
-0.42 -0.42
0.42 0.42
NFDRIVER 1 .44 .44
-0.000727 0
-0.00816 0
-0.44 -0.44
0.44 0.44
NFDRIVER 1 -.45 .45
-0.00415 -0.0126
-0.00415 0.0126
-0.45 -0.45
0.45 0.45
NFDRIVER 1 .5 .5
-0.00383 -0.0295
-0.00383 -0.0295
-0.5 -0.5
0.5 0.5

```

II-10

TABLE 3. POLE PLACEMENT FOR TWO MODE MODEL

NASA/ASEE SUMMER FACULTY RESEARCH FELLOWSHIP PROGRAM

MARSHALL SPACE FLIGHT CENTER
THE UNIVERSITY OF ALABAMA

DEVELOPMENT OF TEST METHODOLOGY FOR
DYNAMIC MECHANICAL ANALYSIS INSTRUMENTATION

Prepared by: Vernon R. Allen, Ph. D.
Academic Rank: Professor
University and Department: Tennessee Technological University
Department of Chemistry
NASA/MSFC
Division: Non-Metallic Materials
Branch: Polymers and Composites
MSFC Counterpart: Dr. W. J. Patterson
Date: August 20, 1982
Contract No.: NGT 01-002-099
The University of Alabama

DEVELOPMENT OF TEST METHODOLOGY FOR
DYNAMIC MECHANICAL ANALYSIS INSTRUMENTATION

By

Vernon R. Allen, Ph.D.
Professor of Chemistry
Tennessee Technological University
Cookeville, Tennessee

ABSTRACT

The high technology requirements for deep-space exploration, for extended periods in near-space, and for an over-riding need for energy conservation demand the development of new materials and for controlled variability of the engineering properties of these materials.

Dynamic mechanical analysis is the study of the mechanical properties, e.g. dynamic tensile storage modulus and energy damping, which define the stiffness and the mechanical energy dissipation (as heat) of the sample under sinusoidal stress. This project was designed to utilize the "dynamic mechanical analysis" instrumentation available for the development of specific test methodology in the determination of engineering parameters of selected materials, esp., plastics and elastomers, over a broad range of temperature with selected environment.

The methodology for routine procedures have been established with specific attention given to sample geometry, sample size, and mounting techniques. The basic software of the duPont 1090 thermal analyser has been used for data reduction which simplify the theoretical interpretation. Although clamp hardware was not available for the testing of 'liquid' resin systems, clamps were developed which allowed 'relative' damping during the cure cycle to be measured for the fiber-glass supported resin. The correlation of fracture energy 'toughness' (or impact strength) with the low temperature (glassy) relaxation responses for a 'rubber-modified' epoxy system was negative in result because the low-temperature dispersion mode (-80 C) of the modifier coincided with that of the epoxy matrix, making quantitative comparison unrealistic.

INTRODUCTION

The exciting technological advances generated by the space program are evidenced by the development of materials that operate at the extremes of the thermal environment - from the high temperatures experienced by the plastic materials which serve as ablative heat shields to the composite structures in the space telescope which must exhibit negligible expansion coefficients to cryogenic temperatures. Achievement of this vast range of the engineering successes is commensurate with the development of new materials having properties previously thought impossible - liquid oxygen-compatible high impact elastomeric resins-, of new processes and new analytical techniques which provide the engineer the necessary data for full utilization of the material properties in structure design. Books (1,2) have been written depicting these "space-age" materials and outlining recent developments in the synthesis, properties characterization and range of applicability of thermally stable engineering resins and of cryogenic compatible exotic plastics and elastomers.

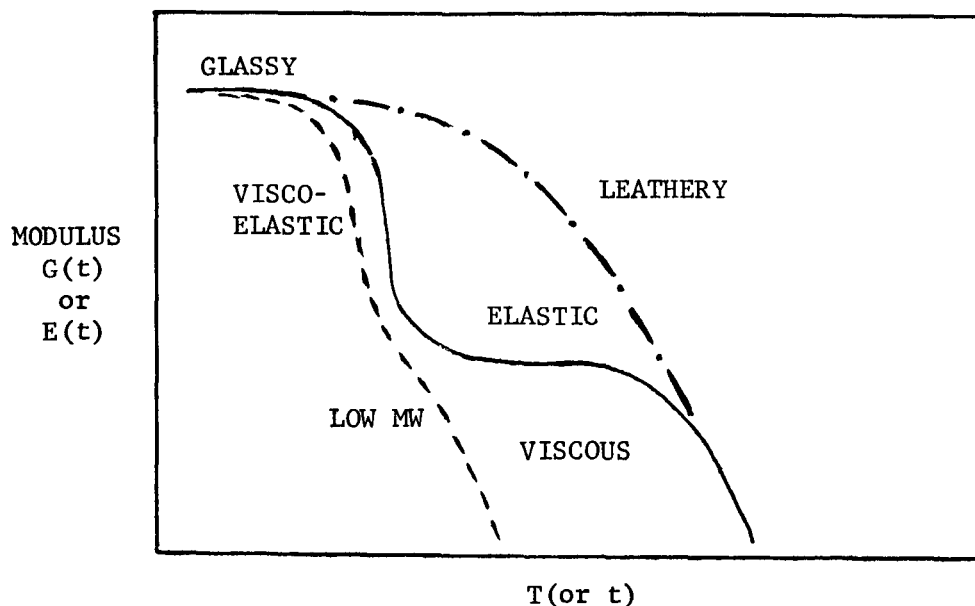
The high technology requirements for deep-space exploration, for extended periods in near-space, and for an over-riding need for energy conservation demand the development of new materials and controlled variability of the engineering properties of these new materials. Consequently, there remains a continuing need for fast, reliable accumulation of the materials engineering data to accelerate design and production of these space-age materials.

The method of dynamic mechanical analysis involves the study of the mechanical properties such as the dynamic storage modulus and the energy damping which define the stiffness and the mechanical energy dissipation (as heat) of the sample under sinusoidal or other periodic stresses. Since, for viscoelastic resins, the stress and the strain are not generally in phase (except at very low temperatures where the sample exhibits brittle-like glassy behavior), these two parameters yield properties evaluation especially sensitive to the chemical and physical structures of the resin, to the influence of the 'thermal history' on the sample properties, and to the effect of processing conditions, e.g. molecular orientation and stress anisotropy, on material stability (3).

This project was designed to utilize the dynamic mechanical analysis instrumentation available in the development of specific test methodology for the determination of engineering parameters of selected materials, especially for epoxy resins, over a broad range of temperature with selected environment.

DYNAMIC MECHANICAL ANALYSIS

The vast range of applicability of polymeric systems is a direct consequence of the wide variety and range of mechanical properties concomitant with these materials. These properties vary from those of viscous liquids to elastomeric solids, through the viscoelastic region, to hard and tough rigid solids. This behavior may be represented by graphing the modulus of the sample (tensile or shear) versus the temperature (or time) as shown.



A number of microstructural and compositional factors influence the magnitude of the moduli and the phase transition temperature, such as the molecular weight, the degree of branching, and the extent of crosslinking, the degree of crystallinity and the crystallite orientation (fibers), and for graft and block copolymers versus the polymer blends, to name a few. For example, the elastic response would not be observed in a low molecular weight sample which has no crosslinks and few chain entanglements (dashed line). The presence of crystallites would tend to mask out the glassy to elastic transition as shown by the (—•) curve above.

In addition to the behavioral factors given, the measured mechanical properties of a given system will be dependent on the type and on the speed of testing, the processing conditions and on the thermal history (stored internal stresses), and on the environmental conditions (humidity induced stress cracking in fatigue). The sensitivity of polymeric systems to temperature (or time) and to the rate of measurement is chiefly a result of the blend of viscous (segmental motion) behavior, in which the strain is proportional to the rate

of strain with viscosity being the constant of proportionality, and of elastic chain coil deformation behavior, in which the strain is proportional to the stress magnitude with Young's modulus (in tensile strain) representing the coefficient of proportionality. It is because of this viscous component of polymeric systems with some of the mechanical energy being converted to heat energy that comparison of mechanical properties and predictions based on such properties must always consider the magnitude of this energy dissipation by including correlation of the rate of strain with the specific stress-strain relaxation mechanism unique to the system.

The concept of 'dynamic mechanical analysis' (DMA) was originally developed more than forty years ago by Mooney and Gerke (4) in which a torsion pendulum was used to investigate the adiabatic heat buildup phenomenon in tires. Nielsen and Buchdahl (5) studied the effect of plasticizers on the glassy transition in polyvinyl chloride and the damping behavior in high-impact polystyrene some thirty years ago using a similar torsion pendulum. The use of the pendulum-based type of instrumentation has been expanded primarily by Gillham and Lewis (6) using glass-fiber braids as mechanical support for uncured liquid resins to allow indepth analysis of the complex mechanism of thermoset cure reaction. The early use of the torsion pendulum by McCrum (7) and by Sinnott (8) of DuPont has evolved into the development of the current modular system for thermal analysis by DuPont Instruments (9-11).

The DuPont 982 Dynamic Mechanical Analyser used in conjunction with the DuPont 1090 Programmer/Data Thermal Processor and with included software provide a system characterized by simplicity of operation with a wide range of materials from soft elastomers to metals and ceramics. A scope of temperature (-150 to 500 C) and time selections may be programmed with marked selectivity of instrument readout (temperature, time, fundamental resonant frequency, and mechanical damping) conversions through preprogrammed software calculations yielding quantitative values of storage and loss moduli, tan delta, and logarithmic functions of these parameters. The software routines allow automatic compensation for sample end effects, instrument compliance, and instrument damping.

The thermal processor system collects and stores real time data in a separate disk drive unit and then plots continuous printouts or tabulated data on command. The complex data analysis routine calculates the standard viscoelastic properties such as tensile storage and loss moduli, tan delta and allows calculation of comparable shear moduli as well. The graphical reports and the tables of calculated or real time data are obtained in a form suitable for publication. The printouts may be further customised using a custom-plotting format. Examples of both types are presented as Figures 1-3. In Fig. 1 there is represented the preprogrammed printout of the real time data for a standard reference sample of an ABS terpolymer.

There is displayed in Fig. 2 the calculated tensile moduli and tan delta for the same sample. The capacity to make comparison plots by recalling real time of calculated data from the disk storage unit for different samples and plotting on fixed axes is shown in Fig. 3 including custom modification to fully identify the samples. Another feature is given in Fig. 4 which contains calculated data in tabular form and with identification of axis specifications. Many other features of this analyser system are described in reference 11.

EXPERIMENTAL

In this section there is described the materials used in this work together with a brief description of the equipment employed. Also, there is included a step-by-step outline of the operation of the DuPont Dynamic Mechanical Analyzer instrumentation.

Materials: The epoxy resin used throughout this work was Shell Epon 828, a low molecular adduct of bisphenol A with diglycidyl ether having an epoxide equivalent of 5.1 equivalents per kilogram. The hardener, Shell Z, a mixture of m-phenylene diamine and methylene dianiline, was added in stoichiometric amount. Both reactants were preheated to 60-70 C, mixed vigorously by stirring, evacuated several minutes under forepump vacuum, and poured into preheated aluminum molds which had been sprayed with Teflon mold-release agent. Samples for cure studies were poured directly into aluminum pans. The resin was allowed to set at room temperature for around sixteen hours, and heated for variable times with a standard cure for mechanical analysis of two hours at 100 C and two hours at 150 C. Samples were removed from the molds after cooling, machined or ground to the desired form and polished with 600 sand paper.

A rubber modified sample was prepared by mixing into the above system 25 phr of WC-8006 (Wilmington Chemical Co.), an epoxy-terminated acrylonitrile-butadiene rubber, and given the same cure cycle.

Equipment: Test sheets of the resin were made by casting into and curing in aluminum molds measuring 20 cm by 10 cm by 0.32 cm (0.125 in) inside dimensions. The milled-out section of the mold was one cm thick and was faced with a 0.64 cm polished slab of aluminum plate. These were secured with four C-clamps, heated to 41 C in an air oven and the warm resin was slowly poured into the slightly tilted mold.

The instrumentation for the measurement of dynamic mechanical analysis was the DuPont 1090 Thermal Programmer/Data Processor, the DuPont 1091 (dual)Disk Drive unit, and the DuPont 982 Dynamic Mechanical Analyzer (see reference 11) with appropriate software (AdvDMA V1.0 data reduction program).

Brief Manual of Operation: Power should always be supplied first to the 1091 Disk Drive unit to prevent disk drive hangup which may occur if the 1090 Processor unit is turned on first. Shutting down and turning back on in proper order will eliminate the hang up should it occur. After a rapid internal self-analysis of the instrument, the display board shows date and time which must be accepted by depressing the Yes key (not Enter). The display then leads the operator through the necessary steps required to provide the required information for real time data obtainment. The final step in this programmed sequence is the Y-axis shift. The New File key is depressed which will automatically add one file unit to the last one

used in either obtaining real time data or in data analysis. Should this new file number already contain data, an error notation will be displayed and the basis for this error will be presented by activation of the Help key. If the operator is uncertain of the correct file number, depressing the File Control key and following the indicated steps allows data files to be identified, deleted, method or sample identification to be changed, and files to be protected from errant deletion. At any time the file contents may be displayed or printed with the identified keys in the List section of the board.

Once the file number has been correctly entered, chart paper must be in place with the chart load red light out before plotter will operate. Depressing the chart Label key will print out and label the axes as entered during the sequence above and will print sample identification, date and time (see Fig. 1). Then the Pen-up key is depressed, which activates the pen to start plotting at the start of the run. The steps in this paragraph may be bypassed if a plot of real time data is not desired. It will be stored and can be recalled as soon as the run is complete.

Actuating the Store key will involve the data storage system. (Should the display already show St or Store on the right side under indicated temperature, depressing the Store key will negate data storage - press again to reactivate). It is mandatory that all entered information be correct at this point because it cannot be changed once the test procedure has been activated by the SET-UP key.

Before the Set-up key is activated, the sample obviously must be in place, centered in the clamps and torqued to 10 in-lb for hard samples and 5 in-lb for soft elastomers. The metal shield must be placed around the sample and the thermocouples - CAUTION - placed very close (1-2 mm) from the sample near the driving arm. WARNING! The clamp screw holding the ceramic thermocouple leads should be carefully tightened with sufficient force ONLY to make it difficult to slide the ceramic rod. Then locking pins are removed from the arms after making sure the arms are parallel - use Length Adjust which slides the driven arm to make parallel - and replace the cover and slide into place the Dewar-type oven assembly and finger tighten connection screws.

With the Y-axis mode reading in millivolts, the display (push Display Axis key) will give the residual load on the LVDT and should be adjusted to zero \pm 10 mv using the LVDT slide-arm wing-nut screw on the back of the module with the mode knob reading Align and 2 showing on the Osc Amplitude potentiometer (0.2 mm amplitude) and 35-40 for A/Z Gain. With a rigid sample in place, turning the mode knob to Cal will cause automatic zero-null of the LVDT. (This step is omitted for non-rigid unsupported samples.) The mode knob is turned to Quant. You are now ready to start the test by depressing the Set-up key, which brings the sample to the preset temperature (displayed temperature may not be exactly the same as the control temperature) and when Ready appears in the lower right corner of the display, actuate the Start key and sit back and relax. The display will indicate when the test is complete. The mode knob on the 982

module should be returned to Align and cooling gas may be introduced to hasten cooling of the oven. Otherwise it takes about thirty minutes to cool to allow sample removal.

For normal type runs using similar type samples, a short hand method follows: with measured sample in clamps, module cover closed with oven in place, and storage disk in disk drive 1

1. Zero LVDT millivolt readout and turn mode to Quant.
2. Actuate Sample ID (Param) and enter data.
3. Actuate Method (Param) and enter data.
4. Enter Axis information (X&Y signal, range and shift).
5. New file selection.
6. Chart paper in place and red light out. Label and Pen-up if real time plot is desired.
7. Heater button IN (upper panel), actuate store, set-up and start.

The system is now in an automatic mode and will begin the test when the pre-set temperature is reached.

Low Temperature Operation: When the test involves below ambient conditions, the DuPont LN₂ tank assembly is attached to the back of the 982 module and the Tank Pressuriser is opened two full turns to give 5 - 7 psi readout - allow 15 min for equilibration. The Liquid valve is opened one-half turn until the temperature reaches -60 C and then closed to one-quarter turn open and the Cool Gas valve opened one-eighth turn. Actuate the Set-up key 30 degrees above start temperature - Ready will be displayed when the correct temperature is reached. Try to maintain the Ready condition at preset temperature for several minutes with the oven heater voltage reading 10-20 volts by slight adjustments of both valves. Press Start and hope that the oven heater voltage stays in the 10 - 20 volt range which will give linear time-temperature dependence. AVOID drastic valve changes. Don't be disappointed if the desired linearity is not always achieved. For an example of how bad it can get, see Figure 6. GOOD LUCK!

Data Playback and Analysis: Actuate Playback Set-up key and Enter the (correct) file number. Select the data to be plotted (X and Y - three Y axis selections) and check for chart load condition. Actuate the AutoScale key (generally) or Fixed Scale and plotting begins. Autoscale selects the axes so that all data points are included. The primary value of real data plotting is for a check of time-temperature linearity and of transition temperatures because the absolute magnitude of instrument readout depends somewhat on sample dimensions, longer and thicker samples give lower frequency, etc. The calculated data, tensile storage and loss moduli and tan delta are independent of sample dimensions - see Figure 7 - so these values are used for sample comparisons.

The data analysis software is actuated by the Data Analysis Set-up key which leads the operator through the selection of type of data readout, continuous or tabular printout - see Figures 3 & 4 - and Auto- or Fixed scales. In this sequence the operator may select all or part of the test information for display so it is convenient to Autoscale the data and use this printout to set range values for fixed scale to allow ease of comparison with other data from other

files or allow expansion of any portion of the test results - see Figures 8 & 9.

The custom-format of the printout is engaged using the Control Param key - enter 5 and the desired information and set the X and Y axis offset. Examples of custom plotting is shown in the Figures 4, 5, 6, 8, and 9.

The many other options included in this instrumentation are detailed in the respective manuals with which you should be familiar and which you should consult whenever questions arise.

RESULTS AND DISCUSSION

The DuPont Thermal Analyzer system has been demonstrated to be a reliable means of obtaining DMA examination of a series of polymeric materials from the thermoplastic ABS resin, Figures 1 & 2, the perfluorinated Kalrez elastomer, Figures 3 & 4, the hybrid graphite-epoxy composite, Figure 5, the glassy and rubber-modified epoxy resins, Figure 8, and the cure study of an epoxy resin, Figure 10.

The sensitivity of this instrument system is shown by the comparison of two runs on the Kalrez elastomer in which a small loss modulus peak was observed in the test piece which previously had been strained to break but the peak was absent in the test piece cut from the same sample which had no strain history. This result also illustrates one application of this type of analysis - that of the effect of processing conditions on the mechanical behavior.

The reproducibility of DMA test data has been thoroughly examined by testing duplicate samples in the study of the effect of addition of rubber-modifier to the base epoxy. The curves shown in Figure 8 represent superposable curves for each system. Also, one series of test runs on the effect of continued heating on the glassy transition temperature - not shown - gave superposable data on three different samples, one of which was markedly different in sample length. Three different test runs using calibration standards of DuPont Lexan test bars were identical both for real time and for the calculated moduli.

Although the reliability of the instrument complex has not been tested in a long time frame, nevertheless, it is significant that over sixty different tests have been performed, in duration from one hour to six hours in the cure study, and over the temperature range from -150 to +200 C, without any instrumental difficulty. The self-analysis software programmed into the processor prevents operator error from generating excess on the components.

In summary, even though the DuPont 1090, 1091, and 982 instrument complex is highly sophisticated, it is, as claimed in reference 11, characterized by simplicity of operation, rapid turnover, a vast range of applicability and accurate and convenient representation of DMA data - all with a minimum of operator attention and effort.

The effort to utilize the DMA system to correlate the fracture surface energy of a series of rubber-modified epoxy resins was not successful as shown in Figures 8 & 9. The low temperature (beta) energy dispersion mode occurs at -20 C in the unmodified epoxy, resulting from the relaxation motions of the glycidyl segments.

As this also happens to be the glassy transition for the rubber modifier, the addition of the rubber to the epoxy matrix does not markedly alter the volume fraction of the low temperature dispersion segments. In fact, as shown in Figures 8 & 9, the unmodified epoxy has the highest tan delta, which may be due to a slight difference in the extent of cure as the stoichiometric ratio of epoxide/amine was the same in both systems with the rubber serving only to dilute the system and so retard the crosslinking reaction.

Some effort has been made to convert the clamps of the 982 module to accommodate a resin-coated fiberglass mat in the horizontal mode. Several variations were used with wire end-clips, bent to form a 90 degree bend, being most convenient since excess resin tended to seize the screws used in the more formal type of clamp and the end-clips were disposable. A typical result of the cure study is shown in Figure 10. It is clear from these curves that the maximum in the damping (dashed) curve corresponds to the transition temperature of the cured resin reaching the cure temperature (150 C). However, it has not yet been possible to identify the time of gelation, which should appear as a smaller damping peak at shorter times. The small shoulder at 15 minutes in Fig. 10 may result from gelation but additional effort will have to be made to justify this conclusion.

CONCLUSIONS AND RECOMMENDATIONS

The investigation of dynamic mechanical properties of polymeric systems is now, with the DuPont thermal analysis modular system, both immediately available and quantitatively reliable. The ease and speed of operation of this system should now allow almost routine of the mechanical properties of polymer resins and of composite materials as they become of interest in the diverse programs of this laboratory. With the impending arrival of other modules which utilize the DuPont 1090 and 1091 units, differential scanning calorimetry (DSC), thermomechanical analyzer (TMA), and thermogravimetric analyzer (TGA), the capability of the laboratory to characterize fully new polymeric systems and to obtain meaningful engineering parameters for structure design will be maximized.

Because of the significance of reliable characterization data, it is recommended that every effort be made to acquaint staff members with the full potential of this valuable thermal analysis equipment.

Further efforts at cure study should be delayed until the DSC and TMA instruments can be used since these methods have proved successful in obtaining positive results in this type of study.

LIST OF REFERENCES

1. C.L.Segal, M. Shen and F.N. Kelley, Polymers in Space Research, Marcel Dekker, Inc. New York (1970) pp 145-159 and 181-215.
2. A. F. Clark, R.P. Reed and G. Hartwig, Nonmetallic Materials and Composites at Low Temperatures, Plenum Press, New York and London (1979) pp 12-26, 123-130 and 267-282.
3. L.E.Nielsen, Mechanical Properties of Polymers and Composites, Vol. 1, Marcel Dekker, Inc. New York (1974) pp 11-17, 123-130 and pp 139-230.
4. M. Mooney and R. H. Gerke, Rubber Chem. Technol., 14, 35(1941).
5. L. E. Nielsen and R. Buchdahl, SPE J., 9, 16(1953).
6. J. K. Gillham and A. F. Lewis, J. Appl. Polym. Sci., 7, 2293(1963).
7. N. G. McCrum, J. Polym. Sci., 27, 555(1958).
8. K. M. Sinnott, J. Appl. Phys., 29, 1433(1958).
9. R. L. Blaine and L. Woo, SPE Tech. Papers 23, 503(1977).
10. R. L. Blaine, P. S. Gill and L. Woo, J. Appl. Polym. Sci., Appl. Polym. Symp., 34, 157(1978).
11. 982 DMA Product Bulletin, DuPont Instruments, E-42397.

Sample: ABS
Size: 50 X 13 X 3 MM
Rate: 10 DEG/MIN

DMA

Date: 20-Jul-82 Time: 14:32:24
File: DMA.03
Operator: ALLEN

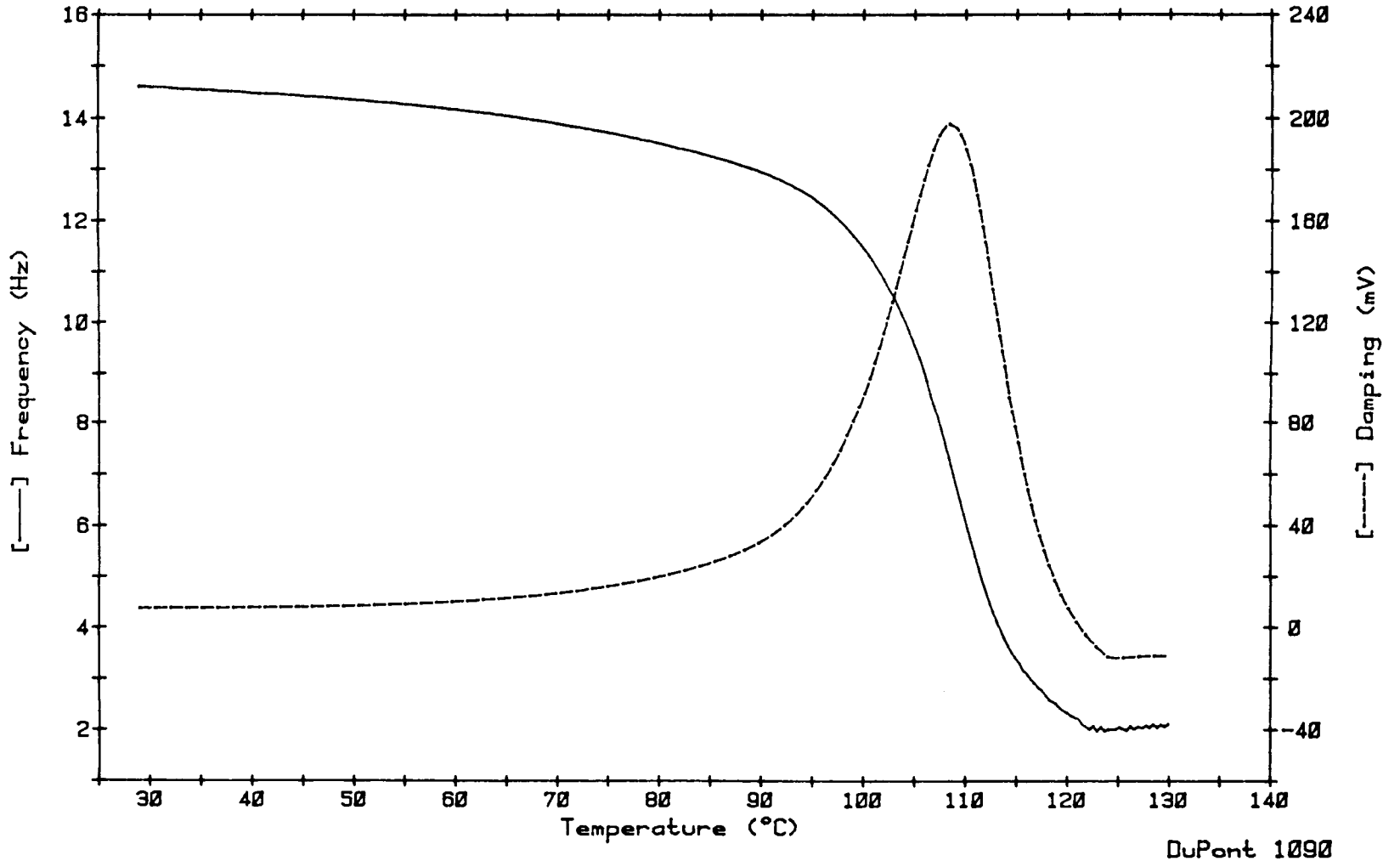
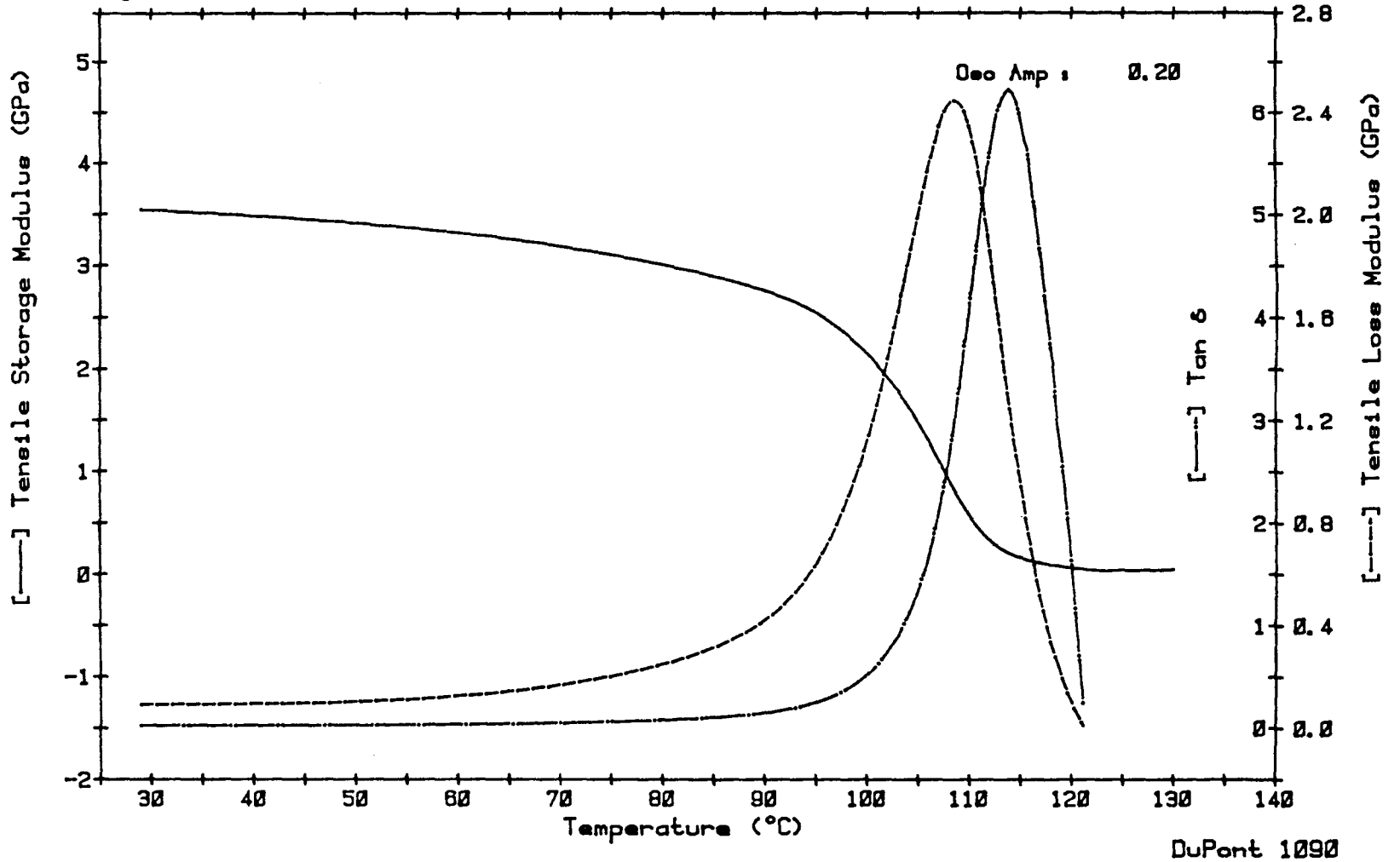


Figure 1. Real Time Data for ABS Resin

Sample: ABS
Size: 50 X 13 X 3 MM
Rate: 10 DEG/MIN
Program: Advanced DMA V1.0

DMA

Date: 20-Jul-82 Time: 14:32:24
File: DMA.03
Operator: ALLEN
Plotted: 19-Aug-82 22:35:17



III-14

Figure 2. Calculated Data for ABS Resin

SI-III
III-15

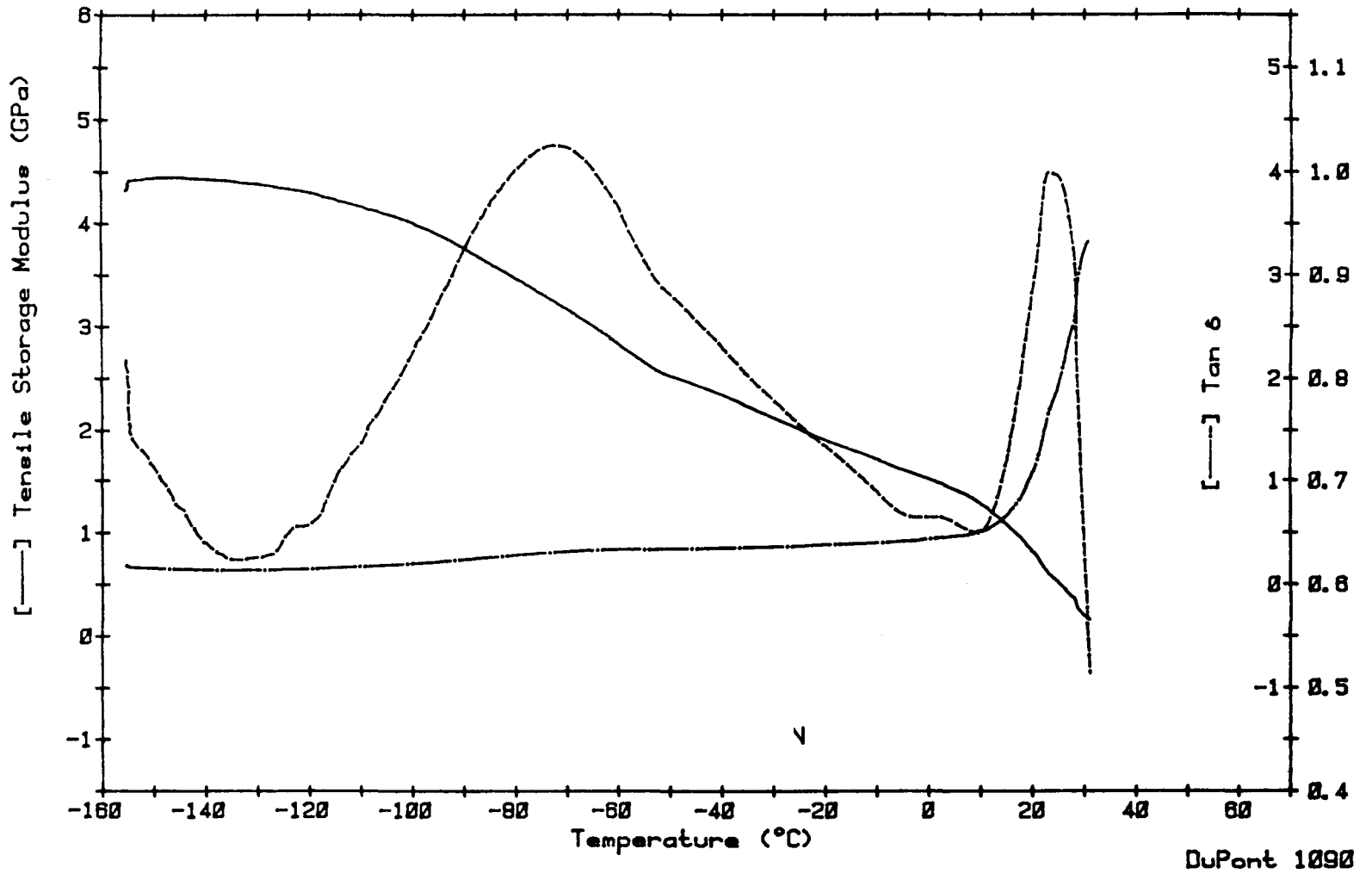


Figure 3. Dynamic Properties of Kalrez Resin

Sample: KALREZ BP-2
 Size: 27.0X9.2X3.3 MM
 Rate: 5 DEG/MIN
 Program: Advanced DMA V1.0

Date: 17-Aug-82 Time: 8:58:28
 File: DMA.41
 Operator: ALLEN
 Plotted: 19-Aug-82 22:56:28

Temp [°C]	Tensile Store [GPa]	Tensile Loss [GPa]	Tan δ
-149.5	4.45	0.709	0.159
-139.8	4.43	0.641	0.145
-129.3	4.38	0.627	0.143
-118.8	4.30	0.659	0.153
-109.7	4.17	0.738	0.177
-99.9	4.01	0.825	0.208
-89.9	3.75	0.927	0.247
-79.9	3.48	1.00	0.290
-69.9	3.16	1.02	0.324
-60.0	2.83	0.987	0.342
-49.9	2.52	0.881	0.349
-39.8	2.33	0.829	0.358
-29.9	2.11	0.779	0.368
-20.0	1.90	0.735	0.368
-9.9	1.70	0.689	0.405
0.1	1.51	0.668	0.442
10.2	1.27	0.653	0.515
20.2	0.811	0.692	1.10
30.0	0.194	0.633	3.28

	Range	Start/Shift
X-Axis:		
Time	20.0 min/om	0.0 min
Temp	10.0 °C/om	0.0 °C
Y-Axis:		
Time	5.0 min/om	0.0 min
Temp	1.0 °C/om	0.0 °C
Sig-A	2.0 Hz/om	2 om
Deriv-A	1.0 Hz/min/om	0 om
Sig-B	20.0 mV/om	3 om
Deriv-B	1.0 mV/min/om	0 om

III-16

Figure 4. Printout of Tabulated Data For Kalrez Resin

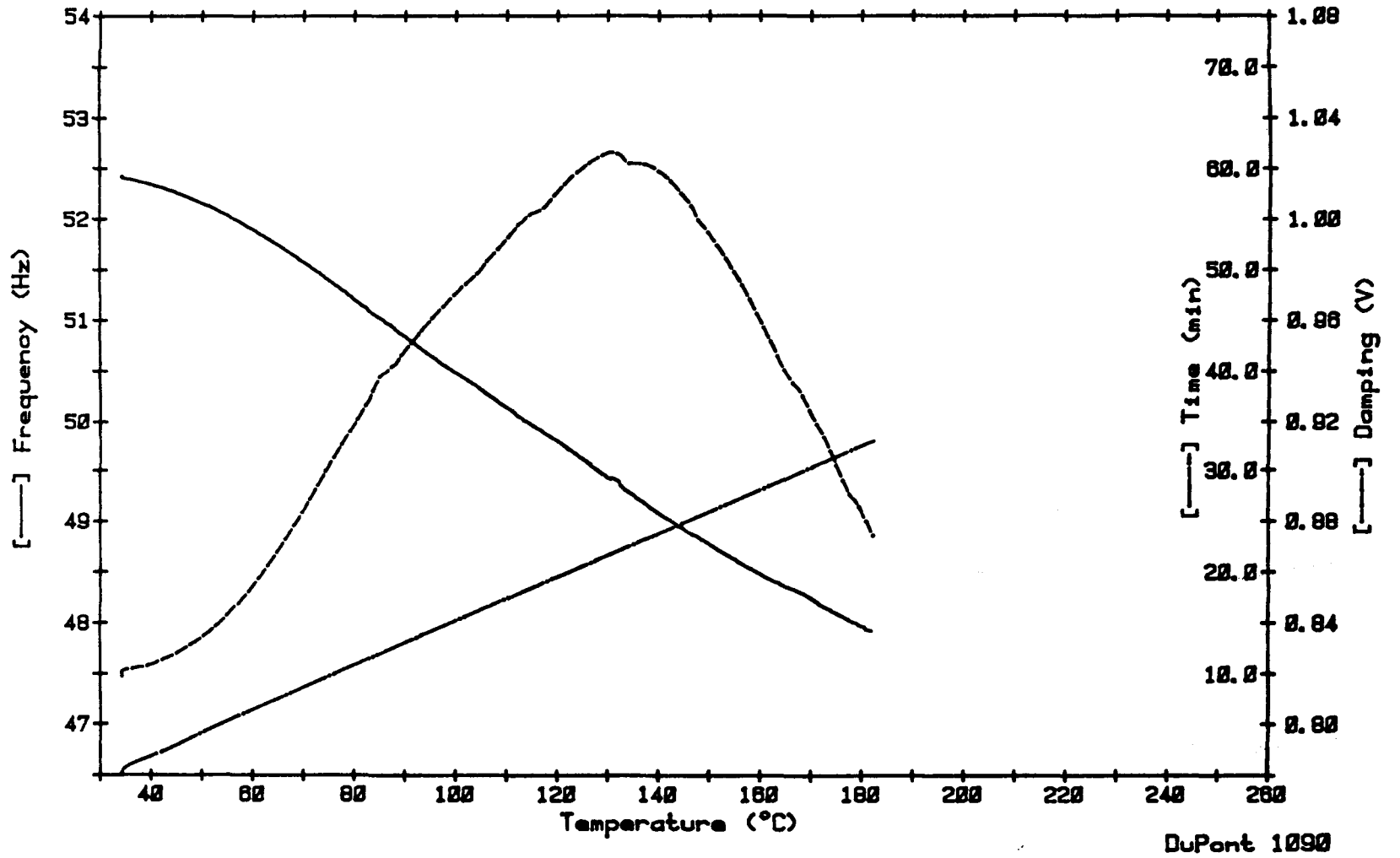


Figure 5. Real Time Data For Kevlar/Graphite/Epoxy Composite

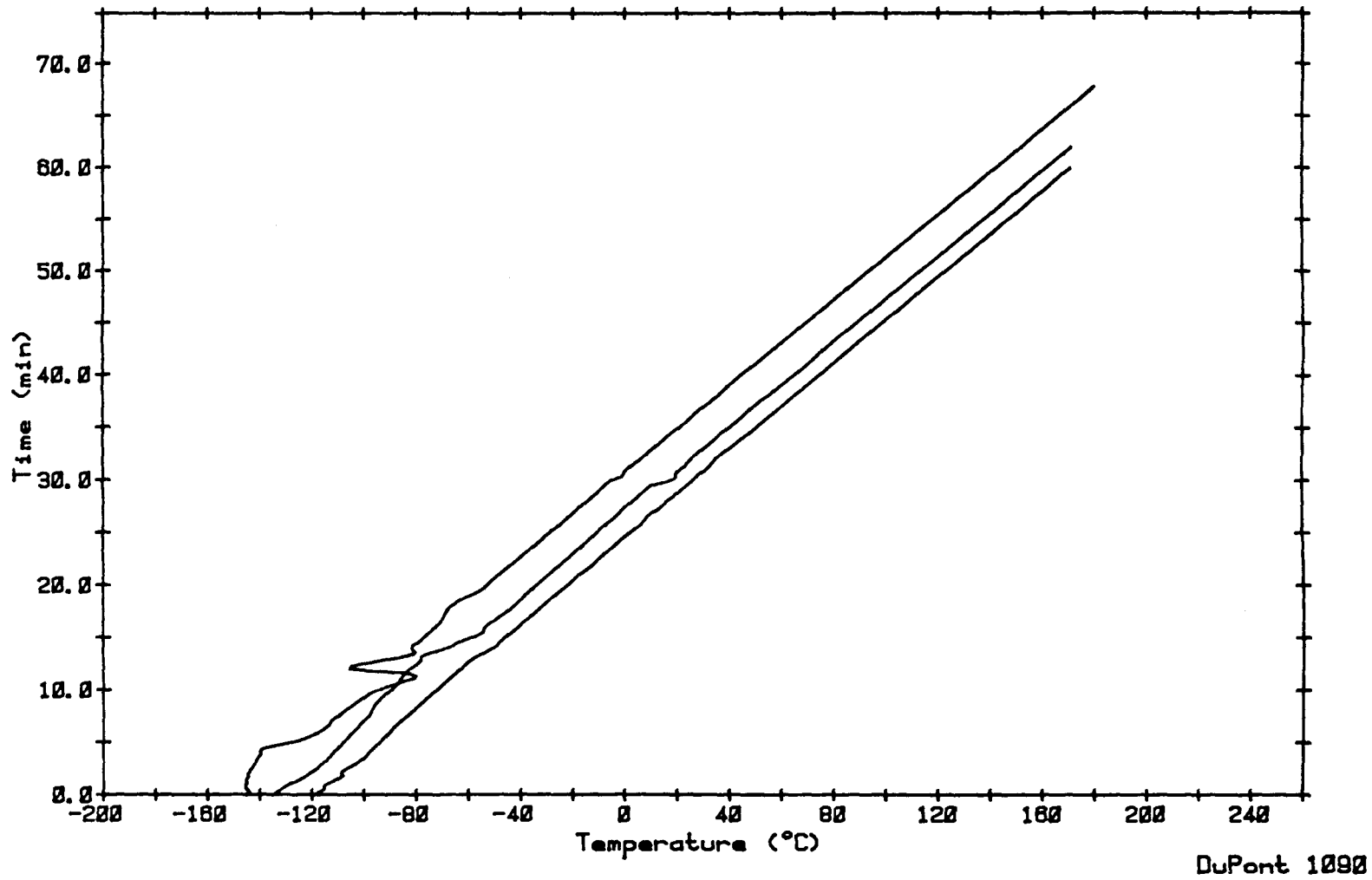


Figure 6. Examples of Good and Bad Control of Temperature In the Below Ambient Temperature Region

61-III

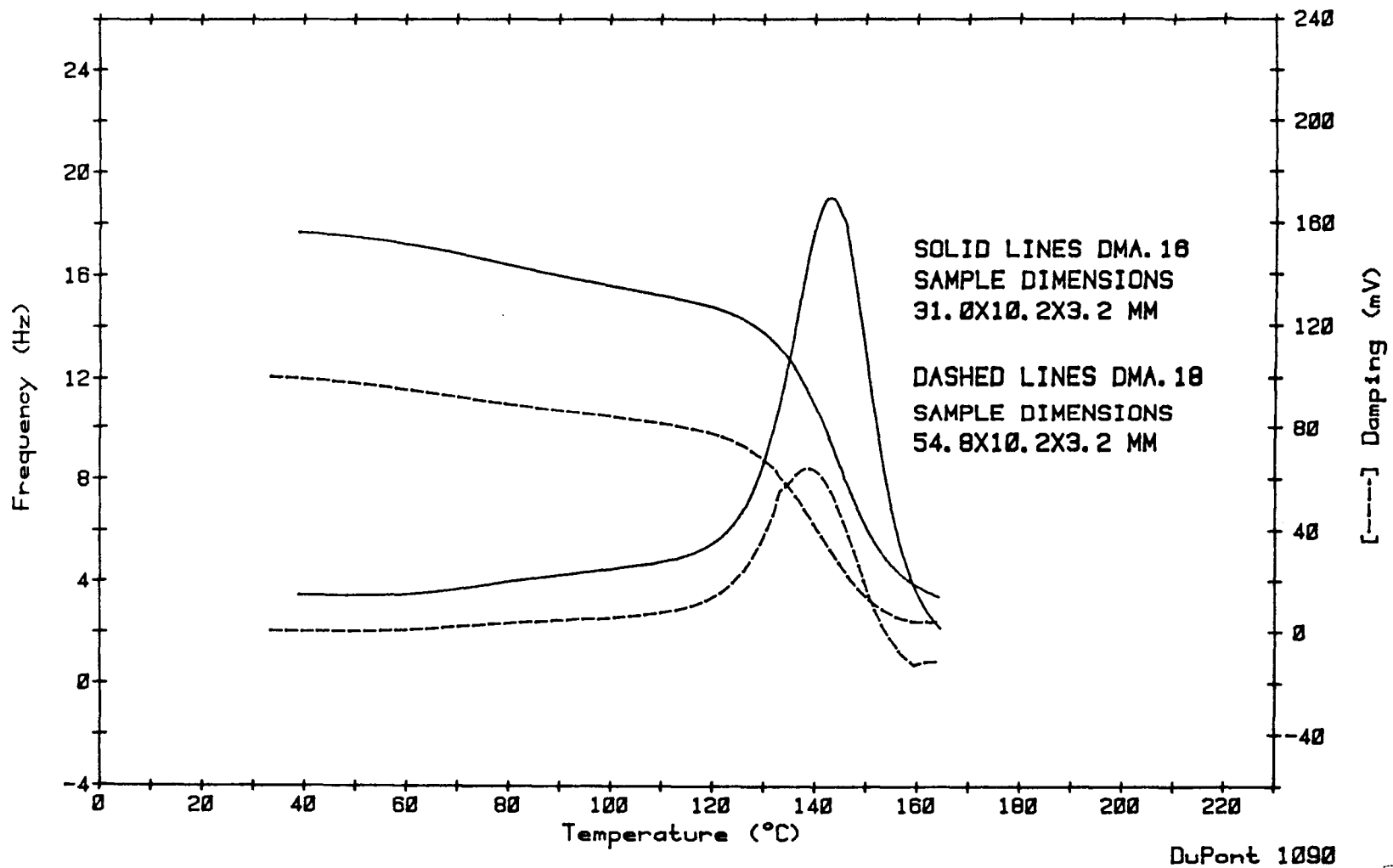


Figure 7. Effect Of Sample Dimensions On Real Time Data

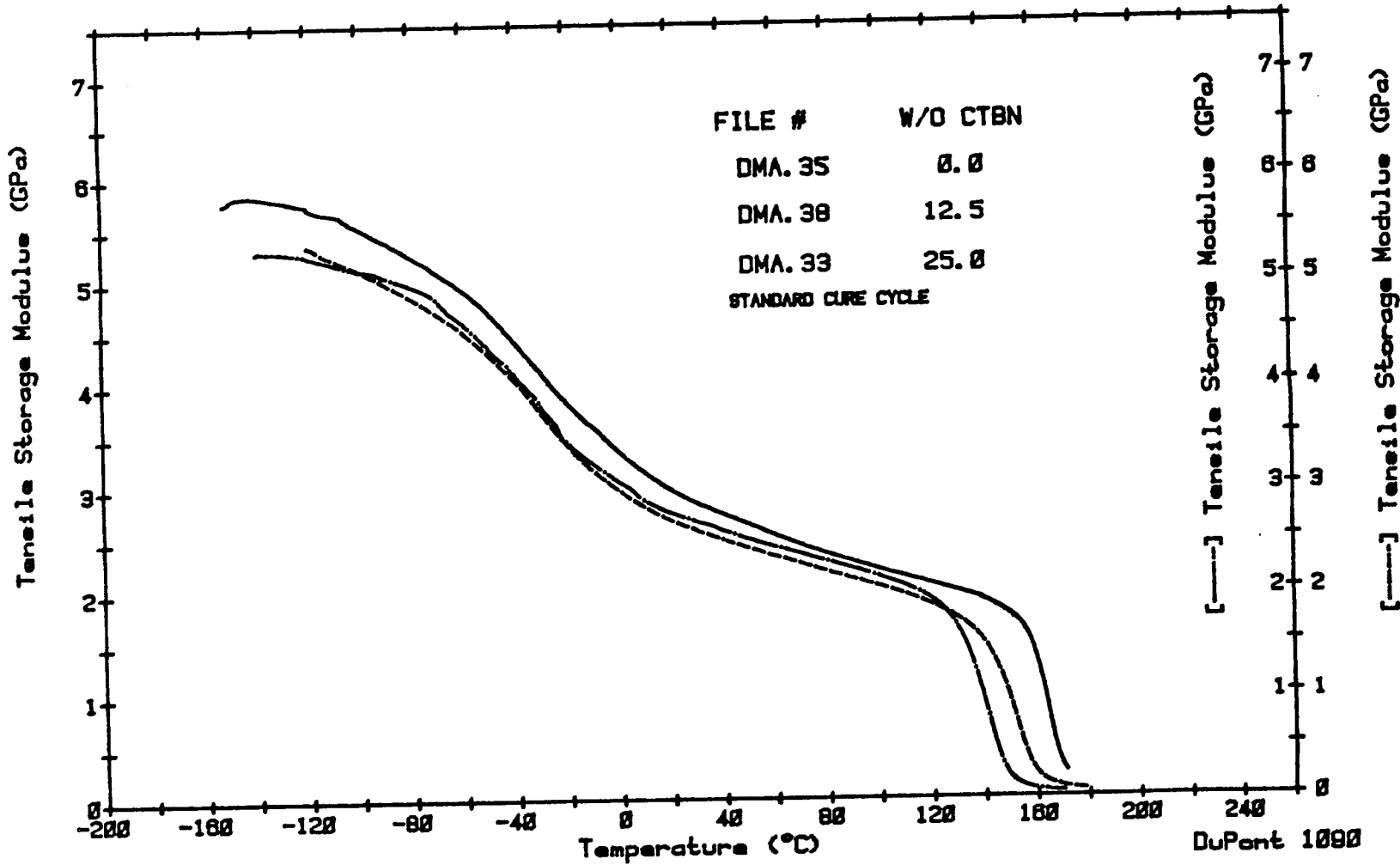


Figure 8. Effect Of CTBN Rubber On Tensile Storage Modulus Of EPON 828/Shell Z Epoxy

DMA

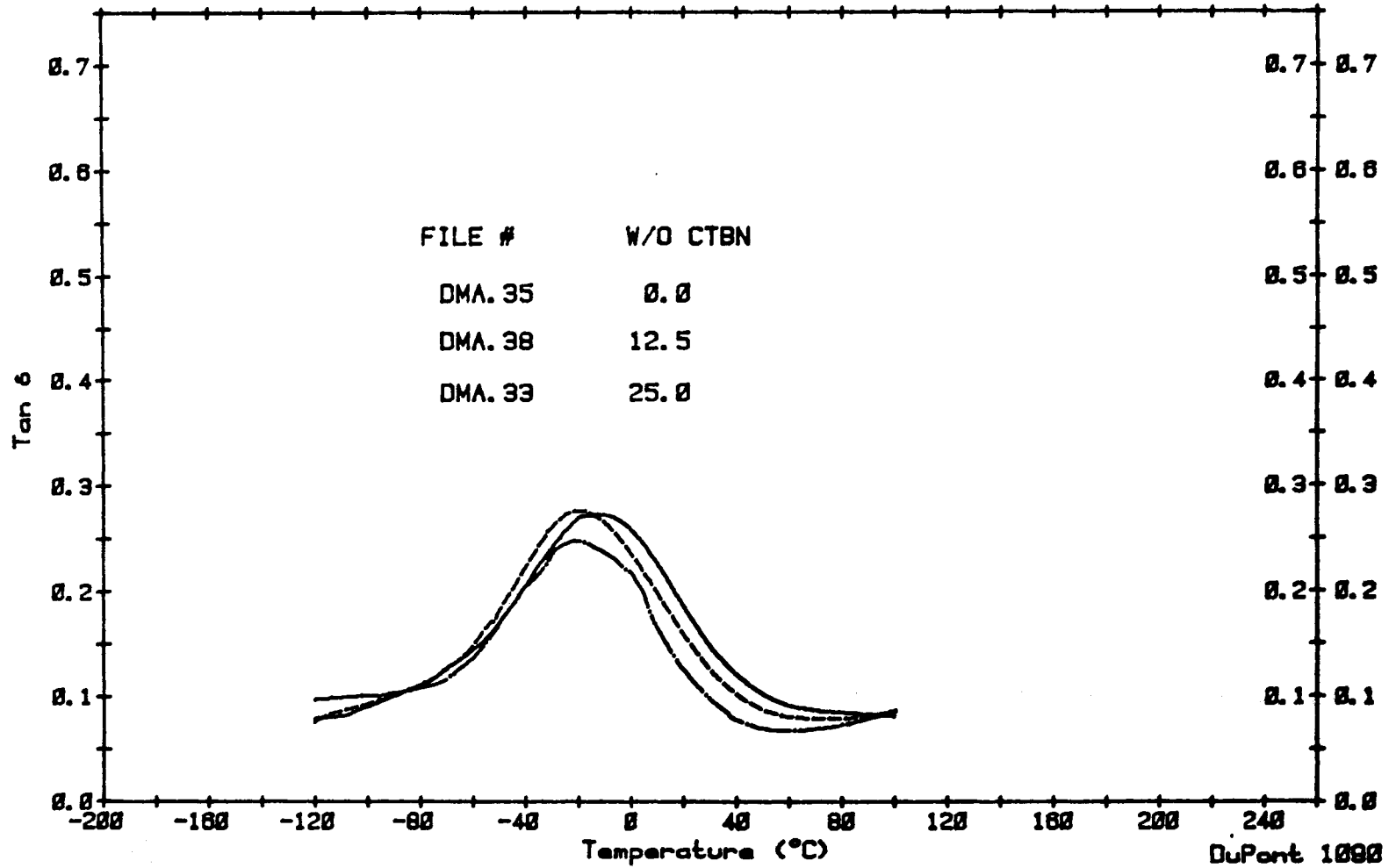


Figure 9. Effect Of CTBN Rubber On Tan Delta Of Epon 828/Shell Z Epoxy

Sample: EPON 828/SHELL Z CURE
Size: 27.0X9.2X3.3 MM
Rate: 10DEG/MIN

DMA

Date: 18-Aug-82 Time: 8:23:47
File: DMA.42
Operator: ALLEN

III-22

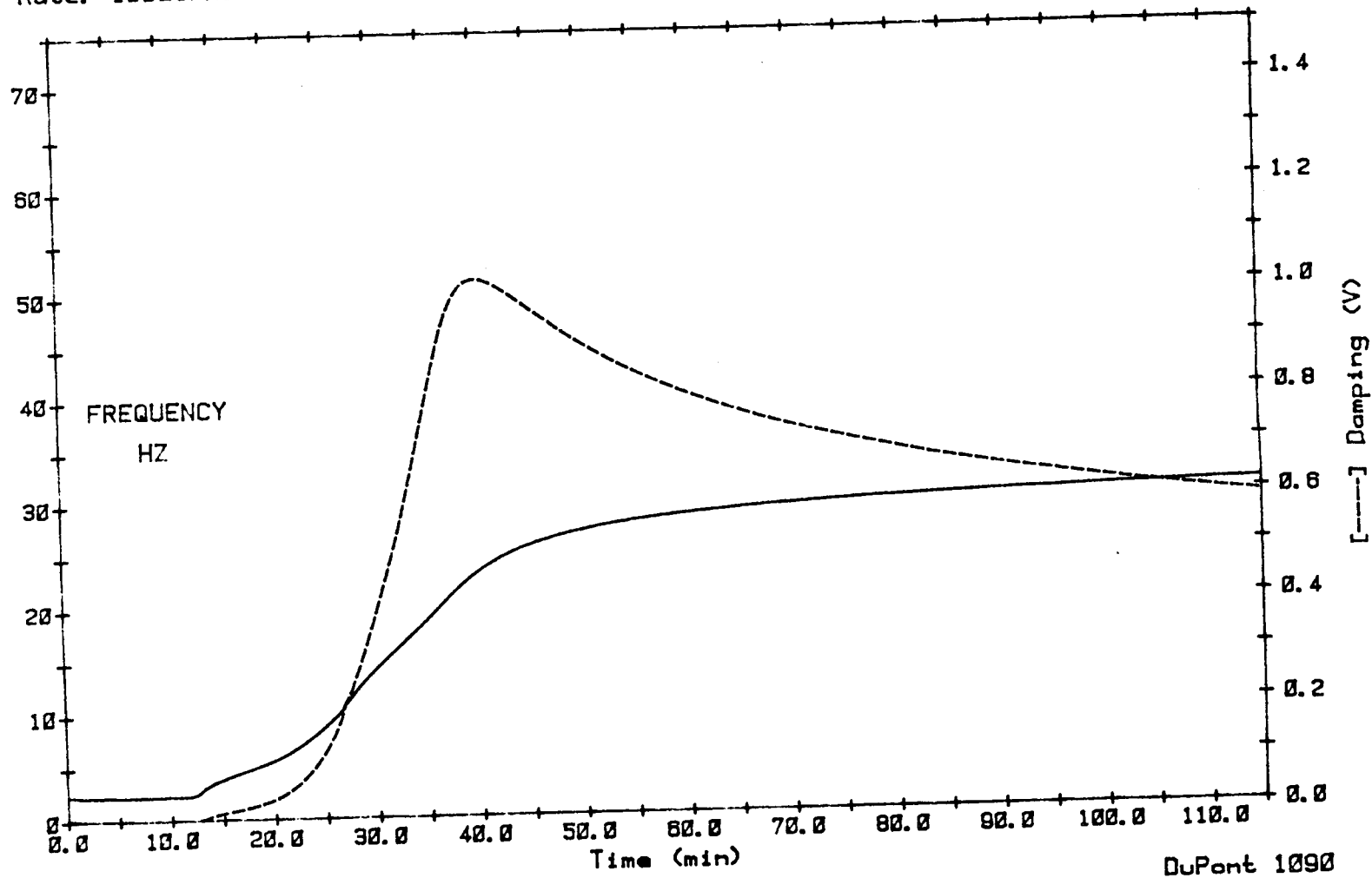


Figure 10. Rate Of Cure Study Of Epon 828/Shell Z
Real Time Data For Resin On Glass Braid

NASA/ASEE SUMMER FACULTY RESEARCH FELLOWSHIP PROGRAM

MARSHALL SPACE FLIGHT CENTER
THE UNIVERSITY OF ALABAMA

INSTABILITY OF A SOLIDIFYING BINARY MIXTURE

Prepared By: Basil N. Antar, Ph.D.

Academic Rank: Associate Professor

University and Department: University of Tennessee Space Institute
Department of Engineering Science and
Mechanics

NASA/MSFC:
(Laboratory) Space Science
(Division) Atmospheric Science
(Branch) Fluid Mechanics

MSFC Counterpart: C. F. Schafer

Date: September 13, 1982

Contract No.: NGT 01-002-099
(University of Alabama)

ABSTRACT

INSTABILITY OF A SOLIDIFYING BINARY MIXTURE

BASIL N. ANTAR

THE UNIVERSITY OF TENNESSEE SPACE INSTITUTE

An analysis is performed on the stability of a solidifying binary mixture due to surface tension variation of the free liquid surface. The basic state solution is obtained numerically as a non-stationary function of time. Due to the time dependence of the basic state, the stability analysis is of the global type which utilizes a variational technique. Also due to the fact that the basic state is a complex function of both space and time, the stability analysis is performed through numerical means.

INTRODUCTION

A great deal of interest has been generated recently in the possibility of producing new materials in the reduced gravity environment provided during the forthcoming missions of Spacelab. The range of possibilities extend from producing large crystals of uniform properties to manufacturing materials with unique properties. Most of these processes involve the solidification of materials from the liquid state. Convective motions within the liquid during solidification can influence the local material composition and the shape of the solid-liquid interface which may result in solids with non-uniform properties and crystal defects. The microgravity environment of Spacelab is being viewed as one in which the buoyancy forces are eliminated so that convection driven by thermal gradients will not occur. It is hoped that this will lead to an improved solidification process. However, convection may occur for other reasons and whether convection is negligible or not during solidification constitutes a vital question bearing on the value of future materials processing in low-gravity environment. Little information exists presently on convection during solidification under such circumstances.

The work reported here is a continuation of an analytical investigation into the nature of convective motion in a binary liquid layer due to surface tension forces during its solidification. The onset of convection will be determined through a stability analysis which is described below.

STATEMENT OF THE PROBLEM

The occurrence of convective motions in a fluid has been studied both theoretically and experimentally for approximately a century. The problem is very well documented in several books and numerous articles with all of its variations. It is obvious that in order to study analytically the detailed convective motions in a fluid in any configuration requires nothing less than the total solution of the Navier-Stokes equations and Energy Conservation equations. This is well known to be a formidable, although not an impossible, task requiring considerable amounts of time as well as financial resources.

In certain applications, it is sufficient to be able to know whether or not under certain conditions a fluid could sustain convective motions. The answer to such a question requires far less work; but, again, the information is essentially just of a binary form. Such information can be obtained through hydrodynamic stability analysis. Essentially one introduces perturbation into a well-known basic state and studies the evolutions of these perturbations in time.

If the perturbations decay with time, then the basic state is said to be stable and no convective motion will ensue. If, on the other hand, the perturbations are found to grow with time, then the basic state is said to be unstable and convective motion will take place. Fundamental to such a stability analysis is the existence of a stationary basic state. Unfortunately, the problem under consideration does not have such a basic. However, it has been shown that it is possible to carry out a meaningful stability analysis of such a basic state through several techniques. We have chosen the energy stability method as the best suited for the problem under consideration. This technique is elucidated in detail in the monographs of Joseph [1].

In this work, we consider the stability of a binary fluid layer which is being solidified from below and has an upper free surface. The fluid layer is assumed to be of infinite extent in the horizontal direction. Since it is assumed that the process is being carried out in the low gravity environment of Spacelab, it is anticipated that the driving force is the surface tension force at the free surface. The solution to the basic state has already been obtained in a previous report (Antar [2]). As is expected, the basic state is a function of both time and space. Thus, the stability analysis used must account for the variations of the basic state with time.

The stability analysis starts with the perturbation equations which may be written in the following form

$$\frac{\partial \underline{u}}{\partial t} + \underline{u} \cdot \nabla \underline{u} + \underline{U} \cdot \nabla \underline{u} + \underline{u} \cdot \nabla \underline{U} = -\frac{1}{\rho_0} \nabla p + \nu \nabla^2 \underline{u} + g[\beta_1 \theta + \beta_2 \gamma] \hat{k} \quad (1)$$

$$\frac{\partial \gamma}{\partial t} + \underline{u} \cdot \nabla \gamma + \underline{U} \cdot \nabla \gamma + \underline{u} \cdot \nabla C = D \nabla^2 \gamma \quad (2)$$

$$\frac{\partial \theta}{\partial t} + \underline{u} \cdot \nabla \theta + \underline{U} \cdot \nabla \theta + \underline{u} \cdot \nabla T = \kappa \nabla^2 \theta \quad (3)$$

where \underline{u} (u, v, w) is the perturbation velocity vector, \underline{U} (U, V, W) is the basic state velocity vector. γ and C are the perturbation and basic state concentration and θ and T are the perturbation and basic state temperature, respectively. ν , D and κ are the kinematic viscosity, thermal diffusivity and the solutal diffusion coefficient, respectively. These equations are for a Boussinesque fluid and subject to the following boundary condition

$$\underline{u} = \theta = \gamma = 0$$

on the lower surface.

While at the upper surface, we must have the following boundary conditions:

$$k \frac{\partial \theta}{\partial z} = -\tau \theta \quad (4a)$$

$$\frac{\partial \gamma}{\partial z} = 0 \quad (4b)$$

$$\mu \left(\frac{\partial w}{\partial x} + \frac{\partial u}{\partial z} \right) = \frac{\partial \sigma}{\partial x} \quad (4c)$$

$$\mu \left(\frac{\partial w}{\partial y} + \frac{\partial v}{\partial z} \right) = \frac{\partial \sigma}{\partial y} \quad (4d)$$

where σ is the surface tension. On all the sidewalls we must have the perturbation function vanishing.

The governing equations are first non-dimensionalized using the fluid depth d for a length scale, d/κ for a time scale, K/d for a velocity scale, $T_1 - T_0$ and $C_1 - C_0$ for temperature and concentration scales respectively. Upon introducing these scales into equations (1) - (4) we get the following equations for the perturbations functions

$$\frac{\partial u}{\partial t} + u \cdot \nabla u + v \cdot \nabla u + w \cdot \nabla u = -\nabla p + P \nabla^2 u + P(R\theta + LR_c \gamma) \quad (5)$$

$$\frac{\partial \theta}{\partial t} + u \cdot \nabla \theta + v \cdot \nabla \theta + w \cdot \nabla \theta = \nabla^2 \theta \quad (6)$$

$$\frac{\partial \gamma}{\partial t} + u \cdot \nabla \gamma + v \cdot \nabla \gamma + w \cdot \nabla \gamma = L \nabla^2 \gamma \quad (7)$$

with the following boundary conditions

$$\theta = \psi = \gamma = 0 \quad (8)$$

on all side except the upper surface and

$$\frac{\partial \theta}{\partial z} + \beta \theta = 0 \quad (9a)$$

$$\frac{\partial \gamma}{\partial z} = 0 \quad (9b)$$

$$\frac{\partial \psi}{\partial z} + M \frac{\partial \theta}{\partial x} + M_c L \frac{\partial \gamma}{\partial x} = 0 \quad (9c)$$

$$\frac{\partial \psi}{\partial z} + M \frac{\partial \theta}{\partial y} + M_c L \frac{\partial \gamma}{\partial y} = 0 \quad (9d)$$

at the upper surface. In these equations we have the following non-dimensional numbers.

$$P = \text{Prandtl No.} = \nu / \kappa$$

$$R = \text{Rayleigh No.} = \beta_1 g \Delta T d^3 / \nu \kappa$$

$$R_c = \text{Solutal Rayleigh No.} = g \beta_2 \Delta C d^3 / \nu D$$

$$L = \text{Lewis No.} = D / \kappa$$

$$B = \text{Biot modulus} = \tau d / \kappa$$

$$M = \text{Marangoni No.} = (-\partial \sigma / \partial T) \Delta T d / \mu \kappa$$

$$M_c = \text{Solutal Marangoni No.} = (-\partial \sigma / \partial C) \Delta C d / \mu D$$

where $\partial \sigma / \partial T$ and $\partial \sigma / \partial C$ are the constants from the surface tension variations with both temperature and concentrations.

Now to obtain the energy equations we first take the dot product equation (5) with u and integrate about the volume under consideration to get

$$\frac{d}{dt} \int_V \rho^{-1} \varphi^2/2 dV = - \int_V \nabla \underline{u} : \nabla \underline{u} dV + R \int_V \omega \theta dV + LR_c \int_V \omega \gamma dV$$

$$- M \int_{z=1} \theta \frac{\partial \omega}{\partial z} dx dy - M_c L \int_{z=1} \gamma \frac{\partial \omega}{\partial z} dx dy \quad (10)$$

Similarly it is possible to obtain equations for $\theta^2/2$ and $\gamma^2/2$ in the following integral form

$$\frac{d}{dt} \int_V \theta^2/2 dV = - \int_V \omega \theta \frac{\partial T}{\partial z} dV - B \int_{z=1} \theta^2 dx dy - \int_V \nabla \theta \cdot \nabla \theta dV \quad (11)$$

$$\frac{d}{dt} \int_V \gamma^2/2 dV = - \int_V \omega \gamma \frac{\partial C}{\partial z} - L \int_V \nabla \gamma \cdot \nabla \gamma dV \quad (12)$$

Now multiplying equation (11) by λ_θ and equation (12) by λ_γ and adding equations (10) - (12) we get

$$\frac{d}{dt} K = - \Delta + \int_V [(R - \lambda_\theta \frac{\partial T}{\partial z}) \omega \theta + (R_c L - \lambda_\gamma \frac{\partial C}{\partial z}) \omega \gamma] dV$$

$$- \int_{z=1} [M \theta + M_c L \gamma] \frac{\partial \omega}{\partial z} dx dy \quad (13)$$

where

$$K = \frac{1}{2} \int_{\sigma} (P^{-1} \dot{q}^2 + \lambda_{\theta} \theta^2 + \lambda_r r^2) d\sigma$$

$$D = \int_{\sigma} [\nabla \underline{u} : \nabla \underline{u} + \lambda_{\theta} \nabla \theta \cdot \nabla \theta + \lambda_r \nabla r \cdot \nabla r] d\sigma + B \int_{z=1} \lambda_{\theta} \theta^2 dx dy$$

Equations (13) can be cast in a symmetric form with the following change of variables

$$\theta' = \sqrt{\lambda_{\theta}} \theta \quad ; \quad r' = \sqrt{\lambda_r} r$$

$$\lambda_{\theta} = M \mu_{\theta} \quad ; \quad \lambda_r = M_c \mu_r$$

$$R = M N \quad ; \quad R_c = M_c N_c$$

which after dropping the primes takes the following forms:

$$\frac{dK}{dt} = -D + \sqrt{M} \Pi \quad (14)$$

where

$$K = \frac{1}{2} \int_{\sigma} (P^{-1} \dot{q}^2 + \theta^2 + r^2) d\sigma$$

$$D = \int_{\sigma} (\nabla \underline{u} : \nabla \underline{u} + \nabla \theta \cdot \nabla \theta + \nabla r \cdot \nabla r) d\sigma + B \int_{z=1} \theta^2 dx dy$$

$$\begin{aligned} \Pi = & \alpha_\theta \mu_\theta^{-1/2} \left(\int_V c_\theta w_\theta dV - \int_{z=1} \theta \frac{\partial w}{\partial z} dx dy \right) \\ & + \alpha_f \mu_f^{-1/2} \left(\int_V c_f w_f dV - \int_{z=1} f \frac{\partial w}{\partial z} dx dy \right), \end{aligned}$$

and

$$\alpha_\theta = \sqrt{\frac{M}{M}}$$

$$\alpha_f = \sqrt{\frac{M_c}{M}}$$

$$C_\theta = N - \mu_\theta \frac{\partial T}{\partial z}$$

$$C_f = L N_c - \mu_f \frac{\partial C}{\partial z}$$

$$M = M + M_c$$

Now let us focus our attention on Eq. (14). Since then, the energy of the perturbation will increase or decrease with time depending on whether $\sqrt{M} \Pi / D \geq 0$. Of course the direct and only way of gaining this information is by solving the integro-differential system explicitly. However Eq. (14) can be written as an inequality in the following form

$$\frac{1}{D} \frac{dK}{dt} = -1 + \sqrt{M} \frac{\Pi}{D} \leq -1 + \frac{\sqrt{M}}{\rho} \quad (15)$$

where

$$e^{-1} = \max_{\tau} \{ \pi \} \quad (16a)$$

with

$$D = 1 \quad (16b)$$

where now the problem is cast as a variational problem defined by (15) and (16).

Let us introduce the lagrange multipliers $M_u(t)$ and $p(x, y, z, t)$ into the variational problem (15) - (16) with the following optimization procedure resulting

$$\delta \left\{ \pi + \int \frac{\partial p}{\partial M_u} (\nabla \cdot u) dV - \frac{1}{M_u} D \right\} = 0 \quad (17)$$

From variational calculus we know that the solution to (17) is the same as the solution of the Euler-Lagrange equation resulting from (17). For the present case, the Euler-Lagrange system of equations are the following

$$\frac{\partial p}{\partial x} - \nabla^2 u = 0 \quad (18)$$

$$\frac{\partial p}{\partial y} - \nabla^2 v = 0 \quad (19)$$

$$\frac{\alpha_B}{\sqrt{M_B}} \frac{M_u}{z} C_B \theta + \frac{\alpha_A}{\sqrt{M_A}} \frac{M_u}{z} C_A \Gamma - \frac{\partial p}{\partial z} + \nabla^2 w = 0 \quad (20)$$

$$\frac{M_u}{z} \frac{\alpha_B}{\sqrt{M_B}} C_B w + \nabla^2 \theta = 0 \quad (21)$$

$$\frac{M_A}{z} \frac{\alpha_F}{\sqrt{M_F}} C_T w + \nabla^2 \gamma = 0 \quad (22)$$

$$\frac{\partial u}{\partial x} + \frac{\partial v}{\partial y} + \frac{\partial w}{\partial z} = 0 \quad (23)$$

with the following boundary conditions

$$\frac{\partial u}{\partial z} + \frac{1}{z} M_A \frac{\alpha_\theta}{\sqrt{M_\theta}} \frac{\partial \theta}{\partial x} + \frac{1}{z} M_A \frac{\alpha_\gamma}{\sqrt{M_\gamma}} \frac{\partial \gamma}{\partial x} = 0 \quad (24a)$$

$$\frac{\partial v}{\partial z} + \frac{1}{z} M_A \frac{\alpha_\theta}{\sqrt{M_\theta}} \frac{\partial \theta}{\partial y} + \frac{1}{z} M_A \frac{\alpha_\gamma}{\sqrt{M_\gamma}} \frac{\partial \gamma}{\partial y} = 0 \quad (24b)$$

$$\beta \theta + \frac{\partial \theta}{\partial z} + \frac{1}{z} M_A \frac{\alpha_\theta}{\sqrt{M_\theta}} \frac{\partial w}{\partial z} = 0 \quad (24c)$$

$$\frac{\partial \gamma}{\partial z} + \frac{1}{z} M_A \frac{\alpha_\gamma}{\sqrt{M_\gamma}} \frac{\partial w}{\partial z} = 0 \quad (24d)$$

at $z = 1$ and

$$u = v = w = \theta = \gamma = 0 \quad (24e)$$

at $z = 0$.

Now as discussed earlier since the basic state itself a function of time then the term II in the energy equation (14) is a function of time. Also, the lagrange multipliers and the term in (16a) are also function of time. Thus, the variational problems (15) - (16) must be solved at each instant of time which requires the solution of the Euler-Lagrange equations at each point in time. Thus, the procedure is to solve the system (18)-(24) at each instant of time and obtaining the optimization parameter $M \mu (\tau)$ as a function of time.

REFERENCES

1. Joseph, D. D., Stability of Fluid Motions I and II. Springer Tracts in Natural Philosophy, Vol. 27 and 28, Springer Verlag, Berlin Heidelberg New York, 1976.
2. Antar, B. N., "Solidification of a Binary Mixture" in Research Reports - 1981 NASA/ASEE Summer Faculty Fellowship Program. Edited by A. Karr, et al., NASA CR - 161855, 1982.

1982

NASA/ASEE SUMMER FACULTY RESEARCH FELLOWSHIP PROGRAM

MARSHALL SPACE FLIGHT CENTER
THE UNIVERSITY OF ALABAMA

PLASMA IGNITION FOR LASER PROPULSION

Prepared By:	Raymond F. Askew
Academic Rank:	Professor
University and Department:	Auburn University Physics and Mechanical Engineering
NASA/MSFC: Laboratory	Structures and Propulsion
Division	Propulsion
Branch	Auxiliary Propulsion
MSFC Counterpart:	T. Dwayne McCay
Date:	September 21, 1982
Contract No.:	NGT01-002-099 (University of Alabama)

PLASMA IGNITION FOR LASER PROPULSION

By

Raymond F. Askew
Professor of Physics and
Mechanical Engineering
Auburn University
Auburn, Alabama

ABSTRACT

The concept of space propulsion, using a remote laser as the continuous energy source for the space vehicle, requires a reliable mechanism to remotely initiate a plasma aboard the space vehicle. It has been suggested that this could be done using a pulsed power laser, properly focused within an onboard combustion chamber.

For a specific optical system a pulsed carbon dioxide laser having an energy output of up to 15 joules has been used to initiate a plasma in air at one atmosphere pressure. The spatial and temporal development of the plasma have been measured using a multiframe image converter camera. In addition the time dependent velocity of the laser supported plasma front which moves opposite to the direction of the laser pulse has been measured in order to characterize the type of wavefront developed.

Reliable and reproducible spark initiation has been achieved. The lifetime of the highly dense plasma at the initial focal spot has been determined to be less than 100 nanoseconds. The plasma front propagates toward the laser at a variable speed ranging from zero to 1.6×10^6 m/sec. The plasma front propagates for a total distance of approximately five centimeters for the energy and laser pulse shape employed.

ACKNOWLEDGEMENTS

Appreciation is expressed to the National Aeronautics and Space Administration for its support through the Research Fellows program. The cooperation and support of all NASA personnel in providing a challenging professional opportunity and environment in which to develop were outstanding. I am particularly in debt to Dr. Dwayne McCay for his continued words of encouragement and collaboration. To David VanZandt, my sincere thanks for his respect, understanding, and patience. And to Charles Smith, my admiration and gratitude for the type of professional and technical support every scientist always dreams of but never expects to receive. I thank you all.

LIST OF FIGURES

<u>Figure No.</u>	<u>Title</u>	<u>Page</u>
1	Laser Propulsion System	V-6
2	Experimental Arrangement	V-8
3	Laser Burn Pattern	V-9
4	Multiple Frame Photographs of Laser Produced Plasmas (100 & 200 ns exposures)	V-11
5	Multiple Frame Photographs of Laser Produced Plasmas (50 ns exposures)	V-12
6	Multiple Frame Photographs of Laser Produced Plasmas (20 ns exposures)	V-13
7	Multiple Frame Photographs of Laser Produced Plasmas (5 ns exposures)	V-14
8	Multiple Frame Photographs of Laser Produced Plasmas (20 ns exposures)	V-16
9	Multiple Frame Photographs of Laser Produced Plasmas (10 ns exposures)	V-16
10	Multiple Frame Photographs of Laser Produced Plasmas (10 ns exposures)	V-17
11	Streak Photographs of Laser Produced Plasmas (200 ns streak duration)	V-18
12	Streak Photographs of Laser Produced Plasmas (200 ns streak duration)	V-19
13	Streak Photographs of Laser Produced Plasmas (200 ns streak duration)	V-20
14	Streak Photographs of Laser Produced Plasmas (100 ns streak duration)	V-22
15	Streak Photographs of Laser Produced Plasmas (100 ns streak duration)	V-23
16	Streak Photographs of Laser Produced Plasmas (50 ns streak duration)	V-24

INTRODUCTION

The placement of satellites into geosynchronous orbit is presently accomplished by direct launch from the earth's surface. The need for such satellites for both commercial communication and defense purposes increases yearly. The space shuttle program provides a mechanism to transport such satellites to a space station at low earth orbit which can be used as a staging area for launching satellites into geosynchronous orbit. Current technology would utilize chemical propulsion for this secondary transfer in order to get the satellite into final orbit within a reasonable time after launch from the platform. This method requires a high fuel-to-pay load mass ratio. Alternative propulsion concepts to the above are needed to accomplish this interorbit transfer. Several have been suggested, among these being a process known as laser propulsion, as described by Kantrowitz⁽¹⁾. This process is shown diagrammatically in Figure 1. A space station power laser system is directed to a rocket which is to transport the satellite to geosynchronous orbit. The on-board fuel is ignited by the focused laser beam and maintained as a plasma within a small volume of the engine. This plasma then transfers energy to the remaining fuel as it flows around the plasma core. The heated gas then exits through the expansion nozzle of the rocket engine thus providing thrust. A system based on this process is most attractive due to the high payload-to-total mass ratio which would be achieved.

It is well known that a focused laser can be used to create a small volume plasma in a gas^{(2),(3)}. However, the plasma so formed has been reported to immediately move toward the laser source^{(4),(5)}. This plasma motion results in the plasma front moving away from the focal volume of the laser beam, thus reducing the beam intensity on the plasma surface. This motion has been measured under limited conditions and theories have been proposed to explain its cause and the dynamics of the motion⁽⁶⁾. Vastly improved time resolved experimental measurements of the early time plasma are needed, along with a better theoretical model of the laser beam-plasma interaction.

OBJECTIVES

The work reported here had as its original objective a broad detailed study of the behavior of the plasma formed by a focused pulsed laser. This included studies of several gases at various pressures using variable laser powers and pulse shapes. Due to time and equipment limitations only preliminary results could be achieved. The effort centered on studying the spatial and temporal behavior of the plasma formed in air at one atmosphere. This included a detailed analysis of the shape and size of the plasma formed and the speed of the plasma front as it moved toward the laser source. The primary intent was to develop an operational system which could achieve the broad objectives envisioned and to demonstrate its reliability while at the same time determining to what degree reproducible results could be obtained.

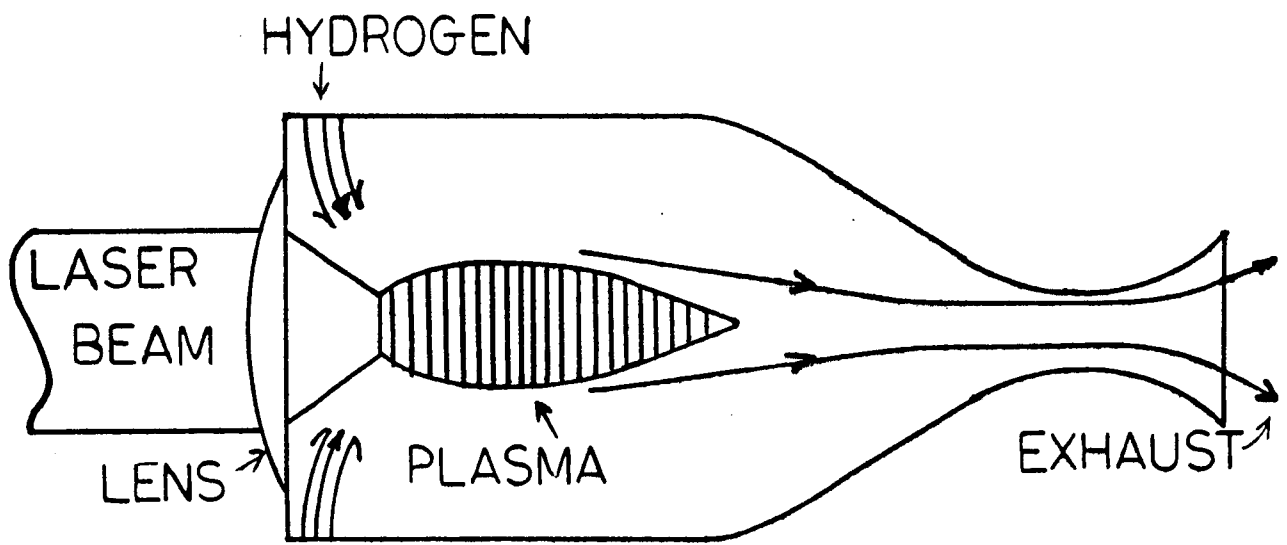


Figure 1. Laser Propulsion System.

EXPERIMENTAL ARRANGEMENT

Apparatus for conducting the experiment was assembled in such a manner as to be compatible with future experiments already planned. A block diagram of the experiment is shown in Figure 2. A Lumonics Model 103 TEA carbon dioxide pulsed laser was used as the energy source. It was modified to perform at approximately the following levels: 15 joules of energy in a pulse having a risetime of 40 nanoseconds, at a peak power of 5×10^7 watts, and with a primary pulse duration of 100 nanoseconds. The pulse had a small second peak with an exponential tail giving a total pulse duration of approximately 400 nanoseconds. The beam had a divergence of 0.6 milliradian half-angle. Time-dependent power measurement devices were not available to the experiment at the time of the studies reported here but will be in place for future measurements.

The turning mirror was front-surface gold-coated flat copper. The lens was NaCl having a focal length of 12 inches. The plasma was created within the enclosed chamber shown and all optical data were acquired through 2 inch diameter, 0.250 inch thick quartz flats. The system was optically aligned using a beam-splitter and a He-Ne laser.

The only diagnostic utilized was a TRW Model 1D1 image converter camera. Framing photographs were taken using Models 4B and 6B plug-in units. Streak photographs utilized Models 5B and 7B units.

The laser system was operated at 40 KV. When the storage capacitors were charged to this potential a trigger pulse was transmitted to a nitrogen filled spark gap. The subsequent breakdown of this gap initiated the current pulse to form the laser discharge.

The trigger pulse to the laser was also used to initiate operation of the image converter system. The system had a variable delay for opening the electronic camera shutter which could be varied from zero to 100 microseconds in increments of 10 nanoseconds. Due to the inherent delay of the laser system, particularly the spark gap, it was necessary to establish the true time delay to the camera shutter to insure that the camera recorded the initiation of the plasma formation. Careful cleaning of the spark gap resulted in a spark gap jitter which was generally less than 20 nanoseconds, with an upper limit of less than 100 nanoseconds. For the system as operated at full laser potential, the delay to the camera from the delay unit was nominally 2.21 to 2.23 microseconds for the streak units and 2.18 to 2.19 microseconds for the framing units.

The image converter camera used a 40 cm focal length, f/5.6 lens to collect light for the image tube. Events were recorded using Polaroid Type 57 (ASA 3000) film.

Alignment of the unfocused beam and evaluation of the beam pattern were performed each day, prior to insertion of the lens, using a thermally sensitive plastic film at the position of the alignment beam splitter, at the mirror position, and at the top of the test chamber. A normal beam pattern is shown in Figure 3.

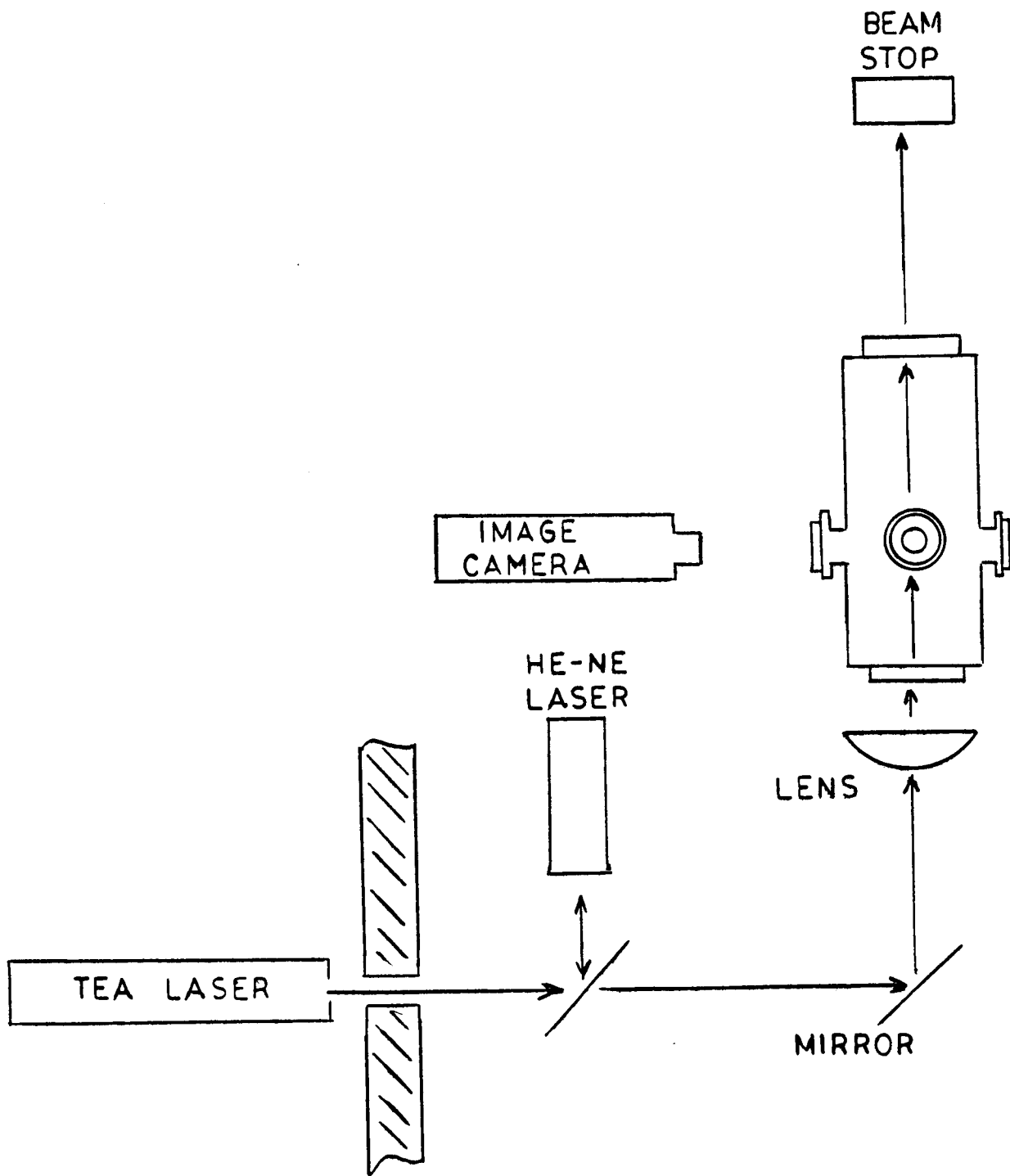


Figure 2. Experimental Arrangement.

Optical magnification of the recording system was accomplished by photographing a precision grid placed in the center of the test chamber and viewed through the quartz window.

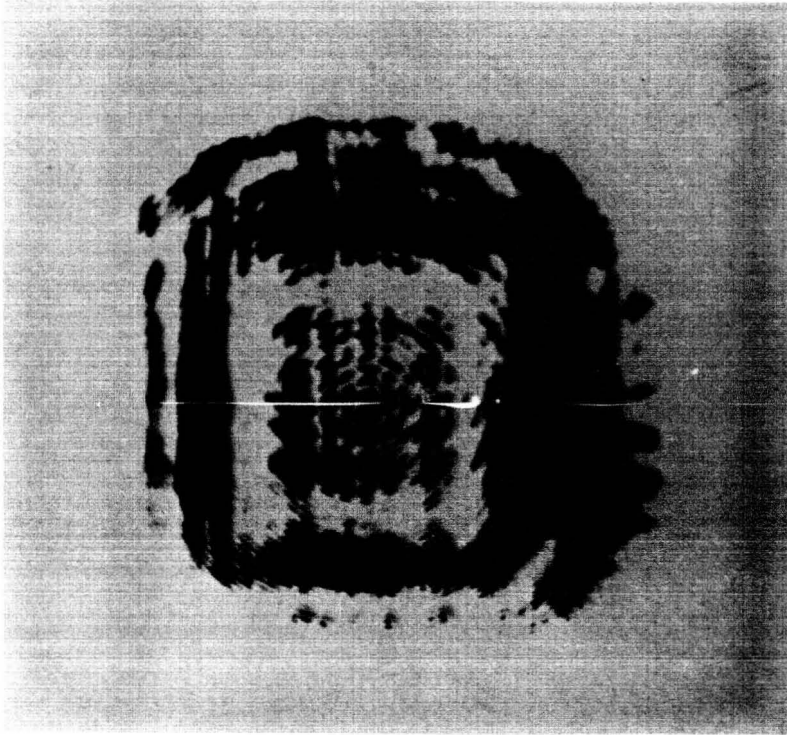


Figure 3. Laser Burn Pattern

Streak and framing times, as well as interframe delays of the image converter system, were carefully measured using a high speed storage oscilloscope. This provided accurate calibration of the time of events and of the streak time on the film.

RESULTS

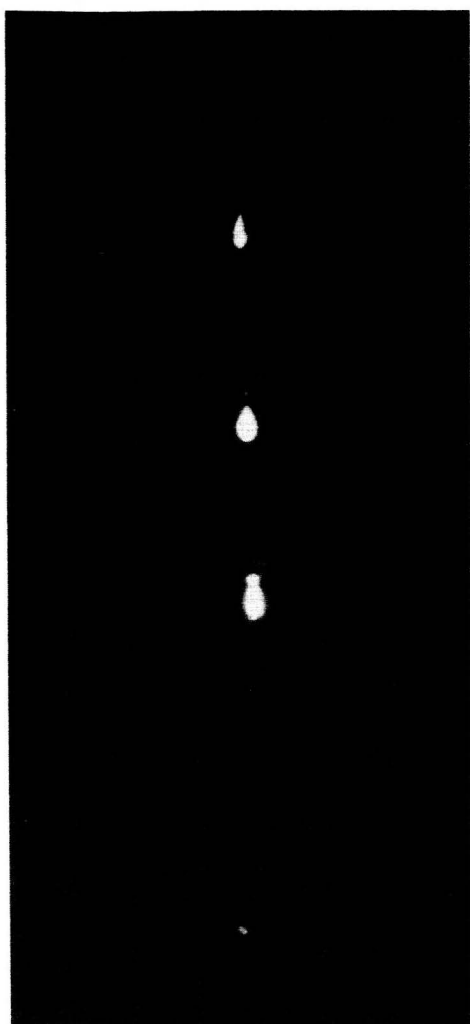
Figure 4 shows two sets of framing exposures of a laser produced plasma, produced under essentially the same conditions. The time of exposure for each frame is 200 nanoseconds (ns) for set (a) and 100 ns for set (b). The interframe delay in each case was 0.5 microsecond (μ s). The first event recorded is at the bottom of each picture, with later events at the top. For orientation, the laser beam was directed from the bottom of the picture toward the top. For scale reference, the length of the plasma shown in (b) is 5 millimeters (mm) in the first frame, 6 mm in the second, and 7 mm in the third. The considerable difference in the detail between the two events as recorded is due to exposure time. The longer exposure (200 ns) results in loss of development detail.

Figure 5 shows six different events, each with multiple frames. The exposure time was 50 ns. The initiation of image recording was prior to the initiation of the plasma in the first set (a). The first frame is therefore blank. The second frame (first image) thus occurred no more than 0.5 μ s after plasma ignition. The considerable plasma shown indicates a very rapidly developing system. The second set of events (b) appears to have begun late in time since the first frame of each is very well developed. For scale reference, the length of the plasma of the first frame of the third event in (b) (lower right corner) is 1.9 cm.

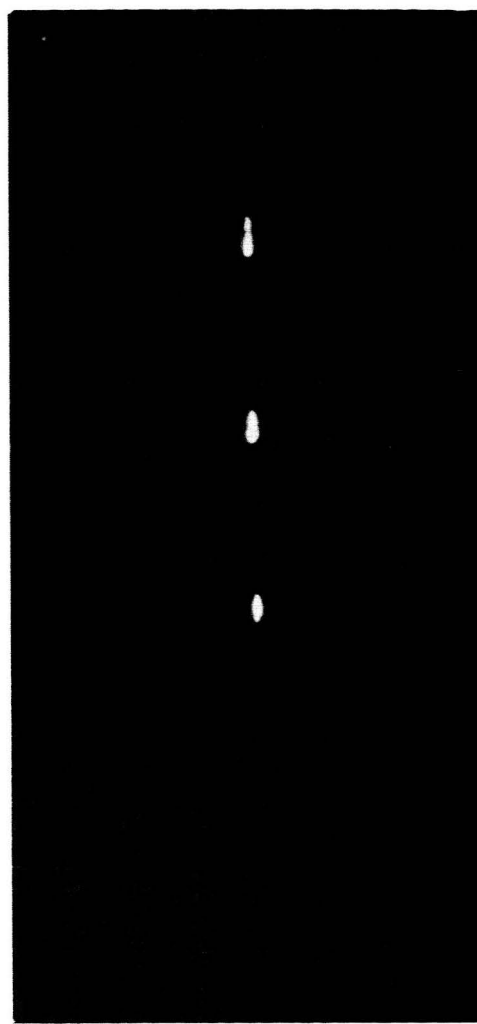
Two observations concerning these photos are appropriate. First, due to the limited aperture of the camera, when the plasma extended below the camera viewing region there was a cutoff of the image. This has occurred in the third frame of all six events of Figure 5. The somewhat flat lower end of each frame is the result of such a cutoff. Secondly, the bright horizontal lines which appear in some frames throughout these data are an effect due to the camera. This occurs at specific geometric locations on the camera screen when the light intensity onto the photocathode exceeds a prescribed limit in those areas.

To obtain better information on the details of development of the plasma, the preceding figures indicate the need for shorter exposures and shorter interframe delays. Figure 6 shows the three frame development of ten events, each having 20 ns exposures. Of special note is the first frame of the third event of (a) (bottom right corner). This event has been recorded very early in time. Since only 50 ns separate the second frame from the first, if one includes the 20 ns exposure of frame 2, the maximum time for the plasma length difference as shown in the first two frames would be 70 ns. The lengths of these two images are 6.6 mm and 13.2 mm respectively. Thus the average speed of the plasma front is 9.4×10^4 m/s. The long faint streak which appears to join the second and third frame images in (a) and (b) is due to using an interframe delay which was not at least four times the exposure time.

Figure 7 shows four events using 5 ns exposures. Considerable detail can be seen in these which would indicate the formation of several distinct events along the plasma length, each changing rapidly in time.



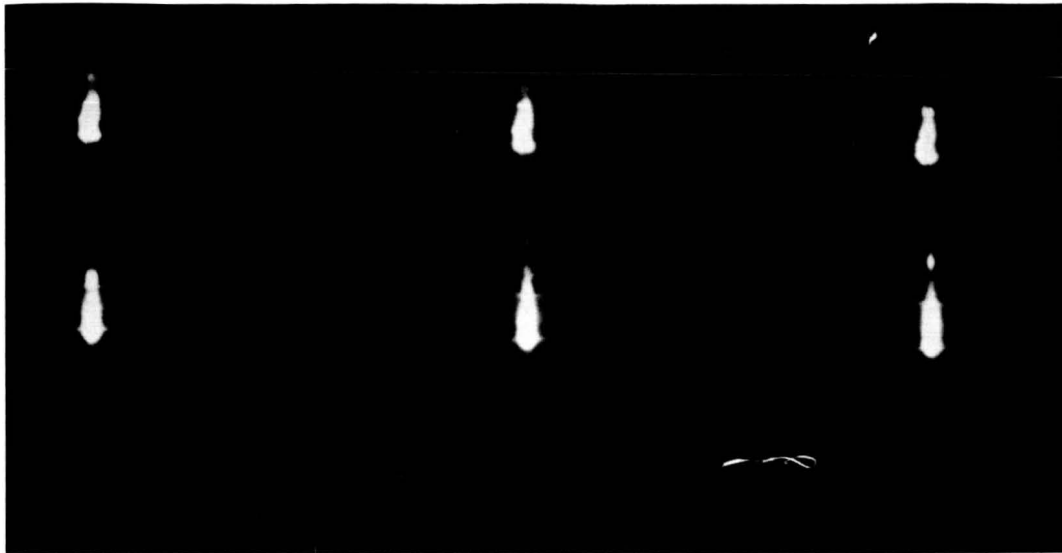
(a)



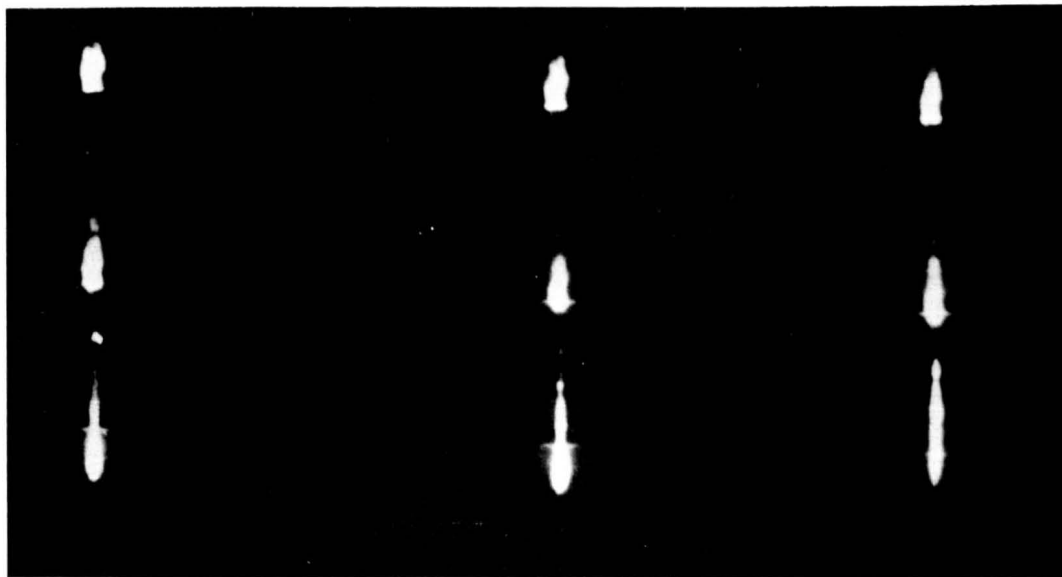
(b)

Figure 4. Multiple Frame Photographs of Laser Produced Plasmas. Air at 1 Atmosphere Pressure.

(a) Exposure: 200 ns; Interframe Delay: 0.5 μ s
(b) Exposure: 100 ns; Interframe Delay: 0.5 μ s



(a)

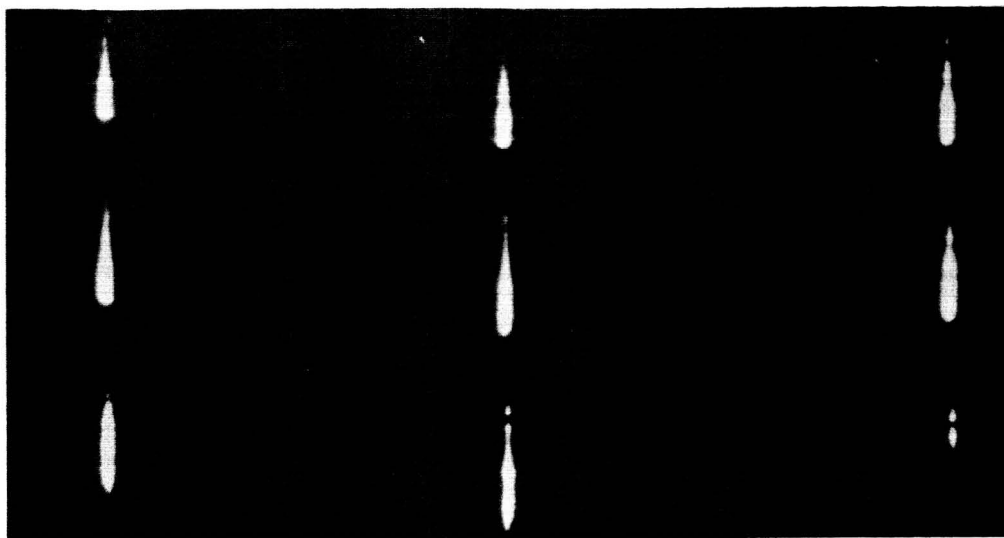


(b)

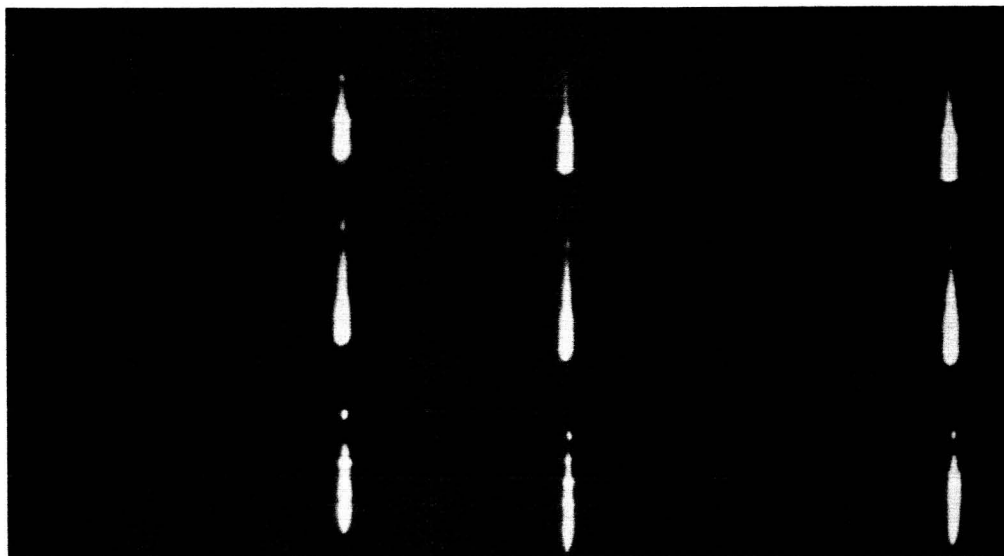
Figure 5. Multiple Frame Photographs of Laser Produced Plasmas. Air at 1 Atmosphere Pressure.

Exposure: 50 ns

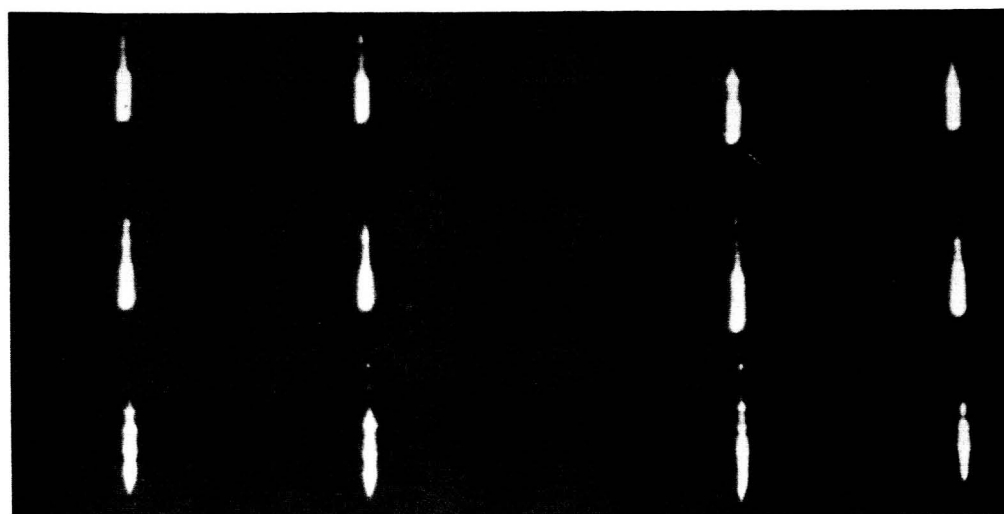
Interframe Delay: 0.5 μ s



(a)



(b)

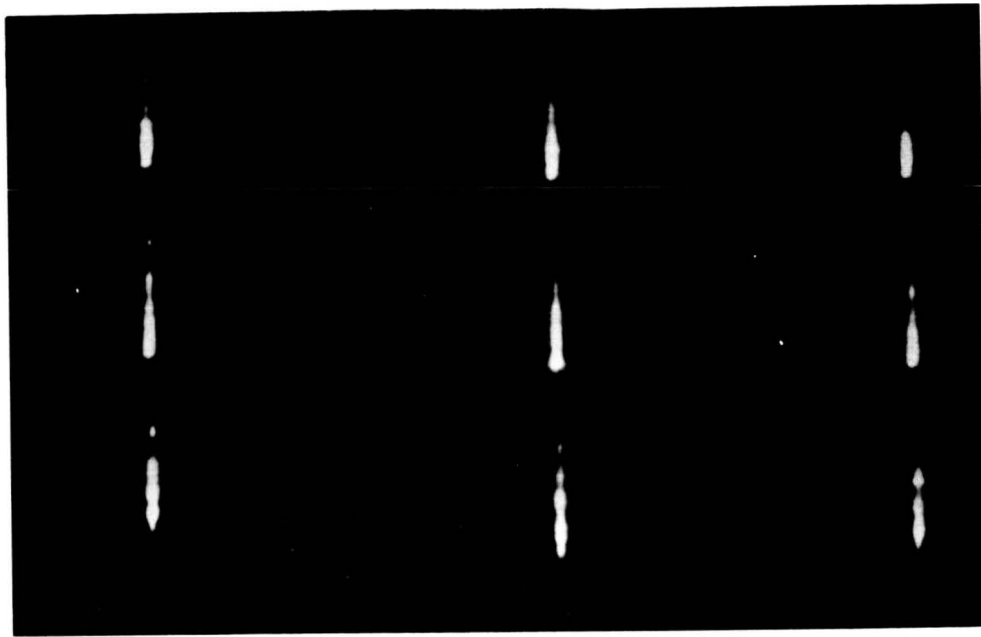


(c)

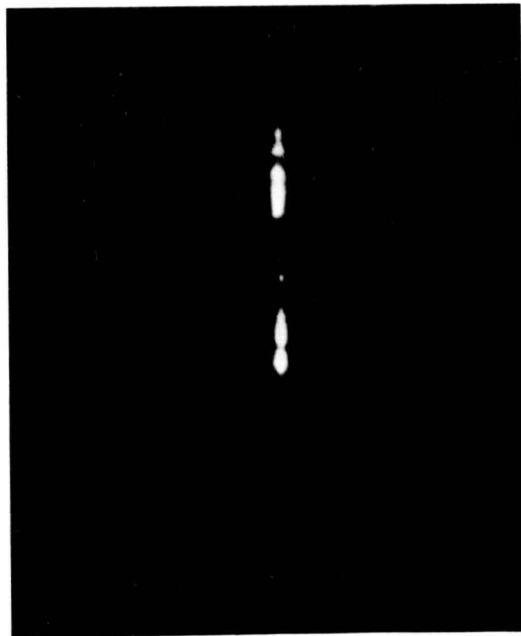
Figure 6. Multiple Frame Photographs of Laser Produced Plasmas. Air at 1 Atmosphere Pressure.

Exposure: 20 ns

Interframe Delay: 50 ns



(a)



(b)

Figure 7. Multiple Frame Photographs of Laser Produced Plasmas. Air at 1 Atmosphere Pressure.

Exposure: 5 ns

Interframe Delay: 50 ns

Figure 8 shows three events having 20 ns exposures at 100 ns interframe delays. These events have been photographed after turning the image through a 90° rotation. The first frame is at the bottom of the picture, the third at the top. The laser source is located to the left and propagates left-to-right. The first frame on the lower left shows an initiation spot to the right extreme with a large separation to a second spot from which the plasma appears to spread irregularly to the left (toward the laser source). The total length of this event is approximately 1.9 cm. Note that the camera aperture terminates the image on the left side for every frame shown in this figure.

Figures 9 & 10 show frames (one to three) for thirteen events using an exposure of 10 ns with an interframe delay of 50 ns. The first frame of the first event (a) in Figure 9 is an extremely early stage development photograph. Noting that the second frame already extends beyond the aperture edge, we can calculate from the expansion of the second spot the average speed of the plasma front. The maximum time between frames would be 60 ns. The total length of the plasma, from first spot to the left edge in frame two is 1.7 cm. The second spot has extended at least 1.4 cm in this time. Thus the average speed must exceed 2.3×10^5 m/s. The remaining events in Figures 9 & 10 show various stages of plasma development. All events have a great deal in common in that each appears to have an initial plasma which is disconnected visually from the following plasma. Considerable structure continues to appear in early time.

Where the initial spot is clear in framing photos, its size appears to never be larger than one millimeter. At times it appears as small as 0.5 mm. The wide plasma glow which appears to move back toward the laser grows to a width of approximately 2 mm in the early times (100 - 150 ns). For the optical geometry chosen the convergence cone of the laser beam after passing through the lens had a half angle of approximately 7°. For the frames shown in Figures 9 & 10, the divergence angle toward the laser source beginning at the initial plasma spot is between 3° and 5° half angle.

Figure 11 shows several very typical streak photographs of the early time plasma formation. All were taken using a total streak time of 200 ns, although each plasma is initiated at a different time following the initiation of the streak. Because of a vertical offset in the image converter orientation, there is an offset to the zero velocity slope on all streak photographs. This has been corrected for in the calculations which were performed to yield velocities.

One can see, particularly in (b) & (c), what appear to be high speed ejections from the already formed plasma front. These ejections, particularly the early time ones, reach speeds of 1.6×10^6 m/s. The speed of the radiating front shows large scale changes several times for each event.

Figures 12 and 13 show streak photographs of fourteen events, all having a 200 ns streak time. The general similarity of all streaks at 200 ns times is excellent. The velocities measured from these images are quite reproducible. The late time velocity approaches 10^4 m/s in all afterglows.

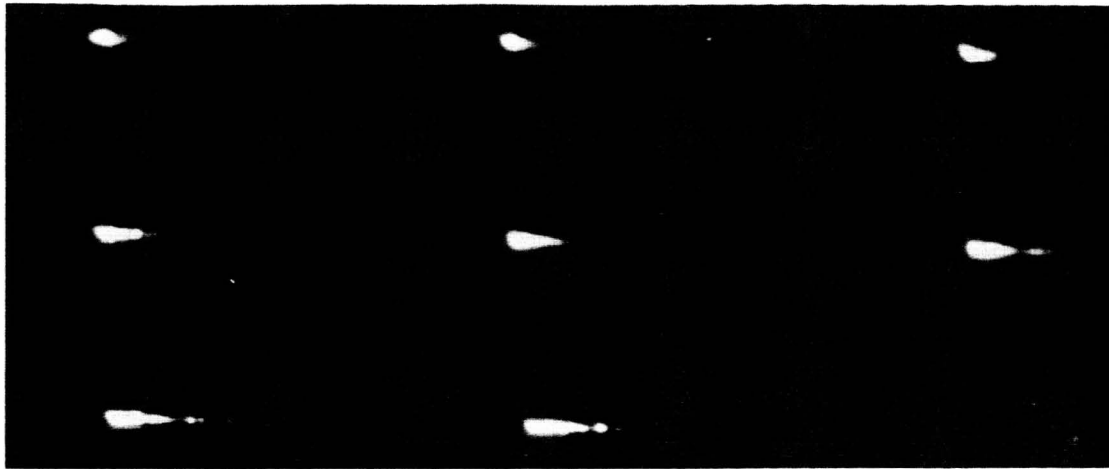


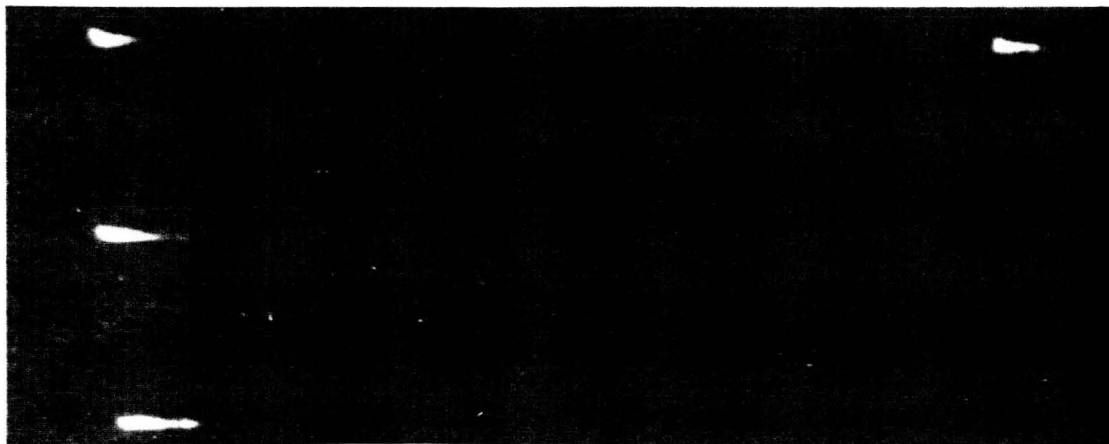
Figure 8. Multiple Frame Photographs of Laser Produced Plasmas. Air at 1 Atmosphere Pressure.

Exposure: 20 ns

Interframe Delay: 100 ns



(a)

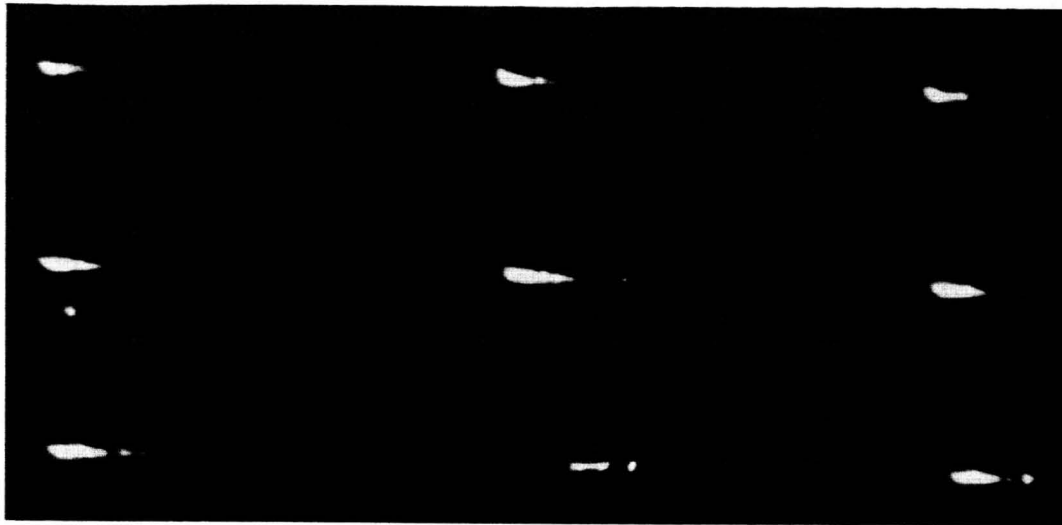


(b)

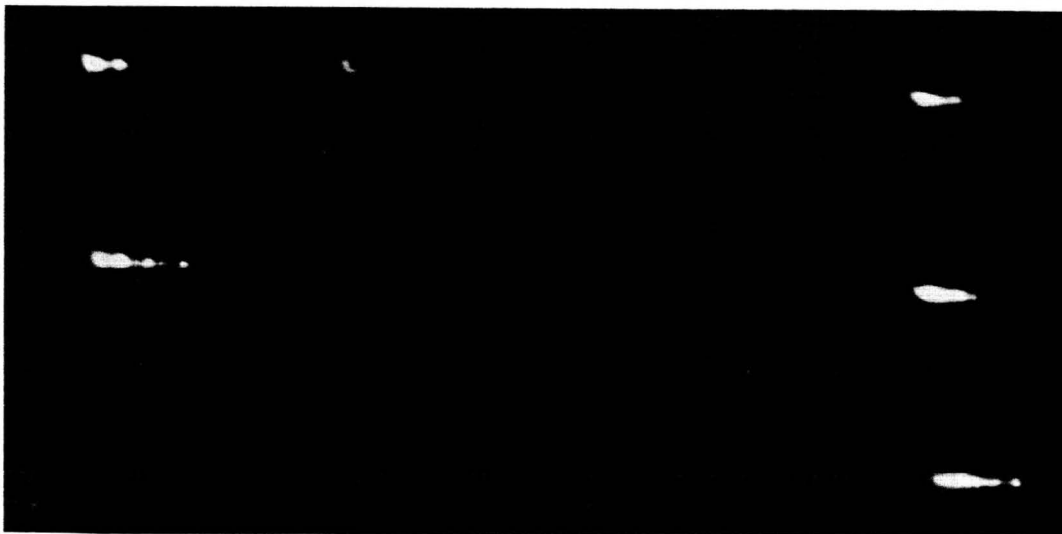
Figure 9. Multiple Frame Photographs of Laser Produced Plasmas. Air at 1 Atmosphere Pressure.

Exposure: 10 ns

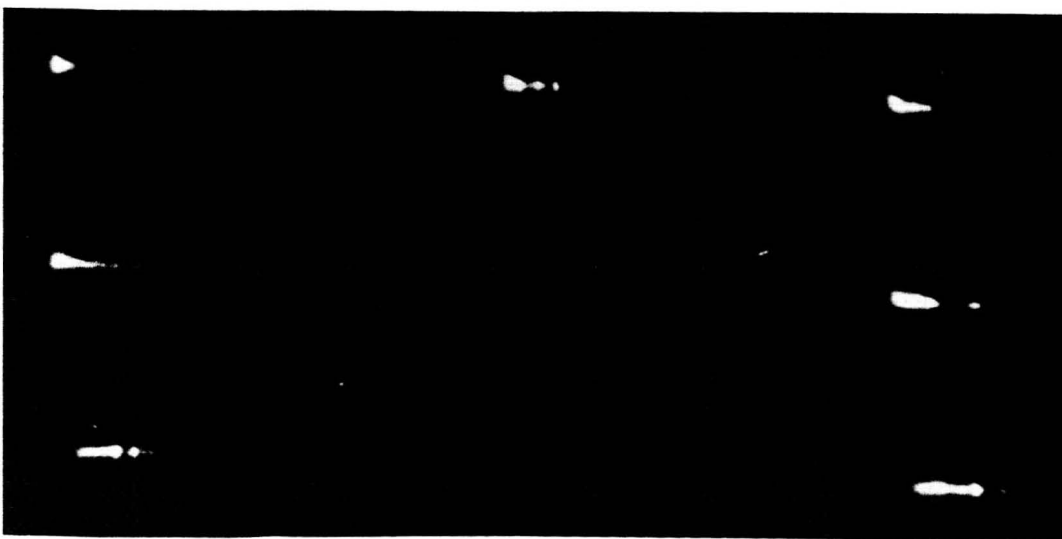
Interframe Delay: 50 ns



(a)



(b)

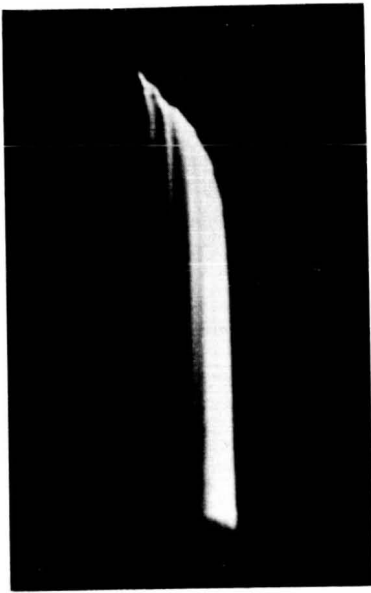


(c)

Figure 10. Multiple Frame Photographs of Laser Produced Plasmas. Air at 1 Atmosphere Pressure.

Exposure: 10 ns

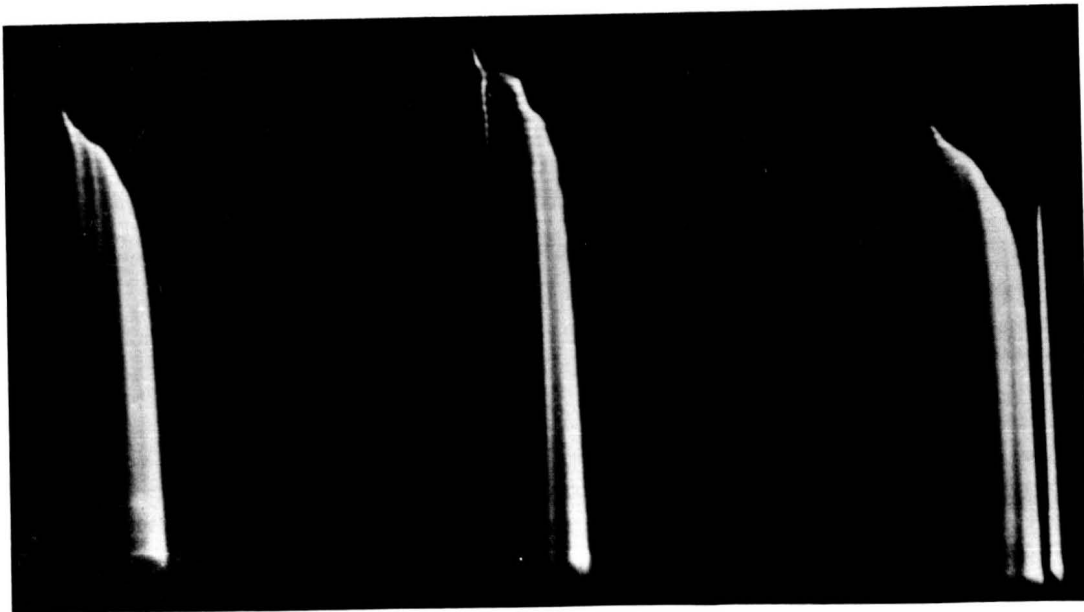
Interframe Delay: 50 ns



(a)

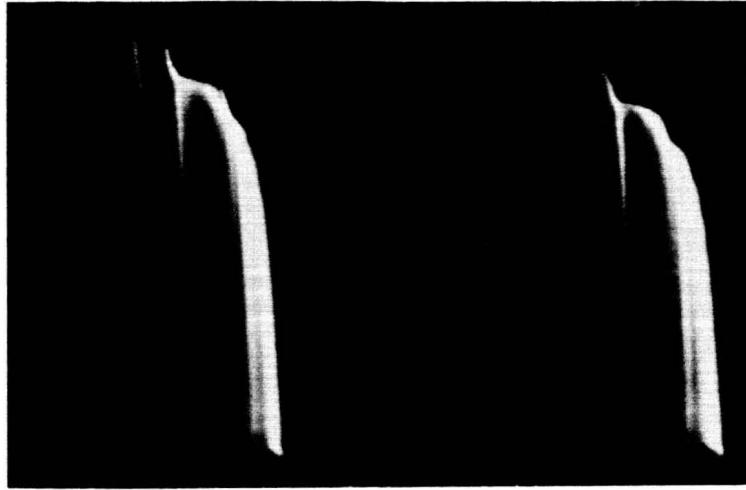


(b)

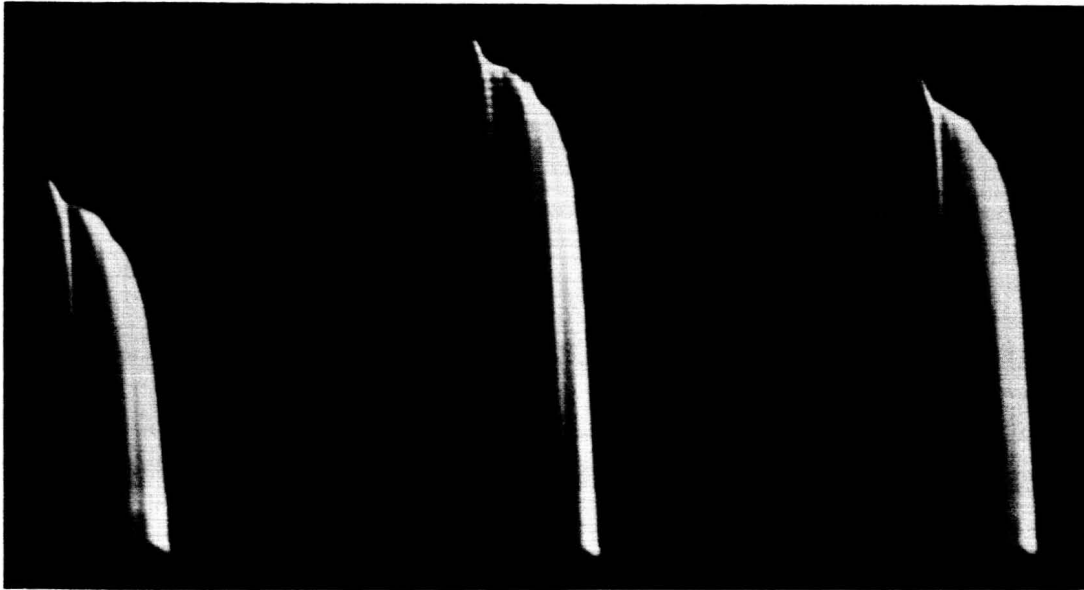


(c)

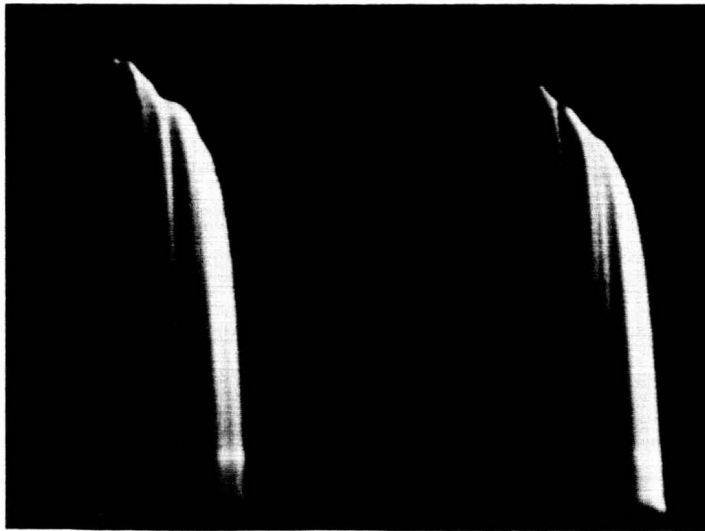
Figure 11. Streak Photographs of Laser Produced Plasmas. Streak Duration: 200 ns. Air at 1 Atmosphere Pressure.



(a)

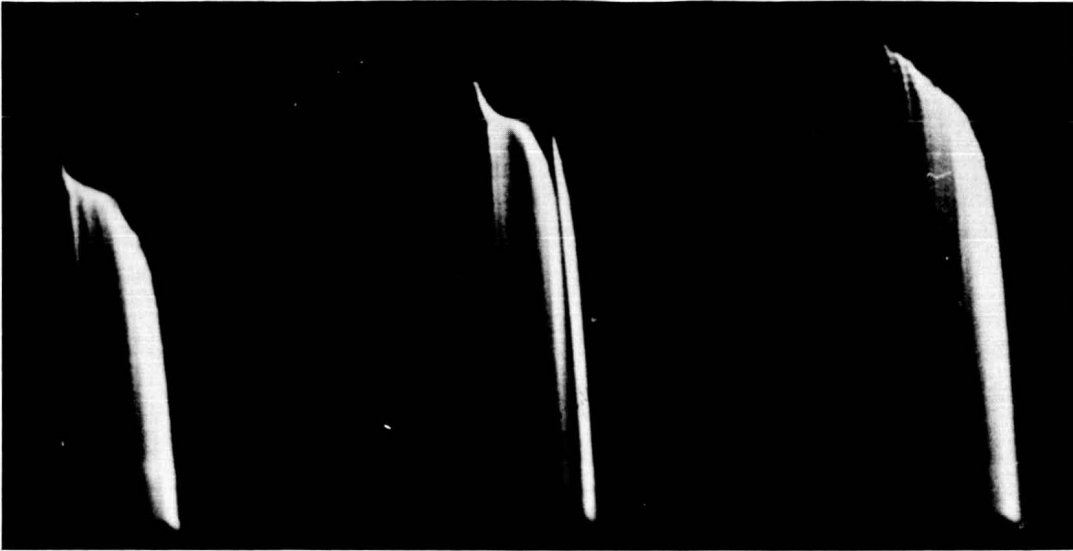


(b)

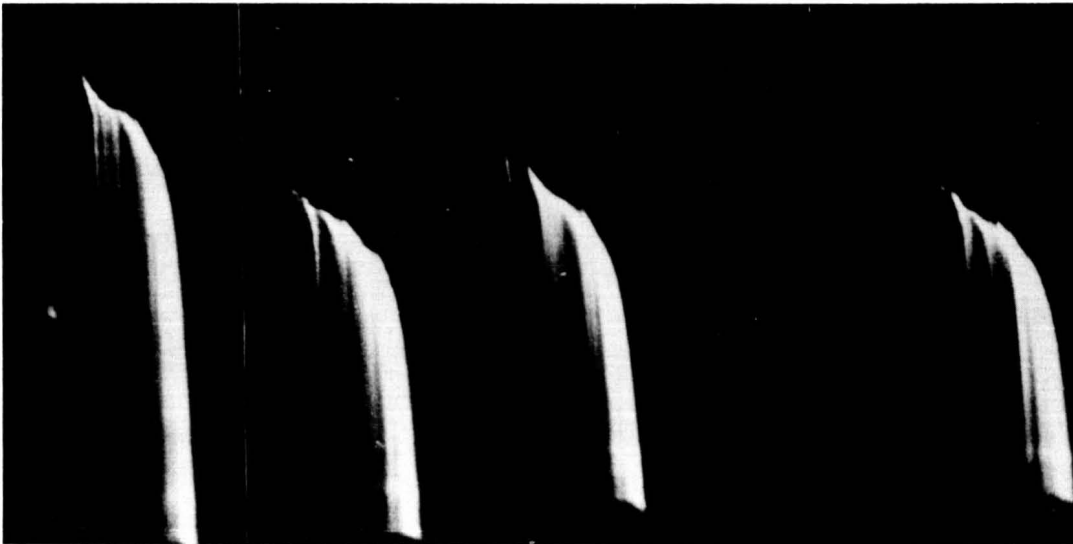


(c)

Figure 12. Streak Photographs of Laser Produced Plasmas. Streak Duration: 200 ns. Air at 1 Atmosphere Pressure.



(a)



(b)

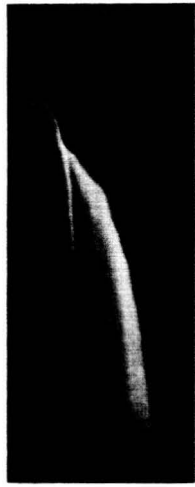
Figure 13. Streak Photographs of Laser Produced Plasmas. Streak Duration: 200 ns. Air at 1 Atmosphere Pressure.

Figures 14 & 15 show thirteen events at streak times of 100 ns. These appear to be two types of structures. One has high speed ejections connecting each portion of the plasma, such as is seen in Figure 14 (a) & (b). Others as seen in Figure 15 show isolated points within the discharge.

To try and obtain better resolution of the streak behavior, streak photographs were taken at 50 ns exposures. These are shown in Figure 16. As can be seen from these images there is considerable structure to the early time plasma. Several separate plasma sources are generated without any apparent physical coupling. The mechanisms involved in the generation of these separate plasmas are not understood at this time.



(a)



(b)



(c)



(d)



(e)



(f)

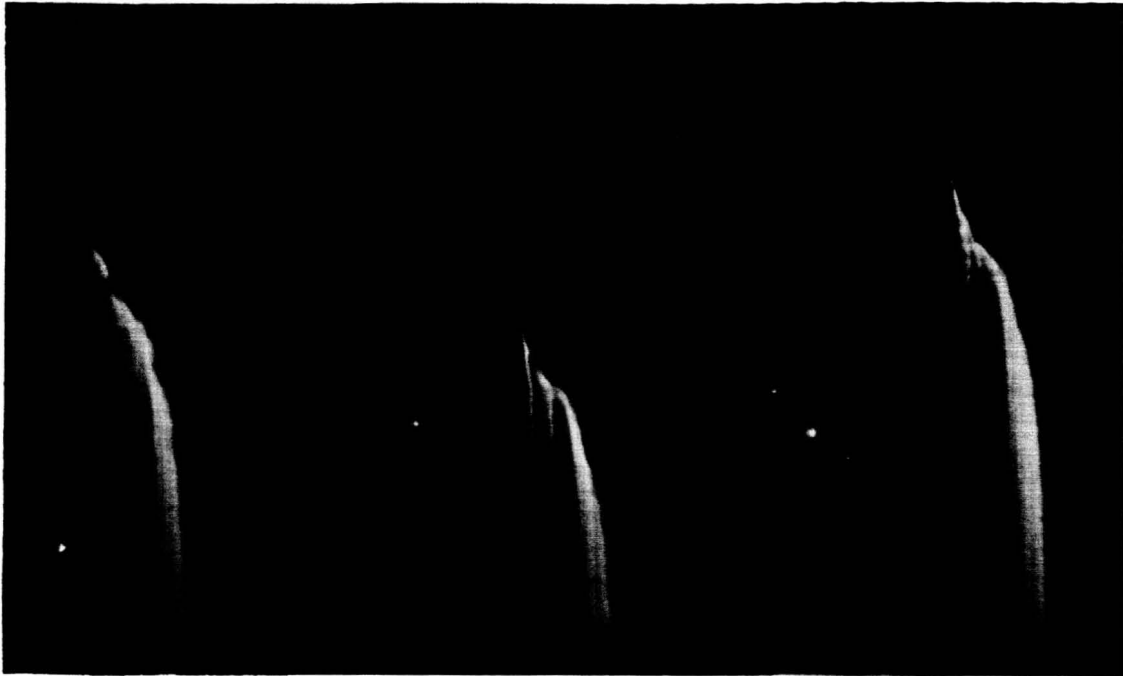


(g)

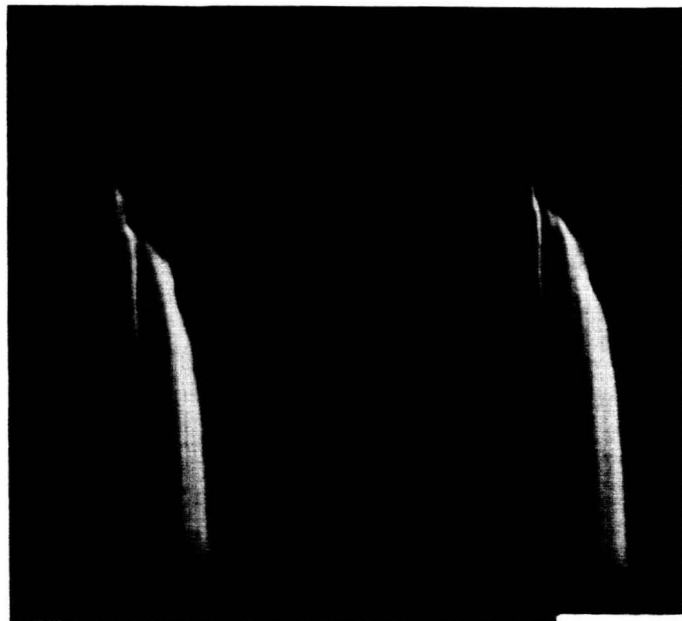


(h)

Figure 14. Streak Photographs of Laser Produced Plasmas. Streak Duration: 100 ns. Air at 1 Atmosphere Pressure.



(a)



(b)

Figure 15. Streak Photographs of Laser Produced Plasmas. Streak Duration: 100 ns.
Air at 1 Atmosphere Pressure.



(a)



(b)



(c)



(d)

Figure 16. Streak Photographs of Laser Produced Plasmas. Streak Duration: 50 ns.
Air at 1 Atmosphere Pressure.

CONCLUSIONS & RECOMMENDATIONS

The apparatus to test and investigate initial spark breakdown phenomena has been assembled and tested. The system has been successfully operated to demonstrate the ability to produce breakdown in air at a predetermined location and to synchronize this event with a high speed image framing and streak camera for both types of operations.

Photographs obtained demonstrate a high degree of reproducibility for plasmas produced by focused laser radiation. The infrastructure of such plasmas has a number of "hot spots" that appear at different points in time following the creation of the first plasma. Earlier image photographs of a plasma similarly produced were reported by Pigott⁽⁷⁾. There is little similarity between the photographs shown here and those of Pigott. The isolated initial spot appears in many of Pigott's photographs. All of his photographs, however, are taken at least one microsecond after plasma initiation. All early time detail has thus been lost.

Streak photographs indicate the presence of high speed ejections from a relatively slow moving front. These ejections are toward the laser source and have speeds up to 1.6×10^6 m/s, whereas the usual speed of propagation of the radiative front is much slower. This value is considerably higher than that reported by Raizer and Kozlov of 1×10^5 m/s. The initial plasma spot never shows a speed in excess of 1×10^4 m/s. Each high speed ejection rapidly (usually in less than 5 ns) slows, soon reaching a somewhat uniform propagation speed of the order of 10^4 m/s. Although we do not observe the total length of the discharge due to aperture cutoff it would appear that the speeds for the plasma front as measured late in time would continue to slow as uniformly as is shown in the streak photographs. This would result in a lifetime for the radiating plasma of the order of 5 μ s, with the plasma having a total length of approximately 5 cm. These numbers are consistent with separate time lapsed photography used to determine the total length, and framing and streak photographs having durations in excess 5 μ s.

Because it was not possible to measure the power levels and energy input to the air, results are only qualitative. To be able to model the phenomena occurring in this plasma, a measure of the energy input as a function of time is necessary. Equipment currently on order will allow for this to be done once in place. In addition, a new chamber facility will be constructed which will allow a view of the entire length of the plasma.

With the new facility and energy measuring equipment the originally conceived program of study over a range of pressures and power levels can be carried out. Because of the consistent shape of the plasma cone produced and the closeness of the cone angle of the converging laser beam to the diverging plasma cone, experiments using lenses of different focal lengths would be desirable.

REFERENCES

1. A. R. Kantrowitz, *J. of Astronautics and Aeronautics*, 9, 34 (1971).
2. D. C. Smith, *J. App. Phys.*, 41, 4501 (1970).
3. N. A. Generalov, V. P. Zimakov, V. A. Masyukov, and Yu. P. Raizer, *Sov. Phys. JETP Lett.* 11, 228 (1970).
4. Yu. P. Raizer, *Sov. Phys. Usp.* 23, 789 (1980).
5. G. I. Kozlov, *Sov. Phys. Tech. Phys.* 24, 37 (1979).
6. N. Kroll and K. M. Watson, *Phys. Rev. A* 5, 1883 (1972).
7. J. C. Pigott, AEDC-TR-71-35, March, 1971.

1982

NASA/ASEE SUMMER FACULTY RESEARCH FELLOWSHIP PROGRAM

KENNEDY SPACE CENTER
THE UNIVERSITY OF ALABAMA

A PRELIMINARY STUDY OF ENVIRONMENTAL
PARAMETERS ASSOCIATED WITH THE FEASIBILITY OF A
POLYGENERATION PLANT AT KENNEDY SPACE CENTER

Prepared By:	Grover D. Barnes, Ph.D.
Academic Rank:	Associate Professor
University and Department:	Jackson State University Department of General Science
NASA/KSC:	
(Directorate)	Design Engineering
(Branch)	Project Engineering Office
KSC Counterpart:	Gary Gutkowski
Date:	August 10, 1982
Contract No.:	NGT-01-002-099 (University of Alabama)

A PRELIMINARY STUDY OF ENVIRONMENTAL PARAMETERS
ASSOCIATED WITH THE FEASIBILITY OF A
POLYGENERATION PLANT AT KENNEDY SPACE CENTER

By

Grover D. Barnes, Ph.D.
Associate Professor of General Science
Jackson State University
Jackson, MS 39217

ABSTRACT

A study is under way to determine the feasibility of a polygeneration plant at Kennedy Space Center. Liquid hydrogen and gaseous nitrogen are the two principal products in consideration.

Environmental parameters (air quality, water quality, biological diversity and hazardous waste disposal) necessary for the feasibility study are being investigated. A National Environmental Policy Act (NEPA) project flow sheet will be formulated for the environmental impact statement. Water quality criteria for Florida waters will be established.

ACKNOWLEDGEMENTS

Special thanks is given to Mr. Gary Gutkowski, my counterpart at KSC, for the fine support given to this participant and to the Polygeneration Team (Walt Feitshans, Frank Howard, Julian King and Larry Manfredi) for their help. I appreciate Mr. Peter Minderman, Director of Design Engineering, asking me to work on the Polygeneration Project.

LIST OF FIGURES

<u>Figure No.</u>	<u>Title</u>	<u>Page</u>
1	A Time Flow Chart for the Environmental Impact Statement (EIS) in a Feasibility Study of a Cogeneration Plant at Kennedy Space Center	VI-8

LIST OF TABLES

<u>Table No.</u>	<u>Title</u>	<u>Page</u>
1	The Criteria of Florida Surface Water Quality in Classified Waters	VI-9

INTRODUCTION

A feasibility study is being done on a polygeneration facility (PF) on the Kennedy Space Center (KSC) in Brevard County, Florida. KSC borders the Indian and Banana Rivers, important estuarine ecosystems.

Extensive surveys for the proposed PF were conducted. Three potential sites have been selected.

The design of the PF facility will utilize a combined cycle coal gasification system to produce 12 tons of liquid hydrogen/day. Best available control technology will be utilized to limit environmental pollution.

The source of make-up water is groundwater from the Florida aquifer or a mixture of groundwater and treated sewage effluent from KSC. If any available technology (Luthy, 1981) is economically feasible, no discharge to surface waters will occur. If wastewater is eliminated, the effluent will be discharged into a turn basin barge canal which empties into the Banana River, a Class III Outstanding Florida Water Stream. Available technology within economic restraints will be utilized to control air pollutant emissions including the removal of sulfur, nitrogen, and particulates.

Outline of the 1982 DOE/ASEE Summer Fellowship Program Objectives

- I. Examine the proposed site for the polygeneration plant
 - A. Order aerial photographs of the proposed area
 - B. Visually examine the site for environmental features: aquatic and terrestrial - especially note endangered and protected species of plants and animals
- II. Attend the short course on ASPEN
- III. Meet key personnel who will be involved in various phases of implementation
- IV. Formulate project environmental flow sheet
- V. Run computer searches for data on air and water pollution produced by polygeneration plants in the following sources: Aquatic Sciences & Fisheries Abstracts, Aqualine, APTIC, CHEM SEARCH, DOE Energy Environmental Biblio, Pollution Abstracts, Water Resources Abstracts, CHEM Industry Notes, and BIOSIS Reviews
- VI. Initiate a draft of the Intent to Prepare a Draft Environmental Impact Statement to include:
 - A. Agency
 - B. Action
 - C. Summary
 1. What the proposed action consists of
 2. Alternatives under consideration
 3. List of significant environmental issues to be analyzed in depth
 4. Description of the scoping process
 5. List of any environmental review and consultation requirements
 6. Expected release date of draft EIS
 7. Discussion of any letter of agreement regarding lead and cooperating agencies

BODY OF REPORT

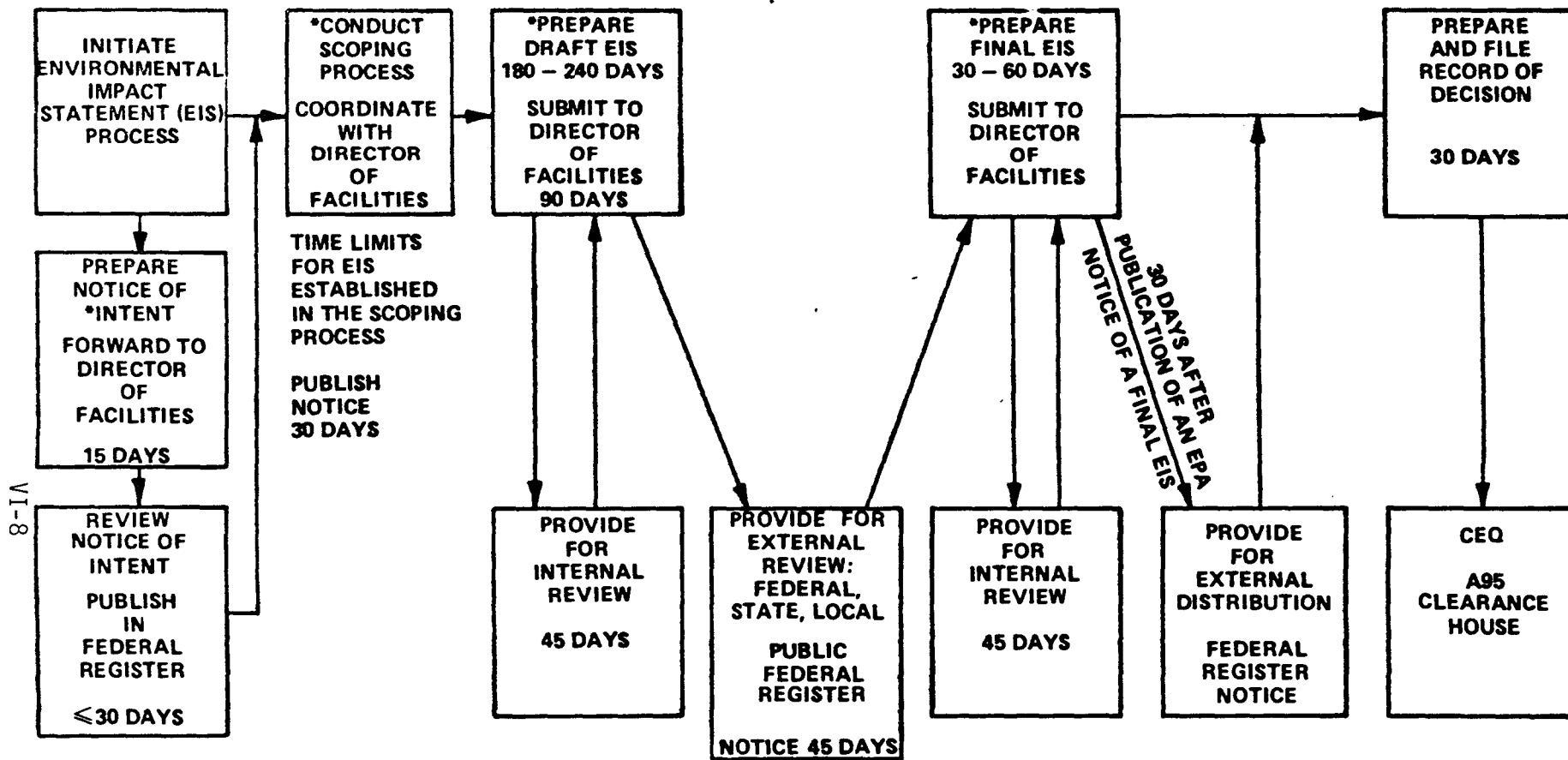
Essentially all of the objectives of the 1982 DOE/ASEE Summer Fellowship Program were done. Aerial photographs were ordered and received.

On two different occasions (22 June and 28 July, 1982), the proposed polygeneration site was observed for endangered and threatened species of plants and animals. Only one threatened species on the Florida State list, the Florida Scrub Jay, was observed. Two jays were seen on the first trip and one on the second trip.

The ASPEN course was conducted from 8 June 1982 to 11 June 1982. This participant attended this course and completed the required assignments.

Various meetings were held to meet individuals involved in various phases of implementation of the polygeneration plan. The following individuals were contacted: Dr. Jim Kanipe, Peggy Hallisey, David Breininger, Dr. Clair Bemiss, David Duns Moor, Bill Brannan, Dr. Al Koller, Bill Knott, Paul Toft, Pablo Auffant and Terry L. Krzywicki.

The polygeneration environmental flow sheet is shown in Figure 1. Computer searches for air and water pollution produced by polygeneration plants were run in the following sources: Water Resources abstracts, DOE Energy, NASA files and Chem Industry Notes. The other sources were not utilized due to cost factors. The criteria of Florida surface water quality is shown in Table I. These criteria are necessary for evaluation of environmental licensing.



* AT EACH MAJOR STEP, MATERIAL WILL BE SUBMITTED TO THE A-95 CLEARING HOUSE. TIME FRAME FOR COMPLETION OF EIS - (540 - 630 DAYS),

Figure 1 - A Time Flow Chart for the Environmental Impact Statement (EIS) in a Feasibility Study of a Cogeneration Plant at Kennedy Space Center

TABLE I

THE CRITERIA OF FLORIDA SURFACE WATER QUALITY IN CLASSIFIED WATERS:

CLASS I-A	Potable Water Supplies - Surface Waters
CLASS I-B	Potable and Agricultural Water Supplies and Storage - Groundwaters
CLASS II	Shellfish Propagation or Harvesting - Surface Waters
CLASS III	Recreation, Propagation and Management of Fish and Wildlife - Surface Waters
CLASS IV	Agricultural Water Supplies - Surface Waters
CLASS V-A	Navigation, Utility and Industrial Use - Surface Waters
CLASS V-B	Freshwater Storage, Utility and Industrial Use - Groundwaters

All Values mg/l Unless Indicated		<u>Surface</u>	<u>Class I-A</u>	<u>Class I-B</u>	<u>Class II</u>	<u>Class III</u>	<u>Class IV</u>	<u>Class V-A</u>
	As	0.05		0.05				
6-IA	BOD	Class Criteria						
	Chlorides	≤ 10% Background						
	Cr	1.0 Total		0.05				
	Cu	0.5	0.03		15.0	15.0		
	Detergents	0.5						
	Fluorides	10.0	1.50	1.50	1.50	5.0		
	Pb	0.05	0.03	0.05		0.03		
	Oils & Greases	5.0						

TABLE I CONTINUED

All Values mg/l Unless Indicated	Surface	Class I-A	Class I-B	Class II	Class III	Class IV	Class V-A
pH	≈ 1.0 unit above or below natural within range: 6.0 - 8.5			≈ 1.0 unit above or below range: 6.5 - 8.5	Same as II	Same as II	5.0 - 9.5 except swamp H ₂ O (down to 4.5)
Phenols	0.001						
01-10 Radioactive (A) radium 226 & 228 (picouries/l)	5.0		5.0				
	(B) Gross alpha particles (picouries/l)	15.0	15.0				
Specific Conductance	Not over 100% Increase in Natural Level						
No Adverse Toxic Substances			X			X	X
No Discharge Resulting in Nuisance Species			X				
Turbidity (Jackson Units)	50.0						

TABLE I CONTINUED

All Values mg/l Unless Indicated	<u>Surface</u>	<u>Class I-A</u>	<u>Class I-B</u>	<u>Class II</u>	<u>Class III</u>	<u>Class IV</u>	<u>Class V-A</u>
Zn	1.0	0.03			0.03		
D.O.		5.0		5.0	5.0	Average 4.0/24 hr Never < 3.0	≥ 2.0
Alkalinity mg/l CaCO ₃		20.0			20.0	600	
NH ₃		0.02			0.02		
Bacteriological Quality/100 ml		1.00		70	200		
Ba		1.00	1.00				
Be		1.10			0.011-1.10	0.10-0.5	
Biological Integrity (Background)		75%		75%	75%		
Cd		0.008-0.012	0.001	0.005	0.005		
Chlorides		250					
Chlorine (Total Residual)		0.01		0.01	0.01		
CN		0.005		0.005	0.005	0.005	0.005

VI-11

TABLE I CONTINUED

	All Values mg/l Unless Indicated						
	<u>Surface</u>	<u>Class I-A</u>	<u>Class I-B</u>	<u>Class II</u>	<u>Class III</u>	<u>Class IV</u>	<u>Class V-A</u>
Dissolved Solids		500					
Fe		0.3		0.3	0.3	1.0	
Hg		0.002	0.002	0.001	0.001	0.002	0.002
Ni		0.1		0.1	0.1	0.1	
NO ₃ (Total N)		10.0	10.0	0.025			
Selenium		0.01	0.01	0.05	0.025		
Ag		0.00007	0.00005		0.00005		
Al				1.5	1.5		
Antimony				0.2	0.2		
Bromine				0.1	0.1		
Bromates				100	100		
Mn					0.1		
P (elemental)				0.0001	0.0001		
Polychlorinated Biphenyls				0.000001	0.000001		
Pb					0.03		
Phthalate esters					0.003		
Boron						0.75	

VI-12

NASA

NOTICE (7 August 1982)

Intent to Prepare a Draft Environmental Impact Statement

AGENCY: National Aeronautics and Space Administrative

ACTION: NOTICE OF INTENT TO PREPARE A DRAFT EIS

SUMMARY:

1. PROPOSED ACTION: A Polygeneration Facility (PF) at Kennedy Space Center (KSC) for producing 12 tons of liquid hydrogen/days and ancillary gaseous nitrogen.

2. ALTERNATIVES UNDER CONSIDERATION:

A. No Action.

With the launch of each shuttle, forty-four trucks are necessary to transport hydrogen from New Orleans, LA, to KSC. Significant increases are expected in transportation costs. The anticipated goal of twenty-four launches will mean that approximately one thousand and fifty-six trucks will be on the road annually with highly explosive materials. This increase in transportation movement increases the statistical chance of accident and public impairment.

With the advent of a petroleum embargo, the possibility exists that no fuel will be available for the hydrogen transportation system. This would preclude shuttle launches and impair national security.

Hydrogen is not the sole product designed by KSC. Nitrogen and electrical generation are additional ancillary products which could be utilized. On-site or near-site generation of hydrogen and other desirable by-products would greatly enhance the feasibility.

B. ACTION

The PF is proposed to be located on/near KSC in Brevard County, FL. The site borders the Indian and Banana Rivers.

Extensive surveys for the proposed PF were conducted. Three potential sites have been selected.

The design of the PF will utilize a combined cycle coal gasification system to produce 12 tons of liquid hydrogen/day. Best available control technology will be used to limit environmental pollution.

The source of the make-up matter is groundwater from the Florida aquifer or a mixture of groundwater and treated sewage effluent from KSC. If any available technology is economically feasible, no discharge into surface waters will occur. If wastewater is eliminated into surface waters, the effluent will be discharged into a turn basin canal which empties into the Banana River, a Class III (outstanding Florida waters) stream. Available technology within economic restraints will be utilized to control air pollutant emissions including the removal of sulfur, nitrogen and particulates.

3. List of Significant Environmental Issues to be Analyzed in Depth in the Draft EIS.

- a. Air quality;
- b. Water quality;
- c. Waste generation, treatment, transportation disposal and storage;
- d. Noise;
- e. Toxic substances
- f. Biotic resources;
- g. Endangered species;
- h. Historical, archaeological and recreational factors;
- i. Wetlands and flood plains;
- j. Economic, population and employment factors, provided they are interrelated with natural or physical environmental factors.

4. DESCRIPTION OF THE SCOPING PROCESS

The proposed schedule for the Polygeneration Facility is as follows:

<u>ACTIVITY</u>	<u>DATE</u>
State/Federal Scoping Meetings	Dec., 1982
Submission of Draft Environmental Impact Statement (EIS)	Sept., 1983
Final EIS	June, 1984
Commence Construction	May, 1985
Operation	Aug., 1987

5. LIST OF ANY ENVIRONMENTAL REVIEW AND CONSULTATION REQUIREMENTS

a. Air monitoring to include ambient air criteria for one year (specific pollutants: sulfur dioxide, ozone, nitrogen dioxide, carbon monoxide, particulates and hydrocarbons). This includes quality assurance monitoring to assess critical environmental parameters for one year near the proposed sites.

b. Phytoplankton and zooplankton sampling for two years to determine ecosystem species diversity and stability of aquatic ecosystems. Bioassays should be conducted to assess possible toxicity of blowdowns at major discharge points in the PF.

c. Hazardous waste disposal and siting must be investigated.

d. Benthic macroinvertebrate sampling surveys should be conducted. Previous data exists which could be utilized in this area.

e. Terrestrial surveys should be correlated with previous studies.

f. Legal assessment and consultation must parallel all environmental work. If legal assistance at local, county, regional and state levels in the environmental areas necessary for the PF is not available or accessible from NASA, then outside legal assistance must be obtained to facilitate legality.

Steps (a), (b) and (d) should be statistically valid.

6. EXPECTED RELEASE DATE OF DRAFT EIS

6 September 1983

7. DISCUSSION OF ANY LETTER OF AGREEMENT REGARDING LEAD AND COOPERATING AGENCIES.

NASA is the initiating agency and there are no cooperating agencies.

8. LOCATION: Kennedy Space Center, Brevard Co., FL 32899

DATE: 7 August 1982

For further information:

Mr. Gary Gutkowski
Polygeneration Project Engineer
DF-PEO
Kennedy Space Center, FL 32899

RESPONSIBLE HEADQUARTERS OFFICIAL:

NASA Headquarters
Attn: NX-2/Gen. Billie J. McGarvey
Washington, D.C. 20546

SIGNATURE: _____

Robert F. Allnutt (Acting)
Associate Administrator for External
Affairs

CONCLUSIONS AND RECOMMENDATIONS

The polygeneration plan appears to be an excellent method for generating liquid hydrogen if environmental control is implemented. Figure 1 should be followed for the development of an environmental impact statement.

Recommendations for the environmental aspects of the EIS include:

a. Air monitoring to include ambient air criteria for one year (specific pollutants: sulfur dioxide, ozone, nitrogen dioxide, carbon monoxide, particulates and hydrocarbons): Quality assurance monitoring to assess critical environmental parameters for one year near the proposed sites.

b. Phytoplankton and zooplankton sampling for two years to determine ecosystem species diversity and stability of aquatic ecosystems. Bioassays should be conducted to assess possible toxicity of blowdowns at major discharge points in the PF.

c. Hazardous waste disposal and siting must be investigated.

d. Benthic macroinvertebrate sampling surveys should be conducted. Previous data exists which could be utilized in this area.

e. Terrestrial surveys should be correlated with previous studies.

f. Legal assessment and consultation must parallel all environmental work. If legal assistance at local, county, regional and state levels in the environmental areas necessary for the PF is not available or accessible from NASA then outside legal assistance must be obtained to facilitate legality.

Steps (a), (b), and (d) should be statistically valid.

REFERENCES

1. Luthy, R. G., "Treatment of Coal Coking and Coal Gasification Wastewaters", Journal of the Water Pollution Control Federation, 53, 3, 325-339.

1982

NASA/ASEE SUMMER FACULTY RESEARCH FELLOWSHIP PROGRAM

MARSHALL SPACE FLIGHT CENTER
THE UNIVERSITY OF ALABAMA

CONTAINERLESS PROCESSING OF Nb-Ge ALLOYS
IN A LONG DROP TUBE

Prepared by:	Robert J. Bayuzick, Ph.D.
Academic Rank:	Professor
University and Department:	Vanderbilt University Department of Mechanical and Materials Engineering
NASA/MSFC: (Laboratory) (Division) (Branch)	Space Sciences Space Processing Solid State
MSFC Counterpart:	M. B. Robinson
Date:	August 12, 1982
Contract No.:	NGT-01-002-099 (University of Alabama)

CONTAINERLESS PROCESSING OF Nb-Ge ALLOYS
IN A LONG DROP TUBE

By

Robert J. Bayuzick, Ph.D.
Professor of Materials Science
Vanderbilt University
Nashville, Tennessee

ABSTRACT

The thirty-two meter drop tube at the Marshall Space Flight Center is being used to study the effect of zero gravity containerless processing on the structure and properties of materials. The concept involves the suppression of heterogeneous nucleation of solid in liquid and, therefore, solidification accompanied by large degrees of undercooling. Under these conditions metastable phases can be formed or, at the very least, unique nonequilibrium microstructures (containing equilibrium phases) with unique properties can be produced.

The drop tube solidification is being applied to niobium base alloys with emphasis on the Nb-Ge binary system in an effort to produce metastable phases with high superconducting transition temperatures in bulk specimens. In the past, only lower Ge alloys (Nb-13 a/o, Nb-18 a/o, and Nb-22 a/o) could be undercooled. However, techniques have now been worked out so that higher Ge alloys (e.g., Nb-25 a/o Ge and Nb-27 a/o Ge) can now be undercooled on a routine basis. Measurement of superconducting transition temperatures and determination of microstructure of the undercooled alloys will now follow.

INTRODUCTION

A potentially useful characteristic of processing materials in space is the capability of containerless solidification. One of the most important aspects of such a process is the elimination of heterogeneous nucleation at container walls thereby resulting in large degrees of undercooling. These large departures from equilibrium can in turn result in the production of unique microstructures and/or metastable phases with unique properties.

Containerless solidification is being studied at the Marshall Space Flight Center through use of drop tubes. A 100 m long tube will soon be available but up until now all the work has been done in a 32 m drop tube (11 cm in diameter). Simply stated, the alloys are electron-beam-melted in vacuum. The molten drops fall off the end of a support wire into the evacuated drop tube and cool by radiation in free fall.

The emphasis of the work has been on Nb-Ge alloys where the motivation is the possible production of metastable phases to give bulk superconductors with high superconducting transition temperatures (T_c). The expectation lies in the fact that the highest T_c measured in any metal or alloy has been in Nb-25 a/o Ge obtained in a thin film by sputtering.⁽¹⁾ The T_c was about 23°K as compared to a T_c of about 7°K in an as-cast alloy of a similar composition. The constituent responsible for the high T_c is the Nb_3Ge compound (A 15 crystal structure) which is unstable with respect to the two phase mixture, β phase plus Nb_5Ge_3 . The β phase is an intermediate solid solution whose Ge-rich limit is about 20 a/o.⁽²⁾ Nb-Ge alloys prepared by other techniques have also exhibited rather high transition temperatures; chemical vapor deposition has resulted in a T_c of 22°K⁽³⁾ and quenching rapidly from the melt has given a T_c of about 17°K.⁽⁴⁾ However, by their very nature these techniques are unable to produce bulk forms. On the other hand it has recently been recognized by Lacy, Rathz and Robinson that high T_c Nb_3Ge in bulk form might be obtainable by drop tube solidification.⁽⁵⁾

Relatively large amounts of undercooling in the drop tube have already been achieved for Nb-18 a/o Ge, Nb-Ge 22 a/o Ge, and in one specimen for Nb-25 a/o Ge. The microstructures developed by the undercooling are unlike arc-melted structures and depend on the rate of quenching at the bottom of the drop tube.⁽⁶⁾ For Nb-18 a/o Ge, dendrites of α (solid solution of Ge in Nb) in a β matrix are seen at a quenching rate of 700°K/sec; when the alloy is splat-cooled at the bottom (for which the quenching rate is orders of magnitude higher), a single phase but highly segregated β is observed. Similarly, for

Nb-22 a/o Ge, a quenching rate of 700°K/sec produces β dendrites with an interdendritic Nb₅Ge₃, but the higher quenching rate of 1700°K/sec gives a segregated single phase β . The Nb-25 a/o Ge alloy also exhibited the segregated single phase β structure when it was splat-cooled at the bottom of the drop tube with large undercooling. It is interesting to note that in each case solidification occurred by impact at the bottom. That is to say, larger degrees of supercooling could be attained in a longer drop tube.

OBJECTIVES

This work is part of a broader cooperative effort that has been underway for about one year and is anticipated to continue. The goals of this effort are:

1. To explore the application of solidifying materials from a deeply undercooled state in order to produce unique microstructures, metastable phases, and amorphous materials.
2. To explore the limitations on undercooling melts in the absence of wall-induced nucleation.

In the narrower context of the work on Nb-Ge in general and of the work connected with the NASA/ASEE program in particular, interest was directed toward developing techniques for undercooling Nb-25 a/o Ge, Nb-27 a/o Ge, and Nb-35 a/o Ge on a routine basis. With respect to the emphasis on producing high T_c alloys, these specific compositions are important. However, with the exception of a single Nb-25 a/o specimen, it has not been possible to undercool these alloys in the past.

NATURE OF EXPERIMENTS

Twenty six different Nb-Ge specimens were dropped during the course of the project. These are tabulated in Table 1 where it can be seen that the breakdown is twelve Nb-25 a/o Ge specimens, eleven Nb-27 a/o Ge specimens, and three Nb-35 a/o Ge specimens.

Slices were hung on a support-wire in an electron beam furnace at the top of the 32 m drop tube. Based on previous experience, a starting mass of 70 mg was chosen. The primary requirement for the choice is the ability to radiate enough heat from the molten drop so as to achieve about 300°C or more undercooling upon arrival at the bottom of the tube. Having chosen the sample size, a support-wire diameter of 5 mils was selected. The basic criteria for this selection is the balance of forces due to surface tension (between the molten alloy drop and the wire) with the forces due to gravity; again the particular choice was based largely on experience. Nb was selected

initially as the support-wire material to minimize contamination by a third element and because its melting point was much higher than the alloy liquidus lines (for example about 600°C higher in the case of Nb-27 a/o Ge).

No undercooling was obtained with the initial configuration. The reason for the failure was clear on microscopic examination. First, it was seen that the Nb support-wire had been partially dissolved. Second, the final drop contained Nb₅Ge₃ in the same morphology as the beginning slice. These observations in conjunction with the realizations that the microstructure of the beginning slice is β plus Nb₅Ge₃, that dissolution of Nb₅Ge₃ in liquid is rather slow, and that Nb₅Ge₃ melts about 280°C higher than β (2180°C versus 1900°C) explains the result. Namely, the Nb₅Ge₃ remains solid while the β melts into a liquid matrix and the Nb support-wire dissolves in the liquid matrix down to a diameter such that gravity forces exceed surface tension forces. The "mushy" drop with solid Nb₅Ge₃ then falls down the tube and the Nb₅Ge₃ causes solidification by heterogeneous nucleation without large undercooling. As shown in Table 1, four more drops with the Nb support-wire were attempted. In these cases the drop mass was reduced to lessen the effect of gravity. The idea was simply to accept some Nb dissolution but to enhance overheating with the smaller mass such that the Nb₅Ge₃ phase would melt. None of these attempts succeeded and the concept was abandoned.

The support-wire was then changed to 5 mil diameter W and, as shown in Table 1, large degrees of undercooling occurred frequently in alloys of the 25 a/o Ge and 27 a/o Ge compositions. Note however that undercooling could not be obtained in the three 35 a/o Ge specimens. In the successful drops dissolution of the support-wire was still evident under microscopic examination but the rate was slow enough to allow sufficient overheating to melt the Nb₅Ge₃. The Nb-35 a/o Ge alloy simply contains a much larger fraction (about 80%) of the high melting Nb₅Ge₃ constituent.

In an effort to minimize W contamination of the 25 a/o and 27 a/o Ge alloys and to increase the undercooling by reducing overheating, 3 mil diameter W wire was tested. This size wire proved to be unfeasible. Lighter drops tended to travel up the wire under the influence of surface tension forces. Slightly heavier drops tended to drop before the Nb₅Ge melted completely.

Table 1 shows another significant characteristic of the experiments. As determined by weight change measurements of the drops and the support-wires, the compositions of the alloys are modified by the process. There is considerable Ge loss by evaporation during melting and, as previously mentioned, addition of support-wire material by dissolution. The Ge content can be decreased by as much as 6 a/o and as much as 1 a/o W can be added.

CONCLUSIONS AND RECOMMENDATIONS

Undercooling of high Ge alloys can be obtained in the 32 m drop tube by electron beam melting. The successful technique involves the use of a 5 mil diameter W support-wire. However, the alloy compositions are modified by the loss of Ge by evaporation and the addition of W by dissolution. Furthermore, solidification is ultimately caused by impact of the drop at the bottom of the drop tube. While not previously mentioned, solidification by impact results in disintegration of the specimen and therefore follow-up analytical work is extremely difficult if not impossible.

The limit of processing of Nb-Ge alloys by electron beam melting in the 32 m drop tube appears to have been reached. Further improvements will necessitate the incorporation of levitation melting. Under these conditions, contamination by the support-wire will be eliminated. In addition, as opposed to the vacuum of electron beam melting, an inert gas atmosphere can be used in the drop tube to accentuate heat removal from the drop. Also, some of the overheating necessary to melt all constituents can be eliminated by simply turning down the power slightly in the melter while continuing levitation of the drop. Both conditions will increase the degree of undercooling in the drop tube and therefore enhance solidification before impact.

Still further improvements in the research will result by application of the 100 m drop tube that is now in the final stages of completion. The longer drop tube with the slightly longer free fall time offers promise even under electron beam melting. However, as is already planned, the ultimate combination would involve the 100 m drop tube with levitation melting. Once this arrangement is in place, experiments will quickly follow.

REFERENCES

1. L. R. Testardi, J. H. Wernick and W. A. Rayer, *Solid State Commun.* 15, 1, 1974.
2. J. L. Jorda, R. Flukiger and J. Muller, *J. of Less-Common Metals*, 62, 25, 1978.
3. J. R. Gavaler, M. A. Janocko, A. I. Braginski and G. W. Roland, *IEEE Trans. on Magnetics*, Mag 13, 192, 1975.
4. B. T. Matthias, T. H. Geballe, R. H. Willens, E. Corenzwit and G. W. Hull, Jr., *Phys. Rev.* 139 A 1501, 1965.
5. L. L. Lacy, T. J. Rathz and M. B. Robinson, *Space Sciences Laboratory Preprint Series No. 81-107*, 1981; to be published in *J. Appl. Phys.*
6. L. L. Lacy, M. B. Robinson, T. J. Rathz, N. D. Evans and R. J. Bayuzick, Proceedings of Symposium on Materials Processing Research in The Reduced Gravity Environment of Space, Elsevier Publishing Co., New York, N.Y., 1982.

TABLE 1. Drop Tube Data for Nb-Ge Alloys

Drop Tube No.	Initial Composition, a/o Ge	Support Wire	Overheating, °C	Undercooling, °C	Change in Composition, a/o
253	25	5 mil Nb	--	None	-2 a/o Ge
254	27	"	153	"	-1.3 a/o Ge
255	25	"	125	"	-0.8 a/o Ge
256	27	"	163	"	-2.4 a/o Ge
257	25	"	118	"	-2.5 a/o Ge
258	27	5 mil W	229	301	
259	25	"	252	288	
260	27	"	240	280	
261	25	"	259	271	
262	27	"	191	279	
263	27	"	198	None	
264	25	"	191	289	
265	25	"	276	264	
266	27	"	--	None	
267	27	"	--	"	
270	25	3 mil W	149	"	
271	25	"	--	"	-3.7 a/o Ge; + 1 a/o
272	27	"	--	"	-6.3 a/o Ge; + 0.4 a/o
273	27	"	--	"	
274	25	"	--	"	
275	25	5 mil W	--	"	
276	27	"	--	280	
277	25	"	--	None	
278	35	"	--	"	
279	35	"	--	"	
281	35	"	--	"	

1982

NASA/ASEE SUMMER FACULTY RESEARCH FELLOWSHIP PROGRAM

MARSHALL SPACE FLIGHT CENTER
THE UNIVERSITY OF ALABAMA

THEORETICAL MODEL OF THE EFFECT OF CRACK TIP BLUNTING
ON THE ULTIMATE TENSILE STRENGTH OF WELDS IN 2219-T87 ALUMINUM

Prepared By:	Robert J. Beil, Ph.D.
Academic Rank:	Associate Professor
University and Department:	Vanderbilt University Department of Civil and Environmental Engineering
NASA/MSFC:	
Laboratory:	Materials and Processes
Division:	Process Engineering
Branch:	Metals Processes
NASA Counterpart:	Arthur C. Nunes, Jr., Ph.D.
Date:	August 6, 1982
Contract No.:	NASA-NGT-01-002-099 (University of Alabama)

ACKNOWLEDGEMENTS

My thanks to Dr. Bob Barfield, University of Alabama, and Mr. Marion I. Kent for their dedication to the continuing excellence of the NASA/ASEE Summer Faculty Research Fellowship Program. My special appreciation, for the second summer, goes to Dr. A. C. Nunes, Jr. who continues to provide interesting problems and devotes much of his time to discussions of the research completed.

My thanks also go to those whose professional expertise provided information concerning the microstructure of the material investigated, James Coston, scanning electron microscopy, Alice M. Dorries, electron microprobe analyses, and Michael Gant, metallography.

I particularly thank Doris Flowers who generously agreed to type this paper and that of last summer, happily and patiently.

THEORETICAL MODEL OF THE EFFECT OF CRACK TIP BLUNTING
ON THE ULTIMATE TENSILE STRENGTH OF WELDS IN 2219-T87 ALUMINUM

By

Robert J. Beil
Associate Professor of Engineering Mechanics
Vanderbilt University
Nashville, Tennessee

ABSTRACT

A theoretical model representing blunting of a crack tip radius through diffusion of vacancies is presented. The model serves as the basis for a computer program which calculates changes, due to successive weld heat passes, in the ultimate tensile strength of 2219-T87 aluminum. In order for the model to yield changes of the same order in the ultimate tensile strength as that observed experimentally, a crack tip radius of the order of .001 microns is required. Such sharp cracks could arise in the fusion zone of a weld from shrinkage cavities or decohered phase boundaries between dendrites and the eutectic phase, or, possibly, from plastic deformation due to thermal stresses encountered during the welding process.

Microstructural observations up to X2000 (resolution of about .1 micron) did not, in the fusion zone, show structural details which changed significantly under the influence of a heat pass, with the exception of possible small changes in the configuration of the interdendritic eutectic and in porosity build-up in the remelt zone.

INTRODUCTION

The ultimate strength for a variable polarity plasma arc butt weld in 3/8-inch plate of 2219-T87 aluminum has been found¹, by experiment, to increase when additional weld heat passes at lower power are made over the weld. Weld heat passes follow the same path as the original weld, but re-melt only a portion of the cast material in the fusion zone as shown in Figure 1a, b, c, d. Yield stress has been found to decrease during the same experimental procedure. The magnitude of these changes, obtained from tensile tests, is shown in Figure 2¹.

This paper presents a theoretical model which indicates that, in the critical region where fracture tends to propagate, coarsening of crack tip radii by a diffusion process which takes place during weld heat passes is feasible and can contribute to increase in ultimate tensile strength.

Characteristics of the physical process of fracture, especially in aluminum, have been studied, using the kinetic theory of materials, for over twenty years. Two review articles^{2,3} describe work at the A.F. Ioffe Physico-Technical Institute USSR Academy of Sciences, Leningrad, where over one hundred materials were tested, by 1970, for confirmation of the applicability of kinetic theory to the failure process. Materials tested included both metal and non-metallic materials, single and polycrystalline materials, alloys, composites, and polymers. By 1980, there, the fracture process during creep tensile tests for aluminum had, through the use of relative density measurements accurate to 10^{-5} , through the use of electron microscopy, x-ray diffraction, et. al., been shown to include, at fracture, large numbers of sub-microscopic discontinuities ($>10^7/\text{cm}^3$) of length less than one-half micron and large numbers of microscopic discontinuities ($>10^6/\text{cm}^3$) of length greater than 1/2 micron in the lateral surface of the test specimen⁴. Creep tests⁵, were performed on polycrystalline aluminum (99.96%) in the temperature range 18-300°C and stress range 1-7 kg/mm². Specimens were loaded for different times and then unloaded to study the build-up kinetics of microdiscontinuities. Researchers at AFIPTI report that rupture during creep develops from "atomic" cracks which arise after the application of the load, grow rapidly, become blunted, and may even change into stable void-shaped discontinuities not larger than 1 μm by the end of the first stage. The mechanism for crack blunting, the mechanism for variations in microcrack concentration in the volume and in surface layers⁶, and the mechanism for coalescence of cracks and voids is a diffusion process most probably involving the emission of vacancies from breaks in continuity to sinks⁷. This paper restricts discussion to the role that diffusion of vacancies might have in blunting of crack tip radii. The reader is referred to related papers⁸⁻¹⁴ which discuss the role of dislocations, the role of original microporosity, and the role of hydrostatic pressure in fracture kinetics which also contain materials which supports the feasibility of the process considered in this paper.

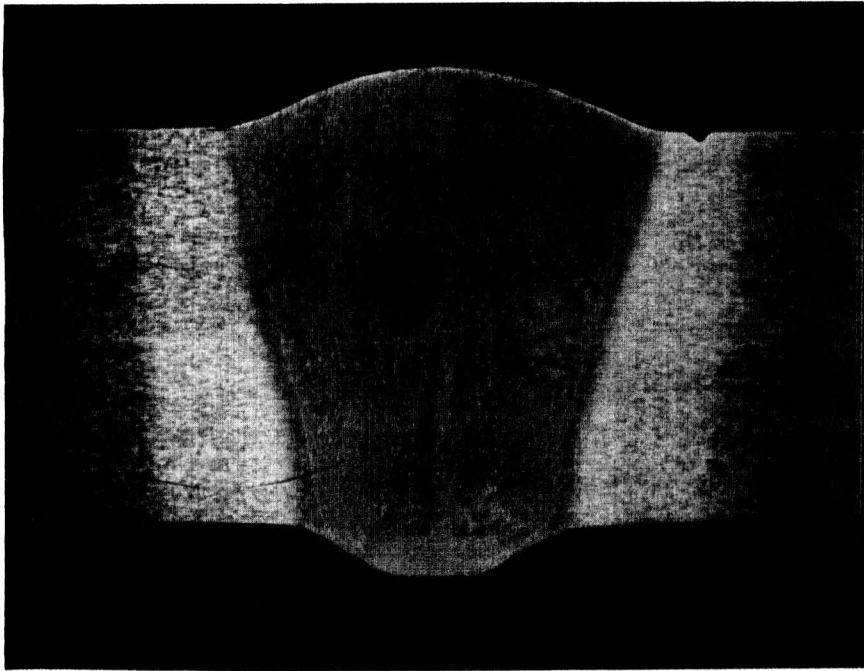


Figure 1a. Initial Weld Cross-
Section. Current= 190 amps.,
Voltage= 31 volts, Weld Speed=7.3ipm
1/16 dia. 2319 wire feed= 60 ipm/
Plate Thickness= 3/8 in.

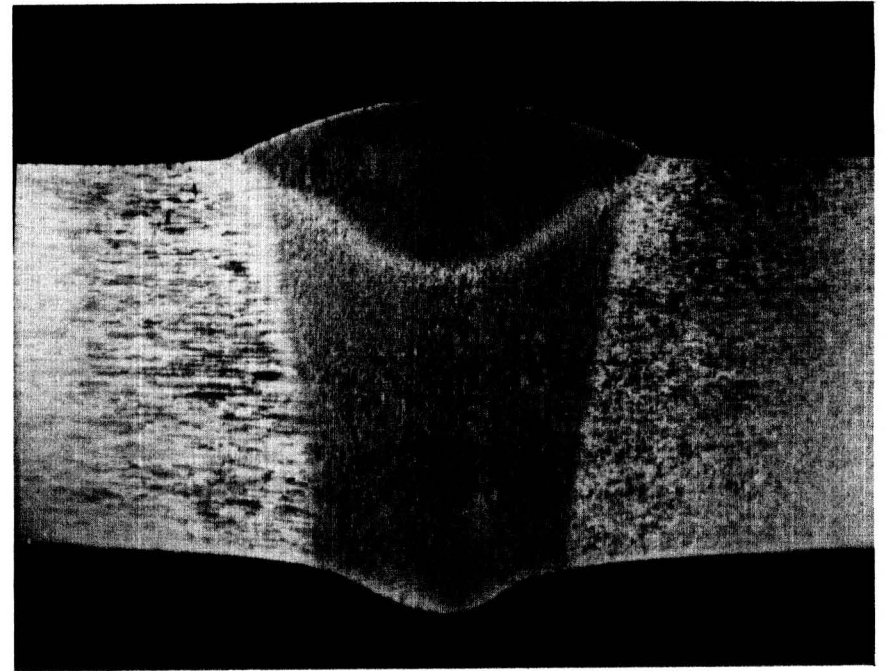


Figure 1b. First Weld Heat Pass
Cross-Section.
Current = 175 amps.
Voltage = 28 volts
Weld Pass Speed = 9 ipm.
No Wire Feed

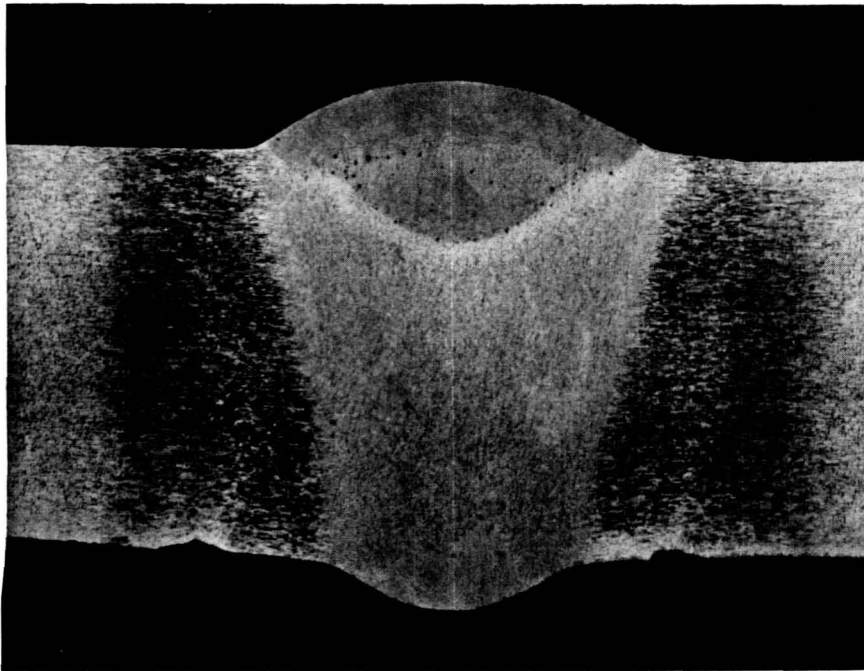


Figure 1c. Second Weld Heat Pass
Cross-Section.
Current= 175 amps.
Voltage= 28 volts
Weld Pass Speed= 9 ipm.
No Wire Feed

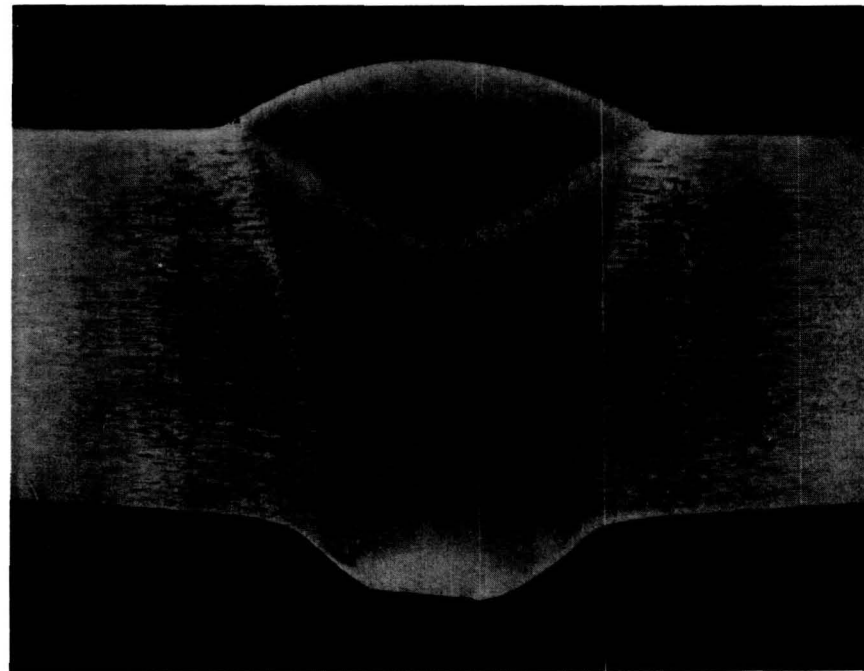


Figure 1d. Third Weld Heat Pass
Cross-Section.
Current= 175 amps.
Voltage= 28 volts
Weld Pass Speed= 9 ipm.
No Wire Feed

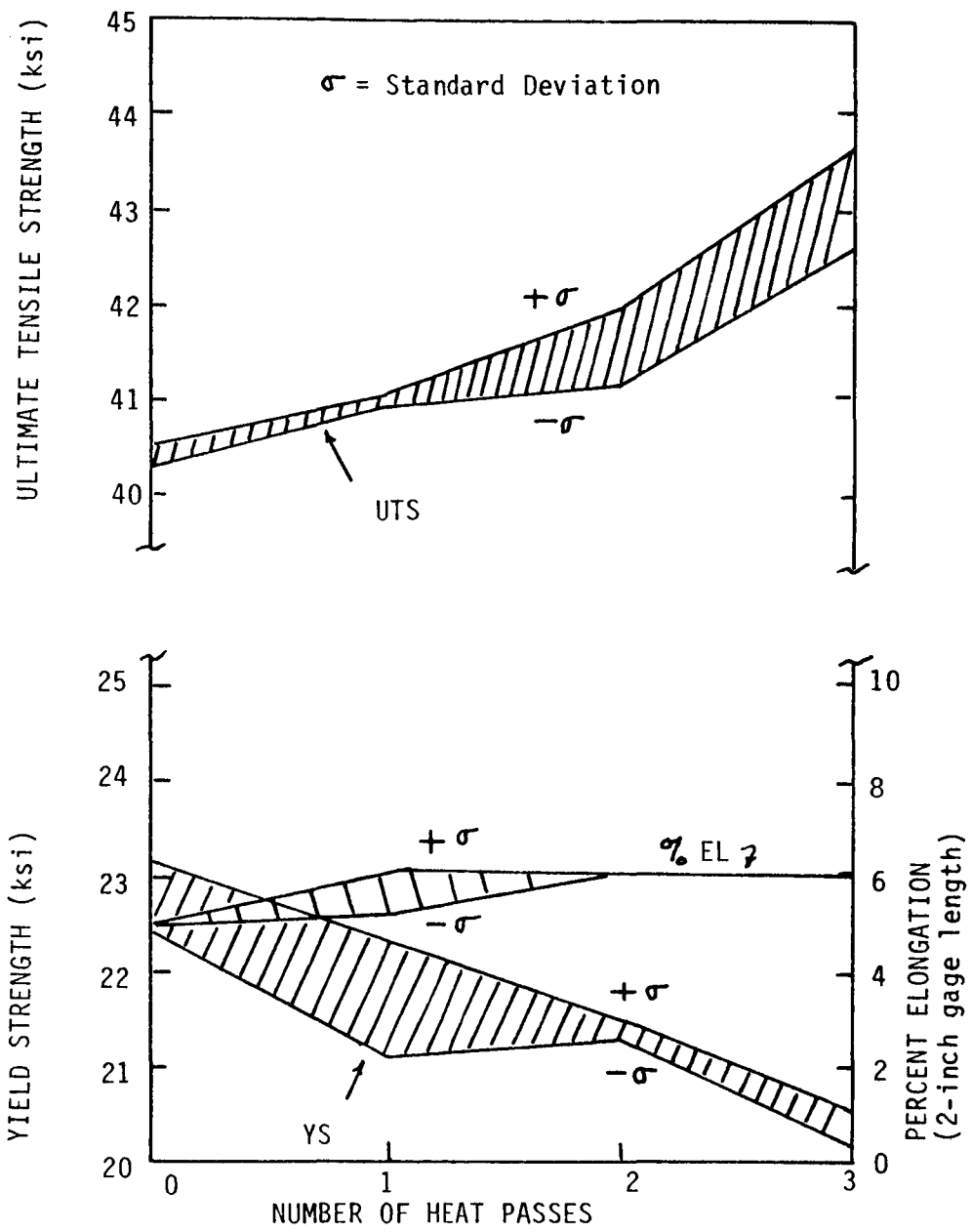


Figure 2. Effect of Multiple Heat Passes on the Strength of a Variable Polarity Plasma Arc Butt Weld in 3/8-inch 2219-T87 Aluminum Plate.

THEORETICAL MODEL

If the local temperature is high enough at a crack tip where the radius of curvature is small and the vacancy concentration is high, vacancies will diffuse to volumes of lower vacancy concentration. They may migrate through the bulk material to other voids or to flat surfaces. It is assumed that the elliptical crack considered is fairly flat at the ends of its minor axis so that vacancies will not need to travel further than half the crack length. The diffusion process increases the radius of the crack tip (blunting or coarsening). It is assumed that the vacancy flow will have little effect on the relatively flat portion of the crack. The diffusion concept is used in Appendix A to develop the differential equation

$$\frac{d\sigma_u}{\sigma_u} = \frac{\Omega(\pi-\alpha)c_0(e^{\frac{\gamma\Omega}{kTR}} - 1) D_s}{4R^2 [\tan(\frac{\pi-\alpha}{2}) - (\frac{\pi-\alpha}{2})] \ln \frac{L}{R}} dt$$

where σ_u is the local ultimate stress

α is the coarsening angle formed by tangents drawn to the assumed circular crack tip

c_0 is the equilibrium concentration of vacancies at the local temperature

T is the local temperature

R is the crack tip radius

D_s is the self diffusion coefficient of aluminum

t is the time

Ω is the atomic volume of fcc aluminum

L is half the crack length

γ is the surface energy of fcc aluminum.

The above formula, the following differential equation, also derived in Appendix A,

$$\frac{d\sigma_u}{\sigma_u} = \frac{dR}{2R} ,$$

and a record of the history of the local temperature during the diffusion process¹⁸ form a system of equations which through iterative calculations determine the local ultimate strength and crack tip radius as a function of time.

CALCULATIONS

Estimate of $\alpha/2$

If a line is drawn tangent to the ellipse shown in Figure 3, then

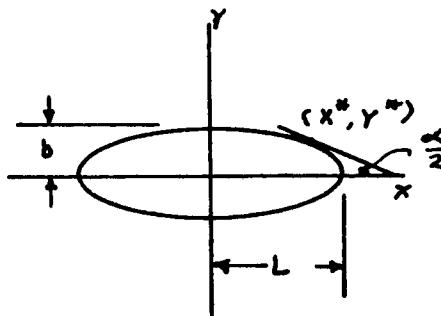


FIGURE 3

Assuming that $b \approx y^*$ and that L is much larger than the radius, R , of curvature of the ellipse at the point $(L, 0)$, so that

$$L \approx x^* \text{ and } R \approx b, \text{ then}$$

$$\text{TAN } \alpha/2 = R/L$$

Calculation of Atomic Volume

The lattice parameter for fcc aluminum is $4.04(10^{-8})\text{cm}$. Hence, the cell volume is $65.94(10^{-24})\text{cm}^3$ which accommodates four atoms. Thus the atomic volume is $16.48(10^{-24})\text{cm}^3/\text{atom}$.

The Self-Diffusion Coefficient, Surface Energy, and Equilibrium Vacancy Concentration

Volin and Balluffi¹⁶ determined, as a consequence of study of the annealing kinetics of voids in aluminum, that the self diffusion coefficient of aluminum was

$$D_s = .176 \text{ Exp } (-1.31 \text{ eV}/kT) \text{ cm}^2 \text{ S}^{-1}$$

in the temperature range $85\text{-}209^\circ\text{C}$, which satisfactorily agreed with the work of Lundy and Murdock, and which agrees satisfactorily with the work by Bass describing the formation and motion energies of vacancies in aluminum¹⁷. The surface energy of aluminum is taken as $1500 \text{ ergs}/\text{cm}^2$ as in the paper by Volin and Balluffi even though calculations suggest that the figure might be slightly lower.

Bass lists the formation energy of a vacancy in aluminum as $.76 \pm 0.02 \text{ eV}$ and the equilibrium vacancy in aluminum as

$$C = C_0 \text{ EXP } (.76 \pm .02 \text{ eV}/kT)$$

where $C_0 = 10^{24} / 16.48 \text{ cm}^{-3} = 6.066 (10^{22}) \text{ cm}^{-3}$
 $k = \text{Boltzmann's constant} = 8.611 (10^{-5}) \text{ eV}/^\circ\text{K}$

and T is the temperature in degrees Kelvin.

Temperature History

The Portion of the computer program which calculates the local temperature as a function of time was developed by Dr. A. C. Nunes, Jr. using a moving point source along with a moving line source to model the heat input. Non-conductive heat losses can be adjusted so that the width of the remelt zone of the fusion zone can be matched.

Five points equally spaced along a line from the edge of the crown to the edge of the root on the opposite side of the fusion zone, as shown in Figure 4, were chosen as local points for calculation. Tensile test specimens show that fracture tends to occur along that line. Point A was taken to be just outside the remelt zone. The computer model for calculating temperature predicted temperatures too high at Point B when non-conductive losses were used to match the width of the remelt zones shown in Figure 1. Hence, higher non-conductive losses were assumed so that the calculated width of the remelt zone was reduced. For the newly calculated remelt zone, the circular part of the remelt zone was slightly larger, but still circular, and the shortest distance of the remelt zone from Point B remained the same. Temperatures for Points B, C, D, and E were calculated using the adjusted parameters. It is felt that this correction gave realistic results for the temperature distribution.

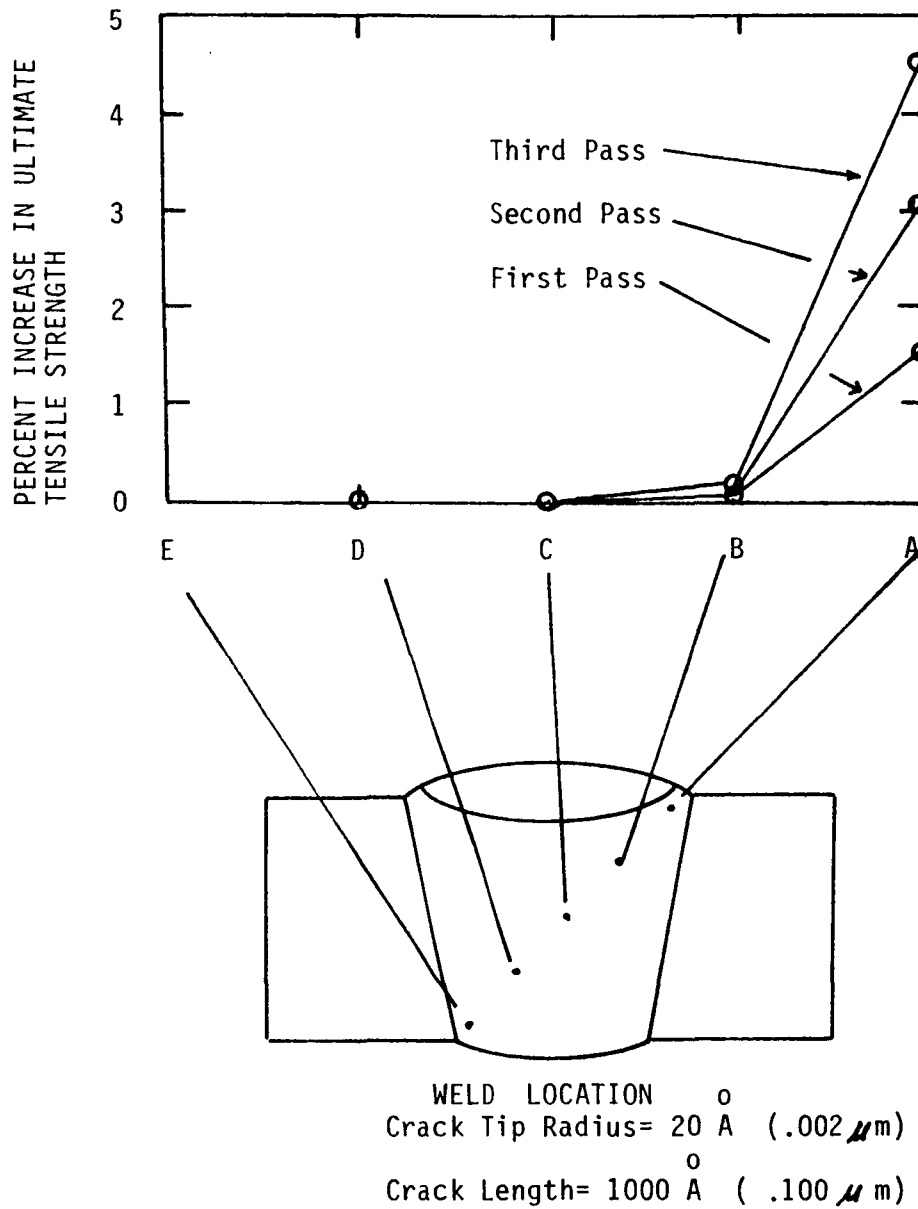


Figure 4. Calculated Effect of Heat Pass on Local Ultimate Tensile Strengths Within the Primary Fusion Zone of a Variable Polarity Plasma Arc Butt Weld in 3/8-inch 2219-T87 Aluminum Plate

DISCUSSION

The amount of coarsening of the crack tip radius and the resulting change in ultimate strength during a weld heat pass is particularly sensitive to

- * the sharpness of the crack tip and,
- * the shape and magnitude of the local temperature versus time curve.

Significant coarsening occurs, due to short heating times, only above temperatures of approximately 650°K or 680°K for crack tip radii of 10\AA or 50\AA respectively. Hence, significant improvement in local ultimate tensile strength takes place at only Points A, B, and possibly C of Figure 4.

The local ultimate tensile strength of Points A, B, C, D and E are not likely to be identical immediately after the initial weld since the cooling rate is different for each of those points. This non-homogeneity does not complicate calculations since the configuration of the system of equations to be used and the iterative process used produce the relative change in ultimate tensile strength. Figure 4 illustrates the percentage relative change at the various points for a crack tip of 20\AA , about four times the lattice dimension of fcc aluminum. The relationship of these changes to changes in ultimate strength observed experimentally is shown in Figure 5, where only the increase in the local ultimate strength at Point A matched the observed values. The 20\AA initial crack tip radius, which provides significant increase in local ultimate tensile strength, is of a size large enough to be observed by the transmission microscope. Preliminary, but extensive, scanning electron microscopy was utilized at powers up to 2000X with good resolution to observe the microstructure of the weld cross section. Micrographs representing the general areas near Points A, B, C, D and E are shown in Figures 6a, b, c, d, and e for a cross section of the fusion zone on a specimen not subjected to weld heat passes. Obviously, 2000X is not enough magnification to see the thin sharp cracks pertinent to this discussion. Replication techniques will permit use of the transmission microscope, which can yield the desired magnification. The micrographs do reveal the dendritic structure in the cast material and the interdendritic eutectic which is a mixture of CuAl_2 and α -aluminum. Microprobe analysis also reveals that a copper depleted zone occurs next to the eutectic similar to those mentioned by Doig and Edington.¹⁹ One can realistically surmise that at the edge of the crown of the weld, where Point A is taken, and where the interdendritic eutectic appears normal to the surface of test specimen, see Figure 6a, cracks of submicroscopic dimensions may initiate in the copper depleted zone after welding. Coarsening of the crack tip radii of these types of cracks, large numbers of which may form during plastic flow prior to fracture under tensile loading, may contribute to the increase in ultimate tensile strength.

It appears, however, that the increase in ultimate strength may be due to more than one mechanism. Ultimate tensile strength increases whether or not the remelt zone overlaps the crown "corner" of the weld or previous weld pass. Hence, refinement of the dendritic structure in the remelt zone, due to more rapid cooling because of lower power, may also contribute to increase in ultimate strength. Further, reconfiguration of the interdendritic eutectic, possibly diffusing into the copper depleted zone or reforming through self diffusion, a slight variation noted in the micrograph study, may play a role in the process.

Coarsening of crack tip radii, then, represents a feasible, but still not certain, or partial explanation, of multiple heat pass strengthening. The process itself is of sufficient practical importance, in fracture mechanics, to be worth investigation in its own right. Although progress has been made, further work is still necessary to pin down the mechanism of multiple heat pass strengthening.

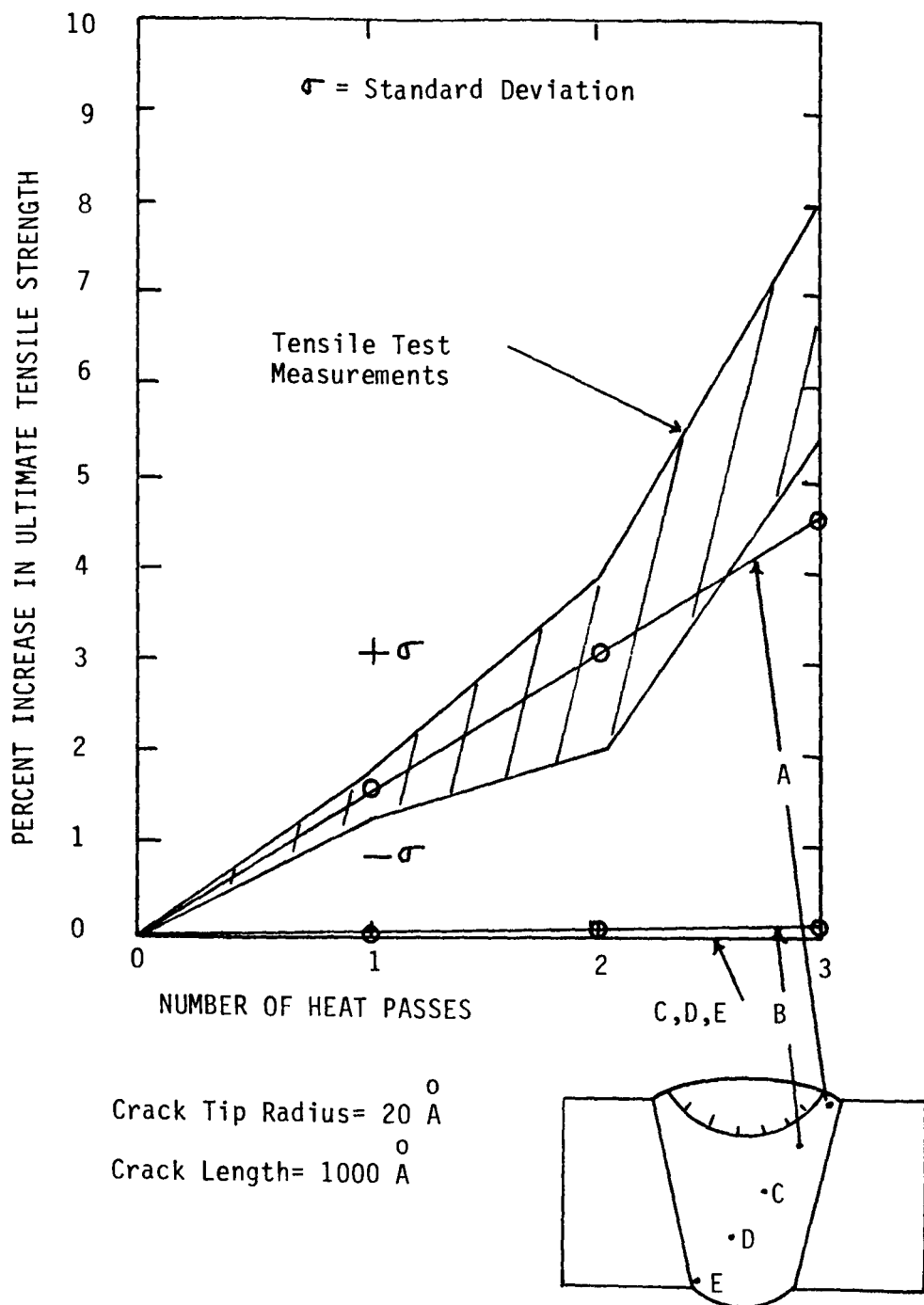


Figure 5. Calculated Effect of Heat Passes on Local Ultimate Tensile Strengths Within the Primary Fusion Zone of a Variable Polarity Plasma Arc Butt Weld in 3/8-inch 2219-T87 Aluminum Plate.

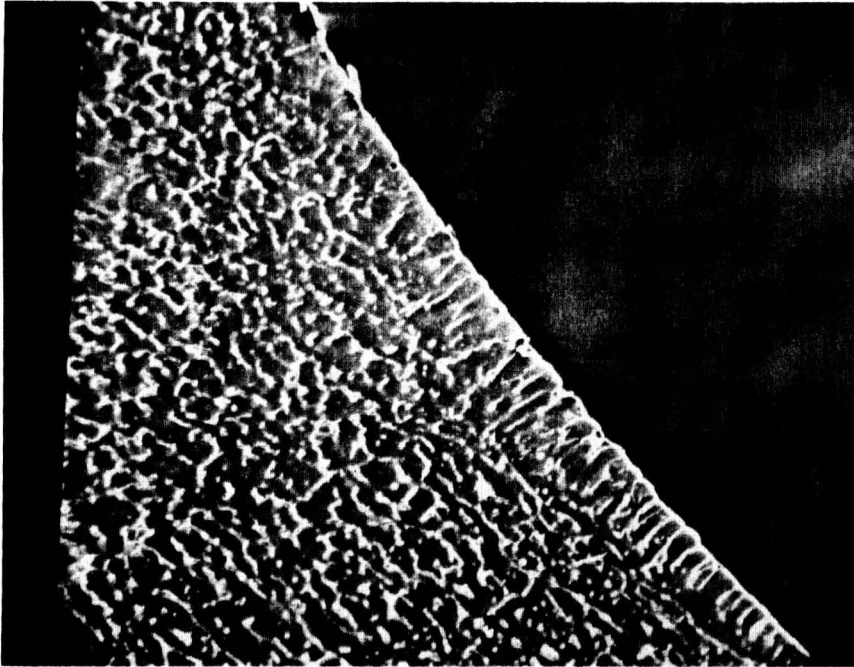


Figure 6a. Point A, Initial Weld.
200X
Alumina Polish
Keller's Etch

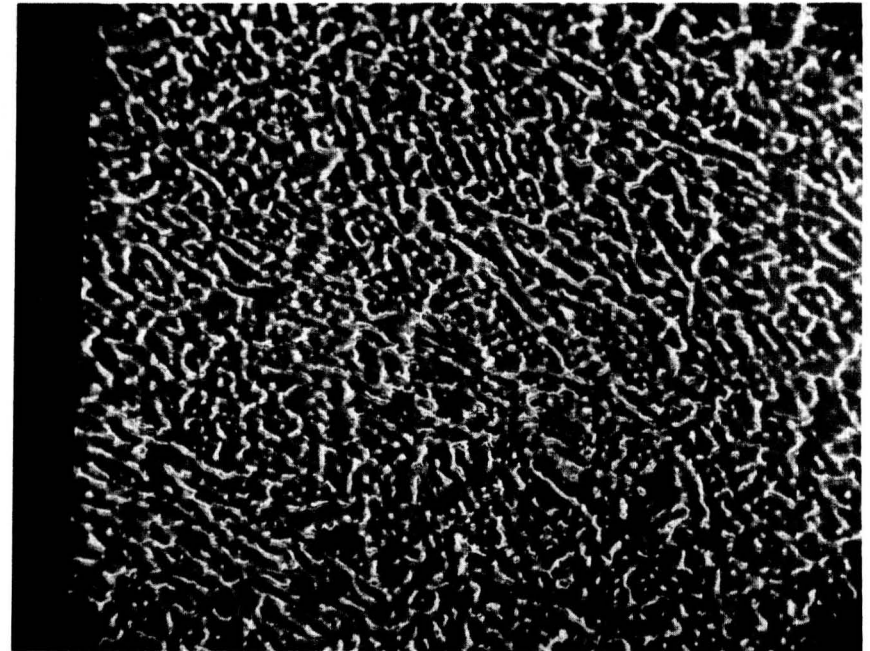


Figure 6b. Point B, Initial Weld.
200X
Alumina Polish
Keller's Etch

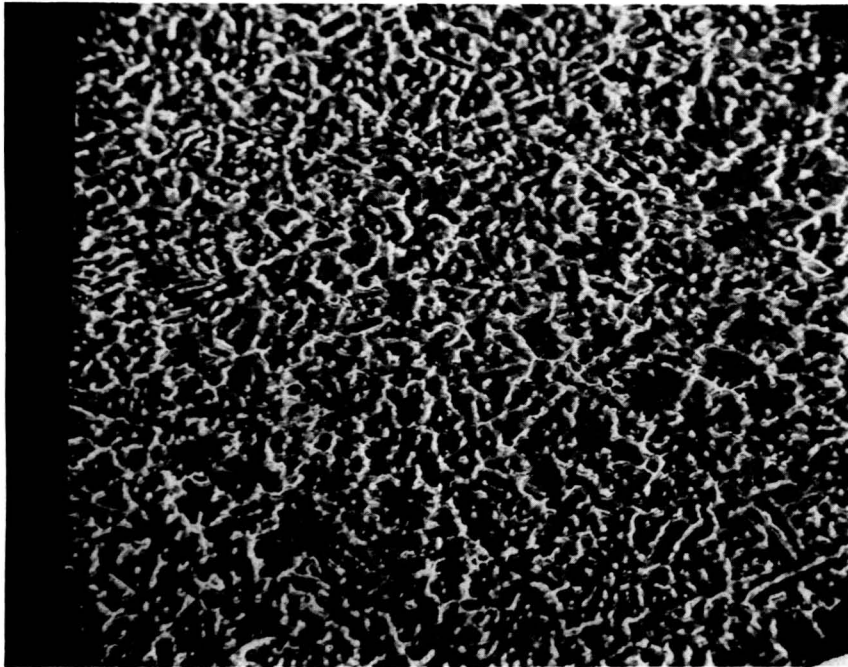


Figure 6c. Point C, Initial Weld
200X
Alumina Polish
Keller's Etch

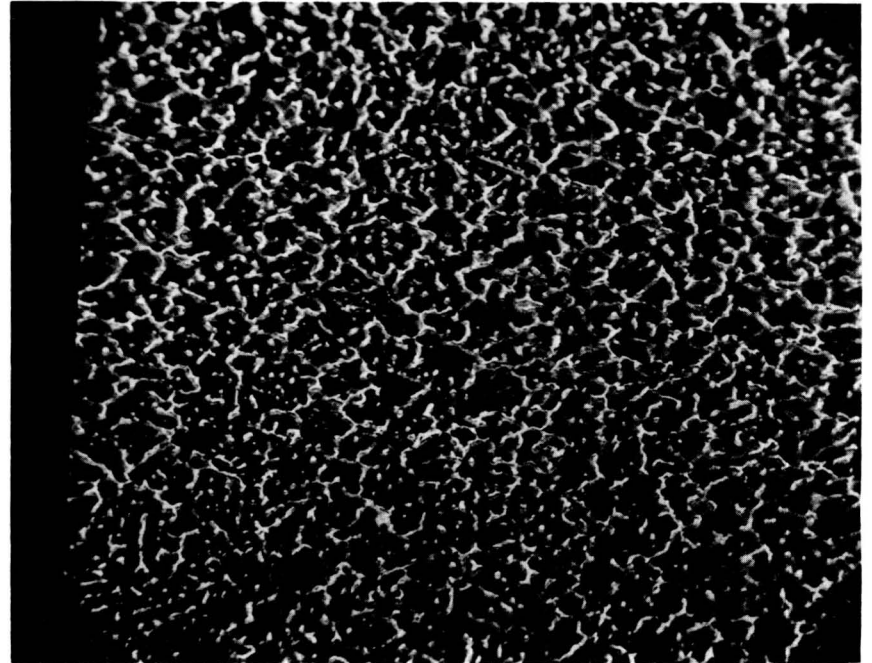


Figure 6d. Point D, Initial Weld.
200X
Alumina Polish
Keller's Etch

VIII-17

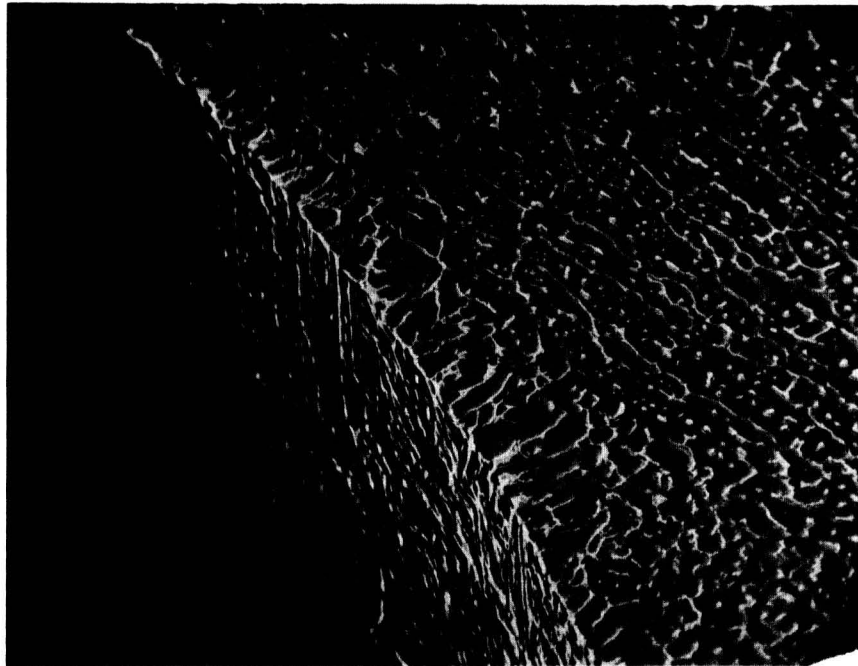


Figure 6e. Point E, Initial Weld.
200X
Alumina Polish
Keller's Etch

RECOMMENDATIONS

The following proposed theoretical and experimental research will help in identifying those processes which characterize fracture and increase ultimate strength in welded 2219-T87 aluminum.

- *...to better understand the fracture process. Proposed experimental research should include microscopic examination, both low power, SEM, and replication TEM, of cross sections of the weld of tensile tested specimens. Test specimens should be loaded to a particular stress, held at that stress for a period of time, unloaded, and examined. This test procedure may allow identification of critical areas where cracks nucleate and characterize the growth pattern to failure.
- *...establish a more accurate method to determine the local temperature history. Higher order multipoles could improve the present technique. Finite element methods, allowing a variable thermal conductivity throughout the material, have been formulated for solution of boundary value and initial value problems to determine local temperature history such as needed in the paper. Since microstructural processes are so sensitive to local temperature history, computer software should be obtained, if it exists, or developed to determine local temperatures more accurately. Some measurements needed just to set up analyses such as loss parameters are not known. However, checks against the program could be verification by thermocouple readings near the weld and the pattern of the remelt zone after weld heat passes.
- *...to understand the effect of a refined dendritic pattern in the remelt zone after weld heat passes. A theoretical and experimental study should be made of the relationship of the size of the dendritic structure with respect to ultimate stress. The size of the dendritic structure can be varied by varying the weld parameters of weld heat passes or by varying the quenching rate of the material during welding or weld heat passes.

*...to better understand the role of the inter-dendritic eutectic. The diffusion coefficient of copper in aluminum is known as a function of temperature. Hence, various, mechanisms, possibly self-diffusion within the eutectic, or diffusion of copper back into the copper depleted zone as a function of time and temperature might be checked experimentally by heat treatment of cast material from the weld fusion zone and subsequent microscopic examination.

REFERENCES

1. Nunes, A.C., Jr, private communication.
2. Betekhtin, V.I. and Zhurkov, S.N., "Time and Temperature Dependence of Strength in Solids", Problemy Prochnosti, No. 2, pp.39-44, February, 1971 (as translated in Strength of Materials, 1971, pp 157-161).
3. Regel, V.R., Slutsker, A.I., and Tomashevskii, E.E., "The Kinetic Nature of the Strength of Solids", Soviet Physics USPEKHI, Vol. 15, No. 1, July-August, 1972, pp 45-65.
4. Betekhtin, V.I., Vladimirov, V.I., Kadomtsev, A.G., and Petrov, A.I., "Plastic Strain and Fracture of Crystalline Bodies. Communication 1. Strain and Microcrack Propagation", Problemy Prochnosti, No. 7, pp 38-45, July, 1979 (as translated in Strength of Materials, 1979, pp 708-715).
5. Betekhtin, V.I., Savel'yev, V.N., and Petrov, A.I., "Kinetics of the Build-up of Microscopic Discontinuities During Creep and Time-to-Rupture Tests of Aluminum", Fiz. metal. metalloved., 38, No. 4, 834-842, 1974 (as translated in the Physics of Metals and Metallography Vol. 38, No. 4, pp 146-152).
6. Betekhtin, V.I., Kadomtsev, A.G., and Petrov, A.I., "Microfracture of Metals During High Temperature Creep", Met. Sci. Heat Treat., Vol 22, n 11-12, Nov-Dec, 1980, pp 879-881.
7. Petrov, A.I., Dobrovol'skaya, I.P., Savel'yev, V.N., and Betekhtin, V.I., "Annealing of Breaks in the Continuity of Deformed Aluminum", Fiz. metal. metalloved., 34, No. 6, 1319-1321, 1972 (as translated in the Physics of Metals and Metallography, Vol. 34, No. 6, 1972, pp 200-202).
8. Lyubov, B.Ya., and Solov'ev, V.A., "Kinetics of the Decomposition of Dislocation Cracks Into Polygonal Walls of Edge Dislocations", Soviet Physics-Solid State, Vol. 8, No. 6, December, 1966, pp 1345-1349.
9. Levin, B.Ya., Betekhtin, V.I., Vladimirov, V.I., Orlov, A.N., and Petrov, A.I., "Density-Measurement Study of Aluminum Destruction", Soviet Physics-Solid State, Vol. 12, No. 9, March, 1971, pp 2138-2142.
10. Betekhtin, V.I., Myshlyayev, M.M., Petrov, A.I., and Skrivskaya, YE.L., "Effect of Hydrostatic Pressure on the Dislocation Structure and Development of Fracture in Deformed Aluminum", Fiz. metal. metalloved., 36, No. 4, 863-865, 1973. (as translated in the Physics of Metals and Metallography, Vol. 36, No. 4, 1973, pp 175-177).

11. Savelev, V.N., Betekhtin, V.I., and Slutsker, A.I., "Peculiarities of Small-Angle X-Ray Scattering in the Surface Layers of Deformed Metals", Fiz. metal. metalloved., 37, No. 1, 211-213, 1974, (as translated in the Physics of Metals and Metallography, Vol. 37, No. 1, 1974, pp 204-206).
12. Betekhtin, V.I., Petrov, A.I., and Kadomtsev, A.G., "Influence of The Original Microporosity on the Life of Aluminum", Fiz. metal. metalloved., 40, No. 4, pp 891-892, 1975 (as translated in The Physics of Metals and Metallography, Vol. 40, No. 4, 1975, pp 202-204).
13. Betekhtin, V.I., Kadomtsev, A.G., Petrov, A.I., and Vladimirov, V.I., "Reversibility of the First Stage of Fracture in Metals", phys. stat. sol. (a), 34, 1976, pp 73-78.
14. Petrov, A.I., Kadomtsev, A.G., and Betekhtin, V.I., "Features of the Influence of Hydrostatic Pressure on the Different Stages of Metal Creep", Fiz. metal. metalloved., 46, No. 6., 1314-1317, 1978. (as translated in The Physics of Metals and Metallography, Vol. 46, No.6, 1978, pp 171-174).
15. Kadomtsev, A.G., Petrov, A.I., and Betekhtin, V.I., "Peculiarities of Microfracture at Small Stresses and High Temperatures", Fiz. metal. metalloved., 46, No. 6, 1321-1324, 1978, (as translated in The Physics of Metals and Metallography, Vol. 46, No. 6, 1978, pp 178-181).
16. Volin, T.E. and Balluffi, R.W., "Annealing Kinetics of Voids and the Self-Diffusion Coefficient in Aluminum", phys. stat. sol., 25, pp 163-173, 1968.
17. Bass, Jack, "The Formation and Motion Energies of Vacancies in Aluminum", Phil. Mag. 15, pp 717-730, 1967.
18. Nunes, A.C., Jr., private communication.
19. Doig, P. and Edington, J.W., "The Influence of Solute Segregation to Grain Boundaries on the Stress Corrosion Susceptibility of Aluminum Alloys", Grain Boundaries in Engineering Materials, Proceedings of the Fourth Bolton Landing Conference, June 9-12, 1974, pp 461-476.

APPENDIX A

EFFECT OF DEFECT EDGE RADIUS COARSENING ON ULTIMATE TENSILE STRENGTH

The preliminary version of the analysis was prepared by
Dr. A. C. Nunes, Jr.

Ductile fractures generally occur by coalescence of voids within the fracturing material. Voids often form around defects such as cracks or weakly bonded second phase particles. The limitation on the ultimate tensile stress, σ_u , is set by the critical stress for propagation of internal voids. The maximum stress supportable by the defects within the metal should be that for initiation of a void from the defect,

If the defect has a sharp edge of suitable orientation, the concentration of stress at the edge should be where the void starts. The stress concentration for an ellipsoidal crack of length $2L$ and radius of curvature ρ at the crack edge raises the nominal stress σ_m to a higher local effective stress σ_e according to the Inglis relation:

$$\sigma_e = 2 \sigma_m \sqrt{\frac{c}{\rho}}$$

Assuming that the nominal stress becomes the ultimate tensile strength at a critical value of σ_e , σ_{ec} then

$$\sigma_u = \frac{\sigma_{ec}}{2} \sqrt{\frac{\rho}{c}}$$

If the radius of the sharp edge of the defect changes, the ultimate tensile strength changes, then, according to the relation:

$$\frac{d\sigma_u}{d\rho} = \frac{\sigma_u}{2\rho}$$

If two faces of a defect come together at angle α to a radius ρ as shown in Figure A-1, then a loss of defect volume at the edge would result in a change of radius $\Delta\rho$.

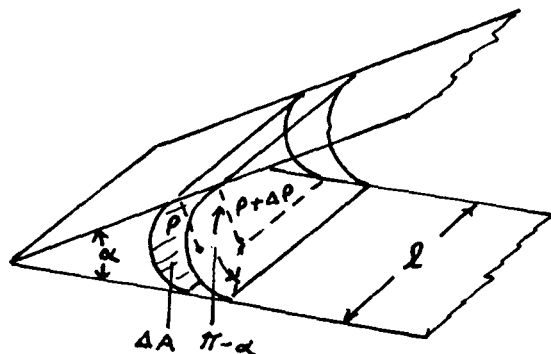


FIGURE A-1. EDGE OF A DEFECT SHOWING CHANGE OF RADIUS OCCURRING WITH LOSS OF VOLUME ΔV

The shaded area, ΔA can be shown to be

$$\Delta A = \{2\rho \Delta\rho + (\Delta\rho)^2\} \{\cot(\alpha/2) - (\pi - \alpha)/2\}$$

so that
$$\frac{dV}{d\rho} = 2\ell\rho \{\cot(\alpha/2) - (\pi - \alpha)/2\}$$

disregarding second order terms.

The kind of volume reduction at the defect edge shown in Figure A-1 takes place because of a difference in chemical potential, $\Delta\mu$, for solutes (or vacancies) on surfaces of different curvature. When a solute atom or vacancy moves from a cylindrical surface of radius ρ_1 to one of radius ρ_2 causing a volume loss Ω to the first cylinder and a volume gain of Ω to the second, a net change ΔA in surface area results

$$\Delta A = \Omega \left(\frac{1}{\rho_1} - \frac{1}{\rho_2} \right)$$

If the surface energy of the cylinders is γ per unit area then the chemical potential difference between the surfaces is:

$$\Delta\mu = \gamma\Omega \left(\frac{1}{\rho_2} - \frac{1}{\rho_1} \right)$$

Assuming that the activity of the solute or vacancy is proportional to its concentration, then the equilibrium concentration C_ρ at the curved surface is related to the equilibrium concentration C_∞ at a flat surface ($\rho = \infty$) according to the equation:

$$C_\rho / C_\infty = e^{\frac{\gamma\Omega}{kT\rho}}$$

It is further assumed here that the surface reaction rates are fast enough so that equilibrium concentrations are maintained at the surfaces and that the relatively lengthy time required for diffusion of solute atom or vacancy from regions of high concentration to regions of low concentration is what holds back the coarsening process.

Fick's first law relating mass flux \dot{j} in atoms or vacancies per area per unit time to the concentration gradient in the radial direction r is assumed to hold:

$$\dot{j} = -D \frac{\partial C}{\partial r}$$

where D is the solute or vacancy diffusivity.

A steady cylindrically symmetrical flow of \dot{m} atoms or vacancies per unit time yields a flux:

$$\dot{j} = \frac{\dot{m}}{2\pi r \ell}$$

Which, with Fick's first law, requires a concentration C_r varying with the radius according to the relation:

$$C_r = C_\rho - \frac{\dot{m}}{2\pi \ell D} \ln\left(\frac{r}{\rho}\right)$$

Where C_ρ is the concentration at radius ρ .
Hence:

$$\dot{j} = \frac{D(C_\rho - C_r)}{r \ln\left(\frac{r}{\rho}\right)}$$

Assuming that there is so much more flat surface ($\rho = \infty$) than curved edge that the bulk mean solute or vacancy concentration C_0 is determined by the flat surface, then:

$$C_p - C_r \approx C_p - C_0$$

for large r and

$$C_p - C_0 = C_0 \left(e^{\frac{\gamma \Omega}{kT\rho}} - 1 \right)$$

The loss of volume v from the sharp edge of a defect is given by:

$$\frac{dv}{dt} = \Omega(\pi - \alpha) r l j$$

or

$$\frac{dv}{dt} = \frac{\Omega(\pi - \alpha) L D C_0 (e^{\frac{\gamma \Omega}{kT\rho}} - 1)}{\ln(L/\rho)}$$

Where L is half the crack length and assumed an approximate maximum upper bound distance to a flat surface.

The ultimate tensile strength then varies according to the relation:

$$\frac{d\sigma_u}{dt} = \frac{d\sigma_u}{d\rho} \cdot \frac{d\rho}{dv} \cdot \frac{dv}{dt}$$

so that

$$\frac{d\sigma_u}{\sigma_u} = \frac{\Omega(\pi - \alpha) C_0 (e^{\frac{\gamma \Omega}{kT\rho}} - 1) D}{4\rho^2 \left\{ \cot \frac{\alpha}{2} - \frac{(\pi - \alpha)}{2} \right\} \ln\left(\frac{L}{\rho}\right)} dt$$

APPENDIX B

VIII-25

```

10 REM *** RAPID DIFFUSION ANNEALING ***
20 REM *** INCREASE IN ULTIMATE STRENGTH ***
30 CLEAR
35 PRINT "INPUT 1 IF MAX PRINTED OUTPUT WANTED, 0 OTHERWISE."
36 INPUT P0
40 PRINT "THIS PROGRAM CALCULATES INCREASED ULTIMATE"
50 PRINT "STRENGTH DUE TO RAPID DIFFUSION ANNEALING"
52 PRINT "(BLUNTING) OF MICROCRACKS, TEMPERATURES AT"
54 PRINT "A MATERIAL POINT ARE TO BE ENTERED FOR DISCRETE"
56 PRINT "TIMES OR CALCULATED FROM THE ATTACHED SUBROUTINE."
60 PRINT
62 PRINT "INPUT 0 TO SKIP ALL PRINTING EXCEPT THE LAST."
63 PRINT "INPUT 1 TO GET TEMP, POINT DATA, ET. AL."
64 INPUT ZA
70 PRINT "ENTER 0 IF THE SUBROUTINE IS TO BE CALLED."
72 PRINT "ENTER 1 OTHERWISE"
80 INPUT B
81 PRINT "INPUT THE NUMBER OF HEAT PASSES NOT INCLUDING THE WELD PASS."
82 INPUT WP
83 PRINT "INPUT NPTS-1 ACROSS THE DIAGONAL."
84 INPUT LU
85 DELETE UP,RP,TU,TR
86 DIM UP(LU),LU),RP(WP,LU)
87 DIM TU(WP,LU),TR(WP,LU)
88 FOR II=0 TO WP
90 IF B=1 THEN 2030
200 REM *** HAS TEMPERATURE HISTORY ***
210 REM *** DATA INPUT ***
230 PRINT "PLEASE SELECT THE NUMBER OF THE METAL TO BE WELDED"
240 PRINT "FROM THE LIST BELOW." PRINT PRINT PRINT
250 PRINT "0. UNLISTED METAL" PRINT
260 PRINT "1. 2219 ALUMINUM" PRINT
270 PRINT "2. 302 STAINLESS STEEL" PRINT
280 PRINT "3. 321 STAINLESS STEEL" PRINT

```

```

290 PRINT "4. INCONEL 718" PRINT
300 INPUT Q
310 IF Q=1 THEN 550
320 IF Q=2 THEN 570
330 IF Q=3 THEN 590
340 IF Q=4 THEN 610
350 PRINT "WHAT IS THE METAL TO BE WELDED?" PRINT PRINT PRINT
360 INPUT M#
370 PRINT "PLEASE WRITE IN THE LOWER AND UPPER LIMITS OF THE MELTING"
380 PRINT "TEMPERATURE RANGE OF THE ALLOY TO BE WELDED. USE UNITS OF"
390 PRINT "DEGREES FAHRENHEIT. SEPARATE THE TWO VALUES BY A COMMA."
400 PRINT "NOTE: A GOOD SOURCE REFERENCE FOR THIS KIND OF DATA IS THE"
410 PRINT "AEROSPACE STRUCTURAL MATERIALS HANDBOOK." PRINT PRINT PRINT
420 INPUT LT,UT
430 PRINT "WHAT IS THE THERMAL CONDUCTIVITY OF THE ALLOY IN BTU'S PER"
440 PRINT "HOUR PER FOOT PER DEGREE FAHRENHEIT?" PRINT PRINT PRINT
450 INPUT K1
460 LET K1=K1*2.441E-05
470 PRINT "WHAT IS THE SPECIFIC HEAT OF THE ALLOY IN BTU'S PER LB"
480 PRINT "PER DEGREE FAHRENHEIT?" PRINT PRINT PRINT
490 INPUT C1
500 PRINT "WHAT IS THE DENSITY OF THE ALLOY IN LBS PER CUBIC INCH?"
510 PRINT PRINT PRINT
520 INPUT P0
530 LET A1=K1/P0/C1*56.83
540 GOTO 630
550 LET UT=1190 LET LT=1010 LET K1=2.44E-03 LET A1=5.56
560 LET M#="2219 ALUMINUM" GOTO 630
570 LET UT=2650 LET LT=2550 LET K1=4.27E-04 LET A1=5
580 LET M#="302 STAINLESS STEEL" GOTO 630
590 LET UT=2550 LET LT=2500 LET K1=4.03E-04 LET A1=66
600 LET M#="321 STAINLESS STEEL" GOTO 630
610 LET UT=2437 LET LT=2300 LET K1=3.83E-04 LET A1=71
620 LET M#="INCONEL 718" GOTO 630
630 PRINT "THE METAL TO BE WELDED IS NOW CHARACTERIZED. WE NOW"

```

```

640 PRINT "TURN TO THE WELDING PROCESS PARAMETERS."
650 PRINT "WHAT IS THE AMBIENT TEMPERATURE OF THE METAL IN DEGREES"
660 PRINT "FAHRENHEIT? IF THE METAL IS PREHEATED, GIVE THE PREHEAT"
670 PRINT "TEMPERATURE AS THE AMBIENT TEMPERATURE."
680 INPUT T0
760 PRINT "PLEASE SPECIFY WELD POWER IN KILOWATTS."
770 PRINT
780 INPUT P0
790 PRINT "PLEASE SPECIFY WELD SPEED IN INCHES PER MINUTE."
800 PRINT
810 INPUT U1
820 PRINT "WHAT PERCENT OF TOTAL BEAM POWER IS LOST FROM THE WELD"
830 PRINT "PUDDLE DUE TO PROCESSES OTHER THAN CONDUCTION BY THE PLATE?"
840 PRINT "THESE LOSSES INCLUDE RADIATION AND METAL EVAPORATION FROM"
850 PRINT "THE VICINITY OF THE PUDDLE."
860 INPUT F1
861 PRINT "INPUT THE NEW NON-CONDUCTIVE PERCENT LOSSES FOR DEEP PTS."
862 INPUT NC
863 CC=F1
870 PRINT "WHAT PERCENT OF THE REMAINING BEAM POWER IS ABSORBED CLOSE"
880 PRINT "TO THE METAL SURFACE SO AS TO FORM THE EB WELD NAILHEAD?"
890 PRINT "THIS WOULD BE THE PERCENTAGE OF THE BEAM CURRENT LACKING"
900 PRINT "SUFFICIENT POWER DENSITY TO VAPORIZE THE METAL."
910 PRINT
920 INPUT F2
940 DIM KD(150),TS(150),US(150),R(150)
950 IF II<>0 THEN 1140
960 PRINT "PLEASE SELECT LENGTH OBSERVED: 0.5, 2.5, 5, 10, 25 INCHES."
970 PRINT
980 INPUT XB\LET XB=XB/5\LET XA=-4*XB
990 PRINT "PLEASE SELECT MAXIMUM TEMPERATURE: 1000, 2000, 5000, 10000 DEG F."
1000 PRINT
1010 INPUT TG
1020 PRINT "INPUT HALF THE CRACK LENGTH IN CENTIMETERS."

```

```

1030 INPUT L
1040 PRINT "INPUT THE LOWER MELTING TEMPERATURE( DEG. KELVIN)."
1050 INPUT L0
1060 PRINT "INPUT THE RADIUS OF THE TIP OF THE CRACK(CM)."
1070 INPUT R(0)
1080 REM R IS ASSUMED MUCH LESS THAN L
1090 PRINT "INPUT THE ULTIMATE STRESS."
1100 INPUT US(0)
1102 FOR MM=0 TO LU
1103 UP(0,MM)=US(0)
1104 RP(0,MM)=R(0)
1105 NEXT MM
1106 PRINT
1110 PRINT "INPUT ONE HALF THE ROOT WIDTH, ONE HALF THE CROWN WIDTH,"
1112 PRINT "AND THE PLATE THICKNESS(DIMENSIONS IN INCHES)."
1120 INPUT BH,TH,W1
1125 DELETE YY,ZZ,MU,MR,SU,SR
1130 DIM YY(LU),ZZ(LU),MU(LU),MR(LU),SU(LU),SR(LU)
1140 FOR MM=0 TO LU
1145 IF II<>0 THEN US(0)=UP(II,MM)
1146 IF II<>0 THEN R(0)=RP(II,MM)
1150 Y=-BH+(TH+BH)*MM/LU
1160 Z=-W1*(Y-TH)/(BH+TH)
1170 YY(MM)=Y
1180 ZZ(MM)=Z
1190 GOSUB 3000
1200 WAIT 1500
1210 PAGE
2020 GOTO 2130
2030 PRINT "INPUT ONE LESS THAN THE NUMBER OF DISCRETE"
2040 PRINT "TEMPERATURES TO BE CONSIDERED."
2050 INPUT M
2060 DIM K(M),TS(M)
2070 DIM US(M),R(M)
2080 FOR I=0 TO M

```

```

2000 PRINT "INPUT TEMPERATURE( DEG. KELVIN), TIME( SECONDS) "
2100 INPUT K0(I), TS(I)
2110 NEXT I
2120 GOTO 2220
2130 FOR I=0 TO 150
2140 TH(I)=5*TA(I)/9+255.37
2150 NEXT I
2160 DT=(2*XB)/U1
2170 M=150
2180 FOR I=0 TO 150
2190 K0(I)=TH(150-I)
2200 NEXT I
2250 AL=2*ATH*(R0)/L)
2300 PI=4*ATH*(1)
2310 OM=16.48*10^(-24)
2340 PAGE
2341 IF PU=0 THEN 2420
2350 PRINT "Z=";Z;"Y=";Y;"L=";L;"R(0)=";R(0)
2360 PRINT "AL=";AL;"US(0)=";US(0)
2370 PRINT
2380 PRINT "K0(I)      DS      RA      RR      US(I)      R(I)"
2390 PRINT "A          C0      S        D          LG"
2400 PRINT
2410 PRINT
2420 FOR I=1 TO M
2430 IF K0(I)/=L0 THEN 2470
2440 US(I)=UP(0,MM)
2450 R(I)=RP(0,MM)
2452 IF ZA=0 THEN 2460
2455 PRINT II;I,MM;K0(I),R(I-1),US(I-1)
2460 GOTO 2510
2470 IF B=0 THEN LET DS=DT
2480 IF B=1 THEN LET DS=TS(I)-TS(I-1)
2490 A=(OM*(PI-AL)*DS)/(4*(SINK(PI-AL)/2)/COS((PI-AL)/2))-(PI-AL)/2))
2500 C0=6.056*10^(-22)*EXP(-8478/K0(I))

```

```

2502 IF ZA=0 THEN 2510
2505 PRINT II;I,MM;K0(I),R(I-1),US(I-1)
2510 S=EXP(1500/OM*(1.381*10^(-16)))/R(I-1)/K0(I))-1
2520 D=176*EXP(-15213/K0(I))
2530 LG=LOG(L/R(I-1))
2540 RA=HFC0+S*D)/(LG*(I-1)/2)
2550 RP=2*RA
2560 R(I)=R(I-1)+RP*(I-1)
2570 US(I)=US(I-1)+PA*US(I-1)
2575 IF PU=0 THEN 2630
2580 PRINT
2590 PRINT K0(I),DS,RA,RP,US(I),R(I)
2600 PRINT A,C0,S,D,LG
2610 PRINT
2615 IF PU=0 THEN 2630
2620 PRINT K0(I),L0,I
2630 NEXT I
2632 IF II=MP THEN 2640
2635 UP(II+1,MM)=US(150)
2636 RP(II+1,MM)=R(150)
2640 MU(MM)=(US(150)-UP(0,MM))/UP(0,MM)
2650 MR(MM)=(R(105)-RP(0,MM))/RP(0,MM)
2652 SU(MM)=MU(MM)
2654 SR(MM)=MR(MM)
2655 TU(II,MM)=MU(MM)
2656 TR(II,MM)=MR(MM)
2660 NEXT MM
2665 WAIT 1500
2700 SU=(SU-(MINK SU))/(MAX(SU)-MINK SU)
2710 SR=(SR-(MINK SR))/(MAX(SR)-MINK SR)
2720 PAGE
2724 IF II=MP THEN 2730
2725 IF ZA=0 THEN 2800
2730 PRINT "MAX DUTS/UTS= ",MAX(MU)
2740 PRINT "MIN DUTS/UTS= ",MINK(MU)

```

```

2750 WINDOW -BH,TH,0.1
2760 VIEWPORT 250,750,100,600
2770 SETGR TICS 5,5,GRAT 5,5
2780 XYPLOT YY,SU
2790 PRINT "A-E-W-A-L"
2800 NEXT II
2803 PAGE
2810 PRINT "DTS/UTS FOR WP=0,3"
2812 PRINT "E","D","C","B","A"
2814 FOR QQ=0 TO WP
2816 PRINT TUC(QQ,0),TUC(QQ,1),TUC(QQ,2),TUC(QQ,3),TUC(QQ,4)
2818 PRINT
2820 NEXT QQ
2840 PRINT "DR/R FOR WP=0,3"
2842 PRINT "E","D","C","B","A"
2844 FOR QQ=0 TO WP
2846 PRINT TR(QQ,0),TR(QQ,1),TR(QQ,2),TR(QQ,3),TR(QQ,4)
2848 PRINT
2850 NEXT QQ
2855 WAIT 1500
2860 PRINT "A-E-W-A-L"
2865 WAIT 1500
2900 STOP
2910 END
3000 REM *** COMPUTATION OF HAZ TEMPERATURE HISTORY ***
3005 IF II=0 THEN 3009
3006 IF MM=LU THEN 3009
3007 F1=HC
3008 GOTO 3010
3009 F1=CC
3010 P1=P0*(1-F1/100)
3015 PRINT II,MM,LU,F1
3020 P2=P1*(1-F2/100)
3030 P1=P1-P2
3040 LET N=150

```

```

3050 DIM XX(N),TAC(N),TE(N)
3060 LET TE=LT
3070 FOR I=0 TO N
3080 LET XX(I)=XA+(XB-XA)/N*I
3090 NEXT I
3110 FOR I=0 TO N
3120 LET X=XX(I)
3130 GOSUB 3290
3140 LET TAC(I)=M2
3145 IF TAC(I)>LT THEN LET TAC(I)=LT+10
3150 NEXT I
3160 REM *** PRINTOUT OF RESULTS ***
3170 PAGE
3175 IF ZA=0 THEN 3280
3180 PRINT "WELD TEMPERATURE PROFILE:";Y;"INCHES FROM CENTERLINE."
3190 PRINT "PROFILES TAKEN AT ".Z/W1*100;" % PLATE DEPTH."
3200 FOR I=0 TO 10 PRINT NEXT I
3210 PRINT "TEMP" PRINT PRINT
3220 PRINT "(DEG F)"
3230 FOR I=0 TO 16 PRINT NEXT I
3240 PRINT "DISTANCE FROM HEAT SOURCE (INCHES)"
3250 WINDOW XA,XB,0,TG
3260 SETGR WINDOW,TICS 5,10,5,5,GRAT 6,6,3,3
3270 XYPLOT XX,TA
3275 PRINT "A-E-W-A-L"
3280 RETURN
3290 REM *** SUBROUTINE TO COMPUTE TEMPERATURE OF HEAT SOURCE AHEAD ***
3300 LET Z2=Z
3310 LET M2=0
3320 LET O3=0
3330 LET O2=2*XW1
3340 GOSUB 3650
3350 GOSUB 3510
3360 LET M2=M1+T0+T2
3370 LET M3=M2

```

```

3320 LET D3=D3+D2
3330 GOSUB 3430
3400 IF (M2-M3)<.01*M2 THEN GOTO 3420
3410 GOTO 3370
3420 RETURN
3430 REM *** SUBROUTINE TO ADD NEXT TWO HEAT SOURCES ***
3440 LET Z2=D3+Z
3450 GOSUB 3650
3460 LET M2=M2+M1
3470 LET Z2=D3-Z
3480 GOSUB 3650
3490 LET M2=M2+M1
3500 RETURN
3510 REM *** SUBROUTINE TO COMPUTE LINE HEAT SOURCE TEMPERATURE
3520 REM DISTRIBUTION ***
3530 LET I0=0
3540 LET T2=0
3550 LET AR=U1/2/A1*X
3560 LET Z3=U1/2/A1*SQR(X*X+Y*Y)
3570 IF AR>88 THEN 3640
3580 GOSUB 3730
3590 IF AR<0 THEN 3620
3600 LET T2=P2/W1/6.2832/K1/EXP(AR)*K0
3610 GOTO 3640
3620 LET AR=-AR
3630 LET T2=P2/W1/6.2832/K1*EXP(AR)*K0
3640 RETURN
3650 REM *** SUBROUTINE TO COMPUTE TEMPERATURE ***
3660 LET S1=SQR(X*X+Y*Y+Z2*Z2)
3670 IF S1=0 THEN LET M1=UT+1000\IF S1=0 THEN 3720
3680 LET AR=U1/2/A1*(S1+X)
3690 IF AR>88 THEN LET M1=0
3700 IF AR>88 THEN GOTO 3720
3710 LET M1=P1/2/3.1416/K1/S1/EXP(AR)
3720 RETURN

```

```

3730 REM *** MODIFIED BESSEL FUNCTION, SECOND KIND, ZEROth ORDER ***
3740 REM *** POLYNOMIAL APPROXIMATION ***
3750 IF Z3>2 THEN 3820
3760 GOSUB 3870
3770 LET G2=Z3*Z3/4
3780 LET K0=((7.4E-05*G2+1.075E-04)*G2+2.62698E-03)*G2
3790 LET K0=((K0+.0348853)*G2+2306976)*G2
3800 LET K0=((K0+.4227842)*G2-.5772157)*.5*LOG(G2)*I0
3810 GOTO 3860
3820 LET G2=2/Z3
3830 LET K0=((5.3208E-04*G2-2.5154E-03)*G2+5.87872E-03)*G2
3840 LET K0=((K0-.01062445)*G2+.02189568)*G2
3850 LET K0=((K0-.07832358)*G2+1.253314)/SQR(Z3)/EXP(Z3)
3860 RETURN
3870 REM *** MODIFIED BESSEL FUNCTION, FIRST KIND, ZEROth ORDER ***
3880 REM *** POLYNOMIAL APPROXIMATION ***
3890 IF Z3>3.75 THEN 3950
3900 LET G1=Z3*Z3
3910 LET I0=((5.923979E-10*G1+6.56017E-08)*G1+6.80123E-06)*G1
3920 LET I0=((I0+4.3394E-04)*G1+.0156252)*G1
3930 LET I0=(I0+.25)*G1+1
3940 GOTO 3990
3950 LET I0=((153.445/Z3-171.822)/Z3+73.2919)/Z3
3960 LET I0=((I0-15.2595)/Z3+1.81198)/Z3
3970 LET I0=((I0-.0830909)/Z3+.0316855)/Z3
3980 LET I0=((I0+.0498222)/Z3+.3983423)*EXP(Z3)/SQR(Z3)
3990 RETURN

```

READY
*


```

10 REM *** RAPID DIFFUSSION ANNEALING ***
20 REM *** INCREASE IN ULTIMATE STRENGTH ***
30 CLEAR
35 PRINT "INPUT 1 IF MAX PRINTED OUTPUT WANTED, 0 OTHERWISE."
36 INPUT PU
40 PRINT "THIS PROGRAM CALCULATES INCREASED ULTIMATE"
50 PRINT "STRENGTH DUE TO RAPID DIFFUSION ANNEALING"
52 PRINT "(BLUNTING) OF MICROCRACKS. TEMPERATURES AT"
54 PRINT "A MATERIAL POINT ARE TO BE ENTERED FOR DISCRETE"
56 PRINT "TIMES OR CALCULATED FROM THE ATTACHED SUBROUTINE."
60 PRINT
62 PRINT "INPUT 0 TO SKIP ALL PRINTING EXCEPT THE LAST."
63 PRINT "INPUT 1 TO GET TEMP , POINT DATA, ET. AL."
64 INPUT ZA
70 PRINT "ENTER 0 IF THE SUBROUTINE IS TO BE CALLED."
72 PRINT "ENTER 1 OTHERWISE"
80 INPUT B
81 PRINT "INPUT THE NUMBER OF HEAT PASSES NOT INCLUDING THE WELD PASS."
82 INPUT WP
83 PRINT "INPUT NPTS-1 ACROSS THE DIAGONAL."
84 INPUT LU
85 DELETE UP,RP,TU,TR
86 DIM UP(WP,LU),RP(WP,LU)
87 DIM TU(WP,LU),TR(WP,LU)
88 FOR II=0 TO WP
90 IF B=1 THEN 2030
200 REM *** HAZ TEMPERATURE HISTORY ***
210 REM *** DATA INPUT ***
230 PRINT "PLEASE SELECT THE NUMBER OF THE METAL TO BE WELDED"
240 PRINT "FROM THE LIST BELOW." \PRINT \PRINT \PRINT
250 PRINT "0. UNLISTED METAL" \PRINT
260 PRINT "1. 2219 ALUMINUM" \PRINT
270 PRINT "2. 302 STAINLESS STEEL" \PRINT
280 PRINT "3. 321 STAINLESS STEEL" \PRINT

```

```

290 PRINT "4. INCONEL 718"\PRINT
300 INPUT Q
310 IF Q=1 THEN 550
320 IF Q=2 THEN 570
330 IF Q=3 THEN 590
340 IF Q=4 THEN 610
350 PRINT "WHAT IS THE METAL TO BE WELDED?"\PRINT\PRINT\PRINT
360 INPUT M$
370 PRINT "PLEASE WRITE IN THE LOWER AND UPPER LIMITS OF THE MELTING"
380 PRINT "TEMPERATURE RANGE OF THE ALLOY TO BE WELDED. USE UNITS OF"
390 PRINT "DEGREES FAHRENHEIT. SEPARATE THE TWO VALUES BY A COMMA."
400 PRINT "NOTE: A GOOD SOURCE REFERENCE FOR THIS KIND OF DATA IS THE"
410 PRINT "AEROSPACE STRUCTURAL MATERIALS HANDBOOK." \PRINT\PRINT\PRINT
420 INPUT LT,UT
430 PRINT "WHAT IS THE THERMAL CONDUCTIVITY OF THE ALLOY IN BTU'S PER"
440 PRINT "FOOT PER FOOT PER DEGREE FAHRENHEIT?" \PRINT\PRINT\PRINT
450 INPUT K1
460 LET K1=K1*2.441E-05
470 PRINT "WHAT IS THE SPECIFIC HEAT OF THE ALLOY IN BTU'S PER LB"
480 PRINT "PER DEGREE FAHRENHEIT?" \PRINT\PRINT\PRINT
490 INPUT C1
500 PRINT "WHAT IS THE DENSITY OF THE ALLOY IN LBS PER CUBIC INCH?"
510 PRINT\PRINT\PRINT
520 INPUT R0
530 LET A1=K1/R0/C1*56.83
540 GOTO 630
550 LET UT=1190\LET LT=1010\LET K1=2.44E-03\LET A1=5.56
560 LET M$="2219 ALUMINUM"\GOTO 630
570 LET UT=2650\LET LT=2550\LET K1=4.27E-04\LET A1=.5
580 LET M$="302 STAINLESS STEEL"\GOTO 630
590 LET UT=2550\LET LT=2500\LET K1=4.03E-04\LET A1=.66
600 LET M$="321 STAINLESS STEEL"\GOTO 630
610 LET UT=2437\LET LT=2300\LET K1=3.83E-04\LET A1=.71
620 LET M$="INCONEL 718"\GOTO 630
630 PRINT "THE METAL TO BE WELDED IS NOW CHARACTERIZED. WE NOW"

```

```

640 PRINT "TURN TO THE WELDING PROCESS PARAMETERS." \PRINT \PRINT \PRINT
650 PRINT "WHAT IS THE AMBIENT TEMPERATURE OF THE METAL IN DEGREES"
660 PRINT "FAHRENHEIT? IF THE METAL IS PREHEATED, GIVE THE PREHEAT"
670 PRINT "TEMPERATURE AS THE AMBIENT TEMPERATURE." \PRINT \PRINT \PRINT
680 INPUT T0
760 PRINT "PLEASE SPECIFY WELD POWER IN KILOWATTS."
770 PRINT \PRINT \PRINT
780 INPUT P0
790 PRINT "PLEASE SPECIFY WELD SPEED IN INCHES PER MINUTE."
800 PRINT \PRINT \PRINT
810 INPUT V1
820 PRINT "WHAT PERCENT OF TOTAL BEAM POWER IS LOST FROM THE WELD"
830 PRINT "PUDDLE DUE TO PROCESSES OTHER THAN CONDUCTION BY THE PLATE?"
840 PRINT "THESE LOSSES INCLUDE RADIATION AND METAL EVAPORATION FROM"
850 PRINT "THE VICINITY OF THE PUDDLE." \PRINT \PRINT \PRINT
860 INPUT F1
861 PRINT "INPUT THE NEW NON-CONDUCTIVE PERCENT LOSSES FOR DEEP PTS."
862 INPUT NC
863 CC=F1
870 PRINT "WHAT PERCENT OF THE REMAINING BEAM POWER IS ABSORBED CLOSE"
880 PRINT "TO THE METAL SURFACE SO AS TO FORM THE EB WELD NAILHEAD?"
890 PRINT "THIS WOULD BE THE PERCENTAGE OF THE BEAM CURRENT LACKING"
900 PRINT "SUFFICIENT POWER DENSITY TO VAPORIZE THE METAL."
910 PRINT \PRINT \PRINT
920 INPUT F2
940 DIM KD(150), TS(150), US(150), R(150)
950 IF II<>0 THEN 1140
960 PRINT "PLEASE SELECT LENGTH OBSERVED: 0.5, 2.5, 5, 10, 25 INCHES."
970 PRINT \PRINT \PRINT
980 INPUT XB \LET XB=XB/5 \LET XA=-4*XB
990 PRINT "PLEASE SELECT MAXIMUM TEMPERATURE: 1000, 2000, 5000, 10000 DEG
F."
1000 PRINT \PRINT \PRINT
1010 INPUT TG
1020 PRINT "INPUT HALF THE CRACK LENGTH IN CENTIMETERS."

```

```

1030 INPUT L
1040 PRINT "INPUT THE LOWER MELTING TEMPERATURE(DEG. KELVIN)."

```

```

2090 PRINT "INPUT TEMPERATURE(DEG. KELVIN),TIME(SECONDS)"
2100 INPUT KD(I),TS(I)
2110 NEXT I
2120 GOTO 2220
2130 FOR I=0 TO 150
2140 TA(I)=5*TA(I)/9+255.37
2150 NEXT I
2160 DT=(2*XB)/U1
2170 M=150
2180 FOR I=0 TO 150
2190 KD(I)=TA(150-I)
2200 NEXT I
2290 AL=2*ATN(R(0)/L)
2300 PI=4*ATN(1)
2310 OM=16.48*10^(-24)
2340 PAGE
2341 IF PU=0 THEN 2420
2350 PRINT "Z=";Z;"Y=";Y;"L=";L;"R(0)=";R(0)
2360 PRINT "AL=";AL;"US(0)=";US(0)
2370 PRINT
2380 PRINT "KD(I)      DS      RA      RR      US(I)      R(I)"
2390 PRINT "A          C0      S        D        LG"
2400 PRINT
2410 PRINT
2420 FOR I=1 TO M
2430 IF KD(I)<=L0 THEN 2470
2440 US(I)=UP(0,MM)
2450 R(I)=RP(0,MM)
2452 IF ZA=0 THEN 2460
2455 PRINT I;I;MM;KD(I),R(I-1),US(I-1)
2460 GOTO 2610
2470 IF B=0 THEN LET DS=DT
2480 IF B=1 THEN LET DS=TS(I)-TS(I-1)
2490 A=(OM*(PI-AL)*DS)/(4*(SIN((PI-AL)/2)/COS((PI-AL)/2))-((PI-AL)/2)
2500 C0=6.066*10^(-22)*EXP(-8478/KD(I))

```

```

2502 IF ZA=0 THEN 2510
2505 PRINT II; I; MM; KD(I); R(I-1); US(I-1)
2510 S=EXP(1500*OM/(1.381*10^(-16))/R(I-1)/KD(I))-1
2520 D=.176*EXP(-15213/KD(I))
2530 LG=LOG(L/R(I-1))
2540 RA=A*C0*S*D/(LG*R(I-1)^2)
2550 RR=2*RA
2560 R(I)=R(I-1)+RR*R(I-1)
2570 US(I)=US(I-1)+RA*US(I-1)
2575 IF PU=0 THEN 2630
2580 PRINT
2590 PRINT KD(I); DS; RA; RR; US(I); R(I)
2600 PRINT A; C0; S; D; LG
2610 PRINT
2615 IF PU=0 THEN 2630
2620 PRINT KD(I); L0; I
2630 NEXT I
2632 IF II=WP THEN 2640
2635 UP(II+1,MM)=US(150)
2636 RP(II+1,MM)=R(150)
2640 MU(MM)=(US(150)-UP(0,MM))/UP(0,MM)
2650 MR(MM)=(R(105)-RP(0,MM))/RP(0,MM)
2652 SU(MM)=MU(MM)
2654 SR(MM)=MR(MM)
2655 TU(II,MM)=MU(MM)
2656 TR(II,MM)=MR(MM)
2660 NEXT MM
2665 WAIT 1500
2700 SU=(SU-(MIN(SU)))/(MAX(SU)-MIN(SU))
2710 SR=(SR-(MIN(SR)))/(MAX(SR)-MIN(SR))
2720 PAGE
2724 IF II=WP THEN 2730
2725 IF ZA=0 THEN 2800
2730 PRINT "MAX DUTS/UTS= ",MAX(MU)
2740 PRINT "MIN DUTS/UTS= ",MIN(MU)

```

```

2750 WINDOW -BH,TH,0,1
2760 VIEWPORT 250,750,100,600
2770 SETGR TICS 5,5,GRAT 5,5
2780 XYPLOT YY,SU
2790 PRINT "^E^W^E^L"
2800 NEXT II
2809 PAGE
2810 PRINT "DTS/UTS FOR WP=0,3"
2812 PRINT "E","D","C","B","A"
2814 FOR QQ=0 TO WP
2816 PRINT TUK(QQ,0),TUK(QQ,1),TUK(QQ,2),TUK(QQ,3),TUK(QQ,4)
2818 PRINT
2820 NEXT QQ
2840 PRINT "DR/R FOR WP=0,3"
2842 PRINT "E","D","C","B","A"
2844 FOR QQ=0 TO WP
2846 PRINT TR(QQ,0),TR(QQ,1),TR(QQ,2),TR(QQ,3),TR(QQ,4)
2848 PRINT
2850 NEXT QQ
2855 WAIT 1500
2860 PRINT "^E^W^E^L"
2865 WAIT 1500
2900 STOP
2910 END
3000 REM *** COMPUTATION OF HAZ TEMPERATURE HISTORY ***
3005 IF II=0 THEN 3009
3006 IF MM=LU THEN 3009
3007 F1=NC
3008 GOTO 3010
3009 F1=CC
3010 P1=P0*(1-F1/100)
3015 PRINT II,MM,LU,F1
3020 P2=P1*(1-F2/100)
3030 P1=P1-P2
3040 LET N=150

```

```

3050 DIM XX(N),TA(N),TE(N)
3060 LET TE=LT
3070 FOR I=0 TO N
3080 LET XX(I)=XA+(XB-XA)/N*I
3090 NEXT I
3110 FOR I=0 TO N
3120 LET X=XX(I)
3130 GOSUB 3290
3140 LET TA(I)=M2
3145 IF TA(I)>LT THEN LET TA(I)=LT+10
3150 NEXT I
3160 REM *** PRINTOUT OF RESULTS ***
3170 PAGE
3175 IF ZA=0 THEN 3280
3180 PRINT "WELD TEMPERATURE PROFILE:";Y;"INCHES FROM CENTERLINE."
3190 PRINT "PROFILES TAKEN AT ";Z/W1*100;" % PLATE DEPTH."
3200 FOR I=0 TO 10\PRINT\NEXT I
3210 PRINT " TEMP"\PRINT\PRINT
3220 PRINT "(DEG F)"
3230 FOR I=0 TO 16\PRINT\NEXT I
3240 PRINT "          DISTANCE FROM HEAT SOURCE (INCHES)";
3250 WINDOW XA,XB,0,TG
3260 SETGR WINDOW,TICS 5,10,5,5,GRAT 6,6,3,3
3270 XYPLOT XX,TA
3275 PRINT "^\E^W^E^L"
3280 RETURN
3290 REM *** SUBROUTINE TO COMPUTE TEMPERATURE OF HEAT SOURCE ARRAY ***
3300 LET Z2=Z
3310 LET M2=0
3320 LET D3=0
3330 LET D2=2*W1
3340 GOSUB 3650
3350 GOSUB 3510
3360 LET M2=M1+T0+T2
3370 LET M3=M2

```



```

3380 LET D3=D3+D2
3390 GOSUB 3430
3400 IF (M2-M3)<.01*M2 THEN GOTO 3420
3410 GOTO 3370
3420 RETURN
3430 REM *** SUBROUTINE TO ADD NEXT TWO HEAT SOURCES ***
3440 LET Z2=D3+Z
3450 GOSUB 3650
3460 LET M2=M2+M1
3470 LET Z2=D3-Z
3480 GOSUB 3650
3490 LET M2=M2+M1
3500 RETURN
3510 REM *** SUBROUTINE TO COMPUTE LINE HEAT SOURCE TEMPERATURE
3520 REM DISTRIBUTION ***
3530 LET K0=0
3540 LET T2=0
3550 LET AR=U1/2/A1*X
3560 LET Z3=U1/2/A1*SQR(X*X+Y*Y)
3570 IF AR>88 THEN 3640
3580 GOSUB 3730
3590 IF AR<0 THEN 3620
3600 LET T2=P2/W1/6.2832/K1/EXP(AR)*K0
3610 GOTO 3640
3620 LET AR=-AR
3630 LET T2=P2/W1/6.2832/K1*EXP(AR)*K0
3640 RETURN
3650 REM *** SUBROUTINE TO COMPUTE TEMPERATURE ***
3660 LET S1=SQR(X*X+Y*Y+Z2*Z2)
3670 IF S1=0 THEN LET M1=UT+1000\IF S1=0 THEN 3720
3680 LET AR=U1/2/A1*(S1+X)
3690 IF AR>88 THEN LET M1=0
3700 IF AR>88 THEN GOTO 3720
3710 LET M1=P1/2/3.1416/K1/S1/EXP(AR)
3720 RETURN

```

```

3730 REM *** MODIFIED BESSEL FUNCTION, SECOND KIND, ZEROth ORDER ***
3740 REM *** POLYNOMIAL APPROXIMATION ***
3750 IF Z3>2 THEN 3820
3760 GOSUB 3870
3770 LET G2=Z3*Z3/4
3780 LET K0=((7.4E-06*G2+1.075E-04)*G2+2.62698E-03)*G2
3790 LET K0=((K0+.0348859)*G2+.2306976)*G2
3800 LET K0=((K0+.4227842)*G2-.5772157)-.5*LOG(G2)*I0
3810 GOTO 3860
3820 LET G2=2/Z3
3830 LET K0=((5.3208E-04*G2-2.5154E-03)*G2+5.87872E-03)*G2
3840 LET K0=((K0-.01062446)*G2+.02189560)*G2
3850 LET K0=((K0-.07832358)*G2+1.253314)/SQR(Z3)/EXP(Z3)
3860 RETURN
3870 REM *** MODIFIED BESSEL FUNCTION, FIRST KIND, ZEROth ORDER ***
3880 REM *** POLYNOMIAL APPROXIMATION ***
3890 IF Z3>3.75 THEN 3950
3900 LET G1=Z3*Z3
3910 LET I0=((5.923979E-10*G1+6.56017E-08)*G1+6.80123E-06)*G1
3920 LET I0=((I0+4.3394E-04)*G1+.0156252)*G1
3930 LET I0=(I0+.25)*G1+1
3940 GOTO 3990
3950 LET I0=((153.445/Z3-171.822)/Z3+73.2919)/Z3
3960 LET I0=((I0-15.2595)/Z3+1.81198)/Z3
3970 LET I0=((I0-.0230909)/Z3+.0316855)/Z3
3980 LET I0=((I0+.0498222)/Z3+.3989423)*EXP(Z3)/SQR(Z3)
3990 RETURN

```

READY

*

1982
NASA/ASEE SUMMER FACULTY RESEARCH FELLOWSHIP PROGRAM

MARSHALL SPACE FLIGHT CENTER
THE UNIVERSITY OF ALABAMA

REFLECTANCE MEASUREMENTS

Prepared By: Robert A. Brown, Ph. D., P. E.

Academic Rank: Professor of Industrial and Systems Engineering

University and Department: The University of Alabama in Huntsville
Department of Industrial and Systems Engineering

NASA/MSFC:
Laboratory: Space Science
Division: Space Physics
Branch: Optical Physics

MSFC Counterpart: D. R. Wilkes

Date: August 6, 1982

Contract No.: NGT-01-002-099
(University of Alabama)

REFLECTANCE MEASUREMENTS

by

Robert A. Brown, Ph. D., P. E.
Professor of Industrial and Systems Engineering
The University of Alabama in Huntsville
Huntsville, Alabama

ABSTRACT

The measurement of the reflectance of objects is essential to the programs of the Space Sciences Laboratory of the George C. Marshall Space Flight Center.

Stable thermal coatings are required to control the internal temperature of almost all objects placed in space for scientific, commercial, industrial, and military purposes. Likewise, most space objects have optical surfaces subject to degradation and contamination upon exposure to the space environment. Finally, even space objects not having these requirements cannot be allowed to contaminate those in close proximity which do. Thus reflectance measurements of coatings and optics are required to control the environment and performance on every space mission.

Spectroreflectometers are currently used to perform these measurements. These instruments are massive, well-built pieces of laboratory equipment, not optimally designed for high-volume measurement work now beginning to be required. Furthermore the equipment design is approaching twenty years old, and the equipment itself is showing signs of advancing age through the increasing unreliability of its electronics. This study was begun to achieve two major objectives: i. To improve the productivity of the equipment and operating personnel, and ii. To improve the accuracy and sensitivity of the measurements by suggesting advances in the state of the art.

The findings of the study are, in summary, that there is a need for increased optical sensitivity to increase productivity, and that better design of the data collection and processing scheme can eliminate some of the unnecessary present operations. Two promising approaches to increased sensitivity have been identified, conventional processing with error compensation and detection of random noise modulation. The latter of these approaches is of sufficient novelty that it is under investigation to determine its patentability.

INTRODUCTION

It is essential to have a capability for measuring the reflectance of objects in order to carry out the missions of the Space Sciences Laboratory of the Marshall Space Flight Center. Almost all objects placed in space for scientific, commercial, industrial, and military purposes must have some form of special coating to control the internal temperature. These thermal control coatings, either light colored to reflect large amounts of incident radiation or black to best radiate surplus heat into space, have organic binders and other components which are affected by the high vacuum and ultra-violet radiation characteristic of the space environment.

Furthermore, many of these space payloads have optics, either lenses or mirrors, to orient them and collect information. These surfaces are subject to contamination by the outgassing of thermal control coatings, plastic parts and electrical insulation, exhaust plumes from reaction motors, etc. Measurement of the reflectance of these items is also required to permit the evaluation of data collected and prediction of their reliable life.

Simple measurements of reflectance, reflected energy divided by incident energy, are not sufficient. For example, obtaining thermal balance for maintaining the proper internal temperature may require high reflectance in one spectral region to ward off incoming radiation while having low reflectance in another spectral region to promote the outward radiation of heat energy. Thus the reflectance must be measured as a function of wavelength over a wide spectral band. Typically, wavelengths from 200 nanometers (nm.) in the ultra-violet to 2500 nm. in the infra-red are required.

OBJECTIVES

Means currently exist for conducting such measurements. Two Beckman Model DK-2A Spectroreflectometers are in use, and a Cary of similar operating characteristics is to be equipped with auxiliary items to enable its use. These instruments are well-built, massive pieces of laboratory equipment. Unfortunately, their design is now about twenty years old, and the electronics in particular have become unreliable and noisy. Their claimed accuracy is only two per cent; this together with the noisiness can easily obscure effects sought.

Also, these instruments are not designed for high-volume ("production") use. All adjustments must be made by

hand. Frequent zero-ing and setting of the maximum scale value must be carried out by hand in a typical measurement sequence. Some modifications have been carried out to allow computer control of the wavelength selection function, and the reading of the output by the computer has been arranged for after a fashion. However, these modifications have resulted in the measurements being compute-bound because the computer is time-shared with other jobs.

Thus the long term objectives of the study undertaken were twofold:

1. To improve the productivity of the equipment and operators to handle a growing demand for reflectance measurements.

2. To advance the state of the art, if possible, allowing more precise, more repeatable measurement of reflectance in keeping with the growth of instrumentation ability generally due to the switch from vacuum tubes to solid state devices and from analog to digital measurement.

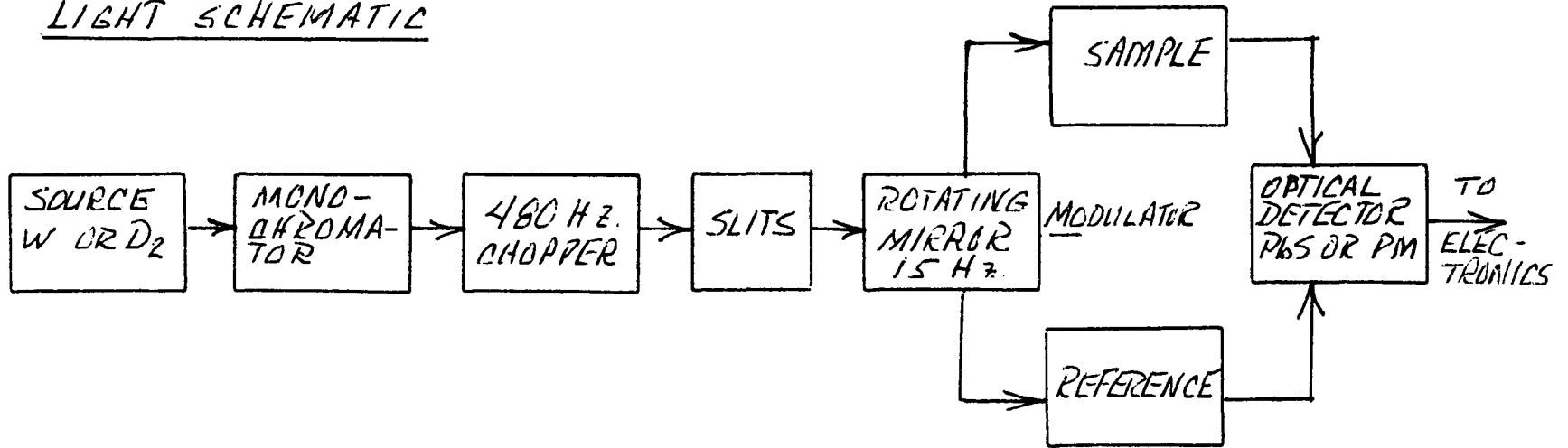
Naturally, it has not been possible to achieve these objectives in nine weeks. A good start has been made toward identifying feasible alternatives for further study. A more detailed description of the problems and the feasible alternatives is presented in the next sections.

GENERAL EQUIPMENT DESCRIPTION AND USAGE

The general functional diagram of the existing equipment is shown in Fig. 1. The upper half of the figure is the path of the information in the optical portion of the instrument; the lower portion shows the electronic schematic.

The monochromator serves to select a narrow band of light wavelengths from the broad-band sources, either a tungsten filament lamp for the visible and infra-red bands or a deuterium lamp for the ultra-violet. The 480 Hz. chopper interrupts the light to provide a (relatively) high-frequency carrier for later alternating current amplification. The slits open and close under servo control to keep the amount of light energy passing to the reference and the sample constant whenever the source is rich enough to permit this constant energy mode of operation. A secondary advantage to servoing the slits is that, with narrow slits, the bandwidth is small and hence the spectral resolution is high. This allows narrow absorption bands to be seen, a very desirable means of identifying contaminants.

LIGHT SCHEMATIC



IX-5

ELECTRONIC SCHEMATIC

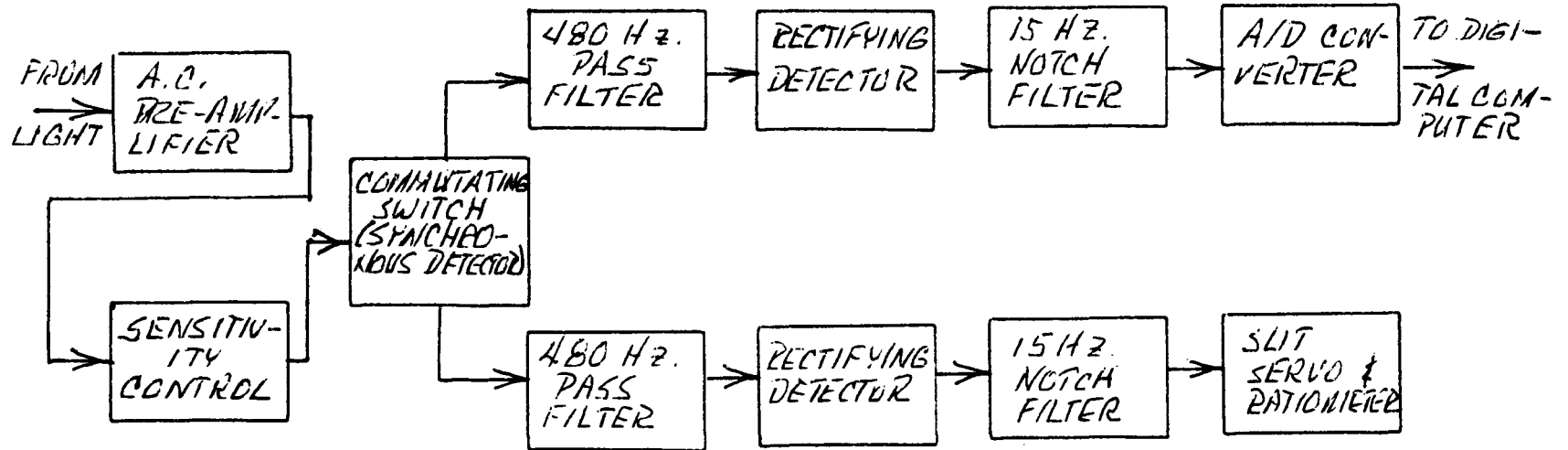


Figure 1 -- Functional diagram of present equipment

The next functional block is a rotating mirror which passes the light along two paths so that it alternates between impinging on the sample and scattering in a diffuse way on the inside of an "integrating sphere". This mirror rotates at 15 Hz., thus modulating the 480 Hz. carrier created by the chopper in a double sideband manner. At this point we now have an audio carrier modulated with a low frequency whose amplitude is the difference between the signal and the reference energies.

The integrating sphere contains the sample and detectors, and is coated on the inside with magnesium oxide to provide the highest possible reflectance. The purpose of the integrating sphere is to provide a field of view for the detectors independent of the geometry of the detectors and the sample, which it does because of the special symmetry properties of the sphere.

The optical signal is now converted into an electronic signal by one of two detectors, a lead sulphide (PbS) cell with 50 volts bias applied to it or a photo-multiplier (PM) tube with 700 volts operating through ten multiplier stages. The PM tube has a swamping resistor network selected by a switch to reduce the sensitivity by a factor of 20 when operating in the visible and near ultra-violet regions. Its photocathode is selected to maximize the response in the ultra-violet, and therefore the lead sulphide detector is the detector of choice for the visible and infra-red regions.

The 480 Hz. carrier with 15 Hz. modulation sidebands is amplified by an AC amplifier to raise the signal level to several volts. The gain of this amplifier is adjustable to control the amplitude of the background noise and, presumably, to prevent overloading and consequent distortion of the signal in later amplifier stages.

The next function is to demodulate (synchronous detect, demultiplex, or homodyne detect are other synonyms) the sample and reference information. This produces two signals which have been amplified by the same amplifier chain, and have therefore been subjected to the same distortions, lack of linearity, etc. Each of these 480 Hz. signals is rectified, and any remnants of the 15 Hz. modulation is removed by notch filters. The sample rectified current is proportional to the light energy returned by the sample, and the reference current is proportional to the energy returned by the perfectly reflecting magnesium oxide sphere wall.

The reference current is next used to servo the slits to keep the reference energy flux constant (if possible). It is also used to manually position the full-scale value (100%) of the built-in ratiometer. Then through a rather complex scheme using the built-in plotter pen positioner

(which is not used for plotting) the sample signal adjusts a potentiometer which provides a voltage proportional to the reflected energy of the sample. This voltage feeds an analog-to-digital converter which ultimately supplies the measured voltage to the digital computer. The digital computer then stores the point pair of wavelength and response.

If the light sources were powerful enough to always provide enough light so that the slits were never wide open, the reference voltage driving the ratiometer and servoing the slits could also be recorded and the reflectance computed immediately. Unfortunately the sources run out of energy at the extremes of the measurement range. Thus the slits open further and further until they are at their maximum opening. At this time the full scale setting on the ratiometer is in error, and the energy reflected from the sample is likewise reduced, not due to low reflectance, but because of lower incident energy. This problem is overcome in the following way.

If the sample is moved aside while still in the sphere, the sample beam will no longer impinge on it but will look at the sphere wall, the same as the reference beam. Thus a run made under these conditions will record the true incident amount of light. Dividing the first (sample) run by the second (reference) run in the digital computer will produce a correct reflectance reading, corrected for the loss of energy in the sources. The price is, of course, a doubling of the time required to obtain a single sample-only reading. The system does work, and works well, but is rather inefficient because of inflexible analog instrumentation. A significant potential source of errors is the long period of time (a minimum of three minutes) between readings of the sample and the (ultimate) reference in the two-pass procedure.

OPERATIONS ANALYSIS

Beside giving attention to the equipment aspects of measuring reflectance, the operational use of the equipment was also studied. An operation process chart of the use of the DK-2A was constructed while samples from the last flight of the Induced Environmental Contamination Monitor (IECM) were being measured. The results are shown in Table I, and summarized in Table II.

The symbols in the first column of Table I are the standard charting symbols used to classify activities. The circle represents a productive operation, something which changes the value of the product or generates information. The D-shaped symbols are delays or idle time. In this case the operations are a classic example of a machine-paced job. The operator idle time is about 80% of the time required to

Table I -- Operation Process Chart of DK-2A Use

Operator	Description	Time
○	Change sample in holder	2 min.
○	Reinstall in sphere, W lamp on	1
○	Set calibration range & zero	1
◐	Reference run, long wavelength	9
○	Expose sample	0
◐	Sample run, long wavelength	8
○	Retract sample	0
○	Set calibration range & zero	1
◐	Reference run, medium wavelength	4
○	Expose sample	0
◐	Sample run, medium wavelength	4
○	Retract sample, D ₂ lamp on	0
○	Set calibration range & zero	1
◐	Reference run, short wavelength	3
○	Expose sample	0
◐	Sample run, short wavelength	3
◐	Plot, store data (if good run)	2

Table II -- Operation Process Chart Summary

Run	31 min.
Recalibrate	3
Change samples	3
Plotting	2
Total	<u>39 min.</u>

perform one complete cycle of the measurement job. Even worse, the idle time is broken up into small chunks of from three to eight minutes, leaving little time for other constructive work. Because technicians and co-op. students are the operators and are highly motivated people, the usual consequence is boredom and distaste for the job.

EXPERIMENTS

Fortunately, the DK-2A with the integrating sphere became available for a period of several weeks for some temporary modifications and measurements. These were carried out primarily to correct some operating deficiencies known to exist and to conduct measurements to provide design constraints for redesign of the electronics.

A relay rack with an oscilloscope and NIM-bins was also available. The NIM-bins are electronic packages designed to be modular elements of nuclear measuring systems. Modules were available in the form of AC broad-band amplifiers (1 Hz.- 100 KHz.), selective amplifiers with Q's up to 100 over the same frequency band, and "lock-in" amplifiers, which are synchronous detectors but may also be used as simple r.m.s. (root-mean-square) AC voltmeters. The theory of the use of these elements will be presented later in connection with the development of a model of modulation and the signal-to-noise ratio of the optical measurements.

EXPERIMENT 1 -- In the first experiment the electronics of the DK-2A were bypassed entirely. Using high-impedance probes to avoid loading any existing circuits, connections were made to the output of the detectors at the wiper of the selector switch. Thus the outputs of the detectors could selectively be applied to the input of the oscilloscope and the NIM-bin amplifiers. For this experiment, only voltages were measured using the calibrated input of the oscilloscope. The following results were obtained:

480 Hz. amplitude on long wavelength band
~1.5 mv. min., 3.5 mv. max.

The noise (non-square wave portion) at the
15 Hz. modulation frequency ~1 mv.

Thus the minimum detectable difference at the claimed accuracy of 2% is not more than

$$(0.02) * (1.5 \text{ mv.}) = 30 \text{ microvolts.}$$

A complete series of measurements across the entire spectrum was taken, showing the maximum voltage to be 310 mv. at 500 and 600 nm. wavelength using the PM tube in its reduced sensitivity (X1) mode. The light output seemed to

be very small using the deuterium (D_2) lamp. The reason for this has not been determined; the source has been changed without noticeable difference.

Other things noticed were:

Shielded probes with short ground leads are necessary to prevent the pick-up of considerable computer generated "hash".

The use of an internal 10 KHz. low-pass filter in the scope eliminated a lot more hash in the detector output.

There was a large 60 Hz. (power line frequency) component in the signals, as well as a large 180 Hz. (third harmonic) component.

At this point a rather serendipitous observation was made. With very low light levels, the current pulses due to the collection of individual photons by the photocathode could be observed on the scope. Individual pulses could still be seen even at high light levels. A few moments' reflection showed that this so-called "shot noise" is composed of rare events; rare events follow a Poisson probability distribution; the standard deviation (root-mean-square AC component) of a Poisson distribution is the square root of the mean (DC component); therefore the shot-noise AC component is related to (correlated with) the DC component, which we wish to measure. Experiment 2 was set up the test a practical way of implementing this technique.

EXPERIMENT 2 -- Just measuring the AC component of the signal would not be a practical method because of the large amounts of computer "hash", power line frequencies and harmonics, and other noise present. A suitably chosen narrow bandwidth would, however, contain noise energy proportional to the shot-noise energy because the individual impulses of which it is composed each have a uniform power spectrum, while avoiding the spurious low frequency content.

The equipment available was set up to accomplish observation of this scheme. The arrangement is shown in Fig. 2. The selective amplifier was set to give a Q of 100 and was tuned from 2.5 KHz. to 10 KHz. Best results were obtained at about 6 KHz. The lock-in voltmeter was operated in its rms. voltmeter mode. While no quantitative measurements were made at this time, the system was sensitive enough to detect the leakage into the integrating sphere of a flashlight played on the darkened room's walls. Similarly, shot noise energy was detected by the PM tube from both the tungsten and deuterium sources across the

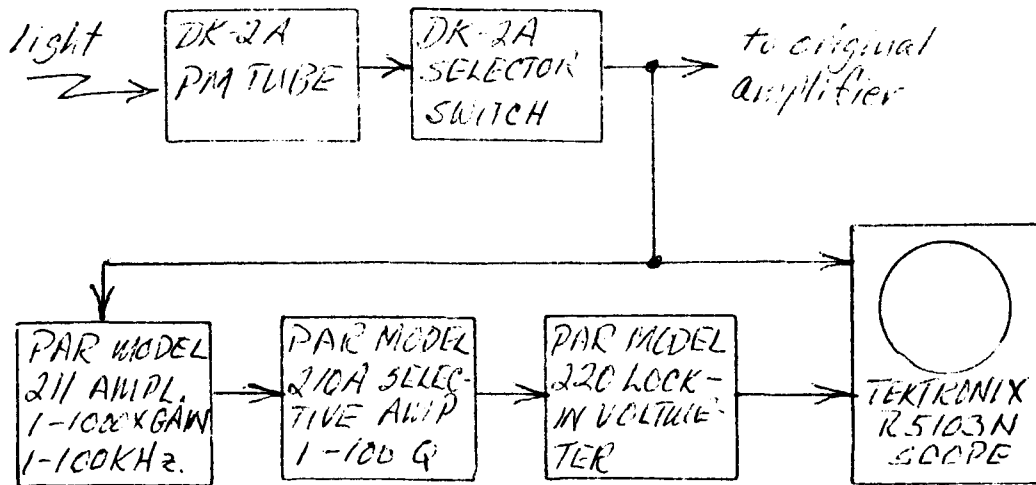


Figure 2 -- Shot noise energy set-up

entire optical spectrum, although this could be spurious radiation not trapped by the monochromator.

A theoretical analysis was conducted to find the form of the response curve and evaluate the sensitivity of the method. Horowitz and Hill, ⁽¹⁾ p. 288-9, give the shot noise due to a DC current as

$$I_{\text{rms}} = (2qI_{\text{DC}}B)^{1/2} \quad (\text{IX-1})$$

where q is the electron charge, $1.6(10)^{-19}$ coulombs, I_{DC} is the DC current, and B is the bandwidth. The ratio of two currents will vary as the square-root of the ratio of the bandwidths over which they are measured:

$$I_1/I_2 = (B_1/B_2)^{1/2} \quad (\text{IX-2})$$

A 1 microA. current has a 10 KHz. bandwidth rms. noise current of

$$[2 * 1.6(10)^{-19} * (10)^{-6} * (10)^4]^{1/2} = 57 \text{ pA.} \quad (\text{IX-3})$$

Across a 1 Mohm load resistor this yields an rms. shot noise voltage of 57 microV. Finally, if the bandwidth is reduced by a resonant filter of $Q = 100$, the shot noise current is reduced by the narrower bandwidth by a factor of $1/10$; but the resonant impedance is 100 times higher, yielding a net gain of 10 for a total rms. noise voltage of 570 microV.

This is easily measured. Again, quantitative measurements were not attempted beyond measuring the peaks of the individual pulses as 100 microV. across a 100 Kohm load.

The method does have two significant advantages which recommend further investigation:

1. The high selectivity permitted and the freedom to locate the center of the narrow band over a relatively wide frequency range give promise of relative immunity to other sources of noise.
2. The square-root relation between rms. noise voltage and average DC voltage means that the dynamic range of the amplifiers can be smaller.

The ideas brought out in Experiment 2 have sufficient novelty that they are under investigation for patentability.

EXPERIMENT 3 -- In the third experiment, the objective was to learn about the sensitivity and nonlinearity of the detectors so that a new electronics package could be designed. To this end the experiment was designed to use the NIM-bins to allow the collection of data independent of the old electronics.

Three different conditions were established to use all the usual combinations of sources and detectors. Since we were interested in finding nonlinearities, manual control of the slit size was elected, and the slits varied from 0.04 mm. to 2 mm. Since the energy varies as the square of the linear slit dimension with the sources used, the energy ratio was 2500 to 1. The lower limit occurred when the source did not have enough energy to be detectable, usually occurring at 0.04 mm.

It was found that at the larger slit openings the amount of energy available was too great for the instrumentation to operate at unity gain without overloading. A three-decade attenuator, matched to the impedances of the detectors and the amplifier, was constructed and used. A modification to the DK-2A was performed to allow the 480 Hz. chopper to be observed via a separate channel. This chopper signal was used to synchronize the synchronous detector in the lock-in amplifier. The general configuration of the equipment is shown in Fig. 3.

The modulation theory used here is thoroughly covered by any modern text in Communication Theory. See, for

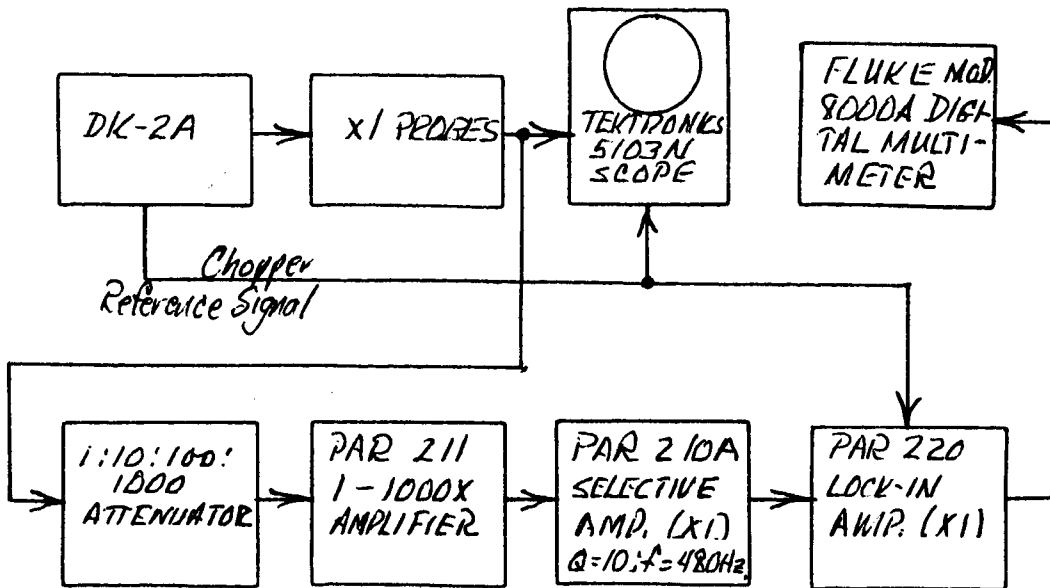


Figure 3 -- Equipment arrangement for Experiment 3

example, Gregg⁽²⁾. We represent the modulating signal by $m(t)$. In our case this is the voltage representing the light energy incident on the detector. A carrier, $c(t)$, the 480 Hz. chopper square wave, produces double sidebands centered around the carrier frequency. The resultant is $s(t)$. After transmission through the communication channel, here the light detector and amplifiers, the signal, now called $r(t)$ is demodulated by some means. The result, $m'(t)$, is a representation of the original which is more or less faithful depending on the nonlinearities and noise encountered in the detectors and amplifiers:

$m'(t) = m(t)$	Perfect rendition
$= m(t) + n(t)$	Additive noise
$= a(t) * m(t)$	Multiplicative noise (not common in non-radio communication)
$= f(m(t)) + n(t)$	Nonlinearities and additive noise

The last two of these are usually avoidable in a well-designed information system. The first one is only an ideal, leaving us to deal with the second form, additive noise.

A full treatment of noise figure and signal to noise ratios is beyond this report (but should ultimately be

done). A briefer, ad hoc derivation of an important relation affecting this study is now given. Consider the ideal optical signal waveform shown in Fig. 4. When the chopper obscures the light beam there is no output except that due to the noise term of the additive noise form above. This has been sketched in Fig. 4 as the wavy line in the two segments of the chopper square wave. The upper horizontal line represents either the true sample reflected energy, S, or the reference reflected energy, R, depending on the position of the sample/reference deflecting mirror in the

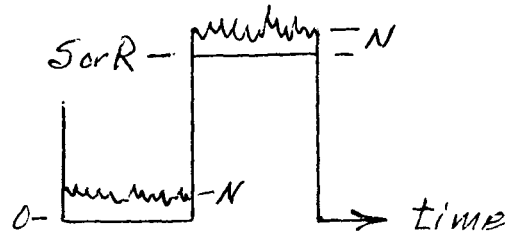


Figure 4 -- Signal showing effect of additive noise

DK-2A. What we wish to measure is the true value of the ratio S/R , but we actually measure $(S + N)/(R + N)$. Is there any way of obtaining the former from the latter? Obviously, if we knew the value of N , the instrumental noise, we could subtract it out of each term of the measurement and get the true S/R . After some algebraic manipulation we can obtain

$$S/R = [(S + N) - N]/[(R + N) + 1]. \quad (\text{IX-4})$$

Although this still doesn't look too hopeful, the terms in parentheses are the measured quantities, and the term on the left is the desired ratio.

Suppose now that we take several measurements on the same sample with the same source, detector, and wavelength combination. Equation 4 can be rearranged, and subscripts added to index measurements and unique measurement errors:

$$(S + N)_i = (S/R) * [(R + N)_i + 1] + N + (\text{unique error})_i \quad (\text{IX-5})$$

This has the linear form

$$y = a + b*x + (\text{unique error}) \quad (\text{IX-6})$$

which is a linear regression! So repeated measurements such as those taken in Experiment 3 with varying slit widths can

be used to estimate both the true reflectance, S/R , and the instrumental noise, N , as long as the signal channel remains linear. The estimators are

$$N = a$$

$$S/R = b$$

$$(R + N)_i + 1 = x_i$$

$$(S + N)_i = y_i$$

(IX-7)

Note carefully the need to add one to each value of the reference reflectance in calculating the regression. This term can be interpreted as arising from having normalized all measurements by the amplitude of the noise.

A similar analysis shows a similar form for errors introduced by phase errors in the synchronizing signal (from the chopper) and by commutation errors caused by lack of symmetry of the open and closed segments of the chopper. They will all contribute to the noise term, N , above. However the signs of these two errors are opposite from that of instrumental noise! This presents some interesting possibilities for cancelling instrumental noise effects by the intentional introduction of phase or commutation errors in the synchronous detection.

The technique derived above was used to fit the data of Experiment 3, with the expectation that the noise term, N , would be of the order of a few microvolts. The results were irregular and disappointing, however. Account was carefully taken of the attenuator setting and the gains of the various amplifiers in the signal amplifiers. After considerable trial and error, it was finally discovered that the experimental measurements only fell into an orderly array when the gain and attenuator settings were ignored! Table III summarizes these results.

Table III \rightarrow Experiment 3 Regression Results

Source	Detect.	Atten.	Gain	# Pts.	N Est.	%R Est.	Coeff. of Determination
W (1200nm.)	PbS	1/10	10	9	0.888mv.	89.2	0.999,991
			100	7	0.828	88.4	0.999,910
			1000	9	0.753	91.1	0.999,860
W (575nm.)	PMx 20	1/1000	1	9	1.194	104.3	0.997,279
			100	6	0.842	94.3	0.999,757
D (575nm.)	PMx 20	1/10	1	6	0.920	94.2	0.999,994
			10	4	0.959	95.7	0.999,992
			100	5	0.967	97.1	0.999,986

The table displays several interesting results. First, the noise estimates approximate one millivolt on an instrument set to read ten millivolts full scale. As already noted, the gain and attenuator settings were disregarded in these calculations, indicating that the 1 mv. noise is being generated in the final stages of the instrumentation. That the results are no fluke is indicated by the fact that the coefficient of determination (square of the correlation coefficient) is very high for most cases. One minus this quantity measures the amount of variation in the dependent variable not explained by the regression equation.

One can only interpret these results as suggesting the instrumentation, probably the lock-in voltmeter, has sufficient internal noise in the synchronous detection process that a noise magnitude approximating 9% of full scale exists.

The table does show that there is some apparent nonlinearity in the detector response, because the corrected values of the reflectance do not remain constant at different incident energy and gain settings. In one case, an impossible result of 104% reflectance was indicated. It is also possible that the lack of agreement is due to the originally anticipated detector noise phenomenon. Pulling this effect out of the data would require a multiple regression analysis; this there was insufficient time to do.

RESULTS AND CONCLUSIONS

In summary, the following results have been obtained:

1. Nonlinearity of the detectors is indicated.
2. Instrumental noise currently limits the investigation.
3. A method of correcting readings for noise and errors, with application to digital computation and control, has been developed.
4. A novel method of measurement based on shot noise modulation has been discovered.
5. A microprocessor-based digital computer has been assembled and made operational for dedicated use in recording, computation, and control of the reflectance measurements.

The following conclusions have been reached:

1. The original study objectives are still valid and achievable.
2. There is a need to locate and eliminate the source of the instrumental noise.
3. Failing this, a theoretical noise study is needed to determine the ultimate capability of the synchronous detection method.
4. Some effort should be expended to further explore the novel noise modulation measurement method.

ACKNOWLEDGEMENTS

My grateful thanks for the opportunity to conduct these investigations go to Mr. Don R. Wilkes, my NASA counterpart and contact for the summer. Thanks are also due Mr. Ray Black for his technical assistance with equipment setups, modifications, etc. Finally, I wish to thank Dr. R. Barfield, ASEE, and NASA for providing the facilitating framework under which this work was performed.

BIBLIOGRAPHY

1. Horowitz, P., and W. Hill, The Art of Electronics, Cambridge University Press, New York, 1980.
2. Gregg, W. D., Analog and Digital Communication, Wiley, New York, 1977.
3. Miller, I., and J. E. Freund, Probability and Statistics for Engineers, Second Ed., Prentice-Hall, Englewood Cliffs, N. J., 1977.
4. Anon., "Instruction Manual, Lock-In Amplifier Model 220," Princeton Applied Research Corp., Princeton, N. J., 1971.
5. ---, "Instruction Manual, Selective Amplifier Model 210A," Princeton Applied Research Corp., Princeton, N. J., 1971.
6. Trujillo, E. F., "Model DK-A Ratio Recording Spectrophotometers," Beckman Instruments, Inc., Fullerton, CA, 1962.
7. Anon., "Illustrated Parts Manual, Model DK-A Ratio Recording Spectrophotometers," Beckman Instruments, Inc., Fullerton, CA, 1963.

1982

NASA/ASEE SUMMER FACULTY RESEARCH FELLOWSHIP PROGRAM

MARSHALL SPACE FLIGHT CENTER
THE UNIVERSITY OF ALABAMA

INVESTIGATION OF MESOSCALE METEOROLOGICAL PHENOMENA
AS OBSERVED BY GEOSTATIONARY SATELLITE

Prepared By:	Kenneth C. Brundidge, Ph.D.
Academic Rank:	Professor
University and Department:	Texas A&M University Department of Meteorology
NASA/MSFC: (Laboratory) (Division) (Branch)	Space Sciences Atmospheric Sciences Fluid Dynamics
MSFC Counterparts:	G. H. Fichtl/J. E. Arnold
Date:	August 6, 1982
Contract No.:	NGT-01-002-099 (University of Alabama)

INVESTIGATION OF MESOSCALE METEOROLOGICAL PHENOMENA
AS OBSERVED BY GEOSTATIONARY SATELLITE

By

Kenneth C. Brundidge, Ph.D.
Professor of Meteorology
Texas A&M University
College Station, Texas

ABSTRACT

Satellite imagery plus conventional synoptic observations are used to examine three mesoscale systems recently observed by the GOES-EAST satellite. The three systems are an arc cloud complex (ACC), mountain lee wave clouds and cloud streets parallel to the wind shear. Possible gravity-wave activity is apparent in all three cases. Of particular interest is the ACC because of its ability to interact with other mesoscale phenomena to produce or enhance convection.

ACKNOWLEDGMENTS

The author is grateful to the American Society of Engineering Education for having chosen him to participate in the 1982 Summer Faculty Fellowship Program. Gratitude also is owed to Dr. J. E. Arnold of the Marshall Space Flight Center who called the author's attention to the phenomena described herein and who spent many hours on the MSFC McIDAS retrieving the satellite imagery and other information needed by the author for this study. Finally, thanks is extended to Dr. G. H. Fichtl, who provided interest and encouragement throughout the program.

INTRODUCTION

Motion systems in Earth's atmosphere cover a broad spectrum of sizes, from roughly hemispheric down to the very small scales of turbulence. A portion of the spectrum has been called mesoscale (Orlanski, 1975), which for our purposes here may be defined to extend from about 400 km to about 1 km. At the large end of this range are the large storm complexes such as squall lines, and at the small end are the individual cumulonimbus clouds. Thus, the mesoscale encompasses phenomena which produce such destructive events as flash flooding, hail damage, tornados, lightning damage and winds affecting aircraft operations.

The study of mesoscale phenomena, particularly at the small end of the scale, by conventional meteorological observations has been essentially impossible because of the horizontal spacing of observation sites. Surface observations generally are 100 km or more apart and upper-air stations generally are several hundred kilometers apart. Therefore, most mesoscale systems cannot be resolved by the observations.

The weather radar has helped overcome some of the deficiencies of the meteorological observation system and a recent development, the meteorological satellite, has made a tremendous impact. As pointed out by Purdom (1979), the Geostationary Operational Environmental Satellite (GOES) has provided the atmospheric scientist a means to see not only the range of atmospheric systems from the synoptic down to the cumulus scale, but also to see the ongoing interactions between scales. Thus, a variety of mesoscale systems have come to be observed and described in the literature such as ocean, lake and river breezes (Purdom, 1976), arc clouds (Purdom, 1973, 1976; Gurka, 1976) and convective complexes (Maddox, 1980). Despite the differences in resolution, it follows that what is needed at this point are studies which combine satellite observations with radar and other conventional data in order to gain an understanding of the conditions that produce or maintain convection which may lead to severe storms.

This report will describe three mesoscale phenomena which have been observed recently by the GOES-EAST satellite. The analysis of these events is in a preliminary stage. The discussion will concentrate on a description of these cases and suggestions as to the physical factors involved, based on related studies reported in the literature.

OBJECTIVES

The immediate objective of this study has been to gain familiarity with some of the mesoscale phenomena which are observed by the GOES satellite. The ultimate objective has been to determine by direct analysis and reasonable inference the physical processes that are involved in producing these mesoscale events. This objective has been only partially satisfied at this time.

CASE 1 - MAY 17, 1982

Figure 1 shows the cloud images over Texas at 1300 GMT on May 17, 1982 as seen by the GOES-EAST satellite with 8 km resolution. Of particular interest is the roughly triangular area delineated by the convective clouds over north, central Texas.

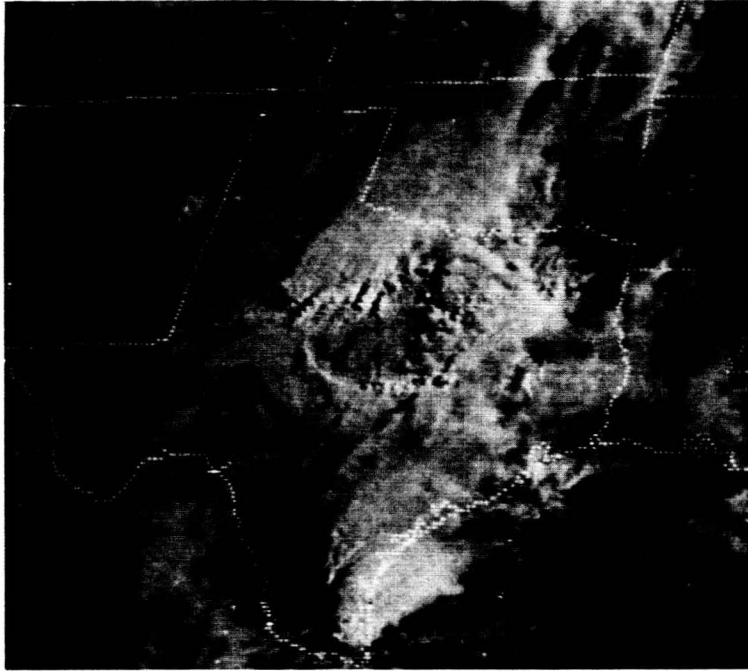


Fig. 1 GOES-EAST visible imagery at 1300 GMT, May 17, 1982 for Texas. The resolution is at 8 km.

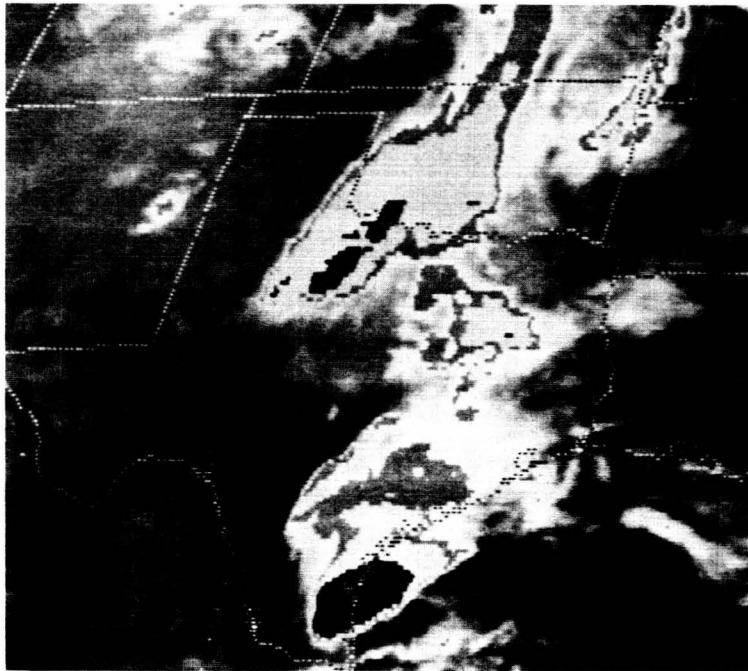


Fig. 2 GOES-E enhanced infrared image for Texas at 1230 GMT on May 17, 1982. The resolution is at 8 km.

Figure 2 shows the enhanced infrared (IR) images at 1230 GMT for the same resolution. The MB color scheme shows some cloud tops in the cirrus shield on the northwest flank of the triangle at temperatures colder than -58°C . The temperatures indicated on the eastern flank of the triangle are generally warmer than -52°C , except at one point. These conditions would seem to indicate that the most intense convection was occurring just north of Abilene, TX (ABI); however, the manually digitized radar (MDR) reports show level 3 values in both areas.

The thin, curved line of cumulus clouds making up the southern side of the triangle in Fig. 1 has no temperature as cold as -32°C and is non-precipitating. The same thing is true of the clouds in the interior of the triangle. Purdom (1973, 1976) has found that this line of clouds marks the edge of a mesohigh in the surface pressure field and has called it an "arc cloud." He also found that the arc cloud is a moving boundary having many of the properties of a cold front, e.g., a wind shift, a pressure jump, and a drop in both temperature and dew point temperature. Where the moving arc cloud intersects other mesoscale boundaries such as fronts, squall lines or other arc clouds is where intense convection is most likely to occur. Also, convection is likely to be enhanced, perhaps even to the intense stage, if an arc cloud moves into a region where some convective clouds already exist (Purdom, 1979). Such was the case in southeastern Texas on this day.

Figure 3 shows the situation at 1600 GMT; the resolution in this figure is 2 km. By this time the convective area north of ABI is beginning to dissipate while that on the eastern flank of the arc cloud has intensified. The arc has expanded normal to itself in the southward direction. This process continues for the next several hours, as seen in Fig. 4 at 1930 GMT. By this time, the convective activity has ceased on the western flank of the arc and the cloud debris in the central portion of the ring has even vanished, probably as a result of substantial subsidence in this area. On the other hand strong convection has been maintained on the east and southeastern flanks of the ring.

The arc cloud for this case is still clearly delineated in deep south Texas in the visible satellite imagery at 2030 GMT (not shown here) but becomes lost to view after this time because the cirrus tops of thunderstorms in Mexico have expanded northward over southern Texas. Note in Fig. 4 that although there is no convection along the western portion of the arc cloud, the penetration of the arc into this region appears to have enhanced the growth of the cumulus cloud lying just to the north of Midland, TX. Intense convection develops northward from this point over far west Texas and eastern New Mexico over the next 8 hours.

The surface synoptic conditions for this case at 1200 GMT in the Texas region are shown in Figs. 5 and 6. The National Weather Service analysis of the pressure field has been modified and replaced with isobars drawn at a 1-mb interval in Fig. 5. Isotherms at a 2°F interval appear in Fig. 6. In both analyses the reported data have been assumed to be correct and have been fully utilized. The thin line or ring with small markings like a cold front represents the estimated position of the arc cloud at this time. It is seen that higher pressure fills the interior of the ring, producing a relative trough in the pressure along the ring.

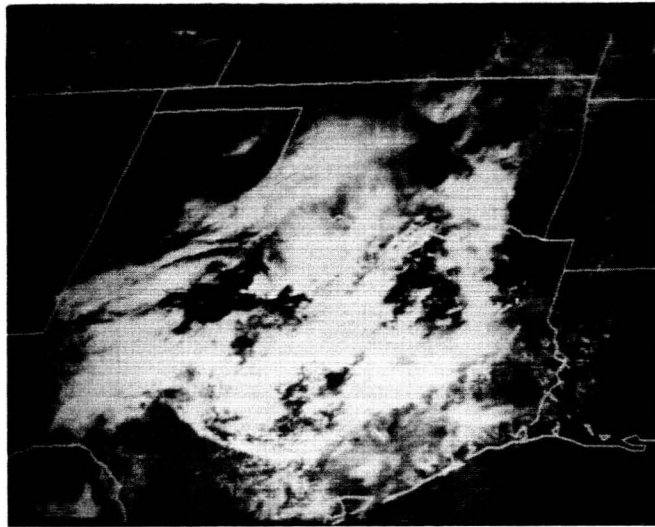


Fig. 3 GOES-EAST visible image at 1600 GMT - 2 km resolution.

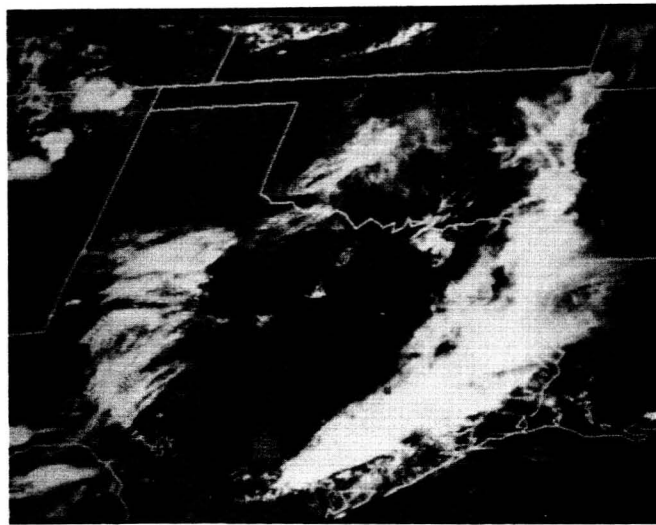


Fig. 4 GOES-EAST visible image at 1930 GMT - 2 km resolution. The two lines of crosses mark the positions of the arc cloud at 1400 and 1600 GMT.

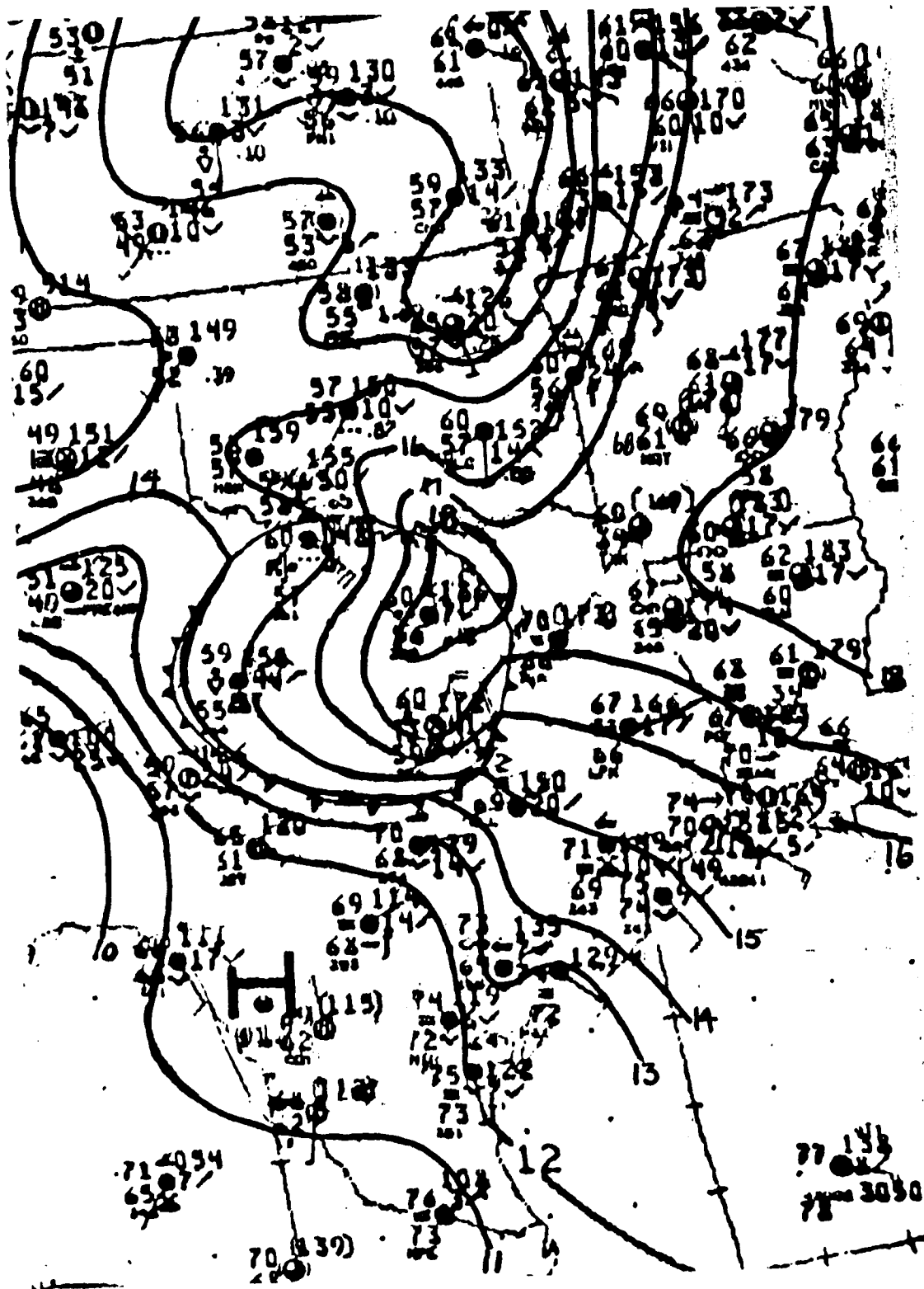


Fig. 5 A portion of the 1200 GMT surface map for 1200 GMT, May 17, 1982. The National Weather Service analysis has been replaced with isobars at 1-mb intervals. The thin line with cold front markings encloses the storm area in northern Texas at this time. A mesohigh is centered over the Dallas-Ft. Worth area.

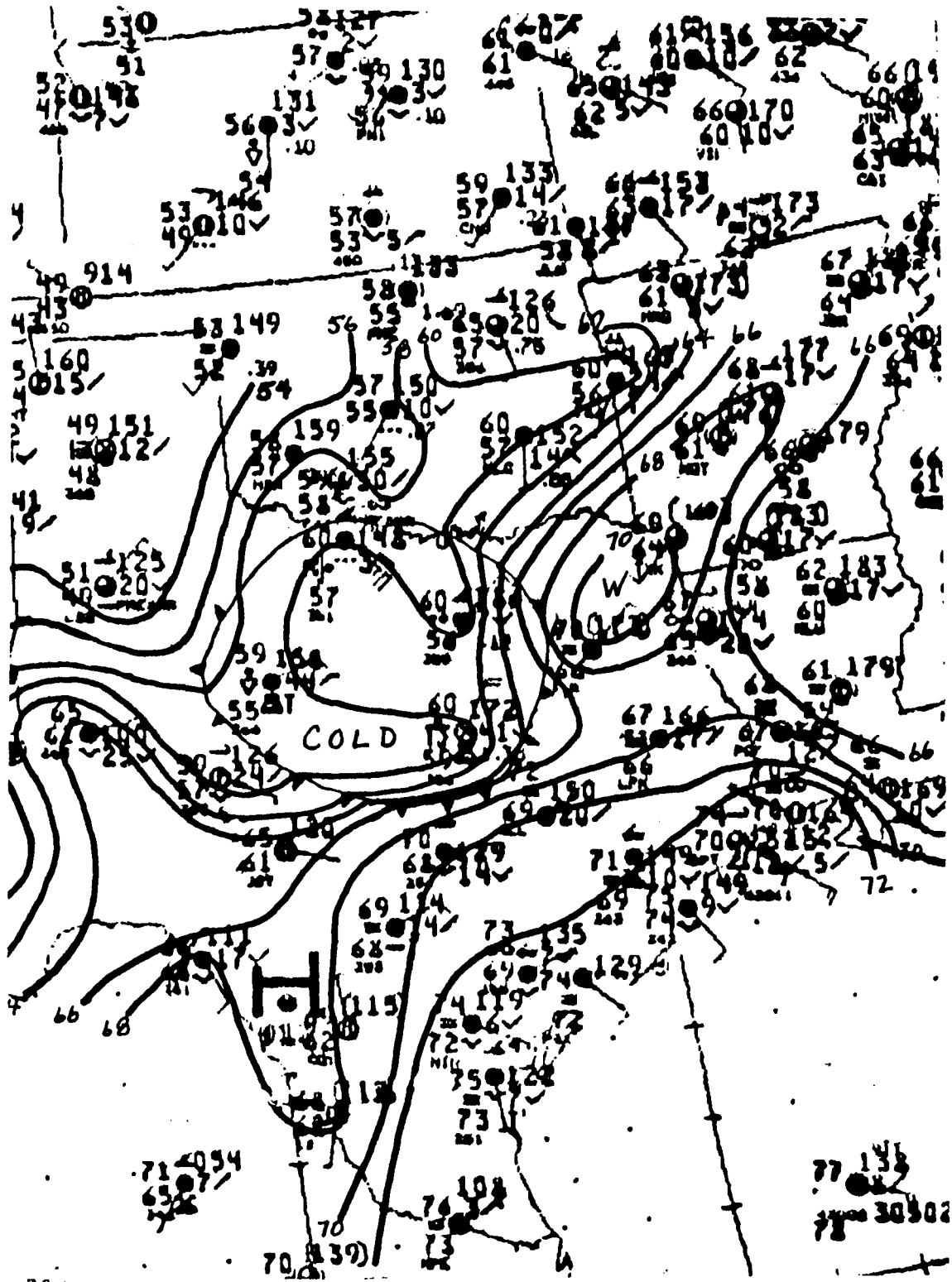


Fig. 6 The mesoscale temperature analysis at 1200 GMT, May 17, 1982. The isotherms are at 2°F intervals.

The isotherms in Fig. 6 indicate temperature gradients on the southern and eastern sides of the arc much like that of a weak cold front. This is even more pronounced in the field of equivalent potential temperature because the cooler air also has a lower dew point temperature. Both Purdom (1973, 1976, 1979) and Maddox (1981) have called attention to the mesohigh associated with large convective complexes but have not shown the coexisting temperature field. Nevertheless, a temperature field much like that in Fig. 6 could be drawn in Maddox's Fig. 5c.

It remains to be determined by future analysis of the pressure and temperature fields at subsequent times if the features seen in Figs. 5 and 6 are maintained over the next 12 hours. This will provide some clues as to the dynamics at play which maintains the identity of the arc cloud for about 12 hours and permits it to propagate a distance of about 300 km. Certainly also there is a great need to understand how the arc cloud interacts with its environment to enhance or produce new convection.

There is one other point of interest involved in this case. It can be seen in Fig. 4 that the middle and high clouds at the western end of the arc cloud have taken on a banded structure. Erickson and Whitney (1973) have reported on a satellite observation of an arc-shaped banded structure in middle clouds which extended from northeast Texas into central Arkansas. They assumed that this structure was the result of a propagating gravity wave initiated by violent thunderstorms to the northwest of the cloud bands. There are no other satellite images to confirm the conjecture that they also were dealing with an arc cloud but their description of conditions and events associated with these cloud bands makes this seem likely. This case has been examined theoretically by Ley and Peltier (1981) as an eigenvalue problem by using the wind and temperature distributions measured by upper-air soundings at Shreveport, LA and Little Rock, AR. The solution mode which they found to have the least horizontal attenuation was ducted vertically, thus confining the energy. This mode also most closely matched the wavelength of the cloud bands (~ 10 km) and the observed phase speed (~ 12 ms $^{-1}$).

CASE 2 - JUNE 7, 1982

Figure 7 gives the National Weather Service analysis of a portion of the 850 mb surface at 1200 GMT on June 7, 1982. The high pressure ridge line extending from east of Hudson's Bay to Louisiana had very little tilt from the surface to the tropopause and was stationary over the next 12 hours. Therefore, the wind over West Virginia, Virginia and North Carolina was essentially free of direction shear with height.

The 1200 GMT soundings for Huntington, WV (HTS) and for Greensboro, NC (GSO) are given in Fig. 8. Subsidence inversions are evident in both soundings and the wind distribution in the boundary layer at GSO approximates the Ekman profile.

The cloud bands seen in Fig. 9 clearly must represent visual evidence of lee waves produced by the movement of the air over the Clinch and Shenandoah Mountain chains. The winds over West Virginia are essentially normal to these mountains. The sounding at HTS indicates that the most likely height of these bands is about 1 km above local average terrain

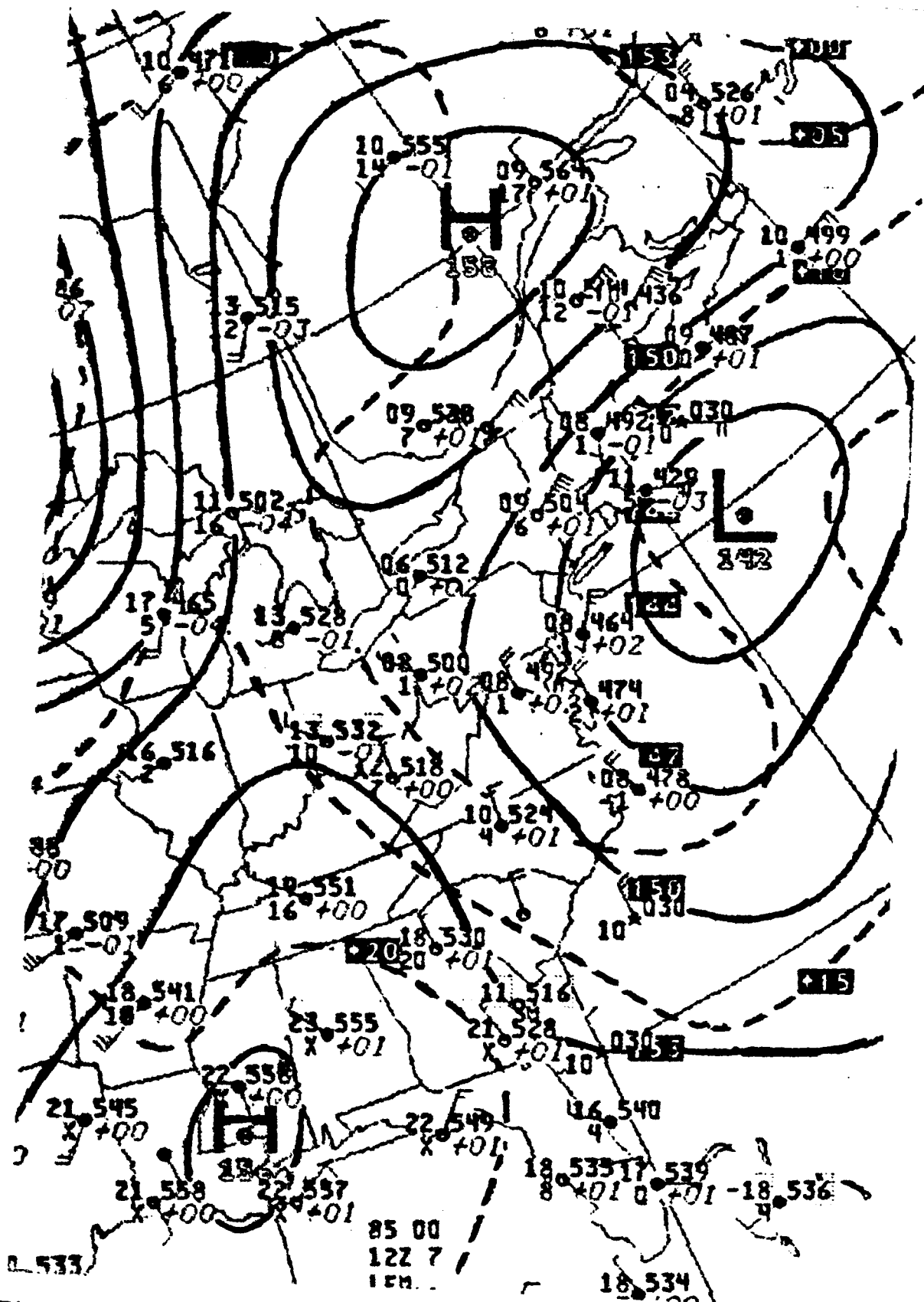


Fig. 7 The 850-mb surface analysis at 1200 GMT on June 7, 1982.

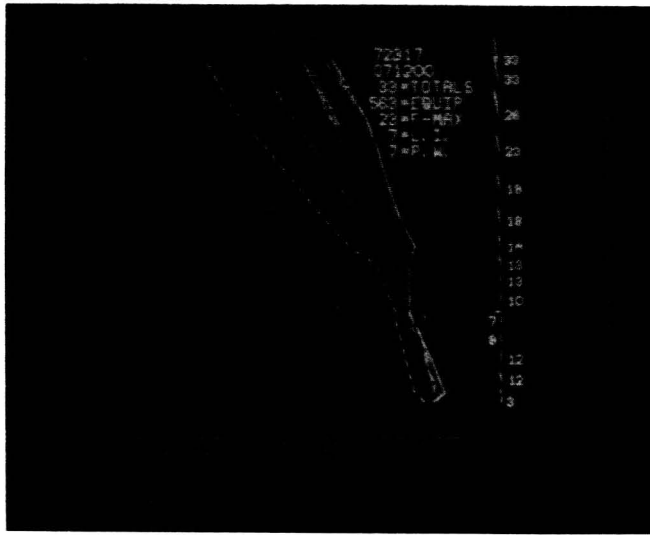


Fig. 8 Soundings at HTS and GSO for 1200 GMT, June 7, 1982.



Fig. 9 GOES-EAST visible imagery at 1330 GMT, June 7, 1982 with 1 km resolution.

height at the base of the weak subsidence inversion. The wavelength of these bands varies from 5 to 10 km and the fact that the bands are stationary, as seen in succeeding satellite images at half-hour intervals (see Figs. 10-13), indicates that the air must be moving through the clouds.

These lee-wave clouds begin to dissipate about 1500 GMT (see Figs. 12 and 13), possibly because convective circulations produced by solar heating of the surface breaks up the wave structure of the flow.

Reviews of the various theories explaining lee-wave formation have been given by Booker (1963) and Gossard and Hooke (1975). A study specifically directed to lee waves over the Blue Ridge Mountains in northern Virginia has been made by Smith (1976).

CASE 3 - JUNE 7, 1982

Figures 10-13 show the lee-wave cloud images as a function of time, as discussed above. However, starting at 1400 GMT (Fig. 10) it is seen that another banded cloud structure suddenly appears just to the west of GSO. These bands of small cumulus are oriented nearly parallel to the wind flow above the planetary boundary layer and have a spacing of about 5 km or less. During the next hour, there is a lateral spread of this pattern as new lines of clouds appear both to the east and west of the original area. The development of cumulus in the morning hours certainly was to be expected in this area, considering the conditions shown in the GSO sounding (Fig. 8). The lower troposphere was quite moist and only a small amount of solar heating at the surface was required to eliminate the shallow nocturnal inversion. The vertical growth of the clouds was suppressed by the stable layer between 830 and 730 mb.

The tendency for low-level clouds to develop in streets parallel to the flow is well-known (Kuettner and Soules, 1966; Kuettner, 1971). One explanation of this phenomena is that the convection is organized by what is referred to as Ekman-layer instability. Various theoretical studies (e.g., Barcilon, 1965; Lilly, 1966) have shown that horizontal roll vortices may develop in the planetary boundary layer (PBL) with their axis making an angle of 10° - 20° to the left of the geostrophic wind vector. The mean flow in the PBL must veer with height in accordance with the Ekman distribution. The wind distribution in the GSO sounding at 1200 GMT veers to a height of 1212 m above sea level. These vortices have been observed in laboratory studies by Faller (1965) and in nature by Angell *et al.* (1968), LeMone (1973) and Berger and Doviak (1979). These studies predict that cloud streets may have a lateral spacing of 2-8 km and may be several hundred kilometers in length. They should move normal to themselves at a very slow rate, on the order of 1 ms^{-1} .

The rapid lateral spread of the cloud streets in this case may simply be a result of local variations in surface heating and/or boundary layer stability. However, this spread seemed to be smoothly continuous rather than random, as would be expected. This implies some organizing influence such as might be provided by a gravity wave.



Fig. 10 Visible imagery at 1400 GMT, June 7, 1982. Surface winds also are shown. 1 km resolution.



Fig. 11 Visible image at 1430 GMT, June 7, 1982. Lee waves normal to the wind and convective cloud streets parallel to the wind are present.



Fig. 12 Cloud images at 1500 GMT, June 7, 1982. Surface winds also are shown.



Fig. 13 Cloud images at 1630 GMT, June 7, 1982.

Gravity waves have received considerable attention in the literature and the citations are too numerous to list here. In view of the behavior of the cloud bands or streets described above, the most pertinent article is that by Jones (1972). If gravity waves are to propagate over any significant horizontal distance, their energy must be confined in a layer. A stable layer embedded in a region of lower stability, such as existed on this day at GSO (Fig. 8), will serve as an energy duct. Jones shows that when there is a vertical shear across the stable layer, there are severe restrictions on the gravity wave modes that can be ducted and still propagate in the direction of the mean wind. These restrictions are removed as the angle between the shear vector and the propagation vector increases. Thus, ducted waves are more likely to be found propagating nearly normal to the shear vector. This should aid in establishing cloud streets parallel to the shear vector.

CONCLUSIONS AND RECOMMENDATIONS

This study has described three mesoscale systems commonly observed in the GOES-EAST imagery. Lee wave clouds and cloud streets have received much study, both through measurements and through theoretical treatment. The literature also is rich with studies dealing with gravity waves and their possible role in producing mesoscale convective bands over a broad range of wavelengths.

On the other hand, the arc cloud and its associated convective complex have received only a descriptive, mainly qualitative treatment of the sort given here. The mesohigh has been attributed to the collective effect of downdrafts and gust fronts from the individual cells making up the convective complex. Starting from this point, Maddox (1980) has attempted to explain in qualitative terms the life cycle of the mesoscale convective complex (MCC). Although his examples of the MCC appear to be very similar to Case 1 described here, there is no evidence of the arc cloud feature nor of an interaction with other convective areas.

The difficulty in developing a theory for the dynamics of the arc cloud complex (ACC) is, as stated previously, that conventional upper-air observations within the ACC generally are not available. Radar observations will not be particularly useful here because by the time the arc cloud becomes defined in the satellite imagery, apparent subsidence is clearing out the precipitation and cloud debris on the interior of the arc ring. Therefore, it is recommended that observations with the Visible and Infrared Spin-Scan Radiometer Atmospheric Sounder (VAS), now mounted on the GOES, be utilized to establish the vertical moisture and temperature distributions in the vicinity of the arc boundary. A number of cases should be studied to determine systematic conditions. A numerical modeling effort also would be useful to see if the common conditions can be simulated.

REFERENCES

- Angell, J. K., D. H. Pack, and C. R. Dickson, 1968: A Lagrangian study of helical circulations in the planetary boundary layer. J. Atmos. Sci., 25, 707-717.
- Barcilon, V., 1965: Stability of a non-divergent Ekman layer. Tellus, 17, 53-68.
- Berger, M. I., and R. J. Doviak, 1979: An analysis of the clear air planetary boundary layer wind synthesized from NSSL's dual doppler-radar data. NOAA Tech. Memo. ERL NSSL-87, 55 pp.
- Booker, D. Ray, 1963: Modification of convective storms by lee waves. Meteor. Monogr., 5, 129-140.
- Erickson, C. O., and L. F. Whitney, 1973: Gravity waves following severe thunderstorms. Mon. Wea. Rev., 101, 708-711.
- Faller, Alan J., 1965: Large eddies in the atmospheric boundary layer and their possible role in the formation of cloud rows. J. Atmos. Sci., 22, 176-184.
- Gossard, E., and W. H. Hooke, 1975: Waves in the Atmosphere, Elsevier, 456 pp.
- Gurka, James J., 1976: Satellite and surface observations of strong wind zones accompanying thunderstorms. Mon. Wea. Rev., 104, 1484-1493.
- Jones, Walter L., 1972: Ducting of internal gravity waves on a stable layer with shear. J. Geophys. Res., 77, 3879-3885.
- Kuettner, J. P., and S. D. Soules, 1966: Organized convection as seen from space. Bull. Amer. Meteor. Soc., 47, 364-371.
- Kuettner, J. P., 1971: Cloud bands in the atmosphere. Tellus, 23, 404-425.
- LeMone, Margaret A., 1973: The structure and dynamics of horizontal roll vortices in the planetary boundary layer. J. Atmos. Sci., 30, 1077-1091.
- Ley, B. E., and W. R. Peltier, 1981: Propagating mesoscale cloud bands. J. Atmos. Sci., 38, 1206-1219.
- Lilly, D. K., 1966: On the instability of Ekman boundary flow. J. Atmos. Sci., 23, 481-494.
- Maddox, R. A., 1980: Mesoscale convective complexes. Bull. Amer. Meteor., 61, 1374-1387.
- Orlanski, I., 1975: A rational subdivision of scales for atmospheric processes. Bull. Amer. Meteor. Soc., 56, 527-530.

REFERENCES

- Purdom, J. F. W., 1973: Meso-highs and satellite imagery. Mon Wea. Rev., 101, 180-181.
- _____, 1976: Some uses of high-resolution GOS imagery in the mesoscale forecasting of convection and its behavior. Mon Wea. Rev., 104, 1474-1483.
- _____, 1979: The development and evaluation of deep convection. Preprints 11th Conf. Severe Local Storms, Kansas City, Mo., Amer Meteor. Soc., 143-150.
- Smith, Ronald B., 1976: The generation of lee waves by the Blue Ridge. J. Atmos. Sci., 33, 507-519.

NASA/ASEE SUMMER FACULTY RESEARCH FELLOWSHIP PROGRAM

MARSHALL SPACE FLIGHT CENTER

THE UNIVERSITY OF ALABAMA

FUEL OPTIMAL MANEUVERS OF SPACECRAFT

ABOUT A CIRCULAR ORBIT

Prepared By:	Thomas E. Carter, Ph.D.
Academic Rank:	Associate Professor
University and Department:	Eastern Connecticut State College Mathematical Sciences
NASA/MSFC: Division: Branch:	Control Systems Division Dynamics & Trajectory Analysis Branch
MSFC Counterpart:	Harry J. Buchanan
Date:	August 20, 1982
Contract No.	NGT 01-002-099 The University of Alabama

FUEL OPTIMAL MANEUVERS OF SPACECRAFT

ABOUT A CIRCULAR ORBIT

By

Thomas E. Carter

Associate Professor of Mathematical Sciences

Eastern Connecticut State College

Willimantic, Connecticut

ABSTRACT

Fuel optimal maneuvers of spacecraft relative to a body in circular orbit are investigated using a point mass model in which the magnitude of the thrust vector is bounded. All nonsingular optimal maneuvers consist of intervals of full thrust and coast and are found to contain at most seven such intervals in one period. Only four boundary conditions where singular solutions occur are possible. Computer simulation of optimal flight path shapes and switching functions are found for various boundary conditions. Emphasis is placed on the problem of soft rendezvous with a body in circular orbit.

ACKNOWLEDGEMENTS

The author expresses appreciation to Stan Carroll of the Dynamics and Trajectory Analysis Branch of the George C. Marshall Space Flight Center whose suggestions and insights were of much value to this project. He also thanks Roger Burroughs of the Flight Mechanics Branch of the George C. Marshall Space Flight Center who wrote the computer program which was used to solve the two-point-boundary value problems and who instructed the author in the use of this program.

LIST OF FIGURES

<u>Figure No.</u>	<u>Title</u>	<u>Page</u>
1	Nature of Fuel Optimal Thrusting Sequence in Deep Space	IX-8
2	Nature of Fuel Optimal Thrusting Sequence about a Point Moving in Circular Orbit	IX-8
3	A Seven Phase Optimal Thrusting Sequence in One Period.	IX-10
4	The Absolute Value of q Over One Period for the Seven Phase Optimal Thrusting Sequence .	IX-10
5	Switching Function and Flight Path for $X(0) = (0, 0)$, $V(0) = (1, 0)$, $X(TF) =$ $(0, 1)$, $V(TF) = (0, 0)$	IX-15
6	Switching Function and Flight Path for $X(0) = (0, 0)$, $V(0) = (0, 0)$, $X(TF) =$ $(1, 1)$, $V(TF) = (0, 0)$	IX-15
7	Switching Function and Flight Path for $X(0) = (0, 0)$, $V(0) = (1, 0)$, $X(TF) =$ $(0, 1)$, $V(TF) = (-1, 0)$	IX-15
8	Switching Function and Flight Path for $X(0) = (0, 0)$, $V(0) = (1, 0)$, $X(TF) =$ $(0, 1)$, $V(TF) = (1, 0)$	IX-16
9	Switching Function and Flight Path for $X(0) = (0, 0)$, $V(0) = (1, 0)$, $X(TF) =$ $(0, 0)$, $V(TF) = (0, 1)$	IX-16
10	Switching Function and Flight Path for $X(0) = (0, 0)$, $V(0) = (1, 0)$, $X(TF) =$ $(0, 1)$, $V(TF) = (0, 1)$	IX-16
11	Comparison of Switching Functions and Flight Paths for Deep Space and 435 KM. Altitude Circular Orbit: $X(0) = (1000,$ $1000)$, $V(0) = (0, 0)$, $X(TF) =$ $(0, 0)$, $V(TF) = (0, 0)$	IX-17

LIST OF FIGURES (CONTINUED)

<u>Figure No.</u>	<u>Title</u>	<u>Page</u>
12	Comparison of Switching Functions and Flight Paths for Deep Space and 435 KM. Altitude Circular Orbit: $X(0) = (0, 1000)$, $V(0) = (10, 0)$, $X(TF) = (0, 0)$, $V(TF) = (0, 0)$	IX-18
13	Switching Function and Flight Path for Different Flight Times for 435 KM. Circular Orbit: $X(0) = (1000, 0)$, $V(0) = (0, 0)$, $X(TF) = (0, 0)$, $V(TF) = (0, 0)$	IX-19
14	Insertion of Mass From Elliptical into 435 KM. Circular Orbit: $X(0) = (0, 1000)$, $V(0) = (0, 0)$, $X(TF) = (0, 0)$, $V(TF) = (0, 0)$, Optimal Maneuver Requires Mid-Course Thrust	IX-20
15	An Optimal Maneuver with Four Thrusts and Three Coasts in One Period (5600 SEC): $X(0) = (0, 0)$, $V(0) = (0, 0)$ $X(TF) = (-73000, 0)$, $V(TF) = (0, 35)$. . .	IX-20

CONTENTS

FUEL OPTIMAL MANEUVERS OF SPACECRAFT ABOUT A CIRCULAR ORBIT

- I. Introduction
- II. Mathematical Analysis
 - 1. Solutions in the Orbital Plane
 - 2. Solutions Out of the Orbital Plane
- III. Computer Simulations
- IV. Conclusions

I. INTRODUCTION

Most of the immediate applications of space involve a body in circular orbit. Fuel optimal maneuvers of a spacecraft relative to such a body constitute the subject of this investigation.

We assume the spacecraft to be a point mass with a variable thrust vector of bounded magnitude. The mass of the spacecraft is assumed constant over a fixed flight time t_f and a minimum fuel maneuver will be regarded as a maneuver in which the integral of the magnitude of the thrust is minimized. The position x and velocity v of the spacecraft are relative to a coordinate system fixed in the rotating body whose angular speed is Ω . The positive x_1 axis is in the direction of the orbital velocity, the positive x_2 axis is toward the center, and the positive x_3 axis completes a right handed system. Relative to this coordinate system, the acceleration of the spacecraft is determined by the applied thrust, a coriolis acceleration, and a centrifugal acceleration.

The case where $\Omega = 0$ is equivalent to the problem of fuel optimal maneuvers relative to a fixed point in deep space. This problem of minimum fuel translation or its mathematical equivalent, minimum fuel rotation, has been discussed by several authors [1-5] and is a special case of other second order linear systems that have been studied [6, 7]. It is well known that the nonsingular solutions of this problem consist of intervals of full thrust and coast with at most one coast interval. Minimum fuel control of other and more general linear systems have been investigated [8 - 12] and, in general, the solutions are not so restrictive. The nonsingular fuel optimal solutions for the case where $\Omega \neq 0$

have also been found to consist of intervals of full thrust and coast but more than one coast interval is possible [13]. We extend that result here to show that as many as three coast intervals can occur for flight times less than or equal to $2\pi/\Omega$ and more can occur for flight times exceeding one period. We show also that there are only four boundary conditions for which singular solutions exist. Finally we present the results of computer simulation of optimal maneuvers for various boundary conditions.

II. MATHEMATICAL ANALYSIS

The problem of minimum fuel maneuvers of a spacecraft about a body moving in a circular orbit is formulated as follows.

Let U denote the set of all Lebesgue measurable functions which map the real closed interval $[0, t_f]$ into the closed unit ball in \mathbb{R}^3 . We seek $u \in U$ to minimize the functional

$$J[u] = \int_0^{t_f} |u(t)| dt \quad (1)$$

(where $| \cdot |$ denotes the Euclidean norm or magnitude) subject to the differential equations

$$\begin{aligned} \dot{x}(t) &= v(t) \\ \dot{v}(t) &= Ax(t) + Bv(t) + bu(t) \end{aligned} \quad (2)$$

which hold a.e. on $[0, t_f]$ and the boundary conditions

$$\begin{aligned} x(0) &= x_0 & x(t_f) &= x_f \\ v(0) &= v_0 & v(t_f) &= v_f \end{aligned} \quad (3)$$

where $x_0, v_0, x_f,$ and v_f are specified points in \mathbb{R}^3 and

$$A = \begin{pmatrix} 0 & 0 & 0 \\ 0 & 3\Omega^2 & 0 \\ 0 & 0 & -\Omega^2 \end{pmatrix} \quad B = \begin{pmatrix} 0 & 2\Omega & 0 \\ -2\Omega & 0 & 0 \\ 0 & 0 & 0 \end{pmatrix} \quad (4)$$

The scalar Ω is the orbital angular speed of the body in circular orbit and the scalar b is the maximum thrust magnitude divided by the mass of the spacecraft.

Since the integrand in Eq. 1 is independent of x and v the Pontryagin Maximum Principle provides both necessary and sufficient conditions for a minimum

[14, Sec. 5.2]. For boundary conditions in which the solution is normal the Hamiltonian is

$$H = |u(t)| + p(t)^T v(t) + q(t)^T Ax(t) + q(t)^T Bv(t) + bq(t)^T u(t) \quad (5)$$

where the functions p and q which map $[0, t_f]$ into \mathbb{R}^3 are absolutely continuous solutions of the adjoint differential equations

$$\begin{aligned} \dot{p}(t) &= -A^T q(t) \\ \dot{q}(t) &= -B^T q(t) - p(t) \end{aligned} \quad (6)$$

and a nonsingular optimal control function is defined a.e. on $[0, t_f]$ by

$$\begin{aligned} u(t) &= 0, \quad |q(t)| < 1 \\ u(t) &= -q(t)/|q(t)|, \quad |q(t)| > 1. \end{aligned} \quad (7)$$

An optimal solution in which $|q(t)| = 1$ on a set of positive Lebesgue measure is called singular on that set.

Equation 7 shows that a nonsingular optimal control function has values that are either on the unit ball or are zero (i.e. either full thrust or coast). Moreover q determines entirely which of these situations occurs. If $q(t)$ is outside of the unit ball a full thrust is required, whereas a coast is required if $q(t)$ is inside the unit ball. Qualitative information about the nature of optimal solutions such as the number of thrusts and coasts or whether or not the solution is singular can be determined from the function q . We shall therefore solve Eq. 6 for q and examine the various forms that this solution can take.

Eliminating $p(t)$ in Eq. 6 we obtain the differential equation

$$\ddot{q}(t) + B^T \dot{q}(t) - A^T q(t) = 0. \quad (8)$$

Before finding the general solution of Eq. 8 we note that $A^T = A$ and $B^T = -B$ so that if we eliminate v in Eq. 2 we obtain

$$\ddot{\bar{x}}(t) + B^T \dot{\bar{x}}(t) - A^T x(t) = bu(t). \quad (9)$$

During a coast interval in which $u(t) = 0$ the differential equations 8 and 9 are identical. For this reason $q(t)$ may be visualized as a point in orbit relative to a body moving in a circular orbit.

Using subscripts to denote the components of the vector $q(t)$, Eq. 8 may be replaced by the following system of scalar equations:

$$\begin{aligned} \ddot{q}_1(t) - 2\Omega \dot{q}_2(t) &= 0 \\ \ddot{q}_2(t) + 2\Omega \dot{q}_1(t) - 3\Omega^2 q_2(t) &= 0 \\ \ddot{q}_3(t) + \Omega^2 q_3(t) &= 0. \end{aligned} \quad (10)$$

Equation 7 shows that a boundary point t between a thrusting and coasting regime of $u(t)$ must satisfy the condition

$$|q(t)| = 1. \quad (11)$$

The function $|q(t)| - 1$ is called the switching function of $u(t)$. A value of t at which the switching function changes sign is called a switch of $u(t)$. Whenever a switch occurs $u(t)$ changes from thrust to coast or from coast to thrust and conversely. Whenever a switch of $u(t)$ occurs the solution of Eq. 10 intersects the unit sphere. Clearly the number of switches cannot exceed the number of intersection points.

The form of the solution of Eq. 10 depends on whether or not $\Omega = 0$. The case $\Omega = 0$ corresponds to a problem of optimal maneuvers in deep space rather than about a circular orbit. In deep space Eq. 8 becomes

$$\ddot{q}(t) = 0 \quad (12)$$

and its general solution is

$$q(t) = -p_0 t + q_0 \quad (0 \leq t \leq t_f) \quad (13)$$

where p_0 and q_0 are constants in \mathbb{R}^3 . Geometrically, this solution describes a straight line segment in \mathbb{R}^3 . This shows, in view of Eq. 11, that an optimal maneuver in deep space can have at most two thrust intervals and one coast interval. A detailed discussion of this case which also includes singular controls can be found in [13].

There is more variety in the type of optimal maneuvers that can occur about a body in circular orbit. In the case where $\Omega \neq 0$ the general solution of Eq. 10 is

$$\begin{aligned} q_1(t) &= 2 \rho \sin(\Omega t + \psi) - 3c_1 t + c_2 \\ q_2(t) &= \rho \cos(\Omega t + \psi) - \frac{2c_1}{\Omega} \quad (0 \leq t \leq t_f) \quad (14) \\ q_3(t) &= a \sin(\Omega t + \psi) + b \cos(\Omega t + \psi). \end{aligned}$$

Geometrically this solution resembles a helical segment if ρ , c_1 , and either a or b is nonzero. Less general situations can occur which we shall consider. Of special interest is the case in which $a = b = 0$. In this case the solution curve is confined to the plane of the circular orbit.

1. Solution in the Orbital Plane

If the third component of each of the vectors x_0 , v_0 , x_f , and v_f in Eq. 3 is zero, then the solutions $u(t)$, $q(t)$, and $x(t)$ from Eqs. 7-9 are each contained in the orbital plane.

In this case the plane curve obtained from Eq. 14 resembles a type of cycloid if c_1 and ρ are nonzero. The relationship to a cycloid can be demonstrated by the following transformation.

$$\gamma_1 = -q_1/2 \quad (15)$$

$$\gamma_2 = -q_2 \ .$$

The curve defined by $\gamma = (\gamma_1, \gamma_2)$ is a type of cycloid. If we introduce the following change of variables:

$$\begin{aligned} \theta &= \Omega t + \psi \\ \alpha &= \frac{3c_1}{2\Omega} \end{aligned} \quad (16)$$

$$c = \frac{-3c_1}{2\Omega} - \frac{c_2}{2} \ .$$

the curve takes the standard form

$$\begin{aligned} \gamma_1 &= \alpha\theta - \rho \sin \theta + c \\ \gamma_2 &= \alpha - \rho \cos \theta + \alpha/3 \end{aligned} \quad (17)$$

This curve is a cycloid if $\rho = |\alpha|$ and $\rho > 0$, a prolate cycloid if $\rho > |\alpha| > 0$, and a curtate cycloid if $0 < \rho < |\alpha|$. In each case the curve is periodic with a period of 2π . For this reason the curve defined by q is a segment of a periodic curve having the orbital period $2\pi/\Omega$. It has periodic loops if and only if $\rho > \frac{3|c_1|}{2\Omega} > 0$.

The nature of the optimal thrusting sequence is determined by the relationship of $q(t)$ to the unit circle in the orbital plane. This is depicted in Fig. 1 for the case where $\Omega = 0$. Since a straight line can intersect a circle in at most two points, it is seen that a fuel optimal maneuver in deep space can have at most two switches. If $\Omega \neq 0$ more switches can occur as is demonstrated in Fig. 2 where $q(t)$ takes a cycloidal shape. There is an essential difference between the deep space case and the circular orbit case even if t_f is small. This is because even

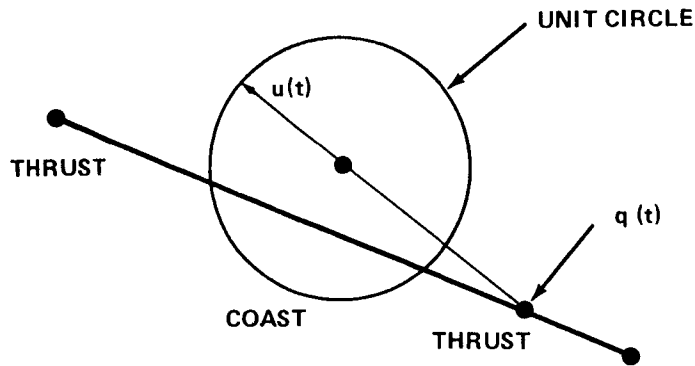


FIGURE 1. NATURE OF FUEL OPTIMAL THRUSTING SEQUENCE IN DEEP SPACE

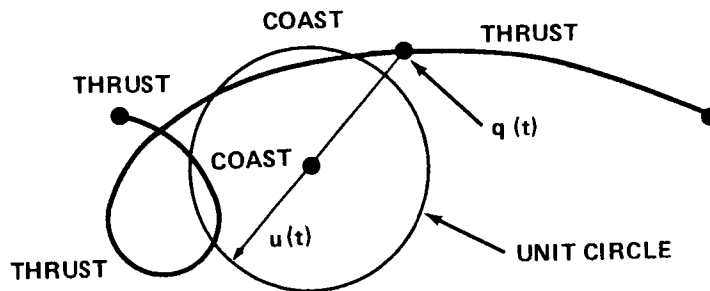


FIGURE 2. NATURE OF FUEL OPTIMAL THRUSTING SEQUENCE ABOUT A POINT MOVING IN CIRCULAR ORBIT

though θ may be restricted to an arbitrarily small interval, there are values of the constants α , ρ , and c so that a prolate cycloid can have a complete loop on that interval. For this reason even if t_f is small there are values of ρ , c_1 , and c_2 so that $q(t)$ can intersect the unit circle more than twice.

Equation 15 transforms the unit circle into the ellipse

$$\gamma_1^2 + 4\gamma_2^2 = 4. \quad (18)$$

This ellipse can intersect the curve defined by Eq. 17 at most six times in one period and more than six times over larger intervals than a period. This indicates that at most six switches are possible during one period of a fuel optimal maneuver about a body in circular orbit and more are possible for longer flight times.

A case where six switches occur is presented in Fig. 3 where the curve $q(t)$ intersects the unit circle at six points. This corresponds to a "thrust-coast-thrust-coast-thrust-coast-thrust" maneuver, a thrusting sequence consisting of seven phases. This information can be seen more easily from Fig. 4 which presents the magnitude of q vs the orbital angle θ which is defined in Eq. 16. The thrust intervals occur where $|q|$ is greater than one and the coast intervals occur where $|q|$ is less than one. A seven phase maneuver can also occur for any smaller flight time if ρ , c_1 , and c_2 are picked correctly but these maneuvers for small flight times may require that some of the boundary conditions defined by Eq. 3 have enormous magnitude.

We now consider the degenerate cases.

If $c_1 = 0$ and $\rho \neq 0$ then $q(t)$ defines a segment of an ellipse whose ratio of major-to-minor axis is two. An ellipse can intersect the unit circle in at most four points so the maximum number of switches that can occur in an optimal maneuver in this case is four in one period although more can occur for flight times exceeding one period.

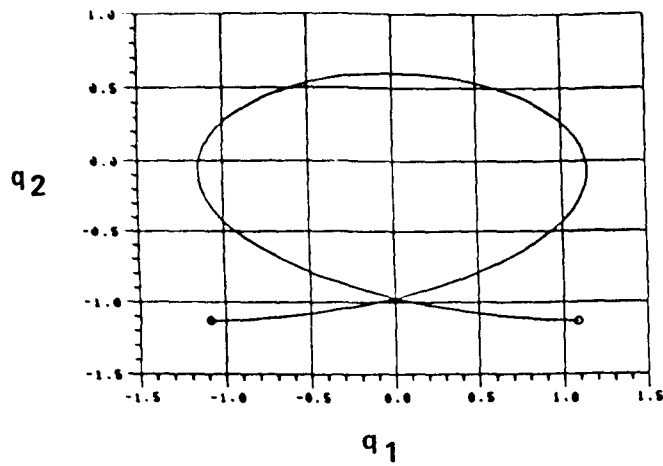


FIGURE 3 : A SEVEN PHASE OPTIMAL THRUSTING SEQUENCE IN ONE PERIOD

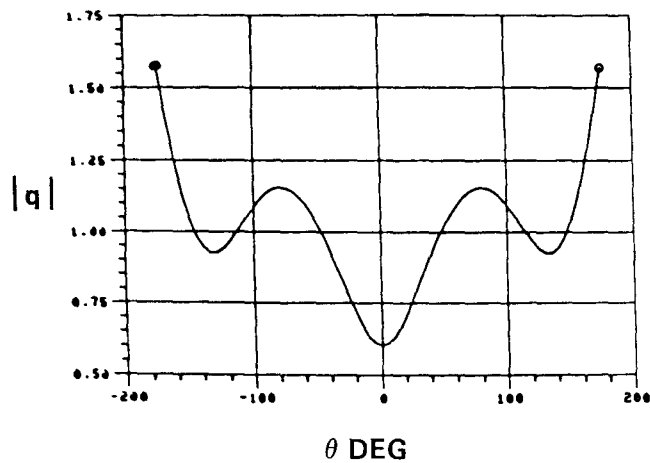


FIGURE 4 : THE ABSOLUTE VALUE OF q OVER ONE PERIOD FOR THE SEVEN PHASE OPTIMAL THRUSTING SEQUENCE

If $\rho = 0$ and $c_1 \neq 0$ then $q(t)$ defines a straight line segment as in the deep space situation and at most two switches are possible.

If both c_1 and ρ are zero, no switches can occur. This is the only situation in the orbital plane case where singular solutions can occur and this happens if $c_2 = \pm 1$. This fact will be shown in the material which follows.

2. Solutions Out of the Orbital Plane

We now examine the other cases where $q(t)$ as defined by Eq. 14 is not in the orbital plane.

We first consider the cases where $c_1 \neq 0$.

We note, first of all, that singular solutions are impossible for these cases because $c_1 \neq 0$ in Eq. 14 shows that Eq. 11 cannot be satisfied identically.

If a and b are not both zero and if ρ is nonzero then the solution of Eq. 14 defines a helical type path that intersects the unit sphere on at most six points during one period. This establishes at most six switches of $u(t)$ during one period of an optimal maneuver.

If $\rho = 0$ and a and b are not both zero then Eq. 14 defines a shifted sine curve. This curve can intersect the unit sphere at six points but not more. In this situation also an optimal maneuver has at most six switches in one period.

We now consider the cases in which $c_1 = 0$.

Singular solutions occur if and only if Eq. 11 is satisfied identically, that is

$$b^2 - a^2 = 3\rho^2, ab = 0, c_2\rho = 0, \rho^2 + b^2 + c_2^2 = 1. \quad (19)$$

Equation 19 is satisfied only in the following cases:

$$\rho = 1/2, c_2 = 0, a = 0, b = \pm \sqrt{3}/2 \quad (20)$$

$$\rho = 0, c_2 = \pm 1, a = 0, b = 0. \quad (21)$$

These are the only cases where singular solutions occur. Equation 20 provides the only cases in which singular solutions exist outside of the orbital plane and Eq. 21 establishes the existence of the singular solutions in the orbital plane previously mentioned.

In the case where $\rho \neq 0$, Eq. 14 defines, in general, an ellipse which either intersects the unit sphere in at most four points or which is identically on the unit sphere. The latter is the singular situation described by Eq. 20. The former indicates that at most four switches in one period are possible for a nonsingular optimal maneuver in this case.

If $\rho = 0$ and a and b are not both zero then Eq. 14 defines a point moving with simple harmonic motion along a line segment. This moving point crosses the unit sphere at no more than four values of t . In this case also no more than four switches can occur during one period of an optimal maneuver.

III. COMPUTER SIMULATIONS

This section presents the flight path and switching function for several fuel optimal maneuvers in a plane, both in deep space and about a body in circular orbit. These results were obtained by solution of a two point boundary value problem using a program written by Roger R. Burrows of the Flight Mechanics Branch of the George C. Marshall Space Flight Center.

Figures 5-10 are presented to illustrate optimal maneuvers in deep space for a variety of boundary conditions. Since only the basic shapes are of interest here Eq. 2 is normalized with $b = 1$ and the flight time t_f is four. Intervals of thrust or coast can be determined from the regions where the switching function depicted on the left is respectively positive or negative.

Figures 11-12 compare an optimal soft rendezvous with a body fixed in deep space and an optimal soft rendezvous with a body in circular orbit for identical initial conditions. These simulations were based on a spacecraft mass of approximately 3400 kilograms, maximum thrust of 267 Newtons, and a flight time of 600 seconds. The upper part of the figures illustrates the optimal switching function and flight path shape for the deep space rendezvous ($\Omega = 0$ rad/sec) whereas the lower part presents this information for rendezvous with a body moving in a 435 kilometer altitude circular orbit ($\Omega = .001122$ rad/sec). The similarities and differences in shape are apparent.

Figure 13 presents an optimal soft rendezvous of a spacecraft in the 435 kilometer altitude circular orbit with a body one kilometer behind in the same orbit for flight times of 600 seconds, one half period (2800 sec), and three fourths period (4200 sec). The mass and maximum thrust are the same as in the previous case.

Figure 14 also presents a soft rendezvous in which the same spacecraft is ferrying a mass nine times heavier than itself to a body in the 435 kilometer circular orbit. The spacecraft begins one kilometer above the body with the same velocity. The flight time is long, six sevenths of a period (4800 sec) and the optimal thrusting function has four switches. The thrusting sequence is "thrust-coast-thrust-coast-thrust."

Figure 15 depicts a situation in which the spacecraft pushes a mass nine times heavier than itself out of circular orbit to a point in an elliptical orbit 73 kilometers behind. This optimal maneuver has a flight time of one period (5600 sec) and the optimal switching function is determined from the curve $q(t)$ presented in Fig. 3. This can be seen from the similarity between Fig. 4 and the switching function shown in Fig. 15. This is an example of an optimal maneuver which has a thrusting sequence requiring the maximum of seven phases in one period.

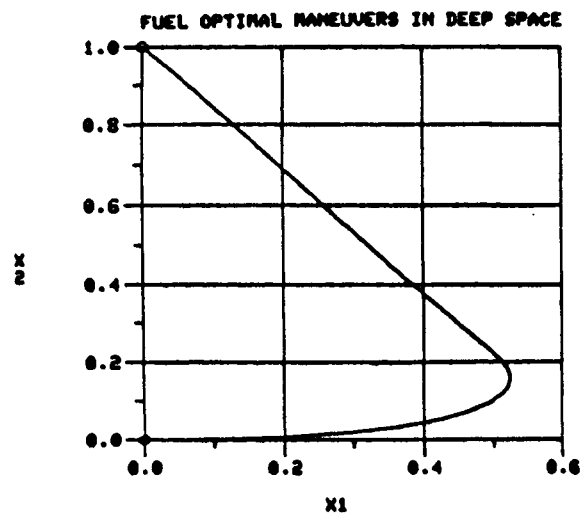
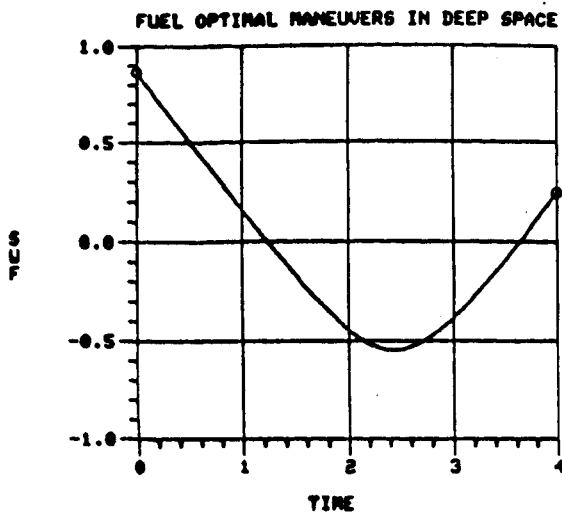


FIGURE 5 : SWITCHING FUNCTION AND FLIGHT PATH FOR $X(0) = (0, 0)$,
 $V(0) = (1, 0)$, $X(TF) = (0, 1)$, $V(TF) = (0, 0)$

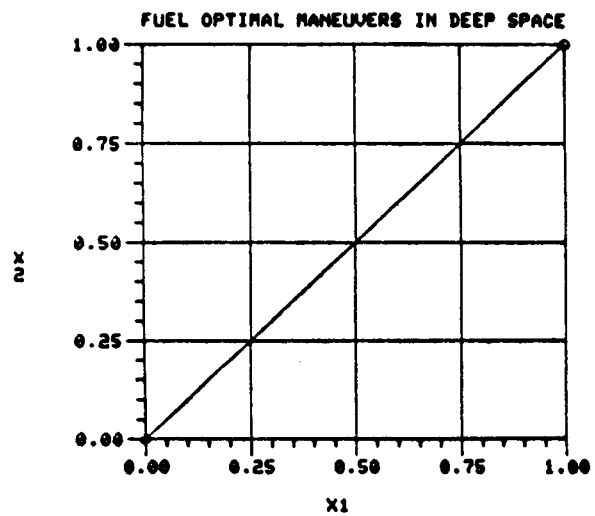
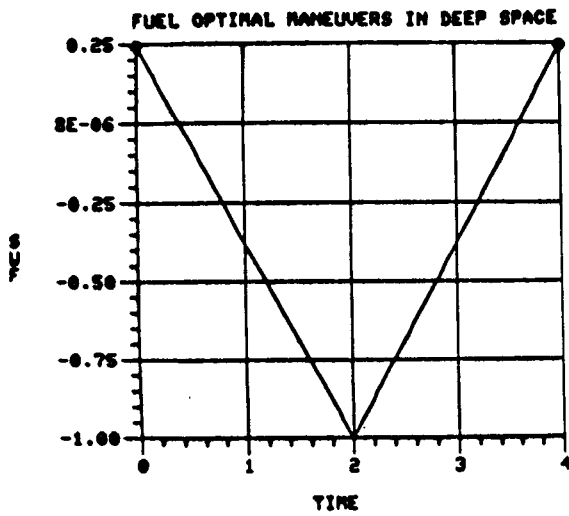


FIGURE 6 : SWITCHING FUNCTION AND FLIGHT PATH FOR $X(0) = (0, 0)$,
 $V(0) = (0, 0)$, $X(TF) = (1, 1)$, $V(TF) = (0, 0)$

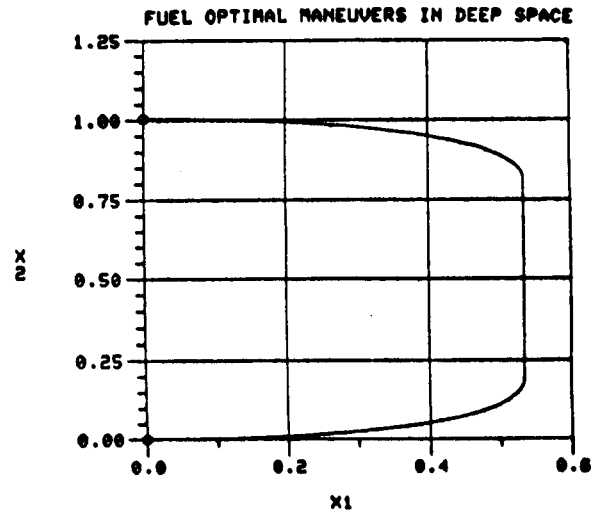
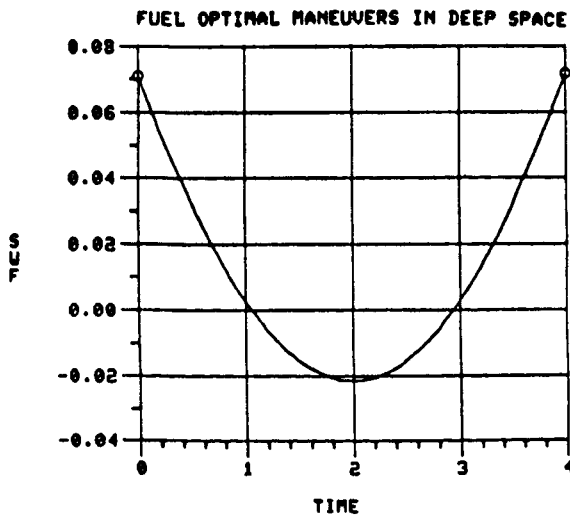


FIGURE 7 : SWITCHING FUNCTION AND FLIGHT PATH FOR $X(0) = (0, 0)$
 $V(0) = (1, 0)$, $X(TF) = (0, 1)$, $V(TF) = (-1, 0)$

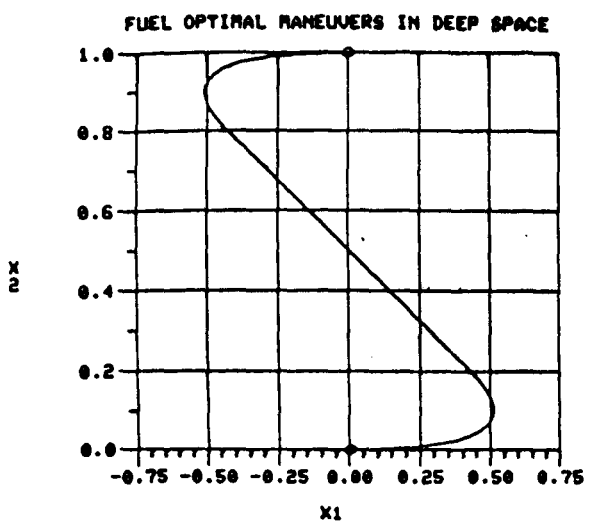
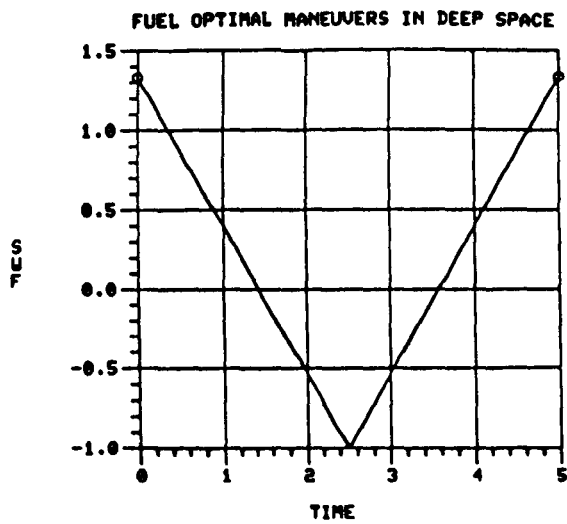


FIGURE 8 : SWITCHING FUNCTION AND FLIGHT PATH FOR $X(0) = (0, 0)$,
 $V(0) = (1, 0)$, $X(TF) = (0, 1)$, $V(TF) = (1, 0)$

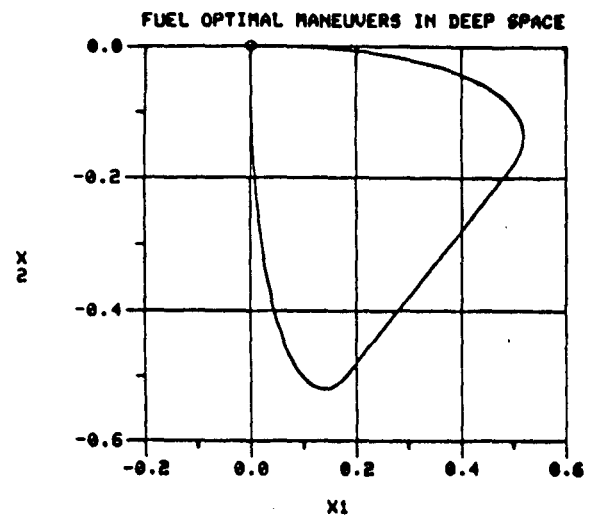
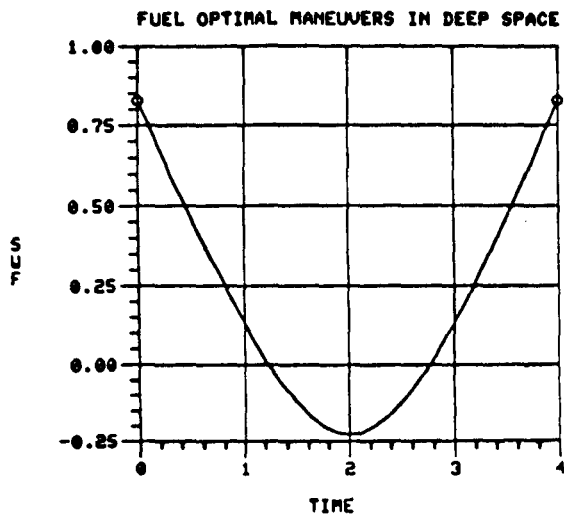


FIGURE 9 : SWITCHING FUNCTION AND FLIGHT PATH FOR $X(0) = (0, 0)$,
 $V(0) = (1, 0)$, $X(TF) = (0, 0)$, $V(TF) = (0, 1)$

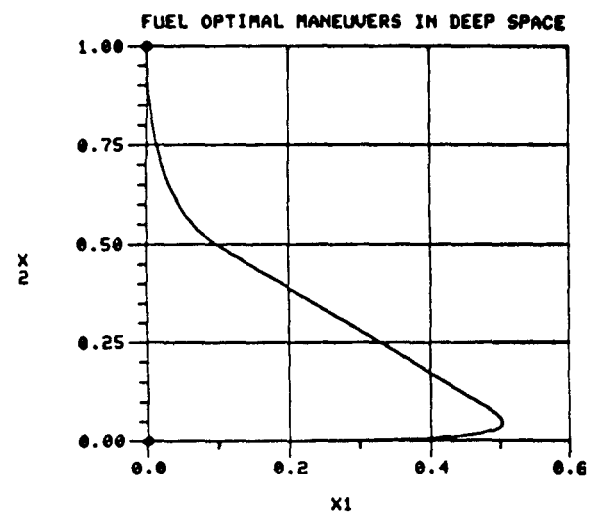
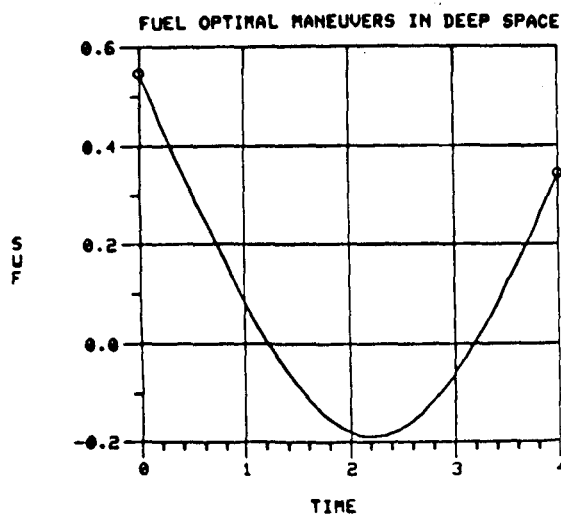
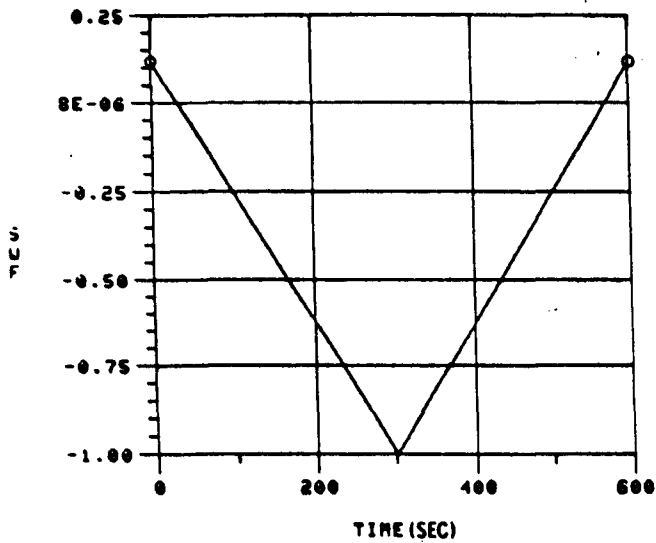
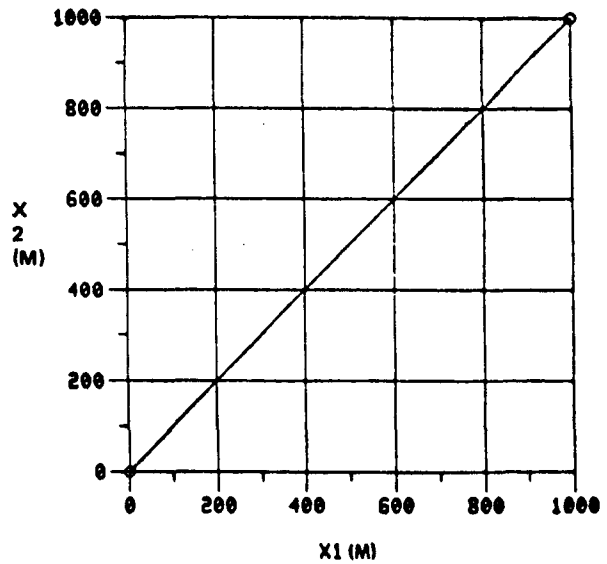


FIGURE 10 : SWITCHING FUNCTION AND FLIGHT PATH FOR $X(0) = (0, 0)$,
 $V(0) = (1, 0)$, $X(TF) = (0, 1)$, $V(TF) = (0, 1)$

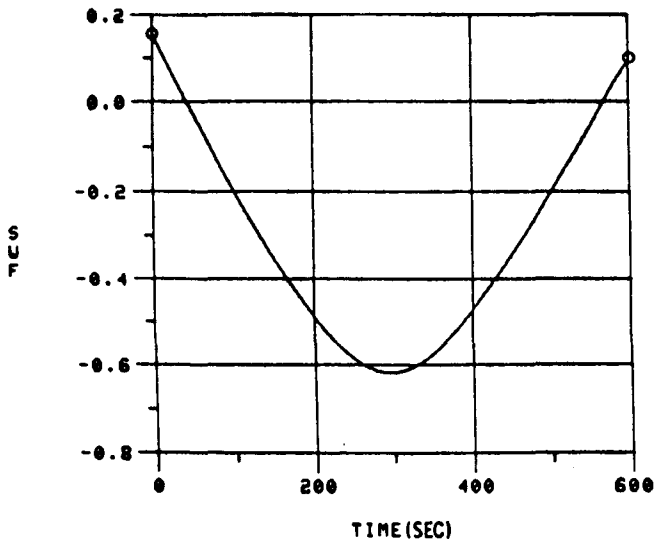
FUEL OPTIMAL MANEUVERS IN DEEP SPACE



FUEL OPTIMAL MANEUVERS IN DEEP SPACE



FUEL OPTIMAL MANEUVERS ABOUT A CIRCULAR ORBIT



FUEL OPTIMAL MANEUVERS ABOUT A CIRCULAR ORBIT

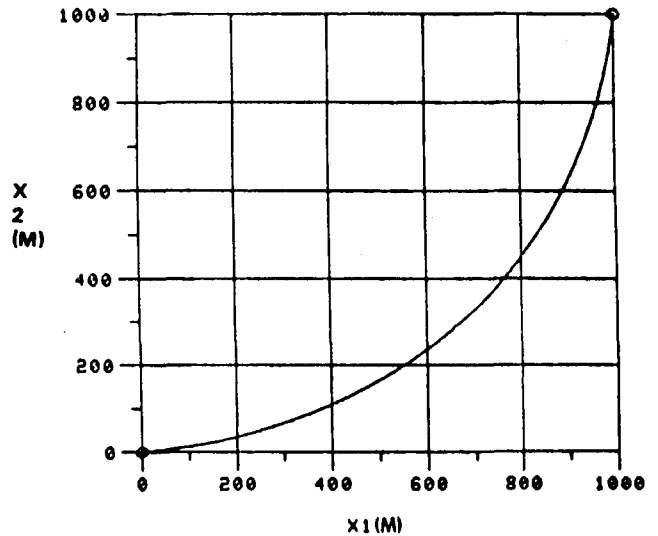
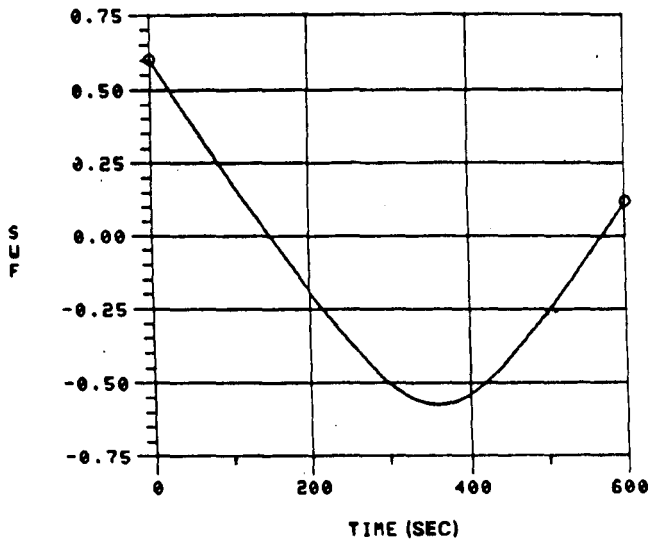
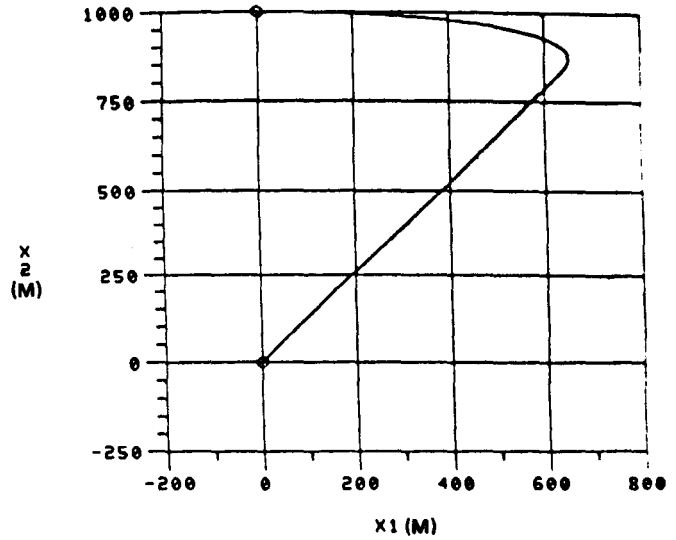


FIGURE 11 : COMPARISON OF SWITCHING FUNCTIONS AND FLIGHT PATHS FOR DEEP SPACE AND 435 KM. ALTITUDE CIRCULAR ORBIT:
 $X(0) = (1000, 1000)$, $V(0) = (0, 0)$, $X(TF) = (0, 0)$, $V(TF) = (0, 0)$

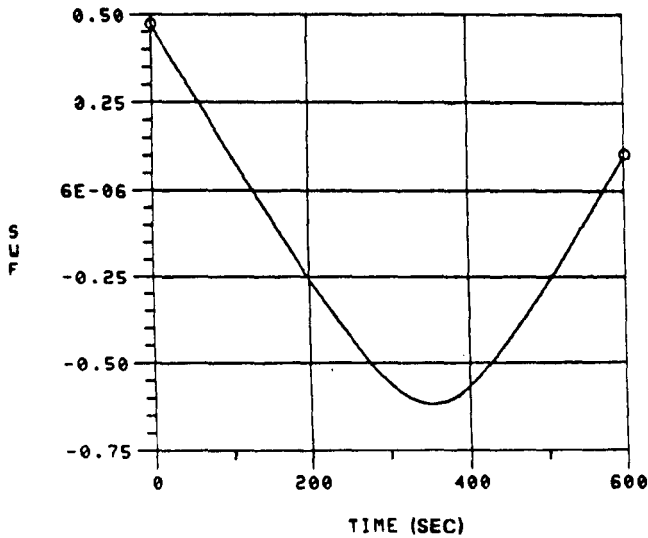
FUEL OPTIMAL MANEUVERS IN DEEP SPACE



FUEL OPTIMAL MANEUVERS IN DEEP SPACE



FUEL OPTIMAL MANEUVERS ABOUT A CIRCULAR ORBIT



FUEL OPTIMAL MANEUVERS ABOUT A CIRCULAR ORBIT

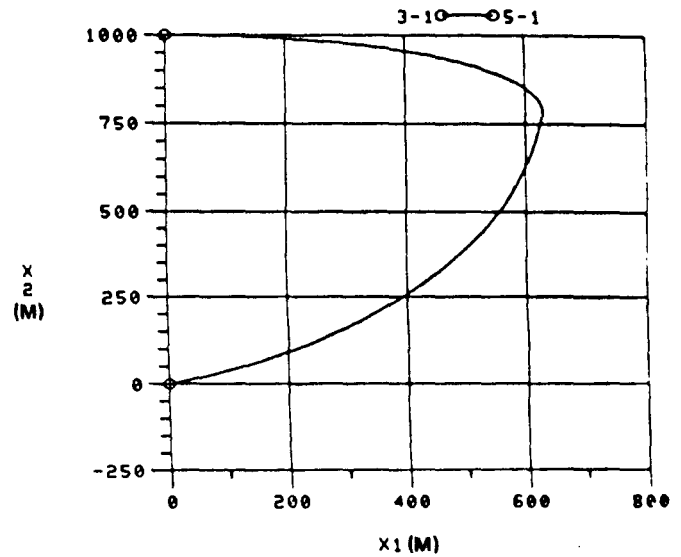
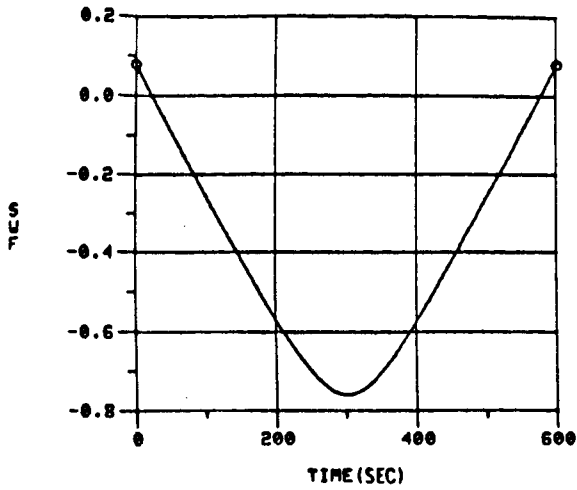
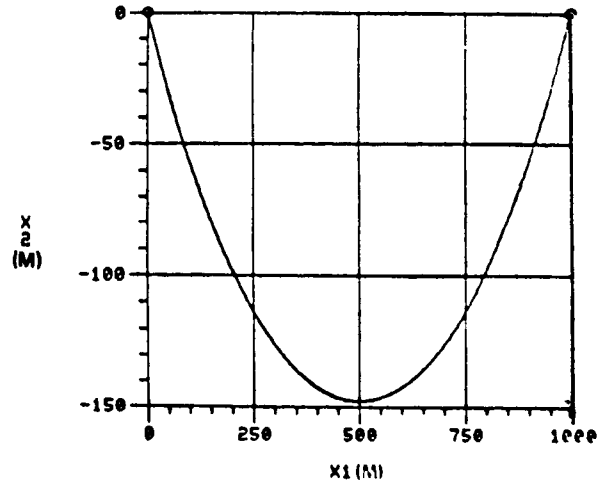


FIGURE 12 : COMPARISON OF SWITCHING FUNCTIONS AND FLIGHT PATHS FOR DEEP SPACE AND 435 KM. ALTITUDE CIRCULAR ORBIT:
 $X(0) = (0, 1000)$, $V(0) = (10, 0)$, $X(TF) = (0, 0)$, $V(TF) = (0, 0)$

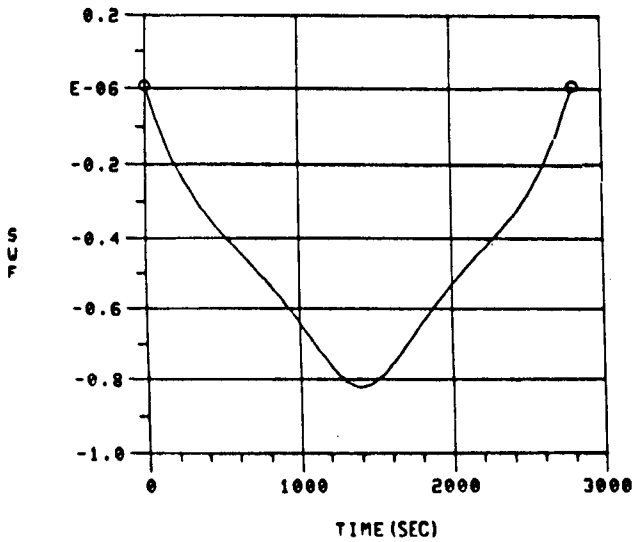
FUEL OPTIMAL MANUEVERS ABOUT A CIRCULAR ORBIT



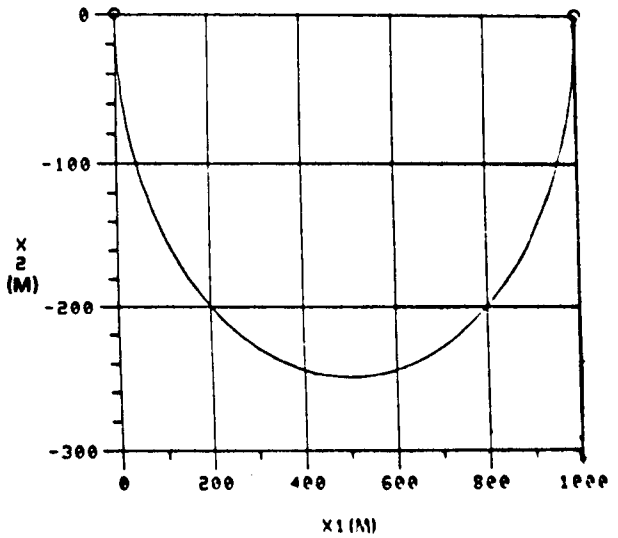
FUEL OPTIMAL MANUEVERS ABOUT A CIRCULAR ORBIT



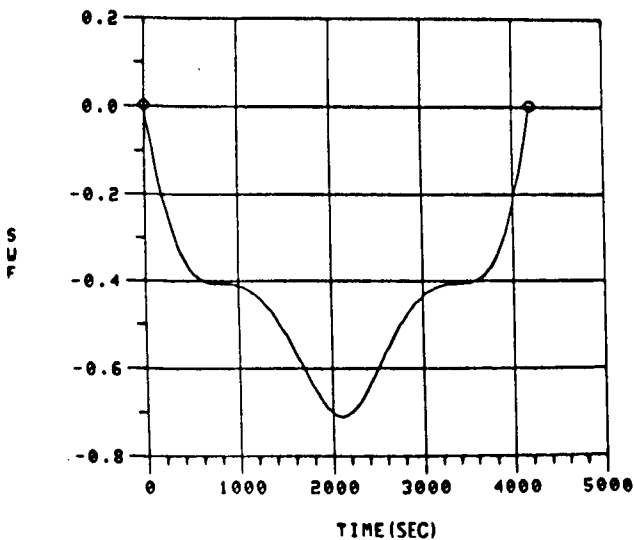
FUEL OPTIMAL MANUEVERS ABOUT A CIRCULAR ORBIT



FUEL OPTIMAL MANUEVERS ABOUT A CIRCULAR ORBIT



FUEL OPTIMAL MANUEVERS ABOUT A CIRCULAR ORBIT



FUEL OPTIMAL MANUEVERS ABOUT A CIRCULAR ORBIT

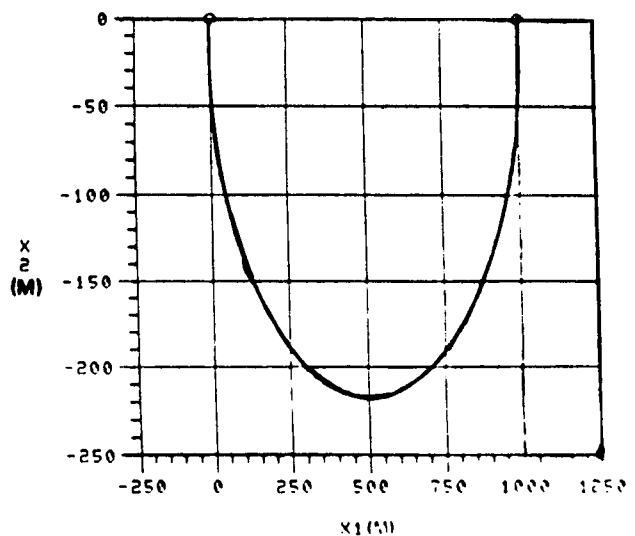
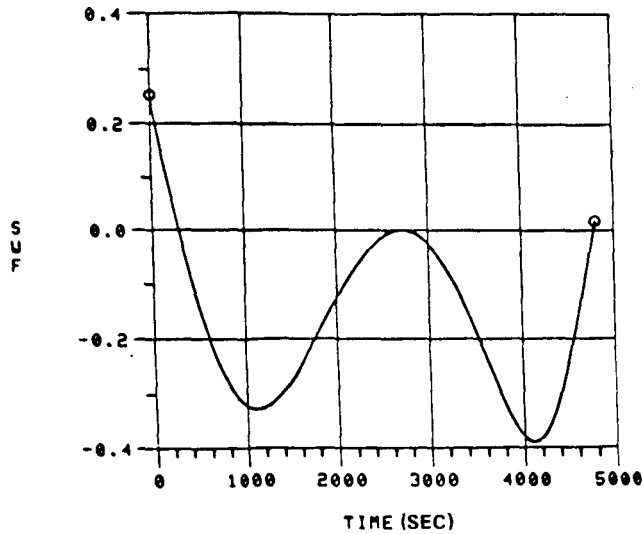


FIGURE 13 : SWITCHING FUNCTION AND FLIGHT PATH FOR DIFFERENT FLIGHT TIMES FOR 435 KM. CIRCULAR ORBIT: $x(0) = (1000, 0)$, $v(0) = (0, 0)$, $x(TF) = (0, 0)$, $v(TF) = (0, 0)$

FUEL OPTIMAL MANUEVERS ABOUT A CIRCULAR ORBIT



FUEL OPTIMAL MANUEVERS ABOUT A CIRCULAR ORBIT

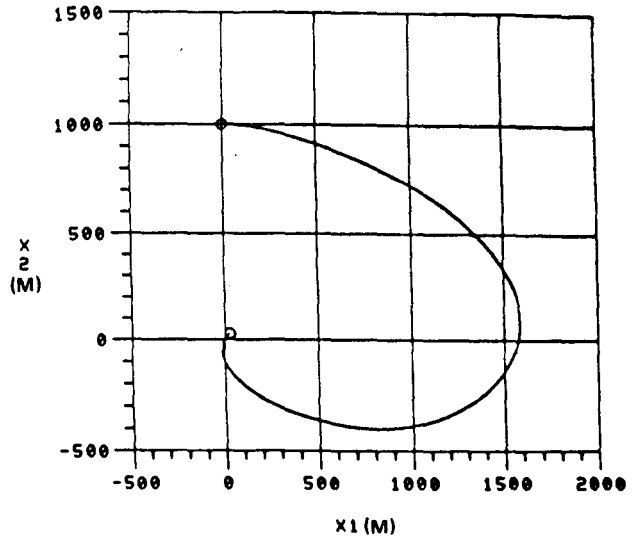
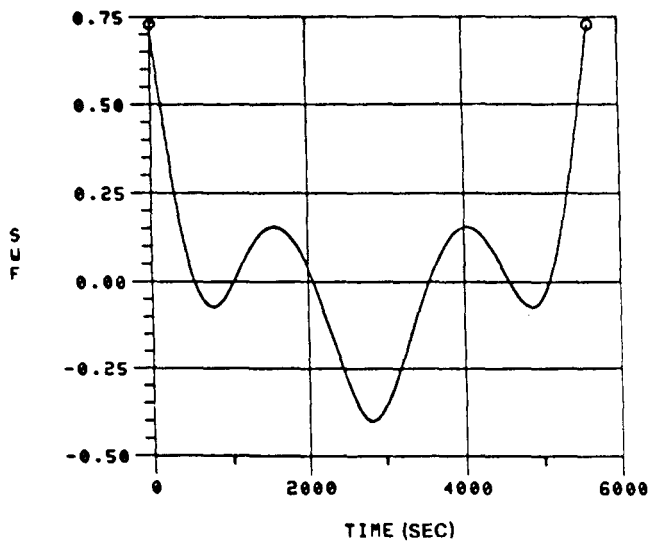


FIGURE 14 : INSERTION OF MASS FROM ELLIPTICAL INTO 435 KM. CIRCULAR ORBIT: $X(0) = (0, 1000)$, $V(0) = (0, 0)$, $X(TF) = (0, 0)$, $V(TF) = (0, 0)$, OPTIMAL MANEUVER REQUIRES MID-COURSE THRUST

FUEL OPTIMAL MANUEVERS ABOUT A CIRCULAR ORBIT



FUEL OPTIMAL MANUEVERS ABOUT A CIRCULAR ORBIT

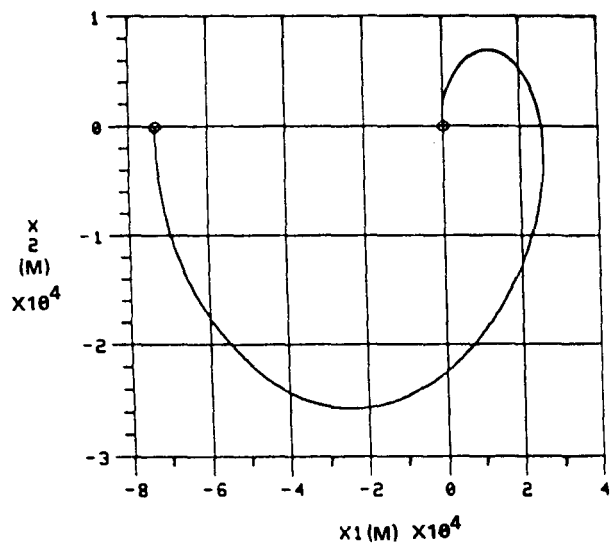


FIGURE 15 : AN OPTIMAL MANEUVER WITH FOUR THRUSTS AND THREE COASTS IN ONE PERIOD (5600 SEC): $X(0) = (0, 0)$, $V(0) = (0, 0)$, $X(TF) = (-73000, 0)$, $V(TF) = (0, 35)$

IV. CONCLUSIONS

Several different forms of solutions to Eq. 10 can occur. If $\Omega = 0$ the solution is a line segment and the optimal control consists of intervals of full thrust and coast with at most two switches. If $\Omega \neq 0$ the solution may be a helical type segment, a shifted sine curve segment, a horizontal straight line segment, a prolate or curtate cycloidal type segment, or a segment of an ellipse. The optimal control consists of intervals of full thrust and coast in each of these cases. More than two switches are possible even for small flight times. If $c_1 \neq 0$ there is a maximum of six switches possible in one period. If $c_1 = 0$ the maximum number of switches that can occur in one period is four.

If $\Omega \neq 0$ only two cases exist in which singular solutions (defined by Eq. 20) can occur outside of the orbital plane. Also only two cases where singular solutions (defined by Eq. 21) exist can occur on the orbital plane.

Computer simulations were run for solution of Eqs. 2, 3, 6, and 7 for cases where $\Omega = 0$ and where $\Omega = 2\pi/5600$ rad/sec. It was found generally that for small flight times and boundary conditions of small magnitudes the optimal maneuvers contained no more than two switches. Boundary value problems whose solutions consisted of four switches and six switches were found.

REFERENCES

1. I. Flugge-Lotz and H. Marbach, "The Optimal Control of Some Attitude Control Systems for Different Performance Criteria," Trans. ASME J. Appl. Mech. (1964) pp. 107-115.
2. J. S. Meditch, "On Minimal Fuel Satellite Attitude Controls," Preprints of the 1963 JACC.
3. L. Schwartz, "Minimum Energy Attitude Control for a Class of Electric Propulsion Devices," Proceedings, 1964 JACC.
4. D. A. Conrad, "Minimum Fuel Closed-Loop Translation," AIAA J. (May 1965).
5. W. F. Keller, "Study of Spacecraft Hover and Translation Modes Above the Lunar Surface," AIAA Preprint 64-341.
6. H. O. Ladd and R. Friedland, "Minimum Fuel Control of a Second Order Linear Process With a Constraint on Time-to-Run," Trans. ASME J. Appl. Mech. (1964) pp. 165-176.
7. D. R. Snow, "Singular Optimal Controls For a Class of Minimum Effort Problems," SIAM J. Control, (1964) pp. 203-219.
8. M. Athans, "Minimum-Fuel Control of Second-Order Systems With Real Poles," 1963 JACC, pp. 232-240.
9. A. J. Craig and I. Flugge-Lotz, "Investigation of Optimal Control With Minimum-Fuel Consumption Criteria for a Fourth-Order Plant With Two Control Inputs: Synthesis of an Efficient Sub-Optimal Control," 1963 JACC.
10. M. Athans, "On Optimal Control of Self Adjoint Systems," 1963 JACC.
11. W. C. Grimmell, "The Existence of Piecewise Continuous Fuel Optimal Controls," SIAM J. Control (1967), pp. 515-519.
12. D. L. Grey and M. Athans, "Computation of Fuel-Optimal Control via Newton's Method - Theory," 1968 JACC.
13. T. E. Carter, "Fuel Optimal Maneuvers for Spacecraft with Fixed Thrusters," NASA CR -161855 (1981).
14. E. B. Lee and L. Markus, Foundations of Optimal Control Theory, Wiley, 1967.

1982

NASA/ASEE SUMMER FACULTY RESEARCH FELLOWSHIP PROGRAM

MARSHALL SPACE FLIGHT CENTER
THE UNIVERSITY OF ALABAMA

SOLIDIFICATION STUDIES
OF MONOTECTIC SYSTEMS

Prepared by:	Kichoon Chang, Ph.D.
Academic Rank:	Associate Professor
University and Department:	Alabama A&M University Department of Chemistry
NASA/MSFC Laboratory:	Space Science Laboratory
Division:	Space Processing
Branch:	Solid State
MSFC Counterpart:	Donald O. Frazier, Ph.D.
Date:	August 13, 1982
Contract No.:	NGT-01-002-099 University of Alabama

SOLIDIFICATION STUDIES
OF MONOTECTIC SYSTEMS

By

Kichoon Chang
Associate Professor of Chemistry
Alabama A&M University
Normal, Alabama 35762

ABSTRACT

It has been suggested that at low or zero gravity critical point wetting and thermal migration of second-phase droplets due to interfacial tension gradient play major roles in phase separation and solidification of a monotectic system.

Understanding of these roles requires estimation of interfacial tensions. However, solid-liquid interfacial tensions are very difficult to measure. Ellipsometric techniques are being investigated to measure liquid film thickness as a means of determining the solid-liquid interfacial tensions at various temperatures and pressures.

INTRODUCTION

Investigation of monotectic and related systems has been of considerable interest in recent years. However, one of the first relatively detailed studies of a monotectic system¹, succinonitrile - water, was reported in 1897.

In the last decade metallic monotectic systems have been of renewed concern within NASA in view of recent space processing experiment.² Currently a number of immiscible organic binary mixtures are under investigation as models for metallic pseudo binary systems.

In a monotectic system two component liquids are miscible in any composition above an upper critical solution temperature. Below the critical temperature and between certain composition limits two immiscible liquid phases are produced, creating a miscibility gap. All such miscibility gaps are two-phase regions. The two liquid phases generally differ in density and separate by Stokes settling in a gravity field.

At the monotectic temperature one of the liquid phases decomposes into a solid phase and the other liquid phase. In all known monotectic phase diagrams the amount of the solid phase produced is always greater than that of the liquid phase produced.³ This liquid phase solidifies at the lower eutectic temperature.

A number of theories have been developed for explaining the separation and solidification phenomena of binary systems.

The motion of bubbles in a temperature gradient in pure liquids and binary liquids and Marangoni convection have been studied by a number of workers. The velocity⁴ of the bubble was related to both the thermal variation of the surface tension and the temperature gradient along which the bubbles moved.

It was shown⁵ that near the critical point one of the critical phases completely wets the third phase and that at some temperature below this point perfect wetting terminates in a first-order transition of the surface.

If the third phase is a container wall which is wetted preferentially by the minority phase, the phase separation by the spreading minority phase, as the temperature is lowered, may be avoided if a crucible which is primarily wetted by the majority phase is chosen. On the other hand, if the majority phase begins to form solid at the monotectic temperature, it will be preferentially wetted by the liquid of the phase because of their closeness in composition.

Cahn⁶ reports that perfect wetting of the monotectic solid by the monotectic liquid occurs whenever the monotectic temperature is close to the critical temperature.

In a study of monotectic systems including Al-In, Cu-Pb, Cd-Ga and succinonitrile-water, Grugel and Hellowell⁷ showed that the solidification behavior of systems containing a

liquid miscibility gap appeared to be related to the height of the gap. They even modified the microstructure of the solids by changing the height of the miscibility gap.

In certain binary solutions the lower of the two liquid phases forms a layer which intrudes between the upper liquid phase and the vapor.⁸ The thickness of the intruding wetting layer was ellipsometrically measured and reported.

Pohl and Goldberg⁹ verified experimentally a predicted transition⁵ from complete to partial wetting at a temperature away from the consolute temperature.

The Gibbs surface excess measurement for two miscibility gap systems, ethyl salicylate - diethylene glycol and hexane-aniline, was reported by NASA workers.¹⁰ Their measurement of the surface excess by use of the Gibbs adsorption equation led to the conclusion that the surface excess increases as the binary solutions approach the conditions of the consolute point. They also observed that near the consolute temperature the surface-active components are switched if the two pure components have a small surface tension difference. The component switching will apparently affect the thickness of the intruding layer and the liquid film thickness on the container wall because of different molecular size and different vapor pressure.

RECENT WORK WITH MODEL MATERIALS

Succinonitrile is a plastic crystal with a small entropy of fusion and freezes like metals, crystallizing with its molecules in random orientations. The crystal grows dendritically into undercooled melt like metals which have small entropies of fusion.^{11,12}

A monotectic system of succinonitrile and water mixture has a convenient temperature range to work with for its solution and solidification. Some of the properties including the phase diagram have been relatively well established.^{1,11,13}

The density difference between the two phases in the miscibility gap is small and can be further minimized by adjusting the amount of H_2O and D_2O to reduce the gravity effect on the phase separation and solidification. Thus the system continues to draw interest within NASA as a model for pseudo metallic systems for investigating composite growth.

Diethylene glycol - ethyl salicylate system has also been studied for excess quantities measurement by NASA workers.¹⁰ The same workers further investigated the miscibility gap system for particle growth and thermal migration by means of holographic techniques.¹⁴

A number of other systems with miscibility gap and metal-like transparent organic compounds have been studied.^{2,7,12,14}

CRITICAL-POINT WETTING AND SPREADING

In solidification of monotectic systems in the absence of gravitation the critical-point wetting⁵ and thermal migration of droplets⁴ appear to play major roles.

Generally, the surface free energy of the system is described by Young's equation

$$\gamma_{SL_2} = \gamma_{SL_1} + \gamma_{L_1L_2} \cos \theta$$

for two immiscible liquids L_1 and L_2 in contact with a non-deforming solid surface of the container. The contact angle θ is between the liquid-liquid interface and the solid surface. For all values of θ

$$\gamma_{L_1L_2} \geq \gamma_{SL_2} - \gamma_{SL_1}$$

In a temperature region below the critical temperature the contact angle vanishes as the critical temperature is reached.⁵ One of the liquid phases, say, L_1 intrudes as a wetting phase between the solid phase S and liquid phase L_2 . At the critical temperature, $\theta = 0^\circ$ and a perfect wetting of the solid by liquid L_1 occurs. This perfect wetting may be expressed in terms of the spreading coefficient of liquid L_1 over solid S

$$\text{spreading coefficient} = \gamma_{SL_2} - \gamma_{SL_1} - \gamma_{L_1L_2}$$

which is greater than zero for a spontaneous spreading.

Thus, for the perfect wetting

$$\gamma_{L_1, L_2} < \gamma_{S, L_2} - \gamma_{S, L_1}$$

and Young's equation no longer holds and the contact angle becomes indeterminate. The inequality sign has reversed.

As solidification occurs at the monotectic temperature



the solid S_1 will be preferentially wetted by liquid L_1 , resulting in a perfect wetting. For this situation, again

$$\gamma_{L_1, L_2} < \gamma_{S_1, L_2} - \gamma_{S_1, L_1}$$

Under these conditions liquid L_2 is a nonwetting phase and monotectic composite can not be grown unless the growth velocity is large enough to overcome the disjoining pressure.⁶

However, Grugel and Hellawell⁷ suggested that if the critical wetting temperature T_w is above the monotectic temperature T_m it may be possible to have steady-state composite growth with solid S_1 being wetted also by liquid L_2 . On the other hand, with T_w lower than T_m for low miscibility gap systems, liquid L_2 is separated due to the preferential wetting of solid S_1 by liquid L_1 and high growth velocities become necessary for composite growth.

OBJECTIVE

As previously discussed, Cahn's theory⁵ predicts that when two fluid phases are near a critical point one of them must completely wet any third phase, excluding the other fluid from contact with the third phase. If the majority phase wets the container preferentially the system is in stable condition. Phase separation could then primarily result from droplet migration due to temperature gradient effect on surface tension.

On the other hand, if the minority phase wets the third phase, the system is unstable and the minority phase droplets will spread over the entire surface. In either case, phase separation follows. Whether or not preferential or perfect wetting of the monotectic solid phase S_1 occurs when a monotectic reaction takes place is to be determined by the location of the critical wetting temperature.⁷

Thus, an attempt is being made to determine critical wetting temperatures in monotectic systems and to investigate the wetting phase on the container walls and the phase preferentially wetting the monotectic solid. This will eventually lead to an examination of Young's equation in these critical wetting regions.

PROCEDURES

Critical wetting occurs when the surface energies of the three phases, two fluids and a solid, are balanced by the equation,

$$\gamma_{L_1 L_2} = \gamma_{S L_2} - \gamma_{S L_1}$$

for which the contact angle θ of Young's equation has approached zero.

Measurement of $\gamma_{L_1 L_2}$ may be made by using a ring method but the surface energies of the solid, $\gamma_{S L_1}$ and $\gamma_{S L_2}$, can not be measured directly.

An alternative is to estimate the surface energies from liquid film thickness X on the surface in question.

If the surface excess of the vapor adsorbed from liquid L_1 or L_2 at a given temperature is substituted in the form of an ideal gas in the Gibbs adsorption equation and integrated over the vapor pressure range, the film pressure π is obtained:

$$\pi = \gamma_s - \gamma_{sv} = \frac{RT}{v^0 \Sigma} \int_0^P X(P) d \ln P$$

where γ_s is the surface free energy of the solid, v^0 the molar volume of the vapor adsorbed at the standard temperature and pressure and Σ the total surface area of the adsorbing solid.

Integration of $X(p)$ over the vapor pressure range gives $\gamma_s - \gamma_{sv}$. By repeating this process at a given temperature

for both liquid phases L_1 and L_2 of the miscibility gap and subtracting one film pressure from the other, the surface tension of the solid (γ_s) is eliminated but the desired quantity, $\gamma_{SL_2} - \gamma_{SL_1}$, which is indeed $\gamma_{SV_2} - \gamma_{SV_1}$ in the experiment because of the equilibrium between the liquid and its vapor, is obtained. With this value together with the measured quantity $\gamma_{L_1L_2}$, the contact angle θ of Young's equation can be calculated at the given temperature.

The entire process can be repeated at different temperatures and the results are extrapolated to estimate the critical-point wetting temperature at which

$$\gamma_{L_1L_2} = |\gamma_{SL_2} - \gamma_{SL_1}|$$

The main task for integrating the equation to obtain the film pressure is in determination of the liquid film thickness as a function of vapor pressure at different temperatures.

Surface Viscosity Method

Migration of gas bubbles or liquid droplets in a liquid phase is retarded by the viscosity of the liquid.⁴ On the other hand, the film pressure Π was shown to be related to the surface viscosity η^s by the equation¹⁵

$$\log \eta^s = \log \eta_0^s + c \Pi$$

where η_0^s is the surface viscosity with the activation energy for flow at zero pressure and c is a constant. The accuracy of this equation was confirmed by the experimental

work on surface films.¹⁶ Thus a well established relationship of the film pressure with the surface viscosity in terms of experimental data will be useful in predicting one quantity from the other.

More recently¹⁷ it was shown for polymers that the thickness adsorbed on the liquid-solid interface is proportional to the intrinsic viscosity over a wide range of thickness in theta solvents such as benzene, cyclohexane and methylethyl ketone.

If the surface viscosity η^s is known, the film thickness X may be calculated from the bulk viscosity η by the equation

$$X = \frac{\eta^s}{\eta}$$

which is a convenient relationship for experimental purposes if surface viscosity can be measured without difficulty.

The measurement of surface viscosity is subject to substantial sensitivity limit. The surface canal method, though more sensitive ($\sim 10^{-5}$ surface poise) than others such as oscillating pendulum and rotational methods, is also limited to surface concentrations which give appreciable film pressures. Furthermore, the method, when applied to soluble adsorbed films, suffers from the disadvantage that the film pressure causes desorption and adsorption as well as sub-phase drag.

Davies and Mayers¹⁸ developed a circular viscous traction

viscometer which can be used for interfacial viscosity measurement with two circular rings held concentrically in the interface. They were able to measure the surface viscosity to an accuracy of 1×10^{-4} surface poise.

Ellipsometric Method

Ellipsometry is sensitive and can detect film thickness as thin as 0.1 \AA and up to tens of thousands of \AA . The technique has been used for measuring oxide films and adsorption of gases and liquids.^{19,20}

The basis of ellipsometry is the fact that the state of polarization of a light beam is altered upon reflection from a bare or film-covered surface. When the light reflects from the specimen, the polarization of the light changes in accordance with the specimen film thickness, the optical characteristics of the film and the surface it is deposited on.

In actual use of the ellipsometer, the compensator (a quarter wave plate) is set at a fixed angle and the polarizer and analyzer circles are rotated until the reflected beam from the specimen is extinguished.

From the angular settings of the polarizer and analyzer at this condition two ellipsometric parameters required to determine the state of polarization are obtained: The amplitude ratio and the phase difference. These parameters are then used to determine the film thickness and refractive index of the film by using graphs, tables or computer programs

provided the optical constants of the substrate are known. The refractive index is independent of the film thickness.

The computer programs are available at the Marshall Space Center for calculating the optical constants (real and imaginary values of the refractive index) and the film thickness.

Kwon et al.⁸ used ellipsometry to measure the thickness of the intruding layer of liquid with He-Ne laser at several temperatures for certain solutions. The result was as predicted by de Gennes' long-range intermolecular potential.²¹

In our preliminary investigation a cell of pyrex glass was designed. Cells with specific angles²² will be designed and tested for maximum sensitivity in the thickness measurement for monotectic systems.

CURRENT INVESTIGATION

A pyrex glass cell was built and is being tested for ellipsometric measurement. Several cells will be designed with specific angles for maximum sensitivity and the investigation will be continued.

On the other hand, each layer of succinonitrile-water miscibility gap is being analyzed for vapor composition by slow distillation and condensation in a specially designed cell below the critical temperature.

The result of this investigation and subsequent experiments with monotectic systems will be reported when significant amount of data are obtained and analyzed.

REFERENCES

1. Schreinemakers, F. H. A., Zeitschr. f. Physik. Chemie, Leipzig, 23, 417(1897).
2. Ang, C. Y. and Lacy, L. L., "Monotectic and Synthetic Alloys, Experiment MA-044," ASTP Preliminary Technical Report, NASA TMX-64956, Sept., 1975; *ibid*, AIAA Progress in Astronautics and Aeronautics, 52, 523(1977); Lacy, L. L. and Ang, C. Y., "Apollo-Soyuz Test Project Summary Science Report," I, NASA SP-412, 403(1977); Gelles, S. H. and Markworth, A. J., "Space Processing Applications Rocket Project, SPAR II Final Report," NASA TM78125, Nov., 1977.
3. Chadwick, G. A., "Metallography of Phase Transformations," Crane, Russak & Co., Inc., New York. Chapter 4.
4. Young, N. O., Goldstein, J. S. and Block, M., "The Motion of Bubbles in a Vertical Temperature Gradient," J. Fluid Mech., 6, 350(1959).
5. Cahn, J. W., "Critical Point Wetting," J. Chem. Phys., 66, 3667(1977).
6. Cahn, J. W., "Monotectic Composite Growth," Met. Trans. A, 10 A, 119(1979).
7. Grugel, R. N. and Hellowell, A., "Alloy Solidification in Systems Containing a Liquid Miscibility Gap," Met. Trans. A, 12A, 669(1981).
8. Kwon, O'D. et al, "Thickness of the Liquid-Vapor Wetting Layer," Phys. Rev. Lett., 48, 185(1982).
9. Pohl, D. W. and Goldberg, W. I., "Wetting Transition in Lutidine - Water Mixtures," Phys. Rev. Lett., 48, 1111 (1982).

10. Nishioka, G. M., Lacy, L. L. and Facemire, B. R., "The Gibbs Surface Excess in Binary Miscibility Gap Systems," J. Colloid and Interface Sci., 80, 197(1981).
11. Glickman, M. E., Schaefer, R. J. and Ayers, J. D., "Dendritic Growth - A Test of Theory," Met. Trans. A, 7A, 1747(1976).
12. Jackson, K. A. and Hunt, J. D., "Transparent Compounds That Freeze Like Metals," ACTA METALLURGICA, 13, 1212 (1965), and references cited therein.
13. Glickman, M. E. and Huang, S. C., "Convective Heat Transfer During Dendritic Solidification," AIAA 16th Aerospace Sciences Meeting, Huntsville, Ala., Jan., 1978, AIAA Paper 78-220.
14. Lacy, L. L., Witherow, W. K., Facemire, B. R., and Nishioka, G. M., "Optical Studies of Model Binary Miscibility Gap Systems," to be published.
15. Glasstone, S., Laidler, K. J. and Eyring, H., Theory of Rate Processes, McGraw-Hill Book Co., Inc. 1941. p. 512.
16. Boyd, E. and Harkins, W. D., "Molecular Interactions in Monolayers: Viscosity of Two-Dimensional Liquids and Plastic Solids," J. Am. Chem. Soc., 61, 1188(1939).
17. Chemistry and Physics of Interfaces, based on the Symposium on Interfaces, June, 1964, American Chemical Society Publications, "Structure of Macromolecules as Liquid-Solid Interfaces."
18. Davies, J. T. and Mayers, G. R. A., "Studies on the Interfacial Viscosities of Monolayers," Trans. Faraday Soc., 56, 691(1960).
19. Archer, R. J., "Determination of the Properties of Films on Silicon by the Method of Ellipsometry," J. Opt. Soc. Am., 52, 970(1962).

20. *ibid*, "Measurement of the Physical Adsorption of Vapors and the Chemisorption of Oxygen on Silicon by the Method of Ellipsometry," Nat. Bur. Std., Misc. Publ. No. 256, 1964. p. 255.
21. De Gennes, P. G., "Some Effects of Long range Forces on Interfacial Phenomena," J. Phys.-Lett. (Paris), 42, L-377(1981).
22. McCrackin, F. L. et al., "Measurement of the Thickness and Refractive Index of Very Thin Films and Optical Properties of Surface by Ellipsometry," J. Res. Nat. Bur. Std., 67A, 363(1963).

1982

NASA/ASEE SUMMER FACULTY RESEARCH FELLOWSHIP PROGRAM

MARSHALL SPACE FLIGHT CENTER
THE UNIVERSITY OF ALABAMA

TOLERANCE ANALYSIS OF OPTICAL
TELESCOPE USING COHERENT ADDITION OF
WAVEFRONT ERRORS

Prepared By:	John W. Davenport, Ph.D.
Academic Rank:	Associate Professor
University and Department:	Georgia Southern College Department of Mathematics and Computer Science
NASA/MSFC:	Optical and R.F. Systems
Division:	Division
Branch:	Optics Branch
MSFC Counterpart:	Donald B. Griner
Date:	August 11, 1982
Contract No:	NASA-NGT-01-002-099 The University of Alabama

ACKNOWLEDGEMENTS

The author would like to express his gratitude to Dr. Bob Barfield for directing a successful summer program. I also wish to express my thanks to my MSFC counterpart, Don Griner, for his consultation and guidance and Charles Jones for his comments and discussion on this project.

A RECURSIVE ALGORITHM FOR ZERNIKE POLYNOMIALS

by

John W. Davenport
Associate Professor of Mathematics
and Computer Science
Georgia Southern College
Statesboro, Georgia

ABSTRACT

Many applications in optics, such as the diffraction theory of optical aberrations, involves the analysis of a function defined on a rotationally symmetric system, with either a circular or annular pupil. In order to numerically analyze such systems it is typical to expand the given function in terms of a class of orthogonal polynomials. Because of their particular properties, the Zernike polynomials are especially suited for numerical calculations. We develop a recursive algorithm that can be used to generate the Zernike polynomials up to a given order. The algorithm is recursively defined over J where $R(J,N)$ is the Zernike polynomial of degree N obtained by orthogonalizing the sequence $r^J, r^{J+2}, \dots, r^{J+2N}$ over $(\epsilon, 1)$. The terms in the preceding row - the $(J-1)$ row - up to the $N+1$ term is needed for generating the $(J,N)^{\text{th}}$ term. Thus, the algorithm generates an upper left-triangular table. This algorithm has been placed in the computer with the necessary support program also included.

INTRODUCTION

An arbitrary function $W(r, \theta)$, such as a wavefront error function over a circular or annular region, can be expanded in terms of an orthonormal series of orthogonal polynomials. If W is defined over a circular or annular region, it is convenient to expand W in terms of the Zernike polynomials, Z_n^l . This

$$W = \sum_{n,l} A_{nl} Z_n^l.$$

It can be shown {3} that $Z_n^l = R_n^l(r) e^{il\theta}$ where R_n^l depends only on the radial coordinate and $e^{il\theta}$ depends only on the angular coordinate. Also, l is the minimum exponent of the polynomials Z_n^l and R_n^l and the numbers n and l are either both even or both odd. The radial polynomials R_n^l are of degree n and satisfy the relation

$$R_n^l = R_n^{-l} = R_n^{|l|}$$

If we write, using only the real part,

$$W(r, \theta) = \sum_{j=0}^{\infty} A_{nj} R_n^{2j} \begin{matrix} \sin j \theta \\ \cos j \theta \end{matrix}$$

the following properties are satisfied.

1. The Zernike polynomials are invariant in form with respect to rotations of axes about the origin {3}.

2. The Zernike polynomials are easily related to the classical aberrations {4}.

3. The function $W(r,\theta)$ is usually found as a best least-squares fit to a collection of data points. Since the Zernike polynomials are orthogonal over an annular region, the well-known minimum-error property of Fourier expressions shows that each term

$$A_{nj} R_{jn+2}^J \begin{matrix} \sin J \theta \\ \cos J \theta \end{matrix}$$

also represents individually a best least-squares fit to the data. Thus, the average amount of each term is given by the magnitude of that term, without the need to do a new least-squares fit.

Because the Zernike polynomials are being applied to an increasing number of physical problems {1,2,5,6}, there is an expressed interest in being able to generate the Zernike polynomials up to a given order. In this paper, we develop a numerical method due to Tatian {8} for generating the polynomials R_{2n+J}^J over an annular region. A discussion of the derivation of the algorithm is presented in section 2 and a general discussion of the computer program that was written to facilitate this algorithm is discussed in section 3.

Bhatia and Wolf {3} have shown that the polynomials $R_{2n+j}^J(r)$ are obtained by orthogonalizing the functions $r^J, r^{J+2}, \dots, r^{J+2n}$ over the interval $\{\epsilon, 1\}$. The constant ϵ represents the inner radius of the annular region and 1

represents the outer radius. Thus $\epsilon = 0$ represents a circular region. We convert this into the associated problem of orthogonalizing $1, u, \dots, u^n$ over $[\epsilon^2, 1]$ with the weight function u^j by substituting $u = r^2$. This follows from

$$\begin{aligned} \left\langle r^{J+2l}, r^{J+2k} \right\rangle &= \int_{\epsilon}^1 r^{J+2l} r^{J+2k} r dr \\ &= \int_{\epsilon}^1 r^{2J+2l+2k} r dr = \int_{\epsilon}^1 (r^2)^{J+l+k} r dr \\ &= \frac{1}{2} \int_{\epsilon^2}^1 u^{j+l+k} du = \frac{1}{2} \int_{\epsilon}^1 u^l u^k (u^j du) \end{aligned}$$

First, let us consider the case $J = 0$. Then $R_{2n}^0(r) = R_n^0(u)$ is obtained by orthogonalizing the sequence $1, u, \dots, u^n$ over $[\epsilon, 1]$ with the weight function 1. This however is a Jacobic problem over the shifted interval $[\epsilon^2, 1]$. Hence,

$$(1) R_{2n}^0(r) = R_n^0(u) = p_n^{(0,0)}(2) \frac{r^2 - \epsilon^2 - 1}{1 - \epsilon^2}$$

where $p_n^{(0,0)}$ is the Legendre polynomial of degree n .

Now, let us consider the case when $J \neq 0$. We will show that R_{2n+2}^J can be obtained by a recursive method over the variable J . Suppose we have solved the problem of obtaining $Q_n^{J-1}(u)$ i.e. orthogonalize $1, u, \dots, u^n$ over $[\epsilon^2, 1]$ with weight function u^{J-1} and we want to obtain $Q_n^J(u)$; orthogonalize $1, u, \dots, u^n$ over $[\epsilon^2, 1]$ with weight function u^J . We obtain a relationship between these 2 polynomials by making use of a special case of the following theorems {7}.

Theorem 1. Let $\{p_n(x)\}$ be the orthonormal polynomials associated with the distribution $d\alpha(x)$ on the interval $\{a, b\}$. Also, let

$$p(x) = c \cdot (x - x_1) \cdot (x - x_2) \cdot \dots \cdot (x - x_l)$$

be non negative in this interval. Then the orthogonal polynomials $\{q_n(x)\}$ associated with the distribution $p(x) d\alpha(x)$ can be represented in terms of the polynomials $p_n(x)$ as follows:

$$p(x) q_n(x) = \begin{vmatrix} p_n(x) & p_{n+1}(x) & \dots & p_{n+1}(x) \\ p_n(x_1) & p_{n+1}(x_1) & \dots & p_{n+1}(x_1) \\ \vdots & \vdots & \ddots & \vdots \\ p_n(x_l) & p_{n+1}(x_l) & \dots & p_{n+1}(x_l) \end{vmatrix}$$

Theorem 2. The following relation holds for any 3 consecutive orthogonal polynomials:

$$p_n(x) = (A_n x + B_n) p_{n-1}(x) - C_n \cdot p_{n-2}(x)$$

if the highest coefficient of $p_n(x)$ is denoted by k_n , we have

$$A_n = \frac{k_n}{k_{n-1}} \quad \text{and} \quad C_n = \frac{A_n}{A_{n-1}}$$

Theorem 3.

$$p_0(x) p_0(y) + p_1(x) p_1(y) + \dots + p_n(x) p_n(y)$$

$$= \frac{k_n}{k_{n+1}} \frac{p_{n+1}(x) p_n(y) - p_n(x) p_{n+1}(y)}{x-y}$$

using Theorem 1 with $p_n(u) = Q_n^{J-1}(u)$, $q_n(u) = Q_n^J(u)$ and $p(u) = u$, we have

$$2.1 \quad u Q_n^J(u) = \frac{1}{Q_n^{(o)}} \begin{vmatrix} Q_n^{J-1}(u) & Q_{n+1}^{J-1}(u) \\ Q_n^{J-1}(o) & Q_{n+1}^{J-1}(o) \end{vmatrix}$$

We note that this formula becomes undeterminate for $u = r^2 = 0$. But we need the values of Q_n^J at $u = 0$ to calculate the next set of polynomials, so expand equation 2.1 and use Theorem 3 to get

$$(2) \quad Q_n^J(u) = \frac{h_n^{J-1}}{(1-\epsilon^2) Q_n^{J-1}(0)} \sum_{i=0}^n \frac{Q_i^{J-1}(0) Q_i^{J-1}(u)}{h_i^{J-1}}$$

where

$$(3) \quad h_n^J = \frac{1}{2} \int_{\epsilon^2}^1 \{Q_n^J(u)\}^2 u^J du$$

is the normalization constant for $Q_n^J(u)$. By substituting the expression in equation 1 for $Q_n^J(u)$ into equation 3 and using Theorem 3, we obtain

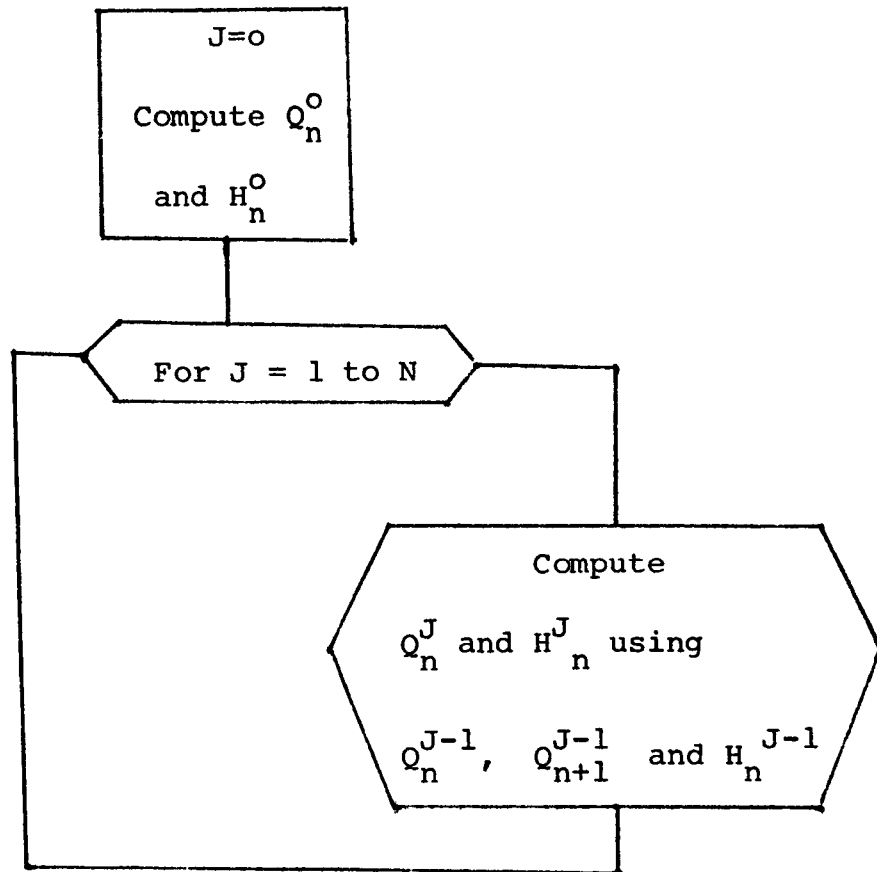
$$(4) \quad h_i^J = \frac{-1}{1-\epsilon^2} \cdot \frac{Q_{i+1}^{J-1}(0)}{Q_i^{J-1}(0)} h_i^{J-1}$$

converting back to the variable r , we have

$$(5) \quad R_{2n+J}^J(r) = r^J Q_n^J(r^2).$$

3. Some comments about the computer program.

The outline for this computer program is:



For a given value of N , the following table shows the values of Q_n^J and H_n^J that are generated.

TABLE 1

Q_n^J or H_n^J	0	1	2	3	·	·	·	N-2	N-1	N
0	*	*	*	*				*	*	*
1	*	*	*	*				*	*	
2	*	*	*	*				*		
3										
·										
·										
·										
N-2	*	*	*							
N-1	*	*								
N	*									

NOTE: Since h_n^J is dependent upon knowing Q_{n+1}^{J-1} , each of the above rows are shorter by 1 entry.

The polynomials Q_n^0 are directly computed from formula (1) namely,

$$Q_n^0(u) = p_n(\alpha, \beta) \quad (\alpha u + \beta)$$

where $p_n(\alpha, \beta)$ is the Legendre polynomial of degree n , $\alpha = 2/(1 - \epsilon^2)$ and $\beta = -(1 + \epsilon^2)/(1 - \epsilon^2)$. Likewise, the constants H_n^0 are directly computed from (3); namely,

$$H_n^0 = \frac{1}{2} \int_{\epsilon^2}^1 (Q_n^0(u))^2 du.$$

NOTE: The above integral is computed in closed form. This is possible because $Q_n^0(u)$ is a polynomial of degree n . This is done via a call to SQPOLY (square the polynomial) and a call to INTGRL (find the integral of a polynomial).

Once the first row is known (Q_n^J and H_n^J for $J = 0$), the recursive algorithm can then be used to compute each succeeding row (Q_n^J and H_n^J for $J = J_0$). The results are then printed via a call to RJN (compute $R_{2n+J}^J = r^2 Q_n^J(r^2)$).

4. Example

A computer run for $n = 3$ is shown below.

ENTER N-LARGEST $R(\emptyset, N)$ DESIRED

?3

$R(\emptyset, \emptyset)$

1.00000

* * * * *

$R(\emptyset, 2)$

NORM: 3.83767639

-.5487 + 1.00000*R** 2

* * * * *

$R(\emptyset, 4)$

NORM: 16.46613630

.2331 - 1.0973*R**2 + 1.00000*R** 4

* * * * *

$R(\emptyset, 6)$

NORM: 71.94691818

-.0981 = .7809*R** 2 - 1.6460*R** 4 + 1.00000*R** 6

* * * * *

$R(1, 1)$

NORM: 1.90923153

1.00000*R** 1 +

* * * * *

$R(1, 3)$

NORM: 8.32586779

-6724*R** 1 + 1.00000*R**3

* * * * *

$R(1, 5)$

NORM: 35,89625267

.3191*R** 1 - 1.2252*R** 3 + 1.00000*R** 5

* * * * *

$R(2, 2)$

NORM: 2.32829044

1.00000*R** 2 +

* * * * *

R(2, 4)
NORM: 11.84460583
-.7897*R** 2 + 1.0000*R** 4
* * * * *

R(3,3)
NORM: 2.6873584
1.0000*R** 3 +
* * * * *

* STOP * Ø

A COPY OF THE ABOVE PROGRAM CAN BE OBTAINED FROM THE AUTHOR.

REFERENCES

1. Baraket, Richard, Optimum Balanced Wavefront Aberrations for Radially Symmetric Amplitude Disturbances; Generalizations of Zernike Polynomials, J. Opt. Soc. Am. 70, (1980).
2. Bezdid'ko, S. N., The Use of Zernike Polynomials in Optics, Sov. J. Opt. Technol., 41, No. 9, Sept., (1974).
3. Bhatia, A. B. and Wolf, E., On the Circle Polynomials of Zernike and Related Orthogonal Sets, Proc. Camb. Phil. Soc., 50, (1954).
4. Nigboer, B. R. A., The Diffraction Theory of Aberrations, Physica (Utrecht) 10, (1947).
5. Noll, R. J., Zernike Polynomials and Atmospheric Turbulence, J. Opt. Soc. Am. 66, (1976).
6. Sumita, H., Orthonormal Expansion of the Aberration Difference Function and its Application to Image Evaluation, Japanese J. Applied Phys., 8, No. 8, Aug. (1969).
7. Szego, G., Orthogonal Polynomials, Am. Soc. Colloquium Pub., v. 23, (1939).
8. Tattain, B., Aberration Balancing in Rotationally Symmetric Lenses, J. Opt. Soc. Am. 64, (1974).

1982

NASA/ASEE SUMMER FACULTY RESEARCH
FELLOWSHIP PROGRAM

MARSHALL SPACE FLIGHT CENTER
THE UNIVERSITY OF ALABAMA

CHROMIUM ION PLATING STUDIES FOR
ENHANCEMENT OF BEARING LIFETIME

Prepared by:	Jack H. Davis, Ph.D.
Academic Rank:	Associate Professor
University and Department:	The University of Alabama in Huntsville Department of Physics
NASA/MSFC: (Laboratory) (Division)	Materials and Processes Engineering Physics
MSFC Counterpart:	Dr. Raymond L. Gause
Date:	August 18, 1982
Contract No.:	NGT-01-008-021 University of Alabama

Abstract

Last summer six 440-C hardened (\sim R.C. 60) stainless steel roller bearing test rods were ion plated with various chromium films of thicknesses from $.2\mu$ to 7μ . During the past six months Dr. B. N. Bhat (Weekly Notes EH23, February 2, 1982) reported that the thinner ($\sim .2\mu$) coating sample had 3X the fatigue life of the unplated (standard) specimens. Contrastingly the samples having thicker coatings (several microns) had short fatigue lives (about 3% of the unplated standard).

This year initially only one specimen has been chromium ion plated ($\sim 10\mu$ thick) as the VTA system has required almost continuous refurbishment. However the VTA system was gradually returned to as good as new condition and during the final week six more specimen rods were ion plated. Thus, the summer objective was met, but little time was available for film characterization or report writing during the final week.

Acknowledgements

I wish to express thanks to the National Aeronautics and Space Administration, the American Society of Engineering Education and the University of Alabama for operating and supporting this program. Special thanks to many who interrupted their higher priority Space Shuttle work to make on-the-spot repairs of the VTA system. Mr. Webster and Mr. Clark performed expert welding on leaks as they were found in delicate parts. Mr. Jack Reed contributed precision machining and general advice. Mr. Long and Willmore provided emergency grinding and lapping. Mr. Bobby Cothren and Charlie Torstenson provided quick replacement parts and help as needed. Alan Biddle, Raymond Gause, B. N. Bhat, and Ann Whitaker provided both suggestions and encouragement.

Introduction

Last year's report¹ provided introductory background material on Ion Plating.

Objective

This year's objective is to ion plate about six roller bearing rods with about 0.3μ of chromium.

Equipment

The ion plating apparatus VTA Model 7375 was custom built by Vacuum Technology Associates and consisted of three main components: (1) a Varian (NRC) vacuum system Model 3117; (2) an electron beam gun system, a Sloan Multi~~earth~~^o 270 gun powered by a Sloan Model Five/Ten power supply; (3) the high voltage power supply for bias voltage (10 KV, .5a), also made by VTA.

General Comments

Testing separate parts of the VTA system is difficult due to vacuum interlocks which shut off the electronics, e.g., without a vacuum the e-beam voltage will not activate. The VTA bias supply is extremely powerful 10KV at 500 ma giving a 5 KW power output which is equal to that of the electron beam itself. Thus insulation and metal may be easily vaporized or melted if the system arcs, producing plating shorts on electrical insulators.

Samples

Eight smooth ($\sim 8\mu$) hardened (R.C. 60) 440-C stainless steel roller bearing test rods, 3-1/4" long by 3/8" diameter, supplied by Dr. B. N. Bhat were similar to those used last year¹ except for some carbon black (from hardening) on the end disks and in the centering cavities.

Experimental Methods

Patience seems to be a chief ingredient in successful electron beam ion plating, e.g., allowing the vacuum system to stabilize at steady state. The bias voltage V_c was slowly increased during discharge cleaning so as not to: (1) damage the feedthrough insulation, (2) evaporate Teflon hydrocarbons into the system, nor (3) cause pressure current runaway. A very low rate of increase of e-beam power minimized the outgassing partial pressure.

Samples 10, 11, 12, 13, 14 and 15 were bead blasted on the ends with a large orifice ($\sim 1/8$ ") while the holes were blasted with a pen type small orifice ($\sim 1/2$ mm) jet. The excess grit was removed by air blown jets and by an acetone rinse. Surface oxygen was removed by a 2 to 2.7 KV d.c. glow discharge at ~ 8 ma for about one hour. Since the substrate is hot water cooled, overheating and arcing to the ground shield occurred at 3 KV after about 30 minutes.

The specimen rod axis was mounted coaxially with the jar axis to produce a symmetric uniform coating. For further uniformity NASA personnel had replaced during the past six months the top center stationary high voltage feedthrough with an NRC rotary feedthrough so the sample could rotate about its own axis. This should provide less destructive vibrations during subsequent bearing testing of samples 9, 12, and 13, but it was unused on #'s 8, 10, 12, and 14. The rotator was switched on only a few seconds at a time because of an increase in arcing with continuous rotation.

Results

The Cr plating thickness in sample #3 varies from +10% to -10% (11μ to 9μ) from the front to the back of the rod although the system had circular symmetry about the rod axis. The 150 mg mass gain predicts an 8.2 average film thickness using the bulk density of Cr of 7.19 gm/cm^3 .

Note that the three thinnest films had the least visibility as expected. Also note that the darkest sample had the highest plating pressure (35μ) in keeping with last year's trend. Optical rechecks of the above estimated film thicknesses should be made by others before any destructive testing.

Refurbishment of VTA 7375 Ion Plating System

Initially the VTA Model 7375 system ion plating system was in only fair condition with a rather high ultimate jar pressure in the 10^{-6} torr range. During the first two weeks a lightning damaged fore pump motor was replaced, a magnetic stress free, quick mounting sample holder was machined, shorts and misadjustments in the e-beam gun were corrected and 440C roller specimen #8 was successfully ion plated with a 10μ chromium film.

Specimen #9 was mounted in the jar but not coated because the ultimate bell jar pressure was too high ($\sim 5 \times 10^{-5}$ torr). Based on the time rate of increase of pressure in the closed system jar, the apparent air leak rate was judged to be a large 5% of the Ar leak rate so that considerable oxygen contamination could be expected. During the third week no leak could be detected with acetone, thermal protection on the diffusion pump failed, thus requiring the system disassembly and methodical decontamination.

During the fourth week the jar pressure level was still poor so a helium leak detector (Veeco MS-9) was acquired on loan from UAH. A large leak was pinpointed in the foreline valve which was eventually corrected by tightening the valve's bellows slot nut.

The blanked-off, i.e., high vacuum valve shut, diffusion pump pressure was then checked at 3×10^{-8} torr (without the cold trap) - a good indication that all was now well at least below the bell jar high vacuum valve. This NRC valve should be watched as the manual shows an O-ring seal but the present seal apparently is formed by a soft elastic flat washer.

Grounded insulator shields were made and installed over the high voltage feedthrough. Filament shields were enlarged and longer e-beam current #10 leads were installed to zig-zag around the above new shields.

During the fifth week the NRC foreline valve leak reappeared so an "extension spreader wrench tool" was fashioned from 5/8" copper pipe which helped to correct the problem. Hand polishing of the top Al plate was begun around the seal areas. Etch marks near the jar seals were found in the stainless steel base plate on the Al top plate which could have contributed to the high pressure. Thus a decision was made to send the top Al plate, the Varian ring and the bottom plate to Building 4705 for resurfacing by lapping. The glass cylinder which had a chipped sealing surface, but not all the way through, was also sent for lapping.

During the sixth week helium leak testing of the e-beam water cooling section was begun; two leaks of greater than 10^{-8} std. cc/sec were found. About eight welds, rewelds and rechecks with the helium detector were required to produce the leak proof welds which are now undetectable on the Veeco MS-9 Leak Detector of sensitivity 10^{-8} std. cc/sec.

During the eighth week helium leak checking indicated a torque of about 50 ft.lbs. is required to stop the leak in the metal to metal Swagelock flange. The carousel hearth showed a slight He leak during rotation but the leak stopped when the rotation stopped. The 18.75" Al top plate was received, the lap (~ 800 grit) looked basically good but several heavy scratch marks had to be hand polished in the O-ring contact area. A set screw induced bulge in the O-ring groove of the center rotary feedthrough was found and resurfaced. This tap hole had been recently added as a terminal for the high bias voltage wire. The center (3/8" shaft) rotary NRC feedthrough was helium tested and found leak free ($<10^{-8}$ std. cc/sec).

The base plate acid pits were lapped but presumably some foreign grit has introduced severe ($\sim .2$ mil. deep) scratches into the base plate and into the Varian ring.

An 18" x 3/4" Al "proof" disk (too big for the Bldg. 4711 lathes) has been machined at UAH to blank off either the top of the Varian ring or the top of the glass jar to isolate troublesome leaky parts of the VTA system without a He leak detector.

Several 58 X Leitz photomicrographs of specimen #8 show that the Cr film peeled away with a knife blade rather easily from the interface with the 440C stainless steel.

During the ninth week the lapping problems were overcome by Mr. Richard Long who ground out the scratches in both surfaces of the Varian ring and both surfaces of the base plate to an estimated 10 microinch finish.

The e-beam gun was left out (the two waterline Con Flat Flanges being blanked off) during initial leak testing of the ring, the new replacement (recleaned in building 4706) glass cylinder jar and the lapped top plate. The suspected combination high voltage (modified for rotation) feedthrough proved leak free. However a makeshift leaky weld of a stainless ($\sim 1/4$ ") tube to a Swagelock fitting at the argon leak inlet was found and rewelded (but not leak tested). An NRC $1/8$ " pipe thread fitting which did not require a weld was used as a replacement. The stainless steel flexible Ar leak line was sprayed with helium with no response on the leak detector which in the above system test had less sensitivity since it was connected by a 6' x .5" I.D. hose to the small fore line ($\sim 1/8$ " I.D.) tap-in valve of the NRC-3117 Vacuum System.

During the tenth week a second ion plating attempt on sample #9 was made. However, the e-beam voltage would not initially come on due to high voltage arcs in the -10 KV feedthrough. Disassembly and subsequent bead blasting of the inside of the feedthrough cleared the short. However the e-beam high voltage still tripped each time it was activated. The 2.5 minute delay timer for the high voltage take was found to be closing but not holding. Mr. C. A. Torstenson found a close substitute timer and wired it into the Sloan Five/Ten power supply.

During the tenth week Mr. Torstenson procured a hot water heater thermostat and wired it into the diffusion pump current line for protection against the previous overheating. This provided an overnight pumping capability which (with LN cold trap) yielded an estimated jar pressure of 6×10^{-7} torr before the first plating with the refurbished system.

During the last week samples 9, 10, 11, 12, 13, and 14 were each ion plated with roughly less than 1μ of Cr. The film thicknesses are not known since most effort was toward coating all samples.

Conclusions

The VTA Ion Plating System operated rather well (once refurbished) plating 0.3μ films compared to a few years ago when 40μ films were attempted. This is not surprising since most of the VTA downtime has been related to film and powder buildup.

REFERENCES

1. Davis, J. H., "Al to Cr Ion Plating Studies for Surface Enhancement," NASA Contract Report, Jan. 1982, NASA CR-161855, p. XXVIII
2. Davis, J. H., "Ion Plating for High Temperature Applications," NASA Contractor Report CR-161511, p. V, Oct. 1980

TABLE I

Sample #	Date Plated	DM (gm) Sample	DM (gm) Source	Color Film	Film Thickness Est T (μ) From DM	Used Step Subst Rotator	T (hr) Dec Tac	Electrode Gap (in.)	CLEANING				PLATING				Comments			
									T (hrs)	Vc (KV)	Ic (ma)	T ($^{\circ}$ C)	P (u)	Vc (KV)	Ic (ma)	Ie (ma)		T (min)	P (t)	
8		150	6	Grey	8	No	10	5.5	1.1	2.2	6	200	23	2	5	400	2	2a	2-discharge cleanings	
9	8-12-82	-10	1 \pm .5	Blackish	41	Yes		6.5	1	2.4	5	170	25	2.4	4	60	5	5	cut depth mark around center	
10	8-13-82	+1	2.2	Bluish	3	No		6.5	2	2.4	6	250	25	2.4	6	80	5	5		
11	8-13-82	-4	.06	Invisible	.08	No		6.5	1.1	2.4	9		25	2.4		40	5	30	Turned out to water	
12	8-16-82	-10	1.6	Bluish	2	Yes		6.5	1	2.7		~200	22	2.2		90	5	30		
13	8-11-82	-15	.67	Invisible	.9	Yes		6.5	1	2.7		~300	20	2.5		60	5	25	some hair	
14	8-18-82	-7	.32	Invisible	.4	No		6.5	1	3(2)		200	20	2		58	5	2b	some arc	
15	Standard			None																

ORIGIN AND CONTROL OF INSTABILITY IN SCR/TRIAC
THREE-PHASE MOTOR CONTROLLERS

Prepared by: John J. Dearth, Ph.D.
 University of Alabama

1982

NASA/ASEE SUMMER FACULTY RESEARCH FELLOWSHIP PROGRAM

MARSHALL SPACE FLIGHT CENTER
THE UNIVERSITY OF ALABAMA

ORIGIN AND CONTROL OF INSTABILITY
IN SCR/TRIAC THREE-PHASE MOTOR CONTROLLERS

Prepared by: John J. Dearth, Ph.D.
Academic Rank: Temporary Assistant Professor
University and Department: University of Alabama
Dept. of Electrical Engineering
NASA/MSFC:
(Laboratory) Information & Electronic Systems
(Division) Guidance, Control and Instrumentation
(Branch) Control Electronics
MSFC Counterpart: Frank J. Nola
Date: August 6, 1982
Contract No: NASA-NGT-01-002-099
(University of Alabama)

ORIGIN AND CONTROL OF INSTABILITY IN SCR/TRIAC
THREE-PHASE MOTOR CONTROLLERS

by

John J. Dearth, Ph.D.
Temporary Assistant Professor of Electrical Engineering
University of Alabama
Tuscaloosa, Alabama

ABSTRACT

An SCR or triac three-phase motor controller employs three sets of antiparallel SCR's or three triacs, one connected in series with each stator winding of the motor. Normally no neutral connection is made to the motor windings. The SCR's or triacs are gated by an electronics package in response to one or more feedback signals. The controller is typically designed to perform soft starting and provide energy savings and reactive power reduction during partial loading, at idle, and during high line voltage conditions. An unusual phenomenon is known to occur in motor controllers of this type. Specifically, if the firing angle is fixed, that is if the feedback loop is opened, the system can go unstable, with low inertial loads.

The energy savings and reactive power reduction functions were initiated by the power factor controller (PFC) invented by Frank J. Nola of NASA. A three-phase PFC with soft start (MSFC size D drawing number 50M28222), developed by Mr. Nola, is examined analytically and experimentally to determine how well it controls the open loop instability, described above, and other possible modes of instability. The detailed mechanism of the open loop instability is determined and shown to impose design constraints on the closed loop system. The Nola design is shown to meet those constraints.

In addition, the Nola design has a pole near 50 Hz and another pole near 200 Hz, neither of which can be moved to a significantly higher or lower frequency without adversely affecting stability. The modes of instability which place the double bounds on these poles were not understood. These are examined and explained and the poles are shown to be located for optimum stability. The Nola design also delays the timing ramps by 6° to allow the firing angle to be adequately delayed at idle without an undesirable change in mode of operation. The details of this are also examined and explained.

Although not part of the stability study, the PFC is shown to reduce the power factor as measured by utilities.

ACKNOWLEDGEMENTS

The author gratefully acknowledges the extensive orientation given by, and many helpful discussions held with his NASA counterpart, Frank J. Nola. In addition, Mr. Nola gave the author free access to several breadboards of his design and some other designs. The author also gratefully acknowledges the valuable support provided by the branch chief, Clyde Jones. The program for the computer plots was written by Ralph Kissel, who "introduced" the author to the HP9845A desk-top computer.

All NASA personnel encountered by the author during his brief tenure were helpful and friendly. It should be noted that funds for the author's stipend were provided through the Technology Utilization Office.

INTRODUCTION

A solid-state three-phase induction motor controller, of the type examined in this report, employs three sets of antiparallel SCR's or three triacs, one connected in series with each stator winding. No neutral connection is made to the motor windings. This configuration provides a practical means to rapidly control the rms voltage applied to the motor. However, an unusual phenomenon is known to occur in motor controllers of this type. Specifically, if the time of the gate trigger is fixed, that is, if no feedback is employed, the system can go unstable with low inertial loads. The instability is characterized by a growing oscillation of the current amplitude with a frequency on the order of 10 Hz. This phenomenon will be referred to as the open loop instability.

Motor controllers of the type defined above were originally considered for speed control [1], but the most common applications today are soft starting and energy savings. The solid-state switches in the controller can also economically serve additional functions, which functions in themselves would not require the speed and proportional control of a solid-state switch. Examples of such functions are over/under voltage protection, overcurrent protection, phase reversal/loss protection, and programmed or remotely controlled operation. It is significant to note that solid-state starters for large motors have been reported to be often cheaper than other reduced voltage starters and in some cases cheaper than full-voltage electro-mechanical starters [2].

The design of motor controllers was radically altered by the invention of the power factor controller (PFC) by Frank J. Nola of NASA. It was the PFC that introduced the energy-saving function into motor controllers. The PFC produces energy savings and reactive power reduction by reducing the rms voltage to the motor during conditions of partial load and idle. A large reduction in idle current is achieved which directly reduces the reactive power drawn at idle and reduces the iron and copper power losses.

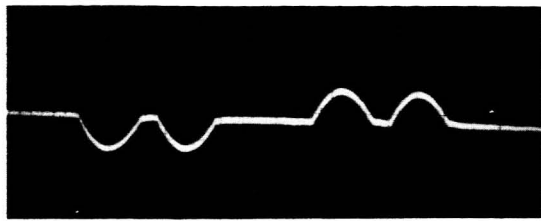
Although other systems are briefly considered, and although the material concerning the open loop instability is applicable to all controllers of this type, the bulk of this report examines a particular controller referred to in this report as the Nola design. It is a three-phase PFC with soft start capability. A complete schematic of this circuit (MSFC size D drawing number 50M28222) is available by contacting Mr. Nola.

The feedback signal in the Nola design is the time, or angle, between the line-to-neutral voltage zero crossing and the moment of current shutoff. This angle will be referred to as the conventional power factor angle, although, due to the nonsinusoidal current waveform, this angle cannot be used in the $V \cos \theta$ formula. The θ in this formula will be referred to as the effective power factor angle. In the Nola design, the conventional power factor angle is sensed for both polarities of all three phases. The time of current shutoff is determined by detecting the voltage across the SCR's/triacs. The DC gain of the feedback loop is carefully restricted to allow the conventional power factor angle to change under load as required to match the rms motor voltage to motor load in order to maximize energy savings. The induced EMF of the motor is also detected and used to advance the firing angle to provide quick response from idle and prevent motor stalling in response to sudden loads. Also, the gain of the feedback loop is increased at idle to enhance speed of response. Under idle conditions, the transfer function of the filter for the feedback signal flattens out below one Hz at approximately 10 dB below its DC gain. A pole occurs near 50 Hz and another pole near 200 Hz. Above idle, the AC gain is lowered somewhat. The output of the filter is compared to timing ramps, one for each phase, to set the time of gate firing. The ramps begin and end 6° past the zero crossings of the line to neutral voltages. When SCR's are used, the gates of both SCR's on a given phase are triggered for both polarities, a condition equivalent to using triacs. The gates are triggered by pulse transformers driven by a 40-kHz "gatepost" oscillator. The trigger signal persists until the end

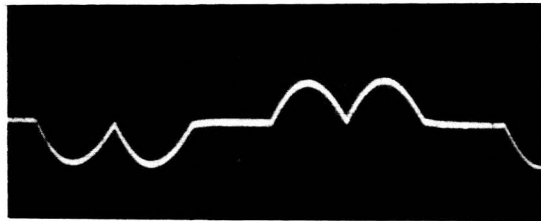
of the timing ramp for that phase to achieve the effect of level firing. Photographs of the current waveform for idle and for various amounts of motor load are shown in Fig. 1. Note that the "double hump" shape of the current waveform is characteristic of all three-phase motor controllers of this general type.

In this report, the Nola design is examined analytically and experimentally to determine how well it controls the open loop instability and other possible modes of instability. To do this, the nature of the open loop instability is studied. Variations in time of current shutoff--that is, variations in the conventional power factor angle--alter the effective voltage applied to the motor, which, in turn, alter subsequent current shutoffs. This was suspected as the mechanism of the open loop instability [3]. However, single-phase motor controllers do not exhibit the open loop instability and three-phase motor controllers exhibit the open loop instability only over a portion of their operating range extending from a little below full on down to a point where the current humps separate. There were problems explaining these observations with the suspected mechanism, but one observation clearly supports the proposed mechanism. An open loop system, the three-phase "light-dimmer" circuit, which tends to correct for disturbances in the time of current shutoff, is known to be stable [3]. (It is significant to note that the "light-dimmer" circuit does not operate in the region where the current humps separate.)

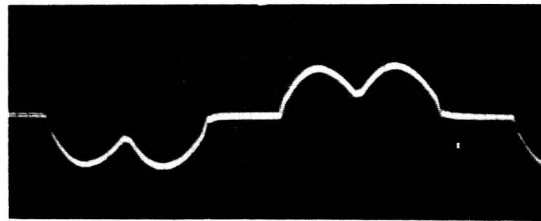
In this report, an improved model for the suspected mechanism is developed by distinguishing between the motoring and generating portions of the cycle and by consideration of the interaction of the three line currents due to Kirchoff's current law in the absence of a neutral connection to the motor windings. The improved model is consistent with the observations listed above, with the observed effect of inertial loads, with the observed effect of connecting the neutral and with some observations made on an antiparallel SCR-diode controller.



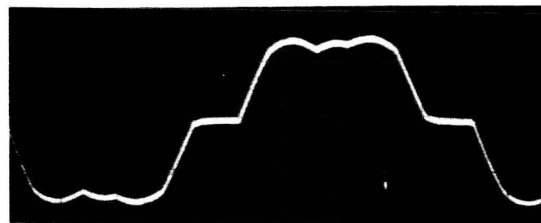
1



2



3



4

Fig. 1. Typical Current Waveforms For A PFC. Photograph 1 is at idle. Load increases in order 1, 2, 3, 4.

A modification of the Nola design was constructed to allow the start of the timing ramps to be referenced to the time of current shutoff and this system is stable in the open loop, as predicted by the improved model. However, this current referenced system is unstable in the closed loop--except when a very slow filter is used. The improved model is shown to impose design constraints on closed loop systems and the Nola design is shown to meet those constraints.

The second section of this report investigates the double bounds known to restrict the location of the 50-Hz and 200-Hz poles. Neither pole can be moved to a significantly higher or lower frequency without adversely affecting stability [3]. The improved model for the open loop instability is used to show that the lower bounds are required in order to control that instability. The upper bound on the 50-Hz pole and the upper bound on the 200-Hz pole are shown to be necessary to control the ripple in order to prevent matching of the ripple to the slope of the ramp, a condition which would result in very high incremental gain and erratic control.

The third section of this report determines why the 6° delay of the timing ramps is required. It was known that the 6° delay was necessary to allow operation in the region where the current humps do not overlap [3]. Operation in this region is essential to achieve maximum savings at idle [3, 4]. If the 6° delays are removed from the circuit, it is observed that at the point where the humps are expected to separate, the second hump apparently ceases to flow and the first hump remains with a somewhat higher amplitude. This posed a paradox, because the same effect is observed in all three phases, and the second hump of any phase is the return current for the first hump of another phase. In this section, it is determined that the gate signal must persist past the zero crossing of the line-to-neutral voltage in order to re-trigger the SCR/triac after the first hump has reached zero. Without the delayed turnoff of the gate signal, both humps disappear at the point in question, and the controller suffers an undesirable change to a new "single hump" mode of operation. The paradox is resolved by noting that the first hump does not actually

remain after the second hump has ceased; instead, both humps cease and a new hump forms in accordance with the new mode. It is significant to note that large delays in gate turnoff would result in premature firing, or misfiring, of the next polarity of current, since the gate signal activates both polarities with this design. However, the 6° delay allows optimum savings at idle, and it is significantly less than the delay at which misfiring commences. Separate polarity triggering is discussed in the section on the optically-coupled trigger option.

The neutral point for measuring line-to-neutral voltage in the Nola design is derived by connecting equal impedances from each line to a common point. Since voltage dividers from this point are also connected to the lines after the SCR's/triacs to detect current shutoff and induced EMF, some noise is introduced into the derived neutral point. This is a consequence of the fact that opening one of the SCR's/triac switches allows the instantaneous sum of the three motor line voltages to be nonzero. Since a suitable neutral line may not be available in a typical application, the capability to operate with a derived neutral is needed. Another possible source of noise is stray coupling of the gatepost oscillation into the input of the voltage comparators which control the gate firings. The Nola design has been observed to be noise resistant and no significant effect was observed to be produced by noise. However, since these noises could be detected by careful observation with the oscilloscope, the fourth section of this report examines them and lists suggested noise reduction techniques which could be used if required by a particular application.

The Nola design was implemented with optically coupled gate trigger circuits in order to experimentally prove that the open loop instability was not a manifestation of the gatepost oscillator. In the fifth section of the report, the open loop instability is shown to occur with optically coupled trigger circuits which use no gatepost oscillator. Also, some design considerations for implementing optical coupling with the Nola circuit are discussed.

During the study covered by this report, the author was shown a copy of a paper which claimed that since the utilities measure power factor at peak demand, the PFC does not reduce the power factor penalty charged by the utilities [5]. While this might be true for a single motor, a typically plant has many motors, some of which would be idling at the time of peak demand. A calculation was made for two motors, one

at full load and one at idle to determine the effect of the PFC on the power factor of the combined load. In the sixth section of this report, the PFC is shown to reduce the power factor for the case described above.

The last section of the report discusses areas for future work.

OBJECTIVES

The basic objectives of the study reported here are to analytically and experimentally investigate the stability of the Nola design--with emphasis on the open loop instability phenomenon--and to analytically verify the choice of some empirically-determined parameters in the design. Some useful incidental information generated during the study is also reported.

OPEN LOOP INSTABILITY

The Nola design can be converted to open loop--to demonstrate the open loop instability phenomenon--by open circuiting the 15K resistor at the input to the feedback-filter amplifier. Although the induced EMF feedback is not designed to function in the operating region which is of interest here, this feedback can also be disconnected from the filter amplifier. The system is now open loop. If the grounded end of the "PFC adjust" potentiometer is, instead, connected to +15 volts, and if the soft start sequence has finished, the firing angle can be set with the PFC adjust potentiometer, as needed. To observe the instability with an unloaded motor, one gradually lowers the PFC adjust from its full negative position until the firing angle is delayed sufficiently to enter the region of instability. The unstable region is observed to begin at a hold-off angle of 5 to 20° depending on the motor observed.

The other side of the unstable region is observed to be precisely limited by the point where the current humps separate as shown in the second photograph of Fig. 1. It should be mentioned that although the open loop instability will not initiate outside the region just described, the instability, once initiated within the region, can grow to where the extremes of the current swings extend beyond the region. A photograph illustrating the buildup of the instability is shown in Fig. 2. Vibration of the motor and jerky rotation of its shaft accompany the current swings. Often the power must be shut off to protect the motor. Sufficient inertia added to the motor shaft prevents the spontaneous growth of the instability, and still more inertia

quickly damps the instability in response to a torque impulse. However, loading the motor does not stop the instability, unless the load contains sufficient inertia. Although all motors exhibit the instability to some degree, some are more unstable than others.

An open loop control system with a damped oscillatory response is, of course, not unusual, but the open loop system, just described, has a negatively-damped oscillatory response--that is, it is an oscillator, and it has no apparent feedback path nor any negative resistance devices. (Although an SCR or a triac exhibits negative resistance when its forward breakover voltage is exceeded, this does not occur for this system.) Therefore an unusual mechanism must be responsible. Since the phenomenon does not occur in induction motors alone, it must be an interaction between the SCR/triac switches and the motor. Because the turn-on time is fixed, interaction can only occur via variations in the turn-off time. Consequently, the oscillations were postulated to arise in the following manner: [3]:

If an inevitable noise disturbs the turn-off of a particular SCR or triac to a time, say, earlier than the previous turn-off, then the earlier opening of the switch means that less rms voltage is applied to the motor. Less voltage, in turn, lowers the slip and reduces the conventional power factor angle as measured at the next current zero, that is, the next turn-off is shifted earlier in time. If its shift exceeds the original disturbance, then the conditions for instability are met.

The most obvious difficulty with the proposed explanation is that it apparently also applies to single-phase motor controllers which are observed to be open loop stable [3]. In addition, the proposed explanation does not allow for the stable portions of the operating region that are observed to exist for three-phase motors, nor for the stable operation that is observed if the motor windings have a neutral connection [3]. (It is important to mention that the neutral connection is normally omitted, because it increases the stator currents required for a given torque [1].)

The model is improved, if one distinguishes between the motoring and generating portions of the cycle. The single-phase case is shown in Fig. 3. Observation of Fig. 3 reveals that at the time of current shutoff the voltage and current have opposite polarities, which implies that power is flowing from the motor to the supply line. Thus an earlier shutoff of the current returns less power to the line and supplies more net power to the motor. This is equivalent to a higher

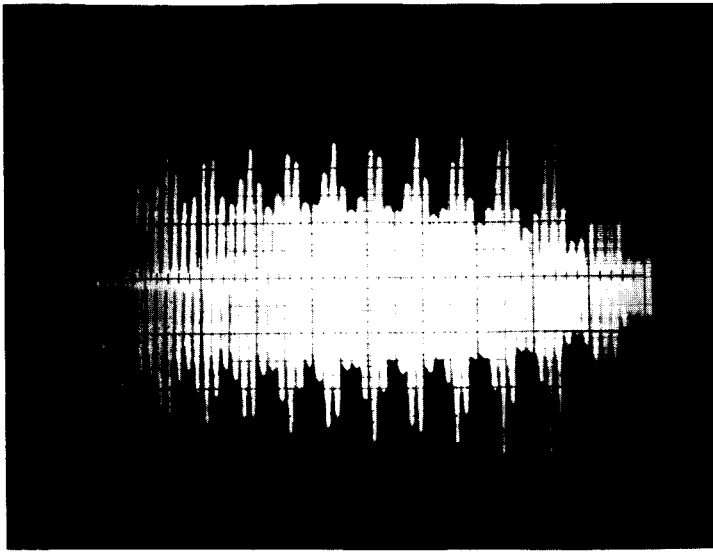


Fig. 2. Photograph Of The Open Loop Instability, Current Vs. Time. Time scale is 0.1 sec/cm.

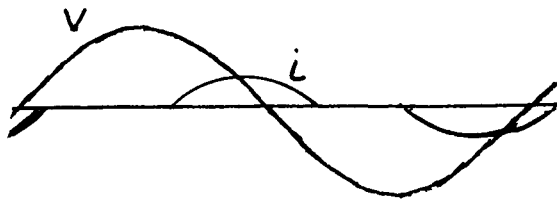


Fig. 3. Voltage And Current Vs. Time Waveforms for Single-Phase PFC.

effective voltage instead of a lower voltage as assumed above. The slip and the conventional power factor angle are now seen to increase and resist the original disturbance for this case, and the model is now consistent with the observed open loop stable behavior of the single-phase system. A stability test based on the improved model can be stated as follows. If the machine is acting as a generator at the moment of current shutoff, then the system is open loop stable. If the machine is acting as a motor at the moment of current shutoff, then the system has the potential to become open loop unstable.

The waveforms for the three-phase case with the motor neutral connected, are the same as the single-phase waveforms shown in Fig. 3, if the voltage waveform is redefined to be the line-to-neutral voltage and if the time axis is appropriately shifted for each phase [3]. With the neutral connected, a disturbance of a current shutoff affects the switching of the voltage applied to only the phase in which the disturbance occurs. Consequently, the stability argument is identical to the single-phase case, and the improved model is thus also consistent with the observed open loop stable behavior of the three-phase neutral-connected system.

When the neutral is not connected, Kirchoff's current law can be applied to the three inward-flowing stator currents i_A , i_B , and i_C to give

$$i_A + i_B + i_C = 0. \quad \text{Eq. 1}$$

This equation clearly shows that a disturbance in the time of current shutoff in one phase also affects the current in at least one other phase. The problem can be stated in terms of voltage as follows. A disturbance in the time of current shutoff in one phase affects the switching of the voltages applied to all of the stator phases which are connected at the time. The model must be further refined to include this interaction. In other words, the effect of a disturbance in the time of current shutoff must be evaluated in terms of its total net impact on all three phases. The total net power supplied to the motor at any instant in time is given by

$$p(t) = (v_{AX})(i_A) + (v_{BX})(i_B) + (v_{CX})(i_C), \quad \text{Eq. 2}$$

where A, B, and C are the terminals of the motor, X is an arbitrary reference point, and the currents are defined as before. For ideal SCR's/triacs, no distinction

is necessary between the motor terminals and the power supply lines in Eq. 2, because, with ideal switches, these points differ only when the current in a phase is zero. A distinction must, of course, be made between the power line neutral and the motor neutral; that is, if point X is selected to be "the" neutral, then the line neutral, or the motor neutral, must be consistently used in all three terms of Eq. 2.

A disturbance of the no-neutral system is easier to evaluate when the current humps are separate, because no more than two phases are connected at any one time during this case. This is the case defined as mode 2 by Lipo in Ref. 1. Typical separate-hump current waveforms, along with the corresponding line-to-neutral voltages are shown in Fig. 4. The quantity $p(t)$ can be found by summing the products of current and voltages for each of three graphs in Fig. 4. This evaluates Eq. 2 with point X as the line neutral. If this is done for a point just before the shutoff of the first positive hump in Fig. 4, the A component of the power is positive, the B component is negative and larger than the A component, and the C component is zero. Since the B current hump is the return current for the A hump, the magnitudes of both currents are reduced identically by a left shift in the time of shutoff. It is thus shown that a early shutoff increases the net power to the motor, because the B term increases more than the A term decreases. Therefore, the shutoff of the first hump is open loop stable. Due to the symmetry of the waveforms, the calculation need not be repeated for the other shutoffs. For example, the second positive hump in A is the return for the first negative hump in C. The improved stability model is thus shown to be consistent with the observed behavior for the separate humps case.

The same calculation is more easily accomplished, if point X is taken to be point A. The waveforms are shown in Fig. 5. The A component of the power is now zero. The B component is negative, and the C component is zero. The disturbance of the A current enters the sum only through the B phase, and the same result as before is obtained directly from the B graph.

Additional insight can be obtained by repeating the calculation once more--this time with point X taken to be the motor neutral. The necessary voltage and current waveforms, along with the electrical torque, are shown in Fig. 6 for one phase. These waveforms are taken from Fig. 4B of Ref. 1. Only one phase needs to be shown, because the power is negative just before every shutoff. Since the symmetry means that this is true for all three phases, all non zero terms in Eq. 2 are shown to be negative just before shutoff. This again leads to the same result as before.

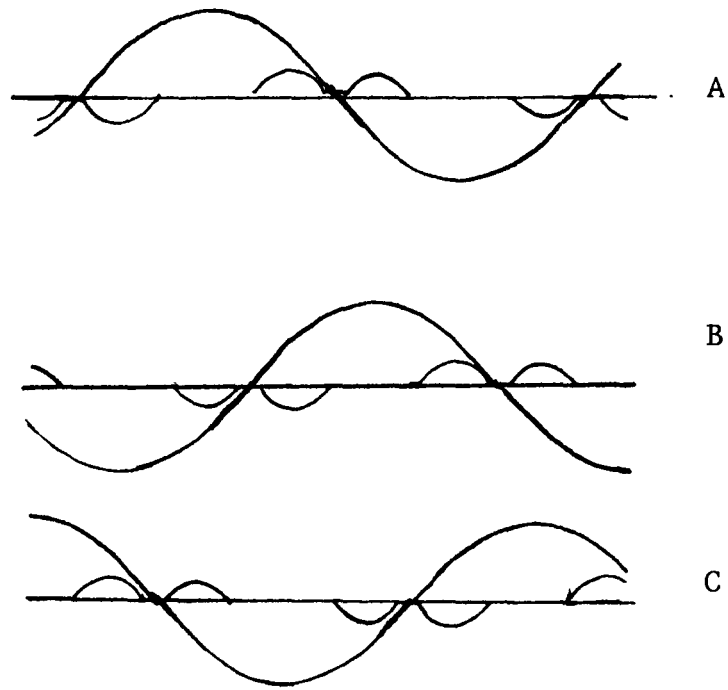


Fig. 4. Three-Phase Separate Current Humps Mode. Line-to-neutral voltages are also shown.

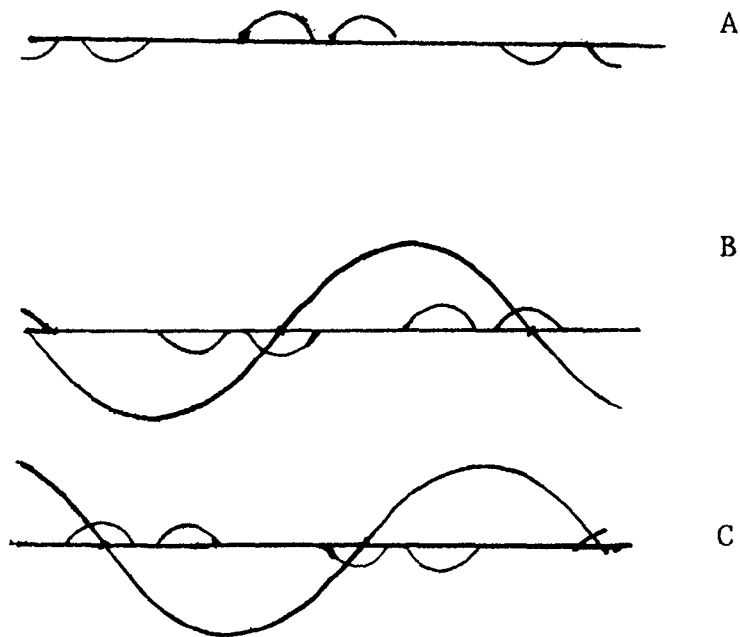


Fig. 5. Three-Phase Separate Current Humps Mode. Line-to-A voltages are also shown.

Observation of Fig. 6, shows that the torque is positive for both the motoring and generating portions of the cycle. This implies that the energy returned to the line during the generating portion of the cycle is energy from the inductors in the machine, not kinetic energy from the motor. Thus, the term "generating portion" is misleading, since it could be confused with the case where the rotor is driven above synchronous speed to produce actual generation.

It is interesting to note that, although a steady-state solution is obtained for the separate-humps, or mode 2, case in Ref. 1, the author of Ref. 1 in 1971 regarded this mode as useless, because it produced little torque. This mode is, of course, essential to achieving maximum power savings, at idle with a PFC.

A disturbance of the no-neutral system is harder to evaluate when the current humps overlap, because all three currents are affected by any shutoff disturbance. The difficulty arises, because a disturbance in, say, i_A is split between i_B and i_C . The problem can be illustrated by the waveforms shown in Fig. 7. Near the positive A shutoff, i_B is positive and i_C is negative. Consequently, Eq. 1 can be rearranged for this case to obtain

$$|i_A| = |i_C| - |i_B|. \quad \text{Eq. 3}$$

A left shift in the A shutoff reduces the magnitude of i_A , and therefore by Eq. 3, the magnitude of i_C must decrease or the magnitude of i_B must increase. Since opening one of the lines to the motor causes the potential of the motor neutral to jump away from ground potential, it is expected that both of these possibilities could occur. If both do occur, then the waveforms in Fig. 7 imply that the A and B terms in Eq. 2 have stabilizing effects, and that the C term has a destabilizing effect for ϕ less than 60° . Therefore, if the splitting factor favors the C term, in this manner, the system has the potential to be open loop unstable with the humps overlapped and ϕ less than 60° . This agrees reasonably well with the experimentally observed open loop unstable region.

Although definitive verification of the proposed open loop instability mechanism is not possible without better knowledge of the splitting factor, the argument for the proposed mechanism is persuasive, because this mechanism is the only apparent mode by which the motor

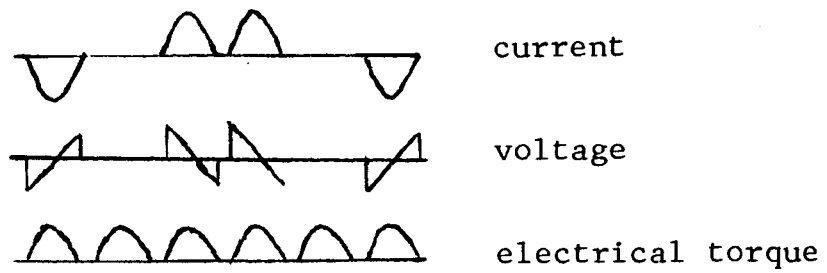


Fig. 6. Three-Phase Separate Humps Mode. Line-to-motor voltage is shown (After Ref. 1.)

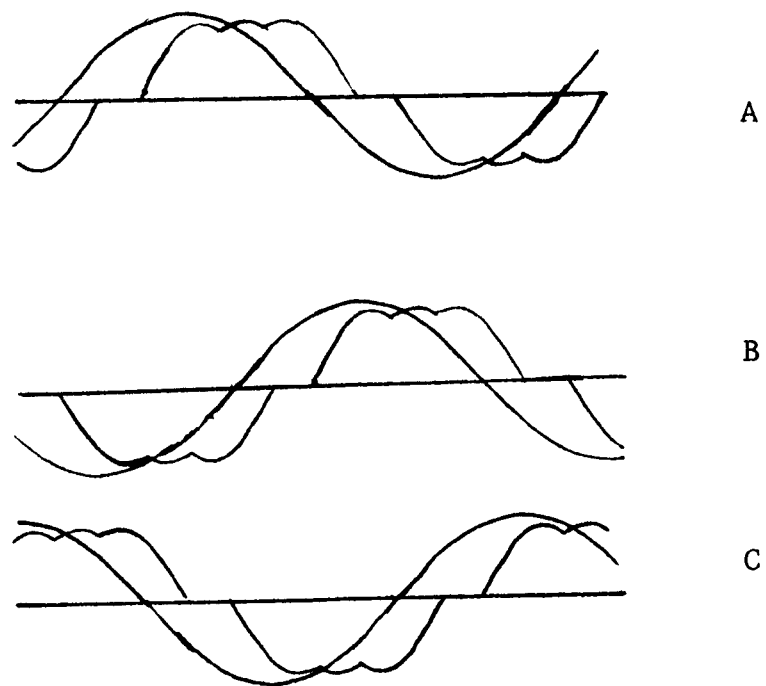


Fig. 7. Three-Phase Overlapped Humps Mode. Line-to-neutral voltages are shown.

can affect the switching of the voltage applied to itself, and because the shutoff time is experimentally observed to vary during the occurrence of the instability, and because the qualified predictions of the refined model agree with the observed stable and unstable cases.

The observed effects produced by adding inertia to the shaft can be readily explained by the model as follows. Sufficient inertia limits the change in slip that is initiated by a shutoff disturbance such that the shift in each successive shutoff is less than the one before and the disturbance is thereby damped out.

Perhaps the strongest experimental evidence to support the model, is that if the firing time is referenced to the previous current shutoff, the system becomes open loop stable. This is demonstrated by both the light-dimmer circuit shown in Fig. 8 and the current referenced modification of the Nola design shown in Fig. 9. This stable behavior is precisely predicted by the model as follows. A left shift of a current shutoff, for example, results in an earlier start for the next timing ramp, which in turn results in a left shift of the next current turn-on which nullifies the effect of the original shift.

As an additional test of the model, some observations were made on an antiparallel SCR-diode controller. No spontaneous initiation of the open loop instability is observed in this system [3]. The waveforms for this system are considerably different, and beyond the scope of this report, but the system is observed to operate in either of two modes. In one mode, no more than two phases are on at the same time and both phases are generators at the moment of shutoff. The waveforms of this mode are not the same as those of the separate-humps case of the SCR's/triac controller, but an almost identical argument can be used to show that this mode is stable. In the other mode, only one current shutoff occurs per cycle per phase. That is, the positive half of the current is not switched off at the zero crossing. Although the waveforms are again different, an almost identical argument can be used to show stability for this mode for ϕ greater than 60° , where ϕ is measured at the negative current shutoff. However, a potential for instability appears to exist for ϕ less than 60° . This is, of course, inconsistent with the observed behavior of this system. Either some other mechanism inhibits the instability or something is wrong with the model. The most obvious difference between the two systems is that the current shutoffs are spaced by 120° in the SCR-diode system, instead of the 60° of the SCR's/triac system. Perhaps the

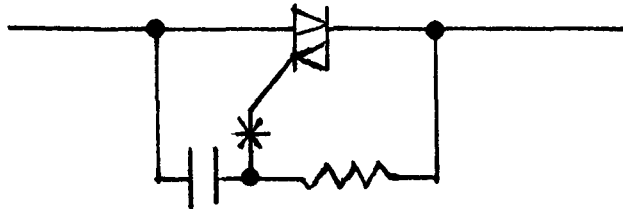


Fig. 8. Light-Dimmer Circuit for Controller.
A unit is required for each phase.

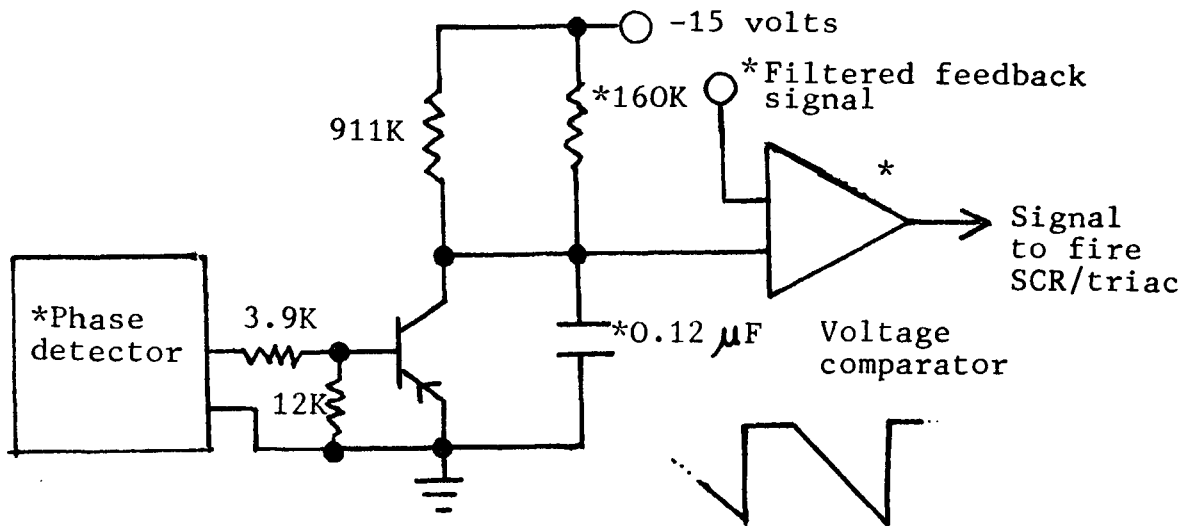


Fig. 9. Current-Referenced Modification of Nola Design. A unit is required to modify each phase. The modified timing-ramp waveform is also shown.

* Parts with * are part of Nola design.

additional time between current shutoffs allows the motor speed to restabilize sufficiently to limit the shift in the next shutoff to less than the original disturbance. This idea is supported by the experimental observation that the SCR-diode system with no added inertia reacts to a torque impulse the same way that the SCR's/triac system does with some inertia added to it; that is, they both exhibit similar damped oscillations in the expected unstable region [3].

The proposed open loop instability mechanism imposes two constraints on a closed loop system: (1) the times of current shutoff, or a parameter which quickly reacts to them must be sensed, and (2) the response of the feedback path must be rapid enough to correct the next gate firing. These design rules are particularly important for a PFC, since many important PFC applications involve operating conditions that could evoke the open loop instability mechanism. Note that the design rules imply that it is best to sense both polarities of all three phases and to independently time the gate firings of each phase. Note also that an optical tach with only one "blip" on the shaft is predicted to provide too slow a sample for the feedback signal.

As described in the introduction, the Nola design clearly meets the first design constraint. The Nola design is shown to meet the second constraint by the graph shown in Fig. 10. The graph is a computer plot of the response of the feedback filter from the Nola design when the input is a 33.3% duty cycle square wave interrupted by a single period with a 16.7% duty cycle. This input simulates a 10° left shift in an otherwise steady-state power factor of 20° . The output clearly responds to the disturbance within the 60° "subcycle" in time to correct the next gate firing, if the slope of the timing ramps is correct. This is verified in the next section.

BOUNDS ON THE 50- AND 200-HZ POLES

Comparison of Fig. 10 with Fig. 11, which is the same as Fig. 10, but without the 200-Hz pole, indicates that the 200-Hz pole acts to smooth (integrate) the points off the ripple. Closer comparison indicates that the 200-Hz pole also reverses the curvature of the "straight" portions of the waveform. The significance of this can be illustrated if the 200-Hz pole is removed from the actual system by disconnecting the $0.056 \mu\text{F}$ capacitor. An operating region can then be found where a ripple slope matches to the slope of a

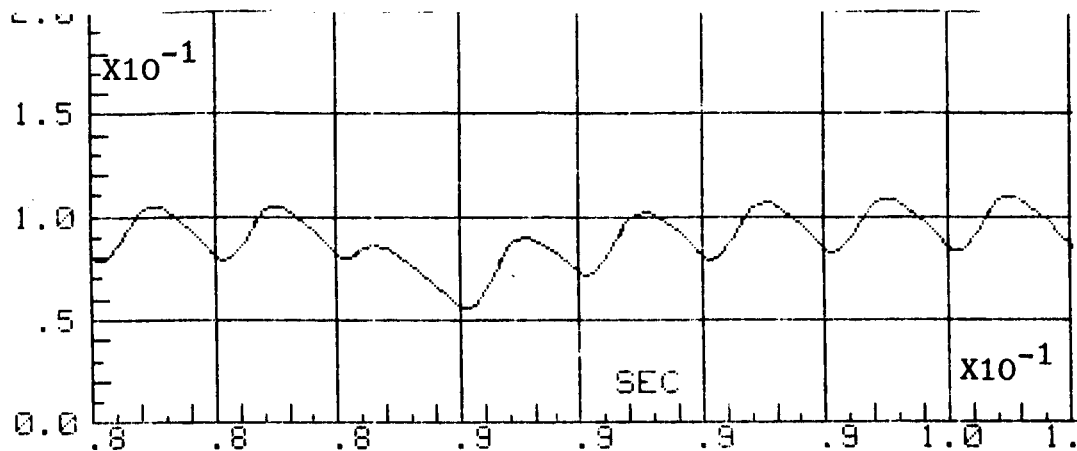


Fig. 10. Normalized Plot Of The Response Of The Feed-back Signal Filter Of The Nola Design To A 10° Left Shift In An Otherwise Constant 20° Conventional Power Factor Angle. To obtain actual voltage, multiply the plot by -11.7 volts. The large horizontal divisions are 60° .

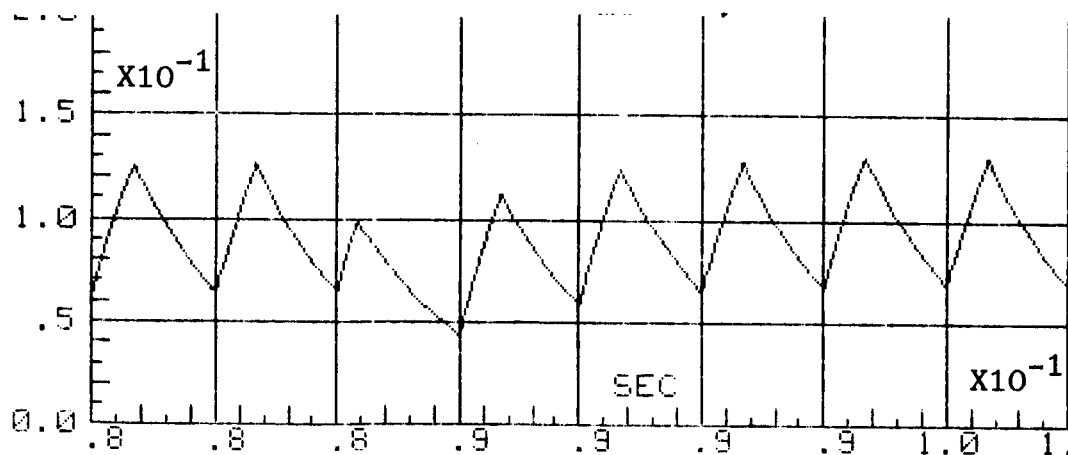


Fig. 11. Same plot as Fig. 10, but with the 200-Hz pole omitted.

timing ramp and the firing point is observed to jump erratically from end to end of the ripple. A photograph illustrating this is shown in Fig. 12.

Since the downward portion of the ripple cannot match to an upward timing ramp, the function of the 200-Hz pole is to shape the upward (on the normalized plots) portion, which lasts some 50° or less for normal "PFC adjust" settings. This response is set in the Nola design by the $0.056 \mu\text{F}$ capacitor and the 12K ohm thevenin resistance which charges it. At the end of 50° , the response of this pole is down to 6%, which is large enough to shape the ripple, yet small enough not to slow the overall response of the filter unnecessarily. That is, the 200-Hz pole is just low enough to shape the ripple without unduly restricting the bandwidth of the filter. The "200-Hz" pole, incidently, is at 189 Hz with the diodes off and at 237 Hz with the diodes on.

The 50-Hz pole needs to be high to provide the fast response required to control the open loop instability, but it cannot be raised too high or the 200-Hz pole cannot shape the ripple. For the necessary curvature, the following inequality must be satisfied:

$$(2\pi f_2)^2 \exp(-2\pi f_2 t) \leq (2\pi f_1)^2 \exp(-2\pi f_1 t), \quad \text{Eq. 4}$$

where f_1 is the 50-Hz pole, f_2 is the 200-Hz pole, and t is the longest expected time for the normalized upward (actual downward) portion of the ripple. For f_2 set by 12K ohms and $0.056 \mu\text{F}$ as before, and $f_1 = 50$ Hz, the curvature will be correct for up to 57° , which means that the 50-Hz pole is properly located to obtain the fastest response while maintaining the curvature.

Observation of Fig. 10 shows that the slope of the ripple is the response of the filter to a shutoff disturbance. Since the response of the 200-Hz pole is virtually over after five time constants, and since the ripple slope is approximately constant, the slope is approximated by:

$$\text{ripple slope} = 2\pi f_1 G_a V_h \exp(-5f_1/f_2), \quad \text{Eq. 5}$$

where G_a is the AC gain of the "flat" portion of the Bode plot between 0.7 and 50 Hz, and V_h is the height of the square wave whose duty cycle represents the power factor angle. For the plot in Fig. 10, V_h is normalized to +1 volt, and the DC gain is normalized to +1. Therefore $G_a V_h$, for the normalized plot, is about 0.22, and Eq. 5 predicts a normalized slope of 20. The slope of Fig. 10 is 17; therefore, Eq. 5 is a reasonable approximation as long as f_1 and f_2 are related properly to control the slope as described above.

The graph in Fig. 10 shows that a 10° left shift

in the time of shutoff results in a 0.025 normalized voltage drop. This corresponds to an actual drop of 0.297 volts. (The DC gain times V_h is 11.7.) The slope of the timing ramp is 781 volts/sec, resulting in a correction of the next firing angle by 8.2° . This means that the slope of the filter is properly set.

FUNCTION OF 6° DELAY

Observation of Fig. 4, which shows a typical idle current waveform, reveals that the second hump starts after the zero crossing of the line-to-neutral voltage. The second hump in the A phase starts when the first hump is triggered in the C phase, but the A phase SCR's/triac must have a gate signal at this time to allow it to switch on and provide the return path for the C phase. This requires the timing ramps to be delayed 6° past the line-to-neutral zero crossings. The necessary delay is provided in the Nola design by the 0.039μ F capacitors in the voltage dividers that sample the line-to-neutral voltage.

DISCUSSION OF POSSIBLE NOISE REDUCTION TECHNIQUES

The photograph in Fig. 13 shows a typical waveform for the noise voltage observed between the derived neutral and the line neutral. As mentioned in the introduction, this noise is not observed to produce any significant effect on the operation of the system. This noise could be reduced, if desired for a particular application, by lowering

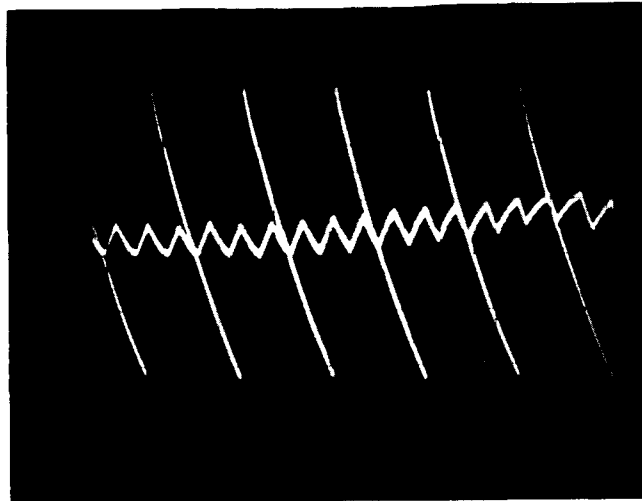


Fig. 12. Matching Of Ripple Slope To The Slope Of The Timing Ramp. Note that the voltage is inverted from the normalized plots. Ground reference is at the top of ramps. The firing point changes on the fourth ramp shown. Vertical scale is 1 volt/div. and the ramps are 60° wide.

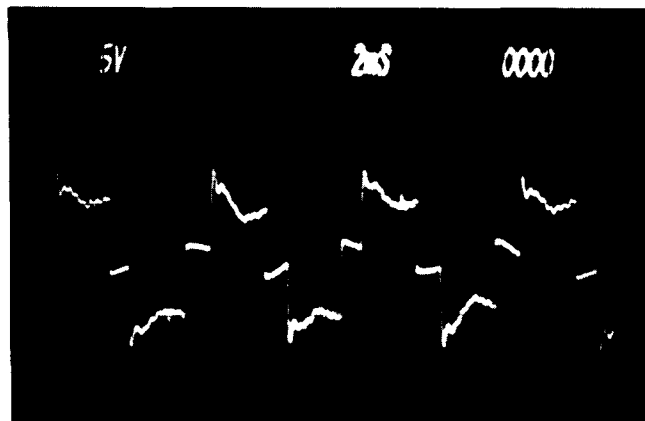


Fig. 13. Typical Noise Observed On The Derived Neutral.

the size of the resistors in the line-to-neutral voltage dividers. The $0.039 \mu\text{F}$ capacitors should be raised as needed to maintain the 6° shift. Alternatively, the derived neutral could be grounded to the line neutral to eliminate the noise, if a suitable line neutral were available (It should be mentioned that the open loop instability is observed to occur even with the derived neutral so grounded.) Also, it is significant to note that the noise on a not-entirely-firm derived neutral might serve a useful function. This is based on the observation that when some faults are deliberately introduced into the circuit, the resulting imbalance of the derived neutral tends to limit the consequences of those faults.

A small amount of noise from the gatepost oscillator can be detected on the inputs of the voltage comparators which control the gate firings. The noise is barely visible on the scope, and it produces no observable effects, but it can be reduced by placing $0.01 \mu\text{F}$ capacitors from these inputs to ground. A significantly larger capacitance should not be used, because it would undesriably alter the feedback filtering. The inputs from the timing ramps of course, need not and should not be filtered.

OPTICAL TRIGGERING OPTION

Experimental observations from two optically coupled trigger circuits are reported in this section. The first circuit is shown in Fig. 14 and the second circuit, which is not shown, differs from Fig. 14 only on the gate side of the coupler, where a DC gate signal is employed. Observations of both circuits demonstrate that the open loop instability occurs without the gatepost oscillator. For example, the photograph in Fig. 1 was taken with DC optical triggering and with the derived neutral grounded.

Switching circuitry to provide separate triggering for each polarity is shown in Fig. 15, in case this is desired for a particular application. However, this circuit is observed to not function properly in the separate-humps mode. The malfunction is probably due to confusion of the power-factor-angle sensor when the off SCR is not triggered between the humps. If so, supplying a signal to "hold on" the angle sensor during the time of the gate trigger should correct the problem. It should be mentioned that optically coupled SCR's--not triacs--should be used for SCR triggering, since triacs, in response to a line transient, might "turn on" the gate of the off SCR without gating the on SCR and this might exceed the reverse gate breakdown voltage of the main SCR and destroy the coupler and/or the main SCR.

CALCULATION OF POWER FACTOR REDUCTION FOR A MIXED LOAD

A loaded 240-volt motor was observed to draw 2700 watts and 8.7 amps. This is a volt-amp draw of 3616.5 VA, which implies a power factor of $2700/3616.5 = 0.75$. The same motor, at idle, drew 315 watts and 5.65 amps. This is a volt-amp demand of 2348.6 VA, which implies a power factor of 0.13. Forming the phasor sum of the currents from both motors shows that the power factor of the combined load would be 0.54.

The same motor, with a PFC, was observed to draw 2700 watts and 8.8 amps when loaded. This is a volt-amp draw of 3658, which implies a power factor of 0.74. The same motor with the PFC was observed to draw 70 watts and only 1.48 amps at idle. This is a volt-amp draw of 615 VA, which implies a power factor of 0.11. This is essentially the same power factor as without the PFC, but yet the reactive current was greatly reduced. The apparent paradox is resolved by calculating the power factor for the combined load with the PFC's. Due to the nonsinusoidal current waveform, the currents were added point by point as shown in Fig. 16. The rms value of the combined currents is 9.7 amps, which implies a volt-amp draw of 4032 VA and a power factor of 0.69--a marked improvement from the 0.54 without the PFC's. The reason that the PFC does not appear to significantly improve the power factor of a single motor, is merely because the PFC reduces the real power in addition to reducing the reactive power. However, the calculation based on Fig. 16, demonstrates that for actual plant conditions the power factor is reduced. It is significant to note that the power factor of a plant would need little power factor correction if some motors were not idling or partly loaded at the time the power factor is measured. This is pointed out by Mr. Nola in the rebuttal published with Ref. 5.

Fig. 14. Optical Triggering Circuit. Three units are required.

Parts with * are part of Nola design.

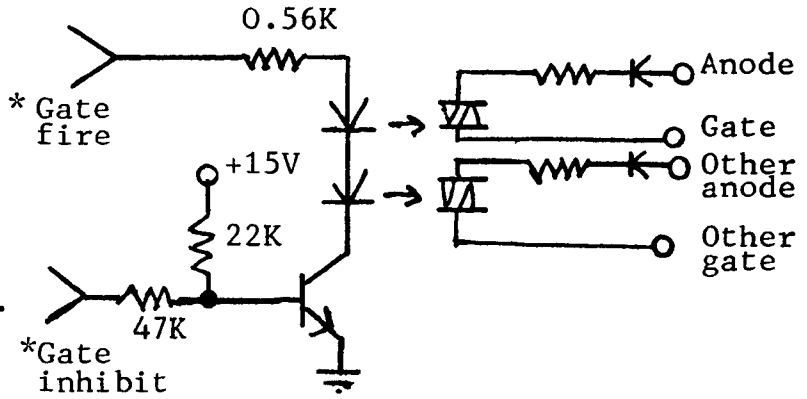
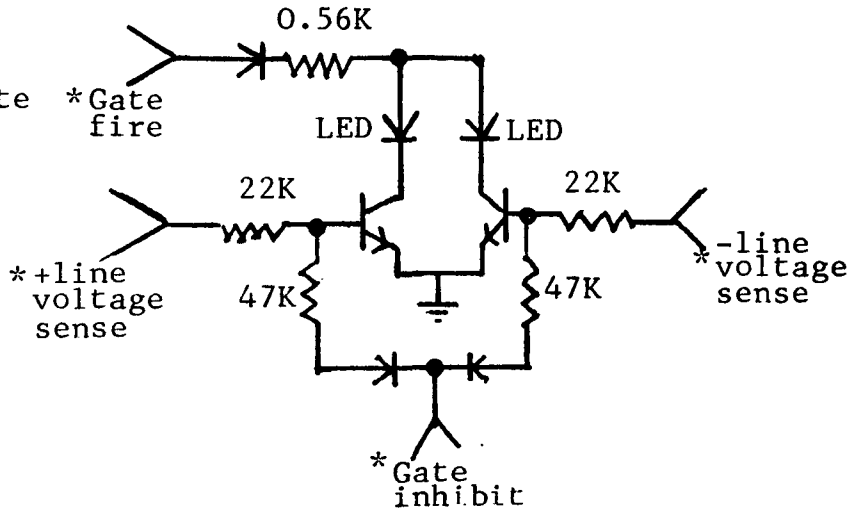


Fig. 15. Alternate Polarity Trigger Circuit. See text.



Outputs of couplers are same as Fig. 14.

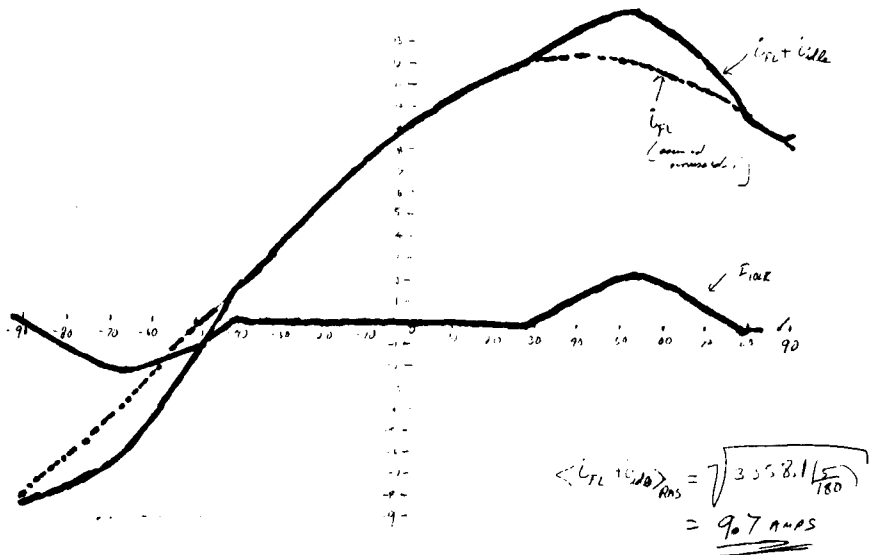


Fig. 16.

GRADUAL ADDITION OF MOTOR CURRENTS AND CALCULATION OF RMS OF THE SUM. SAMPLES EVERY 5° ARE USED TO COMPUTE RMS VALUE.

AREAS FOR FUTURE WORK

The most obvious area for future work is determination of the splitting factor for a disturbance in the time of switching from three lines to two lines. Since the disturbance seems to imply a nonsymmetric shift of the currents, three current probes with a storage scope would constitute a useful means to check the observed disturbance for nonsymmetry and aid further understanding of the phenomenon. Additional observation of the SCR-diode system, perhaps with a specially-constructed low inertia motor, might resolve the question of its stability. A separate-polarity triggering system--probably best implemented with optical coupling--is expected to simplify modification of the system to accept a remote control signal. Investigation of the region where only one line is switched on at a time should also benefit this application. This operating region cannot and need not, occur in the Nola design, but it might occur in a version modified to accept remote control. Contrary to some opinion, current does flow in this region--through the snubber circuits--and this is significant because it might induce violent misfiring, just before the intended turnon of the motor.

CONCLUSIONS AND RECOMMENDATIONS

The Nola design meets the design constraints imposed by the open loop instability mechanism modeled in this report. The empirically determined parameters are optimally set between the limits demonstrated in this report. Equations 4 and 5 might be used to shift the 50- and 200-Hz poles somewhat and maintain a suitable slope and curvature, but this is not needed for any reason considered in this study, and it might adversely affect the good servo loop response that the system was experimentally observed to exhibit. Consequently, it is recommended that the parameters not be changed. Finally, it is strongly recommended that the splitting factor be investigated--not only because it is an interesting academic problem--but also because the open loop instability phenomenon is basic to any SCR's/triac motor controller, with no neutral.

REFERENCES

1. Lipo, T.A., "The Analysis of Induction Motors With Voltage Control by Symmetrically Triggered Thyristors," IEEE Transactions on Power Apparatus and Systems, Vol. PAS-90, No. 2, 1971.
2. Toms, J.W., "Applying Solid State Energy Saver Starters," IEEE 1982 Annual Textile Industry Technical Conference, IEEE Catalog No. 82-CH1777-2, May 1982.
3. Nola, F.J., personal communication.
4. Rowan, T.M. and Lipo, T.A., "A Quantitative Analysis of Motor Performance Improvement by SCR Voltage Control," to be published.
5. Posma, B., "A Sober Look at Power Factor Controllers and Energy Savers," Power Conversion International, to be published Fall 1982.
(See also the rebuttal paper by F. J. Nola in the same issue.)

1982

NASA/ASEE SUMMER FACULTY RESEARCH FELLOWSHIP PROGRAM

MARSHALL SPACE FLIGHT CENTER
THE UNIVERSITY OF ALABAMA

A SCHEDULING ALGORITHM FOR
SPACELAB TELESCOPE OBSERVATIONS

Prepared By: Bob Grone

Academic Rank: Associate Professor

University and Department: Auburn University
Department of Mathematics

NASA/MSFC:
(Laboratory) Systems Analysis & Integration Lab.
(Division) Mission Analysis
(Branch) Mission Integration

MSFC Counterpart: William Askew

Date: August 1, 1982

Contract No.: NGT-01-002-009
(University of Alabama)

A SCHEDULING ALGORITHM FOR SPACELAB

TELESCOPE OBSERVATIONS

by

Bob Grone, Ph. D.
Associate Professor of Mathematics
Auburn University
Alabama 36849

ABSTRACT

An algorithm is developed for sequencing and scheduling of observations of stellar targets by equipment on Spacelab. The method is a general one, but is motivated by the example of a mission organized by the Office of Space Science denoted by OSS-3. This particular mission, along with interactions with NASA personnel in charge of planning the mission has been the basic model for which this method was developed.

In this paper we define and examine the scheduling problem, exhibit and document the method developed for its solution, and make suggestions for further development and implementation of this method.

TABLE OF CONTENTS

- I. Introduction
- II. Files
- III. Functions
- IV. Subroutines
- V. Main Algorithm
- VI. Outputs
- VII. Conclusions and Recommendations

I.

INTRODUCTION

The Spacelab OSS-3 mission includes among other experiments a telescope platform having three telescopes. These are referred to as HUT (Hopkins Ultraviolet Telescope), WUPPE (Winconsin Ultraviolet Spectropolarimeter), and UIT (Ultraviolet Imaging Telescope). The telescopes are not independent, but are aimed along a common axis. Targets are specified for each telescope by a scientist in charge referred to a principal investigator. These targets fall into two categories, faint or bright, depending on their magnitude. Furthermore, each target has a viewing requirement consisting of the number of observances requested and the length of an observance. The distribution of the targets is as follows:

UIT faint	-	48
UIT bright	-	0
HUT faint	-	13
HUT bright	-	35
WUPPE faint	-	45
WUPPE bright	-	37

Since none of the targets involve the Earth or Moon, each target may be considered as being in a fixed location. It is expected that all telescopes will function continuously, and so two of the telescopes will be co-observing a target of the third at any given time.

Each target has certain constraints on the times at which it may be viewed. The first type of constraint is geometric, and requires that the target not be occulted by Earth or Moon. Fainter targets may only be viewed while the Earth is occulting the Sun, and may additionally require they be viewed only if they are at least some fixed angular distance from the Earth and/or Moon. When the Orbiter is over a location in the South Atlantic region characterized by high radiation referred to as the South Atlantic Anomaly (SAA), no viewing is to be scheduled. Hence, each target has certain periods at which it can be viewed during the mission, referred to as observation opportunities. The mission is to last 5 days and encompass 72 orbital periods of 90 minutes each. Each orbital period has 36 minutes of shadow and 54 minutes of Sun, which places a premium on the shadow times of the mission.

Basically the problem is to schedule the observations while obeying the constraints and maximizing viewing time. To do this, one wants to minimize the time spent slewing between targets. If we ignore the constraints this would be a single-machine sequencing problem with sequence-dependent setup times, more commonly referred to as the travelling salesman problem.

In the present situation there are some fundamental differences. In the travelling salesman problem one wants to visit a sequence of n clients in n cities in such a way that minimizes the total distance travelled. In the present situation the analogous problem would also have certain hours at which the clients were available and requirements about how many meetings of what length were required by each client. Another basic difference is that we are trying to maximize clients seen in a fixed time rather than minimize the time (or distance) it takes to see all of the clients. Some aspects of a good schedule are not well-defined and involve facts such as; that some clients may have flexible requirements, some clients may be more important than others, and that a balance should be maintained between three types of clients (HUT, UIT, and WUPPE). In this paper we construct a dispatching-type method to be implemented on a VAX computer for this scheduling problem.

The need for such a schedule is two-fold. A method which in a few minutes constructs a near-optimal or very good schedule would clearly save a lot of man-hours and wages. If there is no particular rush in obtaining a schedule, then a machine-produced schedule could be hand-edited to conform to some of the more nebulous criteria applied to such schedules. In the event that the launch of a mission is delayed or there is a malfunction in orbit, this hand-edited schedule becomes so much wishful thinking, and there is an immediate need for a new schedule. For example, if one of the telescopes were to become inoperable after a few hours, a new schedule would be required which only involved targets corresponding to the other two telescopes. It is clear that time is of the essence in such a situation, and that a computerized method is required.

This paper describes an algorithm to accomplish this task. In the section entitled Files, we describe the format of the data which is fed to the program to produce a schedule. In Functions we define certain quantities obtainable from the file which are involved in the algorithm. In Subroutines we identify some components of the algorithm. In the Main Algorithm section we discuss the principal subroutine as well as the overall method. In the Outputs section we describe the desired format in which the results are to be displayed.

To implement this program we must organize the information corresponding to the set of targets we wish to consider into a form which is compatible with the algorithm. In our general discussion we will let $\{1, \dots, n\}$ index the set of targets we wish to (try to) schedule. For OSS-3 there were 178 such targets and the indexing scheme actually used was slightly different:

Type of experiment	Number of targets	indices
UIT (faint)	48	101-148
HUT (faint)	13	201-213
HUT (bright)	35	301-335
WUPPE (faint)	45	401-445
WUPPE (bright)	37	501-537

With this indexing format, it is easy to keep track of experiment groups of up to 99 targets each. For most of the rest of this paper we will use the $\{1, \dots, n\}$ approach for notational simplicity.

For each $i=1, \dots, n$, the Observation Requirement File lists the quantities r_i and s_i , where

r_i = the number of observances of target i requested

and

s_i = the time (in minutes) required to complete a single observance of target i .

These quantities are provided by the principal investigators. The quantity s_i is taken to be the minimum time necessary to obtain significant information from observing target i . This quantity is largely a function of the magnitude of target i and the sensitivity of the instrument involved.

For each $i = 1, \dots, n$, the Priority File contains an entry p_i which corresponds to the importance of target i . In the algorithm it is assumed that larger numbers denote more important targets so that priority = 2 denotes a more important target than priority = 1. If this were to be reversed the term p_i could be replaced everywhere in the algorithm by $1/p_i$. These priority numbers are decided upon initially by the principal investigators. The following hypothetical situation suggests a question concerning priority values. Suppose a principal investigator groups his targets into four categories of increasing importance. Which of the following assignments of priority values would work best in the algorithm?

1, 2, 3, 4

1, 2, 4, 8

1, 10, 100, 1000

It is hoped that experimentation will suggest an answer to this question. The priority file could also be of use to the scheduling engineer using the algorithm. If a certain target or type of target failed to schedule, then increasing the priority value would cause the algorithm to "try harder" to schedule the target(s).

The Time Periods File consists of an increasing sequence of times:

$$T_0 < T_1 < T_2 < \dots < T_m.$$

The time T_0 corresponds to the time in the mission when the telescope viewing commences, and T_m corresponds to the time when viewing ends. The intermediate times are obtained in one of two ways; consisting of all the ON times in the Shadow File and OFF times in the SAA File. In actuality, there is no Time Periods File since the program has been written to read the relevant information off of the existing Shadow and SAA files. The user must specify T_0 and T_m , however, since we are only interested in the times in these two files which fall between T_0 and T_m . By a time period we mean $[T_{\ell-1}, T_{\ell}]$, $\ell=1, \dots, m$. Hence each time period begins at the start of a shadow portion of an orbit or at the end of a SAA portion of an orbit. Due to the nature of the program it will also be necessary to insert a time into the Time Periods File corresponding to the end of any time interval where viewing is prohibited. This allows the program to "start over" when viewing is again permissible.

The Observation Opportunity File lists the times during which targets may be viewed. The actual format is somewhat different in actuality, but for purposes of simplicity in this discussion we will assume that for each (target) $i=1, \dots, 178$ we have a sequence

$$T_0 \leq t_{1i} < t_{2i} < t_{3i} < \dots < t_{2n_i-1i} < t_{2n_i i} \leq T_m$$

where

$$[t_{1i}, t_{2i}], [t_{3i}, t_{4i}], \dots, [t_{2n_i-1i}, t_{2n_i i}]$$

are the n_i time intervals during which target i may be observed. This file is computed using other programs available at the MSFC, and takes into consideration geometric availability (whether the target is occulted by the Earth or Moon) and other constraints involving the magnitude of the target, sensitivity of the instrument, and amount of direct or reflected sunlight present. The times

$$t_{1i}, t_{3i}, t_{5i}, \dots, t_{2n_i-1i}$$

are referred to as access times (acc-times) for target i, and the times

$$t_{2i}, t_{4i}, t_{6i}, \dots, t_{2n_i}$$

are referred to as loss times for target i.

The Weight File is a list of 54 4-tuples, $(\alpha, \beta, \delta, \gamma,)$ where the values of the entries are:

$$\alpha = 0, .5, 1$$

$$\beta = 0, 5, 10$$

$$\delta = .01, .1$$

$$\gamma = 0, 1, 10$$

These are listed in lexicographic order from $(0, 0, .01, 0)$ to $(1, 10, .1, 10)$ in the Weight File as the rows of a 54-by-4 matrix. Each weight produces a schedule for any given time period which gives the program 54 trial schedules to choose from for any time period.

The Slew Time File is regarded as a 178-by-178 matrix

$$D = [d_{ij}]$$

where d_{ij} is the time required to slew from target i to target j. If the slew rate is a constant, then d_{ij} directly proportional to the angular distance between targets i and j, which is available on another file. In our initial program we are assuming a slew rate of .4 degrees/sec., so if a_{ij} is the angular distance (in degrees) between targets i and j, then

$$d_{ij} = \frac{a_{ij}}{1440} \quad (\text{in decimal hours}).$$

Since D is a symmetric matrix with zero diagonal, the actual file only lists d_{ij} for $i < j$. In this paper we will refer to d_{ij} without restricting ourselves to $i < j$.

The algorithm requires computation of certain quantities in the process of selecting a next target at any time t . In this section we describe the following five functions related in this idea: Local Availability, Total Availability, Initial Selector, Successive Selector, and Reselecter. In addition we define an Objective function which evaluates a schedule over a time period.

The Local Availability function is denoted by $A(t,i)$, and is computed in the following manner:

1. If $t \leq t_{2n_i}$, then $A(t,i)=0$
2. If $t < t_{1i}$, then $A(t,i)=0$
3. If $t_{si} \leq t < t_{s+1i}$, s even, then $A(t,i)=0$
4. If $t_{si} \leq t < t_{s+1i}$, s odd, then

$$A(t,i) = t_{s+1i} - t.$$

This function is 0 unless that t is a time at which target i can be observed. If t is a time at which target i can be observed, then $A(t,i)$ is the amount of time target i can be observed before the observation opportunity ends.

The Total Availability function is denoted by $B(t,i)$ and is the amount of time left in the mission at time t that target i may be observed. It can be computed as follows.

1. If $t \leq t_{2n_i}$, then $B(t,i)=0$.
2. If $t < t_{1i}$, then

$$B(t,i) = \sum_{l=1}^{n_i} t_{2li} - t_{2li-1i}.$$
3. If $t_{si} \leq t < t_{s+1i}$, then

$$B(t,i) = A(t,i) + \sum_{l=\lceil \frac{s+3}{2} \rceil}^{n_i} t_{2li} - t_{2l-1i}.$$

In step 3, the symbol $\lceil \]$ refers to the greatest integer or step function defined by

$$\lceil x \rceil = \text{the largest integer } n \text{ satisfying } n \leq x.$$

In step 3 the computation of $B(t,i)$ involves the quantity $A(t,i)$. This presents no practical difficulty since the algorithm only requires the computation of $B(t,i)$ after $A(t,i)$ has been computed and found to be positive. Hence it is unnecessary to activate the subroutine for $A(t,i)$ in step 3 since it has already been computed.

In fact, it seems natural to compute $A(t,i)$ and $B(t,i)$ in a single sequence of steps in order to simplify the programming.

The Initial Selector function is used to choose a target to be the first viewed in a time period. It is denoted by $F(t,i)$, and calculated as follows:

1. If $r_i=0$, then $F(t,i)=0$
2. Compute $A(t,i)$
3. If $A(t,i) < \delta_i$, then $F(t,i)=0$
4. If $A(t,i) \geq \delta_i$, then

$$F(t,i) = \frac{\rho_i[\alpha + A(t,i)] [\gamma + \delta_i r_i]}{\beta + B(t,i)}.$$

In other words, $A(t,i)=0$ unless there is sufficient local availability at time t to conduct at least one observance of target i . In this case, $F(t,i)$ is given by the formula in step 4.

The Successive Selector function is used to select a next target (j) to follow target i which has been scheduled up until time t . It is denoted by $G(t,i,j)$ and calculated as follows.

1. If $r_j=0$, $G(t,i,j)=0$.
2. Evaluate $A(t+d_{ij},j)$.
3. If $A(t+d_{ij},j) < \delta_j$, then $G(t,i,j)=0$.
4. Evaluate $B(t+d_{ij},j)$.
5. $G(t,i,j) = \frac{\rho_i[\alpha + A(t+d_{ij},j)] \cdot [\gamma + \delta_i r_i]}{[\beta + B(t+d_{ij},j)] \cdot [\delta + d_{ij}]}$.

Step 1 sets $G(t,i,j)=0$ if we have already satisfied the requirement of target j .

Step 3 sets $G(t,i,j)=0$ if there is not sufficient local availability to conduct at least one observance of target j at time $t+d_{ij}$, which is the first time at which viewing of target j can be initiated after viewing target i until time t . If steps 1 and 3 do not establish the value of $G(t,i,j)$, then it is defined by the formula in step 5.

The Reselecter function is denoted by $H(t,i,j,k)$ and is used when target j has been selected to follow target i which finished viewing at time t . In the algorithm, we check to see if target k might be a better choice to follow target i than target j . This could happen if k is not available at time $t+d_{ik}$ but is available at time $t+d_{ij}$.

In such a situation the schedule might be improved by the insertion of idle time. The function is calculated as follows.

1. If $r_k=0$, then $H(t,i,j,k)=0$.
2. Evaluate $A(t+d_{ij},k)$.
3. If $A(t+d_{ij},k) < s_k$, then $H(t,i,j,k)=0$.
4. Evaluate $B(t+d_{ij},k)$.
5.
$$H(t,i,j,k) = \frac{p_k [\alpha + A(t+d_{ij},k)] [\gamma + s_k^n]}{[\beta + B(t+d_{ij},k)] [\delta + d_{ij}]}$$

The careful reader may note the similarities between the functions F, G, and H. In fact, both F and G can be computed by the same subroutine used to calculate H. The relations are as follows.

$$F(t,i) = H(t,i,i,i)$$

$$G(t,i,j) = H(t,i,j,j).$$

For programming purposes the above substitutions would reduce program length and number of subroutines. For purposes of explaining the algorithm we will stick with the various selectors F, G, and H, rather than having a single function (H).

The previous five functions form the basis of the scheduling routine which establishes a schedule for a time period $[T_{k-1}, T_k]$. Since the weight $(\alpha, \beta, \delta, \gamma)$ appears in these functions, we obtain one schedule for $[T_{k-1}, T_k]$ for each of the 54 weights in the weight file. Suppose we denote the schedule obtained from a particular weight by $S(\alpha, \beta, \delta, \gamma)$ and let us further assume that the schedule is presented as follows.

$$\begin{aligned} &(i_1, t'_0, t_1) \\ &(i_2, t'_1, t_2) \\ &(i_3, t'_2, t_3) = S(\alpha, \beta, \delta, \gamma). \\ &\quad \vdots \\ &\quad \vdots \\ &(i_s, t'_{s-1}, t_s) \end{aligned}$$

Here it is assumed target i_1 is scheduled from time t'_0 to time t_1 , target i_2 is scheduled from time t'_1 to time t_2 , etc.. We define an Objective function as follows.

$$O(S) = O(\alpha, \beta, \delta, \gamma) \sum_{\ell=1}^S p_{i_\ell} (t_\ell - t_{\ell-1}').$$

In the algorithm we will choose a schedule $S=S(\alpha,\beta,\delta,\gamma)$ for the time period which corresponds to a maximal value of $O(\alpha,\beta,\delta,\gamma)$. The value of $O(\alpha,\beta,\delta,\gamma)$ (sometimes referred to as the "grade" of $S(\alpha,\beta,\delta,\gamma)$) is simply priority-weighted viewing time, or simply viewing time if $p_i=1$, all $i=1,\dots,178$.

In this section we identify and describe certain portions of the main algorithm. There are several reasons for doing this. For one, it is easier to understand the main algorithm in a modular fashion than all at once. For another, it is convenient to have the main algorithm broken into subroutines for reprogramming purposes. For example, an improvement could be made by rewriting one of the subroutines rather than rewriting the whole program. Also, subroutines can be tested and debugged individually if problems occur.

The first subroutine is referred to as the Initial Selection Algorithm, or INSLA for short. The input to this subroutine is a time t_0 , and the output is (t_0, i_1) where target i_1 has been chosen as the "best" target to schedule at time t_0 , or the message STOP. The procedure is as follows.

1. Input t_0 .
2. Evaluate $F(t_0, i)$, all $i = 1, \dots, n$.
3. If $F(t_0, i) = 0$, all $i = 1, \dots, n$, then STOP.
4. Choose i_1 where $F(t_0, i_1) \geq F(t_0, i)$, all i .
5. Output (t_0, i_1)

In practice we would evaluate $F(t_0, i)$ for $i = 1, \dots, n$, with instructions to save i_{\max} and $F_{\max} = F(t_0, i_{\max})$. The only time the output is STOP is when there is no target to view at time t_0 that is available at time t_0 and has a requirement left.

The Experiment Scheduler Algorithm, or EXSA, has as its input (t_0, i_0, i_1) where target i_0 has been viewed until time t_0 and target i_1 is the next target to view. The EXSA schedules as many consecutive observances of target i_1 , as possible as soon as possible. The output is the message (t_1, i_1) which signifies that target i_1 has been scheduled (consecutively) until time t_1 . The algorithm is described as follows.

1. Input (t_0, i_0, i_1) .
2. Evaluate $A(t_0 + d_{i_0 i_1}, i_1)$.
3. If $A(t_0 + d_{i_0 i_1}, i_1) \geq s_{i_1}$, let $t'_0 = t_0 + d_{i_0 i_1}$.
4. If $A(t_0 + d_{i_0 i_1}, i_1) < s_{i_1}$, let $t'_0 =$ the first $t_{\ell i_1}$ where ℓ is odd and $t_0 + d_{i_0 i_1} < t_{\ell i_1}$.
5. If $t'_0 + s_{i_1} > T$, let $t_1 = t_0$.
6. If $t'_0 + s_{i_1} \leq T$, schedule one observance of target i_1 from t'_0 to $t'_0 + s_{i_1}$ and let $r_{i_1} = r_{i_1} - 1$.
7. If $r_{i_1} = 0$, let $t_1 = t'_0 + s_{i_1}$.
8. If $r_{i_1} > 0$, go back to 1, replacing t_0 with $t_1 = t'_0 + s_{i_1}$ and i_0 by i_1 . (i.e., replace (t_0, i_0, i_1) with (t_1, i_1, i_1)).

The Selector Algorithm, or SELAG, is used to select a next experiment in the middle of a time period. The input to this subroutine is (t_1, i_1) , which represents the fact that target i_1

has been viewed until time t_1 and a new target is to be chosen. The output is either (t_1, i_1, i_2) , which signifies that i_2 has been chosen to be scheduled next, or STOP. The STOP output can occur in the following way. If there is no experiment i_2 which is possible to schedule at time $t_1 + d_{i_1 i_2}$, then STOP occurs. This would happen in a SAA time interval, for example. The Selector Algorithm is composed of two iterations: one each corresponding to the successive selector and reselector functions. It is possible to view the SELAG subroutine as two subroutines, but in this account we will describe the process as one subroutine. The description is as follows.

1. Input (t_1, i_1) .
2. Evaluate $G(t_1, i_1, i)$, all $i \neq i_1$.
3. If $G(t_1, i_1, i) = 0$, all $i \neq i_1$, then STOP.
4. If $G(t_1, i_1, i)$ is not identically zero, then select i_2 which maximizes $G(t_1, i_1, i)$.
5. Evaluate $H(t_1, i_1, i_2, i)$, all $i \neq i_1$.
6. Select i_2 which maximizes $H(t_1, i_1, i_2, i)$, and output (t_1, i_1, i_2) .

Steps 1-4 make an initial selection for a next target and steps 5-6 examine whether a different target might be a better choice if idle time is inserted. If $i_2 = i_1$ (i.e., there is no better choice), then this corresponds to the situation $t'_0 = t_0 + d_{i_0 i_1}$ in EXSA. If $i_2 \neq i_1$ and idle time is inserted, this corresponds to the definition of t'_0 in step 4 of EXSA.

The Descheduler Algorithm, or DESAG is used to fit partial scheduler together and requires some explanation of the main algorithm, which can be obtained in the next section. Briefly, suppose that a partial schedule, say S_k , has been obtained over the first k time periods, (T_0, T_k) . The algorithm next produces a partial schedule for the $(k+1)$ st time period, (T_k, T_{k+1}) . Call this partial schedule S_{k+1} . The Descheduler is designed to combine these two partial schedules into a schedule for (T_0, T_{k+1}) which we will refer to as S_{k+1} . Suppose that the last target in S_k is i_0 which finishes viewing at time $t_0 \leq T_k$, and the first target in S_{k+1} is i_1 , which begins viewing at time T_k . If

$$T_k - t_0 \geq d_{i_0 i_1},$$

then there is sufficient time to slew the telescope from target i_0 to target i_1 , and we combine the two schedules. If

$$T_k - t_0 < d_{i_0 i_1},$$

then the Descheduler deletes the last observance of i_0 until sufficient slew time is available. When DESAG deletes an observance of i_0 it is necessary to let

$$r_{i_0} = r_{i_0} + 1.$$

The input to DESAG is S_k, S_{k+1} , and the output is S_{k+1} .

In this section we define the principal subroutine as well as the main algorithm.

The principal subroutine is the Scheduler Algorithm, or SCHALG, and is designed to produce a schedule, for a time period (T_{k-1}, T_k) . If we let (t_0, T) play the role of (T_{k-1}, T_k) , then SCHALG is described as follows.

1. Input $(t_0, T), (\alpha, \beta, \delta, \gamma)$.
2. Send t_0 to INSLA, T to EXSA.
3. If INSLA yields STOP, then $S = \emptyset$.
4. If INSLA yields (t_0, i_1) , then send (t_0, i_1, i_1) to EXSA and obtain (t_1, i_1) .
5. Send (t_1, i_1) to SELAG and obtain (t_1, i_1, i_2) or STOP.
6. Send (t_1, i_1, i_2) to EXSA and obtain (t_2, i_2) .
7. If $t_2 = t_1$, then STOP.
8. If $t_2 > t_1$, go back to 5, letting (t_2, i_2) play the role of (t_1, i_1) .

Some comments about step 7 are in order. This step is used when target i_1 has been viewed until t_1, i_2 is chosen next by SELAG, and EXSA finds it impossible to schedule i_2 within the current time period. A moments reflection yields that this may occur only when the local availability for i_2 extends past the end of the current time period. This cannot occur if the observation opportunities are all contained within a time period, as was indicated would be the case by the NASA planning personnel assigned to this project. Hence, if everything is in order step 7 will not be used. If the Observation Opportunity Files do not obey this constraint with respect to the Time Periods File, then step 7 will prevent the program from falling into a loop where it repeatedly chooses target i_2 and then is unable to schedule an observation of it. If no such difficulties occur, then the SCHALG will exit on step 5.

The Main Algorithm, or MAINALG, produces a schedule for the time interval (T_0, T_m) . The method is to generate 54 schedules for the first time period, (T_0, T_1) , then pick the best one using the objective function and proceed to the next time period (T_1, T_2) . The DESAG then fits these two schedules together to form a schedule for (T_0, T_2) . Proceeding in a similar fashion, we obtain a schedule for (T_0, T_m) . Before we proceed, we explain the following notation concerning partial schedules.

S_ℓ or $S_\ell(\alpha, \beta, \delta, \gamma)$ denotes a schedule for $(T_{\ell-1}, T_\ell)$,

S_ℓ denotes a schedule for (T_0, T_ℓ) ,

$S = S_m$ is the schedule for (T_0, T_m) .

The MAINALG is described as follows.

1. Let the time period (t_0, T) be $(T_{\ell-1}, T_\ell)$, $\ell = 1$.
2. Let the weight $(\alpha, \beta, \delta, \gamma)$ be $(\omega_{i1}, \omega_{i2}, \omega_{i3}, \omega_{i4})$, $\omega_{i4} = 1$.
3. Send (t_0, T) and $(\alpha, \beta, \delta, \gamma)$ to SCHALG and obtain a schedule $S_\ell(\alpha, \beta, \delta, \gamma)$.

4. Evaluate $O(S_\ell(\alpha, \beta, \delta, \gamma))$ over (t_0, T) .
5. Go back to 2 and increase i by 1 until $i = 54$.
6. Choose S_ℓ from among the 54 trial schedules for (t_0, T) which maximizes $O(S_\ell(\alpha, \beta, \delta, \gamma))$.
7. Use the DESAG to adjoin S_ℓ to $S_{\ell-1}$ to form S_ℓ .
8. Go back to step 1 and increase ℓ until $\ell = m$.

A comment on observation requirements is in order. Since we are examining 54 trial schedules for each time period but only using the best one it is important to not write the program in such a way that it thinks all 54 schedules were performed. In other words, the requirement r_i should be decremented during each of the 54 trial schedules but revert to what it was at the start of the time period when the next trial schedule is to be computed. Then, of course, when the best schedule for the time period is obtained and adjoined to the previous partial schedule by DESAG, then the r_i s are diminished accordingly.

The algorithm described results in a scheduling sequence, say S , which has been constructed from the subschedules for the m time periods. This needs to be presented in some fashion. One method of presenting S would be as follows.

$$\begin{aligned} &(i_1, t_0', t_1) \\ &(i_2, t_1', t_2) \\ &(i_3, t_2', t_3) \\ &\vdots \\ &\vdots \\ &(i_u, t_{u-1}', t_u) \end{aligned}$$

In this scheme target i_1 is scheduled between times t_0' and t_1' , target i_2 is scheduled between times t_1' and t_2' , etcetera. The algorithm produces a schedule which automatically satisfies the two important constraints:

and $(t_{\ell-1}', t_{\ell}') is contained in an i_{ℓ} -window for all $\ell = 1, \dots, u$.$

$$t_{\ell-1}' - t_{\ell-1} \geq d_{i_{\ell-1}i_{\ell}} \text{ all } \ell = 2, \dots, u.$$

It might also be useful to indicate the number of observances as well as the viewing time.

To evaluate the schedule we need to have an objective function to give a grade to the schedule. We define this as follows:

$$\text{Grade} = G(S) = \sum_{\ell=1}^u P_{i_{\ell}} (t_{\ell}' - t_{\ell-1}').$$

This grade is simply priority-weighted viewing time.

We also wish to have the viewing times displayed. For each $i = 1, \dots, n$, we define

$$V(i) = \sum_{i=i_{\ell}} t_{\ell}' - t_{\ell-1}'.$$

These quantities we would not wish to display, but it would be advantageous to be able to call them up if desired. The following six quantities should be displayed along with the schedule.

$$V(100) = \sum_{i=101}^{148} V(i),$$

$$V(200) = \sum_{i=201}^{213} V(i),$$

$$V(300) = \sum_{i=301}^{335} V(i),$$

$$V(400) = \sum_{i=401}^{445} V(i),$$

$$V(500) = \sum_{i=501}^{537} V(i),$$

$$V = V(100) + V(200) + V(300) + V(400) + V(500).$$

Note here that we are referring to the alternate numbering scheme and not to $i = 1, \dots, 178$.

Another desired output is the weight sequence which produced each of the m best subschedules for the time periods. This will show the user which weights were more effective in generating schedules, and will lead to beneficial changes in the weight file. Eventually the number of entries in the weight file should be much less than 54. If a weight is never used it would be dropped from the weight file, where one which appeared many times would be bracketed closely by other weights. Finally, an effective weight file will result. This output could be presented as an m -by-4 or 4-by- m matrix. It is worth pointing out that the overall schedule S is not a function of one particular weight as the subschedule for a time period is. Rather, the overall schedule is a function of the whole weight file rather than one particular weight. As a preliminary guess it seems plausible that each of the parameters $\alpha, \beta, \delta, \gamma$ could have two specified values. This would have the effect of cutting the running time of the program by two-thirds by reducing the number of trial schedules from 54 to 16.

In this section we discuss possible pitfalls in the program as well as suggestions for beneficial modifications. It was hoped that these matters may have been investigated after the algorithm was functioning on the VAX computer. This, however, proved to be impossible to achieve within a ten week period. A programmer has been working on putting the algorithm in the computer, but it was not functioning at the time this report was written. The single attempt to run the program to date was less than auspicious. The machine ran for nearly two hours without scheduling one target observance and then stopped due to programming difficulties. An examination of some of the quantities involved revealed, for example, that $A(t, i)$ and $B(t, i)$ were computed to be the same quantity, which was erroneous. Initially it was planned that the method could be tested, then improved for two to three weeks. Hopefully the following comments may be of assistance to anyone attempting to use the methodology presented in this report, or any part thereof.

One possible source of difficulty lies in the SELAG. In step 3 of SELAG, the algorithm stops if there is no target available at the current time. The MAINALG then proceeds to the start of the next time period. Hence, if there was a "blank spot" in the middle of a time period where no target was available, the whole remaining portion of the time period would remain unscheduled. This would become more likely towards the end of the mission when more of the targets have their requirements satisfied. There are various ways around this problem if difficulty occurs in practice. For one thing, if there are many more targets listed than can possibly be observed, then this problem is unlikely to occur since the SELAG can always find a suitable target. Another method would be to include in the files a bogus target labelled "wait" which would be scheduled for one minute if nothing else was available. The "wait" target would of course have to have variable slew times for effective implementation. The comments about step 3 of SELAG apply equally well to step 3 of INSLA.

The DESAG might also cause difficulties. It is conceivable that the DESAG could unschedule a very long observation, thereby ruining the schedule for the previous time period. This would be as a result of the algorithm insisting on starting the initial observance in a time period exactly at the start of the period rather than adding any necessary slew time. This feature was included at the suggestion of the project engineers who indicated it was preferable to do all possible slewing during the Sun portions of the orbits, thereby saving the valuable Shade portions for viewing. There are ways around this problem if the difficulty occur in actual use. For one, the DESAG could be eliminated. Another approach would be for a secondary program that could be used after this program that would fill in any gaps. For example,

any gaps could be fed to SCHALG after the program had been run. A minor modification might be inserted specifying where the telescope was going to end up at the termination of a gap. Such a "scheduling over" method could be applied to the problem previously discussed regarding SELAG and INSLA.

A feature which has been suggested is a variable requested-time capability. It has been remarked that when a principal investigator specifies a value of s_i , say for example 30 minutes, that what is actually desired is at least 30 minutes, but as much more as can be scheduled consecutively. If that turns out to be a common occurrence, it would be advantageous to have the capability of entering a value of 30+ rather than 30 for s_i .

Another area of investigation we will label as "grouping". The telescope mount has a capability of gimbaling some 17 degrees. It is preferable to use the gimbal mechanism whenever possible to re-aim the telescope since it slews much faster, and it is more efficient to utilize the telescope mount apparatus than to slew by maneuvering the entire Orbiter. To take advantage of this capability it would be first necessary to identify groups of experiments which are in the same portion of the sky (i.e., within 17 degrees of a central point), and all of which can be viewed during some specified time interval. These groups could be identified by the use of some auxiliary software which would examine the Observation Opportunity File and the Angular Distance File. Once these intervals and groups are identified they can be fed as time periods to SCHALG. It would also be necessary to make an adjustment in the Slew Time File to compensate for the faster slew rate of the telescope mount. The identified groups would then be scheduled, using SCHALG, and then the remaining time periods could be scheduled.

1982

NASA/ASEE SUMMER FACULTY RESEARCH FELLOWSHIP PROGRAM

MARSHALL SPACE FLIGHT CENTER
THE UNIVERSITY OF ALABAMA

SHAPE CONTROL OF LARGE SPACE STRUCTURES

Prepared by:	Martin T. Hagan, Ph.D.
Academic Rank:	Assistant Professor
University and Department:	University of Tulsa Electrical Engineering Department
NASA/MSFC: (Laboratory) (Division) (Branch)	Systems Dynamics Control Systems Servo
MSFC Counterpart:	L. Schutzenhofer
Date:	August 6, 1982
Contract No.:	NASA-NGT-01-002-099 (University of Alabama)

SHAPE CONTROL OF LARGE SPACE STRUCTURES

By

Martin T. Hagan, Ph.D.
Assistant Professor of Electrical Engineering
University of Tulsa
Tulsa, Oklahoma

ABSTRACT

The development of the Space Transportation System now makes feasible the erection of large structures in space. Some of these structures will combine large size with very rigorous surface figure error requirements. The most stringent requirements will be made by large optical systems and antennas operating at very high frequencies.

The shape control of these large structures is made difficult because of their flexibility and their distributed nature. Their vibrational modes are numerous, densely packed, and low frequency. In addition, the characteristics of these systems cannot be accurately predicted before flight. The control problem is further complicated by the need to design a controller which has low enough order so that it can be implemented on the onboard computer and yet of high enough order to accurately control the structure.

A survey has been conducted to determine the types of control strategies which have been proposed for controlling the vibrations in large space structures. From this survey several representative control strategies were singled out for detailed analyses. The application of these strategies to a simplified model of a large space structure has been simulated. These simulations demonstrate the implementation of the control algorithms and provide a basis for a preliminary comparison of their suitability for large space structure control.

SECTION 1

INTRODUCTION

The purpose of this project has been to examine procedures for controlling vibrations in large space structures (LSS). This effort has consisted of three major parts:

- A survey of the literature related to LSS control, and control theory in general, to identify candidate techniques for LSS control.
- An analysis of the candidate techniques in order to categorize them and to determine those which have the most promise for successful LSS control.
- Simulation studies of representative techniques from several relevant categories.

This report will present the results of this project. Section 2 outlines the LSS control problem and describes some relevant LSS models. Section 3 discusses the various categories of solution which have been proposed for LSS control. Sections 4 through 8 describe in detail five representative control techniques which have been suggested for use in LSS control and illustrate their application to a common test problem. Section 9 summarizes the results and suggests areas for future investigation.

The scope of this project and of this report has been purposely limited because of time considerations. The control of LSS is a large field, and this report does not attempt to cover it completely. In particular, this report is limited to vibration control and will not consider pointing problems. In addition, the report discusses only continuous time control algorithms and does not treat problems of digital control, sampling rates, etc. Finally, there is no discussion of the hardware implementation of any of the control algorithms in terms of specific actuators, sensors, etc.

SECTION 2

THE MODELS

2.1 The Distributed Parameter Model

The most complete model of a LSS would be a system of partial differential equations of the form

$$m(x)u_{tt}(x,t) + D_0 u_t(x,t) + A_0 u(x,t) = F(x,t) \quad (2.1)$$

where $u(x,t)$ represents the displacement of the structure from its equilibrium position, $F(x,t)$ is the force distribution, $m(x)$ is the mass distribution, D_0 is a differential operator representing the damping of the LSS, and A_0 is a differential operator representing the stiffness of the LSS.

2.2 The Finite Dimensional Model

There are some control procedures which attempt to deal directly with the infinite dimensional distributed parameter model (eg. [1],[2]). However most procedures, including all those discussed in this report, use a finite dimensional approximation of the form

$$M\ddot{q} + D\dot{q} + Kq = f \quad (2.2)$$

where q is an n -dimensional vector representing the displacements of the structure in some generalized coordinate system, f is a vector of generalized forces, M is a real symmetric positive definite mass matrix, K is a real symmetric positive semi-definite stiffness matrix, and D is the damping matrix. Because the damping of the LSS is expected to be very low (~ 0.005), the D matrix will be set to zero for the purposes of the following discussion. The finite dimensional model of (2.2) is normally developed by the finite element method using a computer program such as NASTRAN.

The forces are applied through m actuators in a manner described by

$$f = B_a u \quad (2.3)$$

where u is an m -dimensional vector of inputs to the actuators, and B_a is a matrix which specifies the effects of the actuators on the generalized displacements. There are also k sensors which measure displacements and velocities in a manner described by

$$y = C_d q + C_v \dot{q} \quad (2.4)$$

where y is a k -dimensional vector of measurements, C_d is a

matrix which specifies the position measurements, C_v is a matrix which specifies the velocity measurements.

2.3 The Modal Form

Because of the form of the M and K matrices there exists a unitary matrix U such that

$$U^T M U = I \quad \text{and} \quad U^T K U = W \quad (2.5)$$

where

$$W = \begin{bmatrix} w_1^2 & 0 & \cdots & 0 \\ 0 & w_2^2 & \cdots & 0 \\ \vdots & \vdots & \ddots & \vdots \\ 0 & 0 & \cdots & w_n^2 \end{bmatrix}$$

The values w_1, \dots, w_n are the natural frequencies of vibration of the structure and the columns of U are the corresponding mode shapes. It is now possible to represent the displacements of the structure in terms of the modal coordinates. The relationship between the generalized coordinates and the modal coordinates is given by

$$q = Uv \quad (2.6)$$

where v is an n-dimensional vector of modal coordinates. The model of the LSS can now be written in terms of the modal coordinates

$$\ddot{v} + Wv = U^T B_a u \quad (2.7)$$

$$y = C_d Uv + C_v U\dot{v} \quad (2.8)$$

2.4 The State Space Model

It will be convenient for later discussions to have the finite dimensional model of the LSS in state space form. One possible state space representation would be

$$\dot{x} = Ax + Bu \quad (2.9)$$

$$y = Cx \quad (2.10)$$

where

$$x = \begin{bmatrix} v \\ \dot{v} \end{bmatrix} \quad A = \begin{bmatrix} 0 & I \\ -W & 0 \end{bmatrix} \quad B = \begin{bmatrix} 0 \\ U^T B_a \end{bmatrix} \quad C = \begin{bmatrix} C_d U & C_v U \end{bmatrix} \quad (2.11)$$

2.5 The Reduced Order Model

The LSS model of (2.9) and (2.10) is normally of very high order and therefore it must be simplified in some way before applying any control procedures. The standard method of simplifying the LSS system is to subdivide x into three parts:

- x_p will designate the primary states. These consist of those modes of the system which are most critical to the performance of the LSS (eg. line of sight errors).
- x_s will designate the secondary states. These states consist of those modes which can be accurately modeled but which are not as critical to system performance as x_p . These states can be used in evaluating the control system design.
- x_r will designate the residual states. These states consist of those modes which cannot be accurately modeled.

$$x_p = \begin{bmatrix} v_p \\ \dot{v}_p \end{bmatrix} \quad x_s = \begin{bmatrix} v_s \\ \dot{v}_s \end{bmatrix} \quad x_r = \begin{bmatrix} v_r \\ \dot{v}_r \end{bmatrix}$$

The state space representation of (2.9) and (2.10) can now be written

$$\begin{bmatrix} \dot{x}_p \\ \dot{x}_s \\ \dot{x}_r \end{bmatrix} = \begin{bmatrix} A_p & 0 & 0 \\ 0 & A_s & 0 \\ 0 & 0 & A_r \end{bmatrix} \begin{bmatrix} x_p \\ x_s \\ x_r \end{bmatrix} + \begin{bmatrix} B_p \\ B_s \\ B_r \end{bmatrix} u \quad (2.12)$$

$$y = \begin{bmatrix} C_p & C_s & C_r \end{bmatrix} \begin{bmatrix} x_p \\ x_s \\ x_r \end{bmatrix} \quad (2.13)$$

where A_p , A_s and A_r are defined in a manner analogous to A in (2.11).^p (Appendix A gives an example of such a model for a simplified representation of a LSS.)

Once the model has been partitioned as in (2.12) and (2.13) the problem is simplified by ignoring all secondary and residual modes to obtain the reduced order equations

$$\dot{x}_p = A_p x_p + B_p u \quad (2.14)$$

$$y = C_p x_p \quad (2.15)$$

It is clear from (2.12) and (2.13) that this reduced order model has two potential sources of error. First, states other than x_p influence the output y , and yet the terms $C_s x_s$ and $C_r x_r$ have not been included in the observation equation (2.15). These terms have been called "observation spillover" [3]. Secondly, the input u affects not only the primary states x_p but also x_s and x_r . The terms $B_s u$ and $B_r u$ are called "control spillover". If control and observation spillover are ignored it is possible that a controller could be designed which is stable for the reduced order model of (2.14) and (2.15) but unstable for the model described in (2.12) and (2.13).

To summarize this section, we have divided the modes of the LSS into the following categories

- Primary modes - These are the modes which have the largest effect on system performance.
- Secondary modes - These modes are not specifically controlled but may be used in evaluating the control design.
- Residual modes - These modes are included in the finite element model, but their accuracy is suspect and they would not be included in the design process.
- Unmodeled modes - The distributed parameter system (2.1) is truly infinite dimensional. These are the modes which are not included in the finite element model.

SECTION 3

METHODS OF CONTROL

Now that the LSS control problem has been outlined and the models have been described, this section will provide a brief overview of the categories of control methodology which have been proposed for active LSS vibration control. Later sections of this report will examine several specific control procedures in some detail.

3.1 Direct Output Feedback

The simplest feedback control is direct output feedback (DOFB) which is characterized by the following control law:

$$u = Gy \tag{3.1}$$

where G is a constant matrix of feedback gains. With this control law in force the closed loop equations for the controlled states - ignoring spillover - would be

$$\dot{x}_p = \begin{bmatrix} A_p & - B_p G C_p \end{bmatrix} x_p \tag{3.2}$$

The various methods which use DOFB have the same on-board computational requirements since they use the same control law (3.1). They are distinguished by the criteria by which they choose G . Some methods ([4],[5]) choose G in order to obtain a desired level of damping in the controlled modes. These methods are by far the easiest methods to implement and are the most robust methods in terms of closed loop stability. Their main problem stems from the fact that they were designed to obtain relatively small amounts of damping (up to approximately .2). This may not be a practical limitation, however, because of the large power requirements which would be needed to obtain large amounts of damping with any method.

Other types of DOFB choose G in such a way as to place the poles of the closed loop system (3.2) in some desired locations. There are a number of procedures for pole placement ([6]-[8]). Their advantage over the damping augmentation methods would appear to be the increased flexibility in placing the closed loop poles. However, the number of poles which can be positioned is limited by the number of sensors and actuators which are used, and there is no guarantee that those poles which are not placed will remain stable. Furthermore, even if the reduced order model of (2.14) and (2.15) is stable there is no guarantee that the total closed loop system will be stable.

A third type of DOFB chooses G so as to minimize a performance index of the form

$$J = \int_0^{\infty} [x_p^T R_1 x_p + u^T R_2 u] dt \quad (3.3)$$

where R_1 is a symmetric positive semi-definite matrix, and R_2 is a symmetric positive definite matrix. Procedures of this type are described in [9] and [10], and a stochastic version is given in [11]. The main advantage of these optimal output feedback methods lies in the performance index (3.3). The weighting matrices R_1 and R_2 can be chosen by the designer, and this allows great flexibility in choosing the design criteria. Each mode can be weighted according to its relative effect on the performance of the LSS. The main disadvantage of optimal output feedback is the computational burden. Although, as with all DOFB methods, the on-board computation is minimal, the computational requirements for determining the optimal gains can be prohibitive for problems of the magnitude of most LSS systems.

3.2 Modern Modal Control

The methods of the previous subsection were characterized by the minimal on-board computational requirements of (3.1). This subsection will discuss methods which require more on-board computation but which hold the potential for increased flexibility in affecting LSS performance. These methods, instead of using direct output feedback, estimate the state of the system and use these estimates for feedback. For the reduced order model of (2.14) and (2.15) the estimator (filter/observer) would take the form

$$\dot{\hat{x}}_p = A_p \hat{x}_p + B_p u + K_f [y - C_p \hat{x}_p] \quad (3.4)$$

The control law would take the form

$$u = K_c \hat{x}_p \quad (3.5)$$

As with DOFB, the various modern modal control (MMC) design methods [3] are distinguished by the manner in which they determine the gains K_f and K_c . There are two basic methods. The first method calculates the gains so as to place closed loop system poles in some desired locations. In contrast with DOFB, in which there are constraints on the number of poles which can be placed, there is no theoretical limit on the number of poles of the reduced order system which can be placed using MMC (assuming that the system is controllable). In addition, the procedures for pole positioning using MMC are more straightforward and present a smaller computational burden than those for DOFB. Of course,

just because the poles of the reduced order model are stable this does not guarantee that the total distributed parameter system will be stable.

The second approach to MMC is to choose the gains in order to minimize a performance index in the form of (3.3). This optimal MMC is different from optimal DOFB in that the computational burden in calculating the gains is decreased considerably, although the on-board computation is increased. Both methods have the advantage of choosing the gains based on a performance index which is very flexible and can be used, for example, to mitigate the effects of modeling error. Optimal MMC will be discussed in detail in a later section.

3.3 Suppression of Spillover

In all of the methods discussed so far the controller has been designed based on the reduced order model, ignoring all secondary and residual modes. As was mentioned earlier the effect of spillover from these modes can degrade the performance of the system and in some cases may cause instability. This subsection will provide an overview of some of the methods which have been designed to reduce the effects of spillover.

The first method is a variation of optimal MMC. It is called Model Error Sensitivity Suppression (MESS) [12]. In this procedure the control spillover to the secondary modes is weighted in the performance index (3.3). In this way the control gain is chosen so as to minimize spillover to the secondary modes. Of course there will still be spillover to the residual and unmodeled modes.

A second type of technique for spillover suppression is to include filters in the controller in order to reduce the controller bandwidth. This is done in order to limit spillover to the residual modes, which are of higher frequency than the primary and secondary modes. There are several approaches to this type of control (eg. [13]-[15]). The value of this method is that the high frequency modes cannot be accurately modeled and therefore it is not possible to weight these modes in the performance index, as is done in MESS. Filtering enables the designer to suppress spillover to the residual modes without having accurate knowledge of their characteristics. The disadvantage of these methods is that they require more on-board computation. It is necessary to implement the filter as well as the observer (3.4) (if an observer is used).

Another method of control system design which can be used to reduce the effect of spillover is multivariable

frequency domain design [16]. Because the design is done in the frequency domain it is possible to limit the effect of the controller on high frequency modes. The disadvantage of this procedure is that it is difficult to apply to very high order systems. The design procedure is not as well defined as those discussed previously, and the design is based to a larger extent on subjective decisions of the designer. This process becomes much more difficult as the dimension of the problem increases.

A further discussion of the spillover problem and combinations of methods which can be used to control it is given in [17].

3.4 Adaptive Control

The finite dimensional model of the LSS (2.7), which is normally developed using the finite element method, often contains substantial errors in the modal frequencies and mode shapes. In addition, these system parameters can change during flight due to changes in temperature, vehicle orientation, etc. For these reasons it may be necessary to design LSS control systems which will tune in on the true system parameters ([18],[19]).

These adaptive control techniques can be divided into two basic categories. The first is indirect adaptive control. The indirect methods first identify the parameters of the system and then use the parameter estimates to adjust the control law. The second is direct adaptive control. The direct methods do not explicitly identify the system parameters but rather directly adjust certain parameters in the control law.

Adaptive control has several disadvantages:

- It requires much more on-board computation than other control methods.
- The stability properties for adaptive control of distributed parameter systems are not well understood.
- Very little work has been done on the development of adaptive control procedures for LSS control.

3.5 Conclusions

This section has provided a brief overview of some of the methods which have been proposed for vibration control of LSS. It has suggested that there are two, often conflicting, requirements which these methods must satisfy:

- The computational requirements of the algorithm must not exceed the capacity of the on-board computer.
- The procedure must be robust. The controller which is designed for the reduced order model must perform adequately when applied to the distributed parameter LSS system whose characteristics cannot be accurately estimated.

The methods discussed in this section have ranged from simple output feedback controllers with small on-board computational requirements, to adaptive control systems with considerable computational requirements but with a potentially increased robustness. At this point in time the LSS control problem has not been sufficiently analyzed to significantly narrow the list of potential LSS control systems.

The remainder of this report will investigate in more detail some representative LSS control systems and will illustrate their application to a simplified model of a LSS. The control systems which are covered have been chosen to have a range of complexity from simple output feedback to MMC with filters for spillover suppression.

SECTION 4

MODAL DASHPOTS

This section describes a method for adding damping to specific modes of a LSS through output feedback [4]. This is one of the simplest methods for LSS control and requires a minimal amount of computation - both for calculation of feedback gains and for on-board algorithm implementation.

Consider again the finite dimensional LSS model of (2.7) and (2.8)

$$\ddot{v} + Wv = U^T B_a u \quad (4.1)$$

$$y = C_d U v + C_v U \dot{v} \quad (4.2)$$

If we now consider only the primary modes and ignore all secondary and residual modes we obtain the reduced order model

$$\ddot{v}_p + W_p v_p = U_p^T B_a u \quad (4.3)$$

$$y = C_d U_p v_p + C_v U_p \dot{v}_p \quad (4.4)$$

where the primary mode shapes make up the columns of U_p . The method of modal dashpots uses velocity feedback only so that the closed loop model can be written

$$u = Gy \quad (4.5)$$

$$\ddot{v}_p + W_p v_p = U_p^T B_a G C_v U_p \dot{v}_p \quad (4.6)$$

or

$$\ddot{v}_p - U_p^T B_a G C_v U_p \dot{v}_p + W_p v_p = 0 \quad (4.7)$$

The principle of modal dashpots is to provide a specified amount of damping to the primary modes. This could be done by restricting the damping matrix of the closed loop system to be

$$-U_p^T B_a G C_v U_p = \begin{bmatrix} 2\zeta_1 \omega_1 & 0 & \cdots & 0 \\ 0 & 2\zeta_2 \omega_2 & \cdots & 0 \\ \vdots & \vdots & \ddots & \vdots \\ 0 & 0 & \cdots & 2\zeta_p \omega_p \end{bmatrix} = \Lambda \quad (4.8)$$

The following decoupled controller is chosen

$$G = -[U_p^T B_a]^T [U_p^T B_a (U_p^T B_a)^T]^{-1} \Lambda [(C_v U_p)^T C_v U_p]^{-1} (C_v U_p)^T \quad (4.9)$$

It can be shown [4] that if the feedback gain matrix is symmetric then under minor restrictions the closed loop system will always be stable. This can be assured by requiring that the sensors and actuators be colocated, ie.

$$B_a = C_v^T \quad (4.10)$$

Another restriction is that the number of sensor/actuator pairs be greater than the number of primary modes. This is necessary to ensure that the inverse matrices in (4.9) exist.

It should be emphasized that this discussion has ignored all secondary and residual modes. The spillover from these modes will cause the damping of the system to be different than the designed damping in Λ . However, the system will remain stable under minor restrictions [4].

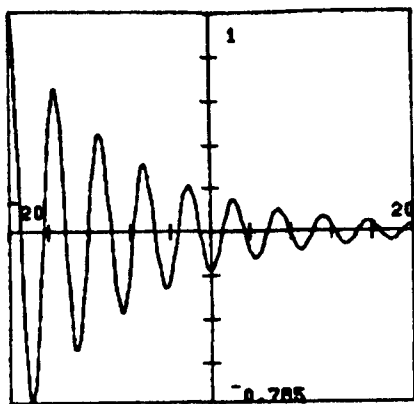
The modal dashpot method has been applied to the CSDL tetrahedral model which is described in [21]. The feedback gains were computed for three values of damping in the primary modes - .1, .2 and .3. As an example, for .1 damping the desired damping matrix would be

$$\Lambda = \begin{bmatrix} 0.27 & 0 & 0 & 0 \\ 0 & 0.33 & 0 & 0 \\ 0 & 0 & 0.51 & 0 \\ 0 & 0 & 0 & 0.68 \end{bmatrix} \quad (4.11)$$

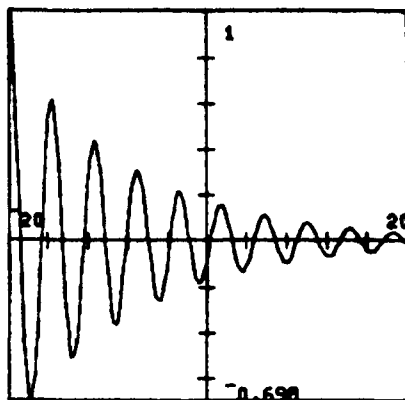
and the gain matrix was calculated from (4.9) to be

$$G = \begin{bmatrix} 3 & 0.35 & -1.0 & -2 & -0.61 & -2.1 \\ -0.35 & 3 & 2.1 & -0.61 & -2 & -1.0 \\ -1.0 & 2.1 & 7.4 & 4.6 & -6 & -7.2 \\ -2 & -0.61 & -4.6 & -0.61 & -0.49 & -6 \\ -0.61 & -2 & -6 & -0.49 & 0.0 & 4.6 \\ 2.1 & -1.0 & -7.2 & 6 & 4.6 & 7.4 \end{bmatrix}$$

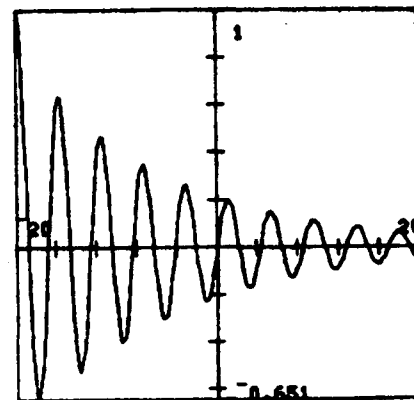
For each of the three values of damping the response of the closed loop system to an initial disturbance in the first mode was simulated. The response of the first mode for each case is shown in Figure 4.1. Notice that the actual maximum damping occurs for the system designed for .1 damping. This occurs because of increased spillover. The secondary and residual modes were ignored during the design process, and as the design attempts to obtain more damping in the primary modes spillover from the other modes degrades system performance.



0.1 Damping



0.2 Damping



0.3 Damping

Figure 4.1

Response to Initial Disturbance - Modal Dashpots

SECTION 5

LOW AUTHORITY CONTROL

Low authority control (LAC) [5] is a method for adding a moderate amount of damping to the primary modes of the system. It is similar in concept to modal dashpots.

Consider again the reduced order state space model (2.14) and (2.15)

$$\dot{x}_p = A_p x_p + B_p u \quad (5.1)$$

$$y = C_p x_p \quad (5.2)$$

where

$$x_p = \begin{bmatrix} v_p \\ \dot{v}_p \end{bmatrix} \quad A_p = \begin{bmatrix} 0 & I \\ -W_p & 0 \end{bmatrix} \quad B_p = \begin{bmatrix} 0 \\ U_p^T B_a \end{bmatrix} \quad (5.3)$$

$$C_p = [0 \quad C_v U_p]$$

with output feedback

$$u = Gy = GC_p x_p \quad (5.4)$$

Combining equations (5.1), (5.2) and (5.4) we obtain

$$\dot{x}_p = A_p x_p + B_p GC_p x_p \quad (5.6)$$

or

$$\dot{x}_p = A_p^* x_p \quad (5.6)$$

where

$$A_p^* = \begin{bmatrix} 0 & I \\ -W_p & U_p^T B_a GC_v U_p \end{bmatrix} \quad (5.7)$$

LAC considers the changes in the eigenvalues of A_p^* from those of A_p when the feedback gain G is small. The eigenvalues of A_p are p

$$\lambda_n = \pm j\omega_n \quad n = 1, \dots, p$$

Aubrun [5] has shown that the changes in the eigenvalues for small gains will be approximately

$$d\lambda_n \approx \frac{1}{2} [U_p^T B_a G C_v U_p]_{nn} \quad (5.8)$$

where $[]_{nn}$ denotes the n, n element of the matrix. Because the matrices in (5.8) are all real, it follows that the new root $\lambda_n + d\lambda_n$ now has a real part. The definition of the damping ratio now gives

$$2\zeta_n \omega_n \approx -[U_p^T B_a G C_v U_p]_{nn} \quad (5.9)$$

To illustrate the method for computing G , let

$$B^* = U_p^T B_a \quad C^* = C_v U_p \quad (5.10)$$

Then (5.9) can be written

$$\sum_j \sum_k B_{nj}^* C_{kn}^* G_{jk} = -2\zeta_n \omega_n \quad (5.11)$$

There is in general more than one solution for G which satisfies (5.11). By using a pseudo-inverse it is possible to compute G in such a way as to minimize

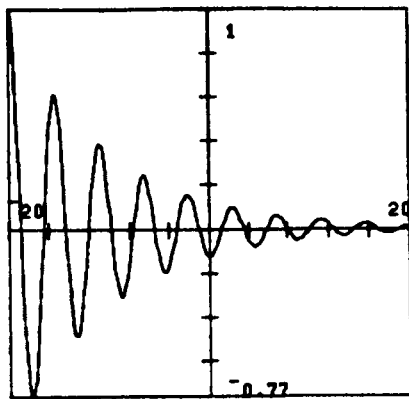
$$\sum_i \sum_j G_{ij}^2 \quad (5.12)$$

The gains were calculated in this manner for the CSDL tetrahedral model. Three values of damping in the primary modes - .1, .2 and .3 were used. The gain matrix for .1 damping is

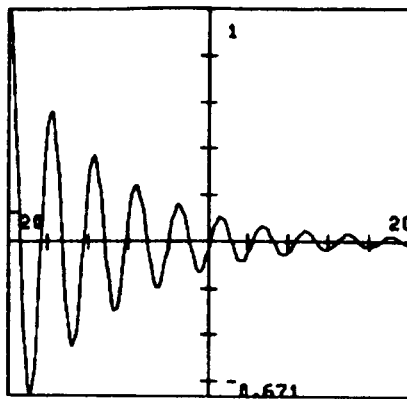
$$G = \begin{bmatrix} -4.8 & -0.49 & -3.9 & -3.1 & -0.22 & -4.3 \\ -0.49 & 4.8 & 4.3 & -0.22 & -3.1 & -3.9 \\ -3.9 & 4.3 & 6.4 & 1.6 & -2.7 & -6.2 \\ -3.1 & -0.22 & 1.6 & 4.2 & 2.8 & 2.7 \\ -0.22 & -3.1 & -2.7 & 2.8 & 4.2 & 1.6 \\ 4.3 & -3.9 & -6.2 & -2.7 & 1.6 & 6.4 \end{bmatrix} \quad (5.13)$$

Notice that this matrix is significantly different than the modal dashpot .1 damping gain matrix (4.12).

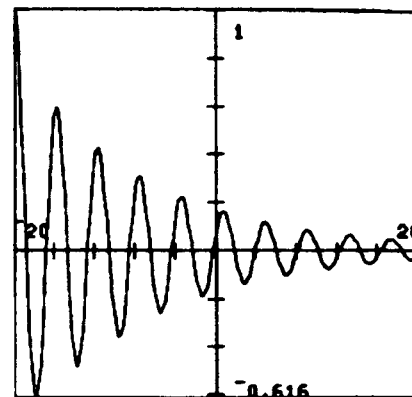
For each of the three values of damping the response of the closed loop system to an initial disturbance in the first mode was simulated. The response of the first mode in each case is shown in Figure 5.1. The results here are very similar to those for modal dashpots. Spillover causes a deterioration in performance if one tries to obtain large amounts of damping.



0.1 Damping



0.2 Damping



0.3 Damping

Figure 5.1

Response to initial disturbance - LAC

SECTION 6

OPTIMAL CONTROL

The theory of optimal control is well described in many textbooks (eg. [20]). This section will state the problem and the principle results in order to introduce the appropriate notation.

The theory of linear optimal control assumes that the system can be characterized by the differential equation

$$\dot{x} = Ax + Bu + w_1 \quad (6.1)$$

$$y = Cx + w_2 \quad (6.2)$$

where w_1 and w_2 are disturbance vectors containing white, Gaussian noise processes with intensities V_1 and V_2 respectively. With the exception of the disturbance vectors this model is the same as the LSS state variable model (2.9), (2.10).

It can be shown that the control

$$u^* = -K_c x \quad (6.3)$$

is optimal in the sense that it minimizes the performance index

$$J = E \left\{ \int_0^{\infty} [x^T R_1 x + u^T R_2 u] dt \right\} \quad (6.4)$$

where R_1 is positive semidefinite and R_2 is positive definite, if the control gain

$$K_c = R_2^{-1} B^T P \quad (6.5)$$

is computed from the algebraic Riccati equation

$$A^T P + PA - PBR_2^{-1} B^T P + R_1 = 0 \quad (6.6)$$

Because x is not measured directly it cannot be used in (6.3). For this reason an estimate of x is found from the filter/observer

$$\dot{\hat{x}} = A\hat{x} + Bu + K_f [y - C\hat{x}] \quad (6.7)$$

where the steady state filter/observer gain

$$K_f = QCV_2^{-1} \quad (6.8)$$

is computed from the algebraic Riccati equation

$$A^T Q + Q A - Q C^T V_2^{-1} C Q + V_1 = 0 \quad (6.9)$$

The estimate \hat{x} is optimal in the sense that it minimizes the mean square estimation error.

The optimal control law was found for the reduced order model (primary modes only) of the CSDL tetrahedral structure. The following weighting matrices were used

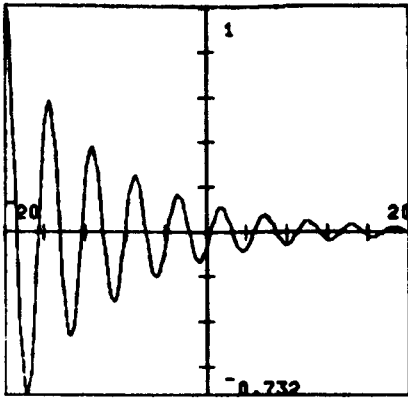
$$R_1 = I_8 \quad R_2 = \rho_c I_6 \quad V_1 = I_8 \quad V_2 = \rho_f I_6 \quad (6.10)$$

Where ρ_c is used to change the relative weighting, in the performance index, of control energy and regulation error. As ρ_c is decreased the system regulation error will decrease while the required control energy will increase. The ρ_f parameter serves an analogous role for the filter/observer.

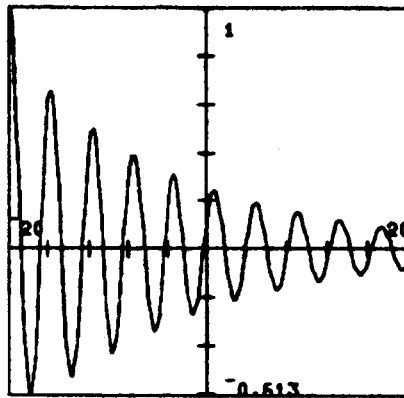
Optimal gains were computed for a number of values of ρ_c and ρ_f using the reduced order model. The response of the full order closed loop system was then simulated for various combinations of ρ_c and ρ_f . The results show the same major effect that was seen with the method of modal dashpots and LAC. As one attempts to achieve decreased regulation error (more damping) there comes a point at which the spillover from secondary and residual modes begins to cause a degradation in system performance and limits the actual damping which can be obtained.

Figure 6.1 shows the response of the system to an initial disturbance in the first mode for three combinations of ρ_c and ρ_f . It is clear that as the control energy is allowed to increase (decreasing ρ_c) the damping actually decreases after a certain point. Note that the initial peak does decrease with decreasing ρ_c , but as the secondary and residual modes are excited the spillover causes subsequent peaks to remain high.

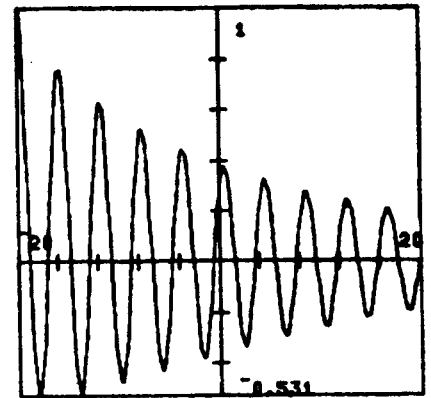
A comparison with Figures 4.1 and 5.1 show that optimal control, even though it requires significantly more on-board computation, does not significantly out-perform the simpler LAC and modal dashpots methods. Of course these results are of a preliminary nature, since the simulations performed were not exhaustive.



$\rho_C = 0.1$
 $\rho_f = 0.001$



$\rho_C = 0.01$
 $\rho_f = 0.001$



$\rho_C = 0.0001$
 $\rho_f = 0.0001$

Figure 6.1

Response to Initial Disturbance - Optimal Control

SECTION 7

MODEL ERROR SENSITIVITY SUPPRESSION

Model Error Sensitivity Suppression (MESS) is a method for reducing spillover from secondary modes. It is essentially the same as the optimal control method of the previous section except in the manner in which the weighting matrices R_2 and V_2 are determined.

Consider the primary, secondary and residual modes of (2.12) and (2.13) taken separately

$$\dot{x}_p = A_p x_p + B_p u \quad (7.1)$$

$$\dot{x}_s = A_s x_s + B_s u \quad (7.2)$$

$$\dot{x}_r = A_r x_r + B_r u \quad (7.3)$$

We want to include in the performance index some penalty on control spillover to the secondary modes - $B_s u$. Therefore the performance index (6.4) is changed to

$$J_2 = E \left\{ \int_0^{\infty} [x_p^T R_1 x_p + (B_s u)^T W_s (B_s u) + u^T R_2 u] dt \right\} \quad (7.4)$$

In terms of implementation this will require a change in the R_2 matrix to be used in (6.5) and (6.6)

$$R_2^* = R_2 + B_s^T W_s B_s \quad (7.5)$$

It is also possible by using a dual argument to develop a similar procedure for penalizing observation spillover by changing the V_2 matrix which is used in (6.7) and (6.8).

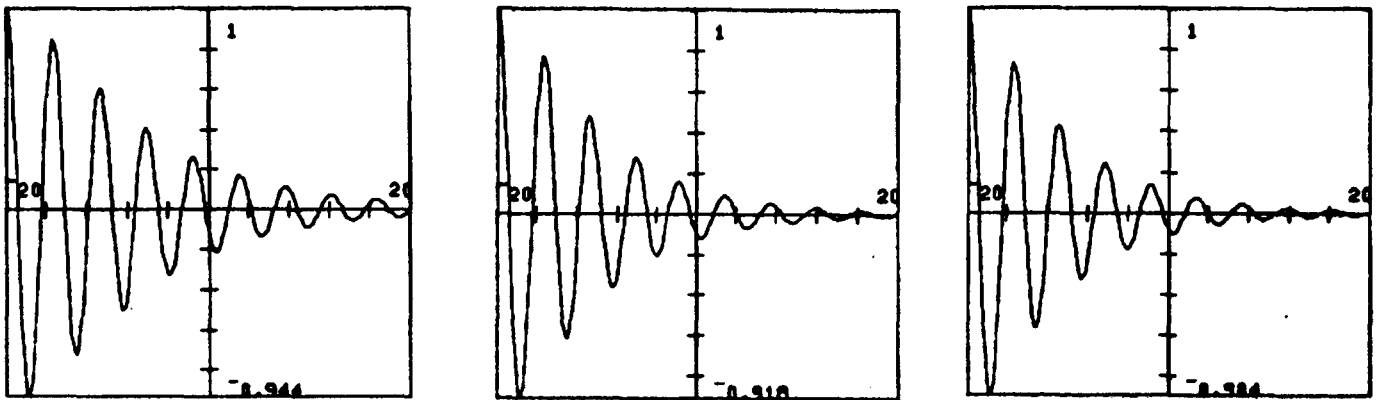
As with the other control methods MESS was simulated on the CSDL tetrahedral model. The spillover weighting matrix which was used was

$$W_s = I_6 \quad (7.6)$$

The R_1 , R_2 , V_1 and V_2 matrices were the same as those of (6.9).¹ Figure 7.1 shows the response of the system to an initial disturbance in the first mode for three combinations of ρ_c and ρ_f . Notice that by comparison with Figure 6.1 the MESS^c technique has reduced the spillover problem significantly. It is now possible to achieve a greater level of damping. It should be emphasized that these are preliminary results, and that there are many possible combinations of weighting matrices and disturbance inputs which have not been investigated.

It should be noted that no attempt is made to reduce spillover to residual modes. This is because it has been assumed that knowledge of residual mode characteristics is

very inaccurate and therefore that B_f cannot be accurately computed. A method for reducing spillover to residual modes will be discussed in Section 8.



$$\rho_c = 0.1$$
$$\rho_f = 0.01$$

$$\rho_c = 0.01$$
$$\rho_f = 0.001$$

$$\rho_c = 0.0001$$
$$\rho_f = 0.0001$$

Figure 7.1

Response to Initial Disturbance - MESS

SECTION 8

FREQUENCY SHAPED COST FUNCTIONALS

The method of Frequency Shaped Cost Functionals (FSCF) [14] is an extension of the standard optimal control procedure of Section 6. The basic purpose is to minimize excitation of high frequency modes by the controller. To accomplish this consider the performance index written in the frequency domain

$$J = \frac{1}{2} \int_{-\infty}^{\infty} [x^*(j\omega)R_1x(j\omega) + u^*(j\omega)R_2u(j\omega)]d\omega \quad (8.1)$$

In its present form the weighting matrices are not a function of frequency, but we can generalize (8.1)

$$J = \frac{1}{2} \int_{-\infty}^{\infty} [x^*(j\omega)R_1(j\omega)x(j\omega) + u^*(j\omega)R_2(j\omega)u(j\omega)]d\omega \quad (8.2)$$

which will allow us to penalize high frequency activity of x and u . The problem is to translate this into an equivalent time domain problem which can be solved using the standard Riccati equation. Under certain restrictions on $R_1(j\omega)$ and $R_2(j\omega)$ this can be done [14]. Assume that $R_1(j\omega)$ and $R_2(j\omega)$ can be factored:

$$R_1(j\omega) = P_1^*(j\omega)P_1(j\omega) \quad (8.3)$$

$$R_2(j\omega) = P_2^*(j\omega)P_2(j\omega) \quad (8.4)$$

where P_1 and P_2 are rational matrices. Define

$$P_1(j\omega)x = x_+ \quad (8.5)$$

$$P_2(j\omega)u = u_+ \quad (8.6)$$

Equations (8.5) and (8.6) can also be written as differential equations. For example, let

$$R_2(j\omega) = I (w^2 + w_0^2)/w_0^2 \quad (8.7)$$

This would penalize controls at high frequencies. R_2 can be factored so that

$$P_2(j\omega) = I(j\omega + w_0)/w_0 \quad (8.8)$$

Equation 8.6 can now be written as a differential equation

$$\dot{u} + w_0u = w_0u_+ \quad (8.9)$$

We now augment our reduced order design model

$$\begin{bmatrix} \dot{x}_p \\ \dot{u} \end{bmatrix} = \begin{bmatrix} A & B \\ 0 & -w_0I \end{bmatrix} \begin{bmatrix} x_p \\ u \end{bmatrix} + \begin{bmatrix} 0 \\ w_0I \end{bmatrix} u_+ \quad (8.10)$$

(To simplify the example we will assume that R_1 is a constant, although it can be handled in a manner similar¹ to R_2 .) The performance index can now be written

$$J = \frac{1}{2} \int_{-\infty}^{\infty} [x^*(j\omega)R_1x(j\omega) + u_+^*(j\omega)Iu_+(j\omega)] d\omega \quad (8.11)$$

or in the time domain

$$J = \int_0^{\infty} [x^T R_1 x + u_+^T I u_+] dt \quad (8.12)$$

which is equivalent to

$$J = \int_0^{\infty} \{ [x^T u^T] \begin{bmatrix} R_1 & 0 \\ 0 & 0 \end{bmatrix} \begin{bmatrix} x \\ u \end{bmatrix} + u_+^T I u_+ \} dt \quad (8.13)$$

Equations (8.10) and (8.13) can now be used to set up the Riccati equation which will be used to find the control law:

$$u_+ = -[K_1 \quad K_2] \begin{bmatrix} x \\ u \end{bmatrix} \quad (8.14)$$

Combining (8.9) and (8.14)

$$\dot{u} = -w_0(I + K_2)u - w_0K_1x \quad (8.15)$$

which is the FSCF control law. Of course \hat{x} will replace x when implementing (8.15).

The FSCF method was applied to the CSDL tetrahedral model. The R_1 , R_2 , V_1 and V_2 matrices were chosen to be the same as those of (6.9). The filter parameter w_0 was set to .5. For all values of ρ_c and ρ_f which have been tested the closed loop full order system has been unstable. It appears that this procedure may be sensitive to filter bandwidth, and further testing needs to be done.

SECTION 9

CONCLUSIONS

9.1 Summary

The LSS vibration control problem can be stated:

How can one restore figure shape to an acceptable accuracy within a reasonable length of time when the structure is subjected to a large impulsive disturbance (or maintain figure shape at an acceptable accuracy in the presence of small continuous disturbances) when there exists limited computational capacity and limited knowledge of structural characteristics?

This report has discussed a variety of active control techniques that attempt to solve this problem - from simple damping augmentation techniques which use direct output feedback, to optimal control strategies with filtering to suppress spillover. Preliminary results seem to indicate that the simple damping augmentation methods provide performance which is comparable to the more sophisticated procedures with a fraction of the computational requirement. The MESS method does show promise, and when combined with some sort of filtering to suppress spillover to residual modes (as has been suggested in [13]) it may provide significantly better performance.

9.2 Future Work

Now that a test procedure has been organized and has been applied to several control algorithms, it would be useful to subject other methods to the same test procedure (eg. filter accommodated control, adaptive control, etc.). This would allow direct comparison of the methods and would make clear the relative advantages and disadvantages of each algorithm, and might suggest improvements. In addition, the test procedure should be expanded to test more aspects of the control systems. For example, it should test response to initial disturbances in secondary and residual modes, response to continuous type disturbances, effect of errors in system models on performance, effect of changes in system parameters on performance, etc. In this way a more complete analysis could be made and a more accurate comparison of their capabilities would result.

REFERENCES

- [1] Gibson, J.S., "Convergence and Stability in Linear Modal Regulation of Flexible Space Structures", Proceedings of the Second VPI&SU/AIAA Symposium on Dynamics and Control of Large Flexible Spacecraft, June 1979.
- [2] Weeks, C., "Static Shape Determination and Control for a Large Space Antenna", Proceedings of the 20th IEEE Conference on Decision and Control, 1981.
- [3] Balas, M., "Feedback Control of Flexible Systems", IEEE Trans. Autom. Cont., Vol. AC-23, No. 4, August 1978.
- [4] Canavin, J., "Control Technology for Large Space Structures", AIAA Conference on Large Space Platforms, Los Angeles, Calif., Sept. 1978, paper 78-1691.
- [5] Aubrun, J.N., "Theory of the Control of Structures by Low Authority Controllers", AIAA Conference on Large Space Platforms, Los Angeles, Calif., Sept. 1978, paper 78-1689.
- [6] Kimura, H., "Pole Assignment by Gain Output Feedback", IEEE Trans. Autom. Cont., Vol. AC-20, 1975, pp. 458-463.
- [7] Davison, E., and S. Wang, "On Pole Assignment in Linear Multivariable Systems Using Output Feedback", IEEE Trans. Autom. Cont., Vol. AC-20, 1975, pp. 516-518.
- [8] Simon, J. and S. Mitter, "A Theory of Modal Control", Information and Control, Vol. 13, 1968, pp. 316-353.
- [9] Levine, W.S., and M. Athans, "On the Determination of the Optimal Constant Output Feedback Gains for Linear Multivariable Systems", IEEE Trans. Autom. Contr., Vol. AC-15, Feb. 1970, pp. 44-48.
- [10] Kosut, R.L., "Suboptimal Control of Linear Time Invariant Subject to Control Structure Constraints", IEEE Trans. Autom. Cont., Vol. AC-15, Oct. 1970, pp. 557-563.
- [11] Johnson, T.L., "Minimum-Variance Fixed-Form Compensation of Linear Systems", Proc. of the 18th IEEE Conference on Decision and Control, Jan. 1979.
- [12] Sesak, J.R., et.al., "Flexible Spacecraft Control by Model Error Sensitivity Suppression", Proc. of the Second VPI&SU/AIAA Symposium on Dynamics and Control of Large Flexible Spacecraft, June 1979.
- [13] Sesak, J.R., et.al., "Filter-Accommodated Optimal Control of Flexible Space Systems", AIAA Guidance and Control Conference, 1981, Paper No. 81-1784.

- [14] Gupta, N.K., "Frequency-Shaped Cost Functionals: Extensions of Linear-Quadratic-Gaussian Design Methods", J. Guidance and Control, Nov.-Dec. 1980, pp. 529-535.
- [15] Skelton, R. and P. Likins, "Orthogonal Filters for Model Error Compensation in the Control of Nonrigid Spacecraft", J. Guidance and Control, Vol. 1, 1980, pp. 41-49.
- [16] Benhabib, R.J., "Discrete Large Space Structure Control System Design Using Positivity", Proc. of the 20th IEEE Conference on Decision and Control, 1981.
- [17] Lin, J.G., "Three Steps to Alleviate Control and Observation Spillover Problems of Large Space Structures", Proc. of the 19th IEEE Conf. on Dec. and Cont., 1980.
- [18] Benhabib, R.J. and F.C. Tung, "Large Space Structures Control: System Identification Versus Direct Adaptive Control", Proc. of the 1980 JACC.
- [19] Montgomery, R.C. and F.J. Thau, "Adaptive Control of Large Space Structures", AIAA Guidance and Control Conference, 1980, Paper No. 80-1739.
- [20] Kwakernaak, H. and R. Sivan, Linear Optimal Control Systems, Wiley 1972.
- [21] Strunce, R.R., et.al., "Actively Controlled Structures Theory", Report R-1338, Vol. 2, December 1979.

NASA/ASEE SUMMER FACULTY RESEARCH FELLOWSHIP PROGRAM

MARSHALL SPACE FLIGHT CENTER
THE UNIVERSITY OF ALABAMA

STRUCTURAL APPLICATION OF HIGH STRENGTH,
HIGH TEMPERATURE CERAMICS

Prepared By: William B. Hall, Ph.D.
Academic Rank: Professor
University and Department: Mississippi State University
Department of Chemical Engineering
NASA/MSFC:
Division: Non-Metallic
Branch: Ceramics & Coatings
MSFC Counterpart: Marshall King
Date: August 9, 1982
Contract No: NGT 01-002-099
The University of Alabama

STRUCTURAL APPLICATION OF
HIGH STRENGTH, HIGH TEMPERATURE CERAMICS

BY

William B. Hall, Ph.D.
Professor of Chemical Engineering
Mississippi State University
Mississippi State, Mississippi

ABSTRACT

The operation of rocket engine turbine pumps is limited by the temperature restrictions of metallic components used in the systems. Mechanical strength and stability of these metallic components decrease drastically at elevated temperatures. Ceramic materials that retain high strength at high temperatures appear to be a feasible alternate material for use in the hot end of the turbopumps. This project identified and defined the processing parameters that affected the properties of Si_3N_4 , one of the candidate ceramic materials. Apparatus was assembled and put into operation to hot press Si_3N_4 powders into bulk material for in house evaluation. A work statement was completed to seek outside contract services to design, manufacture, and evaluate Si_3N_4 components in the service environments that exists in SSME turbopumps.

INTRODUCTION

The Space Shuttle Orbiter is the heart of NASA's space transportation system during the decade of the eighties. This reusable vehicle trims the cost of space travel while increasing NASA's capabilities in space. The system can carry a crew of three, four scientists, and a sixty five thousand pound load into orbit. This Orbiter returns to earth like an airplane and it is anticipated that it can make one hundred round trips into space and back. Although the Shuttle System utilizes the most advanced aerospace technology available to date to achieve economical and useful space flight, it is anticipated various improvements will be made on the system as experience is gained and new technologies emerge. Marshall Space Flight Center has the main responsibility for the Space Shuttle main engine and solid rocket boosters used in this system.

One area in which improvement is desired is in the high-pressure turbopumps, both fuel and oxidizer, in the Space Shuttle main engine. The operation of these pumps is limited by temperature restrictions of the metallic components used in these pumps. Spot melting, oxidation, and erosion-corrosion are some of the problems encountered in the turbopumps.

High strength refractory ceramics are being considered for use as structural materials in these turbopumps. This will alleviate the problems mentioned above and in addition permit a several hundred degree fahrenheit increase in operational temperatures. This increase in temperature will increase the overall efficiency of the space shuttle main engines, which in turn will permit a larger pay load. This ceramic material which appears to have the best possibility of being utilized is silicon nitride, Si_3N_4 .

OBJECTIVES

The objectives of this two year study were:

1. Identify and define the processing parameters that affect the properties of Si_3N_4 ceramic materials.
2. Design and assemble equipment required for processing high strength ceramic.
3. Design and assemble test apparatus for evaluating the high temperature properties Si_3N_4 .
4. Conduct a research program of manufacturing and evaluating Si_3N_4 materials as applicable to rocket engine applications.

ENGINEERING ANALYSIS

Silicon nitride has the desired properties for utilization as a high temperature structural material. These properties include high strength, low coefficient of friction, high decomposition temperature, good corrosion resistance, good oxidation resistance, high wear resistance and good thermal shock resistance. These positive features have been known for two decades and slowly silicon nitride is approaching the fulfillment of its potential. Two problems have slowed the use of silicon nitride. The first is the fabricating of suitable or useful shapes with the desirable properties. The second is the brittleness of silicon nitride, and indeed, all ceramic materials. Traditionally, all engineering design compromises on the selection of a material to use in an application, taking into consideration the total cost of a material and the use properties of that material. The evaluation of these compromises in design generally show that a metallic material has a higher net profit. Because of this, there is very little design experience with structural applications of silicon nitride or other brittle ceramics. It is being considered at this time because of the great need for the potential of Si_3N_4 and the development of computer capability to define the stresses as required for brittle material design.

PROCESSING PARAMETERS

There are three basic methods of forming bulk Si_3N_4 . The first of these three is called "reaction-bonded" Si_3N_4 whereby formed piece of pressed silicon powders is nitrided in nitrogen gas in the range of 1300-1400°C. During this nitridation process, the silicon powders are reacted with N_2 gas to form a mixture of α - and β - Si_3N_4 . The second method is called "hot-pressed" Si_3N_4 . This process entails the nitriding of Si powders to form α - Si_3N_4 powders. These Si_3N_4 powders are mixed with desirable additives and then pressed into a compact in a graphite mold, under a pressure of 1-2 tons/in², at a temperature of 1700-1800°C. This results in a high strength, high density β - Si_3N_4 product. The third process is called "sintered" Si_3N_4 . In the sintered product, α - and/or β Si_3N_4 powders are mixed with desirable additives and then pressed into the desired shape. This pressed bulk is then sintered in a controlled

atmosphere at 1800-1911°C for a considerable length of time. The product of this sintering operation is essentially β -Si₃N₄. Reaction bonded and sintered silicon nitride generally increases in strength with an increase in use temperature up to the 1400°C range and then falls off. Hot pressed silicon nitride is strongest at room temperature and the strength falls off gradually until the 1200°C range and then falls off more rapid. Since reaction bonded and sintered silicon nitride both have lower room temperature strength than hot pressed there is considerable overlap of strengths in the 1200°C to 1450°C range. The exact strength and other properties in this range is very dependent on the starting materials and other processing parameters, such as the specific sintering aid utilized.

In addition to the above parameters, there are two hexagonal crystal structures of silicon nitride, α -Si₃N₄ and β -Si₃N₄, with the α -Structure unit cell being approximately twice the size as the β -Structure unit cell. Since either structure can be produced from the other by rotation of two basal planes, requiring breaking and forming primary bonds, the α - β transformation requires time and energy. Two possible methods are solutioning-precipitation and volatilization-condensation. Both structures can be formed over a wide range of temperatures and both are relatively stable, although β -Si₃N₄ appears to be more stable at temperatures in excess of 1500°C. The formation of Si₃N₄ through a vapor-phase reaction favors the formation of the α -Structure, while precipitation from the liquid state favours the β -Structure formation. The morphology of the formed crystals is important with the fibrous β -Structure preferred because it enhances the strength and toughness of the resulting bulk material.

The processing parameters that are controlled to obtain the desired properties in the silicon nitride include:

- a. Initial particle size and size distribution
- b. Impurities
- c. Milling and Mixing procedures
- d. Sintering aids
- e. Reaction (sintering) temperature
- f. Reaction (sintering) pressure
- g. Reaction (sintering) time
- h. Reaction (sintering) atmosphere
- i. Post heat treatment

Not all of these parameters apply to each of the three types of bulk solid Si₃N₄. Normal impurities present in Si₃N₄ regardless of type are iron, aluminum, calcium, magnesium and oxygen. These elements are usually present in the combined state such as oxides, silicides or silicates.

An excellent article on how all of the above variables affect the final physical properties of the silicon nitride is given in the paper by Larsen et al (Ref. 1) which was presented in 1981.

EQUIPMENT ASSEMBLY

Equipment was assembled and checked out to hot press silicon nitride powders into a bulk shape. The equipment utilized was as follows:

Lepel High Frequency Induction Furnace, model T-20-3-KC-E-H, 45 KVA, 20 KW Radio Frequency Output, 180-450 KC Frequency range, water cooled at a rate of ten gallons per minute.

Corning Precision Deviation Controller model 8810.

Leeds and Northrup Automatic Optical Pyrometer.

BLH Electronics Universal Transducer Indicator, BLH model 350, 25,000 pound load cell at 100%.

Graphite Dies, 1½ inch diameter.

Cavity, dual plungers 1½ diameter and 4 inches in length, outside shell 3½ inch diameter and a height of 6 inches.

Silicon nitride powders, Cerac Pure, Cerac Incorporated, Milwaukee, Wisconsin, -325 mesh, mixture of alpha and beta. Phases, about 2 micron average diameter, 99.9% pure, nitrogen content 38%.

Several runs were completed utilizing this equipment with the final bulk density of the silicon nitride being 99.4% of theoretical. Two problem areas requiring additional effort are:

The sintered silicon nitride bonds to the plungers during the sintering process. It is suggested that small sacrificial dish be inserted between the powders and the plungers.

Water pressure variations causes the safety switch to activate cutting off the Induction Furnace during low pressure periods. Larger lines, or a large surge tank should alleviate this problem.

DESIGN, MANUFACTURING AND EVALUATION OF Si_3N_4 AS A STRUCTURAL COMPONENT OF THE SSME

This portion of the objectives of this research project was beyond the scope of the ASEE-NASA program, and a request for proposal was prepared. The work statement of the RFP follows.

General

It is requested that a contract be negotiated to define the parameters affecting the use of high temperature, high strength ceramics as structural components of the Space Shuttle Main Engine. This contract should be negotiated on a noncompetitive basis and awarded as a cost-plus fixed fee contract.

Background

Operation of the Space Shuttle on a more efficient basis of providing more thrust without additional fuel consumption should directly result in an increase in payload capacity. One means of achieving this increased efficiency is to increase the operational temperature of the turbopumps. The operational temperatures of the turbopumps are presently limited by the capabilities of the superalloys in the turbopump. The use of structural ceramic materials should permit operation of the turbopumps up to 2500°F.

Several materials systems are being developed that may provide the properties necessary for the higher temperature operation. Silicon nitride, silicon carbide, transformation toughened zirconia, and fiber reinforced ceramics appear promising as candidate materials systems for structural applications. The material for this application must possess the properties of high strength at elevated temperatures, good fracture toughness, and thermal shock resistance.

Work Statement

Phase I - Environment Definition

Definition of the environment that the ceramic components of a turbopump will be exposed to will acutely effect the material, processing, and design of the components. The contractor shall define in detail the environments in the turbopumps during start-up, operation, and shut down. The environmental parameters of interest are as follows:

1. Temperature Extremes
2. Rate of Temperature Change
3. Heat Flux Extremes
4. Rate of Change of Heat Flux
5. Gas Mass Flow
6. Gas Composition
7. Combustion Products Composition
8. Change in Gas Composition Ratios
9. Uniformity of Gas Composition Relative to Location
10. Temperature Profile
11. Stress Levels
12. Rotational Speed
13. Pressure Extremes
14. Rate of Change of Pressure
15. Other Stress Sources and their levels
16. Any Other Parameter that would Affect

This data shall be compiled and be available for use in the following phases of this program.

Phase II - Components Study

Based on the data generated in Phase I and knowledge of structural ceramics, the contractor shall conduct a study to identify the components that appear to be candidates for being fabricated from high strength refractory ceramic materials. The rationale utilized to reach these

conclusions shall be provided. Acceptable design criteria such as Wiebull Modulus or other accepted techniques shall be utilized to establish an acceptable degree of reliability for the candidate structures/materials.

Phase III - Design Parameters

The contractor shall apply the results of Phase I and Phase II of this work statement to identify and quantify the critical design parameters of selected components. Included should be the area of utilizing brittle materials as a structural member, where some attention given to:

1. Method of attachment of components
2. Method of joining of components
3. Design concepts to eliminate point contacts
4. Design concepts to maximize compressive loading of ceramics and minimize other types of loading
5. Design concepts to minimize thermal shock effects
6. Design concepts to minimize impact potential and effect

The contractor will also identify any other potential problem areas expected to be encountered and suggest design concepts to minimize these problems. This phase of the project will require the expertise of experienced design personnel in the field of utilization of brittle materials as structural members.

Phase IV - Design Variables

The contractor upon completion of Phase III shall supply a format for the preparation of ceramic components for the turbopumps to be utilized in the Space Shuttle Main Engine. This format shall contain, but not limited to, the following:

1. The selected shapes of the components
2. Materials characterization
 - a. Starting Powders
 1. size
 2. shape
 3. purity
 - b. Required alpha or beta Phase Ratio
 - c. Suppliers
3. Processes
 - a. Forming
Sintering
Final Shaping Tolerance
4. Attachment Techniques

5. Special Handling Required

6. Required Specifications of as Completed Components

This phase will require the collaboration of design personnel and material personnel.

CONCLUSIONS AND RECOMMENDATION:

Si_3N_4 is a viable material candidate for utilization in high temperature structural applications. However, it must be fully evaluated under use conditions and environments before utilization. Main areas of concern are thermal shock, methods of attachment, and reactive atmosphere when considering application in rocket engine turbine. It is recommended that these areas be studied and evaluated under actual environments existing in the turpumps early in the program. These evaluation should continue through the life of the program as long as any change is made in the Si_3N_4 processing parameters. Additional studies could include:

- a. Creep and strength improvement based on different sintering aids
- b. Forming techniques
- c. New processing techniques such as reaction-bonding followed by sintering
- d. Basic studies on the glass bond formed during sintering

References

1. Larsen, D. C., Adams, J. W., Bortz, S. A. and Ruh, R., Evidence of strength degradation by subcritical crack growth in Si_3N_4 and SiC , International Symposium on Fracture Mechanics of Ceramics, Penn. State University, 1981.
2. Larsen, D. C., and Bortz, S. A., Properties of structural ceramics, SAMPE Journal, January, February, 1981.
3. Larsen, D. C. and Ruh, R., The Nature of SiC for use in Heat Engines as compared to Si_3N_4 : An overview of Properties Differences, NATO Advanced Study Institute of Nitrogen Ceramics, University of Sussex, U. K., 1981.
4. Heitman, P. W. Development of Ceramic Gas Turbine Components Detroit Diesel Allison, NASA Contract: Den. 3-17, 1981.
5. Byrd, J. A., Ceramic Applications in Turbine Engines, Detroit Diesel Allison, NASA Contract: Den. 3-17, 1981.
6. Edington, J. W., Rowcliffe, D. J., and Henshall, J. L., The Mechanical properties of Silicon Nitride and Silicon Carbide, Powder Metallurgy International, Vol. 7, No. 2, 1975.
7. Exempt Vol. 7, No. 3, 1975.
8. Jack, K. H., Nitrogen Ceramics, 17th Mellor Memorial Lecture, 1973.
9. Guha, J. P., Goursat, P., and Billy, M., Hot Pressing and Oxidation Behavior of Silicon Nitride with Ceria Additive, Journal of the American Ceramic Society, Vol. 63, No. 1-2, 1980.
10. Jennings, H. M., Danforth, S. C., and Richman, M. H., On a Growth Mechanism for β phase Silicon Nitride, Journal of Materials Science Vol. 14, 1979.
11. Dervisbegovic, H., and Riley, F. L., The Influence of Iron and Hydrogen in the Nitridation of Silicon, Journal of materials Science, Vol. 14, 1979.
12. Lindley, M. W., Elias, D. P., Jones, B. F. and Pitman, K. C., The Influence of Hydrogen in The Nitriding Gas on the Strength, Structure and Composition of Reaction-Sintered Silicon Nitride Journal of Materials Science, No. 14, 1979.
13. Elias, D. P., and Lindley, M. W., Reaction Sintered Silicon Nitride, Part 1, Journal of Materials Science, No. 14, 1979.
14. Jones, B. F., and Lindley, M. W., Reaction Sintered Silicon Nitride, Part 2, Journal of Materials Science, No. 14, 1979.

15. Katz, R. Nathan, High Temperature Structural Ceramics, Science, Vol. 208, 1980.
16. Greskovich, C., and Rosolowski, J. H., Sintering of Covalent Solids, Journal of the American Ceramic Society, Vol. 59, No. 7-8, 1976.
17. Vasilos, T., Cannon, R. M., and Wvench, B. J., Improving the Stress Rupture and Creep of Silicon Nitride, Final Report NASA Contract NAS 3-20088, March, 1979.
18. Richman, M. H., Effect of Processing Parameters on Reaction Bonding of Silicon Nitride, Final Report, NASA Contract NSG-3118, October, 1980.
19. Jack, K. H., Sialons and Related Nitrogen Ceramics, Journal of Materials Science, No. 11, 1976.
20. Longe, F. F., Silicon Nitride Polyphase Systems: Fabrication, Microstructure, and Properties, International Metals Reviews, No. 1, 1980.
21. Vasilo, T., and Cannon, R. M. Jr., Improving and Toughness of Refractory Compounds, Final Report, NASA Contract NAS3-17768, November, 1975.
22. Palm, J. A., and Greskovich C. D., Silicon Nitride for Airborne Turbine Applications, Final Report, Naval Air Systems Command Contract No. 0019-77-C-0259 July, 1978.
23. Sikara, P. F. and Yeh, H. C., Consolidation of Silicon Nitride Without Additives, NASA Technical Memorandum NASATM 73693, 1976.
24. Williams, R. M., Linear Thermal Expansim of Hot-Pressed Si_3N_4 , The Journal of the American Ceramic Society, Vol. 63, No. 1-2, 1980.
25. Moulson, A. J., Reaction-Bonded Silicon Nitride: Its Foundation and Properties, Journal of Materials Science, No. 14, 1979.
26. Personal Communication, Dove Larsen, IITRI; Roger Wills, Battelle-Columbus; Tom Miller, NASA-Lewis.

Orbital Precession, Precessing Accretion Disks and Pulse Timing
Residuals in Binary Systems with Mass Transfer
and
Hydrodynamic Stability of Jets Produced by Mass Accreting Systems

by

Philip E. Hardee

Contract #: NASA-NGT-01-002-099

XIX-i

Abstract

Part I:

We review the existing model for pulsed x-ray emission from the source Hercules X-1. A necessary part of this model is a precessing accretion disk which turns the source on and off with 35 day cycle. It is usually assumed that precession of the primary star in this binary system, Hz Hercules, slaves the disk to its precession rate. This model can account for the systems behavior in a qualitative manner. Precession of Hz Hercules with 35 day period requires precession of the binary orbit. Pulse arrival times from Herc X-1 have been analyzed for orbital precession. The inclusion of precession does not significantly improve the results obtained assuming a non-precessing orbit.

Part II:

Binary configurations like Herc X-1 can produce jets of material ejected perpendicular to the orbital plane. One such galactic binary system is SS433. On a much larger scale this type of system may produce extra-galactic jets whose observed emission is in the radio region of the spectrum. We have considered the fluid dynamical stability of such jets and the possible consequences of Kelvin-Helmholtz instability at the jet surface external medium interface.

The binary star system consisting of Hercules X-1 and Hz Hercules is an example of systems in which there is mass transfer from a primary star (Hz Herc) to a collapsed object (Herc X-1). Material in such systems forms an accretion disk around the collapsed object and material slowly spirals inwards as angular momentum is lost through turbulent and/or magnetic viscosity. Pulsed x-ray emission from Herc X-1 is produced as ionized material from the inner edge of the accretion disk is channeled along magnetic field lines to the polar caps of a rotating neutron star. The constant rotation of the neutron star and x-ray pulse rate of Herc X-1 provides a stable clock which can be used to determine orbital parameters of the binary system. One finds that the orbit is nearly circular with period 1.7 days and stellar separation is $\sim 4 \times 10^{11}$ cm; the neutron star's mass is $\geq 1 M_{\odot}$ and Hz Herc has a mass of approximately $2 M_{\odot}$ (Giacconi et al. 1973). Additionally it is found that the pulsed x-ray emission has a 35 day on-off cycle with approximately 11 days on and 24 days off (Tananbaum et al. 1972). Optical observation of Hz Herc shows variation of 1.5 magnitudes on the 1.7 day orbital period but no 35 day variation (Bahcall and Bahcall 1972). This has been interpreted as a result of heating of Hz Herc by x-rays from Herc X-1 (Bahcall and Bahcall 1972; Forman, Jones, and Liller 1972).

The 35 day on-off cycle of the pulsed x-rays provides evidence for a tilted precessing accretion disk which occults the neutron star for 24 days and precesses with 35 day period (Katz 1973). Such an accretion disk can be created only if the mass is transferred with angular momentum inclined relative to the orbital angular momentum. This can occur if the

spin axis of Hz Herc is inclined relative to the orbital axis, precesses with 35 day period driven by Herc X-1, and mass transfer is periodic (Roberts 1974). In this case the outermost part of the accretion disk is slaved to the precession of Hz Herc. Mass transfer can be periodic in a system with inclined primary as the size of the primary's Roche lobe is a minimum when the secondary (Herc X-1) crosses the equatorial plane of the primary (Avni and Schiller 1982). This implies mass transfer twice per orbit through the inner Lagrangian point. Since disk precession is opposite to the orbital motion, mass transfer occurs preferentially every 0.81 days, half the 1.62 day recurrence of identical accretion disk primary orientation (see Figure 1). Because the precessing disk cannot occult Herc X-1 as seen from Hz Herc, accretion disk parameters and orientation of the observer with respect to the orbital plane are constrained. The disk must be tilted about 30° with respect of the orbital plane with width subtending an angle of about 37° as viewed from Herc X-1, the outer edge of the accretion disk is at distance $> 1.6 \times 10^{11}$ cm from Herc X-1, and the observer's line of sight is about 9° above the orbital plane (Gerend and Boynton 1976) - see Figure 2.

The fluid accretion disk precesses at a rate which is related to the forced precession rate, the transfer of angular momentum outwards from the inner portions of the disk, and the natural precession rate. An accretion disk acting under these driving torques behaves like a series of concentric rings which precess with different rates. The net result is a twisted accretion disk (Petterson 1975). In the Hercules system the natural precession rate of the disk outer edge is faster than the forced precession

rate and is ~ 17 days if the outer edge is at radial distance 2×10^{11} cm. In this case Herc X-1 is obscured before turn-on by the outer edge of the accretion disk and occulted at turn-off by inner portions of the disk. Since the outer portion of the accretion disk is forced to precess with 35 day period rather than its natural 17 day period the outer edge of the disk nutates in addition to the average forced precession. It can be shown that disk tilt, θ , and angle of the line of nodes, ϕ , can be approximated by (Katz et al. 1982)

$$\theta \approx \theta_0 - \frac{\Omega_0 \tan \theta_0}{2(\omega_* - \Omega_s)} \cos 2[(\omega_* - \Omega_s)t - \phi_0]$$

and

$$\phi \approx \Omega_s t - \frac{\Omega_0}{2(\omega_* - \Omega_s)} \sin 2[(\omega_* - \Omega_s)t - \phi_0] + \phi_0.$$

In these expressions θ_0 is the average disk tilt, Ω_s is the average forced precession frequency, Ω_0 is the natural precession frequency - a function of radius, and ω_* is the orbital frequency. Note that $\Omega_0 = -|\Omega_0|$ and $\Omega_s = -|\Omega_s|$ because precession is opposite to the direction of orbital motion, $\omega_* = |\omega_*|$.

Height of the center line of the disk relative to the orbital plane along the observer's line of sight is given by

$$h(t) = a \sin \phi \sin \theta$$

where a is the disk radius. Provided nutation is small

$$h(t)/a \sin \theta_0 \approx \sin(\Omega_s t + \phi_0) \left[1 - \frac{\Omega_0}{\omega_{.81}} \cos(\omega_{.81} t - \phi_0) \right] \\ - \cos(\Omega_s t + \phi_0) \left[\frac{\Omega_0}{\omega_{.81}} \sin \omega_{.81} t \right]$$

where $\omega_{.81} \equiv 2(\omega_* - \Omega_s)$ and has a 0.81 day period. Minimum $h(t)$ corresponds

approximately to the midpoint of the on state and turn-on occurs preferentially when $h(t)$ is most rapidly varying. The behavior of $h(t)$ is shown in figure 3 for $\phi_0 = 0$, i.e., the line of nodes points towards the observer and the center line of the disk is in the orbital plane at eclipse center $t = 0$. The 11 day on state would begin when the center line of the disk is in the shadowed band. The horizontal arrows indicate two possible turn-on points on either side of the vertical arrow which is at eclipse center. In this example turn-on would occur preferentially at about 0.75 or 0.15 orbital phase relative to eclipse center. An analysis by Levine and Jernigan (1982) shows that a solid precessing ring mimics reasonably well the behavior of a fluid ring. Both Katz et al., and Levine and Jernigan claim that nutation can lead to preferential turn-on at orbital phase of about 0.3 and 0.7 relative to eclipse center. This behavior is suggested by the data (Boynton 1980). However, the tendency for turn-on at these orbital phases is marginal (Levine and Jernigan 1982). Following $h(t)$ over several precession periods suggests that turn-on moves in orbital phase as periodicities are not integer multiples of each other. The fact that closely spaced (~ 0.5 day apart) local minima and maxima exist in $h(t)$ resulting from disk nutation suggest the possibility of turn-on followed by an absorption dip or weak turn-on followed by strong turn-on about 0.5 day later. Effects like these are seen in the data. However, the data also reveal so called anomalous absorption dips in the second binary orbit after turn-on. Disk nutation would only seem capable of producing absorption dips within the first binary orbit after turn-on. Recent results also show that turn-on varies by as much as 2 days from

the 35 day average (Boynton, Crosa, and Deeter 1980). This behavior cannot be accounted for by nutation alone. It is possible that a combination of circulating structure on the disk edge and nutation can explain these and one other effect. Material is deposited with 0.81 day periodicity at the disk edge and increased disk thickness may be associated with this deposition. Crosa and Boynton (1980) argue that the Keplerian orbital period of about 15 hours at the disk edge when combined with scale height relaxation after mass transfer can explain absorption dips seen before eclipse. These pre-eclipse dips march to earlier orbital phase relative to eclipse center as the on cycle progresses. This behavior is produced in their model because material is deposited at the disk edge at earlier orbital phase as the on cycle progresses and circulates around the disk into the line of sight occulting Herc X-1 before eclipse at earlier orbital phase as the cycle progresses. It seems likely that a combination of disk nutation at 0.81 day period when linked to mass transfer effects at 0.81 day period will come closer to reproducing the observed effects as the two effects can be complimentary.

While these qualitative explanations for the complex behavior of Herc X-1 are plausible they are difficult to verify. Since the tidal torques acting on the system should have reduced precession of Hz Herc just as they are presumed to have circularized the orbit (Chevalier 1976), there is considerable reason to attempt to verify precession of Hz Herc. If Hz Herc precesses then the binary orbital plane must also precess with 35 day period. This orbital precession leads to x-ray pulse arrival times different from arrival times from a non-precessing orbit. The flight

time of photons from a precessing non-nutating orbit is given by

$$\tau_p = \frac{D}{c} \left(1 - 2 \frac{D_{cm} a}{D^2} [\cos i \{ \cos (\omega_* - \Omega_s)t \sin (\Omega_s t + \phi_o) + \cos \theta_o \sin (\omega_* - \Omega_s)t \cos (\Omega_s t + \phi_o) \} + \sin i \{ \sin \theta_o \sin (\omega_* - \Omega_s)t \}] \right)$$

and for a non-precessing orbit ($\Omega_s = 0$) is

$$\tau_o = \frac{D}{c} \left(1 - 2 \frac{D_{cm} a}{D^2} [\cos i \{ \cos \omega_* t \sin \phi_o + \cos \theta_o \sin \omega_* t \cos \phi_o \} + \sin i \{ \sin \theta_o \sin \omega_* t \}] \right)$$

In these equations D_{cm} is the distance to the systems center of mass, $D = [D_{cm}^2 + a^2]^{1/2}$ where a is the distance of Herc X-1 from the center of mass, ω_* is the orbital frequency, $\Omega_s = -|\Omega_s|$ is the precession frequency, θ_o is the orbital tilt relative to the constant system angular momentum, and i is the inclination of the observer relative to the average orbital plane. The difference between flight times is

$$\Delta\tau = -(a/c)(\theta_o^2/2) \cos i [\sin \omega_{1.62} t \cos (\Omega_s t + \phi_o) - \sin \omega_* t \cos \phi_o] + (a/c) \theta_o \sin i [\sin \omega_{1.62} t - \sin \omega_* t]$$

where $\omega_{1.62} \equiv \omega_* - \Omega_s$. For Herc X-1 $a \approx 2.7 \times 10^{11}$ cm, $\theta_o \sim 0.5^\circ$ (we assume $L_{Hz \text{ Herc}}/L_{orbit} \sim 0.02$ and that Hz Herc is tilted by 30°), $i \approx 9^\circ$, and we find that $\Delta\tau$ can be as large as 20 msec. Arrival time data has been analyzed assuming a precessing orbit and compared to analysis assuming a non-precessing orbit. While the fit was not significantly improved the amount of data was not sufficient to rule out precession of the orbit and Hz Herc. If more data becomes available in the future a better test of orbital precession can be performed.

References

- Avni, Y., and Schiller, N. 1982 (preprint).
- Bahcall, J.N., and Bahcall, N.A. 1972, Ap.J. Letters, 178, L1.
- Boynton, P.E., Crosa, L.M., and Deeter, J.E. 1980, Ap.J., 237, 169.
- Crosa, L.M., and Boynton P.E. 1980, Ap.J., 235, 999.
- Gerend, D., and Boynton, P.E. 1976, Ap.J., 209, 562.
- Giacconi, R., Gursky, H., Kellogg, E., Levinson, R., Schreir, E., and
Tananbaum, H. 1973, Ap.J., 184, 227.
- Katz, J.I. 1973, Nature, 246, 87.
- Katz, J.I., Anderson, S.F., Margon, B., and Grandi, S.A. 1982 (preprint).
- Levine, A.M., and Jernigan, J.G. 1982 (preprint).
- Petterson, J.A. 1975, Ap.J., 201, L61.
- Roberts, W.J. 1974, Ap.J., 187, 575.
- Tananbaum, H., Gursky, H., Kellogg, E.M., Levinson, R., Schreir, E., and
Giacconi, R. 1972, Ap.J. Letters, 174, L143.

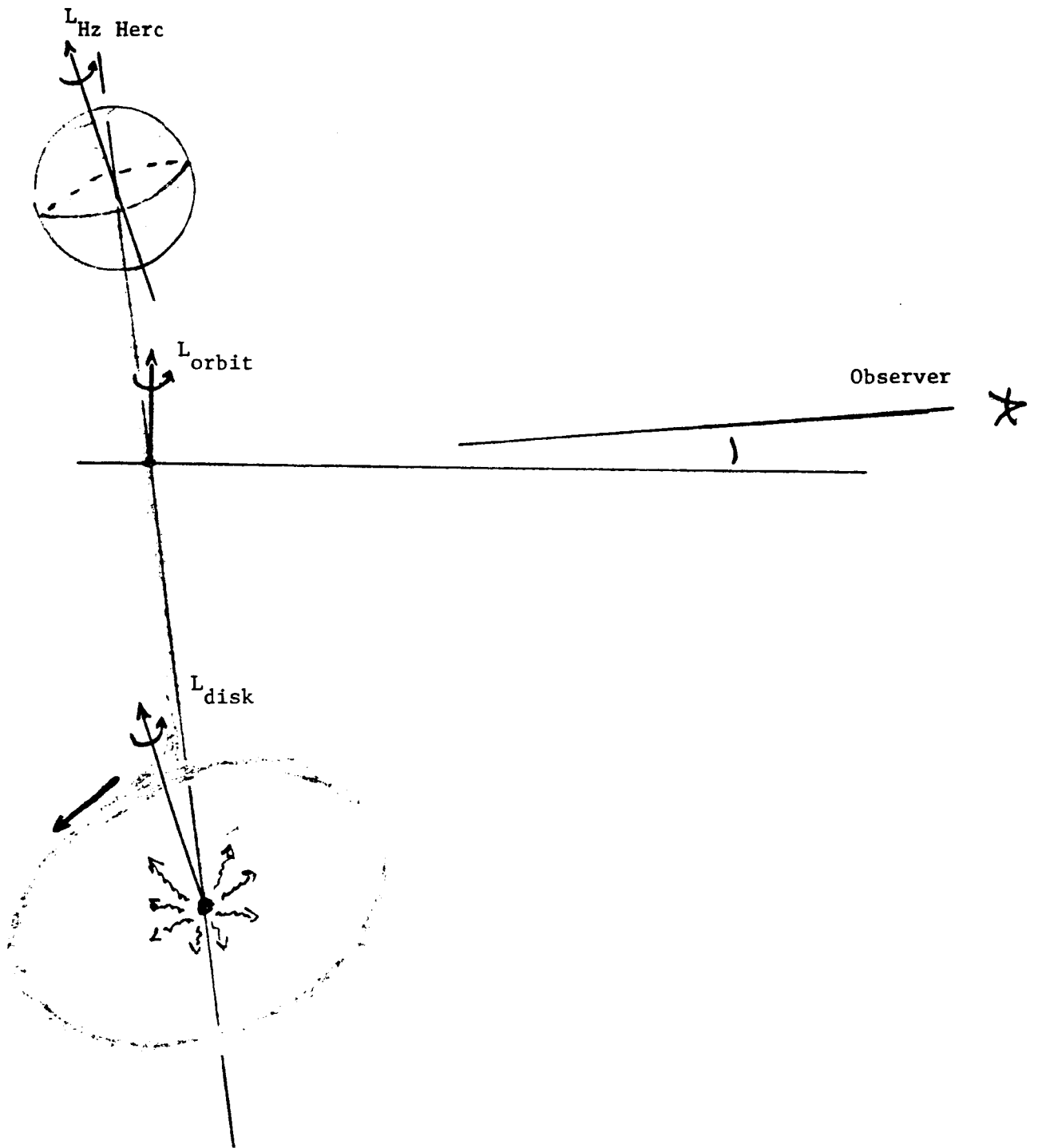


Figure 1: Herc X-1 crosses the orbital plane of Hz Herc and mass is transferred to the outer edge of the accretion disk. Precession is opposite to the direction of orbital motion.

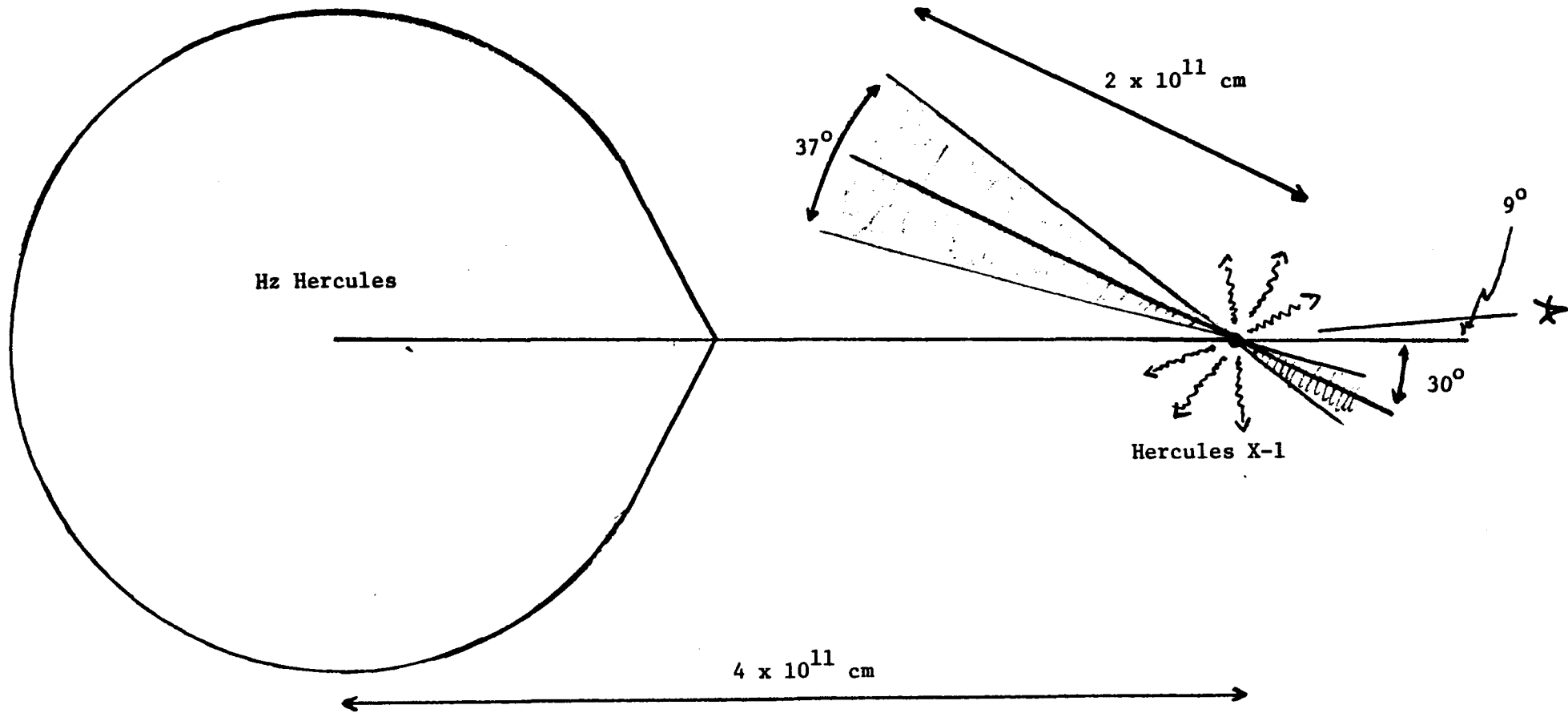
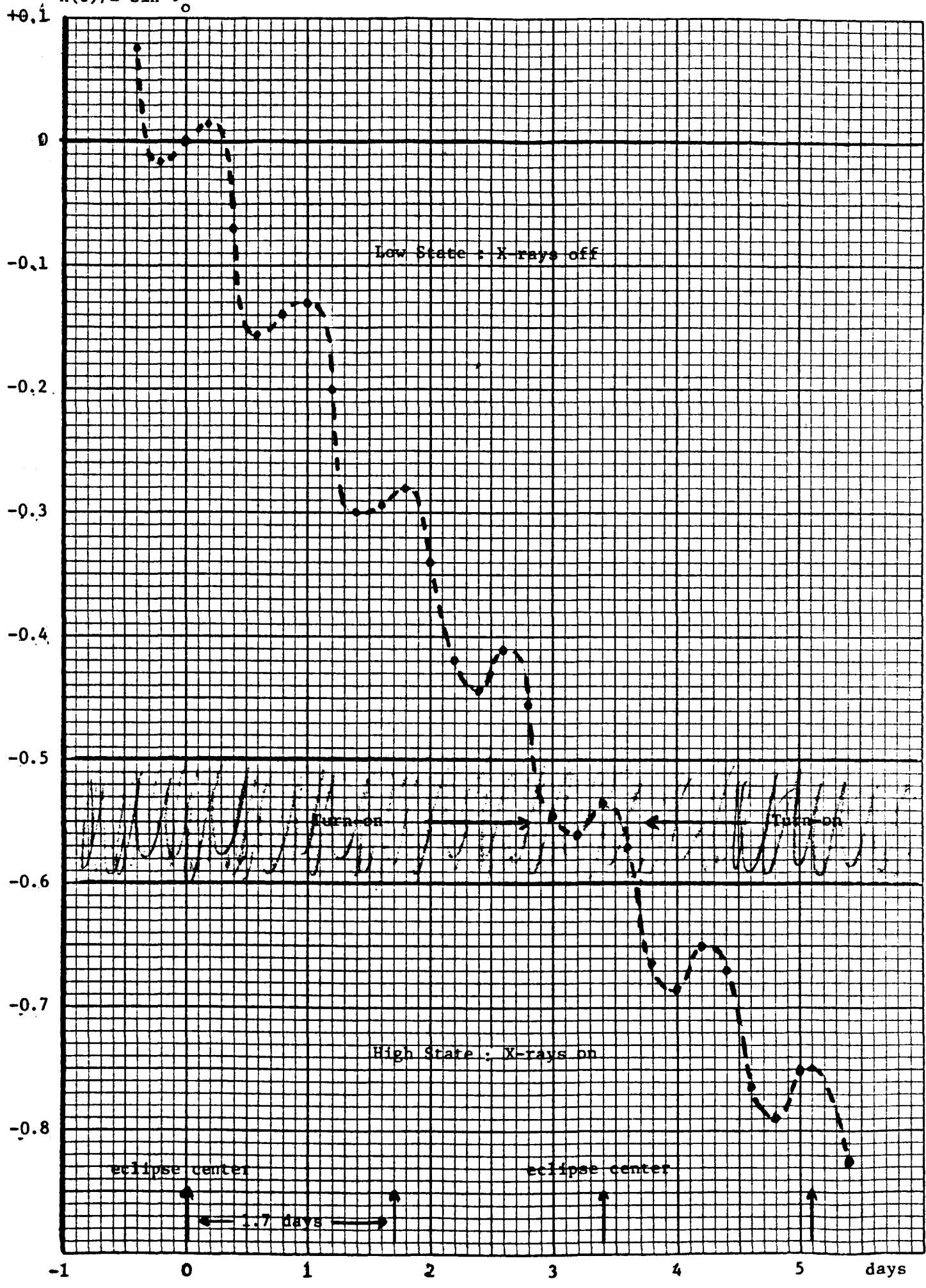


Figure 2: Accretion disk geometry implied by the optical observations of Hz Herc and the pulsed x-rays from Herc X-1.

46 0782

K·E 10 X 10 TO THE INCH 0.7 X 10 INCHES KEUFFEL & ESSER CO. MADE IN U.S.A.



EFFECTS OF THE KELVIN-HELMHOLTZ SURFACE INSTABILITY ON SUPERSONIC JETS

by

Philip E. Hardee

Department of Physics and Astronomy

The University of Alabama

and

NASA/Space Sciences Laboratory

Marshall Space Flight Center, Alabama

Submitted to The Astrophysical Journal

XIX-11

Abstract

We have performed an exact numerical calculation of the linear growth and phase velocity of Kelvin-Helmholtz unstable wave modes on a supersonic jet of cylindrical cross section. An expression for the maximally unstable wavenumber of each wave mode is found. Provided a sharp velocity discontinuity exists all wave modes are unstable. A combination of rapid jet expansion and velocity shear across a jet can effectively stabilize all wave modes. The more likely case of slow jet expansion and of velocity shear at the jet surface allows wave modes with maximally unstable wavelength longer than or on the order of the jet radius to grow. The relative energy in different wave modes and effect on the jet is investigated. Energy input into a jet resulting from surface instability is discussed.

I. Introduction

It has been suggested that surface instabilities such as the Kelvin-Helmholtz instability generate internal turbulence in jets and radio sources which can serve to reaccelerate particles (Pacholczyk and Scott 1976) and Dobrowolny (1972) has shown that the Kelvin-Helmholtz instability generates MHD waves in a collisionless plasma. Several authors have assumed the existence of turbulence in the form of small amplitude MHD waves and used this to investigate particle acceleration. The wave spectrum was assumed to be a power law (Lacombe 1977; Ferrari, Trussoni and Zaninetti 1979) or related to the growth rate of surface instabilities (Eilek 1979). The MHD waves were found to heat the fluid and accelerate particles but did not lead to an appropriate particle energy distribution or emission spectrum if radiative losses were included. These calculations also assumed a uniform input of wave energy throughout a source but energy input at the surface implies that wave energy is not uniformly distributed. This last problem has been addressed by Eilek (1982) who finds that energy input restricted to a thin surface layer produces a turbulent edge in MHD waves and strong limb brightening can occur. However, observed radio jets do not appear to be strongly limb brightened. A partial resolution of these problems may be found through investigation of the behavior of perturbations to a jet surface which is Kelvin-Helmholtz unstable.

Supersonic jets in pressure balance with an external medium are unstable to surface perturbations analogous to the Kelvin-Helmholtz instability of a vortex sheet (Ferrari, Trussoni and Zaninetti 1978; Hardee 1979; Ray 1981). Growing perturbations of long maximally unstable wavelength are pinching and helical wave modes and previous work has provided estimates of wave phase velocity and maximum rate of growth (Ray 1981; Hardee 1982). In addition to

these wave modes a cylindrical jet with sharp velocity discontinuity is unstable to an infinite number of other wave modes with shorter maximally unstable wavelength and more rapid rate of growth. These growing waves convert directed flow energy into wave energy in the jet and external medium. Because initial growth of surface perturbations is rapid several authors have investigated ways of slowing the rate of growth and stabilizing a jet. The maximum rate of growth is decreased as the amplitude of a helical wave increases (Benford 1981) and growth of perturbations to the jet surface can be linear rather than exponential if a jet expands rapidly enough (Hardee 1982). Short wavelength perturbations to a jet surface can be stabilized by the presence of a velocity shear between jet and external medium (Ray 1982). While it may be possible to completely stabilize a jet by a combination of jet expansion and velocity shear, true jet conditions are not yet well known and it seems likely that some instability will be present. For this reason we must consider the behavior of long and short wavelength perturbations to a jet and consider the effect of the resulting growing wave modes on a jet.

In this paper we will proceed by calculating exactly the wave phase velocity, growth rate and maximally unstable wavelength of Kelvin-Helmholtz unstable eigenmodes on a jet of cylindrical cross section. Both jet and external medium are assumed to be isothermal (see Hardee 1982, hereafter H II). The estimates made in H II for pinching and helical wave modes are confirmed and the work is extended to the wave modes describing perturbations of shorter wavelength. Stabilization of these wave modes is investigated. The depth interior to the jet surface affected by a wave mode is derived and relative energy input into a jet is estimated. The consequences for particle acceleration models are discussed.

II. Dispersion Relation and Eigenmodes

It was shown in HII that the wave modes which propagate along the surface of a jet of cylindrical cross section are eigenmodes of the dispersion relation

$$\frac{J'_n(k\Psi\xi_n) H_n^{(1)}(k\Psi\zeta_n)}{J_n(k\Psi\xi_n) H_n^{(1)'}(k\Psi\zeta_n)} \frac{\xi_n}{\zeta_n} = \gamma \eta \frac{(\phi - M_{in})^2}{\phi^2} \quad (1)$$

In equation (1) J_n is the Bessel function and $H_n^{(1)}$ is the Hankel function describing an outward propagating disturbance. The primes indicate derivatives with respect to the arguments of the Bessel and Hankel functions and the meaning of the symbols is

$$\xi_n \equiv \gamma [(\phi - M_{in})^2 - (1 - \frac{u^2/c^2}{M_{in}} \phi)^2 - \frac{n^2}{\gamma^2 k^2} + 2i(1 - \frac{u^2/c^2}{M_{in}} \phi)/\gamma k]^{1/2}$$

and

$$\zeta_n \equiv [\phi^2 - (1 + n^2/k^2 - 2i/k)v]^{1/2}/v^{1/2}$$

where

$$\phi = \omega/ka_{in} \quad M_{in} = u/a_{in} \quad \gamma = (1 - u^2/c^2)^{-1/2}$$

$$\eta = \frac{\rho_{in} + P_o/c^2}{\rho_{ex} + P_o/c^2} \quad v = a_{ex}^2/a_{in}^2$$

The subscript in or ex refers to quantities interior or exterior to the jet respectively. This dispersion relation is valid for jets of constant radius or expanding jets of instantaneous radius $R = r \Psi$ where r is the distance from the origin and $\Psi \equiv \sin \Theta$ where Θ is one half the jet opening angle. In this notation $k\Psi = k_{ex} R$ is the wavenumber normalized to the instantaneous jet radius and $k_{ex} = 2\pi/\lambda$ is the wavenumber. Eigenmodes of the dispersion relation are wave modes with $n = 0, 1, 2 \dots$. A wave mode propagates along the jet surface with form $A = A_n \exp [i(k_{ex} r + n\phi - \omega t)]$.

The $n = 0$ wave mode pinches a jet and the $n = 1$ wave mode helically distorts a jet. In HII it was shown that these two wave modes were maximally unstable at wavelengths $\lambda_0^{(p)} \sim 0.6(M_{in}/\eta)^{1/3}R$ and $\lambda_1^{(p)} \sim 1.6(M_{in}/\eta)^{1/3}R$. The wave mode characterized by $n = 2$ distorts a jet in an elliptical shape; the wave mode characterized by $n = 3$ distorts a jet in a triangular shape, etc.. For convenience we will call all wave modes with $n > 1$, fluting wave modes. These waves will not alter the jet cross section appreciably like the $n = 0$ wave mode or move the jet axis transversely like the $n = 1$ wave mode.

We expect fluting wave modes to be maximally unstable at some wavelength $\lambda_n^{(p)}$ just as we found for the $n = 0$ and $n = 1$ wave modes. To see that this must be the case we take equation 1 and write it in the following form

(Appendix B of HII)

$$\gamma^2 \eta \frac{(\phi - M_{in})^2}{\phi^2} = \frac{\xi_n}{\zeta_n} \frac{[\frac{n}{k\Psi\xi_n} - J_{n+1}(k\Psi\xi_n)/J_n(k\Psi\xi_n)]}{[-\frac{n}{k\Psi\zeta_n} + H_{n-1}^{(1)}(k\Psi\zeta_n)/H_n^{(1)}(k\Psi\zeta_n)]} \quad (2)$$

When $n/k\Psi\xi_n \gg 1$ and $n/k\Psi\zeta_n \gg 1$ equation (2) is easily seen to become

$$\gamma^2 \eta \frac{(\phi - M_{in})^2}{\phi^2} \sim -1 \quad (3)$$

This expression is just the usual expression for Kelvin-Helmholtz instability of a vortex sheet:

$$\omega \sim \left[\frac{\gamma^2 \eta}{1 + \gamma^2 \eta} \pm i \frac{\gamma \eta^{1/2}}{1 + \gamma^2 \eta} \right] k u. \quad (4)$$

We can see that the small wavenumber approximation used to obtain equation (4) remains valid to larger wavenumbers as n is increased. Thus we expect equation (4) to adequately describe the growth and propagation of waves with higher n to larger wavenumber, and we expect faster growth at shorter wavelength as n is increased. We can show that a maximally unstable wavenumber must exist by examining equation (1) in the limit $n/k\psi\xi_n \ll 1$ and $n/k\psi\zeta_n \ll 1$. In this limit equation (1) can be written (Appendix B of HII) in the following form

$$e^{2i\chi_n} \sim \frac{[\phi^2\xi_n + \gamma^2\eta(\phi - M_{in})^2\xi_n + i\frac{n}{k\psi}[\gamma^2\eta(\phi - M_{in})^2 + \phi^2]}{[\phi^2\xi_n - \gamma^2\eta(\phi - M_{in})^2\xi_n - i\frac{n}{k\psi}[\gamma^2\eta(\phi - M_{in})^2 + \phi^2]} \quad (5)$$

where $\chi_n \equiv k\psi\xi_n - \frac{(2n+1)}{4}\pi$.

If we take the natural logarithm of equation (5) then

$$\xi_n \sim \left[\frac{2n+1}{4}\right] \frac{\pi}{k\psi} - \frac{1}{2k\psi} A^{(n)} \quad (6)$$

where $A^{(n)}$ is the logarithm of the right hand side of equation (5). If equation (6) is squared and we use $\xi_n \sim [(\phi - M_{in})^2 - 1]^{1/2}$ and assume that $A_R^{(n)} \gg A_I^{(n)}$ where $A_R^{(n)}$ and $A_I^{(n)}$ are the real and imaginary points of $A^{(n)}$, respectively, it follows that

$$\phi \sim (M_{in} - 1) - i \frac{(2n+1)\pi}{8k^2\psi^2} A_R^{(n)} \quad (7)$$

We need to point out an error in equations (14) and (22) in HII in which the imaginary part needs to be multiplied by a factor of 2. For $\phi_R \lesssim M_{in} - 1$ we

find that $A_R^{(n)} < 0$ and all wave modes are unstable but with rapidly decreasing growth rate as the wavenumber becomes larger. Thus a maximally unstable wavenumber must exist. At a given wavenumber we see that the growth rate in equation (7) becomes larger as n increases.

The maximally unstable wavenumber, maximum growth rate and wave phase velocity of the different wave modes cannot be obtained analytically. We have found exact solutions to equation (1) numerically. In figure 1 we plot the growth rate $\omega_I R$ in cm sec^{-1} , where R is instantaneous jet radius as a function of the normalized wavenumber $k\Psi = 2\pi R/\lambda$ for wave modes n equal 0 through 5 and 7 and 9. The calculations assume a jet 10 times denser than the surrounding medium, $\eta = 10$, that the jet velocity $u = 9 \times 10^8 \text{ cm s}^{-1}$, that $M_{in} \equiv u/a_{in} = 9.9$, and that the jet is expanding with an opening angle $2\theta = 0.08$ radian. We find that the maximally unstable wavenumber is not sensitive to jet opening angle. These exact results when combined with the density and Mach number dependence of the maximally unstable wavenumber from HII which is valid when $\eta > 1$ and $M_{in} \gg 1$ show that

$$k_n^{(p)} \Psi \sim 1.9 \left(n + \frac{1.1}{n^{3/2} + 0.2} \right) (\eta^{1/3} / M_{in}) \quad (8)$$

At large n , $k_n^{(p)} \Psi \sim 1.9n(\eta^{1/3} / M_{in})$. The asymptotic expression is accurate to 10% when $n=3$.

The corresponding relationship for the wavelength is

$$\lambda_n^{(p)} \sim 3.3 \left[\frac{M_{in} / \eta^{1/3}}{n + 1.1 / (n^{3/2} + 0.2)} \right] R \quad (9)$$

For n less than 3 we have that $\lambda_0^{(p)} \sim 0.6 (M_{in} / \eta^{1/3}) R$, $\lambda_1^{(p)} \sim 1.7 (M_{in} / \eta^{1/3}) R$ and $\lambda_2^{(p)} \sim 1.4 (M_{in} / \eta^{1/3}) R$. For larger values of n , $\lambda_n^{(p)} \sim 3.3n^{-1} (M_{in} / \eta^{1/3}) R$ is accurate to better than 10%. The values of $\lambda_0^{(p)}$ and $\lambda_1^{(p)}$ found here are in excellent agreement with the estimates given in HII.

The phase velocity of the different wave modes normalized to the jet velocity u as a function of the normalized wavenumber is shown in figure 2. At wavenumbers much less than the maximally unstable wavenumber the phase velocity, v_{ph} , approaches u or $[\gamma^2\eta/(1+\gamma^2\eta)]u$ for the $n = 0$ and $n > 0$ wave modes, respectively. At wavenumbers much larger than the maximally unstable wavenumber the phase velocity approaches $u - a_{in}$ for all $n \geq 0$. For the $n = 0$ wave mode the minimum phase velocity occurs at wavenumber larger than the maximally unstable wavenumber. The phase velocity at the maximally unstable wavenumber is $v_{ph} \sim u - a_{in}$. This is the result for a small amplitude wave driven by the Bernoulli effect. Larger amplitudes will develop only for smaller wavenumbers and higher phase velocities and any large scale jet pinching should develop with wavelength greater than $\lambda_0^{(p)}$. For all other wave modes the minimum phase velocity occurs near the maximally unstable wavenumber. In general, when $n \geq 1$ we may assume that the dominant wavenumber and wavelength associated with a particular wave mode is within 10% of the value given by equations (8) and (9). We note that the reduction in phase velocity seen at the dominant wavenumber implies more rapid spatial growth than if the phase velocity remained between $[\gamma^2\eta/(1+\gamma^2\eta)]u$ and $u - a_{in}$ as assumed in HII. For $n = 1$ the minimum phase velocity is about 10% less than the value predicted using equation (4). This suggests that spatial growth of the helical wave is 10% faster than was estimated in HII. For other wave modes as n becomes larger the maximum growth rate approaches that predicted using equation (4) with $k = k_n^{(p)}$ and v_{ph} is reduced significantly below that predicted using equation (4) with result that spatial growth is somewhat more rapid than would be predicted using equation (4).

While this result depends on M_{in} and η we find no large change as M_{in} and η are varied. As a consequence when n is sufficiently large, we expect initial wave mode growth at small wave amplitude to be approximated by equation (4) until non-linear effects at larger amplitude become important. Of course, if jet expansion is rapid enough the wave remains in the small amplitude limit and spatial growth is linear as the maximally unstable wavelength increases proportional to $R = r\Psi$ (see HII).

III. Jet Application

Jet expansion can serve to stabilize the wave modes which are maximally unstable at longer wavelength. To see that this cannot be the case for wave modes that are maximally unstable at shorter wavelength recall that $v_{ph} < [\gamma^2 \eta / (1 + \gamma^2 \eta)] u$ and $\omega_I \leq [\gamma \eta^{1/2} / (1 + \gamma^2 \eta)] 2\pi u / \lambda_n^{(p)}$ for all wave modes with $n \geq 1$. We define a spatial growth length as $\ell_e = v_{ph} \tau_e$ where $\tau_e = \omega_I^{-1}$. If we use equation (4) exactly to obtain v_{ph} and ω_I and use $\lambda_n^{(p)} \sim 3.3 n^{-1} (M_{in} / \eta^{1/3}) R$ then $\ell_e \sim 0.52 n^{-1} \eta^{1/6} M_{in} R$. This value of the spatial growth length is sufficiently accurate for our purposes and exact calculation shows the numerical factor is only a weak function of n . Wave amplitude grows as $A = A_0 e^{(r/\ell_e)}$ where r is distance along the jet surface. For an expanding jet $R = r\Psi$ and $(r/\ell_e) \sim 1.9 n / (\eta^{1/6} M_{in} \Psi)$. While the growth rate and phase velocity of growing perturbations will change as wave amplitude increases it is certain that a large value of (r/ℓ_e) implies that large wave amplitudes can occur. For our particular choice of parameters $(\eta^{1/6} M_{in} \Psi) \sim 0.85$ and $(r/\ell_e) \sim 2.2 n$. It is clear that the helical wave mode ($n = 1$) can be restricted to only a few e-folding lengths but this is not the case for $n > 1$. While somewhat more rapid jet expansion is of some help we point out that $M_{in} \Psi < 1$ for a jet in

pressure balance with the external medium. A jet in free expansion with $M_{in} \sim 1$ is stabilized by virtue of its expansion at the sound speed which restricts surface instability to a thin surface region.

If a jet is in pressure balance with an external medium the only way to stabilize the jet surface to wave modes with shorter wavelengths is by velocity and density shear. For a linear velocity shear layer Ray (1982) finds that waves with wavenumber $k \geq 1.28 h^{-1}$ where h is the scale height of the shear layer are stabilized. To apply this result to a cylindrical jet we need to determine the true wavelength of a wave mode at maximum growth. The true wavelength is always less than the wavelength λ at constant angle ϕ (cylindrical or spherical geometry). Figure 3 illustrates the propagation geometry of wave modes on a cylindrical jet of constant cross section. The true wavelength between wave fronts is given by $\Lambda_n = \{ [2\pi R/n] / [(2\pi R/n)^2 + \lambda_n^2]^{1/2} \} \lambda_n$. The true maximally growing wavelength for a wave mode and therefore the true characteristic wavelength of a wave mode is

$$\Lambda_n^{(p)} = \{ [2\pi R/n] / [(2\pi R/n)^2 + \lambda_n^{(p)2}]^{1/2} \} \lambda_n^{(p)} \quad (10)$$

This relation is modified only slightly by jet expansion (see figure 1 in HII) and may be used with confidence with R being the instantaneous jet radius. The stability criterion can be written $\Lambda \leq 4.91 h$. If, for example, the depth of a shear layer were $R/4$ then $\Lambda \leq 1.2 R$ would be stabilized. It is informative to rewrite the stability condition in terms of λ and we find that wavelengths

$$\lambda_n > \lambda_n^{\min} = 2\pi n^{-1} [(1.28R/nh)^2 - 1]^{-1/2} R \quad (11)$$

are unstable and shorter wavelengths are stabilized. Immediately we see that wave modes with $n > 1.28 R/h$ must be completely stabilized. This occurs because no matter the wavelength λ_n for these wave modes, the true wavelength Λ_n is less than the minimum unstable wavelength. Since the maximum

depth of the shear layer is $h = R$ for a cylindrical jet it would not appear possible to stabilize the $n = 1$ helical wave mode by velocity shear. However, it is likely that only wave modes with small n , say $n < 10$, will be unstable. For example, using the parameters $\eta = 10$, $M_{in} = 9.9$ and $h = R/4$ we find $\lambda_1^{(p)} \sim 7.8R > \lambda_1^{\min} = 3.1R$, through $\lambda_4^{(p)} \sim 3.8R > \lambda_4^{\min} = 3.0R$ but $\lambda_5^{(p)} \sim 3.0R < \lambda_5^{\min} = 8.1R$. The maximum rate of growth of the wave mode $n = 5$ is reduced to about that of the $n = 2$ wave mode (see figure 1) and will actually be reduced to less than this if full effects of a shear layer are included (see Ray 1982). Wave modes with $n > 5$ would be absolutely stable. We conclude that only a few wave modes will be unstable on an expanding jet with significant velocity shear.

The observational consequences of the $n = 1$ helical wave mode have already been discussed in detail in HII. It is now necessary to consider the effect of the remaining unstable wave modes on the jet material. The effect of shorter wavelength wave modes on the jet material will be limited by the portion of a jet affected by a surface wave. For a jet of cylindrical cross section the displacement amplitude of jet material interior to the jet surface is given by (HII equation A18)

$$\eta(\theta) = \frac{1}{r} \left[\frac{\rho_{in} a_{in}^2}{\omega_{in}^2 (\rho_{in} + P_o/c^2)} \right] \beta_n^{in} \cos \theta \frac{J_n'(\beta_n^{in} \psi)}{J_n(\beta_n^{in} \psi)} \quad (12)$$

In equation 12 $\beta_n^{in} \equiv k \xi_n$ and spherical geometry is assumed. At the jet surface $\theta = \Theta$ and $\psi = \Psi$. To obtain the amplitude as a function of jet radius we form the ratio

$$\eta(\theta)/\eta(\Theta) = \frac{\cos \theta}{\cos \Theta} \frac{J_n'(\beta_n^{in} \psi)}{J_n'(\beta_n^{in} \Psi)} \quad (13)$$

where $\rho_{in}(\theta)/\rho_{in}(\Theta) = J_n(\beta_n^{in} \psi)/J_n(\beta_n^{in} \Psi)$. Equation (13) can be used to obtain an estimate of the depth affected by each wave mode n .

Provided $n \geq 2$ the characteristic wavenumber for each wave mode can be approximated by $k_n^{(p)} \Psi \sim 1.9n (\eta^{1/3}/M_{in})$ with acceptable accuracy. The arguments of the Bessel functions in equation 13 are proportional to n and we may use the following approximation for the Bessel function:

$$J_n(nz) \sim \left(\frac{4\chi}{1-z^2}\right)^{1/4} \text{Ai}(n^{2/3}\chi)/n^{1/3} \quad (14)$$

where Ai is the Airy function and

$$\frac{2}{3}\chi^{3/2} = \ln \frac{1+\sqrt{1-z^2}}{z} - \sqrt{1-z^2}$$

or

$$\frac{2}{3}(-\chi)^{3/2} = \sqrt{z^2-1} - \arccos(1/z)$$

so χ is real when z is positive (Abramowitz and Stegun 1964). In equation (14) $z = 1.9 (\eta^{1/3}/M_{in})(\psi/\Psi) \xi_n$. If we use equation (4) for $\Phi = \frac{\omega}{ka_{in}}$ at $k_n^{(p)}$ and the fact that $M_{in} \gg 1$ for a supersonic jet it follows that

$$\xi_n \sim \begin{cases} M_{in} & \eta \ll 1 \\ iM_{in}/\eta^{1/2} & \eta \gg 1 \end{cases}$$

As a result we find

$$z \sim \begin{cases} 1.9 \eta^{1/3} (\psi/\Psi) & \eta \ll 1 \\ 1.9 i \eta^{-1/6} (\psi/\Psi) & \eta \gg 1 \end{cases}$$

and in general $|z| < 1$. When $|z|$ is small $\chi \sim (-\frac{2}{3} \ln(2/z) - 1)^{2/3}$, $\text{Ai}(n^{2/3}\chi) \sim \frac{1}{2} \pi^{-1/2} (n^{2/3}\chi)^{-1/4} \exp[-\frac{2}{3} n\chi^{3/2}]$ and $4\chi/(1-z^2) \sim 4\chi(1+z^2)$ can be used with result that

$$J_n(nz) \sim \frac{1}{\sqrt{2\pi n}} \left(\frac{ez}{2}\right)^n \quad (15)$$

Because $J_n'(nz) = \frac{1}{z} J_n(nz) - J_{n+1}(nz) \sim J_n(nz)/z$ it follows that

$$J_n'(nz) \sim \frac{(e/2)^n}{\sqrt{2\pi n}} z^{n-1} \quad (16)$$

The approximate form of the derivative of the Bessel function inserted in equation (13) results in the following relation between the displacement amplitude at the jet surface and inside the jet:

$$\eta(\theta)/\eta(\theta) \sim \frac{\cos \theta}{\cos \theta} \left(\frac{\psi}{\Psi}\right)^{n-1} \quad (17)$$

Equation (17) implies that the wave amplitude interior to the jet surface is

$$A_n \sim A_n^R (b/R)^{n-1} \quad (18)$$

where A_n^R is the surface amplitude and $0 \leq b \leq R$ where b is the radial distance inside the jet. The lack of radial dependence of the $n = 1$ helical wave mode results because the entire jet is displaced.

If conditions are such that $(r/\ell_e) \gg 1$ for a wave mode then it is reasonable to assume that the wave amplitude at the jet surface has grown to its maximum. While maximum amplitudes and associated fluid motions need to be determined by numerical simulation, ordered displacement of the jet surface is limited to motion of the fluid at the sound speed transverse to the flow velocity. Wave modes with $n \geq 1$ appear as sinusoidal displacement of the jet surface $\eta(r) = A_n^R \sin(2\pi r/\lambda_n^{(p)})$ at fixed angle ϕ . The maximum amplitude of such a sinusoidal oscillation is $A_n^R \sim \frac{1}{2\pi} \lambda_n^{(p)} \left[\frac{a_{in}}{u - v_{ph}} \right]$ where $u - v_{ph}$ is the fluid velocity in the wave frame. Because v_{ph} at $\lambda_n^{(p)}$ is only a weak function of n , $A_n^R \propto n^{-1}$. The energy in each wave mode is proportional to $\Delta M (\Delta u)^2$ where ΔM is the jet material participating in motion at velocity Δu . If we continue to assume that $\Delta u \sim a_{in}$ at the jet surface then $\Delta u \propto (b/R)^{n-1}$ independent of $\lambda_n^{(p)}$. To the extent that wave modes are

independent and all of the jet material is involved, the energy in a wave mode interior to the jet surface is $E_n \propto (b/R)^{2(n-1)}$. The total wave energy interior to the jet surface is of the form

$$E \sim E_0 \sum_n \alpha_n (b/R)^{2(n-1)} \quad (19)$$

A fundamental scale size of $\Lambda_n^{(p)}$ exists for each term in the summation and α_n is a weak function of $\Lambda_n^{(p)}$. An upper limit to the summation is set by the depth of the shear layer and a lower limit may be set by jet expansion. Near the upper and lower limits α_n must decrease rapidly. Near the upper limit wave growth is slowed because the fundamental scale size is shifted to longer wavelength and at the lower limit wave growth is slowed and maximum wave amplitude is not reached.

IV. Discussion

Each unstable wave mode can be regarded as driving the jet surface at a length scale $\Lambda_n^{(p)}$ and a frequency $v_{ph}/\Lambda_n^{(p)} = (u - v_{ph})/\lambda_n^{(p)}$. If $\Lambda_n^{(p)}$ is less than the jet diameter it is likely that eddies of size $\Lambda_n^{(p)}$ can be created in the jet fluid. Dissipation in the jet fluid leads to a cascade to eddies of smaller size with a Kolmogorov energy spectrum $W_k = k^{-5/3}$ and with the smallest eddy size governed by dissipation processes in the fluid (Landau and Lifschitz 1959). Wave modes with $\Lambda_n^{(p)}$ larger than the jet diameter cannot generate eddies in the jet and must affect the flow in a more global sense. If we consider $\eta = 10$ and $M_{in} = 9.9$ we find that $\Lambda_1^{(p)} = 4.9 R$, $\Lambda_2^{(p)} = 2.8 R$ and $\Lambda_{n \geq 3}^{(p)} = 5.8 n^{-1} R$. In this case the helical and elliptical wave modes cannot produce eddies in the jet material without disrupting the flow. These wave modes must dissipate jet energy in the external medium and jet by heating of the fluid (Benford 1981). However, each unstable wave mode with $n \geq 3$ can produce eddies in the jet material. Other values of η and M_{in} can reduce $\Lambda_1^{(p)}$ and $\Lambda_2^{(p)}$ to less than a jet diameter. To the extent that each wave mode is independent, each drives a fundamental eddy size with total energy associated with each wave mode given by the appropriate term in equation (19). Wave modes which produce eddies in the jet dissipate energy at a rate $\sim (\Delta u)^3 / \Lambda_n^{(p)}$ (Landau and Lifschitz 1959). The dissipation rate increases as the fundamental scale size decreases. If we continue to assume that $\Delta u \sim a_{in}$ at the jet surface independent of $\Lambda_n^{(p)}$, then energy input into the jet is of the form

$$\epsilon \sim \epsilon_0 \sum_n \beta_n (b/R)^{3(n-1)} \quad (20)$$

where $\beta_n \sim n \alpha_n$.

In equation (20) a lower limit to n is set when $\Lambda_n^{(p)}$ is greater than the jet diameter as dissipation is no longer through fluid turbulence driven at scale size $\Lambda_n^{(p)}$. Modifications to this simple relation will occur if wave modes strongly interact and if fluid turbulence generated at shorter $\Lambda_n^{(p)}$ propagates into the jet faster than perturbations at longer $\Lambda_n^{(p)}$ grow to large amplitude.

The effect of Kelvin-Helmholtz unstable surface waves on the jet interior and external medium is of fundamental importance to an understanding of observed jets. We have found that the presence of velocity shear may stabilize all but one or two of the long wavelength wave modes and that these long wavelength wave modes can be restricted to only a few e-folding lengths and small amplitude by jet expansion. If these conditions are met then we might expect that little of the flow energy would be dissipated in the external medium or internally in the jet because turbulence would be unlikely to develop. However, if the jet edge is relatively sharp then we expect a number of wave modes with $\Lambda_n^{(p)}$ less than the jet diameter and $(r/l_e) \gg 1$. The likely case would be one in which some wave modes with say $2 < n \leq 10$ grow rapidly and those of larger n are suppressed by velocity shear.

It is clear that restrictions on wave mode stability are likely to result in fundamental eddy sizes on the order of the jet radius or suppress the development of short wavelength wave modes and jet turbulence entirely. If wave amplitude is limited by motion of the jet surface at the sound speed then wave energy is proportional to $(\Delta u)^2 \sim u^2/M_{in}^2$ and can be a large or small fraction of the jet flow energy. Interestingly, if $M_{in} \gg 1$, velocity fluctuation in the jet material at the sound speed is a small fraction of the flow speed and the flow can appear well ordered in the observer frame. Even so, the flow would be characterized as strongly turbulent if 10% of the flow energy were converted to eddies in the jet frame.

Our present results suggest that surface instability can affect more than a thin surface layer and probably produces a Kolmogorov energy spectrum in fluid turbulence in a jet. Some of the wave energy converted into turbulence will simply heat the fluid through dissipation but the presence of magnetic field implies the generation of MHD waves (Kato 1968; Dobrowolny 1972). If the fluid is driven turbulent at a single wavenumber or only a narrow range of wavenumbers the MHD waves produced will have an energy spectrum $W_k \propto k^{-3/2}$ (Kraichnan 1965; DeYoung 1980). A Kolmogorov energy spectrum in fluid turbulence allows direct drive to MHD waves at many wavenumbers. The resulting MHD wave energy spectrum is not well determined but is probably as steep or steeper than Kolmogorov (Kato 1968; Henriksen and Eilek 1982). Whatever the exact spectrum, the MHD waves produced in this fashion no longer are confined to a thin surface region (see Eilek 1982) but can exist in a significant fraction of the jet volume with MHD wave energy proportional to the wave energy in fluid turbulence (see equation 19). This MHD turbulence can supply energy to an existing population of relativistic electrons and may produce the observed jet emission (Eilek and Henriksen 1981). Since MHD waves of the appropriate wavelengths for particle acceleration are strongly damped and do not travel far (Eilek 1982) the jet emissivity may be of the same form as equation (20). Such a jet emissivity should result in jets with intensity profiles flatter than if the emissivity were not a function of the jet radius.

Acknowledgments

I would like to thank both Jean Eilek and Dick Henriksen for valuable discussions about the generation of fluid turbulence and the coupling between fluid and MHD turbulence. This work was completed while the author was an NASA/ASEE Summer Faculty Fellow at the Marshall Space Flight Center.

References

- Abramowitz, M., and Stegun, I.A. 1965, Handbook of Mathematical Functions (New York: Dover).
- Benford, G. 1981, Ap.J., 247, 792.
- DeYoung, D.S. 1980, Ap.J., 241, 81.
- Dobrowolny, M. 1972, Phys. Fluids, 15, 2263.
- Eilek, J.A. 1979, Ap.J., 230, 373.
- Eilek, J.A. 1982, Ap.J., 254, 472.
- Eilek, J.A., and Henriksen, R.N. 1981, IAU Symposium 97, Extragalactic Radio Sources, ed. D. Heeschen and C. Wade (Dordrecht: Reidel).
- Ferrari, A., Trussoni, E., and Zaninetti, L. 1978, Astr. Ap., 64, 43.
- Ferrari, A., Trussoni, E., and Zaninetti, L. 1979, Astr. Ap., 79, 190.
- Hardee, P.E. 1979, Ap.J., 234, 47.
- Hardee, P.E. 1982, Ap.J., 257, 509.
- Henriksen, R.N., and Eilek, J.A. 1982, preprint.
- Kato, S. 1968, P.A.S.J., 20, 59.
- Kraichnan, R.H. 1965, Phys. Fluids, 8, 1385.
- Lacombe, C. 1977, Astr. Ap., 54, 1.
- Landau, L.D., and Lifschitz, E.M. 1959, Fluid Mechanics (New York: Pergamon).
- Pacholczyk, A.G., and Scott, J.S. 1976, Ap.J., 203, 313.
- Ray, T.P. 1981, M.N.R.A.S., 196, 195.
- Ray, T.P. 1982, M.N.R.A.S., 198, 617.

Address: Philip E. Hardee

Department of Physics and Astronomy

The University of Alabama

Box 1921

University, AL 35486

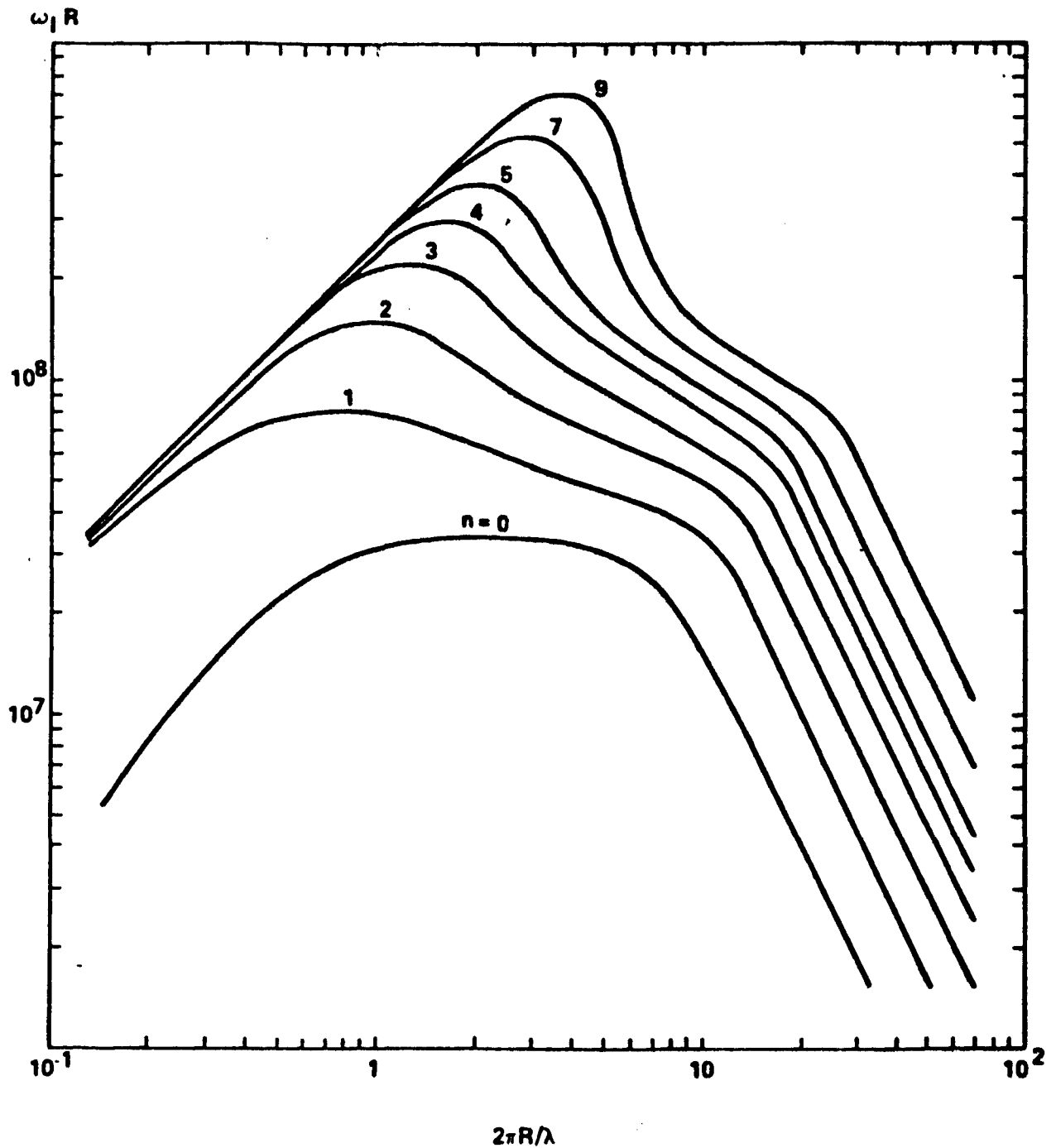


Figure 1: Wave mode growth rate $\omega_I R$ in cm sec^{-1} as a function of wavenumber normalized to the jet radius on a jet 10 times denser than the surrounding medium, Mach number of 9.9 and opening angle $2\theta = 0.08$ radian.

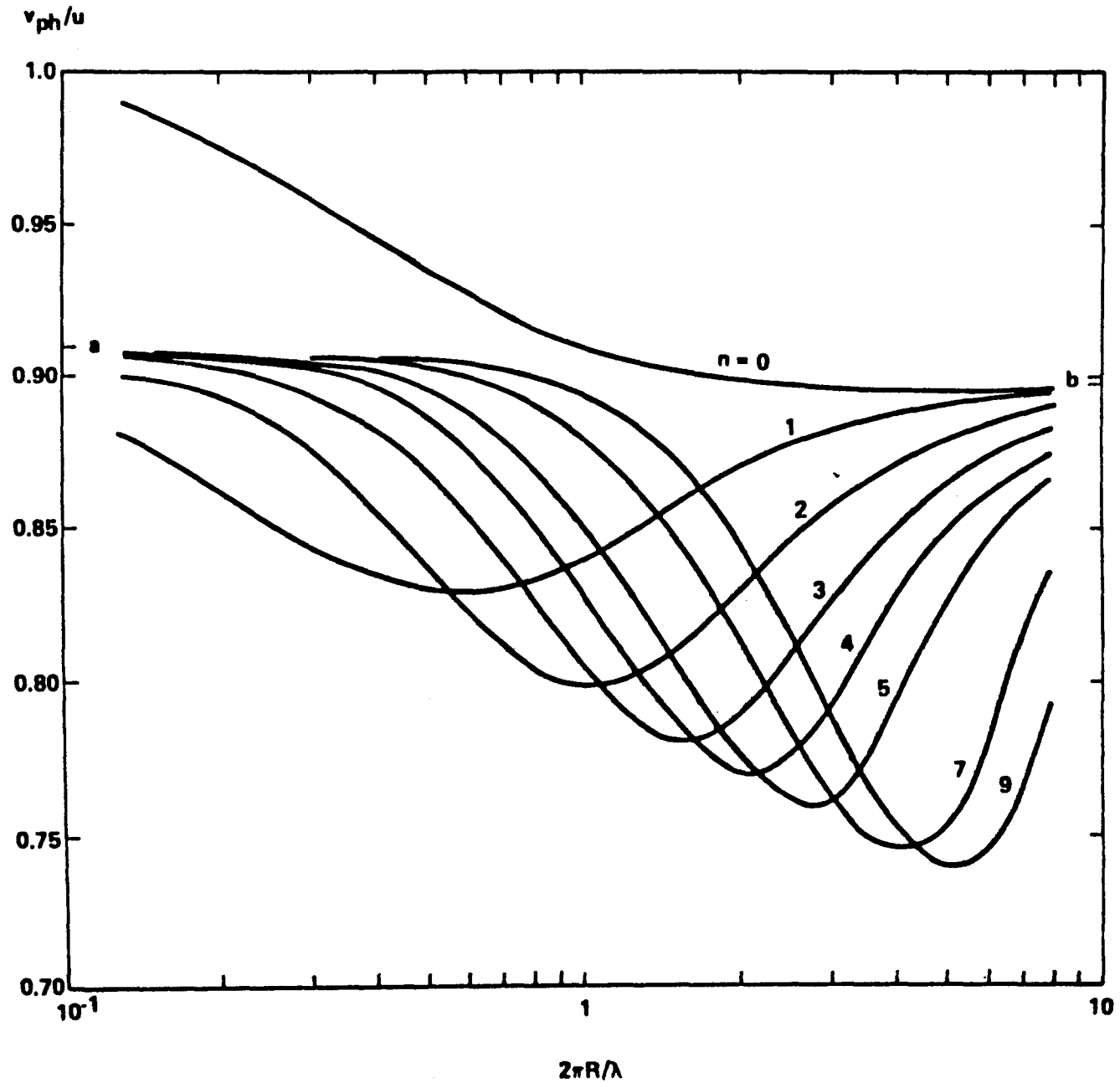


Figure 2: Wave mode phase velocity, v_{ph} , normalized to the jet velocity, u , as a function of the normalized wavenumber for the wave modes shown in Figure 1. The (a) indicates $v_{ph} = [\eta/(1 + \eta)]u$ and the (b) indicates $v_{ph} = u - a_{in}$.

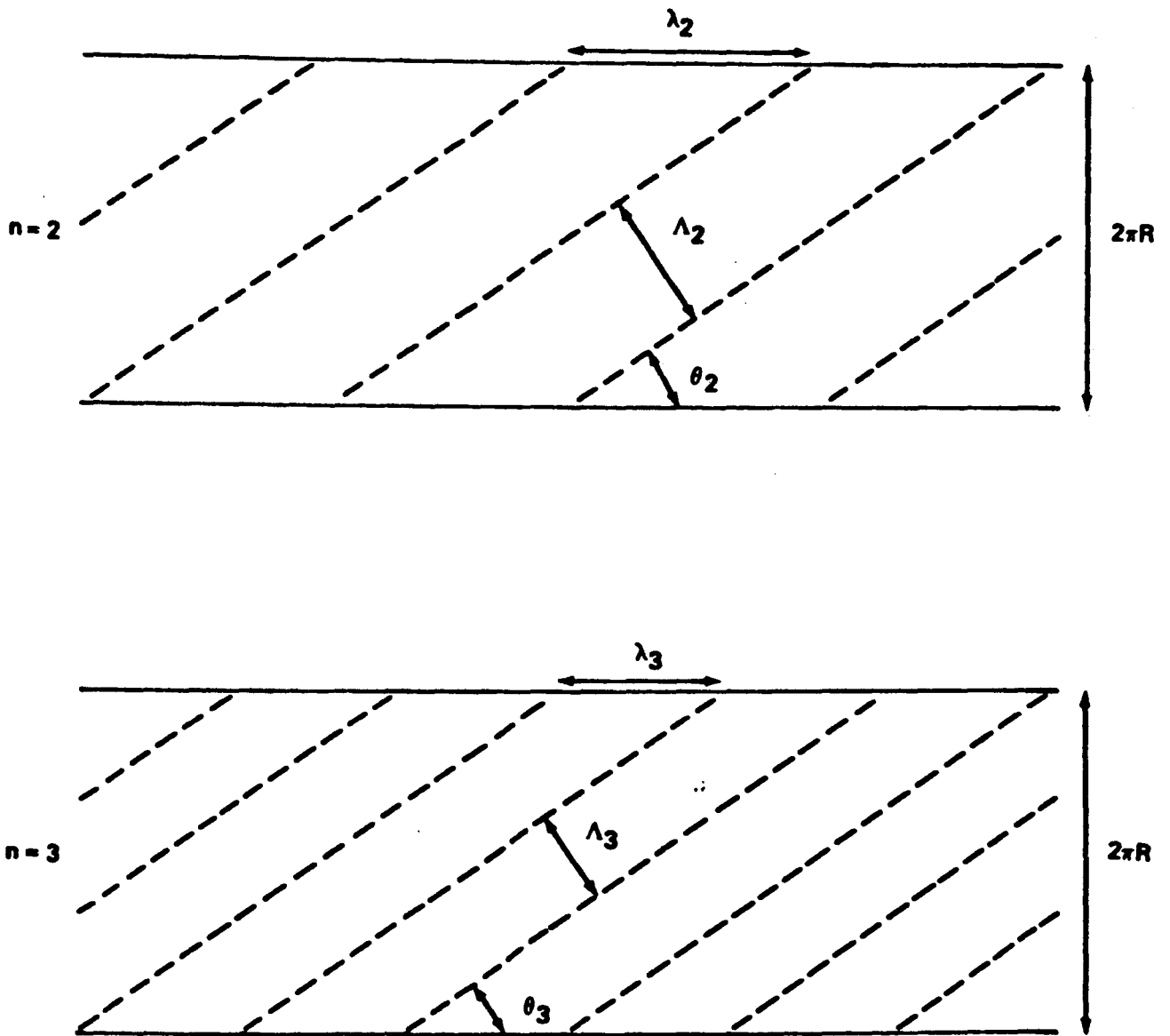


Figure 3. Propagation geometry of wave fronts (dashed lines) of wavemodes $n = 2$ and 3 around a cylindrical jet of circumference $2\pi R$ at equal propagation angle with respect to the flow velocity.

1982

NASA/ASEE SUMMER FACULTY RESEARCH FELLOWSHIP PROGRAM

MARSHALL SPACE FLIGHT CENTER
THE UNIVERSITY OF ALABAMA

FINITE ELEMENT ANALYSIS OF
A DEPLOYABLE SPACE STRUCTURE

PREPARED BY:	DAVID V. HUTTON, Ph. D.
ACADEMIC RANK:	ASSISTANT PROFESSOR
UNIVERSITY AND DEPARTMENT:	WASHINGTON STATE UNIVERSITY MECHANICAL ENGINEERING
NASA/MSFC:	
(LABORATORY)	SYSTEMS DYNAMICS
(DIVISION)	STRUCTURAL DYNAMICS
(BRANCH)	SYSTEMS ANALYSIS
MSFC COUNTERPART:	R. S. RYAN
DATE:	AUGUST 6, 1982
CONTRACT NUMBER:	NGT-01-002-099 (UNIVERSITY OF ALABAMA)

FINITE ELEMENT ANALYSIS OF
A DEPLOYABLE SPACE STRUCTURE

BY

David V. Hutton, Ph. D.
Assistant Professor of
Mechanical Engineering
Washington State University
Pullman, Washington 99164-2920

ABSTRACT

Development of a large-scale Space Station will require similarly large structural elements capable of assembly, fabrication, or deployment in space. Weight and volume constraints of the Space Shuttle orbiter payload bay make deployable structures with minimum on-orbit assembly requirements the favored alternative.

Current deployable structure concepts involve folding, three-dimensional trusses with automated deployment/retraction systems and having high deployed-to-stowed volume ratios. Such designs employ a large number of pin joints to allow the rotational motion required for deployability.

To assess the dynamic characteristics of a deployable space truss, a finite element model of the Scientific Applications Space Platform (SASP) truss has been formulated. The model incorporates all additional degrees of freedom associated with the pin-jointed members. Comparison of results with SPAR models of the truss show that the joints of the deployable truss significantly affect the vibrational modes of the structure only if the truss is relatively short.

LIST OF FIGURES

<u>Figure No.</u>	<u>Title</u>	<u>Page</u>
1	SADE Options	XX-5
2	SASP Ground Test Platform	XX-6
3	SASP Deployment	XX-7
4	Beam Element	XX-10
5	Element Matrices	XX-12
6	SASP Joint Displacements	XX-15
7	Comparison of Model Results	XX-18
8	SASP Parameter Studies	XX-19

INTRODUCTION

The Scientific Applications Space Platform (SASP) Truss is a deployable three-dimensional structure designed to be a building-block element in large space structures. The basic design unit of the SASP truss is a folding cell composed of two bays. When fully deployed each bay has the overall dimensions of a 1.4 meter cube. Theoretically, any number of cells can be joined end to end to create a deployable structure of any length. Alternatively, several independent trusses could be joined to create a composite platform in a variety of configurations such as a "T" shape, for example.

The Structural Assembly Demonstration Experiment (SADE), tentatively assigned to STS 28, includes the objectives of demonstrating shuttle capacity to build a large space structure on-orbit and validating truss design including deployment, assembly, and connectors. As an integral part of three of the five options under consideration for SADE (Figure 1), detailed analysis and testing of the dynamic characteristics of the SASP truss are required. For testing deployment characteristics, the SASP ground test platform (Figure 2) has been fabricated and deployment testing is currently underway. In addition, a mathematical model of deployment was developed by Stoll [1].

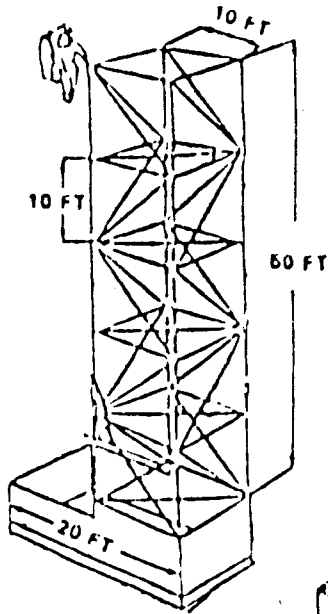
As the relatively low natural frequencies of vibration expected of such large structures could affect shuttle control, analysis of the modal characteristics of the various SADE options is needed. Subsequent articles of this report describe such an analysis for the SASP truss for several configurations using two different mathematical models.

THE SASP STRUCTURE

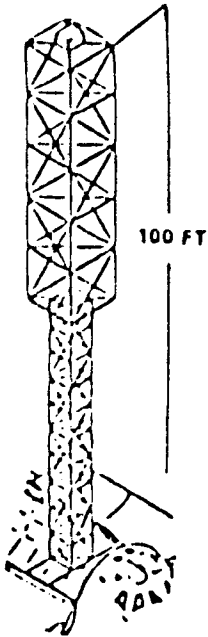
When retracted, the SASP truss resembles a tightly folded accordion with the longitudinal (longeron), diagonal, and transverse members aligned as depicted in Figure 3a. Deployability of the truss is made possible by the telescoping design of the main diagonals and the free rotational motion of certain of the structural members at the joints. In the retraction positions, the length of the telescoping diagonal members is approximately 2.6 meters (104 inches). A deployment cable is strung through the diagonals in sequence and passes across pulleys located at the folding joints and is rigidly attached to the terminal bay of the truss. For deployment, the cable is reeled in via a motor located at the fixed end of the truss. This action produces shortening and rotation of the telescoping diagonals as in Figure 3b. Simultaneously, the longerons rotate about pin connections (effectively) at each joint, and the transverse members execute pure translation in following the joint motion. In the fully deployed position, a locking mechanism on the telescoping diagonals is mechanically actuated, thus preventing further motion and locking each bay into its three dimensional truss configuration.

SADE OPTIONS

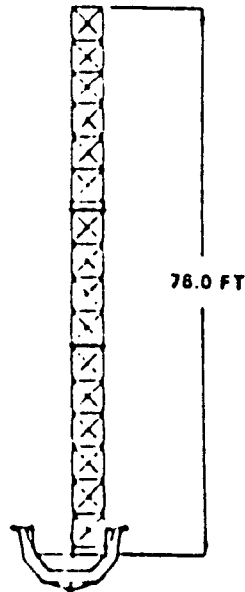
9-XX



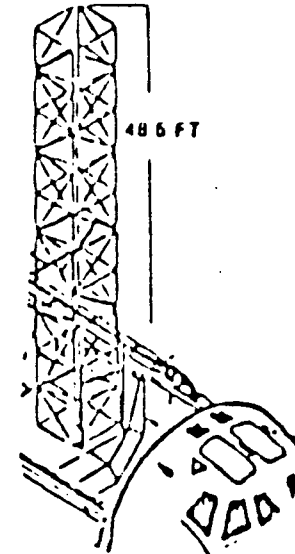
OPTION I
(VOUGHT TRUSS)



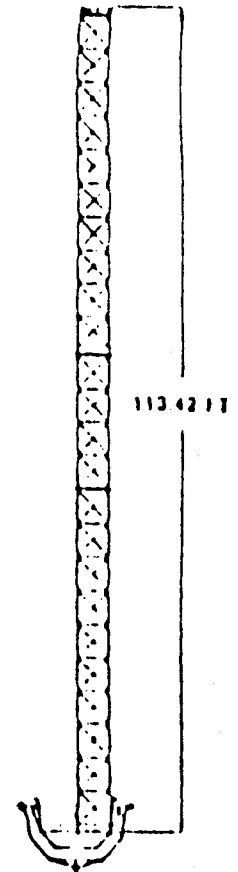
OPTION II
(VOUGHT/SASP TRUSS)



OPTION III
(SASP TRUSS)



OPTION I A
(SASP TRUSS)



OPTION III A
(SASP TRUSS)

FIGURE I

SASP DEPLOYABLE STRUCTURE GROUND TEST PLATFORM

CHARACTERISTICS:

- FULL SIZE PLATFORM HAS 10 BAYS
- DEPLOYED LENGTH = 14.1 M (10 BAYS)
- FOLDED LENGTH = 1.32 M
- FOLDED HEIGHT = 2.74 M
- WEIGHT = 632 LBS
- MATERIAL: 6061 ALUMINUM

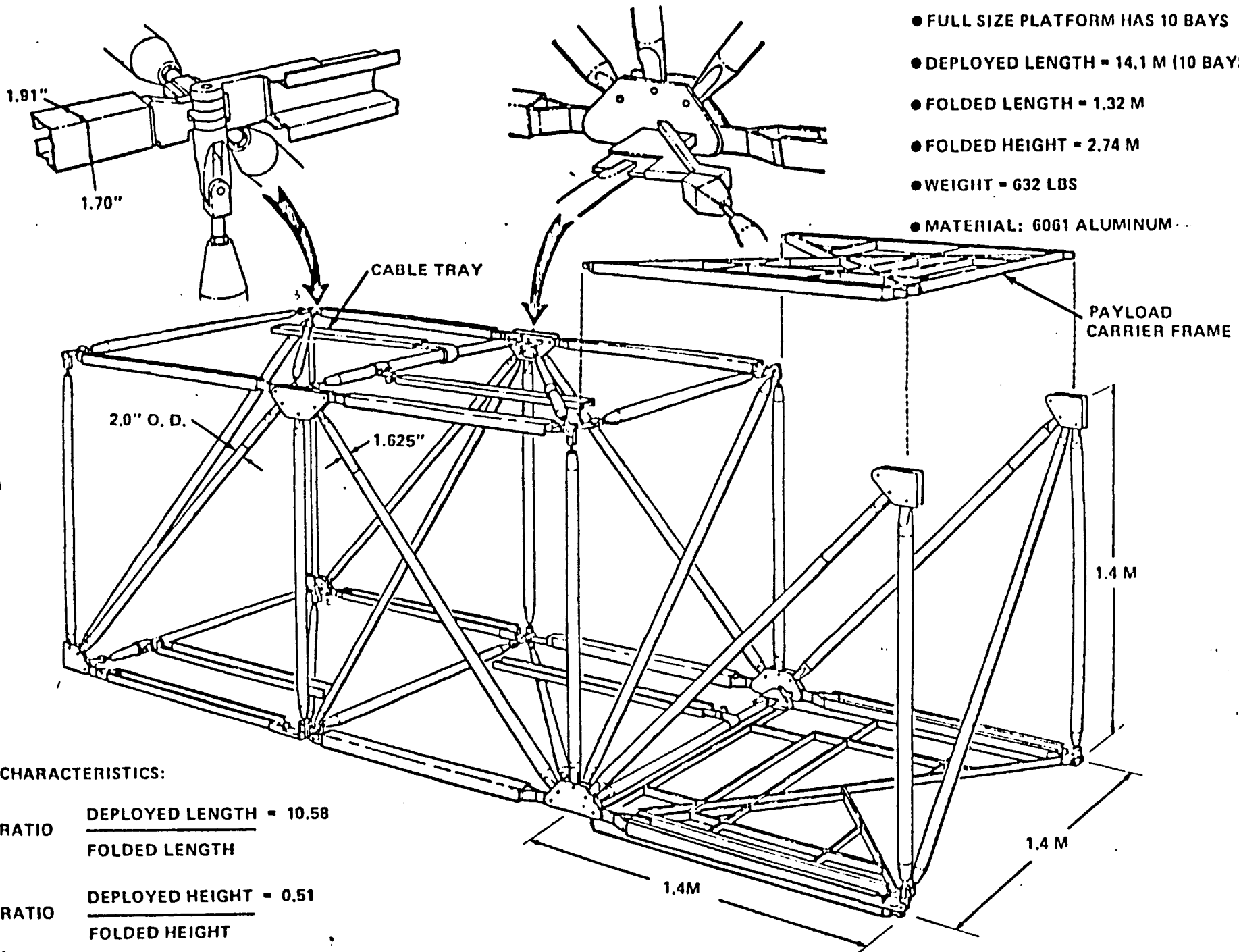


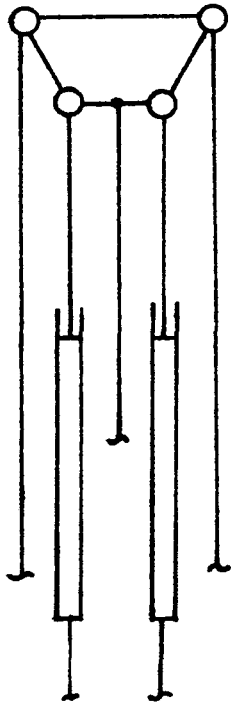
FIGURE 2

XX-6

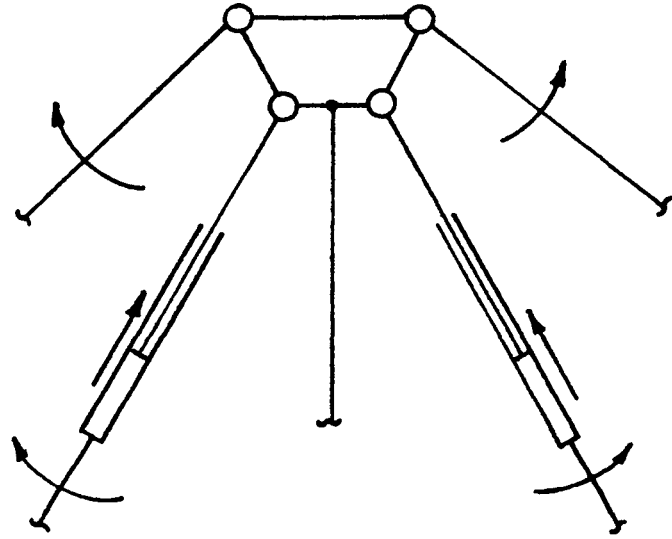
CHARACTERISTICS:

RATIO	$\frac{\text{DEPLOYED LENGTH} = 10.58}{\text{FOLDED LENGTH}}$
RATIO	$\frac{\text{DEPLOYED HEIGHT} = 0.51}{\text{FOLDED HEIGHT}}$

XX-7



(a) RETRACTED



(b) DEPLOYING

FIGURE 3 SASP DEPLOYMENT

The SASP deployment mechanism is a single-fold concept. Telescoping and rotation of structural members occur in a single coordinate plane (actually in two parallel planes). In the two perpendicular planes, the truss configuration remains the same whether retracted or deployed. In these planes, frames designed for payload attachment can be substituted for truss members as suggested by Figure 2.

Excepting the longerons, which are open cross sections designed for nesting, the structural members are 2-inch outside diameter 6061 aluminum tubing having wall thickness of 0.072 inches. Joint fittings, payload carrier frames, and cable trays are of the same aluminum alloy. Each two-bay cell is composed of 26 members. Without payload carriers and accounting for end closure, the ten bay, five cell truss is composed of 135 structural members.

PRELIMINARY ANALYSIS

Initially, several models of the SASP truss were formulated and analyzed using the Structural Performance Analysis and Redesign (SPAR) system [2]. SPAR is a set of computer programs written for general structural analysis using the finite element method. The SPAR programs (referred to as processors) utilize sparse matrix techniques [3] which provide high computational speed and the capability of analyzing very large structures. Finite elements available include bar, beam, plate, shell, solid, and zero-length pure-stiffness elements. However, for analysis of a deployable structure such as the SASP truss, the SPAR system provides no reasonable means for directly modeling the many pin-jointed members. To illustrate this contention, the SPAR models of the SASP truss will be discussed briefly.

The most common approach in modeling planar truss structures is to treat the individual members as bar elements which have axial stiffness only. Effectively, this approach models all structural joints as pin connections since bending and torsion are not supported by the stiffness formulation for bar elements. Consequently, joint rotations are not allowed. For structures loaded symmetrically in the plane of the major load supporting framework, the bar formulation is generally adequate. In the case of the SASP truss, several shortcomings of bar-element modeling are apparent. In this analysis, we seek the natural frequencies (particularly the fundamental frequency) and mode shapes of forced vibrations of the truss in a cantilever configuration. It is not known a priori that the inertial loading associated with free vibration will occur in a plane or planes parallel to a major structural plane of the truss. In fact, considering the structural complexity of the truss, the likelihood of this occurrence is thought to be remote. The other objections to bar elements are rather obvious: all stiffness and inertia terms associated with bending, torsion and shear are ignored in the formulation.

Another possible approach is to model each structural member as a three-dimensional beam element. In this formulation, all stiffness

and inertia terms arising from bending and shear in the principal planes are included as are those associated with torsion. For beam-element modeling, all elements connected to a common joint have identical displacements at the joint location. In the case of the SASP truss, the major joints connect eight structural members. Only two of the members are affixed so as to have displacement identical to those of the joint. Each of the other six has an additional, independent degree of freedom allowed by a pin connection at the joint. A similar situation exists at the smaller joints as well. Thus, straightforward beam-element modeling may result in overspecified stiffness and could give vibrational frequencies which are too large. It may be possible, using SPAR's zero-length, stiffness-only element capability, to produce joint models which more adequately simulate the actual joint construction of the deployable truss. This possibility was given a cursory examination but not pursued in-depth as it appeared to require an excessively large number of joints.

Although several objections to SPAR models of the SASP truss have been delineated above, computer runs using such models have been obtained. These results will be used for comparison with those of a SASP-unique model to be discussed in the next article.

SASP FINITE ELEMENT MODEL

In order to capture, as accurately as possible, the modal vibration characteristics of the SASP truss, a finite element model of the structure has been developed from scratch. Hereafter referred to as SFEM, this model formulation incorporates all additional degrees of freedom associated with the many pin joints in the structure.

In SFEM, each structural member of the SASP truss is treated as a three-dimensional beam element, as in Figure 4. With each element is associated an element reference frame xyz as shown, and the stiffness and inertia properties of the element are defined in terms of this frame. Generalized displacements u_1 through u_{12} represent the three displacements and three rotations of each end of the beam. The element reference frame is assumed to be oriented such that bending is referred to the principal planes of bending.

The stiffness and inertia properties of the beam element are obtained by considering the potential and kinetic energies of the element in conjunction with shape functions $S(x)$ which describe the displacement of any point x along the beam in terms of the displacements at the end of the beam. For axial displacement, for example, we write

$$u(x,t) = S_1(x)u_1(t) + S_7(x)u_7(t) \quad (1)$$

where the shape functions (also known as assumed modes) must satisfy the boundary conditions

XX-10

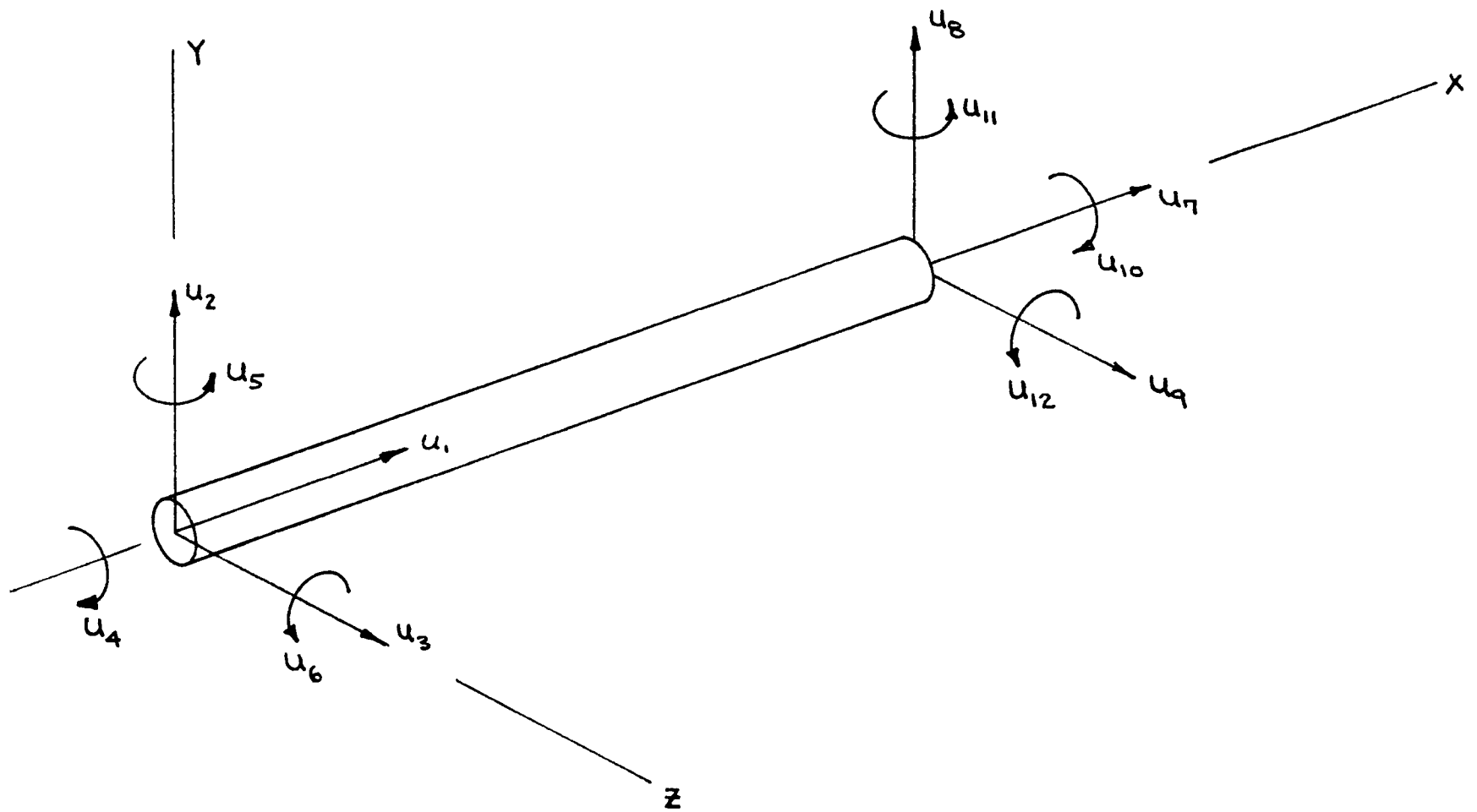


FIGURE 4 BEAM ELEMENT.

$$\begin{aligned} S_1(0) &= S_7(L) = 1 \\ S_1(L) &= S_7(0) = 0 \end{aligned} \quad (2)$$

in order to satisfy $u(0,t) = u_1(t)$ and $u(L,t) = u_7(t)$. The appropriate shape functions are $S_1(x) = 1 - x/L$ and $S_7(x) = x/L$ which are drawn from the solution for axial displacement under static loading. The elastic potential energy of the bar is

$$V = \frac{1}{2} \int_0^L EA (u')^2 dx \quad (3)$$

Using $u(x,t)$ as in (1) the potential energy can be shown to be equivalent to

$$V = \frac{1}{2} (K_{11} u_1^2 + 2K_{17} u_1 u_7 + K_{77} u_7^2) \quad (4)$$

where the stiffness coefficients K_{ij} are defined by

$$K_{ij} = K_{ji} = \int_0^L EA S_i' S_j' dx \quad (5)$$

Similar consideration of kinetic energy

$$T = \frac{1}{2} \int_0^L \rho A (\dot{u})^2 dx \quad (6)$$

will lead to definition of the inertia coefficients as

$$m_{ij} = m_{ji} = \int_0^L \rho A S_i S_j dx \quad (7)$$

If we next consider transverse bending of the beam, we will obtain stiffness and inertia coefficients associated with u_2, u_6, u_8, u_{12} for bending in the xy plane and with u_3, u_5, u_9 and u_{11} for bending in the xz plane. Finally, considering torsional displacements will produce the coefficients associated with u_4 and u_{10} . The specific formulation used here is that of Craig [4] and is based on Bernoulli-Euler beam theory. The resulting element stiffness and mass matrices are as given in Figure 5. The mass matrix so developed is known as the consistent mass matrix since it is based on the same shape functions as the stiffness matrix.

Using the beam elements, the structure is defined by joining the ends of the beams at the appropriate joints and deriving system equations of motion which describe the joint displacements. As an intermediate step in this process, the element stiffness and mass matrices (described in the element reference frame) must be transformed to a common reference frame in which joint displacements will be measured. The latter is known as the Global Reference Frame. This is a straightforward procedure as it involves only a rotation of coordinates defined by a 3 by 3 matrix of direction cosines which will be denoted $[T_c]$. If the element displacements in the global system are represented by $\bar{u}_i, i = 1, 12$, the transformation is given by

$$[u] = [T][\bar{u}] \quad (8)$$

$k =$

$\frac{EA}{L}$						$-\frac{EA}{L}$					
	$\frac{12EI_1}{L^3}$				$\frac{6EI_1}{L^2}$		$\frac{12EI_1}{L^3}$				$\frac{6EI_1}{L^2}$
		$\frac{12EI_2}{L^3}$		$\frac{6EI_1}{L^2}$				$-\frac{12EI_2}{L^3}$		$-\frac{6EI_2}{L^2}$	
			$\frac{GJ}{L}$						$-\frac{GJ}{L}$		
		$-\frac{6EI_2}{L^2}$		$\frac{4EI_2}{L}$				$\frac{6EI_2}{L^2}$		$\frac{2EI_2}{L}$	
	$\frac{6EI_1}{L^2}$			$\frac{4EI_1}{L}$		$\frac{6EI_1}{L^2}$					$\frac{2EI_2}{L}$
$\frac{EA}{L}$						$-\frac{EA}{L}$					
	$-\frac{12EI_1}{L^3}$				$-\frac{6EI_1}{L^2}$		$\frac{12EI_1}{L^3}$				$-\frac{6EI_1}{L^2}$
		$-\frac{12EI_2}{L^3}$		$\frac{6EI_2}{L^2}$				$\frac{12EI_2}{L^3}$		$\frac{6EI_2}{L^2}$	
			$\frac{GJ}{L}$						$\frac{GJ}{L}$		
		$\frac{6EI_2}{L^2}$		$\frac{2EI_2}{L}$				$\frac{6EI_2}{L^2}$		$\frac{4EI_2}{L}$	
	$\frac{6EI_1}{L^2}$			$\frac{2EI_1}{L}$		$-\frac{6EI_1}{L^2}$					$\frac{4EI_1}{L}$

$m = \frac{\rho AL}{420}$

140						70					
	156				22L		54				-13L
		156		-22L				54		13L	
			$\frac{140I_2}{A}$						$\frac{70I_2}{A}$		
		-22L		$4L^2$				-13L		$-3L^2$	
	22L			$4L^2$		13L					$-3L^2$
70						140					
	54				13L		156				-22L
		54		-13L				156		22L	
			$\frac{70I_2}{A}$						$\frac{140I_2}{A}$		
		13L		$-3L^2$				22L		$4L^2$	
	-13L			$-3L^2$		-22L					$4L^2$

FIGURE 5 ELEMENT STIFFNESS AND MASS MATRICES.

where $[T]$ is the 12 by 12 transformation matrix given by

$$[T] = \begin{bmatrix} T_c & 0 & 0 & 0 \\ 0 & T_c & 0 & 0 \\ 0 & 0 & T_c & 0 \\ 0 & 0 & 0 & T_c \end{bmatrix} \quad (9)$$

The total elastic energy of a beam element can be written in matrix notation as

$$V = \frac{1}{2} [u]^T [K] [u] \quad (10)$$

where $[K]$ is the 12 by 12 element stiffness matrix, $[u]$ is the row vector of element displacements and $[u]^T$ is the transpose of $[u]$. Formal substitution of eq. (8) into eq. (10) shows that the element stiffness matrix in the global reference system is given by

$$[K] = [T]^T [K] [T] \quad (11)$$

An identical procedure using kinetic energy gives the transformed mass matrix as

$$[m] = [T]^T [m] [T] \quad (12)$$

As a brief respite from the derivation, we note that the SASP truss is composed of members corresponding to five sets of structural and inertia properties. Thus five sets of stiffness and mass matrices are required. The truss includes eight different element orientations so that eight transformation matrices $[T_c]$ are used in the model.

Having transformed individual element matrices to a common frame of reference, displacement compatibility relations are applied at each joint in the structure to obtain the system stiffness and mass matrices. The procedure used here is known as the direct stiffness method. To obtain the displacement relations we let $\{U\}$ be the column vector of system displacement coordinates, and define, for each element, a locator (or label) matrix $[L_e]$ such that

$$\{\bar{u}\} = [L_e] \{U\} \quad (13)$$

where $\{\bar{u}\}$ is the vector of element displacements in the global frame. Equation (13) does nothing more than assign each of the twelve element displacements a particular system displacement. The locator matrix is composed strictly of zeroes and ones in twelve rows and N columns where N is the total number of system displacements (i.e. degrees of freedom).

Normally the vector of system displacements is composed of the six coordinate displacements (three translations, three rotations) at each joint. For the SFEM this is not the case as additional rotational degrees of freedom are allowed by the pin joints. To include these in the model, the method proposed by Winfrey [5] for analysis of elastic deformation in mechanisms is used. This will be discussed with reference to Figure 6 which is an $X_G Y_G$ plane view of one of the major joints of the truss. In this plane, the joint displacements are U_1 , U_2 , and U_6 corresponding to translation along global axes X_G and Y_G , and rotation about Z_G , respectively. Of the structural members shown, only element 3 is attached such that its displacements are the same as those of the joints. Each of elements 1, 2, 4 and 5 are free to rotate about the pin connections at the joint although the translation displacements are the same as the joint. In this example joint then, there arise four additional degrees of freedom corresponding to U_7 through U_{10} as shown. Extending this procedure we find that a SASP truss with M bays has $24(M + 1)$ system coordinates associated with "standard" joint displacements and $40M + 4$ system coordinates corresponding to the "extra" degrees of freedom.

Having defined the system coordinates as discussed above, final "assembly" of the system equations of motion is possible. The system potential energy can be expressed as

$$V = \frac{1}{2} \sum_{e=1}^N [\bar{u}]_e^T [K]_e [\bar{u}]_e \quad (14)$$

where the summation is over the number of elements in the system. In terms of system coordinates, equation (13) is used to obtain

$$V = \frac{1}{2} \sum_{e=1}^N \{U\}^T [L_e]^T [K]_e [L_e] \{U\} \quad (15)$$

which is equivalent to

$$V = \frac{1}{2} \{U\}^T \left(\sum_{e=1}^N [L_e]^T [K]_e [L_e] \right) \{U\} \quad (16)$$

The summation term in eq. (16) is the assembled system stiffness matrix $[K]$ such that

$$V = \frac{1}{2} \{U\}^T [K] \{U\} \quad (17)$$

Similarly it can be shown that the system consistent mass matrix is given by

$$[M] = \sum_{e=1}^N [L_e]^T [\bar{m}]_e [L_e] \quad (18)$$

in terms of which the kinetic energy is

$$T = \frac{1}{2} \{\dot{U}\}^T [M] \{\dot{U}\} \quad (19)$$

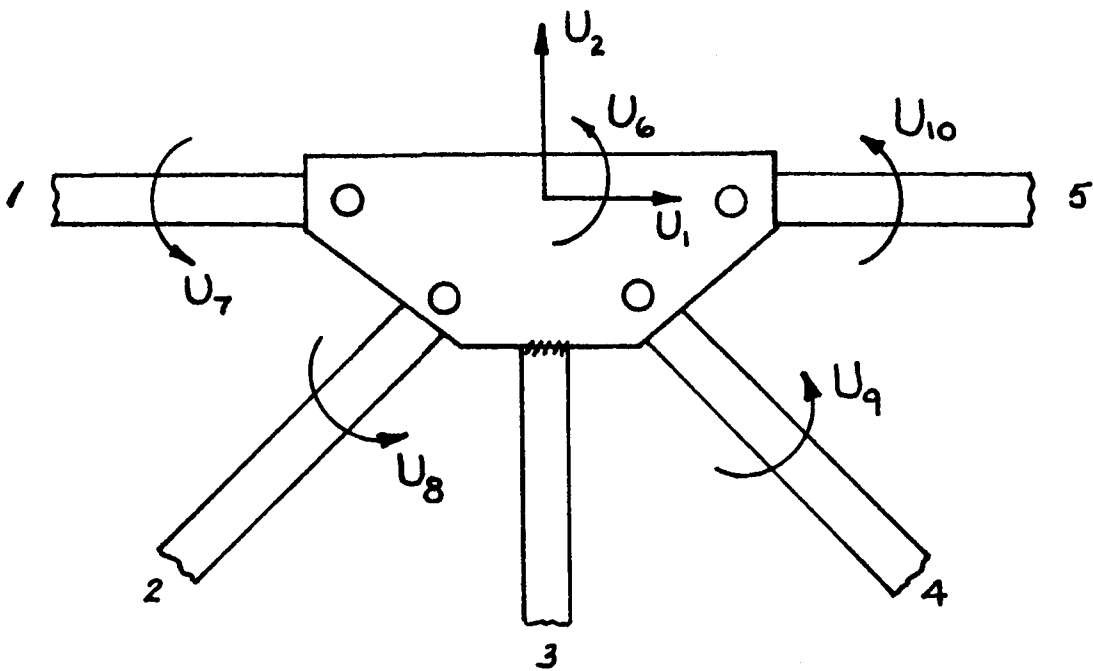


FIGURE 6 SASP JOINT DISPLACEMENTS.

By using eqs. (17) and (19) we obtain the system equations of motion in the matrix form

$$[M]\{\ddot{U}\} + [K]\{U\} = 0 \quad (20)$$

Equation (20) results from application of Hamilton's principle or by forming the Lagrangian and differentiating. Solution of the Eigenvalue problem represented by (20) will yield the natural frequencies and mode shapes of free vibrations of the truss structure.

DISCUSSION OF RESULTS

For simplicity, the SFEM was first applied to a single-cell, two-bay truss composed of 31 elements and constrained in a cantilever configuration. The resulting structural model has 92 active degrees of freedom after eliminating 24 displacements via the constraint conditions. Computer programs were written to sequentially calculate the element stiffness and mass matrices, transform the matrices to the global coordinate system, and assemble the system matrices. As pointed out by Craig, the matrix multiplications involving $[L_e]$ and $[L_e]^T$ do nothing more than locate terms from the element matrices into the proper row and column of the corresponding system matrix. To accomplish this and avoid a great number of matrix multiplications involving mostly zeroes, a locator vector was used for each element. This vector contains simply the row-column data relating element matrix to system matrix.

After assembly of the system matrices, the Eigenvalue problem was solved using the FORMA [6] matrix subroutine package. The results of the first SFEM run gave the fundamental frequency of the two-bay SASP truss as 27.9 Hz. For comparison, a SPAR model of the two-bay truss, using identical elements, resulted in a fundamental frequency of 50.6 Hz. This apparently significant difference in results was not accepted without considerable double checking of the model formulation and the computer program. By eliminating the "extra" degrees of freedom, the SFEM programs should produce the same results as SPAR. When this was done, the first six natural frequencies of the two models were found to differ by less than one percent. On this basis, the accuracy of SFEM was established.

Extending SFEM to the full size ten-bay truss required considerable rework of the computer programs. The ten-bay truss is composed of 135 structural members which leads to 444 degrees of freedom for the model. The huge matrices involved with a model of this magnitude are not amenable to routine manipulation as the computer time and storage requirements are astronomical. To assuage these difficulties, all matrix operations were converted to partition logic to eliminate storage and manipulation of vast number of zero terms. This conversion was readily accomplished since NASA's ZFORMA subroutine package could be used directly. These routines partition all matrices into 60 by 60 (maximum) submatrices for both storage and algebraic manipulation. Using subroutine ZMODEL to solve the Eigenvalue problem, the two lowest natural frequencies of the ten-bay

truss were determined in about eight minutes of actual computer time. The fundamental frequency so determined is 4.6 Hz while the second frequency is 5.4 Hz. Again for comparison, results from a ten-bay model using the SPAR system were obtained. To the surprise of the investigator, the frequencies from the SPAR model were substantially identical. Having learned years ago to believe and disbelieve simultaneously, the investigator again proceeded to check and double check. The partition-logic programs were reduced to the two-bay model to detect software errors which could have arisen in conversion. The results were identical to those previously obtained. On this basis, the ten-bay results were accepted as correct also.

Based on the contradictory comparisons of two-bay and ten-bay truss models using SFEM and SPAR, the programs for each model were run for four-, six-, and eight-bay truss configurations. The results of these runs, as shown by Figure 7, show that the fundamental frequencies given by the two models are convergent with respect to overall truss length. Since the major difference in SFEM and the SPAR model lies in the effective rotational stiffness of the joints, this phenomena can only be explained by surmising that the effects of joint rotations are reduced with increasing truss length not unlike the decreasing significance of transverse shear versus length of a beam.

Per the request of R. E. Jewell (MSFC/ED21), fundamental frequencies of the SASP structure were obtained for truss lengths up to 50 bays (230 feet) and for the ten-bay truss with concentrated mass at one end. In each of these additional cases the cantilever constraint was retained so the length cases apply to SADE Options III and IIIA while the tip mass cases are applicable to Option IA. Fundamental frequency versus truss length as given by SPAR models is shown in Figure 8a. The results of frequency as a function of tip mass are as in Figure 8b. The latter results were again in agreement from both SFEM and SPAR.

CONCLUSIONS AND RECOMMENDATIONS

A detailed finite element analysis of the SASP deployable truss has shown that the fundamental frequencies of vibration are not significantly affected by the extra degrees of freedom associated with the many pin-pointed members except for short overall truss lengths. This leads to the conclusion that simplified models utilizing the SPAR system can be used to adequately assess the dynamic characteristics of the structure for the configurations being considered for SADE.

As additional deployable truss designs evolve or composite platform configurations using SASP are considered, it is recommended that similar analyses be conducted to insure accuracy of simplified models. Detailed modeling similar to SFEM may be required if, in the latter case, a platform concept includes short truss sections to connect payloads for example.

81-XX

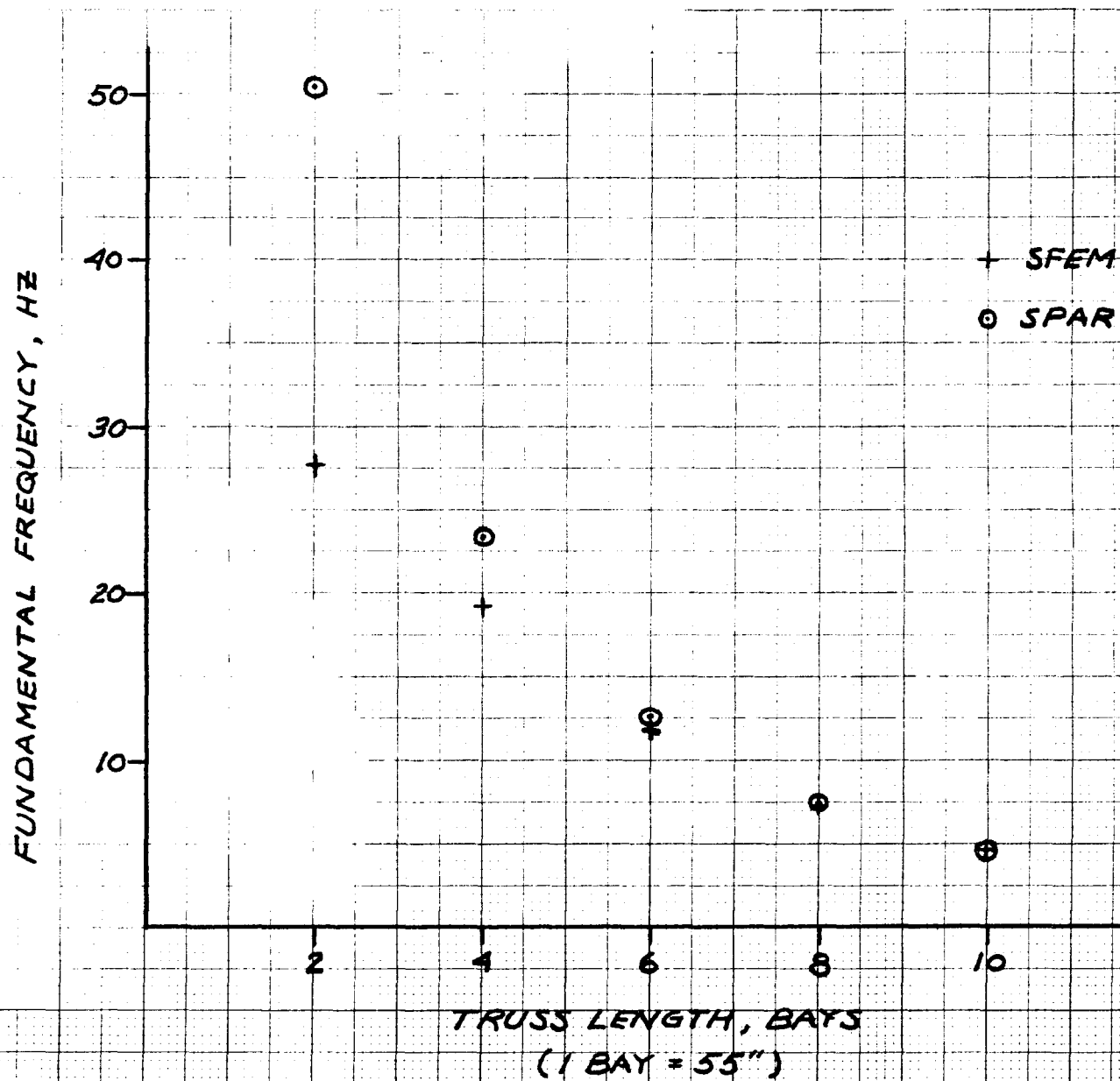
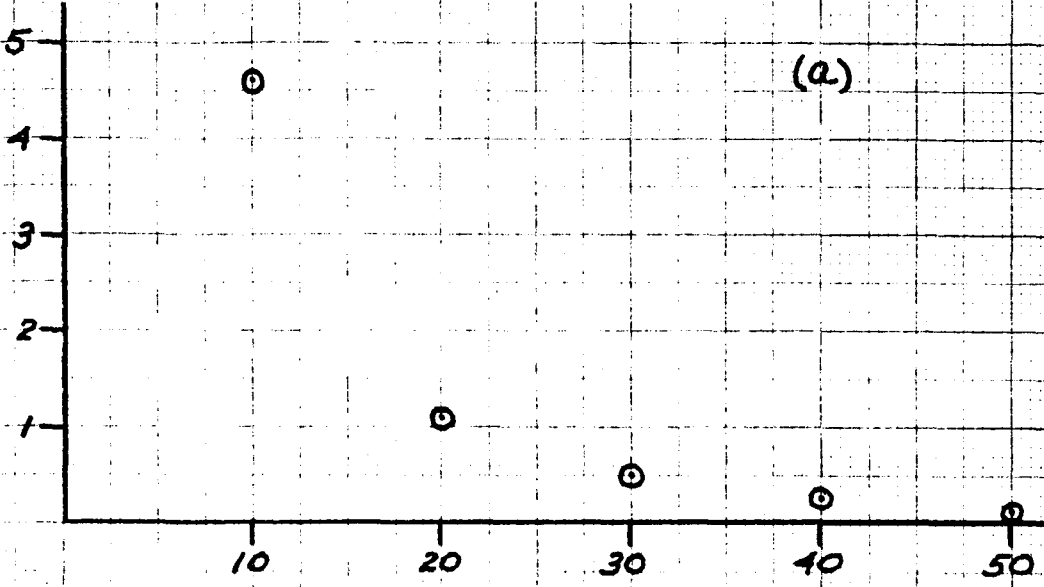


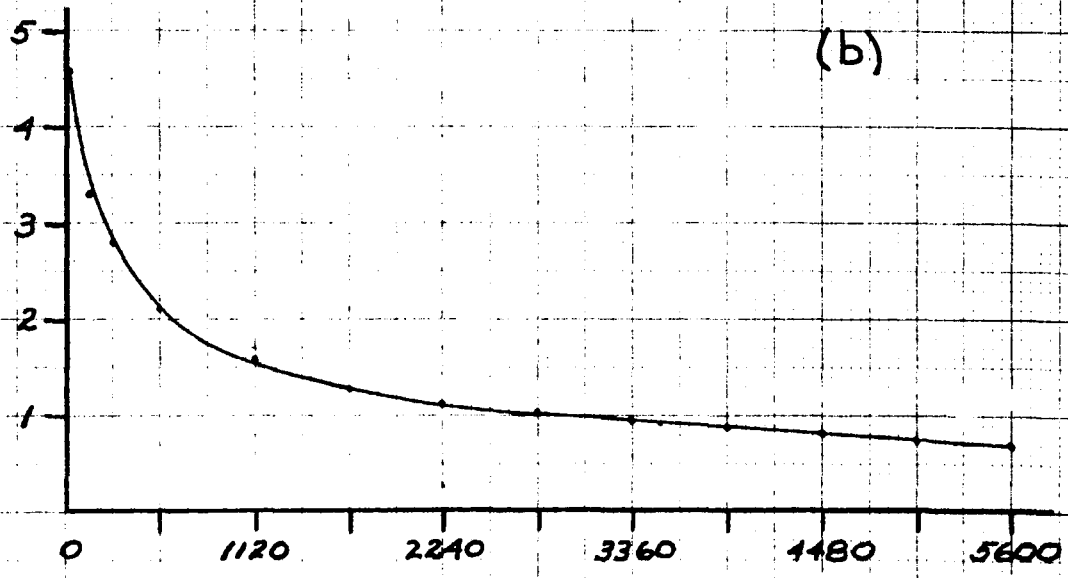
FIGURE 7 COMPARISON OF SFEM AND SPAR RESULTS.

FUNDAMENTAL
FREQUENCY, HZ



TRUSS LENGTH, BAYS
(1 BAY = 55")

FUNDAMENTAL
FREQUENCY, HZ



WEIGHT OF TIP MASS, LB

FIGURE 8 (a) FREQUENCY VERSUS TRUSS LENGTH (SPAR)
(b) TIP MASS EFFECTS ON FREQUENCY (SFEM AND SPAR)

REFERENCES

1. Stoll, H. W., "Computer Simulation for Dynamic Analysis of a Deployable Space Structure", Final Report, Contract No. NAS8-34506, September 1981.
2. SPAR Structural Analysis System Reference Manual, NASA CR158970-2, 1978.
3. Whetstone, W. D., "Computer Analysis of Large Linear Frames", Journal of the Structures Division, ASCE, November 1969.
4. Craig, Roy R., Jr., Structural Dynamics, John Wiley and Sons, New York, 1981.
5. Winfrey, Richard C., "The Finite Element Method as Applied to Mechanisms", Finite Element Applications in Vibration Problems, ASME, New York, 1977.
6. Expansion and Improvement of the FORMA System For Response and Load Analysis, MCR-76-217, Martin-Marietta, May 1976.

1982

NASA/ASEE SUMMER FACULTY RESEARCH FELLOWSHIP PROGRAM

MARSHALL SPACE FLIGHT CENTER
THE UNIVERSITY OF ALABAMA

DETECTION AND ANALYSIS
OF RADIO FREQUENCY LIGHTNING EMISSIONS

Prepared by: Fereydoun Jalali, Ph.D.
Academic Rank: Associate Professor
University and Department: Fort Valley State College
Electronic Engineering Technology
NASA/MSFC:
(Laboratory) Information & Electronic Systems
(Division) Optical and R. F. Systems
MSFC Counterpart: James W. Harper (Retired)
James A. Dunkin
Date: August , 1982
Contract No.: University of Alabama
NGT 01-002-099

DETECTION AND ANALYSIS OF
RADIO FREQUENCY LIGHTNING EMISSIONS

by

F. Jalali
Associate Professor
Electronic Engineering Technology
Fort Valley State College

ABSTRACT

The measurement system developed at MSFC for detection of RF lightning emissions is briefly described and data collected during summer 1982 presented. The system collects emission data at 2 GHz and 251 MHz and simultaneously records the electrostatic field changes. A simple procedure for calibration is devised and made possible due to inclusion of calibration equipment within the system. Data collected from several cloud-to-ground flashes are analyzed and peak signal levels computed. These, converted to 1 KHz bandwidth at 10 Kilometers, yield values between 8-32 $\mu\text{V}/\text{m}$. Examination of the emission data collected so far show distinct signature characteristics associated with the leader and return stroke portions of the cloud-to-ground discharges.

Acknowledgment

The basic concept of the Lightning Recording Facility and its development are due to Mr. James W. Harper who was my counterpart for 1981 and most of summer 1982. It is with pleasure that I express my appreciations to him for his continuous encouragement and support. Also, I would like to thank Mr. James A. Dunkin, my counterpart following Mr. Harper's retirement, for providing the needed continuity in this project and for his very helpful suggestions and assistance. Thanks are also due Kaye Langford for her efficiency and patience in typing this report.

LIST OF FIGURES

<u>Figure No.</u>	<u>Title</u>	<u>Page No.</u>
1	Lightning Emission Recording Facility	XXI-6
2	Calibration Arrangement	XXI-7
3	Vert. Polarized S-Band Calibration Graph	XXI-9
4	Composite Lightning Amplitude Spectrum from Data Presented by Oetzel and Pierce	XXI-12
5	High-Resolution Record of A Cloud-to-Ground Emission	XXI-14
6	Magnetic Tape Record of The Emission Shown in Fig. 5	XXI-15
7	Longer Record Off Magnetic Tape for Emission of Fig. 5 and 6	XXI-16

LIST OF TABLES

<u>Figure No.</u>	<u>Title</u>	<u>Page No.</u>
1	Peak Signal Strength of C-G Emissions at 2 GHz	XXI-10

Introduction

As a result of the interest of many agencies in lightning information, the National Aeronautical and Space Administration has established a program to study the feasibility of developing a satellite-based lightning mapping system. Investigation of the feasibility of detection and location of lightning by sensing its RF and/or optical emissions have been carried out and are continuing. The result thus far favor detection in optical frequencies. However, for an effective system, detection in the RF portion may be necessary either in a hybrid satellite-based system or in ground detection facilities supporting an optical system. Because of the antenna size and propagation constraints, any RF satellite-born system has to operate in or above the VHF. Unfortunately, the lightning characteristics are not adequately known at these frequencies due to lack of data. The RF lightning program at MSFC has undertaken to collect more data above the VHF range. This report describes some aspect of the measurement system and the results obtained to the present.

Objective

Available data on RF emissions from lightning in and above UHF are inadequate both in quantity for any statistical analysis and in resolution for the study of signature characteristics of the emissions. The objectives of this project are: (a) operation and calibration of the RF Lightning Emission Recording Facility set up at MSFC and devising algorithm for efficient data collection and handling; (b) collection of lightning data at 251 MHz and 2 GHz, and (c) initiation of data analysis to determine the peak spectral amplitudes and other signal characteristics at these frequencies.

Measurement System

The system collects RF emission data from lightning at 2 GHz and 251 MHz in both vertical and horizontal polarization modes. In addition, two E-field sensors (slow and fast) are utilized for detection of the electrostatic change during the lightning activity. The above six signals along with the UT time code and a trigger pulse are recorded on magnetic tape producing a long, low-resolution record. (See Figure 1)

Any of the RF signals may be selected from a patch pannel for high-speed digitization and short-term storage. The LeCroy Digitizer/Memory unit employed for this purpose has a maximum sampling rate of 20 Mbs and is triggered when the analog input signal changes through a level which may be adjusted by the operator. The trigger pulse initiates the loading of the digitized data into the unit's 128 Kilo bytes of solid-state memory. Sampling rates of 0.5 to 20 Mbs may be chosen to yield record lengths of 256 to 6.4 milliseconds respectively. Included in the LeCroy unit is a module for memory sweep and D-to-A conversion. This enables displaying the content of the memory immediately following memory fill-up. Any segment of the solid-state memory may be selected and dumped on a hard disk for permanent storage through computer control upon operator instruction.

A TV camera with a ± 20 degree field of view is mounted on the antenna support plate approximately aligned with the antenna cluster bore sight. The camera output, with the UT time as an inset on the video frame, is recorded by a VCR and also displayed on a monitor at the instrumentation site.

Data collection procedure is essentially similar to the routine used previously before the system was expanded to its present stage. However, the addition of the HP1000 computer and hard disc memory have significantly increased the speed of data collection. Also, the video monitoring and recording provisions have improved the accuracy of identification of the discharge event.

Two generators with associated precision attenuators are installed in the instrument trailer and are connected by low loss lines to standard-gain antennas mounted on a post 44 feet from the receiving antennas. A calibration test run can be executed conveniently by aiming the receiving antenna toward the source antenna and setting the source generator output at a desired power level. A simple program is devised to compute received power density and E-field as well as the digitized output level.

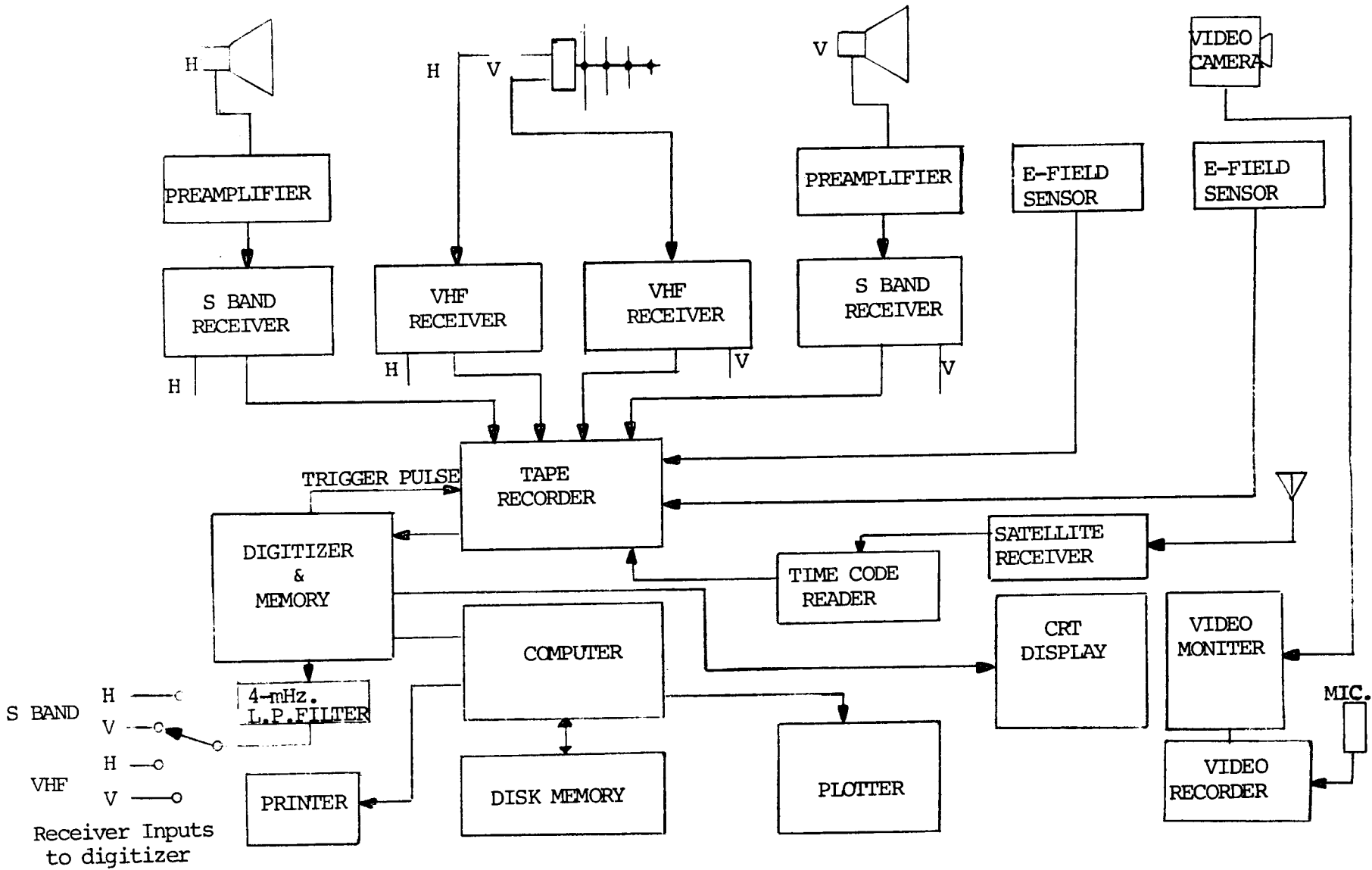


Fig. 1. LIGHTNING EMISSION RECORDING FACILITY

System Calibration and Signal Intensity Computation

Figure 2 shows the part of the system involved in the calibration procedure. The power density, in dB's above $1\text{mW}/\text{m}^2$, at the receiving antenna is obtained by

$$P_{rc}(\text{dBm}) = P_o - P_L + P_{ag} - 10 \log 4\pi r^2$$

in which the terms on the right are: the output power of the RF source, the loss in the line connecting the source to the radiating antenna, the gain of the standard-gain antenna, and the space loss between the two antennas.

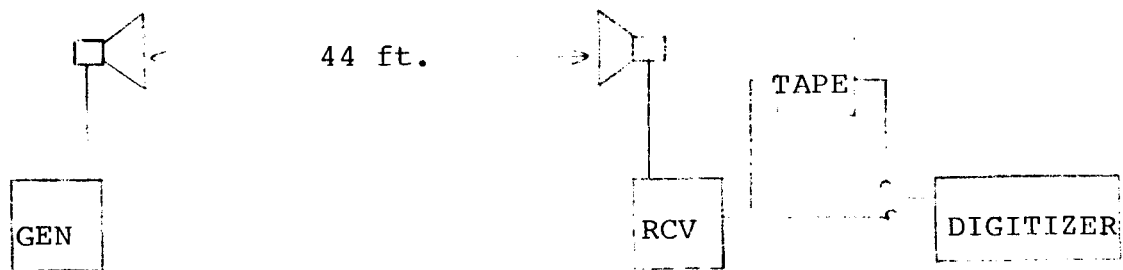


Fig. 2. Calibration Arrangement

The power in W/m^2 at the receiving antenna is computed from above by

$$P_{rcw} = 10^{\frac{P_{rc}}{10}} \cdot 10^{-3}$$

and the electric field by :

$$E_{rc} = (\eta P_{rcw})^{\frac{1}{2}}$$

in which the space intrinsic impedance η is 377 ohms.

The above relations are incorporated in a computer program utilized for the calibration test runs. The procedure requires selecting the desired antenna system and the receiving mode (direct digitization or through the Ampex recorder), adjusting the output of the RF source to a known level, triggering the digitizer, and executing the calibration program. The program

computes the average digitized level of the received signal and the corresponding power density and the signal strength at the receiving antenna. Figure 3 shows the calibration curve for the vertically polarized S-band channel.

For the purpose of comparing the data with those obtained by other workers, the equivalent 1KHz bandwidth signal strength at one statute mile (or at 10 kilometer) may be computed for emissions from lightning events whose distances are known. The loss due to bandwidth conversion to 1KHz is given by

$$10 \log (BW) \left(\frac{BW}{1000} \right)$$

in which BW is the bandwidth of the receiving channel. The gain due to the distance conversion is given by

$$20 \log D \quad (D \text{ in miles})$$

for conversion to one statute mile, and by

$$20 \log \frac{D}{10} \quad (D \text{ in kilometers})$$

for conversion to 10 kilometers.

By combining the conversion relations for bandwidths and distance, the following working equations are obtained:

$$E_{eq} = E_{rc} \cdot D_{mi} \cdot \left(\frac{BW}{1000} \right)^{-\frac{1}{2}} \quad (1)$$

$$E_{eq} = E_{rc} \cdot D_{km} \cdot \left(\frac{BW}{10} \right)^{-\frac{1}{2}} \quad (2)$$

Equation (1) gives the 1KHz-bandwidth equivalent signal strength in V/m at one statute mile, and (2) gives the signal strength at 10 kilometer. E_{rc} is the signal strength at the receiving antenna and D_{mi} and D_{km} are the distance of the discharge from the receiving antenna in miles and kilometers respectively.

6-IXX

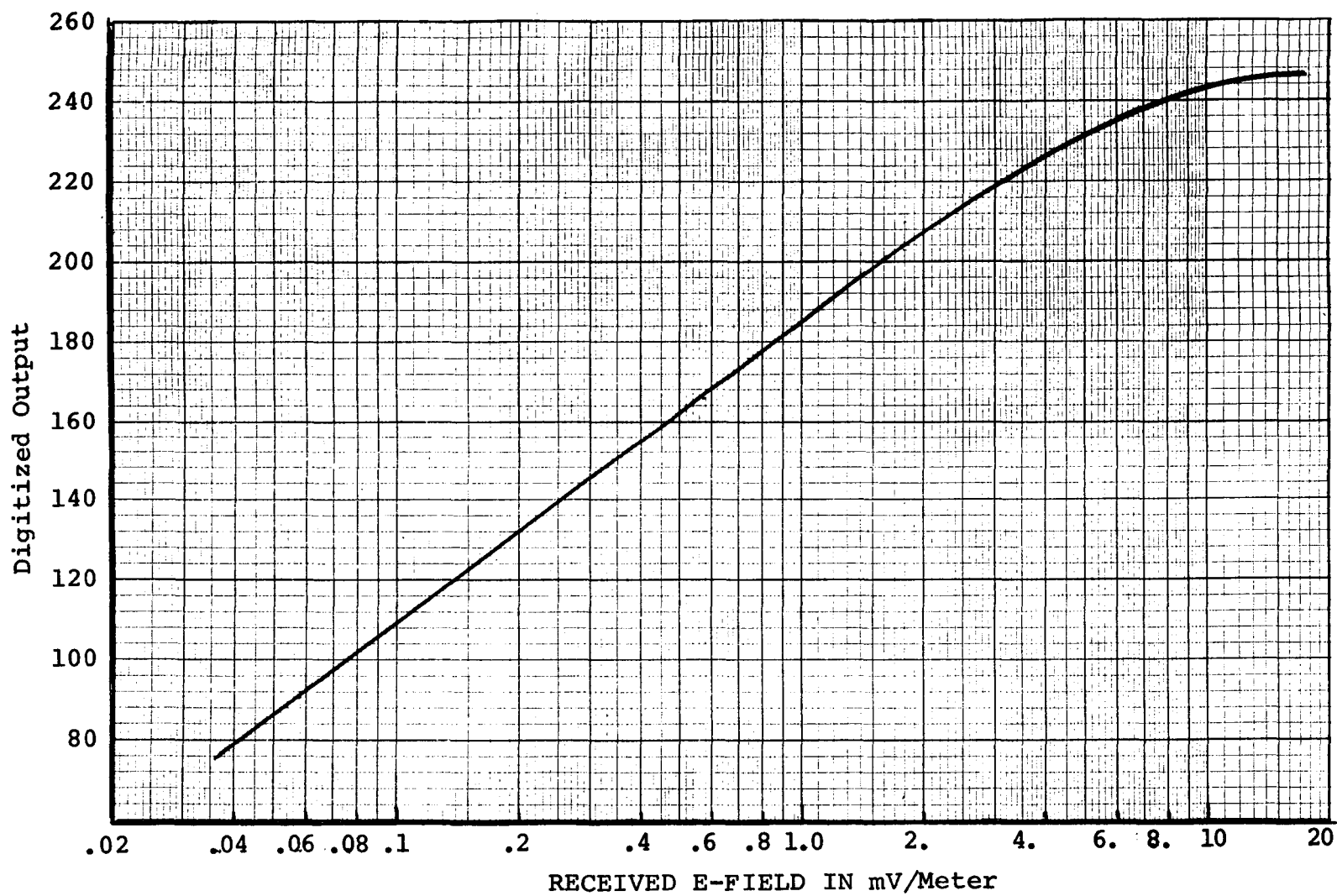


Fig. 3. VERT. POLARIZED S-BAND CALIBRATION GRAPH

Emission Records and Analysis

The RF emission data presented in this report were obtained during four thunder storm activities on July 9, 16, 19, and 22, 1982, between 1:30 to 7:30 p.m. During these sessions, a total of twenty identified discharges were logged. It should be noted that all of the lightning RF emissions are recorded on the low-resolution magnetic tape. However, it was decided that, at this stage of the project, only the emission records for which other relevant information are available be stored in the permanent memory. Thus, the high resolution record (for vertical polarization S-band) of eight emissions were successfully stored on the disk. All of these were cloud-to-ground discharges observed by the field observer directly and/or on the monitor by the instrument operator. The time of the associated thunder was also measured by the field observer using a stop watch. The time measurements were confirmed by the video play back for the flashes which had unambiguous audio records.

The peak signal strength at the receiving antenna is found using the maximum value of the stored digitized record and the calibration curve of Figure 3. Equations 1 and 2 may be used to determine the 1 KHz equivalent E-field at one mile or at 10 Kilometers. Six of the high-resolution records of the cloud-to-ground discharges have been analyzed for peak signal strength and the results are shown in Table 1.

Tabel 1
Peak Signal Strength of C-G Emissions at 2 GHz

Digitized Level	Erc ($\mu\text{V/m}$)	ΔT (Seconds)	Distance (Kilometers)	Eeq (1 KHz, 10 Km) ($\mu\text{V/m}$)
168	600	25	8.3	7.9
175	740	20	6.6	7.7
220	3100	20	6.6	32.5
200	1600	22	7.3	18.5
190	1050	24	8.0	13.2
200	1600	17	5.6	14.3

The results fall, with close agreement, on the experimental lightning amplitude spectrum curve given by Oetzel and Peirce

(1969). Figure 4 shows the experimental curves due to various investigators presented by Oetzel and Peirce. The vertical bar at the 2 GHz shows the range of results obtained in this project, with the circle showing the average. Equivalent emission peaks measured at 2.2 GHz by Rust, et al, (1979) is shown by the X mark.

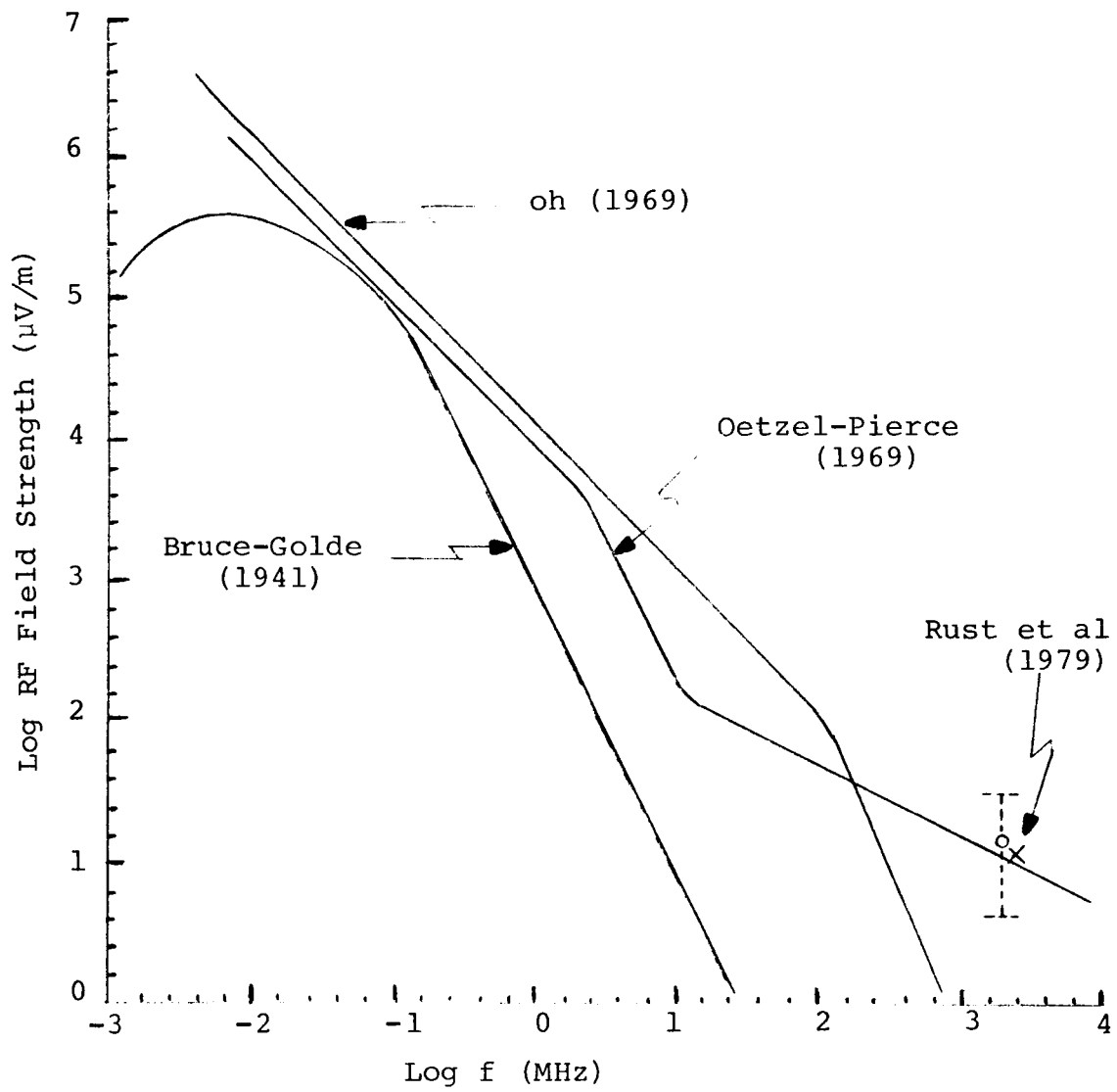


Fig 4. Composite Lightning Amplitude Spectrum from Data Presented By Oetzel and Pierce

Signature Description

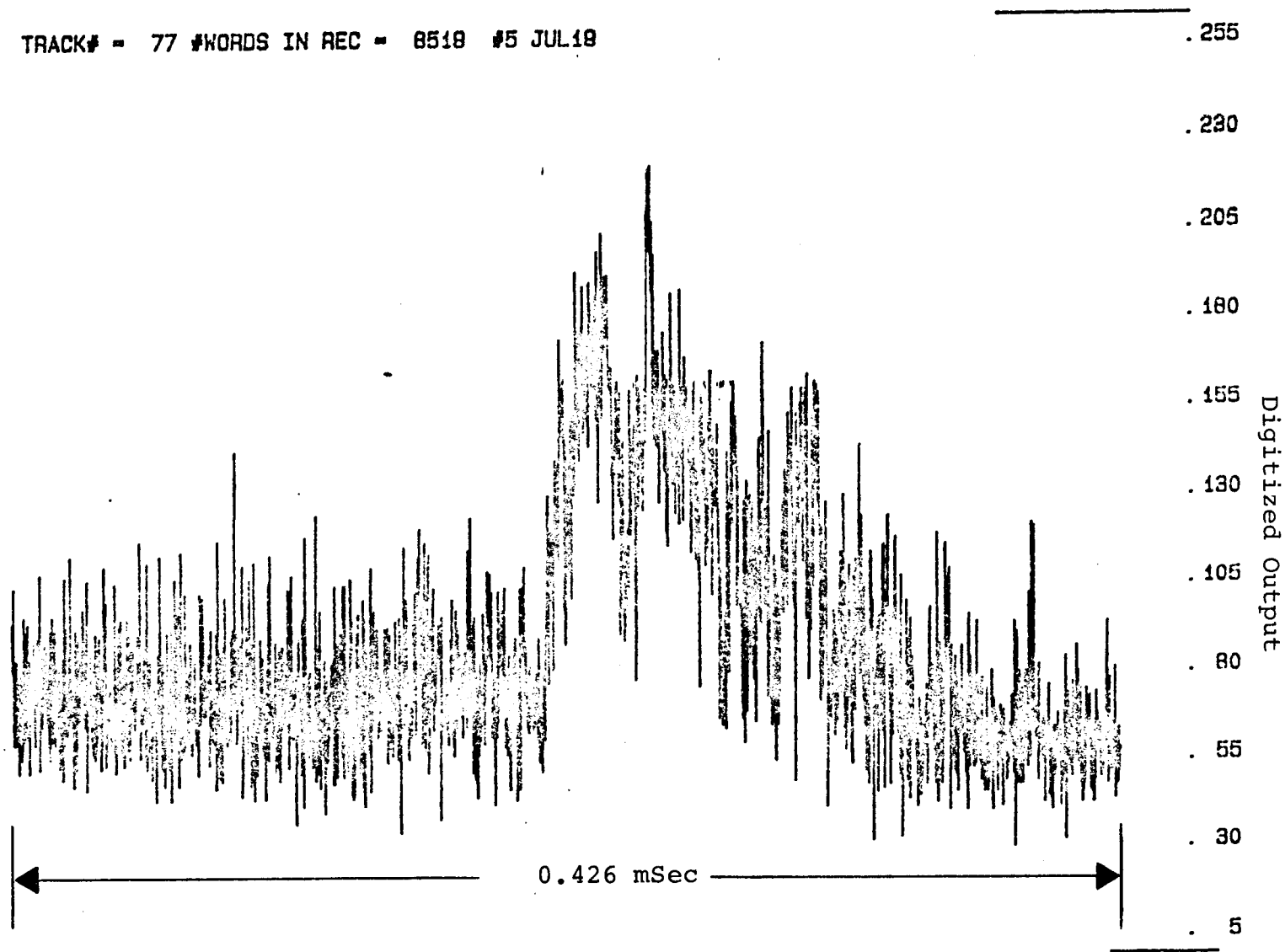
In this section, the graph of a representative emission record is presented and some of the general signature characteristics discussed. Detail and quantitative analysis of these characteristics require more data and maybe done later.

Figure 5 shows the high-resolution record of one of the cloud-to-ground discharges obtained on July 19, 1982. The record is only 0.426 millisecond long (8519 words @ 20Mbs), therefore, its location within the discharge event needs to be determined. For this, the record of the same event stored on magnetic tape is plotted. Various record length off the magnetic tape may be obtained by digitizing the output at different sampling rates (tape speed is kept constant). Also, the system allows some flexibility in the initial point of the reproduced output by operating the digitizer's triggering circuit in Synch mode and varying the trigger level. The two graphs shown in Figures 6 and 7 were obtained in this manner.

The graph of the Figure 6 is almost identical with the high-resolution graph of Fig. 5 except that the high frequency content has been filtered out. This is expected since the high-resolution data was recorded through a 4-MHz channel while the magnetic record has essentially a 40 KHz bandwidths. Now, graphs of Figure 6 and 7 are compared. The large signal region of Figure 6 is clearly identifiable in the last quarter of the graph in Figure 7. This graph shows that the signal strength following the large peak quickly falls to the 55-60 digital level (which is the measured noise level for the S-band). However, prior to the large peak, there is an active region above the noise about 3 millisecond of which extends over the first 3/4 of the graph. This region is followed by the large signal peak. Examination of the long records of the other emissions reveals similar structures.

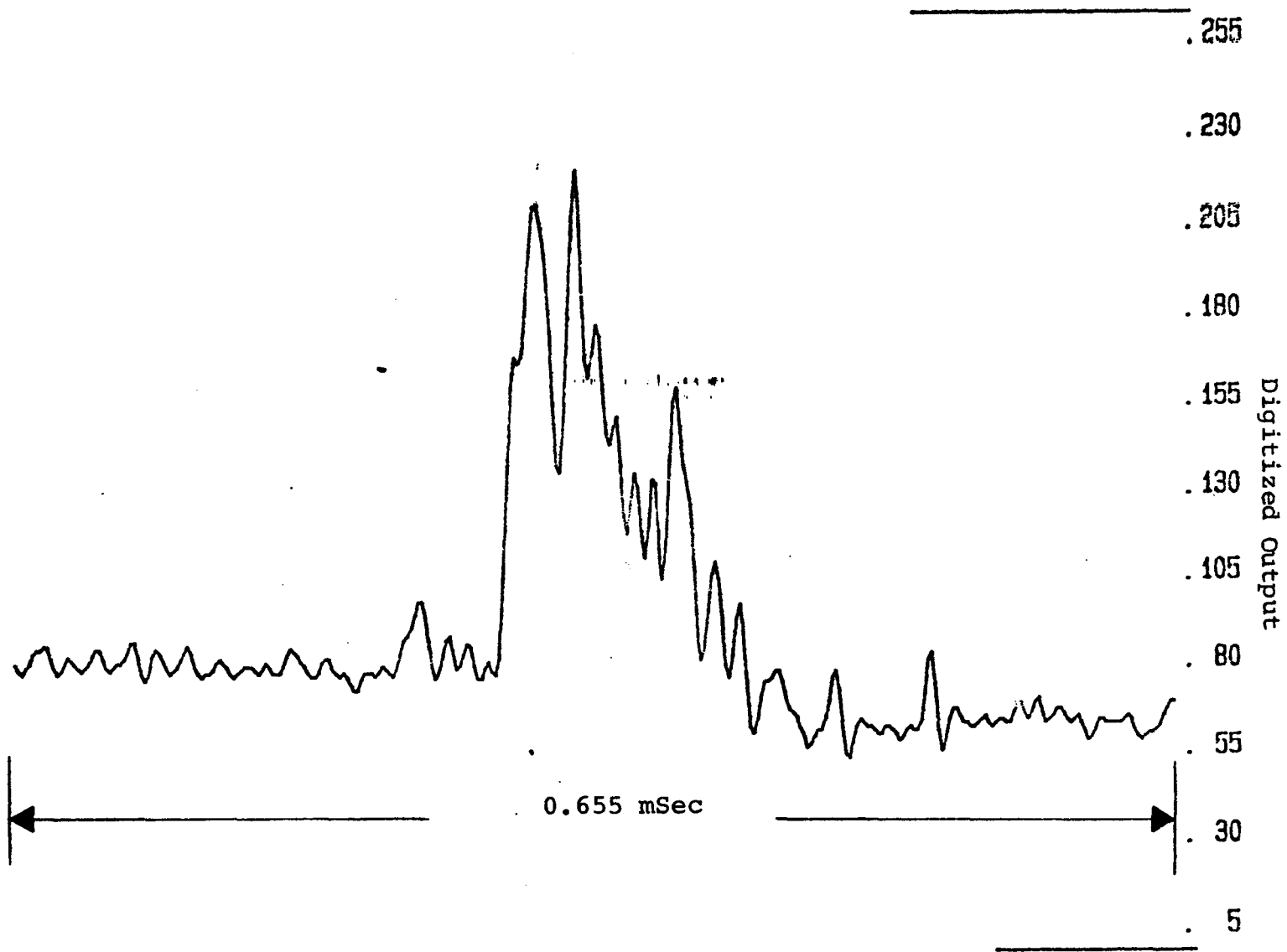
Since all the records considered are for identified cloud-to-ground discharges, it can be safely suggested that the large peak represents the 1st return stroke and the active region prior to that is due to the leader process of the ground flash.

TRACK# - 77 #WORDS IN REC - 8519 #5 JUL19



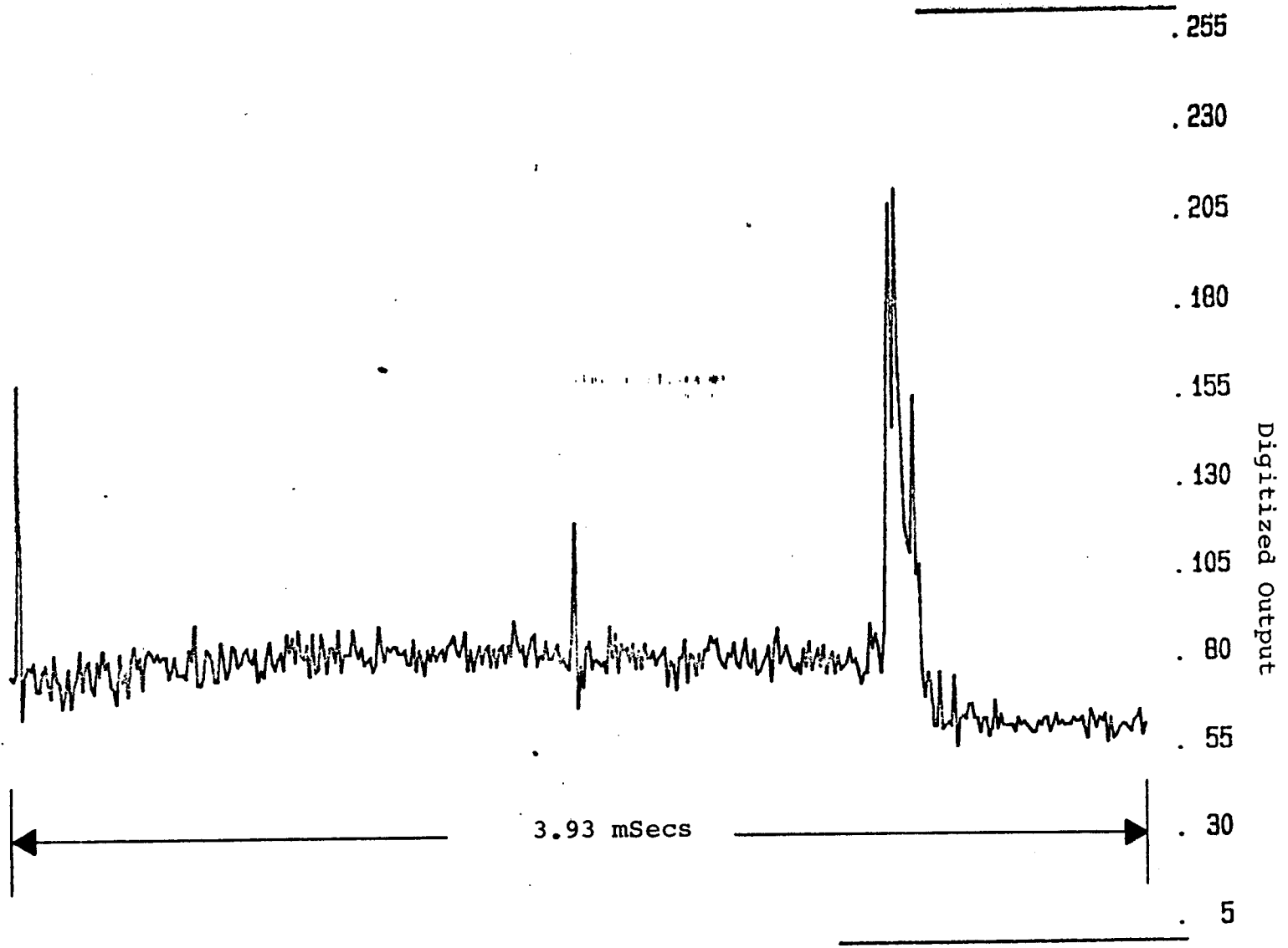
XXI-14

Fig. 5. High-Resolution Record of
A Cloud-to-Ground Emission



XXI-15

Fig. 6. Magnetic Tape Record of The Emission Shown in Fig. 5.



91-1XX

Fig. 7. Longer Record Off Magnetic Tape for Emission of Fig. 5 and 6

Conclusion

The MSFC Lightning Emission Measurement facility has been significantly improved since its setup in 1981 and provides an excellent mean for collecting emission data at the VHF and S-band frequencies. Data collection during summer of 1982 became possible during four thunderstorm activities. Emission records on several cloud-to-ground discharges were obtained. The radiation E-field computed for six cg flashes give peak values (1 KHz at 10 Km) of 8 to 32 $\mu\text{V/m}$. This agrees with the results reported by some of the other investigators.

Preliminary study of signal characteristics suggest distinct signatures are associated with different parts of cg discharges. The high resolution records along with simultaneous S-band, VHF-band, and electrostatic records obtainable with this facility should provide excellent data for signature analysis.

Recommendations:

(a) Several more sessions of data collection with this facility are required to provide the necessary data base for any meaningful statistical analysis. It has been suggested that the facility be maintained operational and efforts be made to collect the necessary data during the early part of Summer 1983.

(b) To facilitate instrument operation during data collection, it is helpful if remote switches are provided for the Reset/Arm of the digitizer and the Stop function of the UT readout. This will eliminate the need for moving between the equipment and hence slightly decrease the "down" time of the digitizer.

(c) Some minor repairs on the Ampex recorder are required. The glass plates associated with the low pressure chambers of the tape guide sections need to be permanently installed for proper recorder operation.

REFERENCES

1. Bent, Rodney B., Operational Applications Committee, Proceedings of the 1979 Workshop on the Need for Lightning Observation from Space, NASA CP-2095, Washington, D.C., 1979.
2. Oetzel, G. N. and E. T. Pierce, Radio Omissions from Close Lightning, Planetary Electrodynamics Vol I, Gordon and Breach Publishers, New York, 1969.
3. Oh, L. L., Measured and Calculated Spectral Amplitude Distribution of Lightning Sferics, IEE Trans. EMC, EMC-11, Nov., 1969
4. Jalali, F., Detection and Analysis of RF Lightning Emissions, NASA/ASEE Summer Faculty Research Fellowship Program Report, NGT 01-008-021, UAH, 1981.
5. Reference Data for Radio Engineers, Howard W. Sams and Co., Inc., New York, Sixth Edition, 1975.
6. Uman, Martin A., Lightning, McGraw-Hill Book Company, New York, New York, 1969.
7. Rust, W. D., P. R. Krehbiel, and A. Shlanta, Measurements of Radiation from Lightning at 2200 MHz, Geophys. Res. Lett., 6, 85, 1979.

1982

NASA/ASEE SUMMER FACULTY RESEARCH FELLOWSHIP PROGRAM
MARSHALL SPACE FLIGHT CENTER
THE UNIVERSITY OF ALABAMA

THERMAL RADIATION VIEW FACTOR
Methods, Accuracy and Computer-Aided Procedures

Prepared By:	Prasanna V. Kadaba, Ph.D.
Academic Rank:	Associate Professor
University and School:	Georgia Institute of Technology School of Mechanical Engineering
NASA/MSFC	
(Laboratory)	Structures and Propulsion
(Division)	Engineering and Analysis
(Branch)	Life Support and Environmental Branch
MSFC Counterpart:	J. D. Moss/L. D. Turner
Date:	August 1982
Contract No.	NGT-01-002-099 (University of Alabama)

THERMAL RADIATION VIEWFACTOR
METHODS, ACCURACY AND COMPUTER-AIDED PROCEDURES

BY

PRASANNA V. KADABA, PH.D
ASSOCIATE PROFESSOR OF MECHANICAL ENGINEERING
GEORGIA INSTITUTE OF TECHNOLOGY
ATLANTA, GEORGIA 30332

ABSTRACT

Exposed orbiting equipment is subjected to temperature variations caused by impinging solar radiation, the reflected energy from the earth, the internal heat sources and sinks and the mutual radiation among themselves. The satisfactory operation of these packages depends on maintaining them within the predetermined acceptable temperature range. The computer-aided thermal analysis programs can predict these results prior to stationing of these orbiting equipment in various attitudes with respect to the sun and the earth.

Principle mechanism of heat transfer in space is by thermal radiation and for thermally diffuse surfaces the heat transfer rates depends on the radiation viewfactors. Complexity of the surface geometries suggests the use of numerical schemes for the determination of these viewfactors.

Basic definitions and standard methods which form the basis for various digital computer methods have been presented followed by a brief discussion of various numerical methods. The physical model and the mathematical methods on which a number of available programs are built have been summarized. The strength and the weaknesses of the methods employed, the accuracy of the calculations and the time required for computations are evaluated and discussed. Based on this study, the situations where accuracies are important for energy calculations have been identified. Methods to save computational times are proposed. Guide to best use of the available programs at several centers and the future choices for efficient use of digital computers are included in the recommendations.

Acknowledgments:

The author of this report wishes to gratefully acknowledge the technical support given in selecting the research topic and presenting the clear perception of the problem by Messrs. J. D. Moss and L. D. Turner as well as Dr. W. R. (Randy) Humphries, Chief, Life Support and Environmental Branch. The arduous task of selecting NASA/ASEE Fellows and matching them with timely topics of interests by the personnel at the University of Alabama (represented by Dr. B. F. Barfield) and at MSFC (represented by Mr. Marion I. Kent) and the immeasurable success they have achieved with limited financial support is noted. It is the sincere wish of this author that such programs be continued with greater vigor and larger numbers in order to expose the academic faculty to the forefront of technologies and carry the message of this mission to the budding generation of students they educate.

The author wishes to acknowledge the careful typing of this manuscript as well as the detailed version by Ms. Loretta Hereford. Without her cheerful and dedicated efforts the successful completion of this project in so short a time would not have been possible. The support of visual aids department in preparing the graphics and tables is worthy of praise. The cordial association of the other members of the team in the Life Support and Environmental Branch, MSFC, is greatly appreciated.

TABLE OF CONTENTS

	<u>Page No.</u>
Abstract	XXII - i
Acknowledgments	XXII - ii
List of Figures	XXII - iv
List of Tables	XXII - iv
 Introduction	 XXII - 1
Basic Concepts	XXII - 2
Radiosity Method	
Hottel's Method	
Gebhart's Method	
Oppenheim's Electric Network	
Analog Method	
 Radiation View Factor	 XXII - 8
Nusselt Method	
Ray Tracing Technique	
Double Integration - Double Summation	
Method	
Hottel's Stretch Film Method	
Contour Integration Method	
Monte-Carlo Method	
 Numerical Procedures	 XXII - 19
Iterative Procedure	
Finite Difference Procedure	
Finite Element Procedure	
Approximate Analytical Solution	
Monte-Carlo Procedure	
 Accuracy and Computational Time	 XXII - 25
 Computer Programs	 XXII - 34
 Conclusions and Recommendations	 XXII - 45
 References	 XXII - 48
 Appendix	 XXII - A1
View Factor Calculations Using	
TRASYS	

LIST OF FIGURES

<u>Figure No.</u>	<u>Title</u>	<u>Page No.</u>
1	Representation of View Factor	XXII - 3
2	Radiosity and Radiative Exchange Between Surfaces	XXII - 5
3	Geometry of Unit-Sphere Method for Obtaining Configuration (View) Factors	XXII - 9
4	Crossed-String Representations for Two-Dimensional View Factors	XXII - 13

LIST OF TABLES

<u>Table No.</u>	<u>Title</u>	<u>Page No.</u>
1	Percentage Error in the Numerical Calculation of the View Factor Between Two Surfaces of Equal Breadth ($L = H$)	XXII - 27
2	Computer Programs Having Heat Transfer Analysis Capabilities Selected for Survey	XXII - 35
3	Survey of Computer Programs Capabilities used in Heat Transfer Analysis	XXII - 39

Introduction

The orbital Space Laboratory with its door open while in the earth's orbit is exposed to the solar radiation, the earth's albedo and the mutual radiation from the parts of the spacecraft itself. Some of the experimental packages are passive and, hence, they experience a wide range of temperatures due to net radiative heat balance. This range of temperatures need to be predicted for various attitudes the space station will be held during its orbit¹. If the upper and low limits of temperatures are beyond the safe limit for satisfactory operation, these packages need to be protected from undesirable radiative heat transfer. Other experimental packages are mounted on coldplates with its ability to heat sink either heat generated from the equipment itself or the extraneous radiative heat transfer. The nature of their arrangements suggests that these components need to be held in a narrow range of temperature limits for their satisfactory operation and control by the crew members. A successful space laboratory mission requires optimization of thermal performance of all the components of the system consistent with the critical weight/cost considerations. It is to be expected that the predicted temperature variations of components of the space laboratory obtained from analytical methods will be verified by selective monitoring of the temperature sensors.

The expected temperature variations of the surfaces of the space laboratory experiments require nodal heat balance among the heat absorption, the heat generation, the heat conduction and the heat lost to outer space. Successful tracking of these parameters leads to unsteady state heat transfer problem since all the suggested parameters are time varying functions, often in asynchronous manner. It is natural to expect coincident spikes and valleys giving rise to the expected range in the temperature excursions of the space laboratory components. Here, the heat flow mechanism is radiative mode to and from the surfaces. Its evaluation is influenced by mutual radiation view factors² among the surfaces of the space laboratory as well as the views to the sun, the earth, and the celestial space. This report will discuss the methods available for their computations, the need for accuracy of these computations and the efficient use of the available computer programs to achieve these goals.

1

In the recently concluded space shuttle -4 mission (June-July), the shuttle was flown for 10 hours with its belly showing to sun in order to drive out possible moisture under the heat shield tiles by taking advantage of the temperature rise due to net radiative heat transfer to the surface.

2

Some of the other names are form factor, shape factor, configuration factor, geometric factor, etc.

Author's Note:

This report has been hurriedly put together due to lack of time at the tail end of the ten week-Fellowship program. The reader will come across open spots in a line. It should not be viewed as missing information. At other places there are evidences of overcrowding. It is hoped that the concerned readers will overlook these shortcomings and lack of professionalism in preparing this report. Thank you very much for your understanding.

Basic Concepts:

Basic definitions of geometric view factors for Lambertian surfaces³ are illustrated in Figure 1. The differential view factor between elemental areas dA_i and dA_j as illustrated in Figure 1-(a) is given by

$$F_{dA_i-dA_j} = \frac{1}{\pi} (\cos \beta_i d\omega_j) = \frac{\cos \beta_i \cos \beta_j dA_j}{\pi r^2} \quad (1)$$

where $d\omega_j$ is the solid angle made by dA_j at the centroid of the area dA_i . $\cos \beta_j dA_j$ is the projection of dA_j normal to the radius vector r . Eq. 1 represents the fraction of hemispherical radiation leaving surface dA_i that is intercepted by the surface dA_j shown in Figure 1-(a). For a selected value of dA_j , the solid angle $d\omega_j$ subtended at the centroid of dA_i reduces as the square of the distance represented by the radius vector. This is of importance in the computer representation of this equation. By considering several such dA_j 's in the area A_j as shown in Figure 1-(b) the geometric viewfactor between the differential area dA_i and the finite area A_j is given by

$$F_{dA_i-A_j} = \int_{A_j} \frac{\cos \beta_i \cos \beta_j dA_j}{\pi r^2} \quad (2)$$

In computer programs the integration represented in Eq. 2 is replaced by the summation and the accuracy of the result depends on the individual size of dA_j 's and r the length of the radius vector. Similarly, by considering several dA_i 's as shown in Figure 1-(c), the total radiation view factor is given by

$$F_{ij} = F_{A_i-A_j} = \frac{1}{A_i} \int_{A_i} \int_{A_j} \frac{\cos \beta_i \cos \beta_j}{\pi r^2} dA_i dA_j \quad (3)$$

Again, it is possible to replace the double integration by the double summation in the computer programs, the accuracy of which depends on maintaining a typical small value of $d\omega_i$ defined in Eq. 1. This statement suggests that the choice of the sizes of dA_i and dA_j should be small when the distance between them is small, opposite being true when the distance is large in order to speed up computational time consistent with required accuracy. By multiplying Eq. 1 by dA_i the right hand side is rendered symmetric suggesting the reciprocity relation

$$dA_i F_{dA_i-dA_j} = dA_j F_{dA_j-dA_i} \quad (4)$$

Similarly from Eq. 2

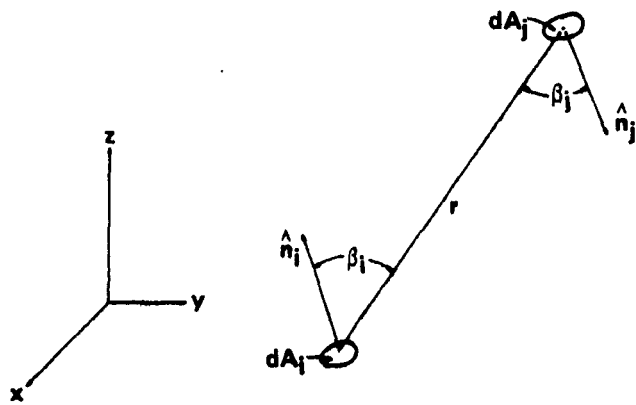
$$dA_i F_{dA_i-A_j} = A_j F_{A_j-dA_i} \quad (5)$$

and from Eq. 3

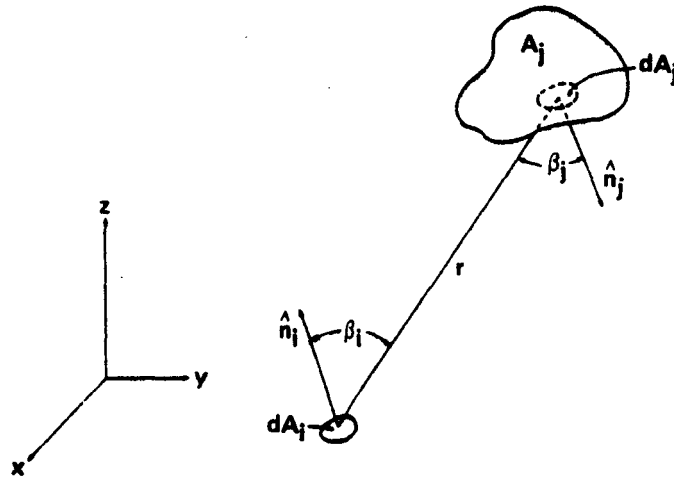
$$A_i F_{ij} = A_j F_{ji} \quad (6)$$

³

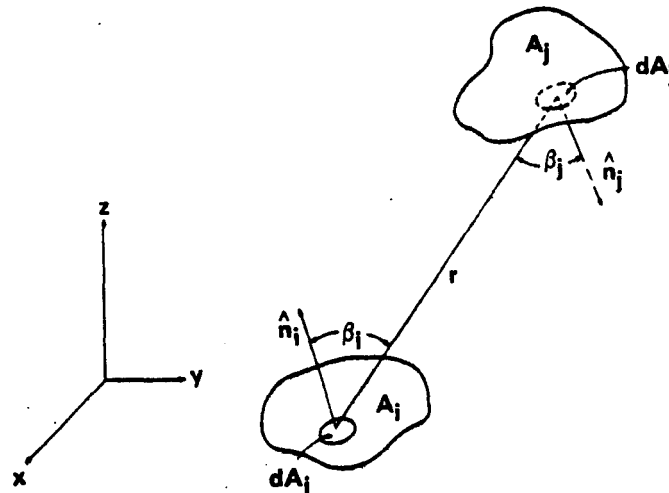
Emission and reflection from such surfaces are perfectly diffuse obeying Lambert's Cosine Law



(a) CONFIGURATION FOR INTERCHANGE BETWEEN TWO INFINITESIMAL ELEMENTS



(b) CONFIGURATION FOR INTERCHANGE BETWEEN AN INFINITESIMAL ELEMENT AND A FINITE SURFACE.



(c) CONFIGURATION FOR INTERCHANGE BETWEEN TWO FINITE SURFACES.

FIGURE 1 REPRESENTATION OF VIEW FACTOR

Equations 4, 5, and 6 represent useful reciprocity relations which can be utilized advantageously in computer program in order to reduce the time of computations. Equations 1, 2, and 3 and the associated reciprocity relationships are satisfactory for black bodies and gray surfaces. In the case of gray surfaces, the net energy transfer between two surfaces differential or finite is proportional to the radiation view factors. Here, the net energy transfer refers to the concept of radiosity⁴, that is the sum of diffusively emitted energy from the gray surface having an emissivity of ϵ and the fraction of diffusively reflected portion of incident energy from the same surface having a reflectivity of ρ . Here $\epsilon + \rho = 1.0$. However, the radiative heat fluxes need to be related to the characteristic temperatures of these diffuse surfaces.

Consider Fig. 2-(a). The radiosity $J_i = \epsilon_i W_{bi} + \rho_i H_i$ the sum of emitted energy from the diffuse gray surface (i) and reflected portion of the incident energy (H_i) from all the surfaces in view. Note $\epsilon_i + \rho_i = 1.0$. Similarly, $J_j = \epsilon_j W_{bj} + \rho_j H_j$. The net radiant flux leaving surface i is given by

$$q_{net,i}'' = J_i - H_i = \frac{\epsilon_i}{\rho_i} (W_{bi} - J_i) \quad (7)$$

Recognizing that the incident energy (H_i) is from the gray enclosure

$$H_i = \sum_{j=1}^N J_j F_{ij} \quad (8)$$

and

$$J_i = \epsilon_i W_{bi} + \rho_i \sum_{j=1}^N J_j F_{ij} \quad (9)$$

Equation 7 can be multiplied by A_i in order to obtain the total heat. Again, A_i can be replaced by dA_i , the sum by integration and F_{ij} by Eq. 1. This leads to integral equation of radiative exchange at the surface. For the case of two surface problems, that is, body and its enclosure (see Figure 2-(c), $F_{11} = 0$, $F_{12} = 1.0$)

$$q_{net,12} = \frac{W_{b1} - W_{b2}}{\frac{\rho_1}{\epsilon_1 A_1} + \frac{1}{A_1 F_{12}} + \frac{\rho_2}{\epsilon_2 A_2}} \quad (10)$$

which illustrates the electric resistance analog leading to network analysis. Recognizing $\epsilon_1 + \rho_1 = 1.0 = \epsilon_2 + \rho_2$, the radiant heat flux leaving surface 1 is

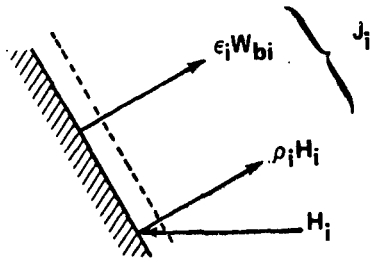
$$q_{net,12}'' = \frac{W_{b1} - W_{b2}}{\frac{1}{\epsilon_1} + \frac{A_1}{A_2} (\frac{1}{\epsilon_2} - 1)} \quad (11)$$

Equation 10 can be generalized to represent the energy leaving gray surface A_i streaming towards another gray surface A_j

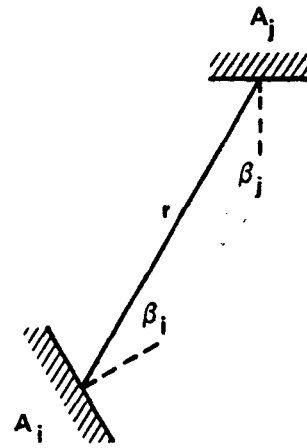
$$q_{net,ij} = \frac{W_{bi} - W_{bj}}{\frac{\rho_i}{\epsilon_i A_i} + \frac{1}{A_i F_{ij}} + \frac{\rho_j}{\epsilon_j A_j}} \quad (12)$$

$$q_{net,ij} = A_i F_{ij} (W_{bi} - W_{bj}) = A_i B_{ij} (W_{bi} - W_{bj}) \quad (13)$$

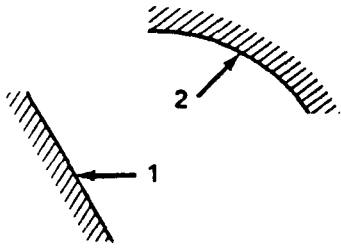
⁴ Hottel calls this term as "Leaving Flux Density" and suggests the word "Radiosity" as an undesirable word.



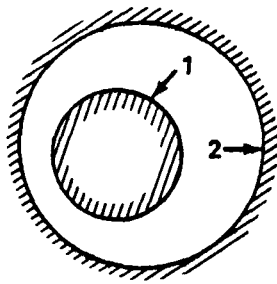
(a) NET RADIATIVE ENERGY TRANSFER AT THE SURFACE



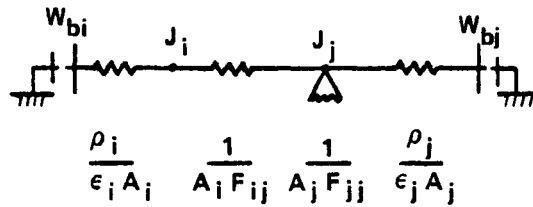
(b) RELATIONSHIP BETWEEN SURFACES



HERE $F_{12} < 1.0$



HERE $F_{12} = 1.0$



GENERAL CASE BETWEEN SURFACES A_i AND A_j

(c) TWO SURFACE PROBLEM – BODY AND ENCLOSURE OR SURFACES THAT CAN SEE EACH OTHER AND THE EQUIVALENT RESISTANCE ANALOGY

FIGURE 2. RADIOSITY AND RADIATIVE EXCHANGE BETWEEN SURFACES

Here, B_{ij} (F_{ij} often used in the textbooks) is the gray surface radiation view factor. For blackbodies $\epsilon_i = \epsilon_j = 1.0$ resulting in $B_{ij} = F_{ij}$ which is purely a geometric factor or configuration factor. A more general definition of patterned after Eq 3 is given by

$$B_{ij} = \frac{\int_{A_i} \int_{A_j} \frac{J_i}{\pi r^2} \cos \beta_i \cos \beta_j dA_i dA_j}{\int_{A_i} J_i dA_i} \quad (14)$$

and for the case of the radiosity being constant over the surface it will reduce to Eq. 3.

The concepts expressed in these equations are important. Various methods that are available to establish the geometric view factors and the associated gray surface will be reviewed in order to appreciate the speed and the accuracy of calculations in a complex enclosure such as the Space Laboratory. The concept of gray surface introduced here and its use instead of real surfaces need to be explained. They are as follows:

1. Each surface considered is isothermal. Here, it means that planar thermal conductivities are high. If a large surface cannot be treated as isothermal it is possible to subdivide the surface to smaller regions each assuring local isothermal conditions.

2. Each surface considered is gray. Here, it means that the emissivity and reflectivity are independent of the temperature, the wave length and they have no directional preferences in the hemispherical enclosure. It is possible to represent strong variation of property with respect to each of the quantities as step function with radiant energy transferred in each of this range. Real surfaces with selective coatings can be approximated in this manner provided the radiative properties are known to a reasonable accuracy and the increase in computational time can be justified. Specularly reflective surfaces can also be handled by the methods reviewed here. Chalk white surfaces have reasonably good diffuse reflectivity, although the tests have shown some specular character. It should be noted that the representation of variation in directional emissivity in the polar and azimuthal direction other than gray surface behavior will add considerable complexity increasing the computational time.

3. The radiosity of each surface is constant along the surface. This assumption makes the computed view factors independent of the magnitude and surface distribution of the radiant heat flux. It is clear that in order to validate this assumption the local isothermal condition of the surfaces should be assured and the incident radiant heat flux be the same at every point on the surface. Again, it is possible to subdivide the main surface in order to improve the accuracy and, hence, the complexity of computational procedure.

Further significances of these assumptions will be discussed later when the power of Monte Carlo method is compared to other numerical methods.

The basic concepts expressed in Figure 2 and Eq. 7 through 14 form the core for various numerical methods that are currently available. Here, the basis for the program development will be discussed.

Radiosity method, proposed by Eckert and Drake. The basic definition is set forth in Fig. 2-(a). From Fig. 2-(c), the heat flow is given by

$$q_i = (W_{bi} - J_i) / \left(\frac{\rho_i}{\epsilon_i A_i} \right) \quad (15)$$

Here q_i represents the heat flow leaving diffuse gray surface towards all parts of enclosure seen by it. This value of q_i need to be broken into n linear equations, solution of which depends on the emissive power of these surfaces which in turn related to the absolute temperatures via Stefan Boltzmann's Law, $W_b = \sigma T^4$.

Hottel's method. Here, the emphasis is placed on evaluation of net heat transfer q_{ij} between the two surfaces. As can be seen in Fig. 2-(c) it is the heat flow in the resistive element between J_i and J_j which is given by

$$q_i = A_i F_{ij} (J_i - J_j) \quad \text{and} \quad q_i = \sum_{j=1,0}^n q_{ij} \quad \text{Although the point of departure is different the calculations involved is same as the radiosity method.}$$

Gebhart's method. Here, the emphasis is on the net heat transfer from surface i to all the n surfaces of the enclosure each characterized by temperature

T_j 's. Adiabatic surfaces (re-radiating surfaces) are treated by substituting $\rho = 1.0, \epsilon = 0$ at these surfaces. The net heat transfer is expressed as difference between the emitted energy from surface A_i and that absorbed at n surfaces forming the enclosure which is given by

$$q_i = \epsilon_i A_i W_{bi} - \sum_{j=1,0}^n B_{ji} \epsilon_j A_j W_{bj} \quad (16)$$

Again $W_b = \sigma T^4$ and B_{ji} is the fraction of the energy emitted by surface j which is absorbed by the i th surface. Evaluation of the absorption factor B_{ji} involve the use of view factor, F_{ji} , the energy emitted and that reflected from the adjoining surfaces which requires all the other view factors of the enclosure. It is given by

$$B_{ji} = \epsilon_j F_{ji} + \sum_{k=1,0}^n \rho_k F_{jk} B_{ki} \quad (17)$$

Differences among the above three methods is in the viewing of the enclosure and the associated radiant exchange. As before, the calculations involved is the same as the previous two methods.

Oppenheim's Electric Network Analog method (1956)⁵. Figure 2-(c) represents such an analog between two gray surfaces.

Such a network can be constructed for an enclosure containing n surfaces. As before the adiabatic surfaces are treated by letting $\rho = 1$ and $\epsilon = 0$. Concave surface which can see itself will have a view factor as shown in Figure 2 -(C), but the net radiation is zero since the equivalent resistance $1/A_j F_{jj}$ is shorted out of the electric network. Radiation to outer space can be represented by treating it as black enclosure ($\rho = 0$) maintained at absolute zero which assures no returning of energy from that surface. The heat flow at any node i is represented by

$$q_i = \sum_{j=1,0}^n A_i F_{ij} (J_i - J_j) \quad (18)$$

and Eq. 7 relates q_i to the

temperature of the i th surface. The unsteady state mode at one or more nodes can be represented by writing the applicable accumulation term. Such a representation permits use of widely understood Kirchoff rules of linear electric circuits. Because of the potentials of this body of knowledge, preference may be given to this method over the remaining three methods. The calculation procedures will not be much different and the results should be identical.

Greater details of the above four methods can be obtained from a paper by Sparrow (1963). All of these methods require radiation viewfactors, and solution to solving linear algebraic equations. The accuracy of the results depends on the extent to which gray surface approximations are valid. Only the overall heat transfer to and from the surfaces can be established. The uniformity of the heat flux depends on the extent to which local isothermal conditions over each surface is established. It is expected that in all but the simplest systems, the leaving radiant flux would likely to be nonuniformly distributed over a surface even if the surface is isothermal and exhibits the character of Lambertian surface. As stated earlier, each of the surfaces can be subdivided, the properties can be represented as step functions increasing the number of algebraic equations and complexity of the problem, and utilize the digital computers for their solutions. The success in reproducing actual result depends on the radiative property of the surfaces as a function of temperature and wave length and their directional character. Sparrow (1978) suggests monochromatic analysis for property dependence on wave length and integrating the results over the entire applicable range of wave lengths. This thought is same as step representation and the number of steps per surface should justify the concurrence between the predicted result and that of experience.

Radiation View Factor:

Nusselt Method.

Basic definition of the radiation view factor has been set forth in Figure 1 and Equations 1, 2 and 3. Such a representation is purely geometric in nature. Figure 3 further illustrates the definitions of view factors between the two differential areas dA_i and dA_j . Here, the total view from the center of dA_i is the "hemispherical space" above it in the viewing plane, which is termed as unity. An area A_j in Figure 3 projects a surface A_s on the hemisphere as viewed from dA_i . This surface is projected on to the base which is shown as A_b in Figure 3. The radius of the hemisphere being unity, the ratio of $A_b / \pi(1)^2$ is the geometric view factor $F_{dA_i-A_j}$ illustrated in the figure which is defined by Equation 2.

$$F_{dA_i-A_j} = \int_{A_j} \frac{\cos \beta_i \cos \beta_j}{\pi r^2} dA_j \quad (2)$$

This illustration forms a basis for explaining, experimentally determining, evaluating by digital computers and developing analytical solutions to the geometric view factor. It is the fraction of the total view. This type of

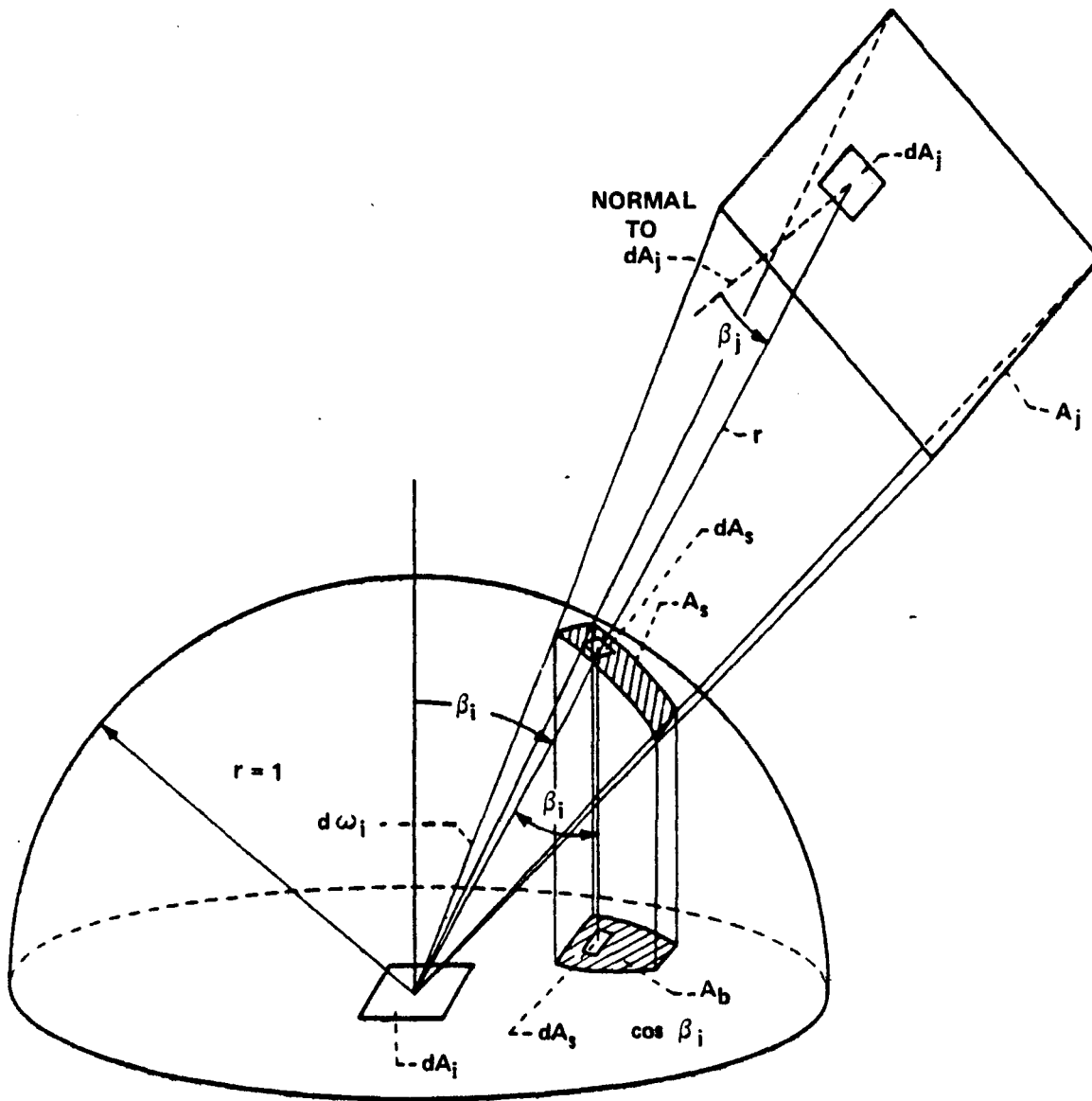


FIGURE 3 GEOMETRY OF UNIT-SPHERE METHOD FOR OBTAINING CONFIGURATION FACTORS.

representation is known as the "unit sphere method" first proposed by Herman (1900), and suggested again by Nusselt (1928). According to Jakob (1957) at almost the same time Seibert (1928) published a similar method. It is popularly known as Nusselt Unit Sphere Method. It is interesting to note why it was not called unit hemisphere method since the view range of the plane face dA_i is only the hemispherical space above it.

The view factor from the differential plane area dA_i should not be confused with the view experienced by a differential sphere of area dA_i to the enclosure. In this report, the space laboratory experiments in the payload bay are made up of plane, convex and concave surfaces for the determination of the view factors. In the case of the differential sphere having convex surface area dA_i the total view is the spherical space around it. Jakob (1957) shows that as a limiting case view factor of infinite plane with respect to this differential sphere is 1/2 while the view factor of the same infinite plane with respect to differential plane dA_i is unity. This result is easy to visualize. It requires two infinite planes to form a total enclosure around the differential sphere whose view factor will be unity. Same result will be obtained if both sides of the differential area dA_i are active viewing areas. In the determination of view factor only one side of plane or curved surfaces dA_i or ΔA_i is considered. It is important to note this subtlety since the determination of view factors from convex surfaces involve portions of differential areas not being able to see all of the viewing areas A_j , the receiving surface.

The illustration shown in Figure 3 has been the basis for experimental determination of the shape factor by mechanical integrators as developed by Hottel (1931), Hamilton and Morgan (1952) photographic technique proposed by Eckert (1935) Hickman (1961), photo electric method of England and Craft (1942), Jakob and Hawkins (1942) and electric analog developed by Paschkis (1936).

Ray Tracing Technique.

The determination of the view factor as described here recognizes the fact that an infinite number of rays emigrate from a point in a plane in the hemispherical space above it. They are intercepted by adjoining surfaces forming a view (solid angle) with respect to the differential area at the source. Only those portions which can be seen are considered. If all the adjoining surfaces of the experiments in the payload bay, the sun, the earth and the planets as seen by the point do not cover the entire hemisphere the view factor of the remaining area is considered as view to the outer space. Farther is the area with respect to the viewing point smaller is its view factor. Such a ray tracing technique is the basis for determination of all view factor calculations whether it is closed form integration or numerical methods including Monte Carlo based model or experimental methods. In the numerical methods the viewing surface that is under consideration is divided into number of small areas ΔA_i . The view factor to each of the A_j forming the total hemispherical enclosure is estimated. These values of view factors for all ΔA_i forming the area A_i are weighted in order to assure the total view from A_i to all the surfaces A_j will not exceed unity. The accuracy of such numerical methods depend entirely on the sizes of ΔA_i and ΔA_j and the average distance between them as set forth in the definition given by Equation 1 and illustrated in Figure 1 -(a). The choice of the size of ΔA_j

depends on the distance r from ΔA_i and it should be selected in a manner that the typical value of $F_{\Delta A_i - \Delta A_j}$ is about the same small value during the entire field of calculations. This thought suggests that the sizes of ΔA 's should be progressively smaller if their average distances get smaller assuring the same level of accuracy. If the surfaces A_j and A_i have common boundary, the ΔA 's in their vicinity will be the regions for sources of error in the determination of view factors. If the determination of view factor to the space from a surface A_i is obtained by subtracting the sum of all the other view factors from unity, $1 - \sum_{j \neq i} F_{ij}$, it is only natural to expect sources of errors to propagate in the energy calculations and incorrect prediction of maximum and minimum temperatures of the surfaces forming the space laboratory experiments in the payload bay.

Double Integration - Double Summation Method.

The view factor between the surfaces A_i and A_j is given by solution to Equation 3. Here, the differential view factor given by Equation 1 is integrated once over the area A_i and next over the area A_j suggesting double area integration. Closed form solutions to a number of simple surfaces are available in the literature. Here, only two references will be mentioned, namely, NASA TN-2836 by Hamilton and Morgan (1952) and a recent textbook by Siegel and Howell (1981). In all these cases each area is defined by two parameters thus reducing the two area integrals to four line integrals.

For complex surfaces such as in the Space Laboratory mission the luxury of closed form solution is often unavailable resulting in replacing Equation 3 by double summation. Here, the area A_i and A_j are divided into small areas ΔA_i and ΔA_j and the differential view factors as expressed in Equation 1 is computed. First, the view factors over all of ΔA_j 's are summed, representing solution to Equation 2 and its weighted summation over all of ΔA_i 's represents solution to Equation 3. The areas A_i and A_j can be divided into small area in any convenient manner for digital computers and their centroid need to be located for determining the distance r between ΔA_i and ΔA_j as well as the associated differential view factor and weighting factor. The converging of the numerical value of F_{ij} as calculated by such a double summation method to a corresponding exact value that may be obtained from the closed form solution depends on the size of ΔA . Generally, as stated earlier, if the magnitude of the differential view factor is kept about the same small value by considering smaller ΔA as r decreases, there should be satisfactory convergence. It should be possible to compare the view factors F_{ij} 's as generated by the computer programs for the geometries for which closed form solutions are available and develop a level of intelligence for admitting variable sizes of ΔA thus reducing computational time consistent with accuracy.

Hottel's Stretch Film Method.

The surfaces and enclosures that exchange heat by thermal radiation such as in the payload bay of the Space Laboratory are plane, convex or concave surfaces. While any part of the plane or convex surface cannot see itself directly, the concave surface can see itself. In all cases, during the evaluation of view factors, if there are other surfaces partially obstructing the view all parts of surface 1 will not see all parts of surface 2 in order to determine the view factor F_{12} . Care should be exercised in evaluating such view factors

and avoid the possibility of over and/or under estimation of the energy exchange associated with them. Hottel (1954) provides solution to two dimensional cases and the methods is referred to as "crossed - string method". A variation of the same idea expressed by Hottel can be referred to as "stretch-film method".

In Figure 4 - (a1) the enclosure is made up of a complex surface A_1 , a plane surface A_2 and a convex surface A_3 , indicating that the real surfaces can be combination of such contours. The stretched string across A_1 will result in plano - convex surface A'_1 , ($A'_1 < A_1$), replacing the actual surface A_1 . In a three dimensional case the stretched string will be replaced by stretched film generating a cover everywhere there is concave contour very much like cellophane wrap. The shape factor relationship between the body (A_1) and the enclosure (A_2) is given by

$$A_1 F_{12} = A_1 (1 - F_{11}) = A'_1 \quad (19)$$

since $F_{11} + F_{12} = 1.0$ and $F_{1'2} = 1.0$.

Here, $F_{11} > 0$ since part of the surface can see itself. However, the view of the concave enclosure can only be through the stretched film covered over it. Utilizing the view factor algebra for the three surface problem the final expression is given by Hottel (1954) as

$$A_1 F_{12} = (A_1 + A_2 - A_3) / 2 \quad (20)$$

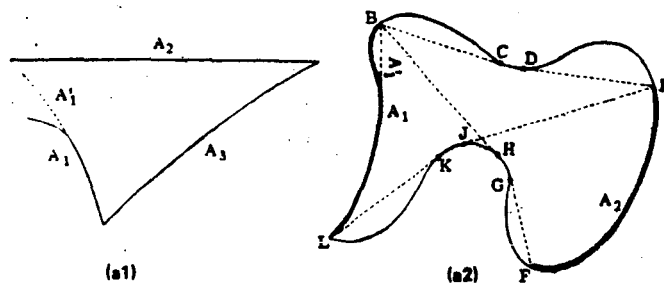
Figure 4 - (a2) represents a more complex enclosure containing areas A_1 and A_2 and bounded by other surfaces. The crossed - string BHGF and EJKL along with stretched - string BCDE and FGHJKL breaks the surfaces into problem represented by Figure 4 - (a1). It is also possible to represent the surfaces A_1 , A_2 under consideration into A'_1 and A'_2 by stretched - string concept. By using Equation 20 Hottel has shown

$$A_1 F_{12} = (EJKL + BHGF) - (BCDE + FGHJKL) \quad (21)$$

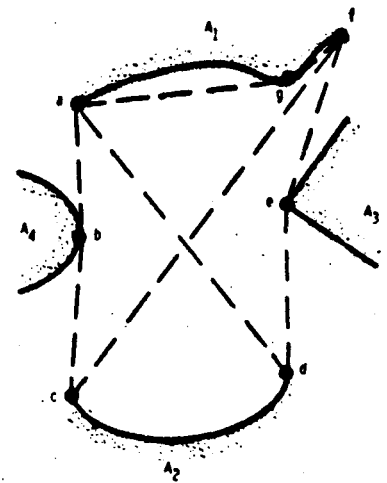
from which F_{12} can be calculated. The right hand side of Equation 21 represents the length of the two crossed - string minus the length of the the two stretched - string between the two surfaces that are considered for the view factor. It should be possible to extend the method of Hottel for the two dimensional geometry to the three dimensional cases. In exploiting such a potential to its fullest extent it should be possible to generate stretched - film surfaces utilizing the geometry of the real surfaces and to break complex enclosure into simpler enclosure by introducing intermediate surfaces, resulting in the utilization of view factor algebra for further reduction in computational time without sacrificing the accuracy. Even if such a convenience cannot be exploited⁶ with the existing programs, the concept expressed in Equation 19, that is the energy crossing across A_1 , consisting of plano convex surface created by the stretched film is the same as that received by A_1 real surface consisting of plano - convex^o - concave surfaces.

⁶

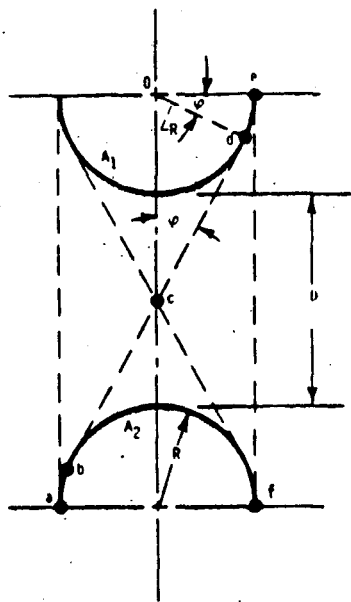
Reader is alerted to CAD programs with associated graphical displays which is capable of drawing various views very accurately which is mind boggling even for the best of living draftsman.



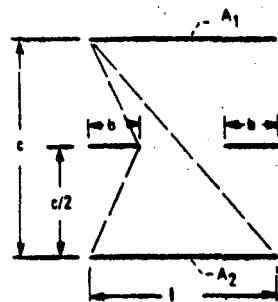
(a) TWO-DIMENSIONAL ENCLOSURES: (a1) THREE-SURFACE SYSTEM;
(a2) ARBITRARY CONFIGURATION.



(b) VIEW BETWEEN ARBITRARY SURFACES WITH OPENINGS TO SPACE



(c) VIEW BETWEEN TWO EQUAL AND PARALLEL CYLINDERS



(d) PARTIALLY BLOCKED VIEW BETWEEN PARALLEL STRIPS

FIGURE 4 CROSSED STRING REPRESENTATIONS FOR TWO-DIMENSIONAL VIEW FACTORS

Figure 4 - (b) represents four real surfaces with spaces between any adjacent pair can be outer space or remote objects forming the enclosure. It is easy to visualize the payload bay of the Space Laboratory to contain such configurations. The shape factor relationship between A_1 and A_2 can be written as indicated in Equation 21 and by constructing a pair of crossed string and another pair of stretched string which in this case

$$A_1 F_{12} = \frac{(A_{cf} + A_{ad}) - (A_{abc} + A_{fed})}{2} \quad (22)$$

which is same as Equation 21.

Figure 4 - c represents two cylinders of equal radius having their axes parallel to each other and a minimum separation of D . It is desired to express the mutual view factor. Note that the halves of the cylinders not seen by each other are not shown in the figure. The pair of crossed string $abcde$ and the pair of the stretched string fe are also shown. Defining $X = [1 + (D/2R)]$ and utilizing Equation 21.

$$F_{12} = \frac{2}{\pi} \left[(X^2 - 1)^{1/2} + \frac{\pi}{2} - \cos^{-1}(1/X) - X \right] \quad (23)$$

An extension of Equation 23 for the case of cylinders of unequal radii, R_1, R_2 ($R_1 > R_2$) and their axes separated by a distance C is given by

$$F_{12} = \frac{1}{\pi R_1} \left\{ R_1 \phi_1 + R_2 \phi_2 + [C^2 - (R_1 + R_2)^2]^{1/2} - [C^2 - (R_1 - R_2)^2]^{1/2} \right\} \quad (24)$$

Where $\phi_1 = \alpha - \beta$, $\phi_2 = \alpha + \beta$, $\alpha = \sin^{-1}(\frac{R_1 + R_2}{C})$, $\beta = \sin^{-1}(\frac{R_1 - R_2}{C})$

For the case $R_1 = R_2$

$$F_{12} = \frac{2}{\pi} \left[(X^2 - 1)^{1/2} + \sin^{-1}(1/X) - X \right]$$

which is same as Equation 23 since $\pi/2 - \cos^{-1}(1/X) = \sin^{-1}(1/X)$ (23)

Figure 4 - (d) represents the view factor between infinite strips A_1 and A_2 in the presence of two other infinite strips forming a slit. The Hottel's crossed-string method yields (see Siegel and Howell (1981)).

$$F_{12} = \frac{1}{l} \left\{ [l^2 + c^2]^{1/2} - 2 [b^2 + (c/2)^2]^{1/2} \right\} \quad (25)$$

The results of Equations 23, 24 and 25 can be checked with TRASYS program for speed and accuracy of the computations resulting in required shape factors.

Contour Integration Method

Determination of the view factor $F_{dA_i - A_j}$ using Equation 2, involves two line integrals while F_{ij} using Equation 3, involves four line integrals. In the contour integration method they can be reduced to one and two line integrals respectively. Here, the line corresponds to the boundary of the areas A_j and A_i thus acquiring the name contour integral. Such a transformation is due to Theorem of Stokes. The method is applicable for a piecewise smooth oriented

surface in space and its boundary be a piecewise simple closed curve. The integration around the closed curve is taken in a manner such that the interior space is to the left of a person walking on the edge of the contour with his head pointing in the same direction as the unit normal. According to Stokes Theorem⁷

$$\oint_C P dx + Q dy + R dz = \int_A \left[l \left(\frac{\partial R}{\partial y} - \frac{\partial Q}{\partial z} \right) + m \left(\frac{\partial P}{\partial z} - \frac{\partial R}{\partial x} \right) + n \left(\frac{\partial Q}{\partial x} - \frac{\partial P}{\partial y} \right) \right] dA \quad (26)$$

where P, Q and R are each functions of x, y and z and they are twice differentiable function and l, m and n are direction cosines of the area dA .

Details of contour integration method can be found in the book of Sparrow and Cess (1978). Here, some pertinent details will be given. In Figure 1 - (b)

$$r^2 = (x_i - x_j)^2 + (y_i - y_j)^2 + (z_i - z_j)^2$$

$$\cos \beta_i = \frac{1}{r} [l_i (x_j - x_i) + m_i (y_j - y_i) + n_i (z_j - z_i)]$$

$$\cos \beta_j = \frac{1}{r} [l_j (x_i - x_j) + m_j (y_i - y_j) + n_j (z_i - z_j)]$$

and using in Equation 2

$$F_{dA_i - A_j} = \int_{A_j} \left\{ l_j [(x_i - x_j)f] + m_j [(y_i - y_j)f] + n_j [(z_i - z_j)F] \right\} dA_j \quad (27)$$

$$\text{and } f = \frac{1}{\pi r^4} [l_i (x_j - x_i) + m_i (y_j - y_i) + n_i (z_j - z_i)]$$

Equation 27 represents the right hand side of Equation 26 setting the stage for the application of Stokes Theorem. Now

$$F_{dA_i - A_j} = l_i \oint_{C_j} \frac{(z_j - z_i) dy_j - (y_j - y_i) dz_j}{2 \pi r^2} + m_i \oint_{C_j} \frac{(x_j - x_i) dz_j - (z_j - z_i) dx_j}{2 \pi r^2} + n_i \oint_{C_j} \frac{(y_j - y_i) dx_j - (x_j - x_i) dy_j}{2 \pi r^2} \quad (28)$$

In practice, in order to simplify the integration where possible select coordinate axes such that one of them is in the same direction as the unit normal of dA_i . Such a choice permits evaluation of only one of the three parts in Equation 28, the other two being zero since the direction cosines are zero. If one or two coordinates of C_j are constant additional simplification of Equation 28 will result. For a complex geometry such a simplification may not be available.

In Equation 28 each of the contour integral can be evaluated independently. The results represents view factor of the surface A_j with respect to three mutually perpendicular dA_i at location i whose normals are coincident with respect to l_i, m_i and n_i . In particular, the absolute value of first part of Equation 28 is for the case $l_i = \pm 1, m_i = n_i = 0$. Both signs of l_i are applicable, they depend on normal to the element along $+x$ or $-x$ axis as it views A_j . Moreover, it is possible that $l_i = +1, m_i = n_i = 0$ may see a portion of A_j and $l_i = -1, m_i = n_i = 0$ may see the remaining portion of A_j such as in the wrap around case. In such cases the contour integral is sum of the two view factors, thus

$$\left| \oint_{C_j} \frac{(z_j - z_i) dy_j - (y_j - y_i) dz_j}{2 \pi r} \right| = F_{dA_i - A_j} (\pm 1, 0, 0) \quad (29)$$

7

Theorem of Gauss converts volume integral to area integral, area being the bounding surface of the volume itself.

Similarly other two parts of Equation 28 can be computed and identified as

$$F_{dA_i - A_j} (0, \pm 1, 0) \quad \text{and} \quad F_{dA_i - A_j} (0, 0, \pm 1)$$

Finally, the required view factor from dA_i having direction cosines, (l_i, m_i, n_i) is

$$F_{dA_i - A_j} = |l_i| F_{dA_i - A_j} (\pm 1, 0, 0) + |m_i| F_{dA_i - A_j} (0, \pm 1, 0) + |n_i| F_{dA_i - A_j} (0, 0, \pm 1) \quad (30)$$

Equation 30 suggests principle of superposition of the view factor. It can be utilized to convert view factor evaluated along the principle axes to any orientation by rotation (vector sum). Such considerations may avoid repetitive calculations besides the advantage of single integration replacing double integration.

Sparrow and Cess (1978) shows that the Stokes Theorem can be applied twice in order to evaluate F_{ij} . The final form of the expression is

$$F_{ij} = \frac{1}{2\pi A_i} \oint_{C_i} \oint_{C_j} (\ln r \, dx_i \, dx_j + \ln r \, dy_i \, dy_j + \ln r \, dz_i \, dz_j) \quad (31)$$

where

$$r^2 = (x_i - x_j)^2 + (y_i - y_j)^2 + (z_i - z_j)^2$$

Equation 28 or Equation 31 can be used. Here, four line integrals traversing entire surface A_i , A_j have been replaced by two line integrals traversing around the contour of A_i , A_j . The closed form integration of Equation 31 is possible for simple shapes. For complex surfaces the integration is replaced by summation and it is more advantageous for computers.

Monte Carlo Method.

Radiative exchange rates at a location is a function of local temperature and energy fluxes that are coming in or going out. This energy can be represented by discrete amounts (bundles) say N , typically of the order of 10,000 emitted from a point in all directions. Accuracy of the method increases with increasing values of N . By assigning energy level to each bundle the total heat flux at the point is satisfied. The Monte Carlo method derives its name from the fact that the laws of probability (chance) are employed in determining the direction of travel of energy bundles and in deciding if a bundle is absorbed, reflected or escapes into space. Some of the other names are "Random Walk" and Markov Chain. The probability of energy bundle leaving a location in a given direction expressed in spherical angles (polar and azimuth) arriving at another location is estimated. This bundle path history is computed by Monte Carlo method. The energy reflected back from the receiving location to the source and then back to receiver is neglected. The accuracy of the method depends on perfect randomness of the process.

Directional distribution of emittance as well as the spectral variations can also be considered. The distribution functions are normalized to give values from 0 to 1. The probability functions for diffusively emitting surfaces are $R_\theta = \sin^2 \theta$ ($0 \leq \theta \leq \pi/2$), $R_\phi = \phi/2\pi$ ($0 \leq \phi \leq 2\pi$) and equal energy is assigned to each bundle. Similar probability functions R_θ, R_ϕ for surfaces having different radiation properties need to be established if the surfaces are not gray. A pair of random numbers R_θ, R_ϕ specifies the direction of departure θ, ϕ of the

energy bundle having a certain magnitude towards the configuration of the enclosure. Its point of impingement on the receiving surface is determined. If the receiving surface has absorptivity α (or $\alpha_{\lambda, \phi}$) a random number R_{α} ($0 \leq R_{\alpha} \leq 1$) is drawn. If the range of α is $0 \leq R_{\alpha} \leq \alpha$ the incident bundle is assumed to be absorbed and it is recorded. The process is repeated for all bundles. If all surfaces are gray the same probability functions can be repeatedly used. In this case, the result of Monte Carlo method is geometric view factor as expressed in Equation 2 since the process is completed for a point on the emitter ΔA_i , to the receiver A_j . The process is repeated for every location of the emitter A_i represented by ΔA_i in order to determine the view factor F_{ij} .

The method described here suggests that the bundle originating from a point not intercepted by any of the surfaces forming the surfaces of payload bay, the sun, the earth can also be recorded. Hence, it should be possible to directly evaluate the view factor of a surface to the sprawling space. The accuracy of estimation of all view factors are upgraded by considering larger values for N suggesting the use of high speed digital computers with large storage capacity. More recent developments of the use of Monte Carlo method for radiation exchange incorporate the time saving schemes by selectively using scaling functions for the probability functions and completing the calculation only when the random numbers R_{θ} and R_{ϕ} impinges on the required surface. As stated earlier, the variation of the radiative properties can easily be accommodated when such information is made available without disturbing the methodology of Monte Carlo procedure.

In the calculation of the view factor, each selected point views the hemispherical space above it (in the direction of unit normal). Since the pair of random numbers R_{θ} and R_{ϕ} selected for each bundle has to intersect either any of the surfaces of interest or not intersect at all (lost to outer space) it should be possible to record all the information and evaluate simultaneously all the radiation view factors from the differential area selected. For a pictorial view of the above statement Figure 3 may be considered. Each of the A_j will create an island A_s on the unit hemisphere with A_b being projection on its base. The sprawling space around the groups of islands obviously represents the shape factor F_{dA_i} space when this area is projected on to the base of the hemisphere. Potential of this procedure should be exploited.

Comparison of Other Methods with Monte Carlo Method

Formulation of equations for radiant exchange by methods other than Monte Carlo method results in integral equation. Correspondingly, the accurate determination of the view factor results in double area integration. Closed form solution can only be obtained for single viewing surfaces. Nusselt Unit Sphere Method is suitable for view factor from a differential (small) area to a finite (large) area. Contour integration reduces the difficulty of double area integration to an extent. The difficulty of all these methods when applied to complex surface is a consequence of 'macroscopic' view point when deriving either the radiant exchange of the view factor to a receiving surface. On the other

hand the use of probabilistic model and Monte Carlo sampling techniques reduces the problem to "semi macroscopic or semi microscopic" depending on the size of N and avoids many of the difficulties inherent in the averaging process of the integral equation formulations. Monte Carlo provides a basis to examine the small parts of the total energy on an individual basis and accumulate the results instead of making an attempt to solve simultaneously the entire behavior of all the energy involved.

The complexity involved in Monte Carlo method is roughly proportional to the complexity of the problem. In all other cases amenable to numerical methods the complexity grows rather rapidly. The closed form solutions for view factors are available only for simple shapes. The complexity of formulation by Monte Carlo method for simple shapes and associated computational time to obtain the numerical result via digital computers makes the procedures undesirable. However, these examples can be used to check on the applicability of the method and its speed and accuracy. As the complexity increases it may be the only method for speed and accuracy of determination of the view factors or energy exchange between real surfaces. The availability of radiative property information is best utilized in Monte Carlo method. The choice of the use of the Monte Carlo method over any one of the other methods and their relative accuracies should be established by running test cases in the available high speed computers. Potential of improvisation to the existing Monte Carlo methods and hybrid situation should not be overlooked.

The determination of view factors and their use in radiative energy exchange involve assumptions such as the surfaces are diffuse - gray emitters and reflectors, they are locally isothermal and the total flux arriving at the surface is evenly distributed across the entire area. In real problems such as in payload bay of the Space Laboratory, the validity of any of these assumptions may be poor. In such cases, the calculation of view factor becomes difficult and their use in energy calculation will not give accurate results. In such cases, and when the geometry of surfaces are nonplanar, Monte Carlo technique may be invaluable. Parametric studies may resolve the issues that are raised here. Potential of the use of Monte Carlo technique to compute radiative heat - transfer directly as against using Monte Carlo technique for the evaluation of view factor and then using auxiliary program for the radiative heat transfer should be explored. Use of Monte Carlo method provides direct answer to the radiative heat fluxes between two surfaces of interest with no restrictions to the variation of surface property characteristics thus bypassing the calculation of radiative view factors. Inability to describe the surface properties will reduce the problem to simpler cases without any loss of generality that will be available for later use when data is made available. Additional details of the method can be obtained by reviewing the references by Howell (1968), Siegel and Howell (1981), Edwards (1981), Sparrow and Cess (1978).

Turner, Humphries, and Littles (1981) have compared results obtained by Monte Carlo method with specialized ray tracing technique and the TRASYS II program when applied to specularly reflecting surface of orbiter door of the payload bay in its open position to the incoming beam of solar radiation. The curved surface have been represented by small planar segments in order to utilize the composite limitations of the programs selected.

One hundred percent specularly reflecting surfaces for the interior of the orbiter door has been considered for comparison. Monte Carlo method accommodates multiple bounce while the specialized ray tracing technique is restricted to single bounce. The pattern of local heat flux variations on the surface of the payload bay compares favorably between the two methods. The total heat flux rate evaluated from the local heating rates compared very well with that obtained by TRASYS II program which allow consideration of specular surfaces. The discontinuities caused by replacing continuous surface by planar segments can be considered by offsetting planar nodes over small increments and changing its orientation accordingly and study the pattern of absorbed heat rate on receiving surface after the reflection from the interior of orbiter door. They can also be compared to smaller segment results. In reality, the existence of planar conduction of the receiving surfaces will naturally smooth out the variations in the heating rates obtained in this paper comparing more favorably with the total heat flux rate.

Numerical Procedures:

The temperature and the radiant heat flux at a point on the surface of any part of the Space Laboratory depends on the conduction heat transfer influenced by internal heat development and/or internal cooling, the diffuse/specular radiative properties at the surface, the radiant fluxes imposed by external sources, the heat exchange among the viewing surfaces and the heat loss to the outer space. Such a consideration for a differential area around the point results in integral equation. The formulation of problem utilizes radiosity concepts which in turn, requires the unknown temperature distribution. The interplay of the radiant energy requires differential view factors. The conduction part related to the first power of temperature and the radiation part related to the fourth power of temperature renders the equations to be nonlinear. It is important to note that the variation of temperature and radiosity over the surface necessitates area integral ruling out the use of contour integral in order to seek the required solution. Thus, the computational efforts are increased enormously if the heat balance of the Space Laboratory equipment in the presence of conductive/radiative environment need to be considered accurately. Replacing real surfaces with gray surface and recognizing large areas of the enclosure to be isothermal reduces computational time greatly. They permit evaluation of radiation view factors, their use in the radiative heat exchange and in the thermal analysis problem providing a means to decouple the problem. Even with this simplification, the computational time for the evaluation of view factors and the associated thermal analysis is considered excessive in the Space Laboratory configuration. The accuracy of the results also need to be established.

Iterative Procedure.

Initial distribution of radiosity is assigned using the radiation exchange formulation between a selected location x_0 and a general location x , a new value of radiosity at x_0 is calculated. Such a numerical procedure is repeated using the updated values of radiosities where available and old values at other locations. The process is repeated until the required convergence at all locations are satisfied. For problems where the nodal radiation is uncoupled with the nodal conduction, the iteration procedure will generally converge without problems of instability. Here, the radiant exchange will be

a linear function of radiosity permitting resistance network analogy leading to algebraic system of equations. With nodal conduction, the nonlinear coupling may display oscillating behavior for successive iterations or even exhibit diverging characteristics. In such cases the consideration may be given to replace the newly computed radiosity with the weighted average of the old and the new values at the same location.

Finite Difference Procedure.

The radiative exchange between any two points represented by integral equation is replaced by a finite sum of terms by dividing the areas to smaller areas, the points located at the centroid of these areas and the radiosity assumed constant over this elemental surface, itself being assumed to be isothermal. The accuracy of the finite difference scheme is comparable to numerical integration by trapezoidal rule, which can be improved by considering smaller element sizes. For the case when radiation is uncoupled with conduction, a number of powerful assortment of techniques are available for the resulting linear algebraic equations. These are standard techniques in the high speed digital computers. It should be expected that the solution to the radiative exchange using finite - difference technique could be carried out over a shorter time when compared to iterative method. In this finite - difference method care should be taken to minimize the loss of accuracy of the final results by insuring against the loss of significant figures associated with solution to the system of linear algebraic equations. Inclusion of nodal conduction to the volume bounded by the elemental area results in nonlinear algebraic equations. Techniques are available for such problems, but they may not be in the form of readily available standard subroutines to the computer programs.

Finite Element Procedure.

The thermal analysis of the complex structures used in the space platform is to predict temperature excursion under varying thermal environment experienced during orbit under various orientations. It will cause thermal stresses which may need to be incorporated at the design stage of these structures. A fast and compatible solution is to break the structures into such elements which can be used in both the thermal and the stress analyses, of which thermal stress is but one part. Finite element method is most popular in the field of stress analysis. Historically, it has replaced the previous finite difference method which is cumbersome because of the odd shapes and contours of the structures. It is natural to expect that the corresponding thermal problem use the same finite element technique in order to make the solution interactive at all stages. Since the finite element structure required for the solution follow the contour of the surface itself, the irregular geometry can be easily accommodated. In the finite difference method these areas are represented by irregular nodes. Emery and Mortazavi (1981) make an excellent comparison of finite difference and finite element methods for the heat transfer calculations. Other useful references for basic aspects of these two methods are the books by Myers (1971) and Chung (1978).

Solution by finite element method requires three new concepts, namely, minimization of a function having one or more variables, calculus of variation laying foundation to this method and the approximation of integrals, besides the representation of derivatives with a finite difference as used in the older finite difference method. Here, the nodal points are ends of the triangular element in contrast to the centroid of the rectangular element in the finite difference scheme. Rest of the computational steps are the same for both the methods. In the finite element method the compatibility of the temperatures at the node of the two elements is assured but not the continuity of the heat flux at these nodes. In finite difference method the continuity of heat flux at the node is also assured. Such a lack of continuity of heat flux in the finite element method causes oscillatory character at the nodes with overshoot at one node compensated by undershoot at an adjoining node. In current computer programs, the automatic mesh generators are available for the finite element method. For a more detailed comparison of the two methods, the reference is made to the paper by Emery and Mortazavi (1981) which also contain relative execution time for same problems. Some of the other points covered by them are assemblage of the global matrix, boundary conditions and irregular meshes and graphical display of results. The comparative examples considered by them are distributed and concentrated heat sources, transient temperatures in one and two dimensions, problems containing singular points, thermal radiation problems and transient phase changes.

The finite difference method is best suited when the boundary conditions are to be treated with high order accurate schemes, for highly nonlinear problems for which iterative solutions are efficient, for problems in which the continuity of the heat flux is important and multi-dimensional problems involving change of phase. The finite element method is best suited for irregular regions for which the automatic mesh generation and highly accurate modeling exists resulting in good temperature profiles, for mildly nonlinear problems requiring a very few iterations, for problems requiring graphical display, for problems involving singular temperature points and concentrated heat sources, for problems in which different approximations are used in different regions and they need to be joined together and problems in which temperature profiles are desired.

Approximate Analytical Solution.

The net radiant interchange from a point in the enclosure results in integral equation since the reflected portion of the energy is a function of incoming radiosity from all points in the enclosure to the point under consideration. If one were to include the conduction into or out of the differential surface area of the body at the point, the resulting representation is integro-differential equation. In general, the close form solution of such an accurate representation of the equation is difficult even though it is desirable. Under certain conditions when the kernel of the integral equation can be approximated by another manageable function it is possible to obtain approximate analytical solution. The choice of this new function should represent the kernel as closely as possible, it should be a differentiable function and some order of its derivative be proportional to the function itself. With such requirements satisfied, it is possible to

reduce the integral equation into a differential equation increasing the possibility of closed form solution. When the kernel can be represented by simple elementary function exact solution is possible. Methods of calculus of variations to represent the kernel results in appropriate solutions which can be made highly accurate. The complexity of the Space Laboratory configuration prevents one to pursue this method. However, when such situation exists the closed form solutions is the simplest and most accurate without any computational time involved.

Monte Carlo Procedure:

It has been stated earlier that Monte Carlo method is best suited for radiation problems in which directional variations, polarization, specular and diffuse characteristics of surfaces and other complicating factors need to be considered. While such relaxation of assumptions permits the solution to be carried out with only slight additional complexity and increased computational time the other procedures fail to generate the required solution. Such an advantage can be compared to potential flow solutions which is governed by Laplace differential equation. The closed form analytical solutions for potential flow can be generated for simple geometries. However, having demonstrated that the potential and flow lines should always intersect everywhere at right angles as represented by Cauchy-Riemann relationships, it is a simple matter to draw such lines for a complex geometry and obtain the heat flow characteristics (conduction shape factors) using the method of curvilinear squares (rectangles). Here too, a method is available to solve practical problem approximately when analytical methods fail and finite difference/finite element methods add degree of complexity for the irregularly shaped bodies. As in this case and in using Monte Carlo method for radiative heat transfer characteristics, the solutions for known cases by the more exact procedures can be compared to the newer techniques for accuracies. The confidence gained in the execution of the procedures and the comparison of the results will aid in the efficient development of procedures for complex situations mentioned here as well as reducing the computational time.

The Monte Carlo procedure utilizes simplified, computerized statistical approach to ray tracing. The radiative properties at the surface suggests the fractions of energy absorbed, emitted, reflected and perhaps transmitted. when the incident energy strikes the surface. The Monte Carlo algorithm compares a random number within the range of probabilities to the theoretical fractions and assigns the whole incident flux to the reflected or absorbed or transmitted wave. Another random number compares with the reflected or emitted flux leaving a point selected randomly in the known surface has arrived at the required surface and assigns this flux. A large number of such samples are considered in order to make the statistical fraction between 0 to 1.0 converge to the expected answers. The Monte Carlo algorithm avoids branching during a ray tracing procedure. Here, the energy is not both reflected and transmitted, instead, it is either reflected or transmitted and one result is traced further till extinction. Similarly, the energy leaving a point either strikes the surface or not arrive at all. One of the two results is counted. The procedure suggests that the surface properties can be recognized by selecting energy level, the surfaces can be combination of plano - convexo - concave orientations, the surfaces can be specular or reflective and the absorptivity/emissivity ratio can be as desired.

The method is ideally suited for directly computing the radiative exchange in real situations, the gray body view factors for diffuse surfaces or in the degenerated case of blackbodies the view factor between surfaces. Modest and Poon (1977), and Modest (1978) have applied Monte Carlo procedure for the determination of radiative exchange heat flux at the deep v-shaped cavity of the opened payload bay doors of the Space Shuttle which was suspected to have potential hot spot. This problem reflects all the complexities stated here and the potential of this procedure is equally applicable for future exposed orbiting equipment such as in Orbiting Space Station. Because of the immediate application of their work to the current problem, it should be illuminating to read their remarks and comparison of the procedure with the experimental result.

Consider a complex enclosure made out of n surfaces and opening to outer space. For the sake of simplicity consider each surface to be isothermal and they exhibit diffuse radiative properties. The view of the Sun and Earth through this sprawling opening can also be treated as surfaces. Thus, there are $n + 3$ surface forming the total enclosure. The net heat balance among the i th surface, the remaining enclosure with n surfaces, the Sun, the Earth and the outer space may be written as

$$q_i = \epsilon_i A_i W_{bi} - \sum_{j=1}^n \epsilon_j A_j W_{bj} - q_s'' A_{os} B_{si} - q_E'' A_{oE} B_{Ei} \quad (32)$$

where A_{os} , A_{oE} are the areas at the sprawling opening covered by the Sun and the Earth as viewed by the surface A_i respectively, and q_s'' , q_E'' are corresponding heat fluxes penetrating towards the surface A_i and the remaining term representing the emitted energy at each of the n surfaces as represented in Equation 16. Here, that portion of emitted energy from the surface A_i lost through the opening not covered by the Sun and the Earth ($n + 3$ rd surface) is lost to the outer space. Each of the terms on the right hand side of Equation 32 can be replaced by heat flow from real surfaces which can be directly calculated by Monte Carlo method. Thus, there is no loss of generality. Here, each of the quantities is proportional to the diffuse radiation view factor B_{ij} or B_{ji} or B_{si} or B_{Ei} . In the Monte Carlo procedure, the statistical sample of energy bundles N_i emitted from the surface A_i is considered. The probabilistic history of N_{ij} bundles being absorbed by the surface A_j either after direct travel or after any number of reflections (for the case $\alpha < 1.0$) is accounted by this procedure. For the case of gray surfaces the final result is

$$B_{ij} = \lim_{N_i \rightarrow \infty} (N_{ij}/N_i) \approx (N_{ij}/N_i) \quad N_i \gg 1.0 \quad (33)$$

For the more general case the right hand side of Equation 33 is modified to directly give the net energy leaving the i th surface and received at the j th surface. The accuracy of the results obtained by this procedure depends on the large numbers of energy bundles selected, its directional and spectral characteristics properly represented and the path traced in arriving at the energy absorbed at the surface (general case), the diffuse radiation view factor (gray surface) and the geometric view factor (blackbodies) being special cases.

The Monte Carlo procedure indicated here suggests that the accuracy of the results depends on the large number of samples considered. The convergence to the true values may be oscillatory. It requires the aid of high speed digital computers with large memory space. Smaller the value of the view factor larger will be the number of energy bundles required to achieve the same level of accuracy. This number increases with each additional parameter required to describe the characteristic of the energy bundle but it will always produce the result to sufficient level of accuracy while the other methods fail to converge on the required answer.

Hybrid program using Monte Carlo procedure to obtain directly the energy absorption/emission characteristics of the exposed orbiting equipment should be preferred to the Monte Carlo program which generates partial information (say view factor) required as an input by another energy analysis program. Here, it is not recommended to use Monte Carlo program to replace TRASYS program only followed by SINDA program, although such an option can be exercised by the developers, and the users of the computer programs.

The Monte Carlo procedure indicated here suggests the possibility of calculating the energy interchanges among $n + 3$ surfaces simultaneously. In the space applications such as in the exposed orbiting equipment, all the information is needed. The time required for this total information is not much more than that required to calculate the energy exchange between the i th and j th surfaces. The reason for this thought is as follows. Having randomly selected the level and characteristic of each energy bundle leaving a point on a surface in a direction, it has to arrive at some point on one of the $n + 3$ surfaces whose absorbing reflecting characteristics are known. The history of the energy level of this originating bundle is traced till its near total extinction takes place as it strikes different points of $n + 3$ surfaces and this information can be stored. This procedure is repeated for all the bundles selected. The stored values for each of the surfaces is the required answer. Again the accuracy depends on the number of the bundles. Selected for each location whose total value represents the energy level. The computational time required for this approach by Monte Carlo procedure is considerably shorter than selecting the surfaces i and j and accumulate the hits or misses of the moving energy bundle in the total enclosure one at a time. According to Edwards (1981) the basic elements of Monte Carlo procedures are randomly choosing a location of emission, choosing a direction of emission, tracing a ray to a wall and determining its node number, deciding whether the ray is absorbed or reflected (or transmitted), choosing the direction of reflection (or transportation) and scoring increments of transfer factor. The number of strikes (arrived at the j th surface) compared to the number of starts (departure from the i th surface) is the expected result, that is, view factor, F_{ij} diffuse radiation factor, B_{ij} or the energy absorbed.

A modification to the Monte Carlo method is called 'The Exodus Method' has been suggested by Emery and Carson (1968). This modification reduces computational time and improves accuracy. It is not dependent on the random number generator and may be applied to any problem which admits nodal network. This modification is the limiting case of the improvement first proposed by Klahr (1960). In this limiting method, the Exodus method, a large number of bundles (usually million) is dispatched simultaneously in directions controlled by the probabilities of going from one node to its neighbors. As these bundles arrive at the new nodal points, they are continually moved according to the probabilities until a set number have reached the boundaries (say 99.99 percent). According to the authors in this procedure, the Monte Carlo method smoothly approaches Exodus method. The use of the Exodus method in a computer program is slightly more difficult since two maps of nodal points are required - one just prior to the movement of the bundles and another after the movement has taken place. However, this complexity is more than compensated by the reduction in computational time and the accuracy. The nodal network representation of the physical systems sets the probabilities P_i a priori. Rectangular and triangular elements are acceptable. Even the transient problem can be solved by the Exodus method.

Modest (1978) suggests number of time saver techniques to speed up the Monte Carlo procedure. In problems where the spectral and directional dependences of the emissivity are separable, one random number can represent different wave lengths. Two more random numbers will establish direction of emission which is same for all temperatures. Further simplification is possible if the surfaces are purely specular reflectors which exhibit direction of reflection independent of wave length. Since the incoming solar energy exhibit such a specular characteristics in the narrow wave length band it can be considered in this manner. The computational time can be saved if the overall enclosure can be broken up into small numbers of basic surfaces dictated by the geometry and each surface can be further broken up into smaller isothermal subsurfaces. If these surfaces are parts of plane or convex surfaces, the leaving bundle will not make direct hit on the same surface. The bundle that is directed towards outer space through the sprawling openings including that towards the Sun and the Earth will never return. All these situations should be exploited since the trends of the results are known apriori and the information can be easily assessed. Probability theory can also be used to define the minimum number of bundles that should be considered consistent with the accuracy.

Accuracy and Computational Time:

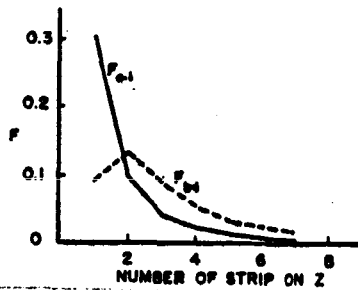
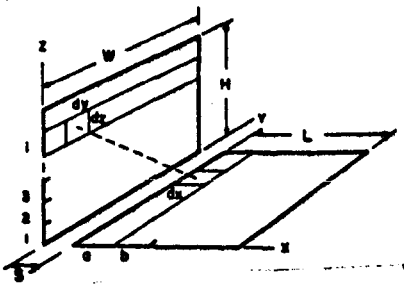
Evaluation of view factor as depicted in Equation 2 and 3 by numerical methods involve summation instead of integration. In order to approach exact value it is necessary to subdivide the basic areas under considerations into smaller elements such that dA/r^2 is kept as small as possible. This approach is satisfactory only at the expense of increased computational time. When the two areas share a common boundary it is difficult to assure small value of dA/r^2 for the area elements in its vicinity. Hence, the results of numerical methods will be inaccurate unless special care is taken to subdivide the area elements in this zone in order to assure the same overall accuracy. The added complexity and additional computations will increase the time of execution. These radiation view factors are converted to radiative conductors in energy exchange calculations. It is possible that the two adjoining surfaces may have similar temperatures or the radiant heat flux exchanged by them be small. In such instances, the accuracy in the computation of view factors will hardly affect the end result. If the user has apriori knowledge of these facts it can be used advantageously. However, if the view factors from the basic surfaces to the space are computed by subtracting the sum of all the other view factors from unity, the user is left with no choice but to improve the accuracies in the computation of view factors to a considerable degree at the expense of increased time of execution. It is only appropriate to consider possible alternate methods of computing the view factors from the bodies to the sprawling space directly, instead of running the risk of increasing computational time in order to approach exact value which is at best asymptotically reached.

Consider a value of the view factor between two surfaces of 0.005. This value of view factor is for a rectangle 0.1 by 0.16 units seen from a point located one unit from one of its corners, the viewing planes being parallel to and seen by each other. This value of view factor is also obtained by a rectangle 0.1 by 0.66 units seen from the same point located one unit from one of its corner, but in this case, the viewing planes being perpendicular to and seen by each other. These examples serve to illustrate that the elemental areas in the numerical calculations must be much smaller in order to assure the indicated accuracy of 0.005 in the overall computational scheme.

Feingold (1966), considered the closed form solution of two rectangles having common edge first treated by Hamilton and Morgan (1952). He points out that in order to assure the accuracy of the results of the view factor equation to eight (8) digits the individual terms of this equation need to be evaluated to sixteen (16) digits. This situation is classical when the numbers of the same order are being subtracted. The discrepancy in the computed values by the original authors were discovered by using reciprocity relationships resulting in the need to generate higher level of accurate results. Even in the present case, similar higher level of accuracy need to be assured in order to evaluate the view factor from the body to the space by using all other component view factors. This illustration points out that for complex surfaces where such closed form solutions are unavailable and double area integrals are replaced by double summation even greater concern should be exercised. Again, Feingold considers the evaluation of the view factor of the regular hexagonal faces of a honeycomb structure by using the view factor values of the six adjoining faces of the enclosure with respect to the face. Recognizing, $F_{FF} = 1 - 6 F_{FS}$, an error of 0.0002 in evaluating view factor F_{SF} for a side/height ratio of 0.1 and using the reciprocity theorem as well as the suggested equation resulted in 57 percent error in F_{FF} , a value that can be directly calculated. Here was a case of Lambertian surface with closed form solution (extension of Hamilton and Morgan's solution) which resulted in enormous error. In complex geometries with directional and spectral variation of properties, it is tempting to blame the built in accumulated computational errors on the existence of non-Lambertian surface instead of having the luxury of evaluating the configuration view factors rather accurately and use them in energy calculations. These examples highlight the problems involved in working with geometrics having common edge and situations where dA/r^2 have not been kept below a certain low value when using double summation method. Even with the provision of idealized Lambertian surfaces for exposed orbiting equipment, the predicted results for the temperature variations can be erroneous since the energy loss to space may have been misrepresented.

It has been pointed out that the evaluation of view factor by contour integration instead of double area integration saves two line integration resulting in considerable simplicity. For the case of diffusively gray surfaces of complex geometries these line integrals can be represented by summation. Emery, Mortazavi and Kippenhan (1981), considered two rectangles of length = height $L = H$ having common edge and placed at right angles. The spacings S/L between the two rectangles of 0.0 (common edge) and 0.1 have been considered. Their results showing the percentage error generated by the numerical solutions using the above two methods when compared to the exact solutions (available for this problem) have been reproduced here as Table 1. Numerical method for the contour integration is very accurate. The double area integral solution obtained by double summation method is highly inaccurate. The reason for this error is again the proximity problem with dA/r^2 being too large for the elements close to the common edge.

Table 1. Percentage Error in the Numerical Calculation of the View Factor between two Surfaces of Equal Breadth (L=H)



View factors between surfaces at right angles to each other and separated by the distance S.

Error based on exact solution to this problem $dA = dx.dz$ or $dy.dz$

Infinite Strip		Contour Integration Finite Area		Double Area Integral			
				Infinite Strip		Finite Area	
d/L	S=0.0%	S=0.0		S=0.0	S=0.1 L	S=0.0	S=0.1 L
1.0	0.2%	<u>3.7</u>		20.7	21.5	59.1	57.6
0.5	0.	0.8		12.9	11.2	32.0	24.1
0.3		0.4		9.1	6.6	21.8	12.1
0.2		0.1		5.7	2.8	13.2	4.9
0.1		0.		2.9	0.7	6.7	1.2
				1.5	0.2	<u>3.4</u>	0.3

$d = dx=dy=dz$ for the Double Area Integration
edge segment length for the Contour Integration

S = Separation distance along the x coordinate

S = 0.0, common edge problem

For example, using the numerical method for contour integration and treating the finite rectangles having common edge as single strips, the error when compared to exact solution is 3.7 percent. Contrary to this result, in the case of numerical summation for double integration using 400 elements per rectangle, the error is still 3.4 percent. It is amazing! Needless to state that the ratio of the computational time will be enormous! In the case of double summation method, for the same case with a spacing equal to 10 percent of the sides, the error has dropped to 0.3 percent. This differential from 3.4 percent is entirely due to proximity of the area at the common edge.

This above example illustrates convincingly that even for Lambertian surfaces having common edge or proximity to each other, it is necessary to further subdivide the area in its vicinity reducing the value of dA/r^2 to a small value consistent with overall accuracy. This comparison also suggests that in order to compute view factors between surfaces the subdivision of areas be done so as to preserve same value of dA/r^2 , thus assuring local accuracy of $F_{dA_i-dA_j}$ is about the same order of the required global accuracy F_{ij} between areas A_i and A_j as defined in Equation 1 and 3. It is this type of sensible use of computer codes which will cut down computational time while preserving both local and global accuracies as required by the user in the prediction of the true temperature excursions, even with the assumption of diffusively gray surfaces.

It has been pointed out that contour integration cannot be used for non-Lambertian surfaces and it takes considerable longer time when double summation is considered since it becomes necessary to consider the differential energy exchanges. This thought suggest the possibility of using Monte Carlo method.

Improvements in the accuracy of the basic view factor calculations can be achieved by specifying a small value, C , for the differential view factor $F_{dA_i-dA_j}$ as stated in Equation 1. In using numerical method, it is indeed $F_{\Delta A_i-\Delta A_j}$. If this calculated value is much smaller than the specified value (say 0.001) it points out that the initial subdivision of areas for double summation method (as used in TRASYS) is too small. On the otherhand, whenever the above differential view factor is above the specified value C that particular element need to be subdivided till the local differential value falls below the specified limit. Such a "do - loop" is standard in all computer programs. It should be noted that in the evaluation F_{ij} between surfaces A_i and A_j , the initial subdivision of areas may be such that the range of differential view factors contributing to F_{ij} may lie on either side of C , the specified limit. They indicate that the value dA/r^2 is either too small or too large. In order to add intelligence to the existing programs it is suggested that the initial subdivision of areas A_i and A_j be coarse and let the program do - loop containing the specified limit C divide them into sub areas so as to generate the same order of values for the differential view factors. This procedure will not only increase the global accuracies of individual view factor between two finite surfaces, but also saves considerable time. In adopting such a procedure care should be taken in situations where two surfaces sharing common boundary or near proximity to each other, since the value of dA/r^2 has been used as a guide to subdivide the areas. It may indeed cause unnecessary expenditure of computational time to assure accuracy which may be inconsequential in energy analysis. The test cases for such improvisations should indeed be the known problems having common edge for which the closed form analytical solutions do exist. As stated earlier, if the mutual surfaces have similar temperatures resulting in minimum exchange of heat the guideline for C , the specified limit can be relaxed.

The geometric view factors between two surfaces always satisfies the basic reciprocity relationships, i.e., $A_i F_{ij} = A_j F_{ji}$. The program should be instructed to evaluate the larger of the two values F_{ij} or F_{ji} which can easily be recognized since the information about A_i and A_j is available in the computer. Such an instruction will also aid in improving the accuracy and reducing the time. It is recognized that A_i and A_j are that portions of surfaces seen by each other, although each of ΔA_i need not see all of ΔA_j . The literature on radiative heat transfer mentions modified reciprocity theorems. The complexities of the surface arrangements in exposed orbiting equipment may not lend itself to take advantage of these theorems.

The evaluation of view factor from the surface A_i to space S can be calculated directly. However, some programs do evaluate this value by subtracting sum of all the other view factors by unity and listing only the positive values. The possibilities of negative results have been used to check the calculations that led to impossible results provided they are beyond the expected overall accuracy. This procedure does not exclude the error involved in computing this important view factor to the space even when positive values are indicated. If the indirect method to evaluate the geometric view factor to the space is the only method, instead of using

$$F_{i-S} = 1 - \sum_{j=1}^N F_{ij} \quad (34)$$

where the total enclosure contain outer space and N surfaces, it is suggested to use

$$F_{\Delta A_i - S} = 1 - \sum_{j=1}^N F_{\Delta A_i - A_j} \quad (35)$$

and

$$F_{A_i - S} = \frac{1}{M} \sum_{i=1}^M F_{\Delta A_i - S} \quad (36)$$

where M is the number of equal area elements the surface A_i is divided in the evaluation of Equation 35. If the surface A_i is divided into unequal areas it is possible to modify Equation 36 to reflect weighted area in the evaluation $F_{A_i - S}$ the important view factor to the space. Such a modification may be viewed as semi-indirect method of evaluation of the view factor to the space. The work of Sawyer (1978) considers view factors between enclosing surfaces in the presence of occluded cylinders (surfaces). The basic concepts of this study can be extended to the current problem of exposed orbiting equipment in space. The work of Sawyer is a part of VIEWFAC program which also contains formula for octal memory required in the computer for typical problems.

The accuracy of view factor as determined by finite element method is comparable to finite difference method, using double summation. Chung and Kim (1982) compares the results obtained by analytic solution with that of contour integration and finite element method. For the case of opposite faces of a cube, the finite element method require 3x3 elements to generate the view factor comparable to analytic solution and contour integration method. In order to obtain similar comparative results for adjacent faces it requires 40x40 elements. For the adjacent faces with angle less than 90° (say 60° and 30°) the values for 40x40 elements did not converge to the analytic values (2.73 and 10.9 percent error). The contour integration method provided the values for the view factors in close agreement with the analytic solution (0.36 and 0.9 percent error). The error indicated for the 40x40 mesh finite element method is unacceptable pointing again to the effect of dA/r^2 in the numerical evaluation. Wu, Ferguson and Altgilbers (1980) considered the application of finite element method to the interaction of conduction and radiation in an absorbing, scattering and emitting medium. They point out that for a 200-node problem it requires 40,000 (40K) words of storage to define the radiosity equation. The use of peripheral mass storage and "out of core" matrix inversion algorithms permit enlarging the number of nodal elements, limited only by the computer economics at the upper end.

Vogt (1981) in a paper on recent developments in Thermal Radiation Analysis System (TRASYS) recommends evaluation of view factor to space directly in order to improve the accuracy. The accuracy depends on the method employed but certainly avoids built in accumulated error when it is obtained by subtracting all the other view factors of the adjoining surfaces from unity. The new Form Factor Calculation (FFCAL) link, described by Vogt, automatically chooses between the double summation and the unit sphere methods in order to improve the accuracy of the nodes that are close to each other. The reduction in computational time with such a frequent switch over has been expected to be 40 percent. Another interesting paper in this area is by Farrell (1976) which discusses the determination of view factors of irregular shapes such as the sprawling space as seen by a point. It is based on the unit sphere concept introduced by Herman (1900). The paper describes the development of the scintiloscope which uses the perspective projection concept aptly describing the geometric view factor as stated by Equation 2, between a point to an object in space (here, sprawling space surrounded by the objects of exposed orbiting

equipment). The idea of Farrell can be computerized in order to evaluate all the required geometric view factors directly. The accuracy of these geometric view factors to important surfaces which exchanges significant energy can also be increased very much like subdividing the interval in numerical integration in order to increase the convergence.

The accuracy of view factors obtained by Monte Carlo method depends on the size of the bundles and randomness of the path selected. Early effort to use this procedure has been branded as one requiring large memory space and inefficient use of computer time. However, the concepts of the procedure is ideally suited to produce accurate results for real surfaces having directional and spectral property variations and integrated approach (for example, coupling of TRASYS and SINDA) is used in energy calculations. Modest and Poon (1977) comment about the accuracy and convergence of the Monte Carlo method when applied to the determination of the geometric view factor between square parallel plates separated by a distance equal to fourth of their sides. They point out that the sets of random number for the Monte Carlo procedure had to be generated on the computer using analytical schemes which can never be truly random. They can at best be called as "quasi-random" which depends on the initial starting value. They indicate that this starting value had considerable influence on the convergence of the view factor to the analytic value, suggesting optimization to select this starting value. For the illustration they considered with a starting value of "unity" even after 5000 bundles the convergence is poor. However, when optimized starting value of "12,345" is selected, initial convergence at 1000 bundles is indicated. They use random number generator contained in NASA - Houston software package for their UNIVAC 1110 in obtaining these values. For larger size bundles the result oscillated around expected value and damping indicated only after using 4000 bundles.

The work of Modest and Poon under NASA/JSC Grant No. NAS9-15109 was to determine the three dimensional radiative exchange factors for the Space Shuttle by using Monte Carlo method. In particular, their study has been directed to radiation exchange between the curved Shuttle door, and radiating panels forming cavity in the open configuration, both being exposed to solar radiation at various angles of incidences. The surfaces were specularly reflective and the problem was directed to predict rather accurately the energy concentration near the hinge between the door and the panel. For black surfaces the Monte Carlo procedure with the optimized starting value of 12,345 showed good convergence with expected values of view factors obtained by Hottel crossed-string method using only 1000 to 2000 bundles.

Modest and Poon (1977) have compared the results obtained by TRASYS and Monte Carlo with the experimental data obtained by Scheps and H. R. Howell (1976) of Vought Corporation under contract with NASA/JSC. The test facility simulated the cavity formed by the Shuttle door and radiator panel, with a baseline deployment angle between them being 38 degrees. In the simulator, Xenon lamps represented the beam radiation from the Sun. The panels were about 3x5 meters. The doors and panels had a coating of silver/teflon material. A white blanket made out of beta cloth bonded to thin aluminum sheet was used to cover the door and assess the effect of diffuse surface coating on the

net radiation trapped in the cavity. The back of the door contained 10 to 20 layers of aluminized mylar in order to minimize the heat leaks. For purposes of evaluating the local view factors to space using measured local heat fluxes, the door and the panel have been divided into strips and each strip into zones. The comparison of experimental results of Scheps and Howell with the Monte Carlo method on a zone-by-zone basis has been made by Modest and Poon. Except for the zones near the hinge (indicating the effect of proximity of two surfaces), the Monte Carlo method using the absorptivity of silver-teflon material (at room temperature) as 0.78 predicted about the same values of gray surface radiation view factors (B_{ij}) on a zone-by-zone basis. In this comparison, each strip has been divided into three zones. The end zone cavity view factor to space as predicted by Monte Carlo method is not symmetric (about one percent or less difference). This is due to inherent oscillation around the expected value associated with the statistical nature of the method itself, and use of limited bundles in increments of hundreds. It should be noted that the asymmetry is much larger with the experimental result (about 3 percent), which is to be expected. The results of view factors from the flat strips (three zones) of the cavity to space, obtained by TRASYS (1973) using diffusively gray emitting surfaces having absorptivity of 0.78, is consistently higher than the experimental values which agrees closely with Monte Carlo predictions. The paper of Modest and Poon contain more detailed comparison of view factors between strips and each strip to space as determined by experiments and Monte Carlo method. It also contains comparison of view factors between the front opening and the strips on the radiator panel facing the door due to solar irradiation. Here, the solar absorptivity of 0.06 for 46 degree angle opening gave a reasonable good agreement between the Monte Carlo method and the experiment. With increasing angle of opening the solar absorptivity had to be artificially increased in order to obtain better agreement between the two methods. It should be noted that at an opening of 77 degrees both the concave door and the back of the radiator panel are fully sunlit. The comparison is also made with TRASYS results using a diffuse solar absorptivity of 0.15. The agreement is inferior when compared to Monte Carlo method. The availability of more complete radiative properties of the surfaces will no doubt improve the comparison between the theory and the experiment.

Sowell and O'Brien (1972) describes F - matrix method in order to efficiently compute view factors within the enclosure. The method is based upon the fact that one view factor in each row of the F - matrix must be determined by conservation equation of that row, that is algebraic sum of the view factor be equal to unity. The reduction of the method to evaluate all the required view factors utilizes reciprocity relationships. They utilize CONFAC II program by Toups (1965) for basis view factors which forms the elements of F - matrix. A Fortran computer procedure is presented. Details of the procedure can be found in the Ph.D dissertation of Sowell (1972). A method to evaluate view factors between surfaces that are partially occluded by other surfaces has been presented by Wiebelt (1972). The computational time required for this program is about twice that of CONFAC II. However, this program uses coarser grid and the expected accuracy is within 2 percent when the occluding surface is close to the viewing plane.

Vogt (1981) points out that in the evaluation of view factors in a complex enclosure such as exposed orbiting equipment, 90 percent of CPU time in the TRASYS program is used up in shadow routines. A significant reduction in time can be achieved if the shadow tables for the specific attitude and orbital position are used. These tables need to be generated and stored prior to computations of view factors. The expected reduction in time is about 50 percent. The newly available FFCAL link for TRASYS II (1977) utilizes the unit sphere method and double summation method interchangeably in order to save computational time by about 40 percent. The FFCAL link utilizes the accuracy specified by the user and Equation 1 in determining the grid sizes. (See Appendix B, TRASYS II, 1977). This method will automatically subdivide the nodes in the region where the surfaces are close to each other. Number of other improvements, time saving steps as well as improved accuracy which are part of TRASYS II indicated by Vogt are; explicit form factor to space (GBCAL link), identical form factor request matrix, restart tape form factors update, trajectory tape input, extended orbit generator capabilities and possible shadower.

Emery, Mortazavi and Kippenhan (1981) point out that the key to reducing computation time is the early detection of obstructions between the elements ΔA_i and ΔA_j . They have not found effective method for such an early detection. They recommend fixed pattern of checking and repeating the same at every location of ΔA_i . The thought expressed by them suggest development of shadow pattern on the surface A_j as viewed from A_i in the presence of occluded surfaces. They emphasize that double area integration for surfaces having common edge leads to inaccurate results, but it is the only method to establish the obstructed view. Hence, such situations should be avoided by properly defining the surfaces. They point to the development of hardware having the capability of generating perspective view with hidden portion of surfaces identified which is as yet unavailable. Utilizing the fixed pattern of checking for obstructions they have shown that the reduction in computational time of 50 to 75 percent in the two isolated examples they considered.

Vogt (1981) emphasizes that the evaluation of geometric view factors of complex structures can be achieved at a greater speed if a fast interactive program with good graphic capability can be developed. For the present, a combination of contour integration and double summation in concert with ray intersection calculations provides the fastest method of calculations. The use of rays may be regarded as highly adaptive Monte Carlo method.

Monte Carlo methods for radiative heat exchange calculations are considered extremely slow and the accuracies are subjected to the choices of random number generators and sizes of bundles used. They require fast computers with large memory space in order to converge on required answers at reasonable values of CPU time. Emery and Carson (1968) compares the computation times of the Exodus method with Monte Carlo and finite difference methods. In the examples considered by them the Exodus method with million bundles took about 10 percent of time taken by Monte Carlo with about 2000 bundles. The computational time for finite difference method is comparable to Exodus method. While the Monte Carlo method shows oscillatory characteristics in converging to final value, the Exodus method exhibits steady convergence to final value. In passing, it may be noted that the application of Exodus method to matrix inversion is much more efficient than Monte Carlo and it is comparable to algorithms for exact method. Modest (1978) has proposed a number of time saver schemes for Monte Carlo method.

In the future, it should be of interest to apply the improvised porcedures to the problems of current interest and compare the same with Exodus method. Modest in applying the Monte Carlo method with time saver schemes to the problem of cavity formed between Space Shuttle payload bay door and radiative heat rejector panel, has shown the superiority of this method over TRASYS for accuracy since it considers specular properties. The execution time on the UNIVAC 1110 using 10,000 - 20,000 energy bundles to assure an accuracy of ± 0.005 was about 60 sec for each incidence angle of the sun shining into the cavity.

Computer Programs:

There are a number of general purpose heat transfer analysis programs that are available largely due to significant advances made in numerical discretization techniques and the rapid developments achieved in computer hardware and software packages. Noor (1981) claims that there are anywhere up to seventy such programs many of which are being used by government and industries to develop analyses for practical problems. He presents a comprehensive review of 38 such programs by categorizing their features under various classifications of heat transfer problems itself, methods available, computer facilities that can be used and the methods of representation of the solutions. Here sixteen of these programs⁸ have been selected which have capabilities for radiation, convection and internal conduction required for solving problems of exposed orbiting space equipment with its convective loops to hold the temperatures of the individual units at the required temperature. Table 2 gives the list of the programs selected, the addresses of program developers, the computer language used and the contact person, where available, for further information. The programs ASAS HEAT, BERSAFE (FLHE) and TAU are from England and SAMCEF (THERNL) is from Belgium. The remaining twelve programs are from the United States out of which six of them coming from California based agencies.

Here, in this laboratory, SINDA (Systems Improved Differencing Analyzer) program (1971) is utilized. It employs finite difference scheme with lumped parameter representation of physical problems governed by diffusion mode. It features resistor capacitor (R-C) network representation. It is backed up by TRASYS (Thermal Radiation Analysis System), a digital computer software, having capability to solve radiation related aspects of thermal analysis problems such as view factors. In combination with SINDA the heat transfer mechanism in space is represented as radiation conductor, suitable for thermal network analysis. TRASYS utilizes view (form) factor accuracy (FFACC) specified by the user in conjunction with Equation 1 representing differential view factor between surfaces ΔA_i and ΔA_j . Having specified FFACC, the smallest ΔA_i is given by

$$\Delta A_i = \frac{FFACC (\gamma_{ij})^2}{\cos \beta_i \cos \beta_j}$$

When the two surfaces A_i and A_j are close to each other the average distance \bar{r} or \bar{r}_{ij} is smaller and Equation 37 suggests consideration of smaller area elements for the evaluation of view factor F_{ij} needed for radiation heat transfer analysis. It should be noted that even with the use of Equation 37 to define minimum size of ΔA_i , the regions of A_i and A_j where the local values of r is smaller than the average value of \bar{r} , the errors in view factor calculations should be expected. The seriousness of this problem is aggravated when areas having common boundary is encountered. The consequences have been discussed in the previous section titled, "Accuracy and Computational Time."

Letters of communication to our William C. Patterson by Mr. J. D. Gaski suggest that Mr. Gaski is the originator of SINDA (1971), his contributions being detailed discussions of the thermal network error correction package and the sensitivity temperature error program. Mr. Gaski is in the process of completing

⁸

At the time of writing this report a separate effort of the author to secure technical backgrounds (theoretical manuals) of these programs in order to independently evaluate the potentials was unsuccessful. The time limitation of the Fellowship program itself was also a factor.

TABLE 2: Computer programs having Heat Transfer Analysis capabilities selected for survey (taken from Ahmed K. Noor, NASA/CP 2216 (1981).

1. AGTAP

Advanced General Thermal Analyzer Program. Grumman Aerospace Corporation, Bethpage, New York, 11714. FORTRAN IV.1000 thermal nodes with 2000 each conductive and radiation connectivities. Contact: Dr. John G. Roukis, mail stop B22/35.

2. ANSYS

Swanson Analysis Systems Inc., P. O. Box 65, Johnson Road, Houston, PA 15342
ANSI FORTRAN.

3. ASASHEAT

Linear/Nonlinear Thermal Analyzer of the ASAS Range of Finite Elem.Program. Atkins Research and Development, Parkside House, Woodcote Grove, Ashley Road, Ebsom, Surrey, England. Portable ANSI FORTRAN 66.

4. BERSAFE (FLHE)

Flow of Heat by Finite Elements. Central Electricity Generating Board, Berkeley Nuclear Laboratories, Berkeley, Gloucestershire, GL13 9PB, England. FORTRAN IV developed by Dr. T. K. Hellen and colleagues. Contact: Mr. G. Marshall.

5. MARC

MARC Analysis Research Corporation, 260 Sheridan Avenue. Suite 200, Palo Alto, CA 94306. FORTRAN IV.

6. MITAS II

Martin Marietta Interactive Thermal Analysis System, Version 2.0. Martin Marietta Corporation P. O. Box 179, Denver, Colorado, 80201. CDC FORTRAN 2.4. Developed by R. E. Kannady, Jr. R. J. Connor and C. E. Shirley. Contact: Roy E. Kannady, Jr., (303) 977-3075 .

7. MSC/NASTRAN

The MacNeal - Schwendler Corporation - NASA Structural Analysis. The MacNeal - Schwendler Corporation, 7442 North Figueroa Street, Los Angeles, CA 90041. FORTRAN IV, contact: MSC Regional Office at Los Angeles (213) 254-3456.

8. NNTB

Nodal Network Thermal Balance Program. NASA-Goddard Space Flight Center, Code 732, Betsville, Maryland, 20771. 300 Nodes Capability. FORTRAN IV. Contact: COSMIC, Suite 112, Barrow Hall, The University of Georgia, Athens, GA 30602.

TABLE 2: (Continued)

9. SAHARA

Sandia National Laboratories, Livermore, CA 94550. CRAY-CFT and CDC-FTN FORTRAN. Developed by V. K. Gabrielson, Organization 8331. Contact: V. K. Gabrielson.

10. SAMCEF(THERNL)

Systeme d'Analyse des Mileax Continus Par Elemets Finis (Thermique Non Linearie). L.T.A.S., Aerospace Laboratory, University of Liege, Rue Ernest Solvay 21, B-400 Liege, Belgium, FORTRAN IV. Contact: L.T.A.S., Aerospace Laboratory.

11. SINDA

Systems Improved Numerical Differencing Analyzer. Program Developers: Chrysler Corporation, Space Division, New Orleans, LA; TRW Systems, Redondo Beach, CA ; TRW Systems, Houston, TX; LTV Aerospace Corporation, Dallas, TX; Lockheed, Houston TX. FORTRAN>Contact: COSMIC, Suite 112, Barrow Hall, University of Georgia, Athens, GA 30602.

12. SPAR

Engineering Information Systems, Inc. 5120 West Cambell Avenue, Suite 240, San Jose, CA 95130. FORTRAN V Contact: James C. Robinson, Loads and Aeroelasticity Division, Mail Stop 243, NASA Langley Research Center, Hampton, VA 23665.

13. TACO

Sandia National Laboratories, Livermore, CA., 94550. ANSI FORTRAN Contact: W. E . Mason, Applied Mechanics Department.

14. TAC3D

Thermal Analysis Code - Three Dimensional. General Atmoic Company, P. O. Box 81608, San Diego, CA 92138. FORTRAN V.

15. TAU

Thermal Analysis of Uncle. U. K. Atomic Energy Authority (UKAEA), Risley Nuclear Power Development Establishment, Warrington, Cheshire WA3 6AT, England. FORTRAN IV,Developed by J. A. Enderby.

16. TEMP (NTEMP)

Temperature Analyzer (New Temperature Analyzer). Dr. A.F. Emery, Dept. of Mechanical Engineering, University of Washington, Seattle, Washington 98195. FORTRAN extended, Cost \$250.00.

"New SINDA" program. He claims that the existing versions of the SINDA program and their many modifications created by various users have deficiencies, inaccuracies, incompleteness, errors and insufficient global documentations. According to Mr. Gaski the new SINDA will have the following features:

- Substantially reduced core size requirements as well as reduced computational time for processing and solution phases.
- Increased problem size capability with several mnemonic data options.
- Operational on CDC and UNIVAC computers with possibility of CRAY and IBM computers.
- Use of CAD color graphics packages such as PATRAN coupled with translators or emulators which allow the user to automate the input to large analysis code such as new SINDA, NASTRAN (NASA Structural Analysis), NEVADA (Net Energy Verification and Determination Analyzer) etc., which offer order of magnitude reductions in overall problem execution times.
- Improvement in Interanalysis Communication and Coupling.
- Estimated 90 percent reduction in preprocessor time and close to a 50 percent reduction in execution time.
- Total rewrite of preprocessor with an entirely different structural base and internal operation instead of patch up jobs that have occurred in 10 years.
- Anticipated submodel definition which will allow several models to serve as input with overlapping number systems. This feature will slow down the overall preprocessor speed, but should not effect execution timing.

Current status of New SINDA, according to the telephone conversation on August 5, 1982 with Mr. J. D. Gaski, (SINDA Industries Inc., P. O. Box 8007 Fountain Valley, CA 92708, Telephone (714) 557-2080). The New SINDA is 80 percent coded and 50 to 60 percent has been checked out. Old SINDA (Revised 82) is available at Aerospace Corporation. The 83 version of Old SINDA with pressure node is in the making for them. The NOPACK version that is available utilizes larger core space, but it runs faster. In SINDA (1971), source data block had lots of errors which have been removed. New SINDA will have Monte Carlo version which directly calculates the gray surface radiation view factor B_{ij} in a single pass instead of TRASYS II which does the same in two passes, first, computing the geometric view factor F_{ij} and then B_{ij} . New SINDA will accept both TRASYS II and NEVADA (Monte Carlo). It is expected that for 1000 nodes or larger NEVADA Monte Carlo method is faster which agrees with other independent claims. moreover, the Monte Carlo method is more versatile. At present, Mr. Gaski is working with Aerospace Corporation on Space Shuttle thermal models for the U. S. Force. NASA, Houston is expected to review these results and based on the satisfactory outcome of comparisons between the two SINDA programs they will authorize the use of New SINDA at the various NASA centers.

Table 3 presents a detailed summary of the capabilities of the sixteen programs depicted in Table 2 for comparison. The information for this table is entirely due to Noor (1981). The tabular survey will be useful in the initial selection of a program or two for heat transfer analysis. The final selection of the suitable program has to be based on a detailed examination of the documentation as outlined in theoretical, programmer's and user's manuals. Since the computer softwares continuously change, often at a rapid rate, most up-to-date information should be sought in order to make final selection. Noor, in a panel discussion with Mr. Sidney Dixon (1981) as moderator, points out that many of the recent advances in computational structural and fluid mechanics have not been used in heat transfer analysis. Such an integration is essential and should be forthcoming. At present finite element methods are lagging behind finite difference method for heat transfer analysis, but their superior advantages in terms of mesh design, formulative aspects coupled with integrated design features and capabilities for transient analysis will be the tool of the future. The availability of a number of large general purpose software, the ushering in of super computers, array processors and microprocessors will also play important role in advancing computational methods including heat transfer models.

Some general comments about Table 3 are as follows:

- All of the programs except four have been updated during 1981. One of these programs is SINDA (1975) which is being updated and it is being reviewed at NASA/JSC for future use at all NASA centers.
- Ten out of sixteen programs utilizes finite element method of analysis. SINDA uses finite difference method. If the anticipated revision (NEW SINDA) utilizes current state of the art of finite difference methods such as curvilinear grids and higher order finite difference techniques, it should be comparable to finite element methods.
- All the programs have temperature as fundamental unknown. Four of these programs considers heat flux as also fundamental unknown. SINDA is not one of them.
- All the programs considers temperature dependent thermo-physical properties.
- All the programs except two considers interelement convection and radiation.
- Only MSC/NASTRAN and TACO have enclosure radiation with view factor calculations internal to the program. Others require supporting programs.
- All of the programs have restart capabilities.

Based on detailed review of the theoretical manuals of these programs, it should be possible to select two or three programs for further scrutiny. Here it is recognized that standard problems which exploits capabilities of these final selection of programs should be used to compare the accuracy, the consistency and the efficiency of computations.

TABLE 3. SURVEY OF COMPUTER PROGRAMS CAPABILITIES USED IN HEAT TRANSFER ANALYSIS

SCOPE AND CAPABILITIES OF THE PROGRAMS	AGTAP	ANSYS	ASAS HEAT	BERSAFE (FLHE)	MARC	MITAS II	MSC/NASTRAN	NNTB	SAHARA	SAMCEF (THERNL)	SINDA	SPAR	TACO	TAC 3D	TAU	TEMP (NTEMP)
	80	81	81	81	81	81	72	67	81	81	75	81	80	69	81	81
MOST RECENT UPDATE/FIRST RELEASE	80	81	81	81	81	81	72	67	81	81	75	81	80	69	81	81
GOAL OF PROGRAM SYSTEM: G - GENERAL PURPOSE B - ALSO RESEARCH CAPABILITIES	G	G	B	B	B	G	B	G	G	B	B	G	G	B	B	G
METHOD OF ANALYSIS: E - FINITE ELEMENT D - FINITE DIFFERENCE	D	E	E	E	E	D	E	D	D	E	D	E	E	D	E	E
FORMULATION - FUNDAMENTAL UNKNOWN: T - TEMPERATURE, B - ALSO HEAT FLUX	T	T	T	T	T	B	T	B	T	B	T	B	T	T	T	T
- CAPACITANCE REPRESENTATION: C - CONSISTENT, L - LUMPED, B - BOTH	L	B	C	C	B	L	B	L	L	B	L	B	B	L	C	B
- CONVECTION REPRESENTATION: N - NATURAL (FREE), F - FORCED, B - BOTH	F	B	N	B	B	B	-	-	B	F	B	B	B	-	B	B
- INTERELEMENT CONVECTION AND RADIATION: Y - YES, N - NO	N	Y	Y	Y	N	Y	Y	Y	Y	Y	Y	Y	Y	N	Y	Y
TEMPERATURE DEPENDENT PROPERTIES: Y - YES N - NO	Y	Y	Y	Y	Y	Y	Y	N	Y	Y	Y	Y	Y	Y	Y	Y
CONDUCTIVITY	Y	Y	Y	Y	Y	Y	N	N	Y	Y	Y	Y	Y	Y	Y	Y
SPECIFIC HEAT	Y	Y	Y	Y	N	N	Y	N	N	Y	Y	Y	N	Y	Y	Y
DENSITY	N	Y	Y	Y	Y	Y	Y	Y	N	Y	Y	Y	Y	Y	Y	Y
ABSORPTIVITY/EMISSIVITY	Y	Y	Y	Y	Y	Y	Y	N	Y	Y	Y	Y	Y	Y	Y	Y
CONVECTION COEFFICIENTS	Y	Y	Y	Y	Y	Y	Y	N	Y	Y	Y	Y	Y	Y	Y	Y
INITIAL CONDITIONS N - HOMOGENEOUS, U - USER SUPPLIED V - VARYING THROUGHOUT THE REGION A - ALL THREE ENTRIES	U	H	A	A	A	U	A	H	H	A	A	A	H	U	A	H
								V	V				V	V		V

XXI-39

* REVIEW THE NUMBER OF FOOTNOTES DESCRIBING CHARACTERISTICS GENERALLY COMMON TO ALL SIXTEEN PROGRAMS WHICH ENABLED TO CAST THIS TABLE INTO MORE COMPACT FORM. INFORMATION TAKEN FROM AHMED K. NOOR, NASA/CP2216 (1981)

CONTINUED

SCOPE AND CAPABILITIES OF THE PROGRAMS	AG TAP	ANSYS	AS AS HEAT	BERSAFE (FLHE)	MARC	MITAS II	MSC/NASTRAN	NNTB	SAHARA	SAMCEF (THERNL)	SINDA	SPAR	TACO	TAC 3D	TAU	TEMP (NTEMP)	
BOUNDARY CONDITIONS AND THERMAL LOADS: - RADIATION AND CONVECTION FROM SURROUNDINGS TO SURFACE AND VICEVERSA S - STEADY STATE, T - TIME DEPENDENT, B - BOTH - RADIATION BETWEEN NARROW GAPS. Y - YES, N - NO - RADIATION BETWEEN 'n' SURFACES WITH USER SUPPLIED VIEW FACTORS, I - INTERNALLY CALCULATED VIEW FACTORS, B - BOTH SEE ALSO FOOTNOTES, 'BOUNDARY CONDITIONS'	T	B	B	B	B	B	B	S	B	B	B	B	B	B	T	B	B
SOLUTION TECHNIQUES AND OTHER CAPABILITIES: - LINEAR STEADY STATE; D - DIRECT, I - ITERATIVE, O - OTHERS - NONLINEAR STEADY STATE; I - ITERATIVE, N - INCREMENTAL, O - OTHERS - TRANSIENT DIRECT INTEGRATION: E - EXPLICIT, U - IMPLICIT WITH USER SPECIFIED STEP, A - IMPLICIT WITH AUTOMATIC TIME STEP SELECTION, C - COMBINED EXPLICIT/IMPLICIT - THERMAL STRESS ANALYSIS WITH FINITE ELEMENT METHOD: C - COUPLED U - UNCOUPLED - ENCLOSURE RADIATION WITH VIEW FACTOR CALCULATION Y - YES, N - NO - HEAT INPUT/OUTPUT AT CONSTRAINED BOUNDARIES: Y - YES, N - NO - RESTART CAPABILITY: Y - YES N - NO	-	D	D	D	D	I	D	D	I	D	I	D	D	D	D	D	D
	-	I	I	I	I	I	I	D	I	I	I	I	I	I	I	I	I
	E	U	U	U	U	E	U	A	U	E	E	E	U	U	U	U	U
	-	C	U	U	U	C	C	-	-	U	-	U	-	-	U	-	-
	N	N	N	N	N	N	Y	N	N	N	N	N	Y	N	Y	N	N
	N	Y	Y	Y	Y	Y	Y	Y	N	Y	N	Y	N	N	Y	Y	Y
	Y	Y	Y	Y	Y	Y	Y	Y	Y	Y	Y	Y	Y	Y	Y	Y	Y

CONTINUED

SCOPE AND CAPABILITIES OF THE PROGRAMS	AG TAP	ANSYS	ASAS HEAT	BERSAFE (FLHE)		MARC	MITAS II	MSC/NASTRAN	NNTB		SAHARA	SAMCEF(THERNL)	SINDA	SPAR		TACO	TAC 3D	TAU	TEMP (NTEMP)
PROGRAM OPERATIONAL USING: - C - CDC, I - IBM, U - UNIVAC A - ALL THREE M - MIMICOMPUTERS, S - SUPER COMPUTERS, B - BOTH	I -	A B	I M	I M		A B	C -	A B	I M		C S	A M	A B	C -		C S	U -	I -	C -
DOCUMENTATION: P - PROGRAMERS MANUAL T - THEORETICAL MANUAL, U - USERS' MANUAL, A - ALL THREE E - EXAMPLE PROBLEM MANUAL, V - VERIFICATION/VALIDATION MANUAL, P - PRE- AND POST- PROCESSORS' MANUAL A - ALL THREE, N - NONE	A E P	T A A	A A A	A A A		A A E	U E A	A A A	T U N		U E P	T A P	T U P	T U E		T E P	P N A	U A E	P P P
INPUT FORM: F - FIXED FORMAT, L - LIST DIRECTED (FREE) FORMAT P - PROBLEM ORIENTED LANGUAGE, A - ALL THREE	F P	L L	L A	A A		F L	L P	A A	F F		F L	P L	L L		F F	F L	L P	L L	L P
INPUT SEQUENCE: U - USER DIRECTED, S - SYSTEM DIRECTED P - PART OF USER SUPPLIED SUBROUTINE, A - ALL THREE	U P	U U	S S			U P	S P	S P	S P	S S	U P	U P	S P	A P		U P	S P	U P	S P
MODEL GENERATION AND CHECKING: AUTOMATIC OR SEMI-AUTOMATIC GENERATOR FOR: N - NODAL POINT COORDINATES, E - ELEMENT CONNECTIVITIES, C - SYMMETRY AND BOUNDARY CONDITIONS CONSTRAINTS, A - ALL THREE S - SUBSTRUCTURE CONNECTIVITY, R - REPETITION OF IDENTICAL SEGMENT, O - OTHERS ELEMENTS: - O - ONE DIMENSIONAL T - TRIANGULAR, Q - QUADRILATERAL, A - ALL THREE ELEMENTS: - B - BODY OR SHELL OF REVOLUTION, 3 - THREE DIMENSIONAL SOLID, 2 - TWO DIMENSIONAL SHELL, A - ALL THREE	C R -	A R -	A S A	A R A		A R B	-	A S 3	-		N -	A R A	-	N O 3		A O B	N -	A T B	N A B

CONCLUDED

SCOPE AND CAPABILITIES OF THE PROGRAMS	AG TAP	ANSYS	AS AS HEAT	BERSAFE (FLHE)	MARC	MITAS II	MSC/NASTRAN	NNTB	SAHARA	SAMCEF (THERNL)	SINDA	SPAR	TACO	TAC 3D	TAU	TEMP (NTEMP)
MODEL GENERATION AND CHECKING (CONTINUED): DATA CHECKING FACILITIES: L - LINE PRINTER, P - PLOTTER, I - INTERACTIVE GRAPHICS, A - ALL THREE PLOTS AND GRAPHICS DISPLAY MODEL: C - COMPLETE ANALYSIS OF REGION WITH 'BLOW-UP' OPTION H - HIDDEN LINES OR SURFACES, O - ORTHOGRAPHIC VIEWS P - PERSPECTIVE AND ISOMETRIC VIEWS, S - SECTION VIEW OF ARBITRARY PLANE, A - ALL FIVE OTHER FACILITIES: D - DIGITIZER INPUT, R - AUTOMATIC RENUMBERING OF NODES, ELEMENTS OR EQUATIONS, T - TABLE LOOKUP OF DATA, A - ALL THREE	L I	A	A	A	A	L P	A -	-	L I	A P	L A	A	L	L	L	A
RESULT OUTPUT FORM: T - TABULAR OUTPUT, F - FIXED SET, U - USER DEFINED SET AND SEQUENCES, A - ALL THREE M - MAXIMUM AND MINIMUM QUANTITIES B - AVERAGE AND MAXIMA FOR BLOCK OF NODES T - TEMPERATURE OR FLUX EXCESSES, A - ALL THREE PLOTS: C - CONTOURS OF TEMPERATURE/FLUX, S - SURFACE FUNCTIONS, O - SELECTIVE OUTPUT BY ELEMENTS OR REGIONS, H - HISTORIES, A - ALL FOUR	U U	F U	T F	A	F U	F U	U F	F	F U	F U	F U	A	F	U	F	F U
INTERACTIVE INPUT AND CONTROL: P - PARAMETER SPECIFICATION (e.g., TIME OR FLUX STEPS) S - SINGULARITY CHECK, E - ERROR CORRECTION/RECOVERY M - USER CONTROL OF MATRIX DECOMPOSITION, A - ALL FOUR	E	P E	S M	-	S	P	- -	-	-	P S E	-	A	-	-	-	-

XXII-42

FOOTNOTES TO TABLE 3 DEPICTING GENERALLY COMMON CHARACTERISTICS
APPLICABLE TO SIXTEEN PROGRAMS OF THIS SURVEY

- All have three dimensional space capabilities except TACO.
- All have linear/nonlinear steady-state and transient response capabilities except AGTAP which has only nonlinear capability and TAC3D which has only linear capability.
- All have models for internal conduction represented by elemental matrices.
- All have models for radiation except AGTAP and TAC3D.
- Multilayered capabilities only for MITAS II, TAU, and TEMP.
- All accommodate time dependent thermal properties except ANSYS, MSC/NSTRAN, and NNTB.

Boundary Conditions

- All accommodate steady-state prescribed temperatures and steady-state thermal flux input except AGTAP and TAC3D.
- All accommodate time dependent prescribed temperatures.
- All accommodate temperature dependent thermal flux input except AGTAP, ANSYS, NNTB, SAHARA, and TAC3D.
- All accommodate time varying thermal flux input except AGTAP and TAC3D.
- All accommodate forced convection except ASAS HEAT, NNTB, SAHARA, and TEMP.
- All accommodate prescribed fluid flow except ASAS HEAT, MARC, NNTB, and TACO.
- Those that accommodate boundary layer convection are; ASAS HEAT, MARC, MSC/NASTRAN, SAHARA, and SPAR.
- All accommodate gap thermal resistance except AGTAP, ASAS HEAT, NNTB, and TEMP.
- All accommodate boundary conditions/loads added or removed during analysis except NNTB and TACO.

Solution Techniques

- All programs using finite element methods of analyses have the feature to transmit temperature field data directly from heat transfer modules to thermal stress modules except TEMP.
- Cyclic symmetry capability is available only for MSC/NASTRAN and TAU.
- Repeated use of identical substructures capability is available only for ANSYS, MSC/NASTRAN, and SAMCEF (THERNL).
- Mixing linear and nonlinear substructures capability is available only for ASAS HEAT, MSC/NASTRAN, and SAMCEF (THERNL).
- All programs have suitable file output for user post-processing and plotting except NNTB, TAC3D, and TEMP.

Conclusions and Recommendations:

This report is based on the literature reviews related to the thermal radiation view factor as it applies to computations of temperature variations in the exposed orbiting equipment. The thermal balance of such an equipment depends on impinging solar radiation, the reflected energy from the earth, the energy lost to sprawling space, the mutual radiative heat transfer among the surfaces, the internal heat generation and the heat transfer from the convective loops. This report provides a broad brush approach discussing the various methods available for calculating thermal radiation view factors, the accuracy of procedures when computer-aided procedures are used and the computational time required to achieve satisfactory results.

The current procedure at the MSFC Laboratory requires two pass approaches, that is, calculation of radiation view factors (TRASYS) and convert them to space conductors (SINDA) in order to perform thermal balance. Besides discussing the basic concepts involved in determining the geometric view factor, in developing the radiation thermal resistance analogy and the assumption involved, this report contains interpretation of the basic methods available for radiation geometric view factor calculations such as Nusselt projection (Unit-Sphere) method, the ray tracing technique for the same, the double integration/summation method, the Hottel's stretch film (Crossed-String) method the contour integration method and the Monte Carlo method. The last method is suitable for directly calculating energy transfer between surfaces having known radiation properties (one pass approach) essentially for Lambertian gray surfaces. This report also contains discussion and status of the available numerical procedures such as iterative procedure, finite difference and finite element procedures and Monte Carlo procedure. More efficient ways available in the literature that are applicable for these basic procedures are also discussed.

In order to aid in the future search for a more efficient, more accurate and less time consuming computational procedure capable of predicting the temperature excursions under time varying conditions, a summary of current state-of-the-art of sixteen programs have been presented. The tabular summary will aid in the preliminary review and selection process. More meaningful comparison is difficult. It can be accomplished by detailed examination of code and by comparing the output of the problems having same identical input. Accuracy and computational times can also be compared. Pertinent comments related to the new SINDA which may be the tool of the future at NASA Laboratories is also presented.

The view factor to space and its importance in dissipating the energy in a thermal balance model of exposed orbiting equipment is important. Currently, this important view factor is being calculated by subtracting all the other view factors from a surface to the objects in the enclosure. This approach imposes tremendous burden on the computer-aided procedures used in calculating all the individual view factor very accurately. Such an accuracy is tied up with the value of dA/r^2 (FFACC - form factor accuracy) factor selected in the double summation method of the view factor calculations. Besides the Monte Carlo method this method is the only other procedure currently available for complex enclosures. When there is a common edge the FFACC criterion cannot be locally met causing global inaccuracies. References have been made to such situations. New and

novel approaches should be sought in order to improve global accuracies without undue expenditure of computational times.

In a complex enclosure such as exposed orbiting space equipment, the calculation of view factors is complicated by the presence of occluded surfaces. At present, considerable amount of time is being spent (about 50%) in identifying such situations. However, the layout of such objects in a mission is fixed. This thought suggests the possibility of developing shadow table and making use of the information in rapidly evaluating the geometric view factors. Reference has been made suggesting significant reduction in computational time. At present, Monte Carlo method is considered too slow and time consuming. It may be competitive when there are 1000 or more modal points. However, there are several time saving techniques and modification to basic procedure itself that are available. In the future there is the potential to successfully use this method for fast and accurate computations in a complex enclosure having non-Lambertian surfaces. In this report a comparison between Monte Carlo method and TRASYS has been made. Similarly comparative advantages of finite element and finite difference methods are indicated.

Schemes to improve the accuracy while making every effort to reduce the computational time should be the future goal. They go hand-in-hand in space research because of the expected one-to-one correspondence between the predicted results and experimental observation. In order to achieve this realistic but elusive goal several ideas are worth considering.

In the evaluation of radiation view factors since the reciprocity relationships are satisfied, every effort should be made to calculate the larger of the two view factors between the two surfaces. Computer programs should have such an intelligence.

It should be possible to recognize those surfaces and surfaces to planets or space which exchange significant energy and calculate these view factors rather accurately. Surfaces having common edge should be avoided or integrated, particularly if their thermal conditions are similar.

Where possible less time consuming contour integration, Hottel's stretch film method should replace slow double summation method. Here it may be possible to reduce the complex enclosure to a number of simple enclosures containing real plano-convex surfaces and artificially introduced plane surfaces covering the concave enclosures. The radiation streaming across these artificially created surfaces can be used as subsidiary surfaces whose thermal balances with respect to enclosed cavity can be completed. The potential of such an implosion or inward travel leading to real surfaces will improve the global accuracy of the results.

The view factors related to the earth's albedo, the sprawling space and the sun are important in the energy circulations. A method to directly calculate these view factors should be explored. Recognize that the view factor from the elemental space to the hemispherical enclosure is unity. Depending on the accuracy of the form (view) factor, it should be possible to construct a number of rays emitting from the centroid of the element towards the hemispherical space above it. Each ray can be traced in order and a record of the surface (including sprawling space, the earth's albedo and the sun) it touches can be kept. Such an accumulation of information will simultaneously evaluate all the differential

view factors (See Eq. 2) $F_{dA_i-A_j}$ satisfying their sum to be unity. This is identical to Herman - Nusselt projection (unit sphere) method which is the basis for number of experimental devices determining such a differential view factor. Here, this procedure can be computerized. The differential view factors from each element of a surface can be weighted according to the area of the elements themselves in order to evaluate F_{ij} , the finite view factors. The availability of computer graphics and the abilities of computers to project surfaces will greatly aid in the success of this procedure.

At a future date Monte Carlo procedure may be integrated with the above mentioned ray tracing method which will not only preserve the rather accurate view factor evaluation but also integrate the rather accurate energy balance consideration required in problems of space exploration. In this connection the potentials of the improved Monte Carlo method (Emery's Exodus method and the time saver techniques of Modest) should be thoroughly explored.

A subset of available computer program for heat transfer analysis based on Noor's work, presented here, and the information contained therein will aid in preliminary selection of a program or two for detailed study. The architect of SINDA (Mr. J. D. Gaski, SINDA Industries, Inc.) after almost ten years of obscurity, is in the process of completing New SINDA. It is scheduled to be reviewed by NASA/JSC and based on their judgment, it will be made available to all NASA centers. It should be of interest to closely scrutinize the improvisation contained in the theoretical manual of New SINDA against the number of recommendations suggested here. Such a scrutiny with our active participation will pave the way to hybrid all the available techniques in order to arrive at efficient and accurate techniques for thermal analyses simultaneously reducing the computational and turn-around times currently being posted.

REFERENCES

1. Chung, T. J., "Finite Element Analysis in Fluid Dynamics," McGraw Hill Book Company (1978)
2. Chung, T. J., "Radiation View Factors by Finite Elements," to appear in Journal of Heat Transfer ASME (1982)
3. Dixon, Sidney, (Moderator), "Panel Discussion - Concerns, Issues, and Future Directions (In Computational Aspects of Heat Transfer Structures)," Proceedings of a Symposium held at NASA Langley Research Center, Hampton, VA, NASA CP 2216, pp.453-486, Nov. 3-5, 1981
4. Eckert, E., "Bestimmung des Winkelverhältnisses beim Strahlungsaustausch durch das Lichtbild" Z. Ver. deut. Ing. Vol. 79, pp. 1495-6, (1935)
5. Eckert, E. R. G. and R. M. Drake, Jr., "Heat and Mass Transfer," McGraw Hill Book Company (1959)
6. Edwards, D. K., "Radiation Heat Transfer Notes," Hemisphere Publishing Corporation, (1981)
7. Emery, A. F. and W. W. Carson, "A Modification to the Monte Carlo Method - The Exodus Method," Transaction of ASME, Journal of Heat Transfer, Vol. 90, No. 3, pp. 328-332, August 1968
8. Emery, A. F., H. R. Mortazavi, "A Comparison of the Finite Difference and Finite Element Methods for Heat Transfer Calculations," Proceedings of a Symposium on Computational Aspects of Heat Transfer in Structures, Held at NASA Langley Research Center, Hampton, VA., NASA CP2216, pp. 51-82, Nov. 3-5, 1981
9. Emery, A. F., H. R. Mortazavi, and C. J. Kippenhan, "Interactive Computation of Radiation View Factors," Proceedings of a Symposium on Computational Aspects of Heat Transfer in Structures, ibid, pp. 221-241, Nov. 3-5, 1981
10. England, F. and H. O. Croft, "Radiation Configuration Factors Using Light in Furnace Models," Transactions of ASME, Vol. 64, pp. 691-702 (1942)
11. Farrell, R., "Determination of Configuration Factors of Irregular Shape," Journal of Heat Transfer, Trans C., ASME, Vol. 96, pp. 311-313, May 1976
12. Feingold, A., "Radiation - Interchange Configuration Factors Between Various Selected Plane Surfaces," Proc. Royal Society of London, Series A Vol. 292, No. 1428, pp. 51-60 (1966)
13. Gebhart, B., "Heat Transfer," McGraw Hill Book Company (1961)
14. Hamilton, D. C., and W. R. Morgan, "Radian Interchange Configuration Factors," NACA TN 2836 (1952)
15. Herman, R. A., "Treatise of Geometric Optics," Cambridge University Press, (1900)

16. Hickman, R. S., "Determination of Radiation Configuration Factors," Jet Propulsion Laboratory Technical Report No. 32-154, December 1961
17. Hottel, H. C., "Radiation Heat Transmission Between Surfaces Separated by Non-Absorbing Media," Transactions of ASME, Vol. 53, pp. 265-273 (1931)
18. Hottel, H. C., "Radiant Heat Transmission" in William H. McAdams (ed.), "Heat Transmission" 3rd Ed., Ch. 4, McGraw Hill Book Company (1954)
19. Hottel, H. C. and A. F. Sarofim, "Radiative Transfer," McGraw Hill Book Company (1967)
20. Howell, J. R., "Application of Monte Carlo to Heat Transfer Problems," Advances in Heat Transfer, Vol 5, Edited by T. F. Igvine, Jr. and J. P. Hartnett Academic Press, pp. 1-54 (1968)
21. Jakob, Max, "Heat Transfer," Vol. II, John Wiley and Sons (1957)
22. Jakob, Max and G. A. Hawkins, "A Model of Photographic and Photometric Determination of Heat Radiation Between Surfaces and Through Absorbing Gases," Journal of Applied Physics, Vol. 13, pp. 246-254 (1942)
23. Klahr, C. N., "A Monte Carlo Method for the Solution of Elliptic Partial Differential Equations," in Mathematical Methods for Digital Computers," Eds. Ralston A. and H. Wilf, John Wiley and Sons (1960)
24. Modest, M. F., "Three-Dimensional Radiative Exchange Factors for Nongray Nondiffuse Surfaces," Numerical Heat Transfer, Vol. 1, pp. 403-416 (1978)
25. Modest, M. F. and S. C. Poon, "Determination of Three-Dimensional Radiative Exchange Factors for the Space Shuttle by Monte Carlo," ASME Paper 77-HT-49, (1977)
26. Myers, Glen E., "Analytical Methods in Conduction Heat Transfer," McGraw Hill Book Company (1971)
27. Noor, Ahmed K., "Survey of Computer Programs for Heat Transfer Analysis," Proceeding of a Symposium on Computational Aspects of Heat Transfer in Structures, Held at NASA Langley Research Center, Hampton, VA, NASA CP2216 pp. 487-561, Nov. 3-5, 1981
28. Nusselt, Wilhelm, "Graphische Bestimmung des Winkelverhältnisses bei der Wärmestrahlung," VDI Z., Vol. 72, p. 673 (1928)
29. Oppenheim, A. K., "Radiation Analysis by the Network Method," Transactions of ASME, Vol. 78, pp. 725-735 (1956)
30. Paschkis, V., Electrotech and Maschinenbau, Vol. 54, p. 617 (1936)
31. Patterson, W. C., Letters of Communications about NEW SINDA - by J. D. Gaski, SINDA Industries, Inc., P. O. Box 8007, Fountain Valley, CA, 92708 (1982)

32. Sawyer, Patricia, L., "Numerical Procedure to Determine Geometric View Factors for Surfaces Occluded by Cylinders," NASA TM-78740, Langley Research Center, Hampton, VA (1978)
33. Scheps, P. R. and H. R. Howell, "The Effect of Radiation Trapping within the Spherical Cavity Formed by the Shuttle Forward Radiator and Payload Bay Door," ASME Paper 76-ENAS-55 (1976)
34. Seibert, O., Archiv fuer Waermewirtschaft, Vol. 9, p. 180 (1928)
35. SINDA, "Systems Improved Numerical Differencing Analyzer," User's Manual, Prepared by James P. Smith of TRW for NASA Manned Spacecraft Center, Under Contract NAS 9-10435, April 1971
36. Sowell, E. F., "Environmental Radiation from Fluorescent Ceiling Systems," PhD Dissertation, University of California, Los Angeles, CA, March 1972
37. Sowell, E. F. and P. F. O'Brien, "Efficient Computation of Radiant - Interchange Configuration Factors within the Enclosure," Journal of Heat Transfer, Series C, Trans. of ASME, Vol. 94, pp. 326-328, August 1972
38. Sparrow, E. M., "On the Calculation of Radiant Interchange Between Surfaces," Modern Developments in Heat Transfer, Edited by Warren Ibele, Academic Press, (1963)
39. Sparrow, E. M. and R. D. Cess, "Radiation Heat Transfer," Hemisphere Publishing Corp./McGraw Hill Book Company (1978)
40. Touts, K. A., "A General Computer Program for the Determination of Radiant - Interchange Configuration and Form Factors - CONFAC II," North American Aviation Inc., Space and Information Systems Division, SID Report 65-1043-2, (1965)
41. TRASYS, "Thermal Radiation Analysis System," Developed by Martin Marietta under Contract NAS9-13033, (1973)
42. TRASYS II, "Thermal Radiation Analysis System," Users Manual developed under Contract NAS9-14318 by Martin Marietta, MCR-730105 (Revision 1) August 1977
43. Turner, L. D., W. R. Humphries, and J. W. Littles, "Effect of Specular Orbiter Forward Radiation on Typical Spacelab Payload Thermal Environment," AIAA-81-1074, AIAA 10th Thermophysics Conference, Palo Alto, CA, June 23-25, 1981
44. Vogt, Robert A., "Recent Developments in Thermal Radiation System Analyzer (TRASYS)," Proceedings of a Symposium on Computational Aspects of Heat Transfer in Structures, Held at NASA Langley Research Center, Hampton, VA, NASA CP2216, pp. 243-251, Nov. 3-5, 1981
45. Wiebelt, J. A., "Configuration Factors for Radiation Heat Transfer Analysis when Surfaces Partially Occlude Other Surfaces," AIAA Paper No. 72-304, AIAA 7th Thermophysics Conference, San Antonio, TX, April 10-12, 1972
46. Wu, S. T., R. E. Ferguson, and L. L. Altgilbers, "Application of Finite - Element Techniques to the Interaction of Conduction and Radiation in an Absorbing, Scattering and Emitting Medium," AIAA-80-1486, 15th Thermophysics Conference, AIAA, Snowmass, Colorado, July 14-16, 1980. Also see MSFC/NASA Report done under Contract NAS8-28097.

APPENDIX

View Factor Calculations Using TRASYS*:

The computer program TRASYS used in the determination of form (view) factor utilizes form factor accuracy (FFACC) along with the double summation method. In order to compare the accuracy of the calculations as well as the computational time, two standard problems have been selected. One of them is view factor between a pair of infinite strips having a common edge with included angles of 60° or 90° . The solution to this problem is provided by Hamilton and Morgan (1952) and the revised calculated values by Feingold (1966). The other problem is view factor between a pair of infinitely long parallel cylinders. In order to accommodate these problems in the TRASYS program the length of common edge or the length of the axes had to be finite. Hence, these length dimensions were made sufficiently large in order to assure two-dimensional character of the problem.

Table A-1 compares the results of TRASYS run for the two rectangular strips having a common edge with that of results of Feingold. The form factor accuracy, $FFACC = 0.03$ has been used for the first six cases. The dimensions of the strips as well as the angle between them are also shown in the table. The numerical results of Feingold is available only for the first two cases. The TRASYS values are higher than Feingold's results. They should have been a shade less than Feingold's results because of the end effects on view factors. The differences are 4.2 and 13.6 percent higher than actual values. Considering that on an average there is more influence of common edge effect in case 2 compared to case 1, the trend of departure in the error is to be expected. Table A-1 contains CPU seconds used in each of these calculations. As the angle between the strips decreases it is expected that CPU seconds will increase and the departure from true values will also increase. The cases selected did not provide a direct comparison to demonstrate the above conclusion.

The results of the test cases 3-1 through 6-1 shown in Table A-1 are for $FFACC = 0.05$. As to be expected the view factor calculation with $FFACC = 0.05$ will consider larger minimum element size than that with $FFACC = 0.03$. The trend in the larger view factor seems to be expected recognizing greater error associated with higher value of $FFACC$. There has been considerable reduction in CPU time with larger $FFACC$ which is to be expected.

Examination of view factors for the test cases 3 through 6 indicates that they are too high and the test case 4 posting a view factor greater than unity. This is impossible. The choice of parameters for these cases did not permit direct comparison with Feingold's results. It is expected that these view factors to be less than 0.67. Hence this comparative study is inconclusive.

* The supporting computational work was provided by Ms. Kathy Upshaw, Life Support and Environmental Branch, Engineering Analysis Division, Structures and Propulsion Laboratory, Marshall Space Flight Center, NASA.

*TABLE A-1: View Factors Between Two Rectangular Strips having a Common Edge.

Test Case	Area A_1	Area A_2	Angle of Contact Deg.	Form Factor	CPU Secs	Feingold Results Form Factor	Difference Percent
1	6 x 300	60 x 300	90	0.4858	2.026	0.4662	4.2
2	6 x 300	15 x 300	90	0.4534	2.151	0.3991	13.6
3	3 x 300	6 x 300	60	0.8155	11.0	-	-
4	1.2 x 120	6 x 120	60	1.1947	1.9	-	-
5	0.3 x 300	6 x 300	60	0.9492	4.54	-	-
6	0.3 x 120	6 x 120	60	0.9449	1.46	-	-
3A				0.8647	4.93		
4A				1.206	1.74		
5A				0.9493	4.54		
6A				0.9453	0.935		

* FFACC = 0.03 for Test Cases 1 through 6 and
 FFACC = 0.05 for Test Cases 3A through 6A.

Table A-2 compares the results of TRASYS run for the two cylinders having parallel axes with that of the values evaluated using the equation based on Hottel's crossed-string method. In this report, the solutions are represented by Eq. 23 for the case of cylinders of equal radii and Eq. 24 is for the cylinders having unequal radii. In Eq. 24

$$\phi_1 = \alpha - \beta, \quad \phi_2 = \alpha + \beta, \quad \alpha = \sin^{-1} \left(\frac{R_1 + R_2}{C} \right)$$

and $\beta = \sin^{-1} \frac{R_1 - R_2}{C}$ and $R_1 > R_2$ and C is the distance between the two centers.

Agreement between the TRASYS and Hottel's methods for the case of parallel cylinders is not at all satisfactory. For the same value of FFACC as the cylinder moved apart the TRASYS program is supposed to permit use of coarser grid and consequently smaller values of CPU seconds. That trend seems to be true for unequal cylinders but not for equal cylinders. Another group of comparative cases that can be considered are semi-cylinders with the curved portions facing each other. Here the view factor between the curved portion of the smaller semi-cylinder to the curved portion of the larger semi-cylinder should be slightly smaller than the corresponding full cylinders. It should be possible to evaluate the view factors when the two cylinders share a common line contact.

Hottel's crossed-string method permits easy derivation of equations for the exact values of view factors for a number of two dimensional cases. Each one of them could be test cases for TRASYS program. These examples could cover occluded surfaces for which the derivations are possible. Hence, it is possible to construct a number of test cases for TRASYS program and study systematically the effect FFACC and CPU time used in converging on correct answers as provided by the closed form solutions. Such a study will enhance the efficient use of TRASYS program and through understanding of the future modifications that are in the wings.

*TABLE A-2: View Factors Between Two Cylinders having their Axes Parallel

Test Case	Radii $R_1 \quad R_2$		Center Distance C	TRASYS		Hottel's Crossed String Method Form Factor
				Form Factor	CPU Secs	
1	1	1	4	0.3192	9.263	0.16275
2	1	1	6	0.2108	12.683	0.10712
3	2	1	8	0.155	9.094	0.04033
4	2	1	12	0.103	7.390	0.02668
5	5	1	30	0.1854	3.184	0.01304

* FFACC = 0.05 in all these Cases.

1982
NASA/ASEE SUMMER FACULTY RESEARCH FELLOWSHIP PROGRAM
MARSHALL SPACE FLIGHT CENTER
THE UNIVERSITY OF ALABAMA

STUDIES OF NEUTRON AND PROTON
NUCLEAR ACTIVATION IN
LOW-EARTH ORBIT

Prepared By:	C. E. Laird, Ph.D.
Academic Rank:	Professor
University and Department:	Eastern Kentucky Department of Physics and Astro- nomy
NASA/MSFC:	
(Laboratory)	Space Science
(Division)	Space Physics
(Branch)	Astrophysics
MSFC Counterpart:	Gerald J. Fishman
Date:	August 6, 1982
Contract No.:	NGT-01-002-099 (University of Alabama)

STUDIES OF NEUTRON AND PROTON
NUCLEAR ACTIVATION IN LOW-EARTH ORBIT

BY

C. E. Laird, Ph. D.
Professor of Physics
Eastern Kentucky University
Richmond, Kentucky

ABSTRACT

The expected induced radioactivity of experimental material in low-Earth orbit has been studied in regards to the characteristics of activating particles such as cosmic rays, high energy Earth-albedo neutrons, trapped protons, and secondary protons and neutrons. The activation cross-sections for the production of long-lived (half life > 1 day) radioisotopes and other existing nuclear data appropriate to the study of these reactions have been compiled. Computer codes required to calculate the expected activation of orbited materials have been studied or developed. A computer code developed in this study has been used to predict the activation by trapped protons of materials placed in the expected orbits of LDEF and Spacelab II. Techniques for unfolding the fluxes of activating particles from the measured activation of orbited materials have been studied.

List of Tables and Figures

<u>Figure No.</u>	Title	Pages
1	Trapped Proton Flux	*
2	Fractional Activation of Vanadium	XXIII - 13

Table No.	Title	Pages
I.	Experimental Cross-Sections for Proton Induced Reactions	*
II.	Parameters used in Activation Calculations	*
III.	Results of Activation Calculations . .	XXIII - 14

*Available upon request from Author.

INTRODUCTION

Many experiments and much experimental equipment placed in near-Earth orbit are sensitive to induced radioactivity. The radiation sources producing this activation are cosmic rays, trapped protons, high-energy Earth-albedo neutrons, and secondary protons and neutrons. When the orbit of a spacecraft passes through regions of trapped protons, these protons and their secondaries will dominate the activation. While the flux of the trapped protons is known to within a factor of two or less [1], the fluxes and the effects of the secondaries are not well understood. The viability of many orbital experiments requires a better understanding of the dominate factors involved in induced radioactivity and the ability to predict the effects of induced radioactivity on these experiments.

In order to better understand the fluxes of these activating particles and the effects of their interaction with spacecraft, NASA has scheduled several experiments in low-Earth orbit. One of these is being planned and carried out by the Astrophysics Branch of SSL at MSFC. Several activation samples are scheduled to be flown on the Long Duration Exposure Facility (LDEF) and on Spacelab II. By measuring the activation of these samples after return from orbit information concerning the fluxes of activating particles is to be obtained.

The unfolding of the particle flux from the measured sample activation requires a thorough knowledge of the cross-sections for the particular reaction under study as well as competing reactions contributing to a particular activation. Also, techniques for unfolding the fluxes from the activation must be known. This report contains the results of a study of the various reactions which can activate the samples, of the cross-sections for these reactions, of the anticipated activation of these samples for the proton flux expected in the planned orbit, and of computer codes needed to calculate the expected activation or to unfold the fluxes of activating particles. Particular emphasis, and calculations, is given to activation produced by primary proton fluxes expected in the LDEF orbit. Suggestions are made for further studies, calculations, and experiments.

LDEF and Spacelab II

It is currently planned to fly five activation samples aboard LDEF and Spacelab II. Due to the shortness of the Spacelab II mission (about one week) little activation of the

Spacelab II samples is expected. However, LDEF is scheduled to be in orbit for a minimum of six months so the activation of the samples aboard it will be more significant.

The LDEF is a structure designed to carry 84 trays into which a large number of passive experiments can be placed. It is a cylindrically shaped structure whose cross-section is a regular twelve-sided polygon with its axes perpendicular to the base. It is to be flown with one base directed towards the Earth at an altitude of about 500km with an orbital inclination of 28.5°.

The five activation samples to be flown on LDEF and Spacelab II consist of 2 inch by 2 inch by 1/8 inch thick slabs of naturally occurring Vanadium, Nickel, Cobalt, Indium and Tantalum. These 99.99 percent elementally pure samples are to be mounted on LDEF experiments A0114, M0001, and M0002.[2] On A0114 the samples are to be mounted inside 3/8 inches of aluminum and/or quartz on a tray to be mounted on the leading and trailing sides of the facility. On M0001 the samples should be cut into 1 x 2 x 1/8 inch segments to be mounted between the four heavy-ion detectors sited on the aphelion side of the spacecraft. On M0002 the samples will be mounted behind a thin honey-combed aluminum plate in a quarter tray sited on the Earth side of the spacecraft. On M0001 and M0002 little degradation of the trapped proton flux is expected because of the covering material but on A0114 considerable degradation is expected. This degradation will not be addressed in this report.

Methods for Predicting the Activation from Trapped Protons

The activation of the samples is caused, first, by the nuclear capture of the primary particles and, second, by the capture of the reactant products. Given sufficient energy, these products would include secondary protons, neutrons, photons, and product nuclei. The first three types of secondaries and some of the product nuclei (deuterons - or pn-, tritons - or p 2n -, He-3-or 2pn -, etc) occur predominantly at low energies; i.e., below about 100 MeV. Compound nuclear reactions are the dominant modes of reaction below 50 MeV followed by direct reactions above 50 MeV with spallation processes increasing in strength above about 100 MeV.

The calculation of the product of a given reaction for a very thin target can be given by

$$P(E) = \frac{N_A}{m} \sigma(E) \phi(E) \rho t A \quad (1)$$

where N_A is Avogadro's number, m the isotopic mass of the target, ρ the density of the target, t the target thickness, A the areas of the target, $\sigma(E)$ the reaction cross-section at energy E , and $\phi(E)$ the incident flux (particles per unit time per unit area). However, for thick targets, the incident flux at energy E may be reduced by absorption and energy degradation. The energy degradation of charged particles can be handled with the known stopping powers of the target material. The nuclear absorption comes from the many inelastic reaction channels available at a specific particle energy. Two techniques commonly used to perform such reaction calculations are the nucleon transport codes such as HETC and a straight-forward approach using a modification of Eq. (1) with known cross-sections.

The high energy transport codes HETC [3] which includes evaporation processes in its latest version has been used for incident particles from 15 MeV to 1. TeV. The code assumes an overall geometrical type cross-section and uses Monte Carlo techniques to follow the individual nucleon-nucleon reactions (inside a nucleus) until all primary and secondary reactions cease. The resultant event chain can be interpreted in many ways including the number of radioactive product nuclei produced in the target. This sophisticated computer code including arbitrary target geometries has been applied to the activation of spacecraft material.[4,5]

In comparison with measured cross-sections for various reactions including spallation, the results of this code or of similar codes usually agree within a factor of two. However, its use in this study was negated by it being currently unavailable at MSFC or other local facilities.

The second method, which is used in this report, is the straight-forward technique of using a modification of Eq. (1) with known cross-sections. In doing the activation calculations, Eq. (1) must account for the degradation of energy as the protons pass through the sample. For an incident flux $\phi(E)$ the reaction cross-section "seen" by each proton at position z in the target where it has energy

$$E' = E + \int_0^z \left(- \frac{dE}{dz} \right) dz \quad (2)$$

is a composite of the cross-sections at the mean energy of the proton in each segment Δz . To account for this, we modify Eq. (1) by using

$$\sigma(E) = \sum_{i=1}^N \sigma(E'_i; E, z_i) \Delta z_i \quad (3)$$

where E'_i is the energy at Z_i for protons of incident energy E , and the summation over N covers the range of the particle in the sample or the effective thickness of the target. Also, Eq. (1) must be summed over the total energy spectrum of the particle flux. Thus,

$$\begin{aligned}
 P &= \int P(E) dE \\
 &= \frac{N_A}{m} \frac{A}{(NPHI)(NTH)} \sum_{i=1}^{NPHI} \sum_{j=1}^{NTH} \sum_{k=1}^{NE} \Delta E_k \phi(E_k) \times \\
 &\quad \sum \sigma(E'; E_k \theta_j \phi_i z_i) \Delta z_i \quad (4)
 \end{aligned}$$

where P is the number of nuclei produced per unit flux time, $\phi(E)$ is the differential flux at energy E , $\sum \Delta z_i$ sums over the small increments of effective target thickness, $\sum_k \Delta E_k$ sums over the energy region under consideration, and $\sum_{i,j,k} 1/NPHIX$ account for the omnidirectional character of the proton flux. This equation does not account for secondary activation, for absorption of the protons by all inelastic processes draining the proton flux, or for edge effects caused by the finite width and length of the sample.

Secondary activation can also be calculated in a similar fashion using Eq. (4) or a modification of it. The flux of secondary particles, excluding spallation, show a characteristic evaporation peaking at low energy with direct processes resulting in the addition of line spectra at forward angles and at high energy on the tail of the evaporation spectrum. [6,7] For charged particles, this low-energy peaked distribution will probably not add significantly to the activation. However, secondary neutrons should yield activation of an (n, γ) nature; especially, if moderating material is available. Since secondary neutrons will dominate high-energy Earth-albedo neutrons and since the LDEF samples will give a measure of these neutrons, further study of the characteristics of secondary neutrons and possibly calculation should be undertaken (See Recommendations).

Calculational Techniques

A. Range and Stopping Power

The range and the stopping power for incident charged nucleons can be calculated using the empirical relations reported by Zaiden:

$$-\frac{dE}{dx} = C E^{-3/4} [1 - \exp(-AE)] \quad (5)$$

$$R = .585 C^{-1} E^{7/4} (1 - \exp(-\frac{3}{7}AE)) \quad (6)$$

where $-dE/dx$ is the stopping power in MeV/g/cm² and R is the range in g/cm². Zaidens claims that these equations are accurate to 5 percent but a comparison to range and stopping power graphs [9] indicates the accuracy is about 2 percent in the region of interests; 1 to 200 MeV. Therefore, these equations are used in the activation calculations of this report using the A and C parameters given by Zaidens.[8]

B. Differential trapped Proton Flux

The differential flux of the Trapped Proton for a 300 nm (560 km) 30 degree orbit were supplied by John Watts [10]. Since this is the approximate orbit planned for LDEF, they are used in the activation calculations. Figure (1)* shows a graph of this flux indicating a rapid drop-off up to 1 MeV, leveling off from 1 to about 6 MeV, and an exponential decline above 6 MeV. In the computer calculations, a semilog interpolation was used at energies intermediate to the tabulated values.

C. Geometrical Considerations

The omnidirectional character of the incident protons and the "edge-effects" on the samples should be taken into account in the activation calculations. Both factors are small at low energy increasing in importance at high energy. While the "edge-effects" were considered to be negligible in the present calculations, the omnidirectional effects were known to be significant and were included in these preliminary calculations. They were included by averaging the activation produced at several angles from normal incidence to 90°. The large computer time required for these calculations limited any detailed calculations.

D. Saturation and Decay Factors

While in orbit, the activation samples do not increase in activity linearly but according to the saturation factor. After their return from orbit, the activity dies off exponentially. Thus, the activity at any given time is reduced by the factor

$$(1 - \exp -\lambda T_1) e^{-\lambda T_2}$$

where λ is the decay constant ($\frac{\ln 2}{T_{1/2}}$), T1 is the time of exposure and T2 is the time since the samples were removed from exposure. Since these factors depend on T1 and T2 which will not be known until the samples are studied, they have not been considered in this study.

E. Evaluation and Selection of Proton Reaction Cross-Section

Various compilations [11,12,13,14,15] of proton reaction cross-sections have been made by several authors in the U.S.

and abroad. The reliability of these cross-sections is uncertain since most were measured using stacked-foil methods, chemical separation, beta counting techniques, NaI detectors, and questionable branching ratios. In addition, the Al-27 (p,3pn) Na-24 reaction was often used as a current (proton) monitor but the cross section for this reaction was later corrected downward by nearly 30 percent. Fortunately, recent studies on [16,17,18,19] on V-57, Co-59, and Ni up to about 50 MeV have been done with relatively consistent results being obtained. These studies used stacked-foil techniques, high resolution Ge(Li) spectrometers, and current published nuclear data. In general, their quoted accuracy is 7-10 percent, including cross-section for Fe - 56 common to the three experimental groups, and all agree to within about 20 percent when normalized to common γ -ray branching ratios. Higher-energy cross-section from reference [13] can be added to the recent data when values are consistent or, when inconsistent, normalized by interpolation or extrapolation.

Natural Indium and Tantalum are more difficult. It seems that no excitation functions above 10 MeV for Indium have been done. Cross-section for (p,n) reactions have been published [20] for energies near 18 MeV and the angular and energy distribution of reactant products [6,21] have been studied. The situation for Tantalum is that it has been studied several times [22,23,20] with inconsistent results. The reactant products have also been studied [21]. The cross-sections used in this studies are selected after evaluation and when required the data are normalized.

In the cross-section tables (Table I)* the data used is that indicated reference or by as otherwise indicated reference. Normalized data is referenced and indicated by parentheses (). Extrapolations are indicated by [].

F. Pertinent Nuclear Data

Table II* contains atomic and nuclear data required to calculate proton induced activation of the LDEF samples. Nuclear half-lives, gamma-ray energies, atomic masses, and half-lives are taken from reference (9). Reaction Q values are taken from reference (24) or from reference (16) or reference (17). Stopping power and range coefficients are from reference (18) and densities are taken from reference (25).

Results and Conclusions

A computer code entitled Induced Radioactivity by Trapped Protons (IRTRAP) was developed and used to calculate the induced radioactivity expected from the proton flux given in Fig. (1). The code, in its present form, allows only for averaging of incident flux over angles from $\theta=0$ to 90° and from $\phi=0$ to 360° . No allowance for "edge-effects" or total proton-nuclear absorption is made.

The results for the production of, V-48 and Cr-51 are given in Fig. (2) in terms of fractional activation per day expected for the prominent long-lived isotopes. Although it should be remembered that "edge-effects" and nuclear absorption will reduce the theta-averaged results, the omnidirectional character of the incident flux has a significant effect both on the shape of the activation curve and on the total activation. This should be remembered when proton fluxes are to be unfolded from the actual sample activation. The preliminary nature of these results is such that they should be considered as indicators of the order of magnitude of the activation and of the trend of the fractional activation.

Proton induced reaction cross-sections for Co-59 and V-51 are available from the (p,n) threshold up to or above 200 MeV. However, cross-sections are not available for Indium, are poorly known for Tantalum at all energies and are poorly known for Nickel above 50 MeV. For these reasons no calculations have been done for Tantalum and Indium.

The difficulty of calculating the induced radioactivity of the LDEF samples in a simple geometry indicates the severe problems that will be encountered with complicated geometries and with sample covering materials. The most unambiguous results concerning the fluxes of inducing particles will be obtained for those samples having the simplest geometry and covering material.

Recommendations

1. The development of IRTRAP should be continued so that it includes effects due to the finite dimension of the samples ("edge-effects") and the reduction of the proton flux caused by all nuclear reaction channels. A future test of the code at a high energy proton accelerator should be considered.
2. The search for and review of reaction cross-sections should be continued, as the case warrants, to improve the reliability of the cross-sections data set or to obtain previously unpublished cross-sections. If necessary, properly parameterized nuclear model calculations could yield unmeasured cross-sections or allow for the extrapolation of known cross-section.
3. A technique for determining the efficiency of the gamma-ray detector for an extended radiation source should be made. The activated samples when counted in a low-background counting system do not represent point-sources because of the almost 2π geometry they subtend to the detector. Also, since the targets are relatively thick, self-attenuation of the emitted photons must be corrected for in the analysis. It is recommended that a program to develop a calibration source be initiated as well as one to measure and model the self-attenuation effects. Initial consideration in this project should be given to uniformly depositing a known quantity of a radioisotope standard such as Eu-152 onto a 2 inch x 2 inch thin metal plate and sealing it with a thin layer of plastic. By sandwiching this source between a sufficient number of similar plates and at various distance from the detector data can be obtained for determining the efficiency and self-attenuation.
4. While a limited study of the Zaidens empirical stopping-power and range equations was done in this report a more detailed study in regards to its use in IRTRAP should be undertaken. Furthermore, the effects of proton straggling on the IRTRAP calculations should also be studied. These studies could be performed by undergraduate or graduate students under proper supervision.

5. Since one of the goals of this proposed LDEF experiment is to study the primary sources of activation, the activation of the samples by secondaries created in the sample must be understood. This requires a careful study of the energy and angular distribution of these secondaries as well as the activation produced by them. These distributions can be calculated using nuclear models and the result compared to published values. It is recommended that future plans for such a study be made. Furthermore, some experimental reaction studies may be required to obtain either the actual cross-sections or other parameters needed for these calculations. Besides stacked-foiled techniques, in-beam techniques may be needed for reactions not leading to unstable long-lived isotopes.

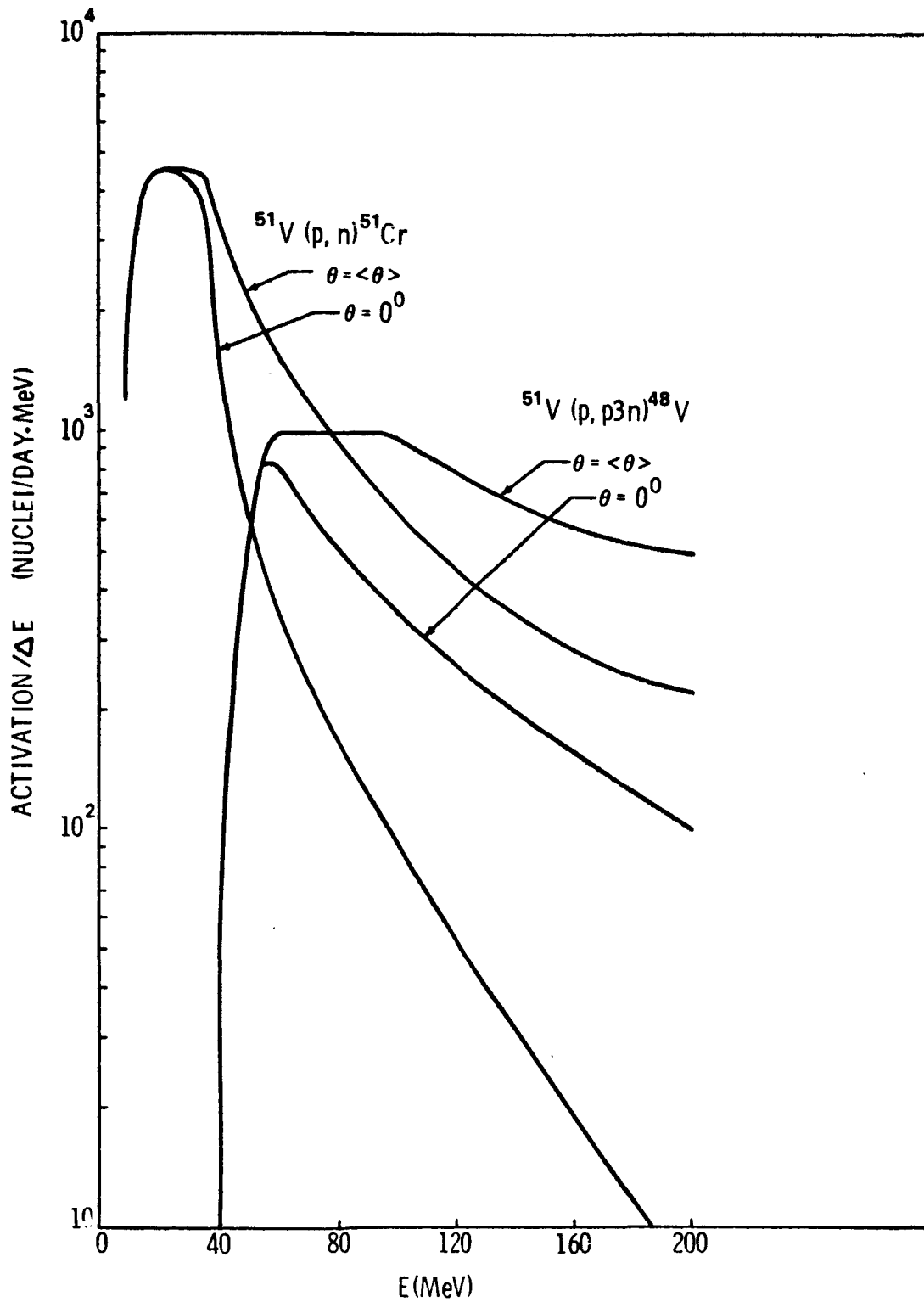


Figure 2. Fractional Activation of Vanadium

Table III: Results of Activation Calculations
 $Q < E < 200 \text{ MeV}$

Target	Isotope	Nuclei/Day	
		Normal Incidence	Theta Average
V-51	Cr-51	143700	244900
	Cr-48	1706	3928
	V-48	52450	117700
	Sc-47	11960	26040
	Sc-46	18290	39900
Co-59	Ni-57	9742	18240
	Ni-56	399	777
	Co-58	547800	1007000
	Co-57	340000	639100
	Co-56	97840	191600
	Co-51	41430	799990
	Mn-54	82060	160000
Nickel	Ni-56	22090	42240
	Ni-57	225000	418000
	Co-55	50620	95070
	Co-56	316000	603500
	Co-57	348900	635000
	Co-58	114000	200000

REFERENCES

- * Figure (1), Tables I and II, and other information are available upon request to the author.
1. The Earth's Trapped Radiation Belts, March 1975, NASA SP-8116.
 2. LDEF MISSION 1, Experiment Description, September 1981. Compiled and Edited by Lenwood G. Clark, LDEF Project Office, NASA Langley Research Center, Hampton, VA 23665.
 3. T. W. Armstrong and B. L. Colborn, "LHI Code Development Study", January 1979, BMDATC report SAI-79-1040-LJ and references therein.
 4. R. G. Alsmiller, G. T. Chapman, J. W. Wachter, and J. Barish, "Photon Spectra from Induced Activity in an Orbiting Spacecraft", ORNL-TM-4345.
 5. R. T. Santoro, R. G. Alsmiller, Jr., and K. C. Chandler, "Shielding of Manned Space Vehicles Against Galactic Cosmic-Ray Protons and Alpha Particles", ORNL-TM-4029.
 6. A. Langsford, P. H. Bowen, and G. C. Cox, Nucl. Phys. A113, 433(1968).
 7. J. R. Wu, C. C. Chang, and H. D. Holmgren, Phys. Rev. C19, 698(1979) and F. E. Bertrand and R. W. Peelle, Phys. Rev. C8, 1045(1973).
 8. C. S. Zaidens, NIM 120, 125(1974).
 9. C. M. Lederer and V. S. Shirley, Table of Isotopes, Seventh Edition, Wiley Interscience, 1978.
 10. John Watts, Space Science Laboratory, Marshall Space Flight Center, private communication.
 11. E. Brunix, "High-Energy Nuclear Reaction Cross-Sections", CERN-61-1 and CERN-62-9.
 12. H. W. Bertini, M. P. Guthrie, E. H. Fickel and B. L. Bishop, "Literature Survey of Radiochemical Cross-Section Data Below 425 MeV", ORNL-3884.
 13. R. Silberberg and C. Tsao, "Cross Sections for Proton-Nucleus Interactions at High Energy", NRL-7593.
 14. "Nuclear Cross Sections for Charged-Particle Induced Reactions", ORNL-CPX-1 and -CPX-2.
 15. Charged particle nuclear data compilation using EXFOR, National Nuclear Data Center, Brookhaven National Laboratory.
 16. R. Michel, H. Weigel and W. Herr, Z. Phys. A286, 393 (1978).
 17. R. Michel, G. Brinkmann, H. Weigel and W. Herr, Nucl. Phys. A322, 40 (1979).
 18. N. C. Schoen, G. Orlov, and R. J. McDonald, Phys. Rev. C20, 88(1979).
 19. E. Gadioli, A. M. Grassi Strini, G. LoBianco, G. Strini, and G. Tagliaferri, Il Nuovo Cimento 22A, 547 (1974).
 20. V. Verbinski and W. R. Burrus, Phys. Rev. 177, 1671 (1969).
 21. C. J. Batty, R. S. Gilmore and G. H. Stafford, Nucl. Phys. 75, 599 (1966).
 22. C. Birattari, E. Gadioli, A. M. Grassi Strini, G. Strini, G. Tagliaferri and L. Zetta, Nucl. Phys. A166, 605 (1971).

23. C. L. Rao and L. Yaffe, *Can. J. Chem.* 41, 2516 (1963).
24. A. H. Wapstra and N. B. Gove, *Nuclear-Reaction Q-Values, Nuclear Data Tables A11*, 127 (1972).
25. H. H. Anderson and J. F. Ziegler, *The Stopping and Ranges of Ions in Matter*.
26. J. L. Zyskind, C. A. Barnes, J. M. Davidson, William A. Fowler, R. E. Mams and M. H. Shapiro, *Nucl. Phys.* A343, 295 (1980).

1982

NASA/ASEE SUMMER FACULTY RESEARCH FELLOWSHIP PROGRAM

MARSHALL SPACE FLIGHT CENTER
THE UNIVERSITY OF ALABAMA

THE MEASUREMENT OF THE STACKING FAULT ENERGY IN
COPPER, NICKEL AND COPPER-NICKEL ALLOYS

Prepared By: H. P. Leighly, Jr.

Academic Rank: Professor

University and Department: University of Missouri-Rolla
Department of Metallurgical Engineering

NASA/MSFC: Materials & Processes Laboratory
Metallic Materials Division
Metallurgical & Failure Analysis Branch

MSFC Counterpart: Paul M. Munafa

Date: August 5, 1982

Contract No.: NGT-01-002-099
(University of Alabama)

THE DETERMINATION OF THE STACKING FAULT ENERGY
IN COPPER-NICKEL ALLOYS

By

H. P. Leighly, Jr.
Professor of Metallurgical Engineering
University of Missouri-Rolla
Rolla, Missouri 65401

ABSTRACT

There is evidence that the hydrogen solubility and the hydrogen embrittlement of high strength, high performance face centered cubic alloys can be related to the stacking fault energy of the alloys. The stacking fault energy is inversely related to the distance between the two partial dislocations which are formed by the dissociation of a perfect dislocation. The two partial dislocations define a stacking fault in the crystal which offers a region for hydrogen segregation.

To examine this hypothesis, the distance between the partial dislocations will be measured using weak beam, dark field transmission electron microscopy. From these data, the stacking fault energy will be calculated. Initially pure copper, pure nickel and copper-nickel single crystals will be used to determine the stacking fault energy. With the development of the technique, the research will be extended to include high performance alloys for which there are data on hydrogen embrittlement.

ACKNOWLEDGEMENT

The author wishes to acknowledge with thanks the assistance of the personnel in the Metallic Materials Division of the Materials and Processes Laboratory.

INTRODUCTION

In face centered cubic metals, the perfect dislocation has a burger's vector, $\bar{b}_1 = \frac{a}{2} [110]$. It has been observed that such a dislocation dissociates into two partial dislocations, $\bar{b}_1 \rightarrow \bar{b}_2 + \bar{b}_3$ where $\bar{b}_2 = \frac{a}{6} [211]$ and $\bar{b}_3 = \frac{a}{6} [12\bar{1}]$. Since the energy associated with a dislocation is proportional to the square of burger's vector, one can readily show that $\bar{b}_1^2 > \bar{b}_2^2 + \bar{b}_3^2$, hence the dissociation of a perfect dislocation is the preferred state.

Dislocation in the face centered cubic lattice lie on the $\{111\}$ planes. If one makes a traverse through the face centered cubic lattice in a direction normal to a (111) plane, i. e. $[111]$ direction, one observes that the atoms are closed packed forming a triangle array in the (111) plane but the sequence from adjacent planes is different. In fact, there are three possible positions for the planes of atoms which can be labelled a, b, and c. The normal stacking sequence can be given as ... a b c a b c If the stacking sequence does not follow this plan, then a stacking fault is present, which results in an increase of the energy of the crystal.

When a perfect dislocation is dissociated into two partial dislocations, the stacking sequence in the region between the two partial dislocations is disrupted hence there will be a stacking fault between the two partial dislocations. The energy of stacking fault, γ , is inversely proportional to the distance, d , between the partial dislocations.

There are several properties of metals that depend upon the stacking fault energy. The stacking fault provides a location for possible hydrogen accumulation which may lead to the embrittlement of high strength, high performance alloys. Textures generated by cold working are strongly dependent upon the stacking fault energy of a metal. The ability to undergo cross slip is dependent upon the stacking fault energy. Cross slip is the movement of a dislocation in a face centered cubic metal from one slip plane to another. This process is strongly dependent upon the distance between the two partial dislocations. If the stacking fault energy is high, the stacking fault is narrow and cross slip is easy. Aluminum is a good example. Conversely, low stack fault energy metals do not cross slip easily because the distance between the partial dislocations is large. Austenitic stainless steel is a good example of an alloy with a low stacking fault energy. This alloy works hardens very rapidly.

Objectives

The initial goal of the project is to determine the stacking fault energy for pure copper, pure nickel and copper-nickel alloys. As the techniques are developed, the effort will be extended to include various high strength, high performance alloys. The resulting data will be correlated with existing information of hydrogen solubility and hydrogen embrittlement.

a. Stacking Fault Energies

The initial experimental methods for determining the stacking fault energy have been indirect and somewhat limited in their precision. Low angle x-ray diffraction of filed, severely deformed metal samples can be used to calculate stacking fault probabilities. A second method relies upon the shape of the shear stress-shear strain curve for a single crystal. State I of the deformation represents single slip, i. e. the parallel movement under applied stress of dislocations on parallel slip planes with only one slip system operating. Stage II, the work hardening stage, involves multiple slip in which dislocation on intersecting planes interact giving rise to tangles. This stage continues as long as dislocation multiplication continues and dislocation movement is not blocked. Stage III occurs when the applied stress is high enough to force dislocations to cross-slip. The value of the shear stress at the beginning of Stage III, τ_{III} , can be used to calculate the stacking fault energy.

With the advent of the 100kV electron microscope, more direct methods of stacking fault determination became available. For metals with high stacking fault energy such as aluminum and the hexagonal close packed metals, zinc and magnesium, quenching from near the melting point will produce vacancy loops. The annealing kinetics of these loops may be used to calculate the stacking fault energy. This technique has been extensively applied by Professor Ray Smallman of the University of Birmingham, England. This method can not be used on metals with low stacking fault energy for the loops that are formed by quenching are irregular in shape and they are not planar so the annealing kinetics for the vacancy loops are difficult to interpret. As an alternative for low stacking fault energy metals, dislocation node size and geometry can be used to obtain the necessary data. A dislocation node is the junction of three dislocations. Unfortunately, there is no metal on which both experimental techniques can be used to obtain the value of the stacking fault by both techniques which will allow a cross check between the techniques.

b. Weak Beam, Dark Field Electron Microscopy

The insertion of a crystal specimen into the electron beam of a transmission electron microscope results in a diffraction pattern. Since this gives very little information, the objective aperture must be inserted which normally is used to block all the diffracting beams, leaving only the transmitted beam resulting in bright field electron microscopy.

There are instances in which one would like to examine one of the diffracted beams. This is done by inserting the Selected Area Diffraction (SAD) aperture to define an area of interest. The objective aperture is removed and the necessary lens currents are adjusted to give a diffraction pattern. By tilting, one can achieve a very bright diffracted beam in contrast to all the other diffracted beams (the two beam condition). This is the case when the K_0 vector for the transmitted beam and K_{hkl} vector for the diffracted beam coincide with the Ewald Sphere. In this case, the value of \bar{s} , the deviation from the reflecting sphere, is zero or nearly zero. By containing the diffracted beam with the objective aperture and removing the SAD aperture one now has a strong beam, dark field image which can be magnified and examined. The image appears to be the same as for bright field illumination except there is an intensity reversal.

Cockayne, Ray & Whelan (1) developed a technique for studying the dislocation strain fields using weak dark field. They use diffraction vector \bar{g}_{220} , for their strong dark field beam image and antipodal diffraction vector, $\bar{g}_{\bar{2}\bar{2}\bar{0}}$, for the weak beam dark field image. They showed theoretical curves which strongly resolved the image of the partial dislocations. They also presented a weak beam, dark field image of a dislocation in Cu + 10 wt%Al in which the two partial dislocations were 120Å apart. By using the anisotropic elastic theory by Stroh (2), one can obtain the stacking fault energy.

Recently, Saka (3) extended this work by measuring the distance between the partial dislocations and by measuring the node size. He prepared his specimens by compressing single crystals to create dislocations. From the deformed crystals, thin segments were sliced with surfaces parallel to (111) planes. These were bent and annealed to develop nodes. From the analysis of the stacking fault energy data obtained from the distance between partial dislocations and the diameter of the nodes, it is possible to determine dislocation core cut-off radius as well as the stacking fault energy.

CONCLUSIONS AND RECOMMENDATIONS

The weak beam, dark field technique is the most powerful, direct method for determining the stacking fault energies. Implicit in the technique is the requirement for single crystal specimens. It is likely that large grain sized specimens could be used as well if care was taken in their selection and it may be possible to successfully prepare specimens from polycrystalline samples which show a strong preferred orientation.

The specimen preparation was difficult and tedious. This was particularly true for the cutting of the specimens from the single crystal. It was necessary to get the spark cutter into working condition in order to cut specimens from a previously oriented crystal.

This author brought with him a eucentric goniometer which he borrowed from the University of Missouri-Kansas City Dental School. The installation caused some delay in the project as did the failure of the high voltage transformer in the transmission electron microscope.

This project was delayed in two ways. Parts of the eucentric goniometer were not brought originally hence this delayed its installation into the microscope. The wire spark cutter had a limited supply of wire which required time to find a supplier. Soon an adequate supply of wire will be on hand. It may be that spark cutting is too damaging for the resulting specimens to be useful. To date, specimens for similar research have been prepared by abrasive wire saws.

This author is eligible for a sabbatical leave. An attempt will be made for this sabbatical leave to be taken in the academic year 1983-84 in this laboratory. If this can be arranged, the author will do preparation of specimens in his own laboratory which will accelerate the research effort.

REFERENCES

1. Cockayne, D. J. H., Ray, I. L. F., and Whelan, M. J., "Investigation of Dislocation Strain Fields Using Weak Beams," *Philosophical Magazine*, 20, 1265, 1969.
2. Stroh, H. N., "Dislocations and Cracks in Anisotropic Elasticity," *Philosophical Magazine*, 3, 625, 1958.
3. Saka, H., "The Dislocation Core Cut-Off Parameter Estimated from the Stacking-Fault Nodes in Cu-Al Alloy," *Philosophical Magazine*, 42A, 185, 1980.

1982

NASA/ASEE SUMMER FACULTY RESEARCH FELLOWSHIP PROGRAM

MARSHALL SPACE FLIGHT CENTER
THE UNIVERSITY OF ALABAMA

ULTRAHIGH MOLECULAR WEIGHT AROMATIC SILOXANE POLYMERS

Prepared by:	Larry M. Ludwick, Ph.D.
Academic Rank:	Professor
University and Department:	Tuskegee Institute Department of Chemistry
NASA/MSFC: (Laboratory) (Division) (Branch)	Materials and Processes Non-Metallic Materials Polymers and Composites
MSFC Counterpart:	William J. Patterson
Contract No:	NGT-01-002-099 (University of Alabama)

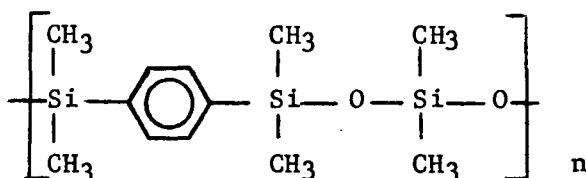
ULTRAHIGH MOLECULAR WEIGHT AROMATIC SILOXANE POLYMERS

by

Larry M. Ludwick, Ph.D.
Professor of Chemistry
Tuskegee Institute
Tuskegee Institute, Alabama 36088

ABSTRACT

The condensation of a diol [(1,4-bis(hydroxydimethylsilyl)benzene)] with a silane [bis(dimethylamino)dimethylsilane] in toluene yields a silphenylene-siloxane polymer.



The reaction of stoichiometric amounts of the diol and silane produced products with molecular weights in the range $2.0 - 6.0 \times 10^5$. Using a multi-step technique the molecular weight of the product was greatly increased.

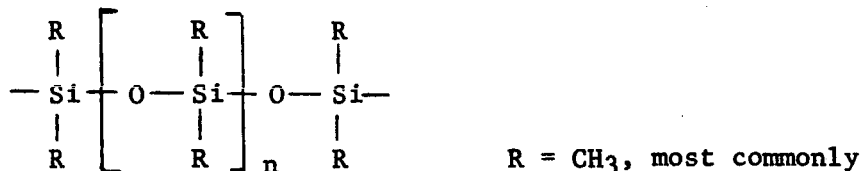
The methodology for synthesis of high molecular weight polymers using a two-step procedure was refined. A prepolymer was prepared and isolated using a 5 mol % deficiency of the silane. This prepolymer was further reacted using incremental additions of the silane. Polymers with weight average molecular weights in excess of 1.0×10^6 were produced using this method. The progress of the second polymerization step was monitored using the gel permeation chromatographic retention time.

Two more-reactive silanes, bis(pyrrolidinyl)dimethylsilane and bis(ϵ -butyrolactam)dimethylsilane, were compared with the dimethylaminodimethylsilane in ability to advance the molecular weight of the prepolymer.

The polymers produced were characterized by intrinsic viscosity in tetrahydrofuran. Weight and number average molecular weights and polydispersity were determined using gel permeation chromatography.

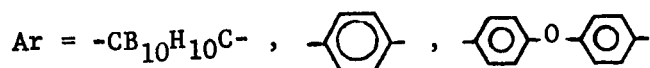
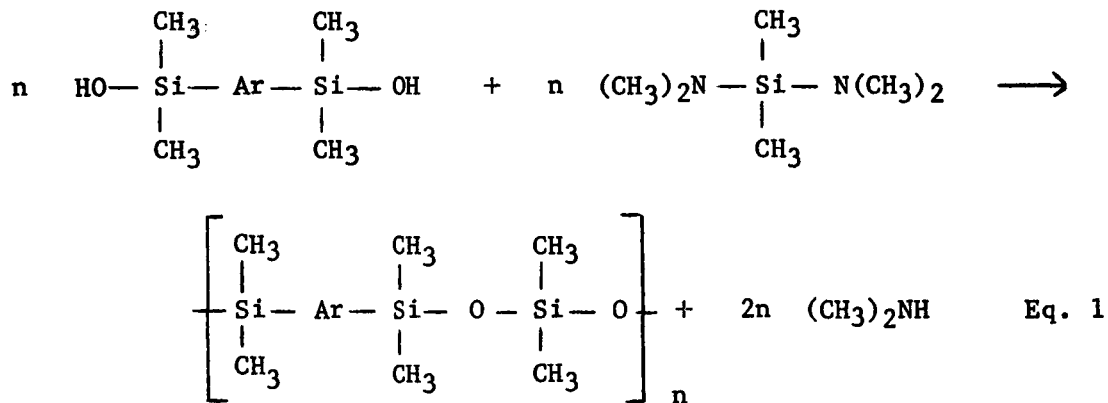
INTRODUCTION

Polyorganosiloxanes have long been known for their unusual and often superior properties(1). These polymeric materials show useful




mechanical properties over an extremely wide temperature range, primarily due to their high thermal stability and low temperature flexibility. Other desirable characteristics include film-forming ability, good dielectric properties and physiological inertness. The properties of these materials depend on the molecular structure of the skeleton as well as the organic substituents on the skeleton. Correspondingly, the silicones, as these materials are commonly called, may be oils, greases, resins or rubbers. Substitution of phenyl groups for the methyls groups can impart greater thermal stability while substitution of vinyl groups can provide reactive centers for crosslinking of the polymers.

With greater molecular weight, desirable increases in tensile strength occur in the polydimethylsiloxanes(2). However, with backbones composed entirely of siloxane units, the polymers are susceptible to degradation by ionic reactions when exposed for long periods to temperatures above 200°C. Improvements in thermal stability as well as low temperature flexibility, mechanical strength and tear resistance of the polydimethylsiloxanes have been sought by insertion of more thermally stable units into the siloxane backbone. Emphasis has been placed on the insertion of arylene units (3-8) and carborane units(9-11). Exactly alternating polymers can easily be prepared by condensation reactions between a disilanol and a silane according to the equation



While the presence of the phenyl groups in the polymer backbone increases the thermal stability, the synthesis of the high molecular weights needed for greater mechanical strength and tear resistance has not been successful. The length of the polymer chains produced by the condensation reaction is greatly influenced by the purity of the monomer starting materials since monofunctional impurities will terminate the chain growth. In addition, the elevated temperatures needed for the condensation and the presence of the reactive amine byproduct may cause degradation of the siloxane polymer. The use of a more reactive silane and a new multistep condensation procedure have shown promise in attaining the high molecular weight polymers, particularly those incorporating D₂-m-carborane into the siloxane skeleton(10).

Current work with silphenylene-siloxane polymers (Ar = ) has achieved molecular weights in the range 2.0 x 10⁵ to 6.0 x 10⁵ (6,7,8,12). The increased molecular weight produces polymers which range from viscous oils to semi-solid gums. The object of this research project was to apply the multistep condensation method to this polymer system and advance the molecular weight to the 1.0 x 10⁶ level. In addition, two more reactive silanes were to be used and compared to the bis(dimethylamine)dimethylsilane in ability to produce high molecular weight products.

EXPERIMENTAL

Materials

Toluene (Fisher Scientific) was distilled from calcium hydride under a nitrogen atmosphere and stored over molecular sieves until used. Methanol and tetrahydrofuran (THF, Burdick and Jackson) were used without further purification. 1,4-Bis(hydroxydimethylsilyl)benzene (Silar Laboratories) was dried in a 50°C vacuum oven overnight before use. Bis(dimethylsilyl)dimethylsilane (Silar Laboratories), N,N-bis(pyrrolidinyl)dimethylsilane (SynMet Inc.) and N,N-bis(γ -butyrolactam)dimethylsilane (SynMet Inc.) were used as obtained from the manufacturers. The silanes were stored in a freezer in closed plastic bags containing Drierite. Before use the bottles were warmed to room temperature and placed in a nitrogen-filled glove bag. Transfers to the septum-sealed reaction systems were made using gas tight syringes.

Polymer Preparations

All polymer preparations were performed in a 3-necked flask fitted with a reflux condenser, thermometer and addition funnel. A positive pressure of dry nitrogen was maintained at all times. Dry toluene was added to the reaction flask as needed to maintain adequate mixing with the magnetic stirring bar. A heating mantle kept the solution at a gentle reflux (109-112°C). Polymer products were recovered by addition of the reaction mixture to rapidly stirred methanol. Solvent removal was by means of overnight drying in a 50-60°C vacuum oven.

Prepolymer Preparation

1,4-Bis(hydroxydimethylsilyl)benzene (50.0 g, 0.221 mol) was placed in a weighed flask and dried overnight in a 50°C vacuum oven. The warm flask was reweighed and fitted with a reflux condenser, thermometer and addition funnel. The system was purged with dry nitrogen for a few minutes and dry toluene (200 ml) was added through the addition funnel. Additional toluene (40 ml) was placed in the funnel and the system sealed with a rubber septum. The reaction mixture was heated slowly to reflux.

Bis(dimethylamino)dimethylsilane (30.9 g, 0.211 mol) was added to the addition funnel through the septum and mixed with the toluene. This mixture was added slowly to the disilanol over a period of about 6 hours. After 24 hours the condenser was removed and a distillation head added. About 150 ml of toluene was distilled from the reaction mixture. At the end of this period the amine production as determined by holding moist acid-base test paper in the effluent nitrogen stream was greatly reduced. The mixture was allowed to cool and poured into about 800 ml methanol with rapid stirring. The viscous oil was transferred to a bottle using a few milliliters of methylene chloride. The solvent was partially removed using a warm water bath and a stream of nitrogen. The product was dried overnight in a 50°C vacuum oven. The recovered polymer weighed 50.0 g (84%, based on the amount of silane used); intrinsic viscosity 0.191 (THF, 30.1 \pm 0.1°C).

Ultra High Molecular Weight Polymer Preparation

Prepolymer (49.0 g, 82% of theoretical yield) was added to a flask and dried overnight in a 50°C vacuum oven. The system was assembled under dry nitrogen purge and 200 ml toluene added. Silane (2.13 g, 0.0146 mol) was added to toluene (40 ml) in the addition funnel. The amount of silane was calculated to be twice the amount needed to remove the 5 mol % deficiency of silane in the prepolymer preparation step. The silane mixture was added over a 4 hour period. During this time additional toluene (about 200 ml) was needed to maintain stirring. After 24 hours the thick solution was cooled and poured into methanol (about 1200 ml). A gum was collected, dissolved in THF (about 200 ml) and reprecipitated in methanol (1000 ml). The polymer (44 g, 74% overall) was placed in a 50°C vacuum oven for two days.

A small portion of the product was dissolved in THF, filtered through a 0.45 μ filter and reprecipitated in methanol. This sample was analyzed by gel permeation chromatography. The intrinsic viscosity was determined in THF (30.1 0.1°C) 2.42.

Comparison of Silanes in Preparation of Ultra High Molecular Weight Polymers

Three separate samples (15.0 g) of a prepolymer prepared using 95 mol % of calculated silane were advanced in molecular weight with three different silanes. Bis(dimethylamine)dimethylsilane (0.72 g, 0.00493 mol), N,N-bis(pyrrolidinyl)dimethylsilane (0.99 g, 0.00500 mol) and N,N-bis(γ -butyrolactam)dimethylsilane (1.23 g, 0.00544 mol) were added in separate trials to toluene (40 ml) in an addition funnel. The silane mixtures were added in four increments at two hour intervals. Preceding each addition of silane, and at the end of 24 hours, samples of the reaction mixture were withdrawn by pipet and precipitated in methanol. After removal of the solvents in a 50°C vacuum oven, the samples were dissolved in THF and analyzed by gel permeation chromatography. The reaction mixtures were then precipitated in methanol and dried in a vacuum oven.

Polymer Characterization

Intrinsic viscosities of the prepolymers and high molecular weight products were determined in THF (30.1 \pm 0.1°C) using a Cannon-Ubbelohde dilution viscometer. Four dilutions (75%, 60%, 43% and 25%) of stock solutions (0.035 - 0.45 g/L) were made.

Molecular weights and polydispersities of all samples were evaluated by gel permeation chromatography using a Waters Associates liquid chromatograph. Four in-line, 30 cm, μ -Styragel, crosslinked, polystyrene-packed columns with pore sizes of 1×10^4 Å (two columns) and 1×10^5 Å (two columns) were used. Tetrahydrofuran was used as the solvent at a flow rate of 1.0 ml/min. Data were gathered and analyzed on a Perkin-Elmer Sigma 15 Chromatographic Data Station with a program to calculate number average and weight average molecular weights and the polydispersity index. A normalized molecular weight distribution could also be plotted with this system. A series of monodisperse polystyrene standards provided a calibration curve.

Typical retention times (retention volumes) along with viscosity and calibration data are shown in TABLE I. With the exception of the highest molecular weight standard, all polystyrene standards were mixed as a single solution. Inclusion of the highest standard caused a loss of resolution among the higher standards.

TABLE I

Calibration Data for Standard Polystyrenes

Peak M ^a	Intrinsic Viscosity ^b η (dL/g)	Peak M x η	Retention Time ^c (min)
2.3 x 10 ⁶	4.92	1.13 x 10 ⁷	22.81 ^d
1.75 x 10 ⁶	3.11	5.44 x 10 ⁶	23.46
6.55 x 10 ⁵	1.86	1.22 x 10 ⁶	25.31
3.70 x 10 ⁵	1.26	4.66 x 10 ⁵	26.87
1.96 x 10 ⁵	0.727	1.42 x 10 ⁵	29.38
1.11 x 10 ⁵	0.521	5.78 x 10 ⁴	30.79
3.45 x 10 ⁴	0.231	7.97 x 10 ³	34.63

^aValues supplied by Waters Associates.

^bTHF (30.1 ± 0.1°C).

^cRetention times reproducible to ± 0.5 min.

^dDetermined separately.

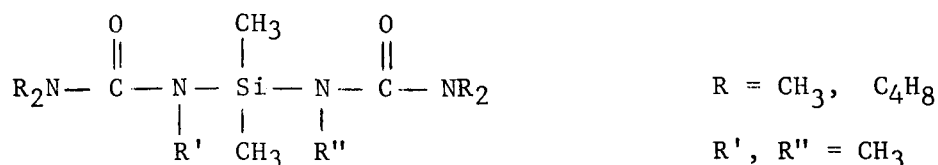
RESULTS AND DISCUSSION

Following established procedures a silanol-terminated prepolymer was prepared according to Equation 1 using a deficiency of the silane. Although no specific study was made, the condensation proceeded rather slowly with the production of gaseous amine (dimethylamine) evident 24 hours after the final addition of the silane. In addition, it was also observed that very little reaction had occurred in a mixture stirred at 85-90°C for over 24 hours, while heating that mixture to temperatures above 100°C produced evidence of considerable reaction. These observations lead to the changes in the technique whereby the silane, as a dilute solution in toluene, was added slowly to the disilanol in refluxing toluene. This procedure then produced a prepolymer in 75-80% yield as precipitated in methanol.

As shown in TABLE II, three of the prepolymer preparations were successfully advanced in molecular weight by the further addition of the silane. As in the first step, the silane was slowly added as a dilute solution. The amount of silane added was twice the amount needed to remove the silane deficiency of the first reaction step. The size of the sample of prepolymer used, based on the theoretical yield in the first step, determined the amount of silane. Due to the slowness of the reaction, it was not determined whether the amount of silane used was in fact sufficient for complete reaction or was an excess. The failure of the second and third trials to advance significantly can perhaps be explained in that the first step produced a relatively high molecular weight product that was less reactive towards the dilute solution of silane added. It may also be that inadequate precautions were exercised to prevent the silane from reacting with atmospheric moisture.

The reaction was scaled up from the initial ten-gram quantities used in Trials 1, 2 and 3 to 50 and 60-gram amounts in Trials 4 and 5. No difficulties were encountered other than the manipulation of the larger quantities of extremely viscous reaction mixtures in the second step. The magnetic stirrer was barely adequate for these situations and it was difficult to assure that the silane was uniformly mixed when added to the reaction flask.

Work with bis(ureido)dimethylsilanes has successfully produced



high molecular weight polymers (7,8,10). These silanes are more reactive than the dimethylamino derivative and thus should condense more rapidly and at lower temperatures. In addition, the amine

TABLE II

Results of Syntheses with Bis(dimethylamino)dimethylsilane

Trial	Prepolymer					High Molecular Weight Product			
	Silane mol %	Viscosity (dL/g)	\bar{M}_w	\bar{M}_w/\bar{M}_n	Retention Time (min)	Viscosity (dL/g)	\bar{M}_w	\bar{M}_w/\bar{M}_n	Retention Time (min)
1	97	0.153	2.1×10^4	9.32	37.2	3.11	1.2×10^6	4.59	24.2
2	98	1.52	6.1×10^5	4.94	26.2	1.56	5.3×10^5	4.37	26.0
3	100	1.46	5.2×10^5	4.43	26.2	2.23	8.9×10^5	5.08	25.3
4	95	0.191	3.6×10^4	2.35	35.9	2.42	1.1×10^6	4.38	25.1
5 ^a	95	---- ^b	----- ^b	1.91	36.5 ^c	--- ^b	----- ^b	4.73	25.5 ^c

^aHigh molecular weight polymer advancement made by four equal additions of silane mixture at 2-hour intervals.

^bNot determined.

^cDetermined by time-slice with maximum area.

byproducts formed are less reactive and thus less likely to degrade the newly-formed polymer. Following these considerations, N,N-bis(pyrrolidinyl)dimethylsilane and N,N-bis(γ -butyrolactam)-dimethylsilane were investigated with respect to molecular weight advancement. These silanes, while more reactive than the dimethylamino compound, avoid the extreme moisture sensitivity of the bis(ureido) derivatives.

The results of identical experiments with the three silanes are shown in TABLE III. It can be seen that the N,N-bis(pyrrolidinyl)-dimethylsilane and the bis(dimethylamino)dimethylsilane produced essentially the same results. As indicated by retention times, the molecular weights of the products in both cases should be nearly the same. Since viscosity measurements were not made on these polymers, \bar{M}_w values could not be calculated with the data reduction system used. The increased reaction time did not appreciably alter the retention time (molecular weight), but did appear to decrease the polydispersity. This was also evident in the normalized distribution curves where the first samples showed broad, often binodal, distributions. Later samples gave more narrow, nearly symmetrical distribution curves. In both cases the recovery of the product was nearly quantitative (greater than 95%) based on the starting prepolymer.

N,N-bis(γ -butyrolactam)dimethylsilane, however, produced much different results. The molecular weight of the product reached a peak at about 6 hours, after 75% of the silane mixture had been added. Additional silane mixture and/or continued heating at 110°C caused the polymer to undergo degradation. With this silane the methanol used for precipitation was cloudy in all cases and the products were all viscous oils and never approached the gum state. It appeared that the silane itself and/or the byproduct amine at elevated temperatures degraded the polymer. The recovery of this product was 87%, indicating a significant loss of material in the methanol. However, since the purity of all three silanes was not determined, it is possible that some impurity may have been responsible for these observations.

TABLE III

Comparison of Silanes in Molecular Weight Advancement

Reaction Time (hr)	% Silane Mixture Added	<u>bis(dimethylamino)-</u>			<u>N,N-bis(pyrrolidinyl)-</u>			<u>N,N-bis(γ-butyrolactam)-</u>		
		Retention Time (min)	$\bar{M}_w \times 10^3$	\bar{M}_w/\bar{M}_n	Retention Time (min)	$\bar{M}_w \times 10^3$	\bar{M}_w/\bar{M}_n	Retention Time (min)	$\bar{M}_w \times 10^3$	\bar{M}_w/\bar{M}_n
0	0	34.9	6.5×10^3	1.9	36.3	5.8×10^3	1.9	36.3	5.6×10^3	1.8
2	25	30.7	9.3×10^5	6.2	29.3	2.1×10^5	4.0	29.9	1.9×10^5	4.6
4	50	25.9	1.7×10^6	5.9	25.9	1.6×10^6	6.4	30.9	8.7×10^4	4.4
6	75	25.5	2.5×10^6	6.0	25.5	1.9×10^6	7.2	29.1	2.3×10^5	4.2
8	100	----	-----	---	25.5	1.8×10^6	6.8	30.1	1.4×10^5	3.8
22	-	25.1	2.3×10^6	4.9	25.5	1.7×10^6	4.6	30.9	8.7×10^4	3.4
26	-	----	-----	---	25.5	1.8×10^6	4.7	30.9	7.9×10^4	3.7

CONCLUSIONS AND RECOMMENDATIONS

A number of points concerning the reaction and the technique remain unanswered. 1) The purity of the silanes, particularly that of the butyrolactam derivative, needs to be characterized and the silanes purified if necessary. This could result in an increase in molecular weight by reducing the possibilities for chain termination. 2) The exact amount of silane needed in the second step to reach the maximum molecular weight should be determined. This is somewhat complicated by the apparent long reaction time. However, if the unreacted silane does degrade the polymer this point is critical.

This study demonstrated that silphenylene-siloxane polymers with a molecular weight in excess of 1×10^6 are easily attainable using a two-step condensation between a silane and a disilanol. These polymers can also be prepared in quantities large enough to permit cure studies and more extensive testing of tensile strength and other physical properties. In addition, the incorporation of other groups such as phenyl or vinyl can readily expand the variety of polymers available. These results are encouraging in terms of producing a polymer with improved mechanical and thermal properties.

REFERENCES

1. Noll, W., "Chemistry and Technology of Silicones" Academic Press, 1968.
2. Kilbourne, F.L., Jr., C.M. Doede and K.J. Stasiunas, Rubber World, 132, 193(1955).
3. Merker, R.L. and M.J. Scott, J. Polym. Sci., A, 2, 15(1964).
4. Burks, R.E., Jr., E.R. Covington, M.V. Jackson and J.E. Curry, J. Polym. Sci. Polym. Chem. Ed., 11, 319(1973).
5. Pittman, C.U., Jr., W.J. Patterson and S.P. McManus, J. Polym. Sci. Polym. Chem. Ed., 14, 1715(1976).
6. Patterson, W.J., S.P. McManus and C.U. Pittman, Jr., Macromolecular Syntheses, 6, 99(1977).
7. Dvornic, P.R. and R.W. Lenz, J. Polym. Sci. Polym. Chem. Ed., 20, 593(1982).
8. Dvornic, P.R. and R.W. Lenz, J. Polym. Sci. Polym. Chem. Ed., 20, 951(1982).
9. Peters, E.N., J. Macromol. Sci., C17, 173(1979).
10. Stewart, D.D, E.N. Peters, C.D. Beard, G.B. Dunks, E. Hedaya, G.T. Kwiatkowski, R.D. Moffitt and J.J. Bohan, Macromolecules, 12, 373(1979).
11. Peters, E.N., D.D. Stewart, J.J. Bohan, R. Moffitt, C.D. Beard, G.T. Kwiatkowski and E. Hedaya, J. Polym. Sci. Polym. Chem. Ed., 15, 973(1977).
12. Patterson, W.J. and N. Hundley, Unpublished results, 1982.

1982

NASA/ASEE SUMMER FACULTY RESEARCH FELLOWSHIP PROGRAM

MARSHALL SPACE FLIGHT CENTER
THE UNIVERSITY OF ALABAMA

IN SITU MEASUREMENTS OF THUNDERSTORM
ELECTRICAL PROPERTIES

Prepared by: Thomas C. Marshall, Ph.D.

Adademic Rank: Assistant Professor

University and Department: The University of Mississippi
Department of Physics and Astronomy

NASA/MSFC:
(Laboratory) Space Sciences
(Division) Atmospheric Sciences
(Branch) Atmospheric Physics

MSFC Counterpart: Hugh J. Christian

Date: August 6, 1982

IN SITU MEASUREMENTS OF THUNDERSTORM ELECTRICAL PROPERTIES

By

Thomas C. Marshall, Ph.D.
Assistant Professor of Physics and Astronomy
The University of Mississippi
University, Mississippi 38677

ABSTRACT

As part of the NASA Storm Hazards project, Marshall Space Flight Center is developing an airplane sensor to measure the charge, size and two-dimensional shape of precipitation particles and large ($>50\mu\text{m}$) cloud particles. We have completed the basic design of this instrument: the transducers and analog electronics, the analog to digital conversion electronics and a microprocessor-based system to run the electronics and load the digital data onto magnetic tape. Although many details of the instrument have yet to be finalized, this project is well underway toward meeting its completion date of April, 1983.

Prototype instrumentation for the proposed NASA Lightning Mapper satellite was tested by flying it in a NASA U-2 aircraft over severe storms in Oklahoma. Data from these flights will be compared to data from ground-based instruments operated by the National Severe Storms Laboratory. The author's involvement in this project is discussed.

INTRODUCTION

As part of the NASA/ASEE 1982 Summer Faculty Fellowship program, I collaborated with Dr. Hugh Christian of NASA on two NASA research projects concerning lightning and thunderstorms: the Storm Hazards project and the Lightning Mapper project. In this report I describe our progress to date on both of these on-going projects. Most of my efforts have been directed at the Storm Hazards project.

STORM HAZARDS

The Storm Hazards project, which is being conducted at NASA/Langley, is a study of the electrical properties of thunderstorms with the twin goals of improving our ability to avoid regions of storms that are potentially hazardous to aircraft and of determining just what risks aircraft will face if they do penetrate strongly electrified clouds. The study is conducted by flying an instrumented F-106 aircraft through thunderstorms while observing the storms remotely in a number of ways (conventional radar, Doppler radar, and several different lightning location techniques). Numerous penetrations of a single storm are made to determine the regions of the storm in which the aircraft is most often struck by lightning, as well as the regions with the worst precipitation and the worst turbulence.

Of course, to avoid hazardous regions of a storm one wants to be able to identify those regions with a remote sensing technique. By comparing the in-cloud locations of lightning strikes to the F-106 aircraft and the in situ aircraft electrical measurements to data from the remote sensing instruments, we should be able to determine the ability of these instruments to locate the hazardous regions.

To determine the risk involved in penetrating thunderstorms, one must learn the magnitude and duration of the electric and magnetic fields associated with a direct strike to the aircraft, the rate of change of these fields, etc. This will be done with on-board aircraft sensors.

As part of the Storm Hazards project Dr. Christian and I are working on an aircraft instrument to measure the charge, size, and shape of individual precipitation particles and larger cloud particles ($>50\mu\text{m}$). These data should allow us to determine, among other things:

- (1) precipitation and cloud particle concentrations and phases (liquid or solid) in various regions of the storm and
- (2) the locations of the dominant charge structures in the cloud (since all of the charge in the cloud should reside on either the precipitation or the cloud particles).

Such information should be quite helpful in determining hazardous regions of the storm. The data will also be important in supporting some of the other aircraft and ground-based measurements: particle concentrations will aid the Heavy Rain Effects experiments and should be useful for comparison with radar-inferred concentrations; charge data should be useful in interpreting the ACEE Charge Patch measurements.

PROGRESS TO DATE

We have completed the basic design of the Charge and Particle (CAP) instrument. A commercial instrument that measures the two-dimensional size and shape of cloud and precipitation particles has been purchased from Particle Measuring Systems, Inc., of Boulder, Colorado. We plan to modify this sensor so that it will also measure the charge of the particles. Since the data acquisition system (DAS) that is normally sold with the particle probe is unsuited for our purposes, we have designed our own DAS to store the charge, size, and shape information for each particle on magnetic tape. The system has been designed to require no human interaction while the aircraft is in the air.

The charge sensor will operate in the same way as the balloon-borne sensor of Marshall and Winn (1982). Although we have yet to produce a detailed drawing for a machinist, the basic design of the charge transducer has been completed; it is conceptually similar to the design of Marshall and Winn with modifications to accommodate the size and shape of the commercial probe. The charge measuring electronics will also be essentially the same as those used by Marshall and Winn. However, since the charges on cloud particles should be substantially smaller than those found on precipitation particles, the electronics will have to be more sensitive.

Our DAS will be built around a single board computer system based on a 6502 microprocessor, since this processor is compatible with (indeed, identical to) some of the computers available in Dr. Christian's laboratory. We plan to store the data on a 67 megabyte magnetic tape recorder cassette. The necessary parts for building the DAS have been ordered. A good bit of software and some hardware have yet to be developed. Until the hardware that we have ordered is in hand, it will be difficult to finalize our design. Much of my time has been spent learning how the commercial particle sizing instrument works so that we could determine what we needed to build our DAS.

Though much work remains, the instrument design is well underway toward meeting our commitment for installation on the F-106 aircraft in April, 1983.

LIGHTNING MAPPER

The Lightning Mapper project is aimed at developing a geostationary satellite to locate lightning flashes and to make quantitative measurements on them. These data will have important practical applications, such as real-time warnings of severe storms, and basic science applications, such as determining the role of thunderstorms in the global electrical circuit. Currently the prototype satellite instrumentation is being tested by flying it over thunderstorms in a NASA U-2 aircraft. The goal of these missions is to compare the U-2 optical and electrical measurements on lightning with similar measurements made from the ground on the same lightning flashes so that the U-2 data can be interpreted correctly.

From 17 May 1982 to 1 June 1982 I was the NASA liaison at the National Severe Storms Laboratory (NSSL) in Norman, Oklahoma, during U-2 operations over severe storms in Oklahoma. My duties at NSSL were threefold:

- (1) To provide weather information (obtained at NSSL) to Dr. Christian and the U-2 pilot so that the aircraft would overfly the most promising electrical storms,
- (2) To ascertain that ground electrical and optical measurements were made on the appropriate storm during U-2 flights (during late night flights, this often meant that I helped operate the NSSL instrumentation), and
- (3) To provide measurements of electric fields inside the severe storms that the U-2 was flying over. This was done using a balloon-borne \vec{E} meter of the type designed by William P. Winn and co-workers (Winn et al 1981).

The Oklahoma U-2 operations were quite successful. The best mission occurred on May 27, 1982, when the U-2 overflew a storm that passed over NSSL. Analysis of both the U-2 data and the NSSL data is in progress.

We have concurrent U-2 and balloon data from only the May 27 storm. The design of the electronics needed to analyze the balloon data has been completed; construction of the electronics is underway.

ACKNOWLEDGEMENTS

Hugh Christian's help has been absolutely vital to me during my stay; I thank him for that and for his refreshingly open-minded and magnanimous views on research. Marion Kent and Bob Barfield eased the red tape burden that threatens to bury us all. O.H. Vaughan helped me find the fastest way through the red tape maze on several occasions. I owe thanks to so many other NASA/MSFC

and USRA personnel as well as other ASEE Summer Faculty Fellows that I despair at trying to list them all; it is a credit to the Space Sciences Laboratory in particular and Marshall Space Flight Center in general that everyone I have encountered here has been so helpful.

Trying to coordinate the U-2 measurements and NSSL ground measurements was tricky at best; it would have been impossible without the aid of Dave Rust and Don Burgess of NSSL. Les Showell and Gene Lee of NSSL made valuable contributions to this work. Again the unnamed supporting cast (this time at NSSL) is large. I am grateful for their aid.

REFERENCES

1. Marshall, T.C. and W.P. Winn, "The Charge and Velocity of Individual Precipitation Particles in a New Mexico Thunderstorm: Lower Positive Charge Centers", Journal of Geophysical Research, in press, 1982.
2. Winn, W.P., C.B. Moore, and C.R. Holmes, "Electric Field Structure in an Active Part of a Small, Isolated Thunderstorm", Journal of Geophysical Research, 86, p. 1187, 1981.

1982

NASA/ASEE SUMMER FACULTY RESEARCH FELLOWSHIP PROGRAM

MARSHALL SPACE FLIGHT CENTER
THE UNIVERSITY OF ALABAMA

POPULATION CONTROL OF SELF-REPLICATING SYSTEMS

Prepared By: Richard L. McCord, Ph.D.
Academic Rank: Professor
University and Department: Middle Tennessee State University
Mathematics and Computer Science
NASA/MSFC:
Laboratory: Space Sciences
Division: Space Physics
Branch: Astrophysics
MSFC Counterpart: Wesley A. Darbro
Date: August, 1982
Contract No.: NASA-NGT-01-002-099
The University of Alabama

POPULATION CONTROL OF SELF-REPLICATING SYSTEMS

By

Richard L. McCord, Ph.D.
Professor of Mathematics
Middle Tennessee State University
Murfreesboro, Tennessee

ABSTRACT

From the conception and development of the theory of self-replicating automata by John von Neumann, others have expanded on his theories. In 1980, Georg von Tiesenhausen and Wesley A. Darbro developed a report which is a 'first' in presenting the theories in a conceptualized engineering setting. In that report several options involving self-replicating systems are presented. One of the options allows each primary to generate n replicas, one in each sequential time frame after its own generation with no restrictions on the number of ancestors per replica.

This study involves determining the state vector of the replicas in an efficient manner. The problem is cast in matrix notation, where $F = [f_{ij}]$ is a diagonalizable matrix. Any element f_{ij} represents the number of elements of type j in time frame $k+1$ generated from type i in time frame k . It is then shown that the state vector is:

$$\bar{f}(k) = \bar{f}(0) \cdot F^k = \bar{f}(0) \cdot S D^k S^{-1},$$

where D is a diagonal matrix whose eigenvalues are precisely those of F .

ACKNOWLEDGEMENTS

Indebtedness is due and appreciation is extended to the following:

Wesley A. Darbro, MSFC counterpart; for his patience, understanding, and encouragement to me and for his mathematical insight, awareness, and contribution in this area of research.

Billy G. Bass, Space Sciences Laboratory; for his concern, comments, introduction, and indoctrination to the Space Sciences Laboratory.

Marion I. Kent, University Affairs; for his influence, interest, support, and cooperation.

B. F. Barfield, University Program Director; for his direction, excellent organization, and administration.

James B. Dozier, Research and Technology; for his programs and unique commentaries.

Gerald R. Karr, and the University of Alabama in Huntsville; for their exceptional hospitality.

LIST OF FIGURES

<u>Figure No.</u>	<u>Title</u>	<u>Page</u>
1	Family tree of replicas	XXVII-11
2	Formation of Matrix $F = [f_{ij}]$	XXVII-11
3	Cumulative diagram of replicas option B, n = 2	XXVII-12

INTRODUCTION

In 1980, Georg von Tiesenhausen and Wesley A. Darbro [5] developed "a first approach to conceptualize self-replicating systems from past and present abstract theories." This development was based on theories composed by John von Neumann in the late 1940's and expanded by others. NASA officials and others have discussed the possible application of self-replicating systems to future space missions.

In the mathematics of self-replication presented in the study cited above and in the paper by Wesley A. Darbro [1], several options are described.

Option A is designed to allow simultaneous replication of a primary; that is, each primary may generate n replicas in each time frame after its own generation until cut-off.

Option B allows each primary to generate n replicas sequentially, one in each time frame after its own generation.

Option C is a special case of option B in which the maximum number m of ancestors is specified.

A primary is an individual capable of replication and may or may not be a replica. The words generates, replicates, and reproduces are synonyms. Production refers to the process of deriving an end product (other than replicas) as a result of work done. The word cut-off indicates the end of replication and the beginning of production.

OBJECTIVES

The aim of this study has been:

1. to review the literature relative to the Fibonacci sequence and the mathematics of self-replication.
2. to determine the state vector of the replicas in an efficient manner, in particular for option B, the system having a fixed number of replicas per primary and no restrictions on the number of ancestors for a replica.

OPTION B

The major concern of this study is option B as presented by Darbro [1]. For this option a primary generates a fixed number n of replicas which in turn become primaries unless cut-off occurs. Each primary generates its replicas in sequential time frames, beginning in the first time frame after its own generation. At cut-off, replication ceases and production begins.

As an example, consider Figure 1 in which $n = 2$. The number s_k of replicas at time frame k for $k = 0, 1, 2, \dots$, forms the Fibonacci sequence $1, 1, 2, 3, 5, 8, \dots$, and

$$s_k = s_{k-1} + s_{k-2}, \text{ if } k \geq 2 \wedge s_0 = 1 = s_1. \quad (1)$$

Also, the cumulative number S_k of replicas at time frame k is given by

$$S_k = S_{k-1} + S_{k-2} + 1 = s_{k+2} - 1 \wedge S_{-1} = 0 = S_{-2}. \quad (2)$$

Particularly, for $k = 6$, $s_6 = 13$ and $S_6 = 33$.

For $n+1$ types of replicas (which are or may become primaries), denote the types by indices $0, 1, 2, \dots, n$, each of which identifies the number of replicas generated by a primary. Consider a square matrix $F = [f_{ij}]$ of order $n+1$, where f_{ij} is the number of replicas of type j in the time frame $k+1$ generated by a primary of type i in time frame k ($0 \leq i, j \leq n \wedge k = 0, 1, 2, \dots$). If $i < n$, let the primary of type i generate one replica of type 0 , and let the primary itself become a primary of type $i+1$. If $i = n$, let the primary remain type i .

In particular, in the example of Figure 1, if $i < 2$, then $f_{i0} = 1$ and $f_{i,i+1} = 1$; if $i = 2$, $f_{22} = 1$; and $f_{ij} = 0$ in all other cases. From Figure 2, a matrix F can be formed;

$$F = \begin{bmatrix} 1 & 1 & 0 \\ 1 & 0 & 1 \\ 0 & 0 & 1 \end{bmatrix}. \quad (3)$$

As presented by Darbro [1] in the framework of Klarner [3], the state vectors may be formed for any time frame k .

Specifically,

$$\begin{aligned}\bar{F}(0) &= [1 \ 0 \ 0] \\ \bar{F}(1) &= \bar{F}(0) \cdot F = [1 \ 1 \ 0] \\ \bar{F}(2) &= \bar{F}(1) \cdot F = \bar{F}(0) \cdot F^2 = [2 \ 1 \ 1] \\ &\vdots \\ \bar{F}(6) &= \bar{F}(5) \cdot F = \bar{F}(0) \cdot F^6 = [13 \ 8 \ 12]\end{aligned}$$

and generally,

$$\bar{F}(k) = \bar{F}(k-1) \cdot F = \bar{F}(0) \cdot F^k. \quad (4)$$

At time frame 6, the state vector indicates: 13 have generated no replicas, 8 have generated one replica, and 12 have generated two replicas.

Continuing with the same example in which $n = 2$, the cumulative diagram (Figure 3) is perhaps more revealing. Since i, j index the number of replicas and ancestors, respectively, for any particular primary, the state vector for any time frame k can be expressed using the following format for ij where $i \leq n$ and $k = 6$.

$$\begin{aligned}i^j: & 0^0 1^0 2^0 0^1 1^1 2^1 0^2 1^2 2^2 0^3 1^3 2^3 0^4 1^4 2^4 0^5 1^5 2^5 0^6 1^6 2^6 \\ \bar{F}(6) &= [0 \ 0 \ 1 \ 0 \ 0 \ 2 \ 0 \ 0 \ 4 \ 1 \ 3 \ 4 \ 6 \ 4 \ 1 \ 5 \ 1 \ 0 \ 1 \ 0 \ 0], \quad (5)\end{aligned}$$

that is,

$$f_{00} = 0, f_{10} = 0, f_{20} = 1, \dots, f_{26} = 0.$$

Since the vector $\bar{F}(k)$, which represents the state of the replicas at time k can be expressed by (4), then

$$\bar{F}(6) = [1 \ 0 \ 0] \begin{bmatrix} 1 & 1 & 0 \\ 1 & 0 & 1 \\ 0 & 0 & 1 \end{bmatrix}^6 = [1 \ 0 \ 0] \begin{bmatrix} 13 & 8 & 12 \\ 8 & 5 & 8 \\ 0 & 0 & 1 \end{bmatrix}, \quad (6)$$

so that

$$\bar{F}(6) = [13 \ 8 \ 12]. \quad (7)$$

From Strang [4], if a square matrix can be diagonalized, then there exists square matrices D , S , and S^{-1} (where D is a diagonal matrix such that its diagonal elements are precisely the eigenvalues of F) such that

$$D = S^{-1}FS. \quad (8)$$

Operating on both sides of (8), first on the left by S and next by S^{-1} on the right, it follows that

$$F = SDS^{-1}. \quad (9)$$

Using associativity for multiplication and the fact that $S^{-1}S = I$, it follows using mathematical induction on k that

$$F^k = SD^kS^{-1}. \quad (10)$$

Then, it follows that

$$\bar{f}(k) = \bar{f}(0) \cdot F^k = \bar{f}(0) \cdot SD^kS^{-1}. \quad (11)$$

It may be pointed out that the columns of S are the eigenvectors of the matrix F.

In the example, since S and S^{-1} exist and D^6 is easily generated from D, then $\bar{f}(6)$ is an immediate consequence.

$$\bar{f}(6) = [1 \ 0 \ 0] \cdot SD^6S^{-1}. \quad (12)$$

Specifically,

$$D = \frac{1}{2} \cdot \begin{bmatrix} 2 & 0 & 0 \\ 0 & 1+\sqrt{5} & 0 \\ 0 & 0 & 1-\sqrt{5} \end{bmatrix}, \quad D^6 = \frac{1}{2^6} \cdot \begin{bmatrix} 2^6 & 0 & 0 \\ 0 & (1+\sqrt{5})^6 & 0 \\ 0 & 0 & (1-\sqrt{5})^6 \end{bmatrix}$$

$$S = \begin{bmatrix} 1 & 1+\sqrt{5} & 1-\sqrt{5} \\ 0 & 2 & 2 \\ -1 & 0 & 0 \end{bmatrix}, \quad S^{-1} = \frac{1}{2^2 \cdot 5} \cdot \begin{bmatrix} 0 & 0 & -20 \\ 2\sqrt{5} & 5-\sqrt{5} & 2\sqrt{5} \\ -2\sqrt{5} & 5+\sqrt{5} & -2\sqrt{5} \end{bmatrix}.$$

CONCLUSIONS AND RECOMMENDATIONS

In option B, the state vector $\bar{f}(k)$ can be generated in several ways.

1. Use of a diagram.
2. Recursively, by using $\bar{f}(k) = \bar{f}(k-1) \cdot F$.
3. Raising F to an exponent, $\bar{f}(k) = \bar{f}(0) \cdot F^k$.
4. Diagonalizing F , $\bar{f}(k) = \bar{f}(0) \cdot S D^k S^{-1}$.

Some areas which may prove to be of interest are:

1. Investigating the state vector for option C which limits the number of ancestors to a maximum value m .
2. Defining and investigating the problems of placement of the replicas as they are generated.
3. Considering the demise of replicas; that is, replicas are no longer productive [2], [1].

REFERENCES

1. Darbro, Wesley A., "Sequences Generated by Self-Replicating Systems", pre-published paper.
2. Hoggatt, V. E., Jr., and D. A. Lind, "The Dying Rabbit Problem", The Fibonacci Quarterly, 7(1969), 482-487.
3. Klarner, David A., "A Model For Population Growth", The Fibonacci Quarterly, 14 (1976), 227-281.
4. Strang, Gilbert, Linear Algebra and Its Applications, Academic Press, New York, 1976, 181-189.
5. Von Tiesenhausen, Georg, and Wesley A. Darbro, "Self-Replicating Systems - An Engineering Approach", July 1980.

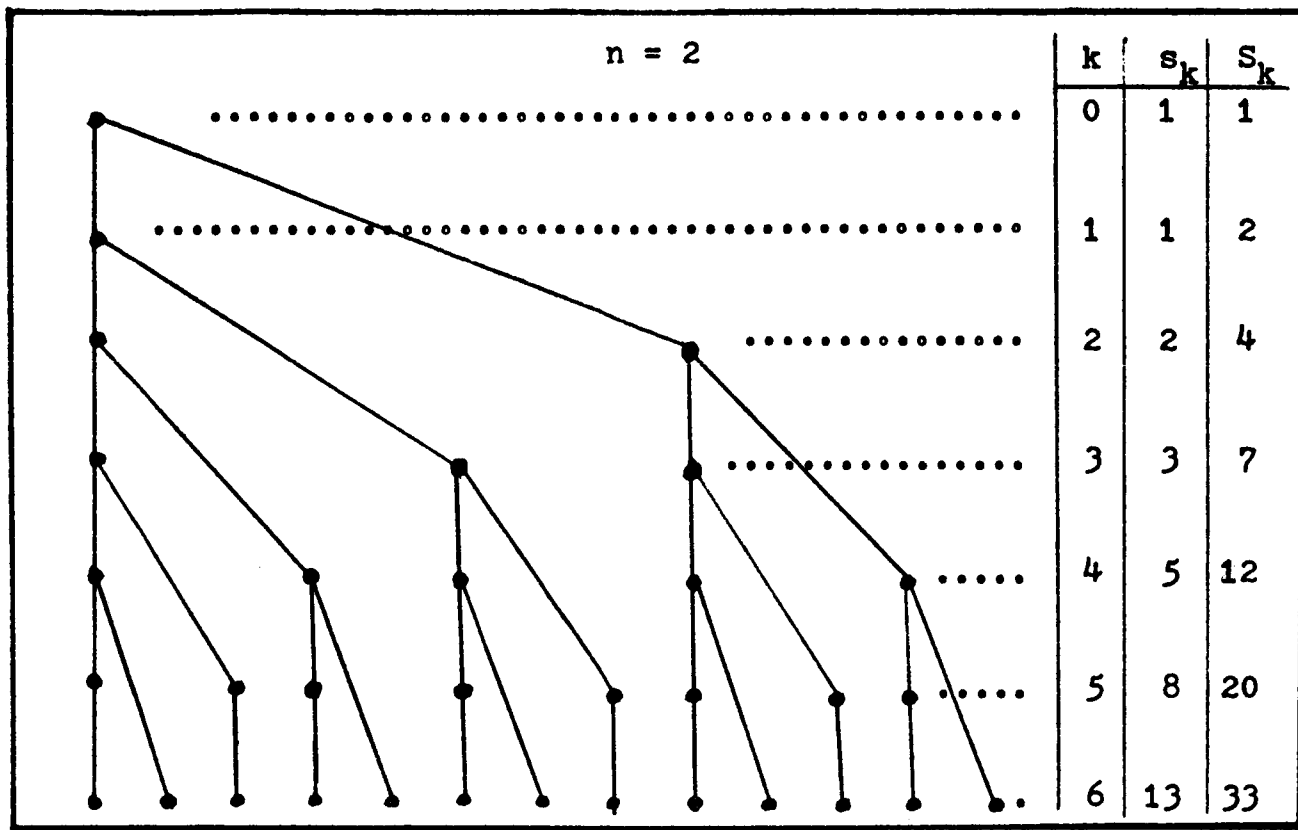


FIGURE 1. Family Tree of Replicas

j	0	1	2
i	1	1	0
0	1	1	0
1	1	0	1
2	0	0	1

FIGURE 2. Formation of Matrix $F = [f_{ij}]$.

$f_{i0} = 1, f_{i i+1} = 1$ when $i < 2$.

$f_{22} = 1$ when $i = 2$.

$f_{ij} = 0$ in all other cases.

XXVII-12

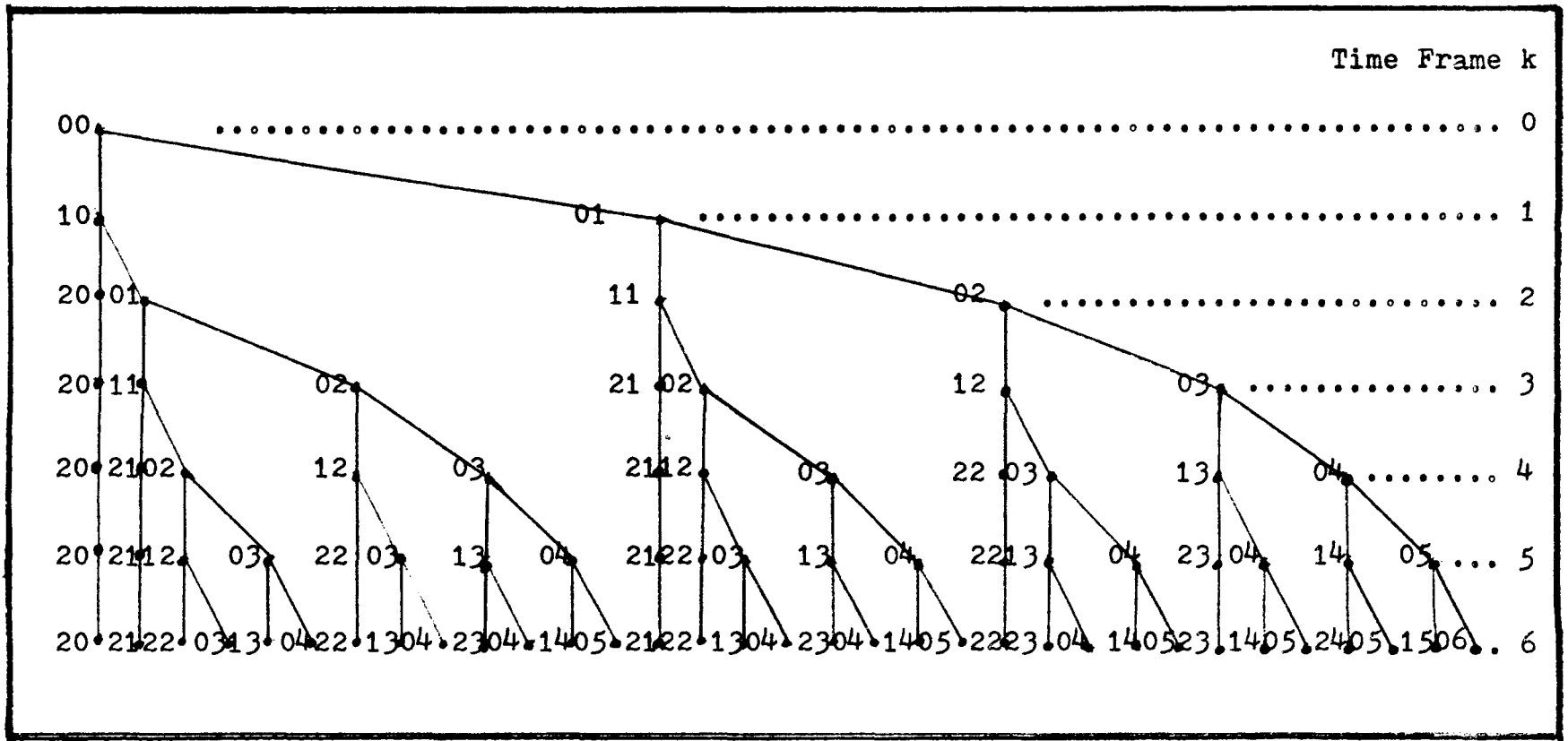


FIGURE 3. Cumulative Diagram of Replicas.
Option B, $n = 2$.

1982

NASA/ASEE SUMMER FACULTY RESEARCH FELLOWSHIP PROGRAM

MARSHALL SPACE FLIGHT CENTER
THE UNIVERSITY OF ALABAMA

STUDY OF AND PROPOSALS FOR THE CORRECTION OF ERRORS IN A
RADAR RANGING DEVICE DESIGNED TO FACILITATE DOCKING OF A
TELEOPERATOR MANEUVERING SYSTEM

Prepared By: Malcolm W. McDonald, Ph.D.
Academic Rank: Associate Professor
University and Department: Berry College
Department of Physics

NASA/MSFC:
(Laboratory) Information & Electronic Systems
(Division) Computers and Communications
(Branch) Communications Systems

MSFC Counterpart: E. H. Gleason
Date: August 9, 1982
Contract No.: NGT-01-002-099

STUDY OF AND PROPOSALS FOR THE CORRECTION OF ERRORS IN A FMCW RADAR RANGING
DEVICE DESIGNED TO FACILITATE DOCKING OF A TELEOPERATOR MANEUVERING SYSTEM

By

Malcolm W. McDonald, Ph.D.
Associate Professor of Physics
Berry College
Mount Berry, Georgia

ABSTRACT

A frequency-modulated continuous wave radar system is being developed in the Communication Systems Branch in the Information and Electronic Systems Laboratory at Marshall Space Flight Center. The system operates in the thirty-five gigahertz frequency range and is to provide millimeter-accuracy range and range rate measurements. This level of range resolution will allow soft docking for the proposed teleoperator maneuvering system (TMS) or other autonomous or robotic space vehicles.

A study has been undertaken to identify sources of error in the operation of the system which tend to limit its range resolution capabilities. Alternative signal processing techniques have been explored with much attention being given to determining the effects of inserting various signal filtering circuits in the system.

A significant result of this investigation has been the identification and elimination of an extraneous low-frequency signal component which was being created as a result of zero-range immediate reflection of radar energy from the surface of the antenna dish back into the mixer of the system. This frequency component there was beating with frequencies of interest due to reflections from the target to produce confusion.

ACKNOWLEDGMENTS

I wish to thank all the persons in the Communications Systems Branch (previously known as the Communication and Tracking Branch) for their generous display of hospitality, helpfulness, and friendliness. I am deeply grateful for their support and acceptance in allowing me (a physicist) to invade their challenging and engagingly interesting area of work and expertise for purposes of participating in this research effort.

I treasure especially the working relationship which developed with Ed Gleason and Bill Reed, my principal and associate research collaborators, respectively. Both are talented engineers, but each has a particular strength that I found to be of inestimable value in supporting this work. Ed seems to have an intimate understanding of every piece of electronic equipment in this laboratory area. He was always able to find any instrument which was needed, install it in support of this research, and have it operating properly in record time. Bill has a commanding understanding of integrated circuit chips and could always find a chip and "breadboard" a circuit to perform any signal processing task I could dream up.

My sincere thanks are extended to Wayne Wagon for his assistance in arranging this research opportunity; to David Mack for sharing office/laboratory space with me during this summer; and to Kaye Langford for deciphering my handwriting and aiding in the typing of this report. Also, I have enjoyed an association with Dr. Al Pujol, another summer faculty research participant, who was working on a project similar to my own.

LIST OF FIGURES

<u>FIGURE NUMBER</u>	<u>TITLE</u>	<u>PAGE NUMBER</u>
1	Basic Radar-Target Geometry	XXVIII-8
2	Block Diagram of Typical Circuit	XXVIII-8
3	Illustration of FM Sweep Parameters	XXVIII-10
4	Effects of Band-Pass Filtering on F vs t Characteristics During One Sweep Cycle	XXVIII-13
5	Signal Delay As A Function of Frequency for Filtering Circuitry	XXVIII-15

INTRODUCTION

In the operations of the proposed teleoperator maneuvering system (TMS) space vehicle, there will be a need for an accurate range and range rate measurement system. This will enable soft docking of the TMS vehicle with a space platform or other space equipment and materials.

A radar system designed to allow such accurate range and range rate measurements is under development in the Communications Systems Branch of the Information and Electronic Systems Laboratory at Marshall Space Flight Center. The present system has evolved from linearly-swept frequency-modulated devices proposed for short range measurements of coal seam thickness in coal mines (ref. 3,4,5). The present device linearly sweeps a 35 gigahertz microwave signal up and down through a frequency deviation of ± 1.25 gigahertz at a rate of 60 Hz.

A portion of the transmitted microwave energy is reflected from the target back into the radar horn after a time delay proportional to the target range. The returning energy is circulated to a mixer where it is superheterodyned with the radar frequency currently being generated in the system to produce a low frequency beat signal output. Analysis of the frequency of the beat signal leads to a determination of the range of the target. Similarly, a calculation of the time rate of change of beat frequency leads to a determination of range rate (time rate of change of range).

OBJECTIVES

Even though the basic method of range determination is straightforward and uncomplicated, various errors do arise in frequency modulated continuous wave radar techniques. The magnitudes of such errors set limitations on the accuracy with which the range of a target reflector can be resolved. The objectives pursued through this investigation are:

1. to analyze the nature and cause of the primary and secondary errors that occur in a FM-CW radar system,
2. to determine the degree to which those errors may be reduced by signal processing techniques, and
3. to develop pertinent criteria for an optimum signal processing technique.

RESEARCH REPORT

I. General Description

The theory and applications of radar systems, in particular frequency-modulated continuous wave (FMCW) systems, are well documented in the literature (see for example ref. 1,2). The work leading to this report involved the study of errors inherent to a FMCW radar range detection system. This system may have applications in the docking and maneuvering procedures of the proposed teleoperator maneuvering system (TMS).

An illustration of the radar-target geometry is presented in Figure 1. Microwave energy of center frequency, $f_c = 35$ GHz, is generated in a voltage-controlled YIG (yttrium-iron-garnet) oscillator in the radar device. Varying a voltage supplied to the YIG driver causes varying frequencies to be generated by the YIG oscillator. A linear ramp voltage was applied to the driver to sweep the YIG oscillator output alternately from a minimum frequency f_1 to a maximum frequency f_2 at a selectable rate. During the early stages of this investigation the frequency sweep rate was 120 Hz. This was changed to 60 Hz during the course of this work. The linear sweep produces a triangular frequency envelope in time, as depicted in Figure 3.

In the radar unit the oscillator output energy is divided into two branches in a hybrid microwave splitter with one branch being directed through a microwave circulator into a waveguide section which feeds the transmit-receive antenna. Energy is reflected from a cubical corner reflector target back into the antenna where it is focussed into the waveguide feed and directed back through the circulator to a microwave mixer. This target-reflected energy superheterodynes in the mixer with a second branch of energy from the hybrid splitter to produce a low-frequency beat signal. For target distances up to 4 meters the beat frequency is less than 10 KHz. The target is mounted on an optical bench to permit high-accuracy range monitoring.

The beat frequency signal is amplified and filtered in preparation for analysis to determine range. A block diagram of a typical filtering sequence is illustrated in Figure 2. The beat signal of frequency F is directed in order through a high-pass circuit with the threshold set at 1.0 KHz, a band-pass circuit which was manually tracked to center on F , and a low-pass filter set at a 10 KHz threshold. During the majority

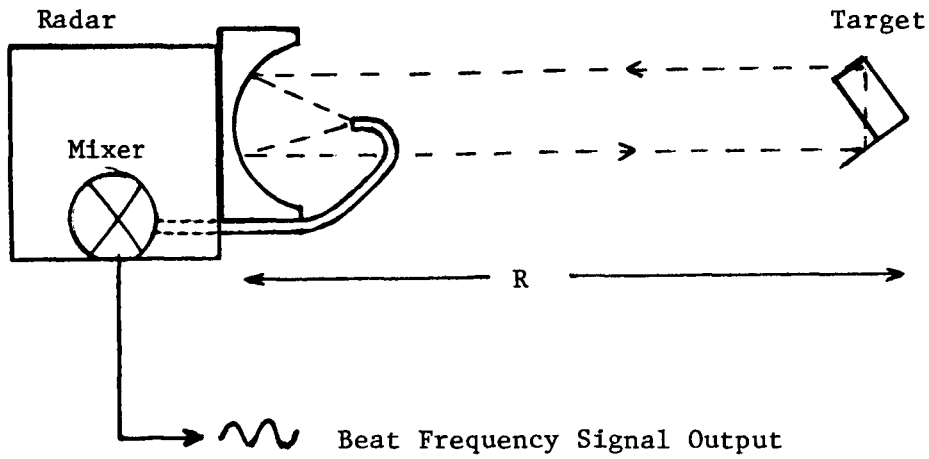


Figure 1. Basic radar-target geometry. The reflecting target is a copper-coated cubical corner reflector.

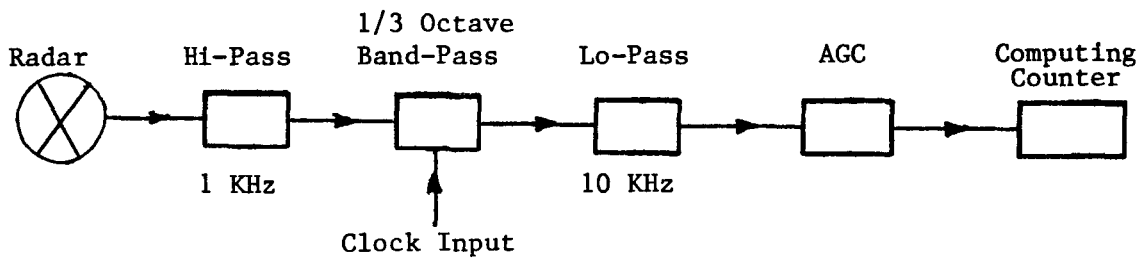


Figure 2. Block diagram of typical circuit.

of the time covered in this investigation the filtered signal was sent to a Hewlett Packard 5360A computing counter where the frequency was measured. After proper range-frequency conversion parameters had been determined the computing counter was programmed to read out range values directly.

In the filtering circuitry illustrated in Figure 2 the low-pass and high-pass filters were set at the indicated cutoff values. The band-pass filter provided a one-third octave bandpass. This was in the form of an EG&G RETICON R5604 16-pin DIP integrated circuit with its center frequency controlled by a variable clock input.

The computing counter was inserted in the system merely to serve as a substitute to simulate the frequency counting function which normally was performed by a separate electronic circuit previously developed in this laboratory. That circuit counts the time duration of a selected counting time window and the number of cycles of the beat frequency signal occurring during that window. The frequency is computed as the quotient of the number of cycles divided by the time duration necessary to count that number of cycles. The counting window is actually of variable time width to enable in all cases the counting of an integral number of beat frequency cycles. This feat is accomplished by opening and closing the window with the first negative-slope zero crossing of the beat signal following two preset times, usually chosen to be two or three milliseconds apart, during each sweep cycle. The timing operations are accomplished at a one megahertz clock rate.

II. Theory of Operation

The frequency modulation of the YIG oscillator occurs as alternating linear sweeps between frequency extremes f_1 and f_2 , as depicted in Figure 3. The solid and dashed line envelopes can be interpreted as representing the frequencies at any instant arriving at the microwave mixer from the hybrid splitter (solid line) and after a time delay τ related to the target range for that energy returned from the target reflector (dashed line). The time delay τ is defined by

$$\tau = 2R / c \quad (\text{Equation 1})$$

where R is the range to the target, and c is the propagation speed of the microwaves in air, or space, (3.00×10^8 meters per second). The

beat frequency F is related to the time delay of the returning signal by

$$F / \tau = \Delta f / T \quad (\text{Equation 2})$$

where $\Delta f = f_2 - f_1$, the total FM sweep range, and T is the time required to complete a single sweep in either the up or down direction. Substituting Equation 1 into Equation 2 leads to an expression for target range as a function of beat frequency,

$$R = cF / 2(\Delta f/T) . \quad (\text{Equation 3})$$

In principle, therefore, the target range R is determined by the beat frequency F , the slope $\Delta f/T$ of the linear FM sweep, and the constant speed of propagation of the waves c .

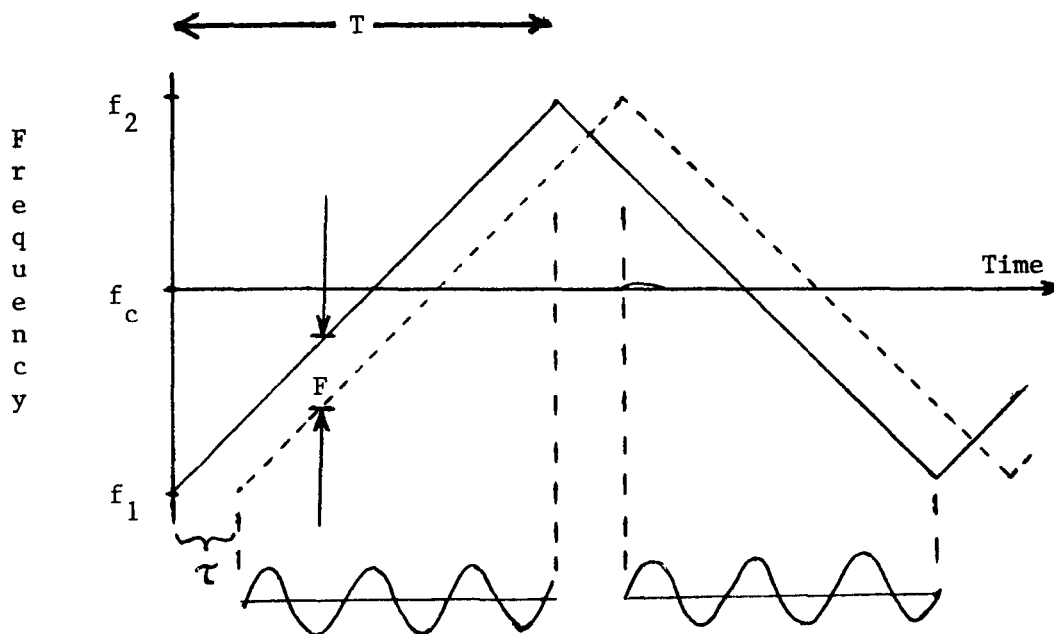


Figure 3. Illustration of FM sweep parameters. The YIG oscillator $f_c = 35$ GHz, and $\Delta f = f_2 - f_1 = 2.5$ GHz. F, T , and τ are described in the text.

III. Sources of Error

An inspection of the range-frequency relationship in equation 3 suggests possible factors which could lead to error or uncertainty in the determination of range. They include:

- type 1: error in the signal processing techniques employed in measuring beat signal frequency F ,
- type 2: error associated with determination of the slope $\Delta f/T$ of the assumed linear sweep, and
- type 3: error caused by actual nonlinearity of the sweep.

An error reduction goal established during the early stages of this project led to a criterion for defining acceptable and unacceptable system errors. The goal was to be able to measure range at approximately one meter range to within one millimeter accuracy. The criterion for deeming sources of error small enough to accept became the fact of whether the error contributed less than plus or minus one part in one thousand to the uncertainty in the range measurement. This would allow an accuracy of ± 1 mm at one meter, ± 2 mm at 2 meters, etc. Sources of error which exceeded these limits were sought and studied at length.

From an ideal standpoint the type 2 errors were quite small since Δf could be determined from the known YIG frequency response to an applied driver voltage and the time length T of the sweep could be measured with more than sufficient accuracy. Since type 3 errors do contribute in the YIG oscillator system (ref. 6), the consideration of type 2 error becomes moot. Analysis of type 3 errors directly is extremely difficult at the high oscillator frequency (35 GHz). Measurement of dynamic sweep non-linearity characteristics of the YIG oscillator were considered to be outside the scope of the present investigation. Instead the linearity of the system was examined from another angle.

As a result of non-linearity of the YIG oscillator response the beat frequency F can not be considered constant throughout the sweep time T . The majority of effort in this investigation was directed to a detailed study of the behavior of the beat frequency generated by the radar circuit during each sweep at a given target range and on ways to produce a more constant beat frequency output at a given range.

Figure 4 demonstrates F versus time curves observed during a single sweep with little filtering of the beat signal (Curve A) and extensive filtering (Curve B) when the target was located at a range of 200 cm. Note that Curve A is shifted downward 0.5 KHz for plotting purposes. Similar plots of F vs. t had similar characteristics at other ranges. These data were obtained by measuring with the computing counter the cycle-by-cycle frequency F generated throughout an entire sweep period T. The time plotted is t_s , the time at which each cycle begins. In Curve A the beat signal was passed through a high-pass filter set at 1.0 KHz threshold and through an AGC circuit only prior to measurement. In Curve B the filtering was done according to the illustration in Figure 2: in order, through the 1.0 KHz high-pass, a one-third octave manually-tracked band-pass, a 10 KHz low-pass filter, and the AGC circuit.

Two facts are evident from examining Figure 4. One is that extensive filtering of extraneous beat signal components is essential, and another is that the beat frequency F produced at a given range R is not at all constant throughout a sweep period.

Attempts during this investigation to measure range with increasing accuracy centered on the belief that there is some measurable average beat frequency which can be linearly related to target range R. Attempts were made to find optimum time width and positioning of a counting window within the sweep period T to permit such measurement.

The counting circuitry developed for measuring F was described partially earlier in this report. That circuit performs a sliding average of the beat frequency measured within the counting window intervals (usually of 2 or 3 milliseconds duration) over the preceding ten sweep cycles. The average is updated with the new data acquired during each sweep cycle. The average beat frequency, thus computed, is used to compute or predict range to the target.

During this investigation one source of error was reduced significantly by a hardware change in the radar unit. At longer ranges of 3 or 4 meters with the returning signal amplitude weakened as a result of the increased distance, rather large amplitude fluctuations in the F vs. t curve were evident, superimposed as a modulation on the F signal with modulation frequency of slightly less than one kilohertz. It was determined that this low-frequency component was arising from zero-range reflection of microwave energy back into the waveguide feed directly from the antenna surface. This component was reduced to almost zero hertz, thus providing a much smoother F vs. t characteristic curve at longer ranges, by inserting an extra length of waveguide between the hybrid splitter and the microwave mixer.

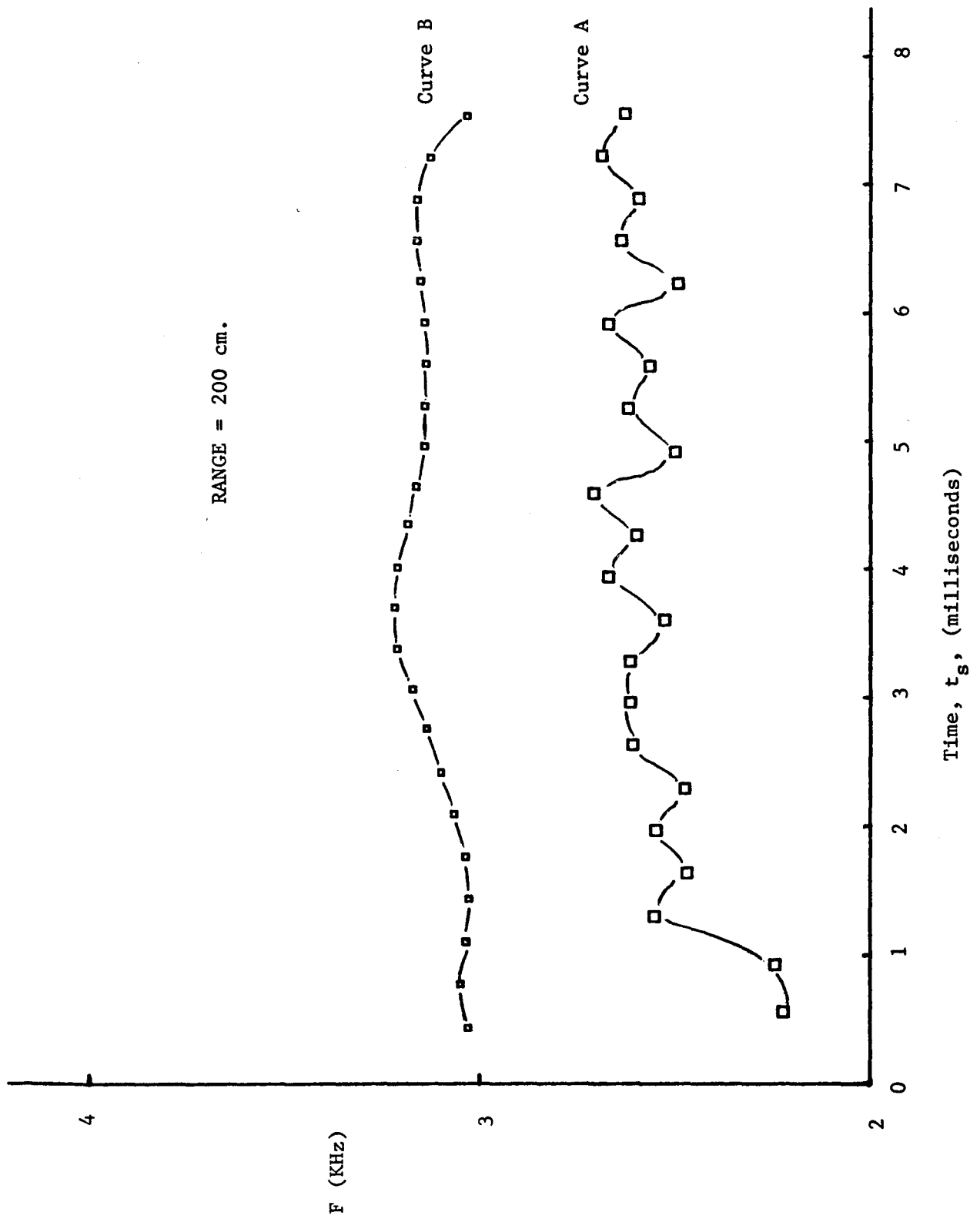


Figure 4. Effects of band-pass filtering on F vs. t characteristics during one sweep cycle. Curve A is shifted down 0.5 KHz.

IV. Results and Conclusions

It was concluded that type 1 errors in determining F are mainly due to the fact that F vs. t does not exhibit the theoretical zero slope over a sufficiently long time during the sweep cycle to enable suitably accurate measurement of beat frequency F . Timing errors in measuring the duration of the counting window are on the order of one part in 2000 or 3000, since a 1 MHz clock rate reduces those uncertainties to the order of one microsecond out of 2 or 3 milliseconds.

The application of the one-third octave tracking filter in the signal processing circuitry presents still another problem. The time delay experienced by the beat signal as it is being processed through the filter circuitry is a function of F which is the center frequency for the bandpass which is in turn a function of range. The delay of a pure sinusoidal signal through the full filter arrangement illustrated in Figure 2 was measured and plotted as a function of signal frequency in Figure 5.

It is believed that a dependable range-frequency (R vs. F) relationship can be established only if the frequency is measured during the same relative time window during the sweep cycle at all ranges. Due to the fact that the signal of interest is delayed in the filter circuitry for a period of time dependent on the center frequency of the band-pass tracking filter it becomes necessary to delay the opening of the counting window by a similar interval. This tends to complicate the simplicity of the system as does the fact that the delay encountered by the signal is also influenced by how accurately the bandpass is centered on the frequency of the signal of interest.

Inherent in the method employed for measuring F is an occasional error which arises, again, from the non-flat F vs. t curve. This error is observed as the target is moved slowly and smoothly through changes in range. Of necessity at certain target locations the zero crossing of a given cycle of the F signal becomes coincident with the pre-set time for allowing the opening of the counting window. At such a point the circuitry forces the window to shift backward in time and commence counting at the next-occurring zero crossing of the beat signal later in the sweep period. This time shift of the counting window corresponds to the period of the beat frequency signal (reciprocal of the frequency) at that point. If F vs. t were a flat curve this would not present a problem. Since F is not constant in time throughout a sweep cycle this occurrence causes a small incremental jump in the predicted range by the system at those range values where this condition occurs.

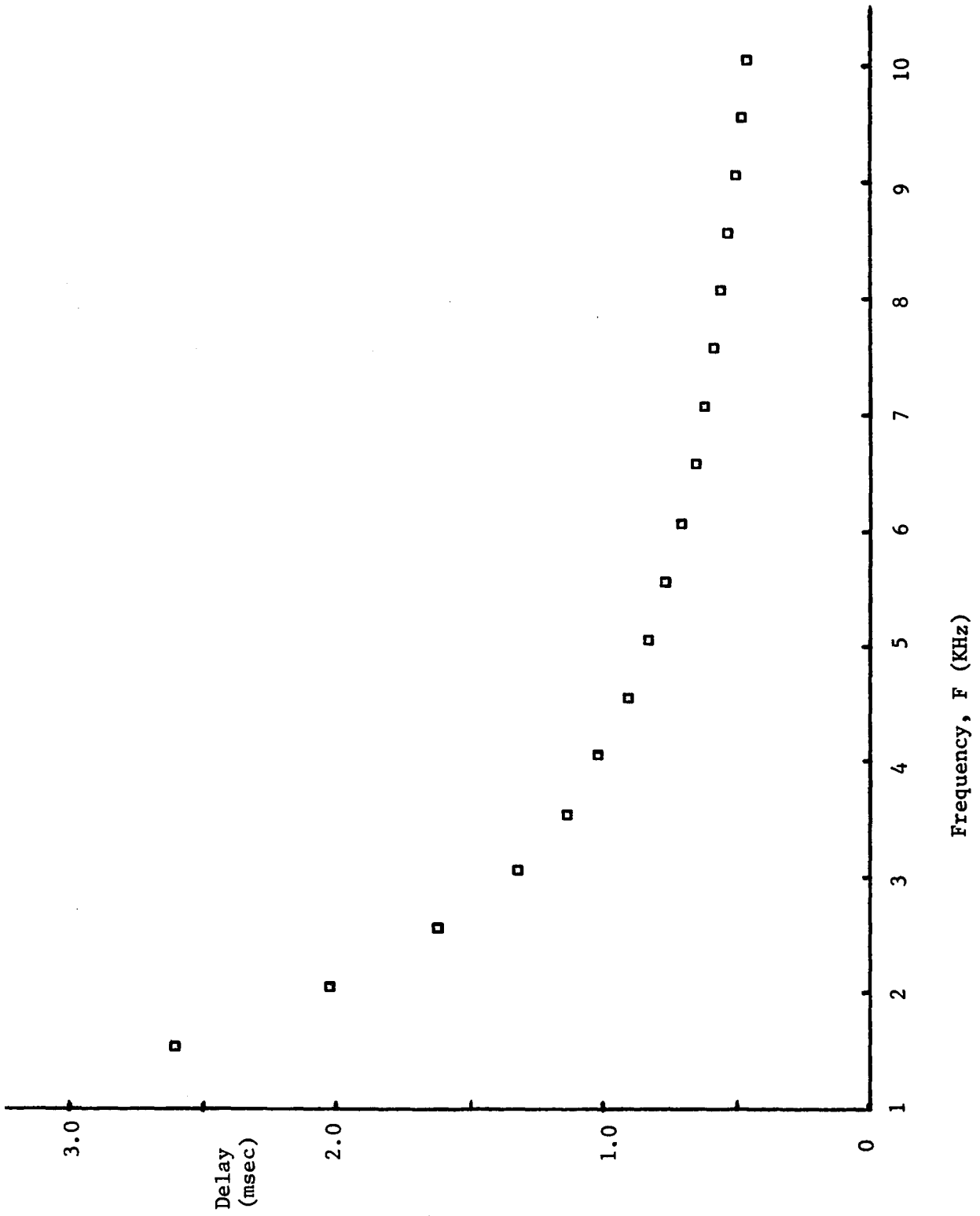


Figure 5. Signal delay as a function of frequency for the filtering circuitry. Details explained in text.

The predominant source of error in limiting the accuracy of range predictions by the system as it has been described in this report is the non-flat character of the F vs. time curve throughout a sweep cycle. Improvements were achieved in flattening that response curve through filtering and hardware revisions described in this report. With relative ease the radar system demonstrated a capability of predicting range to an accuracy of ± 3 millimeters over target ranges up to 4 meters. Unfortunately the ± 1 millimeter accuracy at one meter range can not be met at the time of this writing.

Limitations of time available for this investigation did not allow a full study of possible improvement in the F vs. t curve shape which might be expected by sweeping through a variety of different frequency extremes, f_1 and f_2 . It seems feasible also that a different sweep envelope (perhaps sinusoidal rather than the triangular shape) could be expected to produce a more suitable F vs. t response by eliminating the pronounced oscillator lag which must certainly occur when the present sweep slope discontinuities occur at the beginning of each sweep cycle. It is suggested that this bears further investigation.

REFERENCES

1. Skolnik, M. I., Introduction to Radar Systems, McGraw-Hill Book Company, New York, N.Y., 1962.
2. Nathanson, F. E., Radar Design Principles, McGraw-Hill Book Company, New York, N.Y., 1969.
3. Owen, T. E. and O. Tranbarger, "Volume II - Investigation and Development of a High Resolution FM-CW Radar System for Residual Coal Thickness Measurements," Interim Report to U. S. Department of Interior, Bureau of Mines from Southwest Research Institute, June 12, 1977, Contract No. H0262055.
4. Baghdady, E. J., "Study-Coal Radar Measuring System," Interim Final Report to NASA/MSFC from Infor Systems, Inc., April 27, 1978, Contract No. NAS8-32655.
5. Baghdady, E. J., "Study-Coal Radar Measuring System," Final Report to NASA/MSFC from Info Systems, Inc., July 15, 1979, Contract No. NAS8-32655.
6. Gilbert, K. D., "Dynamic Tuning Characteristics of YIG Devices," Reprint from the Microwave Journal, June, 1970.

1982

NASA/ASEE SUMMER FACULTY RESEARCH FELLOWSHIP PROGRAM

MARSHALL SPACE FLIGHT CENTER
THE UNIVERSITY OF ALABAMA

PRODUCTION OF METAL PARTICLES
AND CLUSTERS

Prepared By: Samuel P. McManus, Ph.D.

Academic Rank: Professor

University and Department: The University of Alabama in Huntsville
Department of Chemistry

NASA/MSFC:
(Laboratory) Space Sciences
(Division) Engineering Analysis
(Branch) Strength Analysis

MSFC Counterpart: Donald O. Frazier, Ph.D.

Date: July 30, 1982

Contract No.: NGT-01-002-099

PRODUCTION OF METAL PARTICLES AND CLUSTERS

by

Samuel P. McManus, Ph.D.
Professor of Chemistry
The University of Alabama in Huntsville
Huntsville, Alabama

ABSTRACT

Finely-divided metal particles and clusters are attracting increasing attention as petroleum feedstocks are projected to dry up and as alternate fuel and organic chemical feedstock sources emerge. Many metals and metal clusters have been found to be catalysts for some chemical reactions which hold promise for the production of alternate fuels and chemical feedstocks. Production of finely-divided metals using current technology leads to larger particles than sometimes desired because the finely-divided materials settle and agglomerate. This study has addressed the feasibility of producing novel metals or metal clusters in a low gravity environment.

The production of coordinately unsaturated metal carbonyls by thermolysis or photolysis of stable metal carbonyls is a research area attracting unusual attention because of the potential for generating novel catalysts by this technique. Our interest has focused on the laser irradiation of certain commercially available metal carbonyls. Our analysis of the literature leads us to the conclusion that laser-induced decomposition of metal carbonyls is feasible for producing a variety of coordinately unsaturated species. Formation of clustered species does occur but is hampered by weak metal-metal bonds.

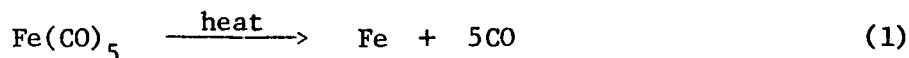
To prevent agglomeration, a coating process has been sought. Research reports on formation of coatings in gas phase systems are rare or difficult to locate. Nevertheless, some photochemical processes which may be applicable to coating of the reactive metal particles have been suggested from previous work. Experimentation on both the metal carbonyl photochemical process and gas phase photochemical polymerization is warranted.

INTRODUCTION

Since the discovery of ferrocene by Peter Pauson shortly after World War II, the chemistry of transition metals has largely dominated inorganic chemistry and has interested organic chemists, biochemists and material scientists. In fact a new subdiscipline of chemistry - - Organometallic Chemistry - - has resulted. Considering the variety of structures possible between transition metals and organic ligands, it is not surprising that the field has had so much room for expansion. However, the growth has come about because of the fascinating properties attributable to the interesting substances we call transition metal organometallics. Indeed, their importance has caused both the theory and practice of this type chemistry to rise to the forefront of basic chemistry.

Of the emerging science of transition metal chemistry, no area holds more promise or has attracted as much attention as that of polynuclear metal clusters - those containing two or more metal atoms bonded to each other as well as to nonmetallic ligands or groups. Some of these clusters, called Chevrel phases, are claimed to be the best superconducting substances in strong magnetic fields yet discovered. Others are implicated as catalysts for a variety of important organic reactions which hold the key to our future supply of chemical raw materials and fuels. Still others are among the photosensitive complexes that may serve to catalyze such important photochemical processes as the conversion of water into hydrogen and oxygen and the conversion of carbon dioxide into carbon and oxygen. Finally, the largest of the known metal clusters are of interest as models of metal surfaces.

Our interest in these materials derives from their use as catalysts in some important, basic organic reactions. Since only small amounts of catalysts are necessary to cause conversion of millions of pounds of reactant substances, it is appropriate to consider production of these substances under low gravity conditions, or in space, if gravity affects the chemistry of their production. In this regard the production of pure metal catalysts is affected by what may, in part, be an effect of gravity depending on the process. For example, high purity iron may be made by thermolyzing (in the gas phase) iron pentacarbonyl, eq. (1) The iron particles



settle out and agglomerate forming iron powder which has considerably less surface area than a much finer powder.

A number of other metal carbonyls are known to be converted to the respective metal or to coordinatively unsaturated species which cluster. Either heat or light serve as energy sources depending on the substance used. For example, when a metal carbonyl is heated or photolyzed a carbonyl group is lost after the absorption of sufficient energy to break the metal-CO bond, eq. (2). If contact is made between

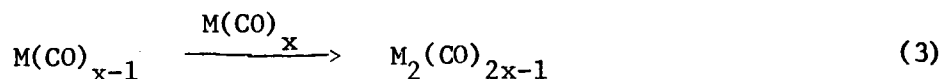
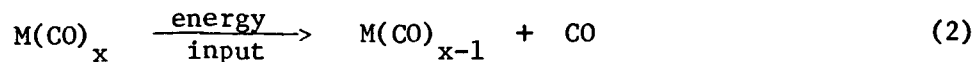


Table 1. Some Representative Group VIII Transition Metal Clusters

Type	Group		
	VIIIa	VIIIb	VIIIc
Dinuclear	$\text{Fe}_2(\text{CO})_9$	$\text{Co}_2(\text{CO})_8$	$\text{Pd}_2(\text{CNR})_6^{2+}$
	$\text{Ru}_2(\text{OCOR})_4^+$	$\text{Rh}_2(\text{OCOR})_4$	$\text{Pt}_2(\text{CNR})_6^{2+}$
Trinuclear	$\text{Fe}_3(\text{CO})_{12}$	$\text{Co}_3(\text{CO})_{11}$	$\text{Pd}_3(\text{CNR})_6$
	$\text{Ru}_3(\text{CO})_{12}$	$\text{Rh}_3(\text{C}_5\text{H}_5)_3(\text{CO})_3$	$\text{Pt}_3(\text{CNR})_6$
Tetranuclear	$\text{Fe}_4(\text{CO})_{13}^{2-}$	$\text{Co}_4(\text{CO})_{12}$	$\text{Ni}_4(\text{CNR})_7$
	$\text{Os}_4\text{H}_4(\text{CO})_{12}$	$\text{Ir}_4(\text{CO})_{12}$	$\text{Pt}_4(\text{CO})_5(\text{PR}_3)_4$
Pentanuclear	$\text{Os}_5(\text{CO})_{16}$		$\text{Ni}_5(\text{CO})_{12}^{2-}$
Hexanuclear	$\text{Ru}_6\text{H}_2(\text{CO})_{18}$	$\text{Rh}_6(\text{CO})_{16}$	$\text{Ni}_6(\text{CO})_{12}^{2-}$

the product of that decarbonylation, now coordinately unsaturated or having an unsatisfied coordination shell, and the saturated metal carbonyl a reaction may occur that will produce a cluster compound, eq. (3). A wide variety of clusters are now known. Some representative examples are given in Figures 1 and 2 and Table 1. Two recent reviews have highlighted important work ongoing in this area and have discussed prospective applications [1,2].

The objective of the present study was to determine the feasibility of producing clustered metals or metal cluster compounds in a low gravity environment by the photolysis or thermolysis of metal carbonyls using a laser source. Additionally, since clustered metals may produce larger particles upon settling out, the feasibility of coating the small particles by the simultaneous polymerization of a light- or heat-sensitive monomer was considered.

RESULTS AND DISCUSSION

A detailed literature search on the laser-induced thermolysis and photolysis of metal carbonyls and on laser-induced polymerization has been carried out. The results of this search are discussed below.

Thermolysis and Photolysis of Metal Carbonyls Using Laser Irradiation. Early into our search we found considerable evidence to indicate that ir laser radiation of metal carbonyls, if iron pentacarbonyl can be considered representative, is complex [3]. In fact, $\text{Fe}(\text{CO})_4$, the first intermediate expected from photolysis or thermolysis of $\text{Fe}(\text{CO})_5$, eq. 4, is claimed to undergo more ir laser induced reactions than any other matrix

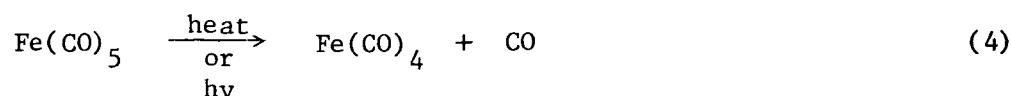


Figure 1.
**Polynuclear clusters come
 in many varieties**

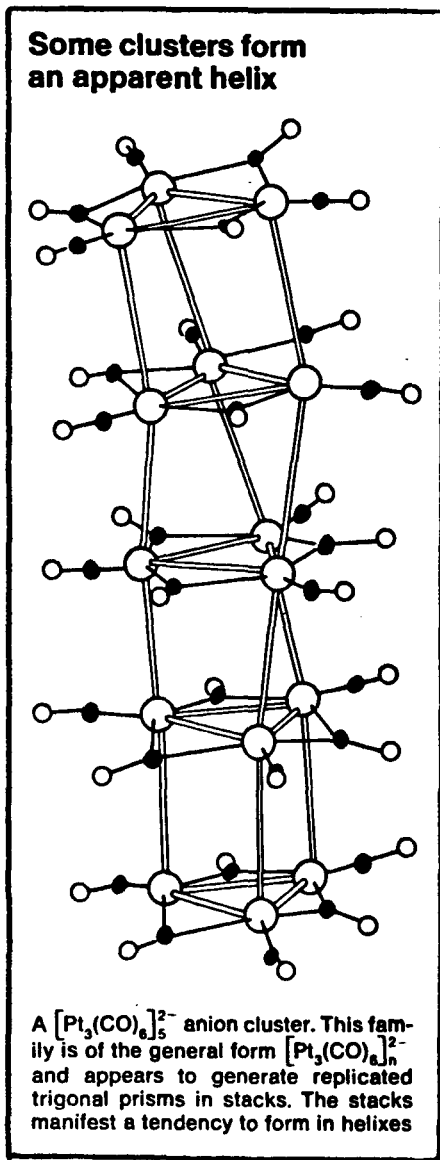
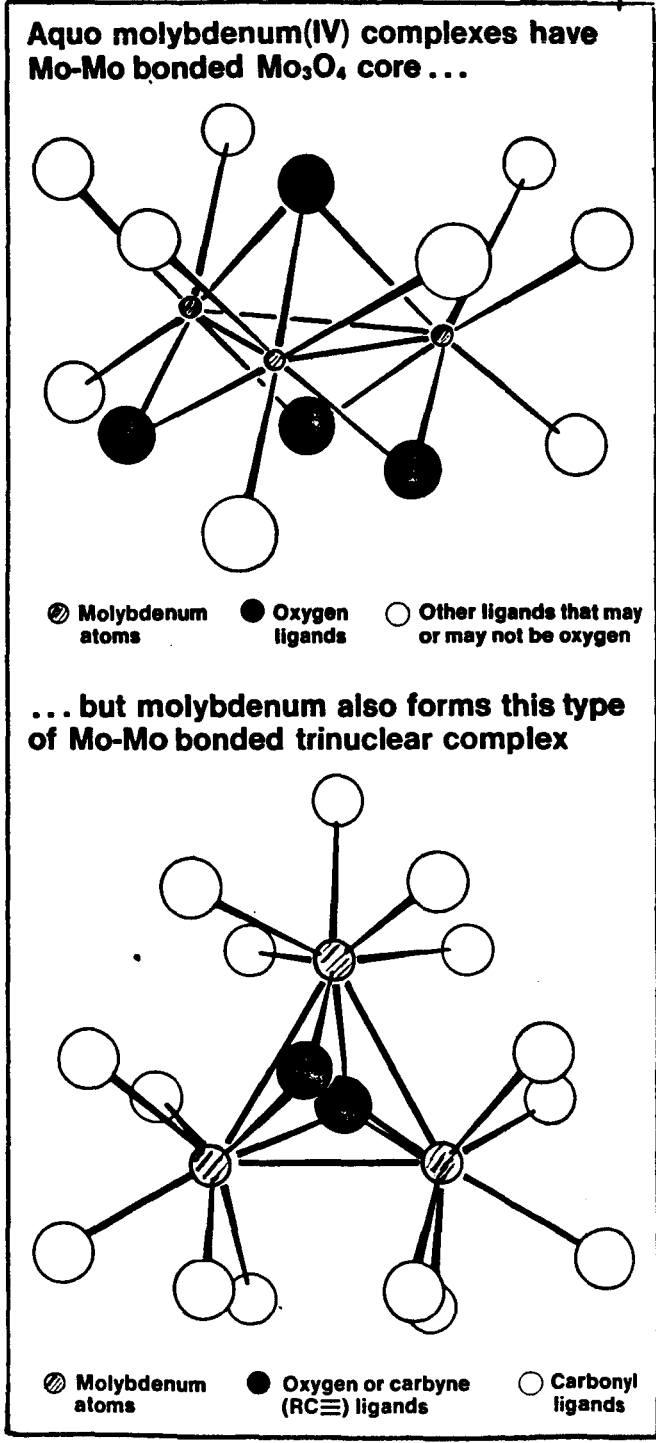
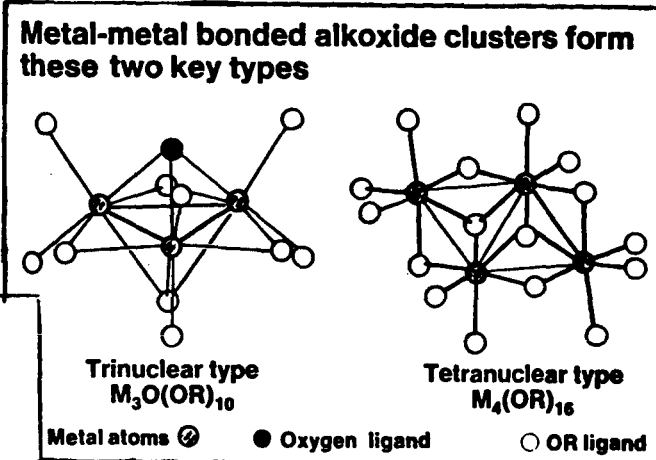
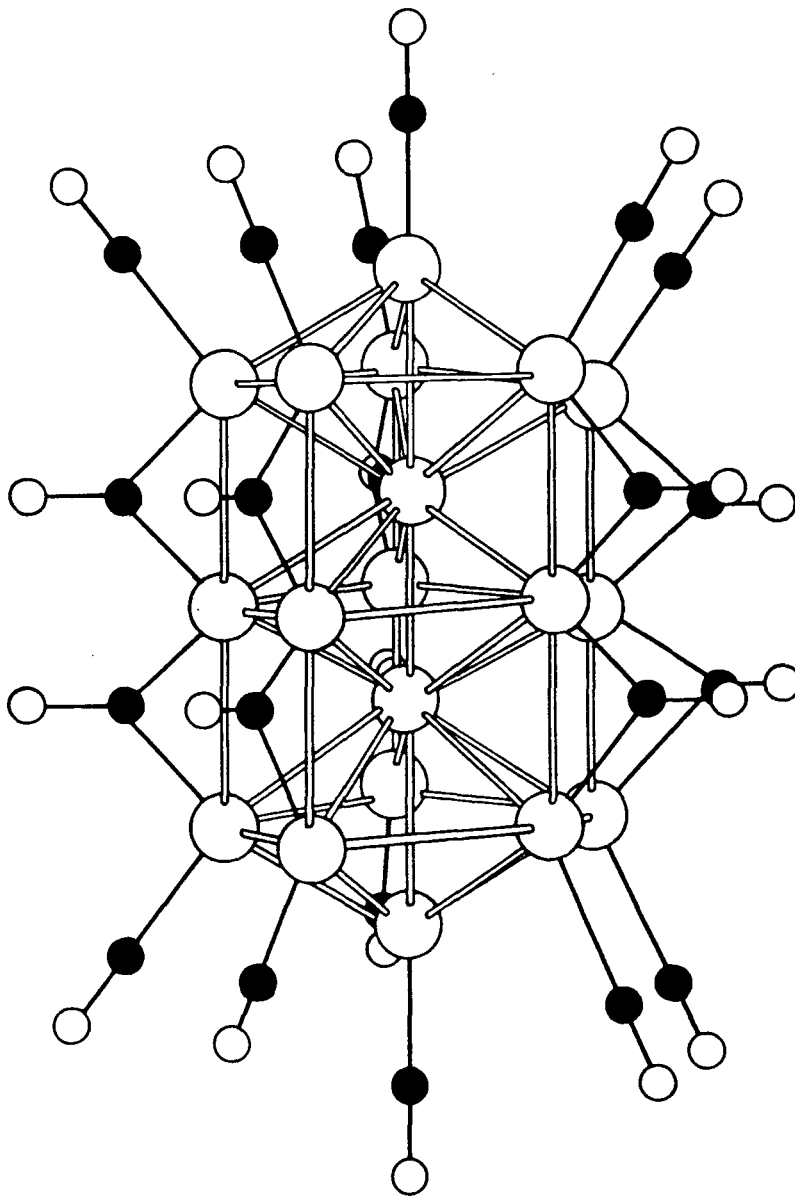


Figure 2.

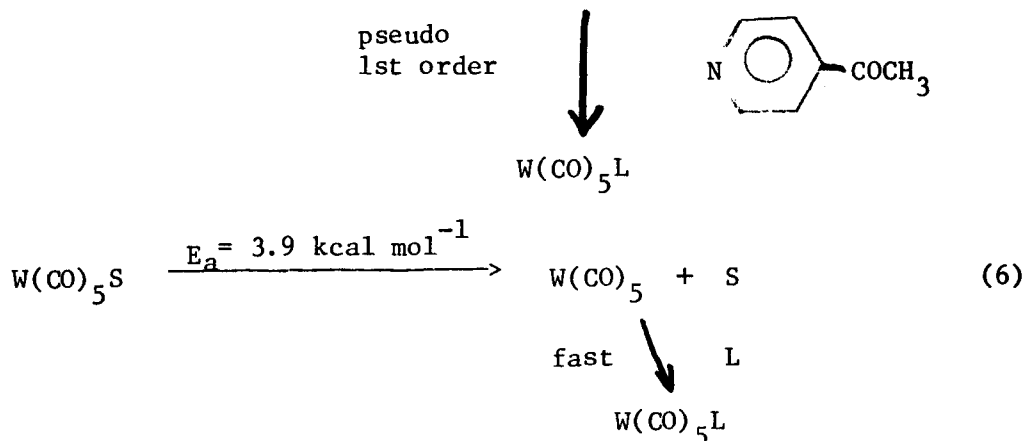
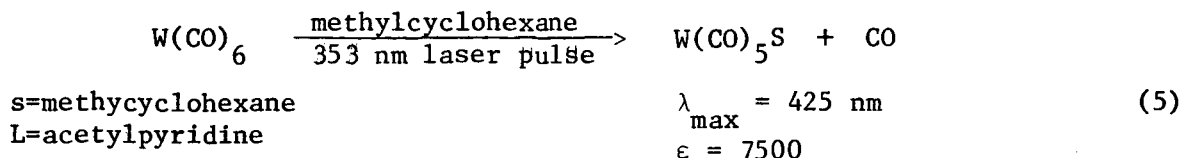
Large cluster is almost macroscopic in size



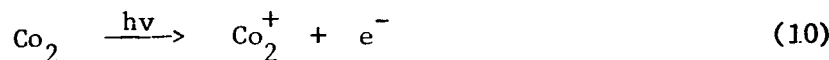
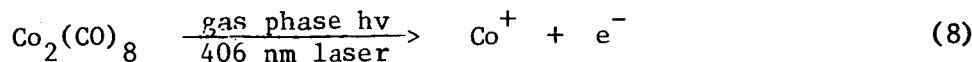
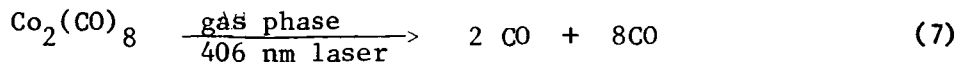
The cluster anion $[Pt_{19}(CO)_{22}]^{4-}$ with dimensions of 8 by 11 Å is one of the larger clusters, approaching very small platinum crystallites in size

isolated molecule for which studies are available. For that reason and because ir heating may cause stability problems, especially in polymer formation (see below), we concentrated our interest on photochemical techniques.

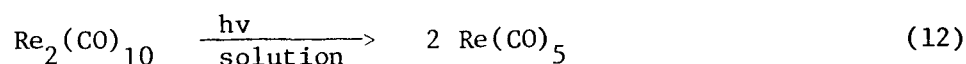
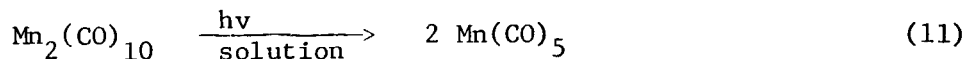
Recent studies have confirmed that loss of a single CO₂ is the first step in the photochemical decomposition of simple metal carbonyls [4-6], i.e. eq. (4). It is also observed that the first-formed coordinately unsaturated derivatives from the iron or tungsten carbonyls, and by analogy any other transition metal carbonyl, react with even the least nucleophilic solvents to form a solvent complex. The chemistry of solvated complexes were investigated by Lees and Adamson [6] in the case of the tungsten complex. A summary of their results are schematically shown in eqs. (5) and (6).



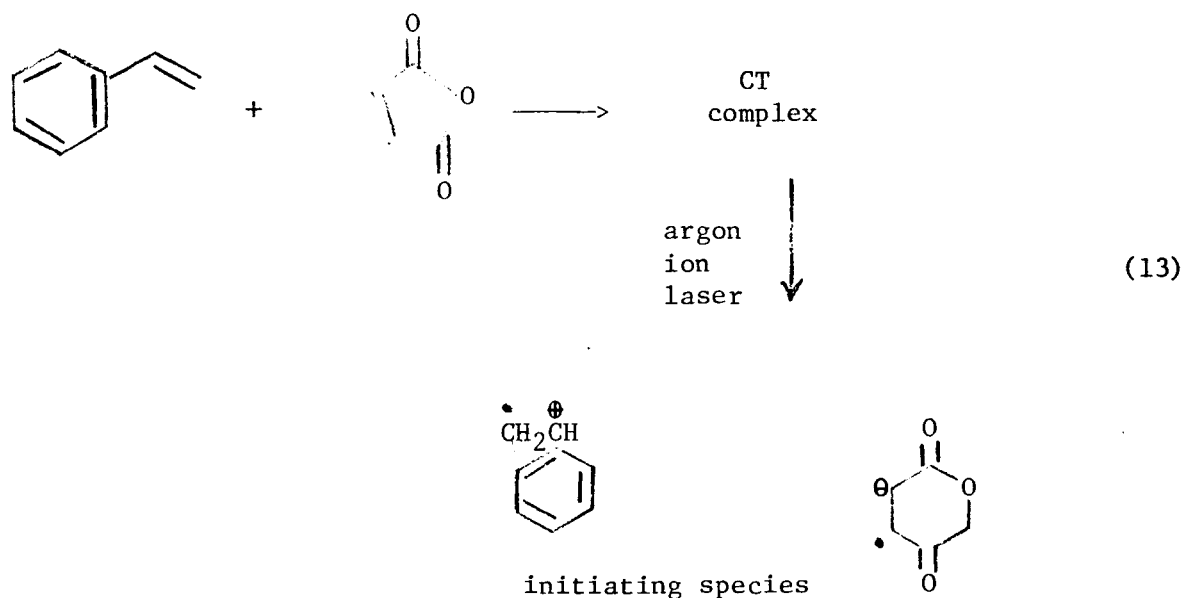
Loss of several carbonyls occurs on extended exposure to a laser source [7-9]. When a polynuclear metal carbonyl is utilized in the experiment, the result is formation of bare metal ions, eq. (7-10) [8].



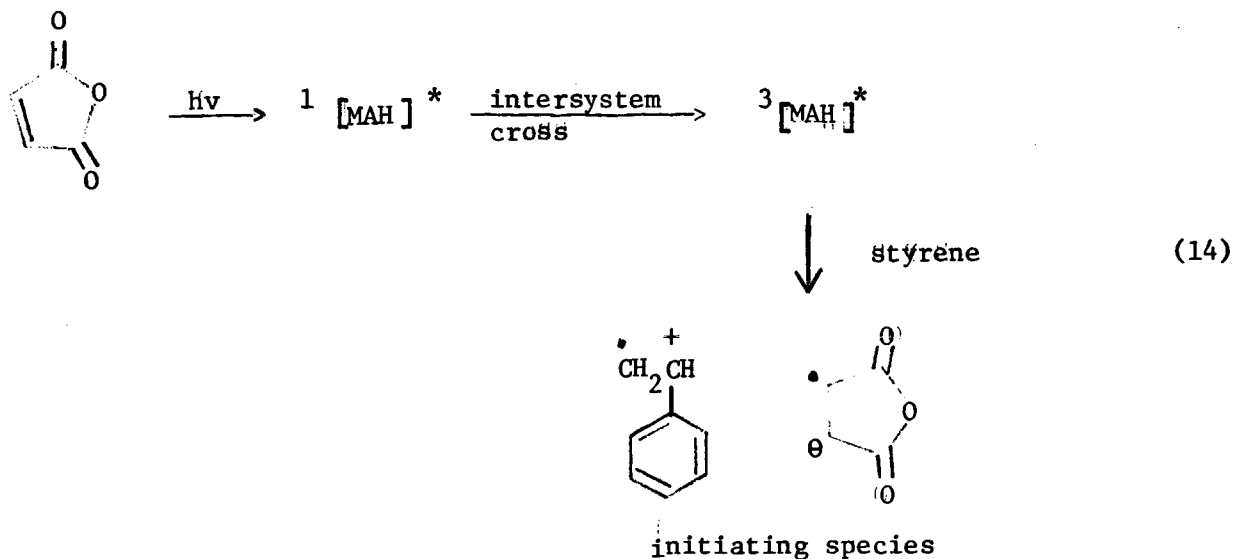
The above experiments provide the basis for suggesting future experiments to form larger bare metal ions and larger cluster molecules. However, the experiments seem to be at odds with other work which indicates that the weakest link is binuclear metal bond [10-12], i.e. eq. (11) and (12).



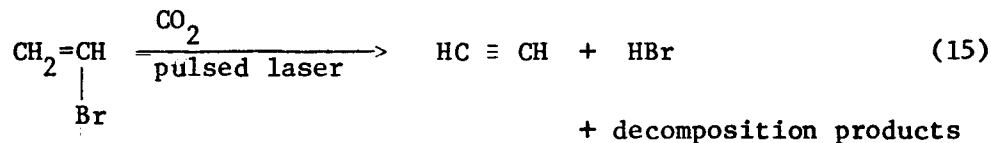
Laser Induced Polymerization. Despite the use of lasers as the energy source to facilitate a wide variety of thermal and photochemical reactions, laser-induced polymerization is rarely a topic in the literature. We have located some isolated examples of polymerization such as by laser-initiated dielectric breakdown [13]. Also, a Russian review on laser radiation in the preparation of coatings (unfortunately unavailable) [14] has been published. Another example is of a more typical photochemical process [15], the photosensitized photopolymerization of acrylamide. The only current work to which we can find literature reference is that of Castle and associates at Westinghouse Corp. [16 and 17]. They have concentrated on comonomer systems which form charge transfer complexes which may be initiated by laser irradiation. The well known maleic anhydride-styrene system is an example, eq. (13). Four experimental facts support the ion-radical mechanism: (i) a light



yellow color forms upon irradiation, (ii) polar solvents enhance polymer yield, (iii) rates are sensitive to substituents on the styrene ring with electron-donating substituents contributing to rate increases, and (iv) there is a tendency toward alternation in the copolymer [17]. Another possible mechanism which would account for the process is that shown in eq. (14). Since MAH forms a strong CT complex in ether solvents when exposed to 360 nm Ar ion laser energy, the second mechanism is favored by the experimenters.



A rather thorough search of the literature turned up no reports of gas phase polymerization using laser excitation. Our own experiments with ir laser irradiation have not been encouraging on the prospects of ir laser irradiation. Vinyl bromide which absorbs readily in the region of the CO₂ laser's maximum output and gives a high vapor pressure, is converted principally to acetylene by thermal HBr elimination [18], eq. (15). Following the lead provided by Castle et. al. seems to be a better approach.



CONCLUSION

Our study suggests that the UV laser-initiated photolysis of metal carbonyls would be an interesting process to study as a route to metal clusters. Also, polymerization using a UV laser source looks promising.

REFERENCES

1. Cotton, F. A. and Chisholm, M. H., "Bonds Between Metal Atoms. A New Mode of Transition Metal Chemistry," Chemical & Engineering News, June 28, 1982, pp. 40-50.
2. Haggin, J., "C₁ Chemistry Spurs Cluster Catalyst Work," Chemical & Engineering News, February 8, 1982, pp. 13-21.
3. Poliakoff, M. and Turner, J. J., "Infrared Laser Photochemistry in Matrixes," Elsevier Publishing Co., New York, 1979, pp. 188-196.
4. Nathanson, G., Gitlin, B., Rosan, A. M. and Yardley, J. T., J. Chem. Phys., 74, 361 (1981).
5. Yardley, J. T., Gitlin, B., Nathanson, G., and Rosan, A. M., J. Chem. Phys., 74, 370 (1981).
6. Lees, A. J. and Adamson, A. W., J. Amer. Chem. Soc., 104, 3804 (1982).
7. Lichtin, D. A., Bernstein, R. B., and Vaida, V., J. Amer. Chem. Soc., 104, 1830 (1982).
8. Vaida, V., Cooper, N. J., Hemley, R. J., and Leopold, D. G., J. Amer. Chem. Soc., 103, 7022 (1981).
9. Tumas, W., Gitlin, B., Rosan, A. M., and Yardley, J. T., J. Amer. Chem. Soc., 104, 55 (1982).
10. Wrighton, M. S. and Ginley, D. S., J. Amer. Chem. Soc., 97, 2065 (1975).
11. Freedmen, A. and Berspjn, R., J. Amer. Chem. Soc., 100, 416 (1978).
12. Meckstroth, W. K., Walters, R. T., Waltz, W. L., Wojcicki, A., and Dorfman, L. M., J. Amer. Chem. Soc., 104, 1842 (1982).
13. Chin, S. L. and Bedard, G., Phys. Lett., 36A, 271 (1971).
14. Klygina, R. V., Kozlov, L. V. and Golovanenkso, B. I., Lakokrasoch. Mater. Ikh Primen., 27-29 (1972).
15. U. S. Pat. 3,477,932, 11 Nov 69, to Monsanto Research Corp.
16. Williamson, M. A., Smith, J. D. B., and Castle, P. M., Polymer Preprints, 22 207, 1981.

17. Sadhir, R. K., Smith, J. D. B., and Castle, P. M., Polymer Preprints, 24, 291, 1982.
18. Riley, C. and McManus, S. P., unpublished results, 1982.

1982

NASA/ASEE SUMMER FACULTY RESEARCH FELLOWSHIP PROGRAM

MARSHALL SPACE FLIGHT CENTER
THE UNIVERSITY OF ALABAMA

AGEOSTROPHIC WINDS IN THE
SEVERE STORM ENVIRONMENT

Prepared By:	James T. Moore, Ph.D
Academic Rank:	Assistant Professor
University and Department:	Saint Louis University Earth and Atmospheric Sciences Department
NASA/MSFC: (Laboratory) (Division) (Branch)	Space Sciences Atmospheric Sciences Environmental Applications
MSFC Counterpart:	James E. Arnold, Ph.D
Date:	August 6, 1982
Contract No.:	NGT-01-002-099 (University of Alabama)

AGEOSTROPHIC WINDS IN THE SEVERE STORM ENVIRONMENT

by

James T. Moore, Ph.D
Assistant Professor of Meteorology
Saint Louis University
Saint Louis, Missouri

ABSTRACT

A study of the three-dimensional ageostrophic wind field is crucial towards understanding the severe storm environment. When viewed from an isentropic perspective, departures from geostrophic, mass-balanced flow can be seen to enhance vertical motions in the vicinity of a baroclinic zone, as well as assist in the release of potential instability. The Atmospheric Variability Experiment - Severe Environmental Storms and Mesoscale Experiment (AVE-SESAME) I data set, consisting of three-hourly rawinsonde data covering the south-central United States over the period 1200 GMT 10 April to 1200 GMT 11 April 1979, provides an excellent opportunity to study ageostrophic winds in the pre-storm and storm environment.

This study is centered on the period from 1200 GMT 10 April to 0000 GMT 11 April 1979, during which time several major tornadoes and severe thunderstorms, including the Wichita Falls tornado occurred. A time-adjusted, isentropic data set was used to objectively analyze key parameters onto an 18 X 15 grid mesh using a 127 km grid interval. Fourth order centered finite differences were used to compute the isallobaric, inertial advective (geostrophic form), tendency, inertial advective (total form), geostrophic and ageostrophic winds. Explicit isentropic trajectories were computed through the isentropic, inviscid equations of motion using a fifteen minute time step. Finally, ageostrophic, geostrophic and total vertical motion fields were computed to judge the relative importance of ageostrophy in enhancing the vertical motion field.

Results reveal that in response to the advance of a strong upper level jet (ULJ) entering western Texas, the inertial advective wind increases in magnitude while crossing to the anticyclonic side of the jet. In this exit region of the ULJ at lower levels, an isallobaric wind develops in eastern Texas helping to form a southerly low level jet (LLJ). The LLJ not only increased warm, moist air advection into the pre-storm environment, but also enhanced upward vertical motion along the Red River Valley by strengthening the cross-isobaric flow across the baroclinic zone, towards the cyclonic side of the ULJ.

Thus, ageostrophy is symptomatic of those mass adjustments which take place during ULJ streak propagation and can, in a favorable environment, act to increase and release potential instability over meso alpha time periods.

ACKNOWLEDGEMENTS

The author would like to thank Dr. Jim Arnold, his NASA counterpart, who offered encouragement, new ideas, and friendship. Mr. Gary Jedlovec assisted in helping the author use the HP-1000 mini-computer and data management. Mr. Paul Meyer also was instrumental in graphics software and fortran program development. Finally, the author is appreciative of Dr. Barfield's efforts on behalf of the NASA-ASEE program in making this summer so worthwhile.

I. INTRODUCTION

As House (1963) has noted, the prediction of severe convective storms centers around those atmospheric processes which control the trend of hydrostatic stability. Thus, a successful prediction scheme must be able to detect the stability trend as well as be able to detect or predict those mechanisms that will release the instability locally. Although unstable regions may cover large volumes of the fluid, convective activity is usually limited in space-time to those regions undergoing low level convergence and/or upper level divergence. This is especially true in those cases of organized severe storms attendant with a spring-time baroclinic wave disturbance.

A study of the three-dimensional ageostrophic wind field and its components is crucial to understanding how low level convergence/upper level divergence is generated in the severe storm environment. When viewed from an isentropic perspective, ageostrophic wind components cause air parcels to cross energy gradients (Montgomery stream function values), which, in the vicinity of a baroclinic zone can cause parcels to descend or ascend adiabatically. In addition, the resulting ageostrophic convergence (divergence) within an atmospheric layer bounded by two isentropic layers will cause the layer to destabilize (stabilize) with time. Importantly, since isentropic surfaces are material surfaces for "dry" air parcels, it is possible to construct trajectories depicting air parcels responding to ageostrophic forcing.

Data available from the Atmospheric Variability Experiment - Severe Environmental Storms and Mesoscale Experiment (AVE-SESAME) I offers a unique opportunity to study ageostrophic motion in the pre-storm and storm environment. This data set consists of three-hourly rawinsonde data, covering the south-central United States over the period 1200 GMT 10 April to 1200 GMT 11 April, 1979. AVE-SESAME I coincided with the formation of two major areas of severe convection. Figure 1 shows locations of these storms and reporting stations in the region. The first area occurred between approximately 1800 and 0200 GMT in the Red River Valley region of Texas and Oklahoma and includes the major Wichita Falls (SPS) tornado. The second area formed later in the day in southwestern Texas near San Angelo (SJT). Moore and Fuelberg (1981) have discussed most of the major synoptic features attending this outbreak.

In the next section, the objectives of this study will be stated. Section Three will set forth the theoretical basis of this study and present some background research. Section Four will then explore ageostrophic wind components for AVE-SESAME I and their role in the severe storm environment. In addition, isentropic vertical

motions and parcel trajectories will be shown to help tie together ageostrophy and vertical motion. Conclusions and some recommendations for future research are presented in Section Five.

2. OBJECTIVES

The major objectives of this study include the following:

- (1) to study ageostrophic wind components in the vicinity of an upper level jet (ULJ) streak as it propagates into the storm region,
- (2) to examine the role of each ageostrophic wind component in organizing a low level jet (LLJ),
- (3) to compare the approximate forms of the ageostrophic wind components to their total forms, and,
- (4) to compute isentropic vertical motions due to geostrophic and ageostrophic flow in order to judge the impact of ageostrophy on vertical motions.

Although conclusions will be limited to the AVE-SESAME I case, this storm scenario is typical of a spring-time, Midwest, severe storm outbreak. Thus, important aspects of ageostrophic flow can still be gleaned from this study.

3. BACKGROUND

The basic equations needed to compute ageostrophic wind components have been detailed by Keyser and Johnson (1982) and appear in Table I. Note that equations (4)-(6) are based upon the geostrophic momentum approximation, i.e.,

$$\left| \frac{d\vec{V}_{ageo}}{dt} \right| \ll \left| \frac{d\vec{V}_{geo}}{dt} \right| \quad (7)$$

and the geostrophic relationship,

$$\vec{V}_{geo} = f^{-1} \hat{k} \times \nabla_{\theta} \Psi \quad (8)$$

Thus, the isallobaric wind, (5), is an approximation of the local wind tendency, (2) and (6) is an approximation of the total inertial advective wind, (3).

TABLE I

EXPRESSIONS FOR COMPONENTS OF FRICTIONLESS ADIABATIC,
AGEOSTROPHIC MOTION IN ISENTROPIC COORDINATES

A. Total Form

$$\vec{V}_{ageo} = f^{-1} \hat{K} \times \left[\underset{A}{\frac{\partial}{\partial t_{\theta}}} + \underset{B}{\vec{V}_{\theta} \cdot \nabla_{\theta}} \right] \vec{V}_{\theta} \quad (1)$$

Term A - Local wind tendency component

$$\vec{V}_{ageo_A} = f^{-1} \hat{K} \times \frac{\partial \vec{V}_{\theta}}{\partial t} \quad (2)$$

Term B - Inertial advective component

$$\vec{V}_{ageo_B} = f^{-1} \hat{K} \times (\vec{V}_{\theta} \cdot \nabla_{\theta}) \vec{V}_{\theta} \quad (3)$$

B. Semi-geostrophic Form

$$\vec{V}_{ageo} = f^{-1} \hat{K} \times \left[\underset{A}{\frac{\partial}{\partial t_{\theta}}} + \underset{B}{\vec{V}_{\theta} \cdot \nabla_{\theta}} \right] \vec{V}_{geo} \quad (4)$$

Term A - Isallobaric wind component

$$\vec{V}_{ageo_A} = f^{-1} \hat{K} \times \frac{\partial \vec{V}_{geo}}{\partial t} = f^{-2} \nabla_{\theta} \frac{\partial \psi}{\partial t} \quad (5)$$

Term B - Inertial advective component

$$\vec{V}_{ageo_B} = f^{-1} \hat{K} \times (\vec{V}_{\theta} \cdot \nabla_{\theta}) \vec{V}_{geo} \quad (6)$$

. A physical interpretation of these ageostrophic wind components is important in evaluating their effects on the mesoscale environment. The isallobaric wind is entirely due to changes in the mass field, measured in isentropic coordinates by ψ , the Montgomery stream function. The isallobaric wind is directly proportional to and directed along the isallobaric descendent vector. Thus, it is an irrotational, ageostrophic wind that is directed towards (away from) ψ falls (rises), as it responds to mass divergence/convergence within the fluid. Saucier (1955) notes that the validity of the isallobaric wind measured from a mass change field is dependent on how well the field of integrated change during the period indicates the field of instantaneous tendency. In general, the longer the time interval for mass change, the greater the discrepancy between indicated and true isallobaric wind fields.

The inertial advective wind in its approximate form (6), is a measure of the effect of horizontal variations in the mass field on accelerations. Thus, an air parcel encountering a weaker (diffluent) mass field will be deflected to the right of the flow and decelerate, while an air parcel moving into a stronger (confluent) mass field will be deflected to the left of the flow and accelerate. Saucier (1955) shows that when this ageostrophic wind lies along the actual wind, the acceleration is centripetal and the motion is parallel to the mass-balanced field. Thus, neglecting (3) is the same as neglecting the gradient wind correction.

Uccellini and Johnson (1979) have shown that terms A and B shown in equations (5) and (6), play important roles in coupling ULJ streaks with LLJ streaks in the exit region of the ULJ. They found the inertial advective component to be the major component of the ageostrophic wind at upper levels while in lower levels the LLJ develops primarily in response to isallobaric forcing. Arnold (1982) has shown that in the AVE-SESAME I case, the ratio of the isallobaric term to the inertial advective term increased, for lower tropospheric layers, as short wave troughs translated through the area. Kocin, et al. (1982), looking at the same case, found evidence supporting Uccellini and Johnson's (1979) thermally indirect circulation enacted by ageostrophic winds in the exit region of the jet. The formation of the LLJ is very important in the mesoscale environment leading to a major severe storm outbreak. The LLJ acts to increase low level moist, warm air advection, since it is usually dominated by southerly momentum. This enhances the potential instability in the pre-storm environment. Secondly, low level convergence is increased over meso α space-time scales, usually to the north and northwest of the LLJ. This acts to localize the area over which the potential instability will be released.

4. AGEOSTROPHIC FLOW AND VERTICAL MOTION ACCOMPANYING THE RED RIVER VALLEY TORNADO OUTBREAK

In this section, the specific role of the various components of the ageostrophic wind will be examined in terms of their contributions to LLJ development and the increase of upward vertical motion in the severe storm environment.

4.1. DATA HANDLING AND COMPUTATIONAL PROCEDURES

Input rawinsonde data from AVE-SESAME I were adjusted to a common release time by performing linear time interpolation as done by Jedlovec (1981). As part of the process, missing data were interpolated in time from available soundings if the time interval was 6 h or less; otherwise, the sounding remained missing. This constant pressure coordinate data set was then transformed to an isentropic data set through a program devised by Duguet (1964). All variables except the wind, are interpolated to isentropic surfaces assuming linearity with respect to P_k . Winds are linearly interpolated with respect to height; direction and speed are interpolated separately. This program yields data in 2 K increments of potential temperature and includes all the necessary parameters for diagnostic isentropic analysis.

Objective analyses of u , v wind components, mixing ratio (q), pressure (P), and Montgomery stream function (ψ) were done through a Barnes (1964) objective analysis scheme. The data is interpolated onto a 18×15 , 127 km grid on a polar stereographic map projection. It is imperative to have a good objective analysis of ψ and P in order to have reasonable ageostrophic wind calculations and isentropic omega fields, respectively. In the case of ψ , a scheme discussed by Inman (1970) was used in which the gradient of ψ surrounding each station is computed, using the geostrophic gradient from the observed wind, and introduced into the error term. In a similar fashion, for P , the pressure gradient surrounding each station is computed using the thermal wind gradient from the observed vertical wind shear and introduced into the error term. Experience with these modified Barnes objective analysis schemes indicates an improvement in resolving the jet core (for ψ) and its associated baroclinic zone (for P).

Calculations of geostrophic and ageostrophic wind components were done using fourth order centered finite differences.* Explicit isentropic trajectories were computed using a technique developed by Petersen and Uccellini (1979). It should be noted that these trajectories were over three hours and were computed using a 15 minute time step. This three hour period is commensurate with

*All calculations based upon these winds, however, were done using second order, centered finite differences.

the temporal period used for time tendency calculations needed for some of the ageostrophic wind components. Typical parcel errors, obtained through a comparison with the ambient, observed wind velocity at the parcel's endpoints, were $\pm 5 \text{ m s}^{-1}$ and ± 10 degrees for speed and direction, respectively.

4.2. UPPER LEVEL AGEOSTROPHIC WINDS

In this section and those following, the period 1800 GMT - 0000 GMT, 10-11 April 1979 will be emphasized since most of the exciting dynamics took place over that time interval. The 324 K isentropic surface slopes from approximately 250 mb over Colorado to 400 mb over the Gulf Coast and, therefore, was chosen as a representative upper level. All maps are representative of three hour averages, unless stated otherwise.

Figure 2a shows the average wind flow from 1800 - 2100 GMT 10 April, where the length of a wind arrow is proportional to the wind speed in m s^{-1} . This pattern reveals an exiting short wave around Missouri and an entering short wave in western Texas accompanied by strong westerly momentum. The ageostrophic wind (not shown) at this time, is northeasterly over western Texas and Oklahoma with speeds of over 25 m s^{-1} , indicating subgeostrophic flow over the area.

The "total" inertial advective wind (displayed with its divergence field) shown in Fig. 2b, is generally strong and from the north-northeast over most of western Texas. The divergence field reveals that the inertial advective wind acts to enhance ageostrophic mass convergence (divergence) on the anticyclonic (cyclonic) side of the jet axis. The tendency wind field, shown in Fig. 2c, also contributes to convergence over most of Texas. Magnitudes of the tendency wind tend to be smaller, in upper levels, than the inertial advective wind.

Figure 3a, which displays the average wind field for 2100-0000 GMT, 10-11 April 1979, shows winds of over 50 m s^{-1} entering western Texas upstream of a short wave trough located over the Red River Valley. The exit region of the latter jet streak is characterized by strong inertial advective winds from the north with speeds of up to 50 m s^{-1} (Fig 3b). The remainder of the inertial advective wind field is far less organized than that near the exit region of the ULJ streak. The ageostrophic divergence/convergence couplet associated with the exit region of the ULJ has increased since the last time period. Importantly, this feature has excellent continuity in space-time, as well, ensuring its association with the ULJ. The tendency wind field and its associated

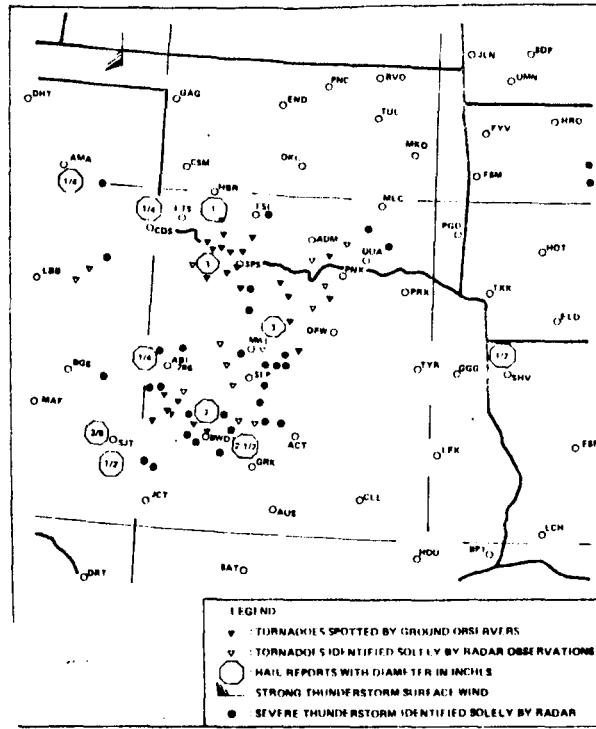


Figure 1. Severe weather reports that occurred during the 24 h period between 1200 GMT on 10 April and 1200 GMT on 11 April 1979 in the south-central United States (after Hill, et al., 1979)

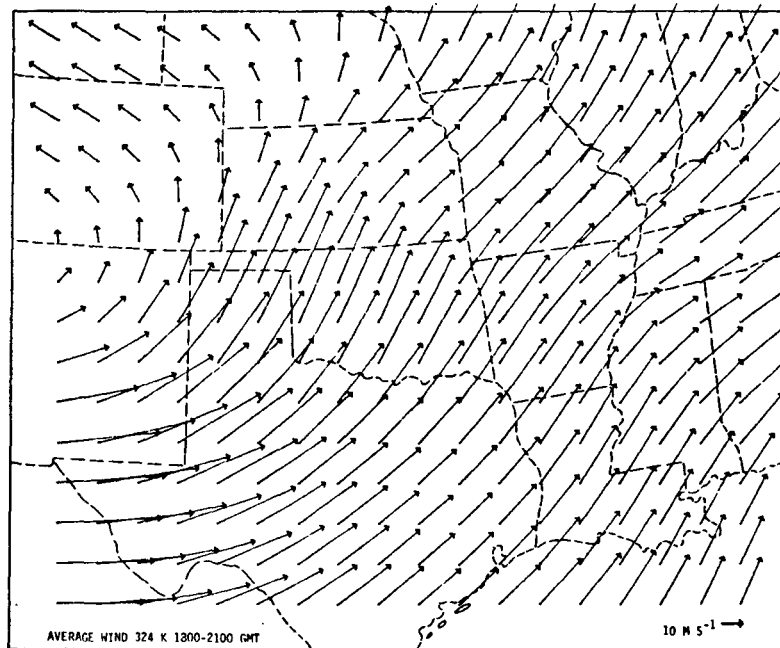


Figure 2a. Average wind from 1800-2100 GMT 10 April 1979 on the 324 K isentropic surface.

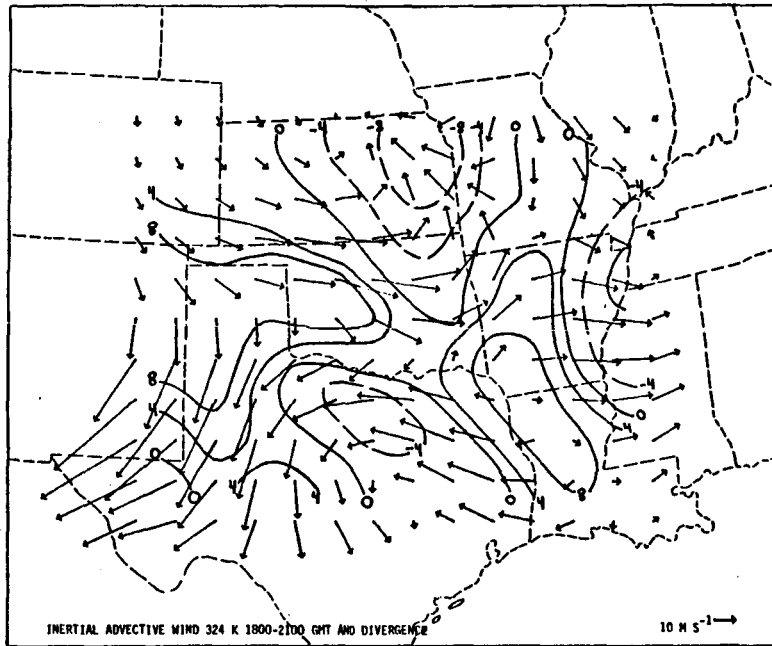


Figure 2b. Inertial advective wind averaged from 1800-2100 GMT 10 April 1979 on the 324 K isentropic surface. Divergence values are $\times 10^{-5}$ second⁻¹.

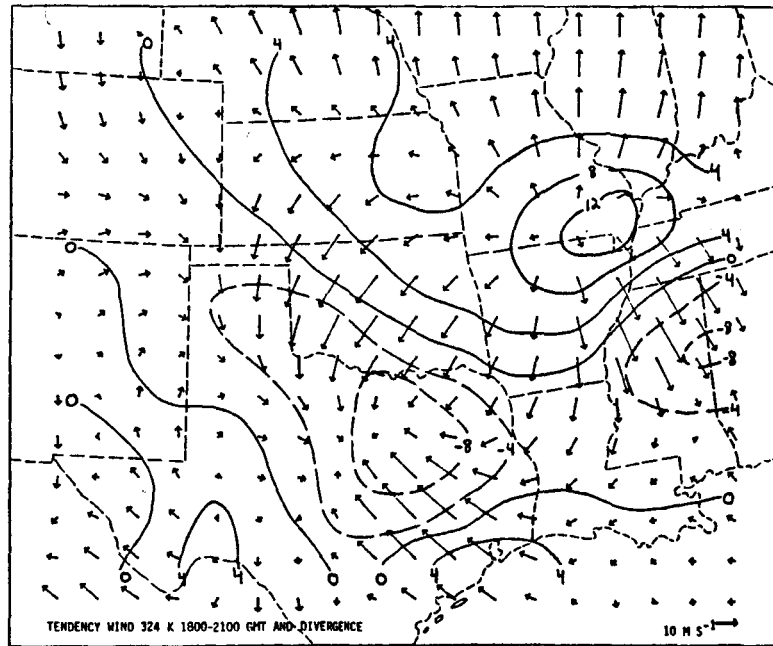


Figure 2c. Tendency wind averaged from 1800-2100 GMT 10 April 1979 on the 324 K isentropic surface. Divergence values are $\times 10^{-5}$ second⁻¹.

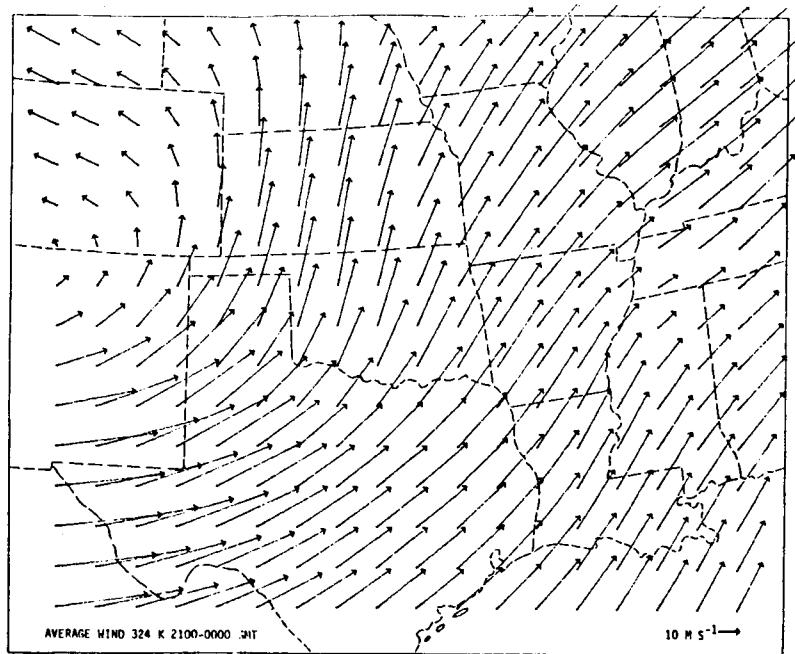


Figure 3a. Average wind from 2100-0000 GMT 10-11 April 1979 on the 324 K isentropic surface.

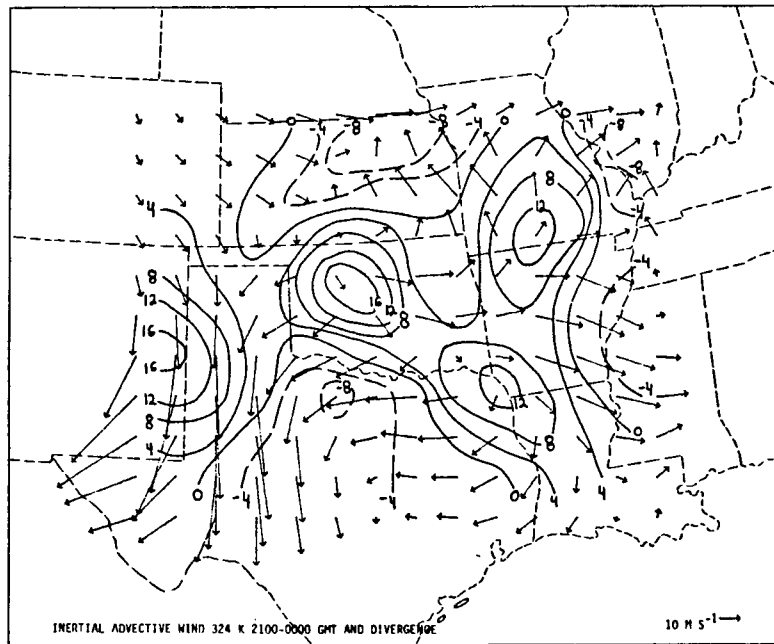


Figure 3b. Inertial advective wind averaged from 2100-0000 GMT 10-11 April 1979 on the 324 K isentropic surface. Divergence values are $\times 10^{-5}$ second⁻¹.

divergence are displayed in Fig. 3c. Continuity with the previous time period's flow is poor, and wind speeds are relatively weak compared to the inertial advective wind. However, it is interesting to note that the tendency wind divergence field, although weaker, is similar to that shown in Fig 3b for the inertial advective field.

4.3. LOW LEVEL AGEOSTROPHIC WINDS

The 304 K isentropic surface was chosen as being representative of low level flow. It intersects the ground, by 1800 GMT, over western Texas and southeastern New Mexico. In other areas, it slopes from about 640 mb over Kansas to near 900 mb along the Gulf Coast.

Figures 4 a-b, taken from Moore and Squires (1982), show the Montgomery stream function and isotach field on the 304 K surface for 1800 GMT and 2100 GMT, respectively. The main feature to note is the development of a 20 m s^{-1} wind maximum in eastern Texas. This wind maximum, composed of primarily southerly momentum developed over only 3 hours! By 0000 GMT (not shown) this incipient LLJ expands and moves into eastern Oklahoma while reaching speeds of over 25 m s^{-1} . What forces may have contributed to this development?

The low level response to the ageostrophic mass convergence/divergence in the exit region of the jet is best illustrated by the isallobaric wind. Uccellini and Johnson (1979) have shown that the isallobaric wind on an isentropic surface is directly proportional to the pressure tendency on that surface as well as the integrated pressure tendency above it. Thus, the isallobaric wind is responsive to net mass divergence/convergence in the column. Secondly, the tendency wind in lower levels can be dramatically affected by sub-grid scale phenomena such as friction, diabatic effects and turbulent mixing. Thus, it tends to be less continuous in space-time than the isallobaric wind.

Figure 4c depicts the isallobaric wind over the period 1800 - 2100 GMT 10 April. Strong, southerly isallobaric flow converges along and north of the Red River Valley. The isallobaric winds shown in Fig. 4c are stronger than the inertial advective winds, in general, at this level. Thus, the isallobaric wind formed underneath the ULJ exit region and was directed towards the cyclonic side of the ULJ. Its presence helps explain the increase in speed of the LLJ and the localized convergence which formed in the Texas Panhandle leading to the development of severe convection. During the next three hours, this isallobaric convergence center moves into northwestern Oklahoma while the southerly ageostrophy decreases due to diminished psi falls to the north.

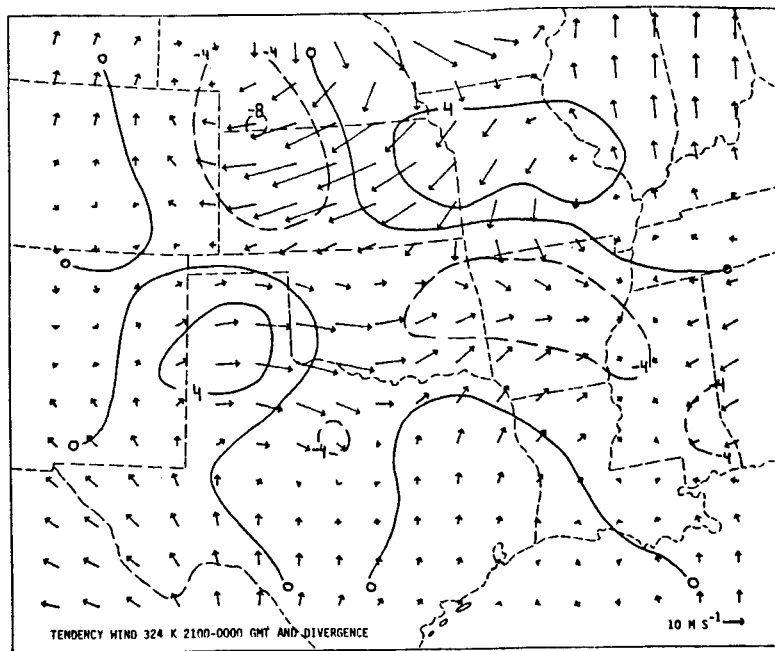
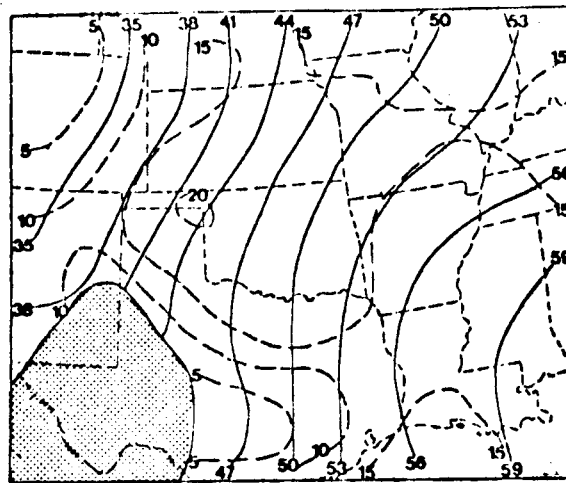
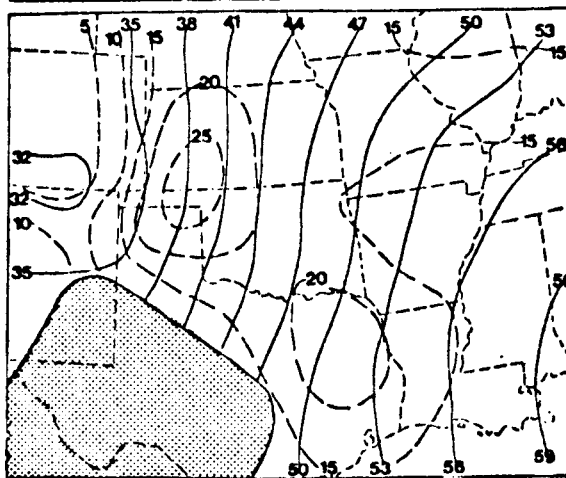


Figure 3c. Tendency wind averaged from 2100-0000 GMT 10-11 April 1979, on the 324 K isentropic surface. Divergence values are $\times 10^{-5}$ second $^{-1}$.



(A)



(B)

Figures 4a-b. Isotachs (m s^{-1}), dashed lines, and Montgomery stream function ($\times 10^6$ ergs gm^{-1} where the preceding 30 has been omitted) for the 304 K isentropic surface at 1800 GMT and 2100 GMT, 10 April 1979, respectively. Stippling indicates 304 K surface is in ground.

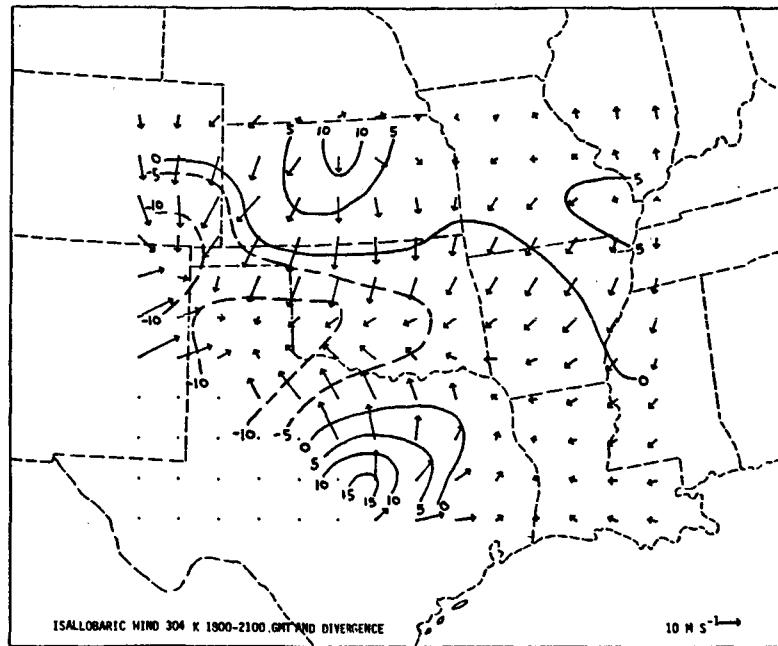


Figure 4c. Isallobaric wind for 1800-2100 GMT 10 April 1979 on the 304 isentropic surface. Divergence values are $\times 10^{-5}$ second⁻¹.

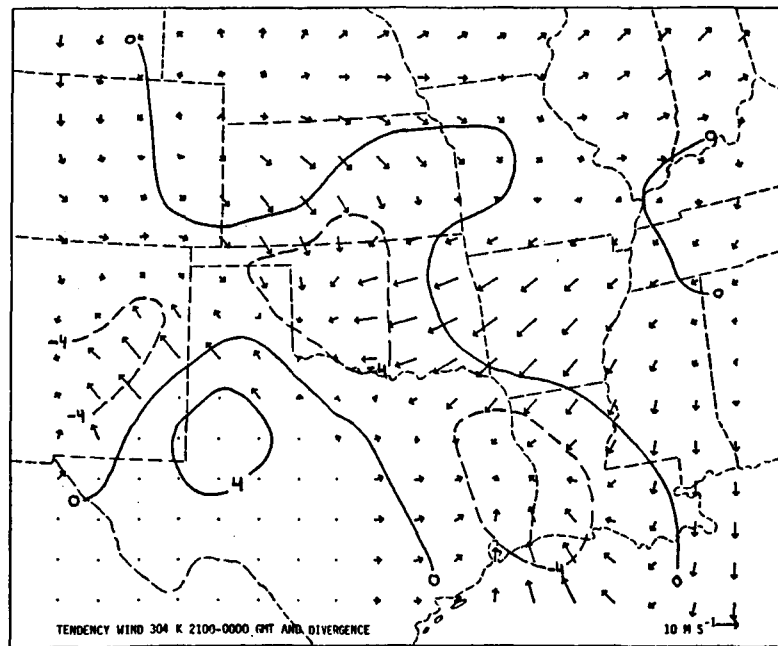


Figure 4d. Tendency wind averaged from 2100-0000 GMT 10-11 April 1979 on the 304 isentropic surface. Divergence values are $\times 10^{-5}$ second⁻¹.

Interestingly, at this time period (2100 - 0000 GMT 10 April) the tendency wind and its divergence field (Fig. 4d) agree more closely with the isallobaric wind and its associated divergence (not shown). It would seem that strong isallobaric forcing in low levels demands a response in the u, v local wind fields with the result that the isallobaric and tendency winds more nearly agree (notwithstanding friction, turbulent mixing and diabatic effects).

4.4. VERTICAL MOTIONS AND AGEOSTROPHY

Vertical motions with respect to an isentropic surface can be expressed as:

$$\omega = \frac{dP}{dt_\theta} = \frac{\partial P}{\partial t_\theta} + \vec{\nabla}_\theta \cdot \nabla_\theta P + \frac{d\theta}{dt} \frac{\partial P}{\partial \theta} \quad (9)$$

If one neglects the diabatic term, then one is measuring the vertical motion for parcels constrained to an isentropic surface. This expression was computed for the 312 K surface over the period 2100 - 0000 GMT, 10-11 April 1979. Average winds and pressures were used and local pressure tendencies were computed for the three hour period.

Figure 5a shows the omega (vertical motion) field on the 312 K surface during said time period, in microbars second⁻¹. A moderately strong center of less than -7 microbars second⁻¹ is centered near the Red River Valley with axes to the northeast and southeast. To see how much of this vertical motion could be attributed to ageostrophic flow, omega values were recomputed using geostrophic winds; these values were then subtracted from the original vertical motion fields. The resultant ageostrophic omega field is shown in Fig. 5b. It depicts a -3 microbars second⁻¹ center in nearly the same area as shown in Fig. 5a. Thus, one can see that ageostrophic flow contributes up to ~ 40% of the upward vertical motion to the severe storm environment. This, of course, neglects the influence of topography, diabatic heating/cooling and friction.

Finally, Fig 5c displays isobars on the 312 K isentropic surface and selected 3 h trajectories for the period 2100 - 0000 GMT 10-11 April 1979. Although even geostrophic flow can cross isobars on an isentropic surface, it is argued here that the ageostrophic component of the real wind enhanced the cross-isobaric flow on lower and middle isentropic surfaces. This enhanced moisture advection to the north and increased the resultant upward vertical motion due to the tight baroclinic zone in the vicinity.

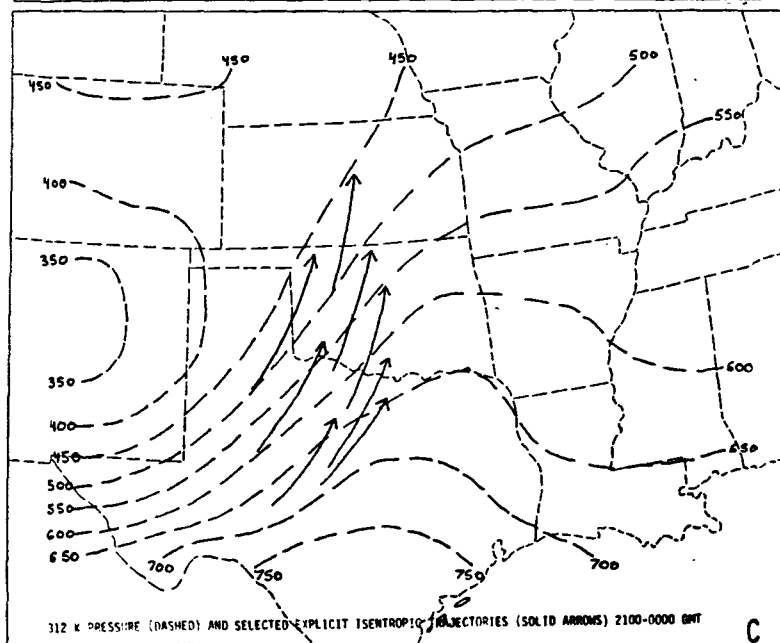
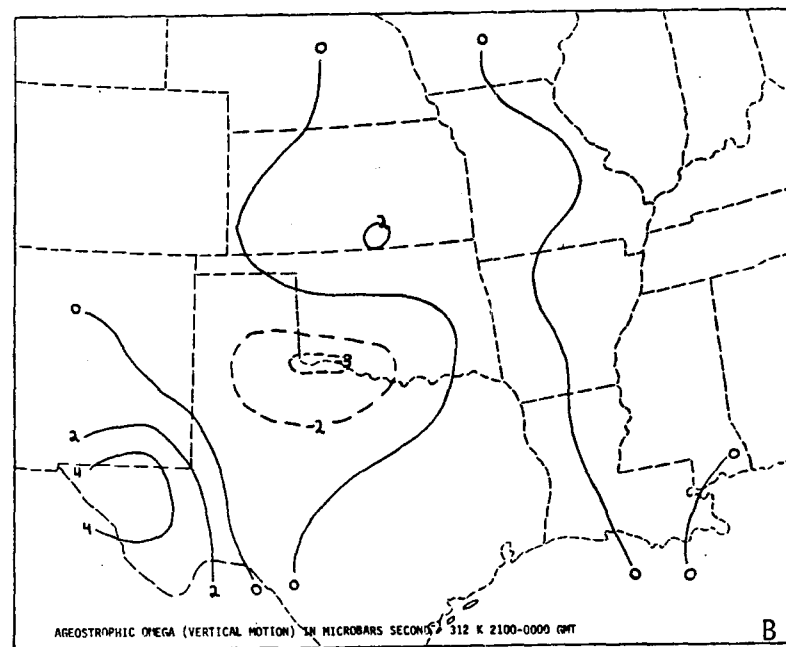
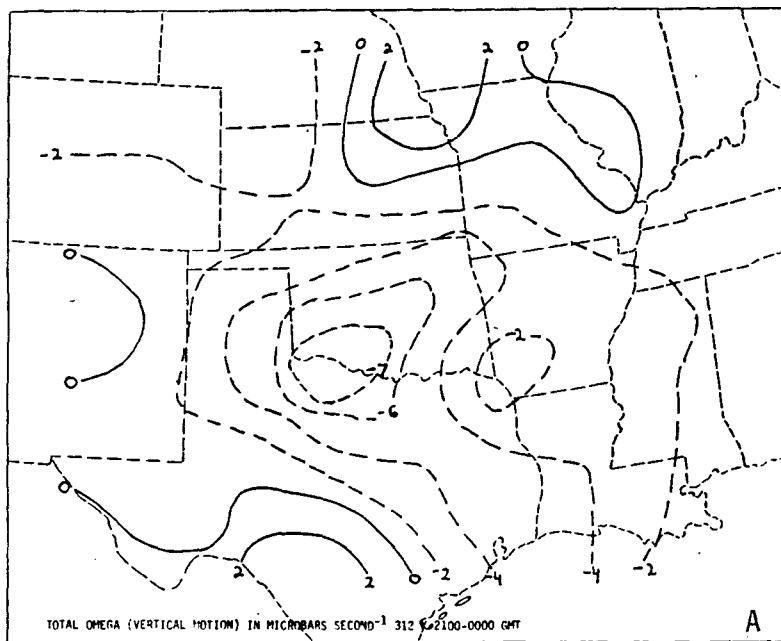


Figure 5a. (upper left-hand corner). Total vertical motion field (microbars second⁻¹) for 2100-0000 GMT 10-11 April 1979 on the 312 K isentropic surface.

Figure 5b. (upper right-hand corner). Ageostrophic vertical motion field (microbars second⁻¹) for 2100-0000 GMT 10-11 April 1979 on the 312 K isentropic surface.

Figure 5c. (bottom left-hand corner). Average pressure (millibars) for 2100-0000 GMT 10-11 April 1979 on the 312 K isentropic surface. Selected explicit isentropic trajectories for the same period are also shown.

5. CONCLUSIONS AND RECOMMENDATIONS

These results lead to the following conclusions:

- (1) the inertial advective wind tends to dominate the tendency wind at upper levels and displays better continuity in time,
- (2) the inertial advective wind in the exit region of the ULJ acts to transport mass to the anticyclonic side of the jet axis,
- (3) in lower levels, the isallobaric wind is a good indicator of mass adjustment processes aloft and displays better continuity than the tendency wind,
- (4) the LLJ appears to have been increased in magnitude as a response to primarily isallobaric forcing,
- (5) the inertial advective wind in low levels at best plays a minor role in the mass adjustment process,
- (6) low level ageostrophy helped to increase upward vertical motion over the Red River Valley, thereby enhancing the initiation and sustenance of severe convection, and
- (7) the approximate forms of the ageostrophic wind components compare favorably to their "total" counterparts in some areas, some times, however, there are significant discrepancies many times. This area warrants further investigation.

This author's recommendations for future research include:

- (1) testing the above concepts on several other AVE-SESAME cases,
- (2) further resolving those mass-momentum structures and synoptic settings under which the approximate forms of the ageostrophic wind components are reasonably close to the total form, and,
- (3) perturbing u , v , and ψ fields with a random number generator, using typical errors from rawinsondes as standard deviations, and rerunning all ageostrophic winds to test for sensitivity (an error analysis).

REFERENCES

- Arnold, J. E., 1982: Characteristics of Ageostrophic Flow in the Vicinity of a Severe Weather Outbreak - AVE-SESAME I. Preprints, Twelfth Conference on Severe Local Storms, San Antonio, TX, pp 205-208.
- Barnes, S. L., 1964: A Technique for Maximizing Details in Numerical Weather Map Analysis. J. Appl. Meteor., vol. 3, pp. 396-409.
- Duguet, R. T., 1964: Data Processing for Isentropic Analyses. Technical Report No. 1, Contract AT (30-1)-3317, The Pennsylvania State University, 36 pp.
- Hill, K., G. Wilson, and R. Turner, 1979: NASA's Participation in the AVE-SESAME '79 Program. Bull. Amer. Meteor. Soc., vol. 60, pp. 1323-1329.
- Inman, R. L., 1970: Papers on Operational Objective Analysis Schemes at the National Severe Storms Forecast Center. NOAA Tech. Memo. ERLTM-NSSL 51, 91 pp.
- Jedlovec, G. J., 1981: A Subsynoptic-Scale Kinetic Energy Study of the Red River Valley Tornado Outbreak (AVE-SESAME I). M. S. Thesis, St. Louis University, 109 pp.
- Keyser, D., A. and D. R. Johnson, 1982: Effects of Diabatic Heating on the Ageostrophic Circulation of an Upper Tropospheric Jet Streak. NASA Contractor Report 3497, NAS8-33222, 122 pp.
- Kocin, P. J., L. W. Uccellini and R. A. Petersen, 1982: The Role of Jet Streak "Coupling" in the Development of the 10-11 April 1979 Wichita Falls Tornado Outbreak. Preprints, Twelfth Conference on Severe Local Storms, San Antonio, TX, pp. 560-563.
- Moore, J. T. and H. E. Fuelberg, 1981: A Synoptic Analysis of the First AVE-SESAME '79 Period. Bull. Amer. Meteor. Soc., vol. 62, pp 1577-1590.
- _____ and M. F. Squires, 1982: Ageostrophic Winds and Vertical Motion Fields Accompanying Upper Level Jet Streak Propagation During the Red River Valley Tornado Outbreak. Preprints, Ninth Conference on Weather Forecasting and Analysis, Seattle, WA, pp. 424-429.

- Petersen, R. A. and L. W. Uccellini, 1979: The Computation of Isentropic Atmospheric Trajectories Using a Discrete Model Formulation. Mon. Wea. Rev., vol. 107, pp. 566-574.
- Saucier, W. J., 1955: Principles of Meteorological Analysis. The University of Chicago Press, Chicago, IL, pp. 240-247.
- Uccellini, L. W. and D. R. Johnson, 1979: The Coupling of Upper and Lower Tropospheric Jet Streaks and Implications for the Development of Severe Convective Storms. Mon. Wea. Rev., vol. 107, pp. 682-703.

NASA/ASEE SUMMER FACULTY RESEARCH FELLOWSHIP PROGRAM

MARSHALL SPACE FLIGHT CENTER
THE UNIVERSITY OF ALABAMA

FABRICATION TECHNIQUES FOR SUPERCONDUCTING READOUT LOOPS

Prepared By: James E. Payne, Ph.D.
Academic Rank: Associate Professor of Physics
University and Department: South Carolina State College
Department of Natural Sciences
NASA/MSFC:
Laboratory: Space Science
Division: Space Physics
Branch: Cryogenic Physics
MSFC Counterpart: Palmer N. Peters
Date: August 6, 1982
Contract No.: NGT 01-002-099
The University of Alabama

FABRICATION TECHNIQUES FOR SUPERCONDUCTING READOUT LOOPS

by

James E. Payne
Associate Professor of Physics
South Carolina State College
Orangeburg, South Carolina

ABSTRACT

The objective of this research project is to develop procedures for the fabrication of superconducting readout loops out of niobium on glass substrates. It is proposed that readout loops fabricated according to current design parameters will be used in the Gravity Probe-B (GP-B) Experiment. A computer program for an existing fabrication system was developed. Both positive and negative resist procedures were investigated for the production of the readout loops. A description of methods used to produce satisfactory loops is given as well as an analysis of the various parameters affecting the performance of the loops.

ACKNOWLEDGEMENTS

I would like to express my appreciation to the NASA/ASEE Summer Faculty Fellowship Program for the research opportunity it has provided. Thanks also are extended to Drs. Bob Barfield, Gerald Karr, and Jim Dozier and to Marion Kent for their very capable administration of this program. Special thanks go to my counterpart, Dr. Palmer Peters, for his suggestions and guidance this summer. Appreciation is also expressed for the help so willingly given by the Space Sciences Laboratory personnel, especially to Mr. Edward Stephens and Mr. Charles Sisk for their technical assistance and to Mrs. Sue Davis for typing this report.

INTRODUCTION

In 1962, the late Dr. Leonard I. Schiff and Drs. Fairbank and Cannon of Stanford University proposed a new and unique test of Einstein's Theory of Gravitation, General Relativity. The experiment they proposed consisted of measuring the precession of ultra-precision gyroscopes in orbit about the Earth. Detailed descriptions of the gyroscope experiment, or Gravity Probe-B Experiment as it is called, have been published in several places (1,2). The design of the experiment is such that advancements in several key technology areas have been required. The research efforts of many personnel at Marshall Space Flight Center and at Stanford University have been directed toward developing the necessary technology.

The gyroscope consists of a niobium-coated spherical quartz rotor that is floated electrostatically inside a quartz gyro housing. The superconducting niobium coating on the quartz ball establishes a magnetic field due to the rotation of the ball (3). A superconducting readout loop is deposited on the gyro housing. Any change of alignment between the spin axis of the quartz ball and the readout loop will produce a current in the readout loop which will be monitored by a SQUID magnetometer.

OBJECTIVES

The main objective of this research project is to develop procedures for the fabrication of superconducting readout loops out of niobium on glass substrates. It is planned that the loops fabricated according to current design parameters (4) will be used in the Gravity Probe-B (GP-B) Experiment. The initial work would involve both positive and negative resist techniques on the glass substrates and if time permitted, a pattern would be produced on a gyro housing half. The various techniques involved and the parameters affecting the quality and performance of the loops would be evaluated.

THE FABRICATION SYSTEM

To fabricate the fine lines, approximately 15 μm wide, that are needed for the GP-B readout loops a system was developed by Dr. Palmer Peters, Mr. Charles Sisk, and Mr. Ed Stephens that uses a mercury arc source focused to a fine point on a movable stage as shown in Figure 1. Since 1979 a considerable amount of work has gone into the fabrication system and the microprocessor control (4). The present system can be positioned to 1 μm (translational) and $.01^\circ$ (rotational) over a 4 inch square area and is capable of producing line widths of less than 10 μm , if required.

The earlier designs of the readout loops, as shown in Figure 2, have been fabricated on glass substrates. This design required that a crossover be made on the readout loop and connecting pads to the SQUID magnetometer be external to the loops.

The present design (5), as shown in Figure 3, contains connecting pads that are an integral part of the readout loops with the cross-over being made by the external wires. The current design parameters are:

- 5 turns
- 2.005 cm starting radius
- .030 cm loop spacing
- 15 μm line width
- 11,500 nm line thickness
- 1.3 mm square contact pads
- .005 cm line spacing around pads.

In order to meet the design parameters it was necessary to program the microprocessor control to produce the pattern as indicated in Figure 3. This was completed and the program with notes is included as Appendix A.

FABRICATION PROCEDURES

Negative Resist Techniques

Initially it was felt that the readout loops could be best produced using negative resist techniques. Although a limited number of samples were produced by each resist technique, it appears that there may be more problems associated with the negative resist than with the positive.

In order to produce preliminary readout loops a three inch square glass substrate was cleaned and a 1000 Å niobium film with a 150 Å gold overlay was sputtered onto it. Initially the samples were not prepared in a manner that should produce superconducting films. When it was demonstrated that the system could produce the desired patterns, films were produced which would give superconducting lines. To produce the type of film needed for the actual readout loops, the pressure in the chamber must be in the low 10^{-6} torr range.

The lab has developed a technique for predicting the transition temperature of a niobium film. If the ratio of the film's resistance at liquid nitrogen temperature to its resistance at room temperature is .72, then the film will be superconducting with a transition temperature of approximately 6° K. This is the goal for the loops.

The completed films were spin-coated with WAYCOAT TYPE 3 negative resist at 3600 rpm. The samples were air dried at room temperature for 2 hours and placed in the system where the pattern was exposed. Since the negative resist is more sensitive than the positive, a beam splitter was included in the system to decrease the sensitivity. It was found that a setting of 20° on the splitter and settings of 5.5 for X, 5.5 for Y and 2.5 for θ on the stepping motor controls produced the correct line widths.

The samples were then developed in xylene and examined under the microscope. Four samples were fabricated that appeared to be

suitable for sputter etching. Of these, two demonstrated that the systems could produce the desired loop configuration but they both had some niobium remaining on the substrate after etching. Attempts to remove all the niobium resulted in part of the loops being removed. The control of the sputter etching rate across the substrate is a problem with the negative resist. It could be due to variations in thickness of the niobium films, oxygen level in the chamber, or asymmetry of the chamber. If negative resist is used, this problem must be solved.

Positive Resist Techniques

The lab has developed positive resist liftoff techniques for the production of step function junctions and Mr. Sisk is quite proficient in the technique. The technique does require one extra step in the sputtering chamber but this presents little problem. There are some additional problems with dust and contamination on the pattern.

Three-inch square glass substrates were also used for the positive resist, but in order for the resist to adhere well the cleaned substrates had to have approximately 50 Å of niobium sputtered onto the surface before the resist was applied. Once the AZ1350J positive resist was applied the samples were dried at room temperature for 12 hours. The pattern was then exposed and the samples were given a 30 minute post-bake at 90° C. After which they were returned to the chamber where the 1000 Å niobium film was sputtered on the substrate. To produce satisfactory superconducting loops a chamber pressure of 2×10^{-6} torr was required before sputtering and the target was presputtered for about an hour. The finished samples were removed from the chamber and the resist was lifted off with acetone in the ultrasonic cleaner. This left the readout loops on a substrate coated with the initial 50 Å of niobium. The samples were sputter etched for about 10 minutes to remove the thin niobium leaving the desired pattern on the substrate. This technique produced sharp lines and the pattern could be examined prior to sputtering the films.

Using this technique four samples with resistance ratios greater than one were produced. These were early samples and the parameters were not watched closely to produce superconducting samples. Two later samples were both superconducting with resistance ratios of .82 and .8 and transition temperatures near 4° K.

Connectors

In order to make resistance measurements on the samples it was necessary to connect .003 inch diameter niobium wire to the 1 mm to 1.3 mm square pads. It was found that if gold was sputtered onto thin niobium sheet, the sheet could be cut and mechanically clamped around the wire to form connecting tabs. These tabs were then soldered to the pads on the readout loops. The joints exceeded the strength of the wire in several cases and held during repeated temperature cycling.

CONCLUSIONS AND RECOMMENDATIONS

This study indicates that the fabrication system described here can produce readout loops for the GP-B Experiment that meet the present design parameters. In addition either positive or negative resist techniques may be used. Although the problems associated with the negative resist could probably be overcome, the positive liftoff technique is more satisfactory. It would have been nice to produce a pattern on a rotor housing half but a limited number of halves and limited time prevented this.

One minor problem remains in the patterns produced in both positive and negative resist. The innermost loop is narrower by approximately 2 μm than the outer loop. This was examined briefly and variables including rotational velocity, exposure, focus and drying time were eliminated. It was concluded that the problem is due to variations in the thickness of the resist and can be eliminated by a higher rpm spin coater.

It is recommended that at least one satisfactory housing half be supplied and a set of readout loops be produced on it for testing in an actual experimental situation.

5-XXXX

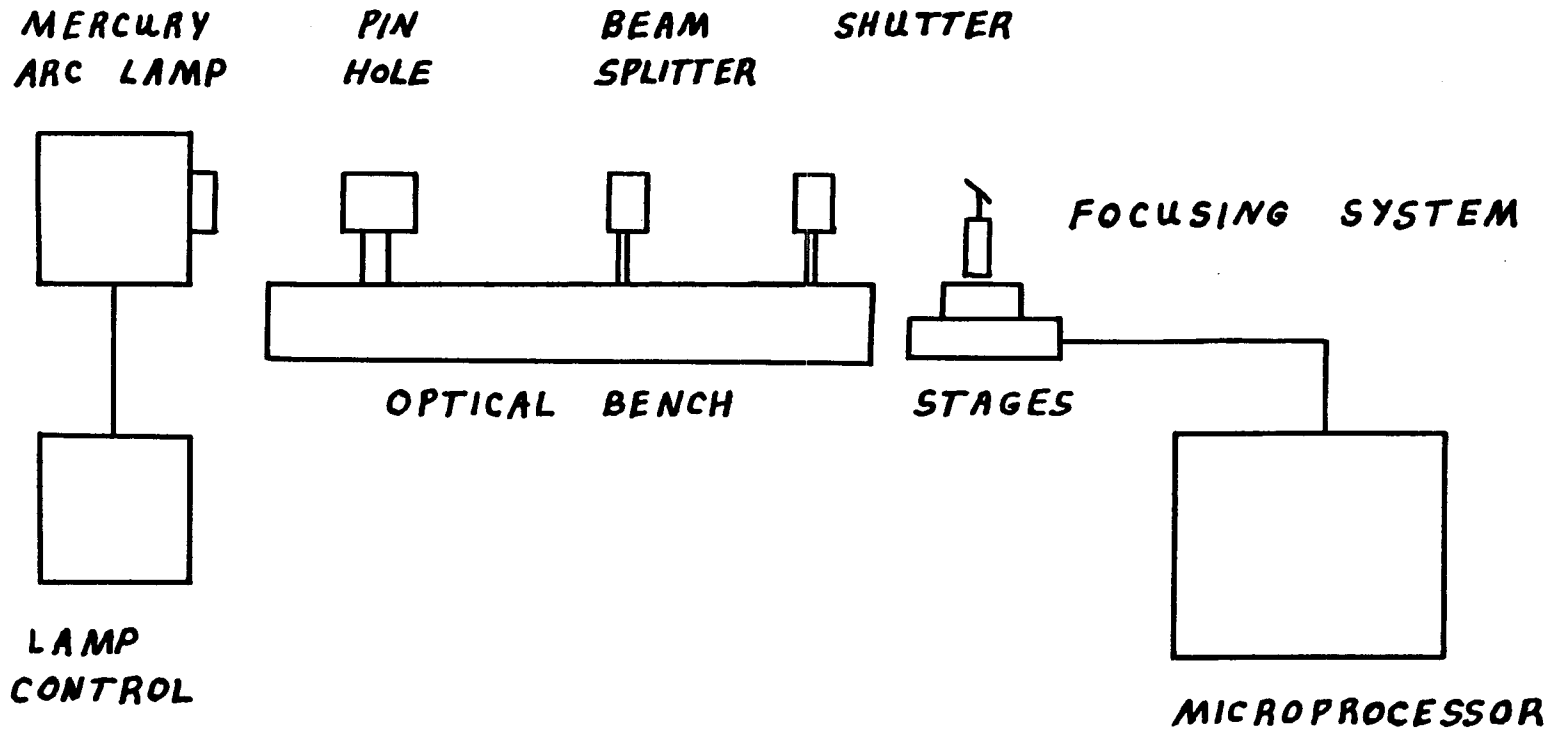


FIGURE 1: FABRICATION SYSTEM

9-XXXX

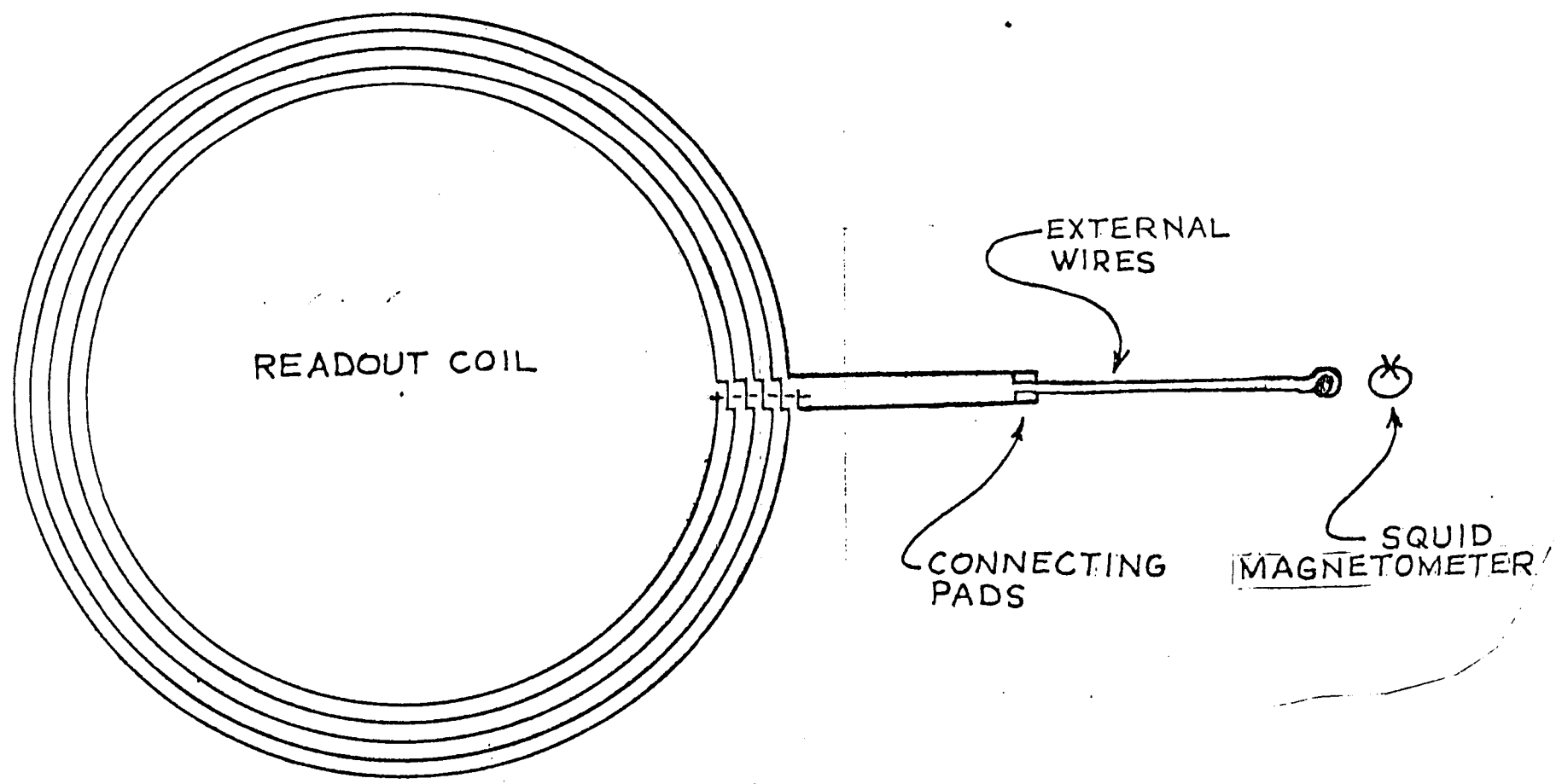


FIGURE 2: READOUT LOOP

XXXX-7

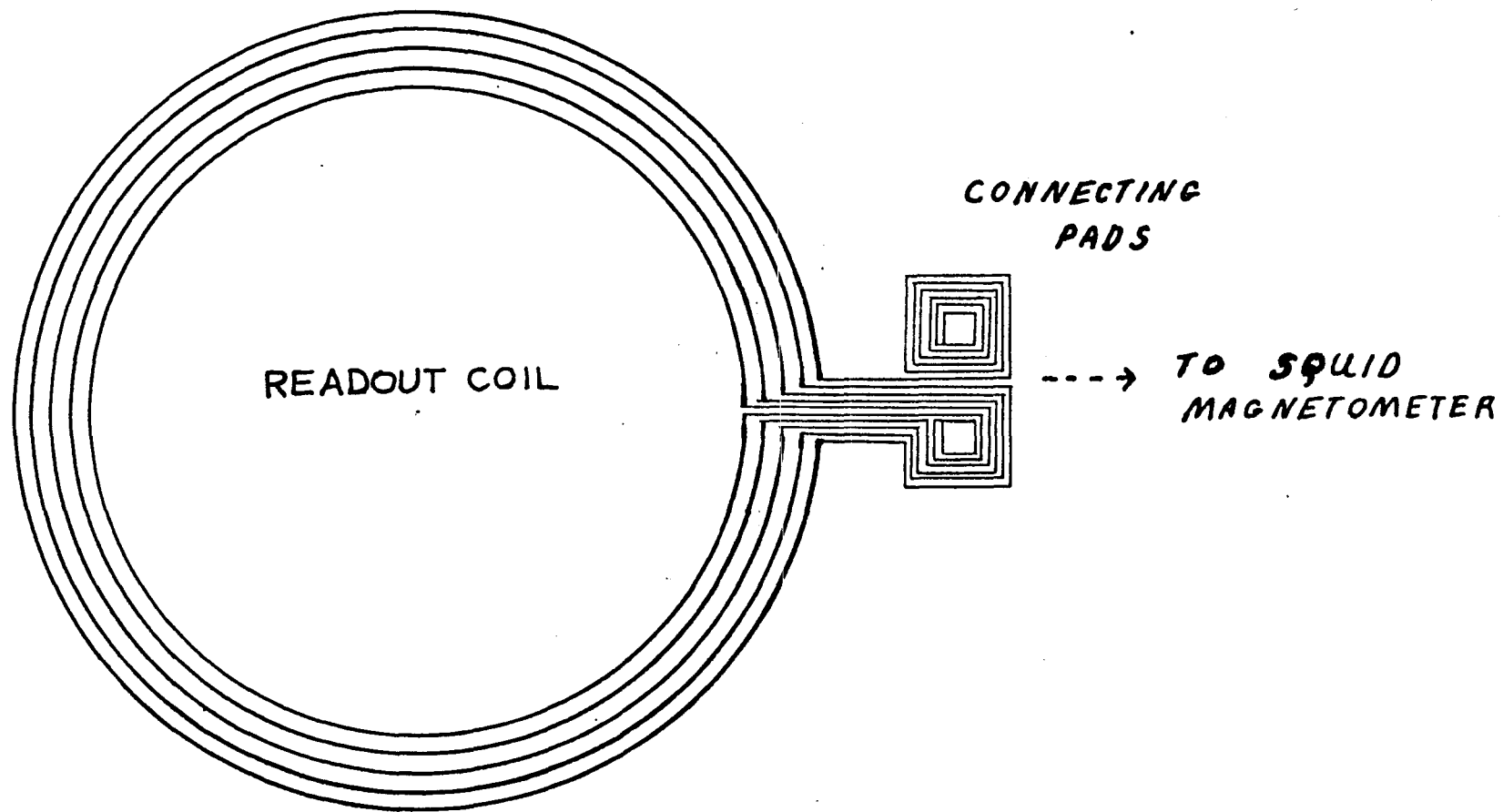


FIGURE 3: CURRENT READOUT DESIGN

X	Y	Θ	X	Y	Θ
+1255	0	0	4	293	0
0	13	0	0	0	78
-1255	0	0	-765	0	0
0	13	0	0	1385	0
+1255	0	0	-1905	0	0
0	13	0	0	-1905	0
-1255	0	0	2985	0	0
0	13	0	0	0	62
+1255	0	0	2	227	0
0	13	0	0	0	35876
-1255	0	0	2	243	0
0	13	0	0	0	66
+1255	0	0	-1145	0	0
0	13	0	0	1385	0
-1255	0	0	-1775	0	0
0	13	0	0	-1775	0
+1255	0	0	1840	0	0
0	13	0	1385	0	0
-1255	0	0	0	0	41
0	13	0	1	147	0
+1255	0	0	0	0	35910
0	13	0	1	178	0
-1255	0	0	0	9	49
0	13	0	-1525	0	0
+1255	0	0	0	1385	0
0	13	0	-1645	0	0
-1255	0	0	0	-1645	0
0	13	0	3485	0	0
1255	0	0	0	0	23
0	13	0	0	82	0
-1255	0	0	0	0	35945
0	7	0	0	113	0
1320	0	0	0	0	32
0	-1320	0	-1905	0	0
-1385	0	0	0	1385	0
0	1385	0	-1515	0	0
1450	0	0	0	-1515	0
0	-1450	0	3730	0	0
-1515	0	0	0	0	5
0	1515	0	0	17	0
1580	0	0	0	0	35981
0	-1580	0	0	48	0
-1645	0	0	0	0	14
0	1645	0	-2285	0	0
1710	0	0	0	1385	0
0	-1710	0	-1385	0	0
-1775	0	0	0	-1385	0
0	1775	0	1385	0	0
1840	0	0	0	65	0
0	-1840	0	-1320	0	0
-1905	0	0	0	13	0
0	1905	0	1255	0	0
2670	0	0	0	13	0
0	0	78	-1255	0	0
4	292	0	0	13	0
0	0	35845	1255	0	0

X	Y	Q	X	Y	Q
0	13	0	-1255	0	0
-1255	0	0	0	13	0
0	13	0	1255	0	0
1255	0	0	0	13	0
0	13	0	-1255	0	0
-1255	0	0	0	13	0
0	13	0	1255	0	0
1255	0	0	0	13	0
0	13	0	-1255	0	0
-1255	0	0	0	13	0
0	13	0	1255	0	0
1255	0	0	0	13	0
0	13	0	-1255	0	0
-1255	0	0	0	13	0
0	13	0	1255	0	0
1255	0	0	0	13	0
0	13	0	-1255	0	0
-1255	0	0	0	13	0
0	13	0	1255	0	0
1255	0	0	0	13	0
0	13	0	-1255	0	0
-1255	0	0	0	13	0
0	13	0	+1255	0	0
+1255	0	0	0	13	0
0	13	0	-1255	0	0
-1255	0	0	0	13	0
0	13	0	1255	0	0
1255	0	0	0	13	0
* 0	13	0	0	7	0
0	13	0			
1255	0	0			
0	13	0			
-1255	0	0			
0	13	0			
1255	0	0			
0	13	0			
-1255	0	0			
0	13	0			
1255	0	0			
0	13	0			
-1255	0	0			
0	13	0			
1255	0	0			
0	13	0			

*Insert
-1250 0 0

REFERENCES

1. Fairbank, W.M. et al: Final Report. NASA Grant 05-020-019, W. W. Hansen Laboratories of Physics and the Department of Aeronautics and Astronautics, Stanford University, July 1977.
2. Fairbank, W.M. et al: Report on Progress of NASA Grant 05-020-019; U.S. Air Force Contract F36615-67-C-1245 and NASA Contract NAS8-32355; W. W. Hansen Laboratories of Physics and the Department of Aeronautics and Astronautics, Stanford University, June 1980.
3. Gravity Probe B Phase A Report: George C. Marshall Space Flight Center, March 1980.
4. Palmer N. Peters, Private Communication (1981).
5. James M. Lockhart, Private Communication (1982).

NASA/ASEE SUMMER FACULTY RESEARCH FELLOWSHIP PROGRAM

MARSHALL SPACE FLIGHT CENTER
THE UNIVERSITY OF ALABAMA

OPTICAL CONTACTING OF QUARTZ

Prepared By: Linda L. Payne, Ph.D.
Academic Rank: Associate Professor of Physics
University and Department: South Carolina State College
Department of Natural Sciences
NASA/MSFC:
Laboratory: Space Science
Division: Space Physics
Branch: Cryogenic Physics
MSFC Counterpart: Palmer N. Peters
Date: August 6, 1982
Contract No.: NGT 01-002-0299
The University of Alabama

OPTICAL CONTACTING OF QUARTZ

by

Linda L. Payne
Associate Professor of Physics
South Carolina State College
Orangeburg, South Carolina

ABSTRACT

The Gravity Probe-B (GP-B) Experiment proposed by Stanford University to test the theories of general relativity requires extremely precise measurements. The quartz components of the instruments to make these measurements must be held together in a very stable unit. Optical contacting has been suggested as a possible method of joining these components. This research will review the fundamental forces involved in optical contacting and will attempt to relate calculations of these forces to the results obtained in experiments.

ACKNOWLEDGEMENTS

I would like to express my appreciation to the NASA/ASEE Summer Faculty Fellowship Program for the research opportunity it has provided. Thanks also are extended to Drs. Bob Barfield, Gerald Karr and Jim Dozier and to Marion Kent for their very capable administration of this program. Special thanks to my counterpart, Dr. Palmer Peters, for his suggestions and guidance this summer. Appreciation is also expressed for the help so willingly given by the Space Science Laboratory personnel, especially to Mr. Ed Stephens and Mr. Charles Sisk for their technical assistance and to Mrs. Sue Davis for typing this report.

INTRODUCTION

In 1962, the late Dr. Leonard I. Schiff and Drs. Fairbank and Cannon of Stanford University proposed a new and unique test of Einstein's Theory of Gravitation, General Relativity. The experiment they proposed consisted of measuring the precession of ultra-precision gyroscopes in orbit about the Earth. Detailed descriptions of the gyroscope experiment, or Gravity Probe B Experiment as it is called, have been published in several places (1,2). The design of the experiment is such that advancements in several key technology areas have been required. The research efforts of many personnel at Marshall Space Flight Center and at Stanford University have been directed toward developing the necessary technology.

The gyroscopes for the experiment and the telescope which will be used to aim the spacecraft will be made of fused quartz. The components of these instruments must be joined together very rigidly and maintain their relative positions under conditions of reduced temperature and pressure. One method which has been proposed for joining the quartz components is the method of optically contacting the surfaces.

OBJECTIVE

Research has been conducted to investigate the strength of the bond between optically contacted quartz surfaces. This paper will review the results of this research and also give an overview of the fundamental forces believed to be involved in optical contacting. Attempts will be made to relate calculations of these forces to the results obtained in experiments.

HISTORY

It has been known for more than fifty years that very flat, clean glass or silica surfaces can be brought into optical contact, that is contact so close that reflection at the interface is very nearly eliminated. Typically, the optical reflectivity at the interface is about four orders of magnitude lower than the reflectivity of a free surface (3,4). When the surfaces are contacted, they are held together by considerable force with no adhesive or clamping. The nature of the forces of adhesion which bind the quartz surfaces has been a matter of speculation for a number of years. Some of the earliest work proposed that the adhesion was due to the presence of a water film on the surface of the quartz and in some cases was enhanced by an electrostatic attraction (5). Water from the atmosphere collects around hygroscopic impurities on the surface of the quartz. The equivalent of about 20 molecular layers is present when the relative humidity is 80% (6). It has been reported that no adhesion occurred in air at a relative humidity below 50% and that a good correlation existed between adhesive strength and surface tension if liquids other than water were placed on the surfaces prior to contacting (7).

However, others reported that the adhesion of quartz was not solely due to a film of water on the surface, but was an actual adhesion of quartz with quartz (8). In order to determine if covalent, ionic, or van der Waals forces contribute to the adhesion, optical contact experiments were carried out in an ultrahigh vacuum chamber where liquid films could be eliminated (9). Adhesion did occur under these conditions which indicates that the optical contact is not an effect due to a liquid film on the surface. It is also unlikely that this adhesion is electrostatic in nature since the vacuum was achieved with ion pumps which would have exposed the quartz surfaces to a glow discharge and eliminated any nonuniform surface charge distributions.

The separation between the contacted surfaces is much less than 1000 Å. Some sources give a mean separation of 200 Å (10) while others quote as little as 10 to 30 Å (3). The mean height of surface irregularities on the optically polished samples is at least 100 Å which renders the exact separation a rather meaningless quantity. It probably ranges from 0 to 200 Å across the surface of the contact. The area of intimate contact is probably only a minute fraction of the total contacted surface. Covalent and ionic bonding require precise near-neighbor separation and orientation and therefore it is unlikely that they contribute significantly to the adhesive forces. It is most probable that the adhesion occurs because of van der Waals forces and it is on this assumption that a theoretical model for the adhesion will be developed.

THEORY

The idea of weak bonds between gas molecules was first presented in the 1880's by Johannes van der Waals. He based his assumption on several experimental observations made for gases at high and low pressures. Van der Waals reasoned that real gases under pressure depart from the pressure-volume relationship for ideal gases

$$PV = nRT$$

due to forces of attraction between gas molecules as the distances between the molecules are decreased. At extremely high pressures, a repulsive force associated with the molecules themselves, or the space they occupy influences the pressure-volume relationship. The famous van der Waals equation

$$\left(P + \frac{a}{V^2} \right) (V-b) = nRT$$

incorporated these forces into the P-V description of real gases. In these equations, P is the pressure, V is the volume, T is the Kelvin temperature, n is the number of moles of gas, R is the Universal gas constant and a and b are constants which are characteristics of the gas.

The presence of these weak bonds between gas molecules is indicated by behavior of gases: adsorption of gases on surfaces, solution of gases in liquids, liquification of gases. All these

procedures would be impossible were there not bonding between the gas molecules or atoms. Such bonds also occur between the molecules of liquids and solids though they are often only evident in the absence of stronger bonds such as covalent, ionic, metallic, or hydrogen bonds.

Basically the van der Waals bonds result from electrostatic forces between the electrons of one atom and the nucleus of another. There are basically three mechanisms by which the van der Waals bonds are formed: the dispersion effect, the orientation effect, and the induction effect. The dispersion effect is the only mechanism for bonding between atoms or molecules with no permanent dipole. When two such molecules approach each other, each exerts an electric field on the other. This in turn produces two mutually induced dipoles which cause the attraction between the molecules. The orientation effect and the induction effect are mechanisms by which bonding occurs in molecules with permanent dipoles. The orientation effect occurs when the positive portion of one molecule is electrostatically attracted to the negative part of another. In the induction effect, a molecule with a permanent dipole may induce an additional dipole in another molecule (which has or has not a permanent dipole) which results in attraction. The dispersion effect is also present in the van der Waals bonds involving permanent molecular dipoles.

Theoretical considerations of the range, nature, and strength of such forces between solids have been made by de Boer (11), Hamaker (12), Casimir (13), and Lifshitz (14). A summary of their work is found in a chapter in Adhesion and Cohesion by Debye (15) and in an article by Bowden (16). At close distances, the electrostatic Coulomb forces are dominant, but they fall off very rapidly with distance. For distances greater than about 20 Å, the attraction is due to the van der Waals force. London (17,18) showed that this force is proportional to $1/r^7$, where r is the distance between atoms. If one is to compute the force between two parallel blocks of material, each atom in one exerts an attractive force on each atom of the other. When summed over all the atoms in both solids, it is found that the attractive force F should vary as $1/d^3$ where d is the distance between the outermost row of atoms in the parallel surfaces (11,12). This relationship is valid for values of d less than a few hundred Angstroms. Casimir (13) and Lifshitz (14) have shown that for distances greater than this, a correction is needed for the time it takes the changing electrostatic field of one fluctuating dipole to propagate information to polarize the second dipole. This retardation effect results in a new force proportional to $1/r^8$ between pairs of atoms and thus the force between parallel surfaces becomes proportional to $1/d^4$. From this one can see that atoms more than a few atomic layers from the surface contribute little to the attraction.

The fact that these van der Waals forces between atoms and molecules give rise to an attractive force between solid bodies has been observed by several experimenters at separations ranging from 1000 to 10,000 Å using optically polished surfaces (10,19,20,21). The

results of these experiments agreed with the microscopic theory of Casimir and Polder (22) and the macroscopic theory of Lifshitz (23). Attractive forces were found to range from 10^9 dyne/cm² for 10-Å separation to 1.5×10^6 dyne/cm² for 100 Å separation for molecularly smooth mica sheet (7) which is in the range of the theoretically calculated van der Waals forces.

Debye (15) reports that for quartz plates, based on the above theoretical models, the force per unit area could be written as

$$F = \frac{B}{d^3}$$

where F is in dyne/cm², d is the separation between the plates in microns and B is a coefficient whose value could be obtained from the Lifshitz work and the dispersion curve of quartz. Since the latter is not well known estimates of this coefficient range from $B = 0.6 \times 10^{-3}$ to 1.6×10^{-3} . This agrees fairly well with B derived from the measured forces.

EXPERIMENTAL WORK

Optical contacting experiments on two types of samples have been conducted in the Space Science Lab at Marshall Space Flight Center. The first involved the contacting of quartz fibers by P. N. Peters (24) and the second involved optical contacting of quartz flats by the author (25). In both of the cases, the results obtained closely agreed with the predicted theoretical values. For the quartz flats, the maximum applied force per unit area was 2.2×10^8 dynes/cm². For this applied force, the contacts did not separate, indicating the forces holding them together to be in excess of this. From the theoretical equation for the force

$$F = \frac{B}{d^3}$$

a calculation for a separation of 10 Å or 1×10^{-3} μm yields a force of 10^9 dynes/cm². Further surface studies must be made to determine if the average separation of the quartz flats is in the range of 10 Å.

CONCLUSIONS AND RECOMMENDATIONS

Results of these preliminary studies indicate that predicted strength of the optical contact bonds between quartz surfaces should be sufficient to withstand the rigors of the launch and the space environment. Contacts of such strength are only obtained between very clean, dust-free surfaces, such that the separation between the flats is less than 100 Å. Recommendations would be to continue testing quartz contacts while developing a reliable method of contacting and surface characterizations of the samples.

REFERENCES

1. Fairbank, W.M., et al: Final Report. NASA Grant 05-020-019, W. W. Hansen Laboratories of Physics and the Department of Aeroanautics and Astronautics, Stanford University, July 1977.
2. Fairbank, W.M., et al: Report on Progress. NASA Grant 05-020-019, USAF Contract F36615-67-C-1245, and NASA Contract NAS8-32355, W. W. Hansen Laboratories of Physics and the Department of Aeronautics and Astronautics, Stanford University, June 1980.
3. Lord Rayleigh, F.R.S., "Proc. Roy. Soc.", A156, (1936), pp. 326-349.
4. Carr, Paul H., J. Acoust. Soc. Amer. 37: 5, 927; (1965).
5. Stone, William, Phil. Mag. ix: 610 (1930).
6. Smith, H. I., J. Acoust. Soc. Amer., 37: 5, 928; (1965).
7. Bowden, F.P., and D. Tabor, The Friction and Lubrication of Solids (Oxford University Press, London, 1954) 2nd ed., p. 299.
8. Tomlinson, T.A., Phil. Mag. vi: 695 (1928).
x: 541 (1930).
9. Smith, H.I., and M.S. Gussenhoven, J. Appl. Phys. 36: 7, 2326 (1965).
10. Sparnaay, M.G., Physica 24: 751 (1958).
11. de Boer, J.H., Trans. Far. Soc. 32: 21 (1936).
12. Hamaker, H.E., Physica, 4: 1058 (1937).
13. Casimir, H.B.G., Proc. Kon. Akad. Wetenschap. Amsterdam 51: 793 (1948).
14. Lifshitz, E.M., C.R. Acad. Sci. U.S.S.R 97: 643 (1954).
15. Weiss, P. (ed.), Adhesion and Cohesion, Elsevier, NY (1962).
16. Bowden, F.P., Fundamentals of Gas - Surfaces Interactions (1967).
17. London, F., Zeit. Phys. 63: 245 (1930).
18. London, F., Trans. Far. Soc. 33: 8 (1937).
19. Kitchener, J.A., and A.P. Prosser, Proc. Roy. Soc. A 242: 403 (1957).

20. Abrikosova, I.I., and B.V. Deriagin, Soviet Phys. JETP 3: 819 (1957). 4: 2 (1957).
21. Abrikosova, I.I., Soviet Phys JETP 6: 615 (1958).
22. Casimir, H.B.G., and D. Polder, Phys. Rev 73: 360 (1948).
23. Lifshitz, E.M., Soviet Phys. JETP 2: 73 (1956).
24. Peters, P.N.: Optical Contacting and Its Application to Gravity Probe-B. NASA Report. Unpublished. August 1981.
25. NASA Contractor Report: NASA CR-161855:XVIII; January 1982.

THE APPLICATION OF DIGITAL SIGNAL PROCESSING TECHNIQUES
TO A TELEOPERATOR RADAR SYSTEM

BY

Alfonso Pujol Jr., Ph.D.
Assistant Professor of Electrical Engineering
University of Tennessee Space Institute
Tullahoma, Tennessee

ABSTRACT

A digital signal processing system has been studied for the determination of the spectral frequency distribution of echo signals from a Teleoperator radar system. The system consisted of a Sample and Hold circuit, an Analog to Digital converter, a Digital Filter, and a Fast Fourier Transform. The system is interfaced to a 16-bit microprocessor. The microprocessor is programmed to control the complete digital signal processing.

The digital filtering and Fast Fourier Transform functions are implemented by a S2815 Digital Filter/Utility Peripheral chip and a S2814A Fast Fourier Transform chip. The S2815 will initially simulate a low-pass Butterworth Filter with later expansion to complete filter circuit (Bandpass and Highpass) synthesizing.

From this study, a later attempt will be made to extract some characteristic parameter that will correlate spectral data to range determination.

ACKNOWLEDGMENTS

The writer wishes to express his appreciation to the NASA/ASEE Summer Faculty Fellowship program for the research opportunity it has provided. Sincere gratitude is extended to Dr. Bob Barfield, Dr. Jim Dozier and Mr. Marion Kent for their very capable administration of this program and to Mr. B. R. Reed and Mr. E. H. Gleason who provided many creative ideas and stimulating conversations.

Credit is given to Kaye Langford for her patience in typing this paper.

LIST OF FIGURES

<u>Figure No.</u>	<u>Title</u>	<u>Page</u>
1	Digital filter processing system.	XXXIII-4
2	Lowpass filter power gain characteristic.	XXXIII-6
3	Butterworth filter power gain for $\epsilon=1$.	XXXIII-6
4a	Cascade of the digital Butterworth filter; $N=10$.	XXXIII-13
4b	Realization of $\tilde{H}_n(z)$.	XXXIII-13

INTRODUCTION

For the past few years, research has been undertaken at the George C. Marshall Space Flight Center (MSFC) for the development of a short range (at present, from 0.5 meters to 4.0 meters) radar system for usage in the areas of Teleoperators, Robotics, and Autonomous Systems. The radar system is an analog system that transmits and receives a Frequency-Modulated Continuous Wave (FM-CW) triangular shaped waveform. The input (echo) signal is processed by passing it through a mixer, amplifier, and a limiter. To remove unwanted frequencies, the processed signal is then sent through a Highpass filter, a Bandpass filter, and a lowpass filter. The filtered signal is then sent through an automatic gain control (AGC) and a computing counting circuit for range determination.

The possibility of doing filtering and other signal processing operations by numerical means (Digital Signal Processing) instead of by traditional analog means has been known and studied for 20 years or longer. Digital signal processing provides a means of determining or identifying characteristic parameters of a signal, or to transfer a signal into a form which is in some sense more desirable.

It is the purpose of this study to apply digital signal processing techniques to the FM-CW radar system and develop the groundwork for (later studies) extracting some characteristic parameter which will correlate spectral data to range determination. For simplicity, the study will consider digital signal techniques applied only to the Lowpass filter (digital filtering) with expansion to the Highpass and Bandpass filters. The study will also present areas for further investigation.

OBJECTIVES

The purpose of this study is to investigate the application of digital techniques to perform functions that traditionally were done by analog circuitry. Microprocessors and Large Scale Integration (LSI) will be utilized to replace analog equivalents. The following objectives are:

1. Define and determine the feasibility of digital signal processing on FM-CW radar baseband signals.
2. Identify those analog functions that may be replaced by digital processing elements.

3. Replace analog filters with digital equivalent.
4. Perform evaluation of selected digital processors.
5. Use Fast Fourier Transforms (FFT) or other transforms to determine the system where frequencies are most likely to be related to range.

DIGITAL SIGNAL PROCESSING SYSTEM

Very Large Scale Integration Chips

As mentioned earlier, the possibility of doing digital filtering and other digital signal processing operations by numerical means instead of by traditional analog means has been known and studied for 20 years or longer. Until recently, the hardware for the physical realization of digital filters has been bulky, power-hungry, and expensive; and for this reason, the digital filter has not been suitable for use as a component in commercial systems. However, Very Large Scale Integration (VLSI) chips has changed this condition drastically. It has reduced the size, power consumption, and cost of digital filters to the point where their use as a system component is both economically feasible and technically desirable.

Discrete and Fast Fourier Transforms

VLSI has also spund on the use of digital signal processing for spectrum analysis, and it is at this point that the Discrete Fourier Transform (DFT) and the Fast Fourier Transform (FFT) comes into its own. The DFT, by virtue of its efficiency, can replace a bank of filters and result in a significant reduction in the computation rate required to execute the function. The FFT is an algorithm for computing the DFT just described.

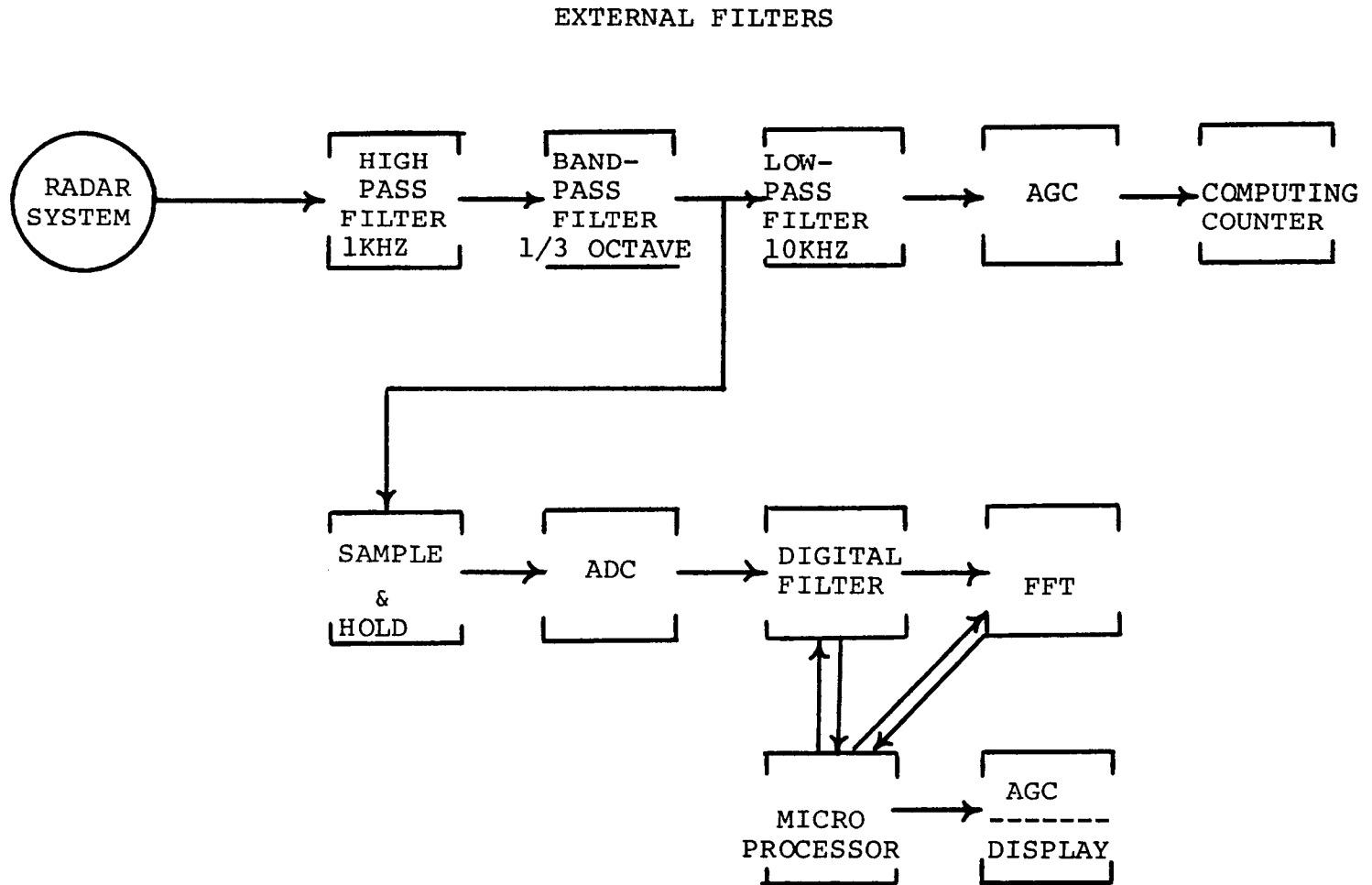
The methods of spectral analysis often require the direct computation of spectra from large sample sets, or repeated computations of spectra from large numbers of sample sets. In these cases the FFT may provide the only possible means for spectral computation within the limits of time and computing cost. The DFT and the FFT are versions of the Fourier Analysis Technique (1, 2) which are suitable for digital implementation, and consequently, for machine computation. They can be realized as programs in a general purpose computer or as pieces of special purpose hardware.

Digital Signal Processing System

Figure 1 shows a block diagram of a digital signal processing system. The input to the system is the signal (maximum frequency of 10KHz) from the Bandpass filter of the FM-CW radar system (refer to the Introduction). The signal is then sampled by a "LH0043 National Semiconductor," sample and hold circuit. With an aperture time of 20n sec., the sampling device will minimize aliasing. A "Model ADC-1131K Analog Device Co." analog to digital converter (ADC) digitizes the stair-step waveform samples from the sample and hold circuit and provides input to the digital processor (Digital filter and FFT). The heart of the analyzer is the "Model S2815 American Microsystems, Inc.," digital filter (3) and the "Model S2814A American Microsystem, Inc.," FFT (4). They are preprogrammed VLSI chips interfaced to a 16-bit "Model TM990/101 MA Texas Instruments Co.," microprocessor.

The S2815 is a microprocessor compatible input-output (I/O) interface with two independent 32 tap transversal filter routines, cascadable into a single 64 tap filter, two recursive (biquadratic) filters providing a total of 16 filter sections, computation functions (two integrating, two rectifying, squaring, and block multiply routines), conversion functions (μ 255 Law, and Linear-to-dB transformations), and generator functions (sine and pseudo-random noise patterns). The S2815 chip is a high speed microcomputer organized for efficient signal processing and contains a data memory, instruction memory and an arithmetic unit incorporating a 12-bit parallel multiplier, as well as control registers and counters. The Instruction ROM contains the mentioned routine which make up the package. The Data ROM contains the coefficients required to execute the functions. One hundred twenty-eight (128) words of Data RAM and an eight (8) word scratchpad are provided to hold the signal data and the jump addresses for cascading routines. The Data memory is arranged as a matrix of 32 X 8 words. Routines will be executed under control of a TM990/101 microcomputer.

The S2814A is also a microprocessor compatible I/O interface. It can perform 32 complex point forward or inverse FFT in 1.3m sec., and operate with any 8 or 16 bit microprocessor. It has a basic resolution of 57dB with a conditional array scaling routine to increase the dynamic range to 70dB, and a window routine to permit use of arbitrary weighting functions. The S2814A is a high speed microcomputer organized for efficient signal processing and contains a data memory, instruction memory, an arithmetic unit incorporating a 12-bit parallel multiplier, as well as control registers and counters.



XXXX
IIII-4

Figure 1. Digital filter processing system.

The Instruction ROM contains the various routines which make up the FFT package. The Data ROM contains the coefficients required to execute the functions. One hundred twenty-eight (128) words of Data RAM are provided to hold the 32 point complex signal data during processing as well as the power spectrum of the output and various other parameters, including the total number of points in the desired transform. The memory is organized as a 32 X 4 matrix, with the data arranged in columns. The S2814A is intended to be used in a micro-processor system, using an 8 or 16 bit microprocessor. It will be used as a memory mapped peripheral, and will be assigned a block of 16 addresses. The TM990/101 microcomputer will control the flow of data, including I/O, and calls the routines to cause the FFT to be executed.

Butterworth Analog Filter

A filter is assumed to be a system for passing the spectral content of an input signal in a certain specified band of frequencies. In other words, the filter transfer function forms a "window" in the frequency domain through which a portion of the input spectrum is allowed to pass.

The design of analog lowpass filters has been a much-explored subject. This design problem, called the "approximation problem," has led to some more-or-less standard analog lowpass designs, such as the Butterworth filter, Chebyshev filter, etc.

The traditional approach to the design of digital filters involves the transformation of an analog filter into a digital filter meeting prescribed specifications. The following discussion will consider the Butterworth filter as the initial filter design of concern. Future investigations will consider other filter designs, such as Chebyshev, Elliptic, etc., to establish the optimum design for spectral-range determination.

Butterworth filters are defined by the property that the magnitude response is maximally flat in the passband. The power gain of the filter is expressed as

$$\text{Power gain} = |H(j\omega)|^2 \quad (1a)$$

or

$$\text{Power gain in dB} = 10 \log_{10} |H(j\omega)|^2 \quad (1b)$$

Referring to Figure 2, there is a cutoff frequency, ω_c , and a rejection frequency, ω_r . Between the two is the

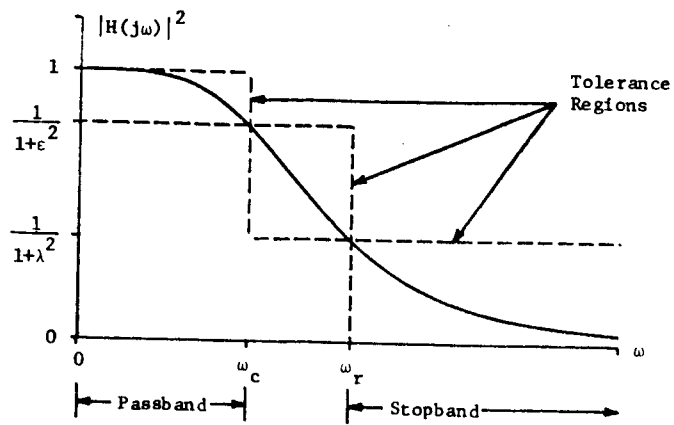


Figure 2. Lowpass filter power gain characteristic.

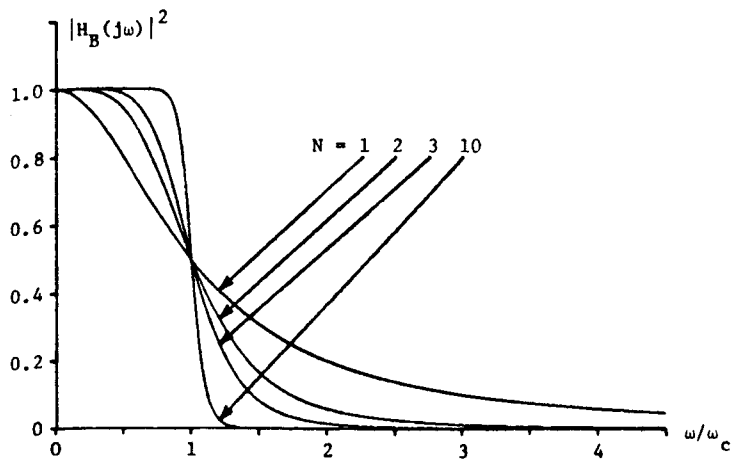


Figure 3. Butterworth filter power gain for $\epsilon=1$.

region in which the power gain rapidly decreases. The gain parameters, λ and ϵ , determine the tolerances the designer is willing to accept, as follows:

$$\text{Passband: } |\omega| < \omega_c; |H(j\omega)|^2 > \frac{1}{1+\epsilon^2} \quad (2a)$$

$$\text{Stopband: } |\omega| > \omega_r; |H(j\omega)|^2 < \frac{1}{1+\lambda^2} \quad (2b)$$

The Butterworth analog filter has a power gain of

$$|H(j\omega)|^2 = \frac{1}{1+\epsilon^2 \left(\frac{\omega}{\omega_c}\right)^{2N}} \quad (3)$$

where N is the order of the filter and ϵ and ω_c are defined by Equations 2a and 3a. The filter is maximally flat near $\omega=0$ and $\omega=\infty$. Referring to Equation (3), when ω equals ω_r ,

$$\begin{aligned} |H(j\omega)|^2 &= \frac{1}{1+\lambda^2} \\ &= \frac{1}{1+\epsilon^2 \left(\frac{\omega_r}{\omega_c}\right)^{2N}} \end{aligned} \quad (4)$$

Solving for N ,

$$N < \frac{\log(\lambda/\epsilon)}{\log(\omega_r/\omega_c)} \quad (5)$$

Thus, the designer must make a choice between the squareness of the power gain characteristic and the smallness of N . The relative improvement of this characteristic as N increases is illustrated in Figure 3 for the case where $\epsilon=1$. The S -plane poles of $|H(s)|^2$ where $s=j\omega$, are found by setting the denominator of Equation 3 equal to zero, such that,

$$\epsilon^2 \left(-\frac{s^2}{\omega_c^2}\right)^N + 1 = 0.$$

Solving for s ,

$$S_n = \omega_c \epsilon^{-1/N} e^{j\pi(2n+N-1)/2N} \text{ for } n=1,2,\dots,2N, \quad (6)$$

where the poles of the transfer function are those in the left-half plane, since

$$|H(S)|^2 = H(S) H(-S) \quad . \quad (7)$$

Multiplying the numerator and denominator of Equation 3 by $\epsilon^{-2\omega_c 2N}$, and referring to Equation 6,

$$H(S) = \frac{(-1)^N S_1 S_2 \dots S_N}{(S-S_1)(S-S_2)\dots(S-S_N)} \quad \text{for } N = 1, 2, \dots, N \quad . \quad (8)$$

The DC power gain is $|H(0)|^2 = 1$.

Digital Filters by the Bilinear Transformation

The bilinear transformation enable designers to take advantage of known analog designs. The bilinear transformation is viewed as a transformation from the S-plane to the Z-plane, which allows the conversion of analog poles and zeroes into digital poles and zeroes. The bilinear transformation is defined as

$$S = \frac{Z-1}{Z+1} \quad . \quad (9)$$

Substituting $S=j\omega'$ and $Z=e^{j\omega T}$ into Equation 9,

$$j\omega' = \frac{e^{j\omega T} - 1}{e^{j\omega T} + 1} \quad ,$$

where T is the sampling interval in seconds.

Solving for ω' ,

$$\omega' = \tan \frac{\omega T}{2} \quad . \quad (10)$$

Thus, for the desired values of ω_c and ω_r (for digital filters),

$$\omega_c' = \tan \frac{\omega_c T}{2} \quad , \quad (11a)$$

$$\omega_r' = \tan \frac{\omega_r T}{2} \quad . \quad (11b)$$

With the information mentioned above, the following section will utilize the Butterworth filter to design a digital filter.

Designing A Butterworth Digital Filter

For an object 0.5 meters away, the Teleoperator echo frequency was 2KH_z (minimum frequency), and for an object distance of 3.5 meters, the echo frequency was 8.4KH_z (maximum frequency). At present the system will not be used for any distances greater than 3.5 meters.

Referring to the Sampling Theorem, "To be able to recover a signal exactly, it is necessary to sample a signal at a rate greater than twice its highest frequency." Since the maximum echo frequency is 8.4KH_z , we will assume for simplicity a maximum frequency of 10KH_z . Therefore, the sampling frequency, f_s , is

$$\begin{aligned}f_s &= 2(10\text{KH}_z) \\ &= 20\text{KH}_z ,\end{aligned}$$

and the sampling interval, T , is

$$\begin{aligned}T &= 1/f_s = \frac{1}{20\text{KH}_z} \\ &= 50\mu \text{ sec.} .\end{aligned}$$

We want the filter to have a cutoff frequency, ω_c , of 1KH_z , with a rejection frequency, ω_r , of 1.2KH_z . In addition, the filter is to have a power gain between 0^z (100% for $H(j\omega)$) and -0.7dB (92.2%) from 0 to 1KH_z and a power gain down to at least -10dB (32%) at 1.2KH_z .

Using Equations 11a and 11b, ω_c and ω_r are transformed to

$$\begin{aligned}\omega_c' &= \tan\left[\frac{\omega_c T}{2}\right] \\ &= \tan\left[\frac{2\pi(1\text{K})(50\mu)}{2}\right] \\ &= \tan [157.0796\text{m rad}] \\ \omega_c' &= 0.1583844 , \\ \omega_r' &= \tan\left[\frac{\omega_r T}{2}\right] \\ &= \tan\left[\frac{2\pi(1.2\text{K})(50\mu)}{2}\right]\end{aligned}$$

$$= \tan [188.4956 \text{m rad}]$$

$$\omega_r' = 0.1907602 \quad .$$

The next step is to design the analog filter using ω_c' and ω_r' . If the minimum passband gain is -0.7dB at ω_c' , then from Equations 1b and 2a,

$$10 \log_{10} |H(j\omega)|^2 = 10 \log_{10} \frac{1}{1+\epsilon^2} = -0.7\text{dB} \quad .$$

Solving for ϵ ,

$$\epsilon = 0.41821 \quad .$$

From Equations 1b and 2b, and with a maximum stopband gain of -10dB at ω_r' ,

$$10 \log_{10} |H(j\omega)|^2 = 10 \log_{10} \frac{1}{1+\lambda^2} = -10.0\text{dB} \quad .$$

Solving for λ ,

$$\lambda = 3 \quad .$$

Having solved for ω_c' , ω_r' , ϵ , and λ , and using Equation 5, the order N of the filter is

$$N \geq \frac{\log (\lambda/\epsilon)}{\log (\omega_r'/\omega_c')}$$

$$N = 10.59391 \quad .$$

For simplicity of this paper, we will let $N = 10$. Therefore, referring to Equations 8 and 6, the transfer function of the analog filter is

$$H(S) = \frac{S_1 S_2 \dots S_{10}}{(S-S_1)(S-S_2) \dots (S-S_{10})} \quad ,$$

where,

$$S_n = \omega_c' \epsilon^{-1/N} e^{j\pi(2n+N-1)/2N} \quad ; \quad n=1,2,\dots,N$$

$$= 0.1728116 e^{j\pi(2n+9)/20}; n = 1, 2, \dots, 10.$$

Finally, using Equation 9 to translate $H(S)$ into $\tilde{H}(Z)$

$$\tilde{H}(Z) = \frac{S_1 S_2 \dots S_{10} (Z+1)^{10}}{\left[(1-S_1)Z - (1+S_1) \right] \dots \left[(1-S_{10})Z - (1+S_{10}) \right]}$$

with S_1 through S_{10} defined by S_n above. The power gain of this digital filter can be foundⁿ by substituting $e^{j\omega T}$ for Z and finding the squared magnitude. $\tilde{H}(Z)$ is the desired Z -transfer function.

The digital transfer function $\tilde{H}(Z)$ can be realized conveniently in a cascade form. Note that S_n and S_{11-n} are complex conjugates where,

$$S_n = R e^{j\theta_n}; R = \omega_c \epsilon^{-1/10}; \theta_n = \theta_{11-n} = \left(\frac{2n+9}{20} \right) \pi,$$

and

$$S_{11-n} = R e^{-j\theta_n}. \quad \text{Factoring } \tilde{H}(Z) \text{ into five parts,}$$

$$\tilde{H}(Z) = \tilde{H}_1(Z) \tilde{H}_2(Z) \tilde{H}_3(Z) \tilde{H}_4(Z) \tilde{H}_5(Z),$$

where,

$$\begin{aligned} \tilde{H}_n(Z) &= \frac{G_m(Z)}{V_m(Z)} = \frac{S_n S_{11-n} (Z+1)^2}{\left[(1-S_n)Z - (1+S_n) \right] \left[(1-S_{11-n})Z - (1+S_{11-n}) \right]} \\ &= \frac{R^2 (Z+1)^2}{\left[(1-R e^{j\theta_n})Z - (1+R e^{j\theta_n}) \right] \left[(1-R e^{-j\theta_n})Z - (1+R e^{-j\theta_n}) \right]} \\ &= \frac{R^2 (Z^2 + 2Z + 1)}{(1+R^2 - 2R \cos \theta_n) Z^2 - 2(1-R^2)Z + (1+R^2 + 2R \cos \theta_n)}, \end{aligned}$$

for $n = 1, 2, \dots, 5$. From the definition of the Z -transform (1,2), it follows that

$$V_m(Z) = \sum_m v_m(mT) Z^{-m},$$

$$G_m(Z) = \sum_m g_m(mT) Z^{-m},$$

where $V_m(Z)$ is the input generated by the Sample and Hold circuit, $G_m(Z)$ is the output from $\tilde{H}_n(Z)$, v_m and g_m are the DFT's of $V_m(Z)$ and $G_m(Z)$, where it is understood that the summation is over all non-negative values of m (m is the sample number).

The realization of $\tilde{H}_n(Z)$ (in the time domain) is diagrammed in Figures 4a and 4b. From the figures, the difference equations relating the input, $v_m(mT)$, to the output, $g_m(mT)$, are

$$\chi^0(n-1) = R^2 v_m(mT) - (1+R^2+2RC_n) g_m(mT) , \quad (12a)$$

$$\chi'(n-1) = 2R^2 v_m(mT) + \chi^0(n-1) + 2(1-R^2) g_m(mT) , \quad (12b)$$

and

$$g_{m,n}(mT) = \left(\frac{1}{1+R^2-2RC_n} \right) (R^2 v_m(mT) + \chi'(n-1)) , \quad (12c)$$

where, the importance of these difference equations lie in the fact that the digital filter operates by calculating values given by the difference equations. These equations are programmed into the S2815 digital filter chip (3) to perform in real time, the multiplications and additions of signal samples and coefficients required to evaluate the above equations for each successive sample of the input, $v_m(mT)$.

$g_{m,5}(mT)$ is then sent to the S2815 FFT chip for real time spectral computations (refer to "Digital Signal Processing System" and "Discussion" sections).

DISCUSSION

The digital signal processing system (Figure 1) consisted of a Sample and Hold circuit, an Analog to Digital converter, a Digital Filter, a Fast Fourier Transform, and a 16-bit microprocessor.

The Sample and Hold circuit provides stair-step output waveforms for continuous-time signal input waveforms. The stair-step waveforms play a central role in the analysis of digital filters and of sample-data systems in general. A basic entity of the Sample and Hold circuit or in any analysis of digital signal processing is the Discrete Fourier Transform (1,2). It is generally applicable whenever samples of a continuous function are involved. It bears the same relation

OVERALL $H(Z)$:

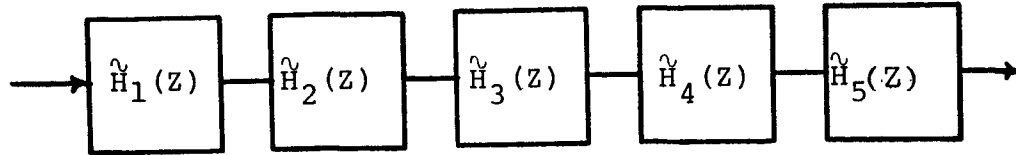


Figure 4a. Cascade of the digital Butterworth filter; $N=10$

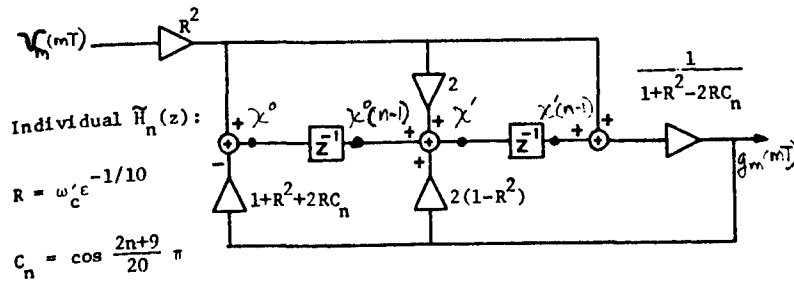


Figure 4b. Realization of $\tilde{H}_n(Z)$

to the digital system that the Fourier Transform bears to the analog system. The Discrete Fourier Transform can be an approximation to the Fourier Integral, Fourier Transform, and most important, to the Sampling Theorem (1,2). Any FFT synthesizing performed in the analog world can also be performed by the DFT in the digital world.

The Analog to Digital converter digitizes the waveform samples (DFT's) from the Sample and Hold circuit and provides input to the digital filter.

The digital filtering will be implemented by a S2815 Digital Filter/Utility Peripheral chip. The digital filter is a digital machine that performs the filtering process by the numerical evaluation of the linear difference equations (Equations 12a, 12b, and 12c) in real time under program control. In most cases, the design of a digital filter involves determining a digital (Z-domain) transfer function having the desired frequency characteristics. This digital transfer function can often be obtained in a straightforward manner (refer to "Designing A Butterworth Digital Filter" section) from an appropriate analog (S-domain) transfer function (refer to "Butterworth Analog Filter" section). A mathematical relation known as the bilinear transformation (refer to "Digital Filters by The Bilinear Transformation" section) proves in many cases (1,2) to be an especially effective tool for converting an analog transfer function into a useful digital transfer function that can be realized as a digital filter in a straightforward manner.

A S2814A Fast Fourier chip will accept the Discrete Fourier Transform data from the digital filter chip and convert it to spectral data. The FFT provides a means for efficient real time computations of the DFT.

The above system is interfaced and controlled by a 16-bit microprocessor.

The real test of the above discussion lies in a hardware implementation of the digital processing system.

CONCLUSIONS AND RECOMMENDATIONS

This paper presented a study on the application of digital signal processing techniques to a short range FM-CW radar system. The study investigated the application of these techniques to functions that traditionally was done by analog circuitry.

The study considered only the Lowpass filter and transformed it to a digital Lowpass filter. With this filter design and rational transformation techniques (very similar to the bilinear transformation), the digital design can be expanded to Highpass, Bandpass, and Bandstop digital filter development. An area for further investigation is to develop and apply these concepts to the short range radar system.

The study showed that with the use of the bilinear transformation, the Butterworth analog filter can be transformed into an applicable digital filter. However, studies should be made to consider the Impulse Invariant transformation and other analog filter types (Chebyshev Type 1, Chebyshev Type 2, Elliptic) for the optimum filter characteristics.

Emphasis must be placed on the completion of the hardware phase of this study. This involves the usage of VLSI chips and microprocessors in place of their analog equivalent. The system, operating in real time, can provide information for data comparison, system modification, and provide a means of investigating areas for further studies. In addition, an analysis can be made to determine the characteristic parameter that correlates spectral data to range.

REFERENCES

1. Oppenheim, A. V., Schafer, R. W., Digital Signal Processing, Prentice-Hall, Inc., 1975
2. Rabiner, L. R., Gold, B., Theory and Applications of Digital Signal Processing, Prentice-Hall, Inc., 1975
3. Advanced Product Description, S2815 Digital Filter/Utility Peripheral, American Microsystems, Inc., Santa Clara, Ca., 1982
4. Advanced Product Description, S2814A Fast Fourier Transformer, American Microsystem, Inc., Santa Clara, Ca., 1982

NASA/ASEE SUMMER FACULTY RESEARCH FELLOWSHIP PROGRAM

MARSHALL SPACE FLIGHT CENTER
THE UNIVERSITY OF ALABAMA

SPIN AND GRAVITATION

Prepared By: John R. Ray
Academic Rank: Professor
University and Department: Clemson University
Department of Physics
and Astronomy
NASA/MSFC: Space Sciences Laboratory
Division: Space Physics Division
Branch: Cryogenic Physics Branch
MSFC Counterpart: Peter Eby
Larry L. Smalley
Date: August 6, 1982
Contract No.: NASA-NGT-01-002-099
The University of Alabama

SPIN AND GRAVITATION

by

John R. Ray

Professor of Physics and Astronomy
Clemson University
Clemson, South Carolina 29631

ABSTRACT

Much work has been done to understand the role of spin angular momentum in gravitational theories. The equation of motion for the spin in general relativity is the basis for the NASA/Stanford gyroscope experiment. This experiment will give us accurate experimental data on the behavior of spin in a gravitational field. Thus, it is important to carry out a very careful and thorough theoretical study of spin in gravitational theories. Using the results from these studies we can formulate specific questions that the gyroscope data will be able to answer. In general relativity this experiment tests a whole complex of ideas which are centered around the question of the treatment of spinning matter in the theory. To discuss the experiment in terms of the so called PPN parameters is really an oversimplification since these parameters do not contain information about different spin equations of motion, or theories that are very much removed from general relativity. [One can prove (Lovelock's theorems) that given the Riemannian structure of general relativity, the field equations are unique.] Thus, in order to put the gyroscope data to maximum use we need to consider theories that are not so closely related to general relativity. One such theory is the Einstein-Cartan theory.

This theory is also interesting because the spin plays an important role in the theory. The basic goal of our work this summer concentrated on the study of macroscopic spin in the Einstein-Cartan theory. New results obtained include: The introduction of torsion into the variational principle for a perfect fluid; a new variational principle for dealing with spinning matter in general relativity; the combination of these two results into a Einstein-Cartan variational principle involving spin and torsion. This variational principle should give a clearer view of the behavior of spin in the Einstein-Cartan theory and allow us to deduce the implications of the gyroscope experiment in this theory.

INTRODUCTION

Our study of spin in gravitational theories makes use of variational principles to arrive at a complete and consistent theory. The study is broken down into two papers. The first of these papers "Perfect Fluids in the Einstein-Cartan Theory" shows how torsion is introduced into the standard perfect fluid variational principle. The second paper gives a new treatment of spin in general relativity. We are presently working on combining these two lines of work to arrive at a description of spin in the Einstein-Cartan theory.

PERFECT FLUIDS IN THE EINSTEIN-CARTAN THEORY

John R. Ray[†]
Space Sciences Laboratory
Marshall Space Flight Center, AL 35812

and

Department of Physics and Astronomy
Clemson University, Clemson, SC 29631

and

Larry L. Smalley
Space Sciences Laboratory
Marshall Space Flight Center, AL 35812

and

Department of Physics
University of Alabama in Huntsville, Huntsville, AL 35899

[†]NASA/ASEE Summer Faculty Fellow

ABSTRACT

We extend the fundamental variational principle for a perfect fluid in general relativity so that it applies to the metric-torsion Einstein-Cartan theory. We thereby deduce field equations for a perfect fluid in the Einstein-Cartan theory.

I. INTRODUCTION

In the Einstein-Cartan(E-C) theory, spinning matter gives a contribution to the gravitational field which is not included in general relativity. The mathematical change engendered by the Einstein-Cartan theory is that the gravitational field is now described by a metric-torsion geometry. Motivation for the E-C theory is contained in the review article by Hehl et al.¹ which also contains many references.

Although most of the discussion of the E-C theory involves the relationship between gravitation and elementary particles, it is possible that the E-C theory, if correct, would be important in some extreme astrophysical and cosmological problems. Here, we have in mind something like the collapse of a spinning star or an early universe with spin. In this paper, we derive and examine a set of equations which describes a macroscopic-perfect fluid in the E-C theory. These equations are derived starting from the fundamental variational principle for a perfect fluid in general relativity.² A preliminary study in this direction was started by Tunyak.³ In Section II, we give a brief review of Ref. (2) and in Section III we present the results for the E-C theory. In the conclusions, we discuss these results and suggest directions for future investigation of this theory.

II. GENERAL RELATIVITY VARIATIONAL PRINCIPLE

Here, we briefly review the variational principle presented in Ref. (2) in order to compare with later results. The Lagrangian density for the gravity-perfect fluid system has the form:

$$\mathcal{L} = c_1 \sqrt{-g} R + c^{-1} \sqrt{-g} F(\rho, s) + \lambda_1 \sqrt{-g} (g_{ik} U^i U^k + c^2) + \sqrt{-g} \lambda_2 (\rho U^i)_{;i} + \sqrt{-g} \lambda_3 X_{,i} U^i + \sqrt{-g} \lambda_4 s_{,i} U^i, \quad (2.1)$$

where we refer the reader to Ref. (2) for the definitions of the above symbols. The quantities λ_1 , λ_2 , λ_3 , and λ_4 are Lagrange multipliers which are introduced in order to impose the constraints in (2.1). The quantities to be varied in (2.1) are ρ , s , X , U^i , g_{ij} , and λ_i , $i = 1, 2, 3, 4$. The variation leads, after simplifications, to the following set of equations:

$$\delta \rho : \lambda_{2,i} U^i = c^{-1} F_\rho, \quad (2.2a)$$

$$\delta s : (\sqrt{-g} \lambda_4 U^i)_{,i} = c^{-1} \sqrt{-g} F_s, \quad (2.2b)$$

$$\delta X : (\sqrt{-g} \lambda_3 U^i)_{,i} = 0, \quad (2.2c)$$

$$\delta U^i : \lambda_1 = -\rho F_\rho / (2c^2), \quad (2.2d)$$

and

$$U^i = -\frac{c^3}{\rho F_\rho} [\rho \lambda_{2,i} - \lambda_3 X_{,i} - \lambda_4 s_{,i}], \quad (2.2e)$$

$$\delta g_{ij} : G^{ij} = \frac{1}{2c_1} [-c^{-2} \rho F_\rho U^i U^j + (F - \rho F_\rho) g^{ij}], \quad (2.2f)$$

$$\delta \lambda_1 : g_{ij} U^i U^j + c^2 = 0, \quad (2.2g)$$

$$\delta \lambda_2 : (\rho U^i)_{;i} = 0, \quad (2.2h)$$

$$\delta \lambda_3 : X_{,i} U^i = 0, \quad (2.2i)$$

$$\delta \lambda_4 : s_{,i} U^i = 0, \quad (2.2j)$$

where the subscripts on F indicate derivatives with respect to the rest density ρ , $F_\rho = \partial F / \partial \rho$, and rest specific entropy s , $F_s = \partial F / \partial s$. The combined first and second law of thermodynamics may be written in the form²

$$Tds = d\varepsilon + pd(1/\rho) \quad . \quad (2.3)$$

The function $F(\rho, s)$ had the form²

$$F = -\rho(c^2 + \varepsilon) \quad . \quad (2.4)$$

When this form for F is used in (2.2e) along with (2.3) we obtain for (2.2f)

$$G^{ij} = \frac{1}{2c} [\rho(1 + \varepsilon/c^2 + P/(\rho c^2))U^i U^j + pg^{ij}] \quad , \quad (2.5)$$

which are Einstein's field equation for a perfect fluid with energy-momentum tensor

$$T^{ij} = \rho(1 + \varepsilon/c^2 + P/(\rho c^2))U^i U^j + pg^{ij} \quad . \quad (2.6)$$

Note as a by-product of this variational principle the four-velocity of the fluid U_i is found to have six-potential representation expressed by (2.2e). In other variational principles for the perfect fluid (see Ref. (2) for references to this subject) this six-potential form of the four-velocity is assumed a priori and hence, these other variational principles are not as general as the one discussed here. For further discussions and references to fluid variational principles in general relativity see Ref. (4). Our variational principle has also been used by Goenner to study fluids in his nonminimal coupling gravitational theories.⁵

III. EINSTEIN-CARTAN VARIATIONAL PRINCIPLE

Here, we start with the same Lagrangian density (2.1) but extend it to the E-C theory where the affine connection Γ_{ij}^k has the form:

$$\Gamma_{ij}^k = \{^k_{ij}\} + S_{ij}{}^k - S_j{}^k{}_i + S^k{}_{ij} \quad (3.1)$$

$S_{ij}{}^k$ is the torsion tensor

$$S_{ij}{}^k = \Gamma_{[ij]}^k \quad (3.2)$$

and $\{^k_{ij}\}$ the Christoffel connection of general relativity. In the E-C theory, the gravitational field is described by the metric g_{ij} and the torsion $S_{ij}{}^k$, which are independent geometrical quantities. To extend the Lagrangian density (2.1) to the Einstein-Cartan theory, we replace the general relativistic connection $\{^k_{ij}\}$ appearing in (2.1) by the connection Γ_{ij}^k . This makes a change in the scalar curvature term $c_1 \sqrt{-g} R$ and in the conservation of mass term, $\sqrt{-g} \lambda_2 (\rho U^i)_{;i}$, which now has the form:

$$\sqrt{-g} \lambda_2 (\rho U^i)_{;i} = \sqrt{-g} \lambda_2 [(\rho U^i)_{,i} + \{^i_{ik}\} \rho U^k - 2S_{ki}{}^i \rho U^k] \quad (3.3)$$

The other terms in (2.1) are not altered. We note that the extension of the fluid Lagrangian density from general relativity to the Einstein-Cartan theory is not unique.⁶ We shall return to this point later.

The variables in our variational principle are the previous variables plus the torsion $S_{ij}{}^k$. The variations after simplifications yield:

$$\delta \rho \quad : \quad (\lambda_{2,i} + 2S_{ik}{}^k \lambda_2) U^i = c^{-1} F_\rho \quad (3.4a)$$

$$\delta s \quad : \quad (\sqrt{-g} \lambda_4 U^i)_{,i} = c^{-1} \sqrt{-g} F_s \quad (3.4b)$$

$$\delta X : (\sqrt{-g} \lambda_3 U^i)_{,i} = 0 \quad , \quad (3.4c)$$

$$\delta U^i : \lambda_1 = -\rho F_\rho / (2c^3) \quad , \quad (3.4d)$$

and

$$U_i = -\frac{-c^3}{\rho F_\rho} [\rho \lambda_{2,i} - \lambda_3 X_{,i} - \lambda_4 s_{,i} + 2\lambda_2 \rho S_{ik}^k] \quad , \quad (3.4e)$$

$$\delta S_{ij}^k : \lambda_2 = \frac{8c_1}{3\rho c^2} S_{jk}^k U^j \quad (3.4f)$$

and

$$S_{ij}^k = \frac{1}{3c^2} S_{rn}^n U^r (U_j \delta_i^k - U_i \delta_j^k) \quad , \quad (3.4g)$$

$$\begin{aligned} \delta g_{ij} : G^{ij} &= \frac{1}{2c} [-c^{-2} \rho F_\rho U^i U^j + (F - \rho F_\rho) g^{ij}] \\ + \frac{4}{3c^2} & \left[\frac{2}{c^2} (S_{rk}^k U^r)^2 U^i U^j + (S_{rk}^k U^r)^2 g^{ij} \right] \quad , \quad (3.4h) \end{aligned}$$

$$\delta \lambda_1 : g_{ij} U^i U^j + c^2 = 0 \quad , \quad (3.4i)$$

$$\delta \lambda_2 : (\rho U^i)_{,i} = 0 \quad , \quad (3.4j)$$

$$\delta \lambda_3 : X_{,i} U^i = 0 \quad , \quad (3.4k)$$

$$\delta \lambda_4 : s_{,k} U^i = 0 \quad . \quad (3.4l)$$

where G^{ij} in (3.4h) is defined in terms of the Christoffel symbols as in Ref. (7). We note first that if we set the torsion S_{ij}^k to zero, the results (3.4) pass back into the results for general relativity (2.2), as of course they must [an exception is (3.4f) which we discuss later].

The torsion equation (3.4g) obtains by solving the field equation $\delta \mathcal{L} / \delta S_{ij}^k = 0$ which is

$$\begin{aligned} S_k^{ij} - S_{ij}^k + S_{ij}^i + 2(\delta_k^j S_r^{ir} - \delta_k^i S_r^{jr}) \\ = -\frac{1}{c} \lambda_2 \rho U^i \delta_k^j \quad (3.5) \end{aligned}$$

The left hand side of this equation comes from varying $\sqrt{-g} R$ while the right hand side, which is the spin energy potential μ_k^{ij} , comes from the remaining terms in $\overset{\cup}{\mathcal{C}}$. Here, we are using the results in Aldersley.⁷ Solving (3.5) yields (3.4f) and (3.4g). Note that here the Lagrange multiplier λ_2 is given in terms of the torsion S_{ij}^k . In order to avoid confusion, we point out that in the limit as $S_{ij}^k \rightarrow 0$, λ_2 does not go to zero since the equation (3.5) used to derive (3.4f) is not then valid.

The variations with respect to g_{ij} yield the equations:

$$\begin{aligned}
 G^{ij} &= \frac{1}{2} g^{ij} (K_m^{mr} K_{nr}^n - K_n^{mr} K_{mr}^n) \\
 &\quad - K_r^{ri} K_m^{mj} + K^{nri} K_{rn}^j \\
 &= \frac{1}{2c_1} [-c^{-2} \rho F_\rho U^i U^j + (F - \rho F_\rho) g^{ij}]
 \end{aligned}
 \tag{3.6}$$

where K_i^{jk} is the contortion tensor

$$K_i^{jk} = -S_i^{jk} + S^{jk}_i - S^k_{ij}
 \tag{3.7}$$

As before, the terms on the left-hand side of (3.6) arise from $\sqrt{-g} R$, while the terms on the right-hand side of (3.6) arise from the other terms in $\overset{\cup}{\mathcal{C}}$.

Using previous results in (3.6) leads to the final form of the δg_{ij} field equation:

$$\begin{aligned}
 G^{ij} &= \frac{1}{2c_1} [\rho(c^2 + \epsilon/c^2 + p/(\rho c^2)) U^i U^j + p g^{ij}] \\
 &\quad + \frac{4}{3c^2} \left[\frac{2}{c^2} (S_{rk}^{kUr})^2 U^i U^j + (S_{rk}^{kUr})^2 g^{ij} \right]
 \end{aligned}
 \tag{3.8}$$

The similarity in (3.8) between terms involving torsion and those not involving torsion is obvious. Note that the right-hand side of

Equation (3.6) is the perfect fluid symmetric energy-momentum tensor; whereas the right-hand side of equation (3.8) is the effective energy-momentum tensor given for comparison with the Einstein case.

IV. CONCLUSIONS

We have extended the variational principle of Ref. (2) to the E-C theory. This theory leads to the field equations (3.4) which are a direct extension of general relativity. As mentioned earlier, these results are not a unique extension.⁶ The reason for this is that one may add divergences to the Lagrangian density in general relativity and then extend the resulting Lagrangian density. For example, in our case, the term $\sqrt{-g} \lambda_{2,i} (\rho U^i)_{;i}$ leads to the same results in general relativity as $-\sqrt{-g} \rho U^i \lambda_{2,i}$ (the two terms differ by a divergence). The extension of these two cases to the Einstein-Cartan theory leads to different theories, and there does not seem to be a way to choose one form over the other. Our only reason for using the given form in (2.1) is that we do not see any reason to add on arbitrary divergences to the basic Lagrangian density of Ref. (2). If we did use the term $-\sqrt{-g} \rho U^i \lambda_{2,i}$, then the torsion equation would have no source, the right-hand side of (3.5) would be zero, and we would be back to general relativity with no torsion.

We have not attempted to find solutions to the field equations (3.4). This is, of course, an important topic for future work. There has been considerable effort devoted to finding solutions to the E-C field equations.² The fluid solutions so discussed have not used equations (3.4) but have used a heuristic approach to introduce fluids into the E-C theory. It would seem that our theory is the simplest extension of the description of fluids in the E-C theory. This same opinion was

first expressed by Tunyak.³ Alternatively, the dynamical effects of spin could be brought directly into the energy-momentum tensor through modification of the thermodynamic law (2.3). The resulting linkup of spin through the equation for the spin potential, (3.5), and hence the torsion, would shed new light on the connection between spin and torsion. We are presently investigating this more fundamental approach.

As a final point, we note from (3.4e) that the four-velocity does not retain the six-potential form (2.2e) in the E-C theory. Thus, the variational principles which assume a six-potential form for the four-velocity will not work for the E-C theory, and one is forced to use the variational principle as given in Ref. (2).

REFERENCES

1. F. W. Hehl, P. von der Heyde, and G. D. Kerlich, Rev. Mod. Phys. 48, 393, 1976.
2. J. R. Ray, J. Math. Phys. 13, 1451, 1972.
3. V. N. Tunyak, Dokl. Akad. Novk. BSSR 19, 599, 1975.
4. J. R. Ray, "Perfect Fluids in General Relativity," MSFC SSL Preprint #81-113, 1981.
5. H. Goenner, Z. Naturforsch. 31a, 1451, 1976.
6. L. L. Smalley, Phys. Rev. D 18, 3896, 1978.
7. S. J. Aldersley, Gen. Rel. Grav. 8, 397, 1977.

SPINNING FLUIDS IN GENERAL RELATIVITY

John R. Ray[†]

Space Sciences Laboratory
Marshall Space Flight Center, AL 35812

and

Department of Physics and Astronomy
Clemson University
Clemson, SC 29631

and

Larry L. Smalley
Space Sciences Laboratory
Marshall Space Flight Center, AL 35812

and

Department of Physics
University of Alabama in Huntsville
Huntsville, AL 35899

[†]NASA/ASEE Summer Faculty Fellow

ABSTRACT

We derive the equations of motion for a fluid with intrinsic spin in general relativity from a variational principle. Our theory is a direct extension of the theory of nonspinning fluids in special relativity.

I. INTRODUCTION

The treatment of spin angular momentum in special and general relativity has received quite a bit of attention. A recent paper by Bailey¹ contains many earlier references. In this paper we consider the field equations in general relativity for a continuous medium with internal spin. It is thought that the spin of "particles"; photogalaxies, turbulent eddies or primeval black holes could play an important role in the early epochs of the universe.^{2,3}

A special relativistic variational principle for a spinning fluid in special relativity was formulated some time ago by Halbwach.⁴ Halbwach's variational principle gives the special relativistic Weyssenhoff theory for a spinning fluid. Here we generalize Halbwach's variational principle to general relativity and obtain the Einstein equations for a fluid with internal spin. It would also be possible for us to treat the Einstein-Maxwell theory in a medium with spin. This would be the general relativistic version of the Lorentz dielectric theory and has been studied in References (1-3). For simplicity we shall just treat the gravitational case.

II. HALBWACHS VARIATIONAL PRINCIPLE

Halbwach⁴ introduces an orthornormal tetrad of vectors a^μ_i which he uses in his variational principle. Here $\mu, \nu, \dots = 1, 2, 3, 4$ label the tetrad vectors and $i, j, \dots = 1, 2, 3, 4$ label the components. These vectors satisfy

$$a^\mu_i a_{\mu j} = g_{ij} \quad , \quad (2.1)$$

$$a_{\mu i} a^i_\nu = \eta_{\mu\nu} \quad , \quad (2.2)$$

where g_{ij} is the spacetime metric and $\eta_{\mu\nu}$ the Minkowski metric.

The vector a^4_i is related to the Eulerian four-velocity of the fluid via

$$a^4_i = U_i/c \quad , \quad (2.3)$$

whereas the spin density of the fluid is described by

$$S_{ij} = \rho\kappa(a^1_i a^2_j - a^1_j a^2_i) \quad . \quad (2.4)$$

In Equation (2.4) ρ is the conserved density of the fluid

$$(\rho U^i)_{;i} = 0 \quad , \quad (2.5)$$

where the semicolon denotes covariant differentiation and κ is a scalar function proportional to the magnitude of the spin of the fluid and has the dimensions of angular momentum per unit rest mass. With the choices (2.3) and (2.4) the spin vector S_i of the fluid is associated with a^3_i

$$S_i = \frac{1}{2c} \eta_{ijkl} S^{jk} U^l = \rho\kappa a^3_i \quad . \quad (2.6)$$

The fluid also satisfies the auxiliary condition

$$S_{ij} U^j = 0 \quad . \quad (2.7)$$

The angular velocity of the spin vector is given by

$$\begin{aligned} W_{ij} &= \frac{1}{2} (\dot{a}^\mu_i a_{\mu j} - a^\mu_i \dot{a}_{\mu j}) \\ &= \dot{a}^\mu_i a_{\mu j} \quad , \end{aligned} \quad (2.8)$$

where the dot denotes differentiation along the fluid flow

$$\dot{a}^\mu_i = a^\mu_{i;j} U^j \quad . \quad (2.9)$$

The spin kinetic energy density of the fluid has the form

$$\begin{aligned} T &= \frac{1}{2} S_{ij} W^{ij} \\ &= -\rho\kappa a^1_i a^{2i}_{;j} U^j \quad , \end{aligned} \quad (2.10)$$

This form for the kinetic energy density was given earlier by Unal and Vigier⁵ who also briefly discuss Halbwach's variational principle. The Lagrangian density for the spinning fluid has the form

$$\begin{aligned}
 \mathcal{L}_f = & \sqrt{-g} F(\rho, s)/c - \sqrt{-g} \rho \kappa a^1_{;i} a^{2i}_{;j} U^j / c \\
 & + \sqrt{-g} \lambda_1 (g_{ij} U^i U^j + c^2) + \sqrt{-g} \lambda_2 (\rho U^i)_{;i} \\
 & + \sqrt{-g} \lambda_3 X_{;j} U^i + \sqrt{-g} \lambda_4 s_{;i} U^i \\
 & + \lambda^{\mu\nu} (g_{ij} a^i_{;\mu} a^j_{;\nu} - \eta_{\mu\nu}) \quad , \quad (2.11)
 \end{aligned}$$

where $\lambda_1, \lambda_2, \lambda_3, \lambda_4$, and $\lambda^{\mu\nu}$ are Lagrange multipliers associated with the various constraints. We have generalized Halbwach's variational principle by considering the entropy s and the Lin particle identity variable X . $F(\rho, s)$ is the energy density of the fluid. The Lagrangian density for a nonspinning fluid, defined here by $a^{1i} = a^{2i} = a^{3i} = 0$, has been discussed in detail in Reference (6) to which we refer the reader.

The variables to be varied in \mathcal{L}_f are $U^i, \rho, a^{\mu i}, s, X, \lambda_1, \lambda_2, \lambda_3$, and $\lambda^{\mu\nu}$. Since a^{3i} does not appear in the kinetic energy terms in \mathcal{L}_f it may be left out of the variations without changing the final results. Also the constraint for λ^{44} is the same as that for λ_1 and these may be combined together into one term whose Lagrange multiplier we call λ_1 . Thus, we have the final form of the Lagrangian density for the fluid

$$\begin{aligned}
\mathcal{L}_f = & \sqrt{-g} F/c - \sqrt{-g} \rho \kappa a^1_i a^{2i}_{;j} U^j/c \\
& + \sqrt{-g} \lambda_1 (g_{ij} U^i U^j + c^2) + \sqrt{-g} \lambda_2 (\rho U^i)_{;i} \\
& + \sqrt{-g} \lambda_3 X_{,i} U^i + \sqrt{-g} \lambda_4 s_{,i} U^i \\
& + \sqrt{-g} \lambda^{11} (g_{ij} a^{1i} a^{1j} - 1) + \sqrt{-g} \lambda^{22} (g_{ij} a^{2i} a^{2j} - 1) \\
& + 2\sqrt{-g} \lambda^{12} g_{ij} a^{1i} a^{2j} + 2\sqrt{-g} \lambda^{14} g_{ij} a^{1i} U^j/c \\
& + 2\sqrt{-g} \lambda^{24} g_{ij} a^{2i} U^j/c \quad . \quad (2.12)
\end{aligned}$$

The spin density of the fluid S_{ij} is defined by

$$\sqrt{-g} S_{ij} = c \left(a^v_i \frac{\partial \mathcal{L}_f}{\partial \dot{a}^v_j} - a^v_j \frac{\partial \mathcal{L}_f}{\partial \dot{a}^v_i} \right) \quad , \quad (2.13)$$

which gives when applied to (2.12)

$$S_{ij} = \rho \kappa (a^1_i a^2_j - a^1_j a^2_i) \quad , \quad (2.14)$$

from which we see that our earlier definition of the spin density is consistent with the field theory definition (2.13). The spin of a fluid particle is given by '7

$$s_{ij} = \kappa (a^1_i a^2_j - a^1_j a^2_i) \quad , \quad (2.15)$$

from which we see that the spin of a fluid particle is proportional to the scalar $\kappa(x)$. Later we shall prove that κ is constant along the flow for our problem.

An equivalent way to introduce spin in field theory is via the Belinfante-Rosenfeld spin tensor τ_{ij}^k

$$\sqrt{-g} \tau_{ij}^k = c F_{ij}^{rs} \frac{\partial \mathcal{L}_f}{\partial \psi^r_{;k}} \psi_s \quad . \quad (2.16)$$

For the spin variables $\psi^r \rightarrow a^{2r}$,

$$F_{ij}^{rs} = \left(\delta_j^r \delta_i^s - \delta_i^r \delta_j^s \right) \text{ and we obtain}$$

$$\tau_{ij}^k = S_{ij} U^k \quad ,$$

the Weyssenhoff convective form for the spin tensor. In Sec. III we carry out the variations that yield the equations of motion for a spinning fluid in general relativity.

III. FIELD EQUATIONS

In order to generalize Halbwach's Lagrangian density \mathcal{L}_f (2.12) to general relativity we only need add on the gravitational Lagrangian density $\sqrt{-g} R$, where R is the scalar curvature. This gives the total Lagrangian density

$$= c_1 \sqrt{-g} R + \mathcal{L}_f \quad (3.1)$$

where $c_1 = c^3/(16\pi k)$ and k is the gravitational constant.

We now outline the results of varying the action associated with (3.1) with respect to the field variables a^{1i} , $a^{2i} U^i$, ρ , s , X and g_{ij} . For more details of this calculation see References (4,6).

Variations with respect to a^{1i} and a^{2i} leads to the field equations

$$- \rho \kappa \dot{a}^2_i / c + 2 \lambda^{11} a_{1i} + 2 \lambda^{12} a_{2i} + 2 \lambda^{14} U_i / c = 0 \quad , \quad (3.2)$$

and

$$\rho \kappa \dot{a}^1_i / c + \kappa \rho \dot{a}^1_i / c + 2 \lambda^{22} a_{2i} + 2 \lambda^{12} a_{1i} + 2 \lambda^{24} U_i / c = 0 \quad . \quad (3.3)$$

Dotting (3.2) with U_i leads to

$$\begin{aligned} \lambda^{14} &= - \rho \kappa \dot{a}^2_i U^i / (2c^2) \\ &= \rho \kappa a^2_i \dot{U}^i / (2c^2) \quad . \end{aligned} \quad (3.4)$$

The same procedure applied to (3.3) yeilds

$$\lambda^{24} = - \rho \kappa a^1_i \dot{U}^i / (2c^2) \quad . \quad (3.5)$$

Next if we dot (3.2) with a^{1i} we obtain

$$\dot{\lambda}^{11} = \rho \kappa a^{1i} \dot{a}^2_i / (2c) \quad , \quad (3.6)$$

whereas the same procedure applied to (3.3) produces

$$\lambda^{12} = - \dot{\kappa} \rho / (2c) \quad . \quad (3.7)$$

If we now dot (3.2) with a^{2i} we obtain

$$\lambda^{12} = 0 \quad , \quad (3.8)$$

which with (3.7) gives

$$\dot{\kappa} = 0 \quad . \quad (3.9)$$

This means that the magnitude of the spin is constant along the flow. Dotting (3.3) with a^{2i} gives

$$\begin{aligned} \lambda^{22} &= \kappa \rho a^{1i} \dot{a}^2_i / (2c) \\ &= \lambda^{11} \quad . \end{aligned} \quad (3.10)$$

If we next multiply (3.2) by a^{1j} , (3.3) by a^{2j} , add the resulting equations we find

$$\begin{aligned} &\rho \kappa (\dot{a}^1_i a^2_j - \dot{a}^2_i a^1_j) / c + 2\lambda^{11} (a_{2i} a^2_j + a_{1i} a^1_j) \\ &- \rho \kappa a^2_j a^1_k \dot{U}^k_i / c^3 + \rho \kappa a^1_j a^2_k \dot{U}^k_i / c^3 = 0 \quad . \end{aligned} \quad (3.11)$$

If we switch i and j and subtract the resulting equation from (3.11) we arrive at the equation of motion for the spin

$$\dot{s}_{ij} + s_{jk} U_i \dot{U}^k / c^2 + s_{ki} U_j \dot{U}^k / c^2 = 0 \quad . \quad (3.12)$$

This equation expresses the fact that the spin undergoes Fermi-Walker transport along the four-velocity U^i and has also been derived in general relativity by Mathisson⁸ and Papapetrou⁹ using considerably different methods than those employed here.

The variation with respect to the density ρ leads to

$$\lambda_{2,k} U^k + \kappa a^1_i \dot{a}^2_i / c = F_\rho / c \quad , \quad (3.13)$$

where $F_\rho = \partial F / \partial \rho$.

Variation with respect to the four-velocity leads to the expression

$$2\lambda_1 U_i + \lambda_3 X_{,i} + \lambda_4 s_{,i} - \rho \kappa a^1_k a^{2k}_{;i}/c + \rho s_{ik} \dot{U}^k/c^3 - \lambda_{2,i} \rho = 0 \quad (3.14)$$

In a nonspinning fluid $a^{1i} = a^{2i} = a^{3i} = 0$ and (3.14) gives the important velocity potential (Clebsch) representation of the four-velocity. For the case of spinning matter the four-velocity does not come out in a potential representation. If we dot (3.14) with U^i and employ (3.13) we find

$$\lambda_1 = -\rho F_\rho / (2c^3) \quad (3.15)$$

This is the same solution for λ_1 as for a nonspinning fluid. The variation with respect to X and s lead to simple equations which are the same as in Reference (6). Since we shall not need these equations explicitly in this paper we shall not write them out. If one were to differentiate (3.14) to obtain an expression for \dot{U}_i then these equations would have to be used to eliminate λ_3 and λ_4 from the resulting equation, which would be the generalized Euler equation.

The variation with respect to the metric g_{ik} leads to the Einstein equations for a fluid with internal spin. This calculation is somewhat tedious and we give only the final result which is

$$G^{ik} = \frac{8\pi\kappa}{c^4} \left(-\rho F_\rho U^i U^k / c^2 + g^{ik} (F - \rho F_\rho) + \frac{1}{c^2} \rho U^{(i} s^{k)} \dot{U}_l + \rho U^{(k} s^{i)} j_{;j} + [\rho U^{(k}]_{;j} s^{i)j} \right) \quad (3.16)$$

where the brackets () around indices imply symmetrization

$A_{(ik)} = \frac{1}{2}(A_{ik} + A_{ki})$. If we make use of the form for $F(\rho, s)$,

$F = -\rho(c^2 + \epsilon)$, where ϵ is the rest specific internal energy then (3.16) can be written

$$G^{ik} = \frac{8\pi k}{c^4} \left(\rho(1 + \epsilon/c^2 + P/\rho c^2)U^i U^k + g^{ik} P + \frac{1}{c^2} \rho U^{(i} S^{k)\ell} \dot{U}_\ell + \rho U^{(k} S^{i)j}{}_{;j} + [\rho U^{(k} S^{i)j}{}_{;j}] \right), \quad (3.17)$$

where P is the pressure $P = \rho^2 \left(\frac{\partial \epsilon}{\partial \rho} \right)_S$. The first two terms on the right hand side of (3.17) give the energy-momentum tensor for a fluid without spin

$$T_F^{ik} = \rho(1 + \epsilon/c^2 + P/\rho c^2)U^i U^k + g^{ik} P. \quad (3.18)$$

The remaining terms on the right hand side of (3.17) give the intrinsic spin contribution to the energy-momentum tensor

$$T_S^{ik} = \frac{1}{c^2} \rho U^{(i} S^{k)\ell} \dot{U}_\ell + \rho U^{(k} S^{i)j}{}_{;j} + [\rho U^{(k} S^{i)j}{}_{;j}] \quad (3.19)$$

As far as we are aware this spin contribution to the energy-momentum tensor has not been derived previously although it is a straight-forward generalization of Halbwach's treatment of spinning fluids in special relativity. The symmetric energy momentum tensor T^{ik}

$$T^{ik} = T_F^{ik} + T_S^{ik}, \quad (3.20)$$

satisfies the Bianchi identities $T^{ik}{}_{;k} = 0$ which lead to the relativistic Euler equation for the fluid.

IV. CONCLUSIONS

We have given a detailed treatment of the equations for a spinning fluid in general relativity. Our procedure was to follow Halbwach's introduction of a tetrad to represent both the spin density and four-velocity of the fluid. We were then able

to formulate an Eulerian variational principle, which is correct in special relativity, to derive the form of the Einstein equations. The resulting energy momentum tensor for a spinning fluid is given in (3.17) and has apparently not been previously derived. An alternative derivation of T^{ik} is to calculate the canonical energy momentum tensor t^i_k

$$\sqrt{-g} t^i_k = c \delta_i^k \mathcal{L}_f - c \frac{\partial \mathcal{L}_f}{\partial \psi^r_{;k}} \psi^r_{;i} \quad (4.1)$$

which has the form

$$t^i_k = \delta_i^k F - \delta_i^k \rho \kappa a^1_j \dot{a}^{2j} + \rho \kappa a^1_r a^{2r}_{;i} U^k - c \lambda_2 \rho U^k_{;i} - c \lambda_2 U^k_{\rho,i} - c \lambda_3 U^k_{X,i} - c \lambda_4 U^k_{S,i} \quad (4.2)$$

and then to carry out the Belinfante-Rosenfeld symmetrization procedure. This again, of course, leads to the symmetric energy momentum tensor given in (3.17).

The equations of motion of the fluid also follow from the variational principle. The spin s_{ij} undergoes Fermi-Walker transport and the generalized Euler equations follow from the Bianchi identities or by differentiating U_i in (3.14) and using the other equations from the variational principle.

There are several suggested applications of the results of this paper. First one could study exact solutions to the Einstein equations for a spinning fluid in general relativity. In a cosmological context the galaxies would be the spinning particles of the fluid. The study of such a fluid of galaxies in various anisotropic Bianchi universes would give an indication of how the spin interacts gravitationally with the anisotropy of the space-time. Israel² studied a simple model in a Bianchi I universe

and found that spin induces a Lense-Thirring rotation of the local inertial axis relative to the directions along the spin of the fluid.

The work by Bailey and Israel References (1-3) is the closest to that presented in this paper. Their study does not make use of an explicit Lagrangian density, as we have done, but derives various relations which must be satisfied via Noether's theorem. Their theory is therefore valid for arbitrary Lagrangian densities. Our work, on the other hand, deals with a specific Lagrangian density that describes spinning fluids in special relativity. The work by Israel and Bailey also allows for other fields to be present in the Lagrangian density. This we can do by adding more terms to describe these fields. For example, Maxwell's theory and the generalized Lorentz dielectric model would be a first step.

Our formulation of spinning fluids in general relativity can also be used to investigate the equations of motion for a spinning fluid in the Einstein-Cartan metric-torsion theory. In a preliminary study¹⁰ we have investigated the introduction of torsion into the fluid variational principle of Reference (6). We can now extend this work using the results of this paper to give the first variational derivation of the equations of motion for a spinning fluid in the Einstein-Cartan theory. We are presently studying this problem.

REFERENCES

1. I. Bailey, *Ann. Phys.* 119 76 (1979).
2. W. Israel, *Lett. Nuovo Cim.* 7 860 (1973).
3. I. Bailey and W. Israel, *Commun. Math. Phys.* 42 65 (1975).
4. F. Halbwach, *Theorie Relativiste Des Fluides A Spin*
(Gauthier-Villars, Paris 1960).
5. B. C. Unal and J.-P. Vigiier, *Comptes Rendus*, 245 1890 (1957).
6. J. R. Ray, *J. Math. Phys.* 13 1451 (1972).
7. F. Halbwach, *Prog. Theo. Phys.* 24 291 (1960).
8. M. Mathisson, *Acta Phys. Pol.* 6, 163 (1937).
9. A. Papapetrou, *Proc. R. Soc. London* A209, 248 (1951).
10. J. R. Ray and L. L. Smalley, "Perfect Fluids in the Einstein-Cartan Theory" NASA/MSFC preprint, 1982.

ACKNOWLEDGEMENTS

I have enjoyed the hospitality of everyone I came in contact with at the MSFC. In particular I thank Pete Eby, Larry Smalley and Al Fennelly for interesting discussions.

1982

NASA/ASEE SUMMER FACULTY RESEARCH FELLOWSHIP PROGRAM

MARSHALL SPACE FLIGHT CENTER
THE UNIVERSITY OF ALABAMA

AUTONOMOUS ONBOARD CREW OPERATIONS:
A REVIEW AND DEVELOPMENTAL APPROACH

Prepared By: Jon G. Rogers Ph.D.
Academic Rank: Professor
University and Department: The University of Alabama Huntsville
Department of Psychology

NASA/MSFC

(Laboratory) Systems Analysis and Integration
(Division) Operations Development
(Branch) Man/Systems Integration

MSFC Counterpart: Harry H. Watters
Date: August 2, 1982
Contract No.: NGT-01-002-099 (University of Alabama)

AUTONOMOUS ONBOARD CREW OPERATIONS:
A REVIEW AND DEVELOPMENTAL APPROACH

by

Jon G. Rogers Ph.D.
Professor of Psychology
University of Alabama Huntsville
Huntsville, Alabama

Abstract

A basic goal for Space Platform and Space Shuttle is to move toward autonomous onboard crew operations. Autonomous operations is regarded as a necessary milestone in the development of future mission profiles for several reasons. Reliance on ground control to perform certain critical mission support functions delimits the flexibility of mission profile planning. Further, the involvement of ground control centers manned 24 hours a day for the duration of a mission is expensive and inefficient.

A review of the literature generated by an intercenter Mission Approach and Consolidation Team and their contractors was performed to obtain background information on the development of autonomous operations concepts for future missions. These concepts were compared to the Space Platform Operations Concepts and Requirements as they are now formulated.

The Boeing 757/767 flight management system was examined to determine the relevance for transfer of the developmental approach and technology to the performance of the crew operations function. In specific, the engine indications and crew alerting system were studied to determine the relevance of this display for the performance of crew operations onboard the vehicle.

It was concluded that the developmental approach and technology utilized in the aeronautics industry would be appropriate for development of an autonomous operations concept for Space Platform. It is recommended that a high level NASA Administrative Directive be issued to implement the autonomy objectives formulated by the Mission Approach and Consolidation Team over a decade ago.

Acknowledgments

I would like to express my deep appreciation to the following NASA personnel who spent hours of their time in support of this project:

Harry H. Watters, EL15

Michael Naumcheff, EL12

Jonathan B. Haussler, EL12

The cooperation and generosity of Mr. Peter M. Morton, Senior Project Engineer for the 757 flight deck; Mr. B. C. Hainline, Chief Engineer, Systems Technology; and Mr. T. R. Cole, Boeing Public Relations for making available a great deal of information, some of which is proprietary so that this project could be completed.

LIST OF FIGURES

<u>Figure No.</u>	<u>Title</u>	<u>Page</u>
1	Four Computer Complex for the Performance of Onboard Functions	
2	Space Platform Free-Flyer Operation Concepts	
3	Functions Performed in SPCC	
4	Functions Performed in PCC	
5	Functions Performed in DHF	
6	Alert Information Flow	
7	Configuration of the Flight Control System for the 757/767	
8	Location of EICAS on Display Panel	
9	LICAS in Full Alert Format with Alert Messages	

INTRODUCTION AND OBJECTIVES

A basic program goal for Space Platform and Space Shuttle is to move toward autonomous onboard crew operations. Autonomous operations is regarded as a necessary milestone in the development of future mission profiles for several reasons. Reliance on ground control to perform certain mission support functions delimits the flexibility of mission profile planning. Further, the involvement of ground control centers manned 24 hours a day for the duration of a mission is expensive and inefficient.

It is the objective of this study to examine the issue of autonomous onboard crew operation using the following approach:

- o Review the literature generated by a NASA intercenter Mission Approach and Consolidation Team
- o Compare the Consolidation Team's recommendation in relationship to the proposed Space Platform Operations Concepts and Requirements
- o Select a sample function (crew operations) to be converted to onboard operation
- o Review an existing and parallel autonomous system (Boeing 757/767 Flight Management System) to determine relevance for transfer of the developmental approach and technology to Space Platform
- o Review a specific existing alerting system (EICAS) in terms of its usefulness to Space Platform
- o Recommend an approach to implementation of an autonomous operations concept.

BACKGROUND

In 1969, an intercenter Mission Approach and Consolidation Team was convened to establish a simplified mission operations approach for the 1975-85 era. A major milestone to be addressed by all three centers was to define new operations concepts for future programs which have a greater reliance upon onboard system self-monitoring and decreased dependence on ground control. The steering committee assigned the initial study to eight study teams. Team three addressed the issue of autonomy and partitioned their study into two phases. In phase one the objectives were to identify and examine the types of onboard systems that could be implemented in the area of checkout, flight control, and data handling to provide spacecraft autonomy. Complexity, weight volume, power requirements, and costs were to be identified. In phase two, existing ground-based support of missions versus the use of onboard autonomous systems was studied. The proper future mix between the two extreme approaches was to be determined.

Several ground control functions were examined. For example, the checkout functions were examined. Checkout involves the monitoring of critical parameters in such subsystems as the environmental control system, the guidance and navigation system, the propulsion system, the data management system, the altitude control system, and the experiments. Flight control functions were evaluated. Flight control includes routine guidance and navigation, rendezvous navigation, mission timeline generation, and contingency planning. The experiment data handling function includes real time requirements, preprocessing and data compaction, and storage of data for use onboard or for transmittal to the ground. The astronaut health and skill maintenance function includes monitoring of vital signs and any data processing necessary to determine crew health status. The technical feasibility of performing these functions onboard was assessed and trade-offs were evaluated.

In approaching these evaluations it was necessary first to determine mission assessment objectives and an operational philosophy. Mission assessment objectives were developed and emphasized crew safety, information transfer, cost and efficiency, and the development of a configuration management system. Other objectives included nominal and off-nominal system performance evaluation, resupply and refurbishment requirements, mission scheduling, operational techniques for future missions, and development and long term biomedical data requirements for follow-on phases and future programs.

The operational philosophy specifically developed an approach to autonomy which is very likely valid in the current time frame. First it was necessary to develop criteria for onboard/ground tradeoffs which involved the development of ground and onboard functional requirements and necessary interfaces. These criteria were determined for the development and shakedown phase as well as the operational phase. The final step was the development of ground and onboard computational requirements. Several interface assumptions are noteworthy. It was assumed that a central ground facility would be used for communication and data interface between space vehicles and the ground with continuous voice and emergency data communications capability. Software was to be developed and checked out on the ground and be interchangeable; i.e., flight software can be operated on the ground.

The results of the analysis suggested that a variety of functions should be transferred onboard. These functions included the following: crew safety, operations, cost and efficiency, information transfer, resupply and refurbishment, scheduling, configuration management, performance evaluation, and information dissemination to follow-on missions and programs. The onboard operations and crew safety function displayed all parameter outputs to the lowest replaceable unit on demand, performed automatic checkout and diagnostics on all systems continuously, predicted trends leading to systems degradation and failure, and displayed the current configuration of all systems with the capability to reprogram software and logic limits as required.

Because of the cost incurred from placing and sustaining man in space, efficiency of operations is synonymous with cost. As a result, several cost and efficiency functions are important. Systems must be designed to facilitate maintenance which implies onboard trend and diagnostic capability. Hardware and software should be compatible to as many systems as feasible. The onboard system should be capable of selective data processing in order to eliminate wasted time, materials, and payload capability. Redundant data should be removed onboard where feasible.

The information transfer function requires a Data Management System (DMS) capable of transmitting variable formats, with appropriate parameter identification to facilitate onboard and ground display and storage. The DMS should provide data routine and sequencing control. The DMS should have adequate storage capacity and computational speed to handle nominal and off-nominal operations. Onboard and ground computers should be compatible for data interface, i.e., one computer can input to another without any software changes.

It is assumed that long term scheduling will be performed on the ground and short term scheduling onboard. The onboard scheduling system displays functions to be performed with appropriate timeline information and suggested priorities. It can be updated by the crew or the ground and is capable of scheduling maintenance and changing timelines based on unforeseen events. The system stores and is capable of producing the previous days schedule on demand.

The configuration management system displays the current configuration of any system or experiment on demand as well as current available inventories. Current maintenance status of systems can be displayed on demand.

The performance evaluation function provides the capability of all system outputs to be evaluated to the line replaceable unit level. Trend data are generated for critical systems to detect impending failures and consumables expenditure. Logic limits and trend data can be updated. Data storage is provided so as to assess trends.

The major objective of the information dissemination function is the rapid dissemination of data to the general public and scientific community and involves voice communication with the ground, the transmission of scientific and applications data to the ground, and some onboard selected data processing. The data collected from each mission expands the baseline data base and determines requirements and operational procedures for future missions.

The resupply and refurbishment function requires maintaining inventory control of all expendibles and consumables. Constant surveillance of current onboard configurations is required to provide input to the maintenance and refurbishment cycle. Trend data are used to predict refurbishment requirements. Required maintenance and replacement of equipment are flagged and programmed into the mission timeline. A warning system is required which notifies the crew of impending problems before they actually occur.

Computer requirements for these systems were presented for Space Station, a Mars Mission, Space Shuttle, and a Lunar Orbital Space Base. These requirements are too lengthy to be presented here and were based on state-of-the-art computers in the late 1960's (i.e., IBM SAH No. 1169-234, 236, and 242). Current computer technology would provide the capability of implementing the 1969 four computer complex onboard. This concept is shown in Figure 1.

The trade-off study for the Space Station concluded that all operational and experiment assessment will be done onboard. The ground was to maintain: documentation control, configuration and change control, documentation data bank, and performance data relevant to system evaluation as it applies to future long duration missions. It was assumed that the bulk of these data would be accumulated onboard and transported to the ground by means of the Shuttle.

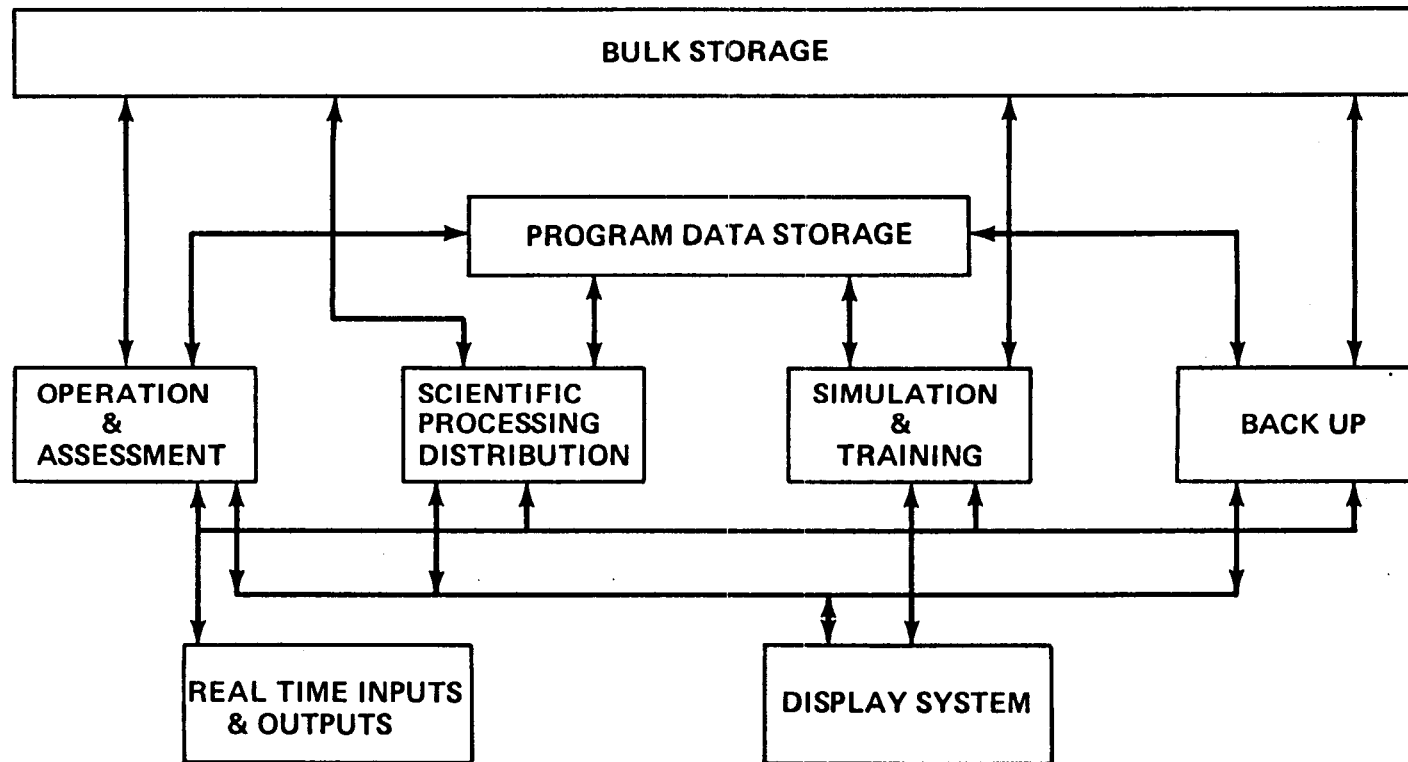


FIGURE 1. THIS CONCEPT DEFINES A 4-COMPUTER COMPLEX WITH ALL COMPUTERS BEING IDENTICAL & HAVING ACCESS TO THE SAME RANDOM STORAGE & BULK STORAGE TO PERFORM ONBOARD FUNCTIONS

SPACE PLATFORM OPERATIONS CONCEPTS AND REQUIREMENTS

The operations concept for Space Platform in the free flyer mode is diagramed in figure 2. This concept shows the Data Handling Facility (DHF) Space Platform Control Center (SPPO), and the Payload Control Center (PCC) as separate entities. As you can see in figure 2, all communications pass through the Tracking Data Relay Satellite System (TDRSS). This, of course, is consistent with the recommendation of the intercenter Mission Approach and Consolidation Team regarding a central ground facility. All commands to the Space Platform are generated in or pass through the SPCC. Downlink telemetry goes to the DHF for distribution, and multiple PCC's can be accommodated.

It is difficult to determine, from a review of the anticipated functions for each control center or facility, whether the specific recommendations of the Consolidation Team regarding onboard functions have been implemented (see figures 3, 4, and 5). Figure 3, for example, states that the SPCC will "monitor and control Space Platform subsystems operations and performance; generate and transmit real time and stored command messages; monitor and control resource envelopes; plan and schedule experiment operations; command experiment." With the SPCC and the PCC performing such a broad array of functions it is unclear if a discriminable step is being taken toward autonomy.

Had the Consolidation Team's recommendation regarding autonomy been implemented, experimental data would have been transferred to the ground by the Shuttle. The Space Platform operations concepts call for a large telemetry system requiring continuous monitoring.

Indeed it would appear that the concept of autonomy is not a visible part of the operational philosophy for Space Platform. The word autonomy is rarely used in the operations concept and requirements, and no list of functions for onboard operations is given. If the proposed operations concepts are implemented as proposed, the platform would basically be operated from the ground with the vehicle and crew continuing to be dependent upon the ground control centers for all major functions.

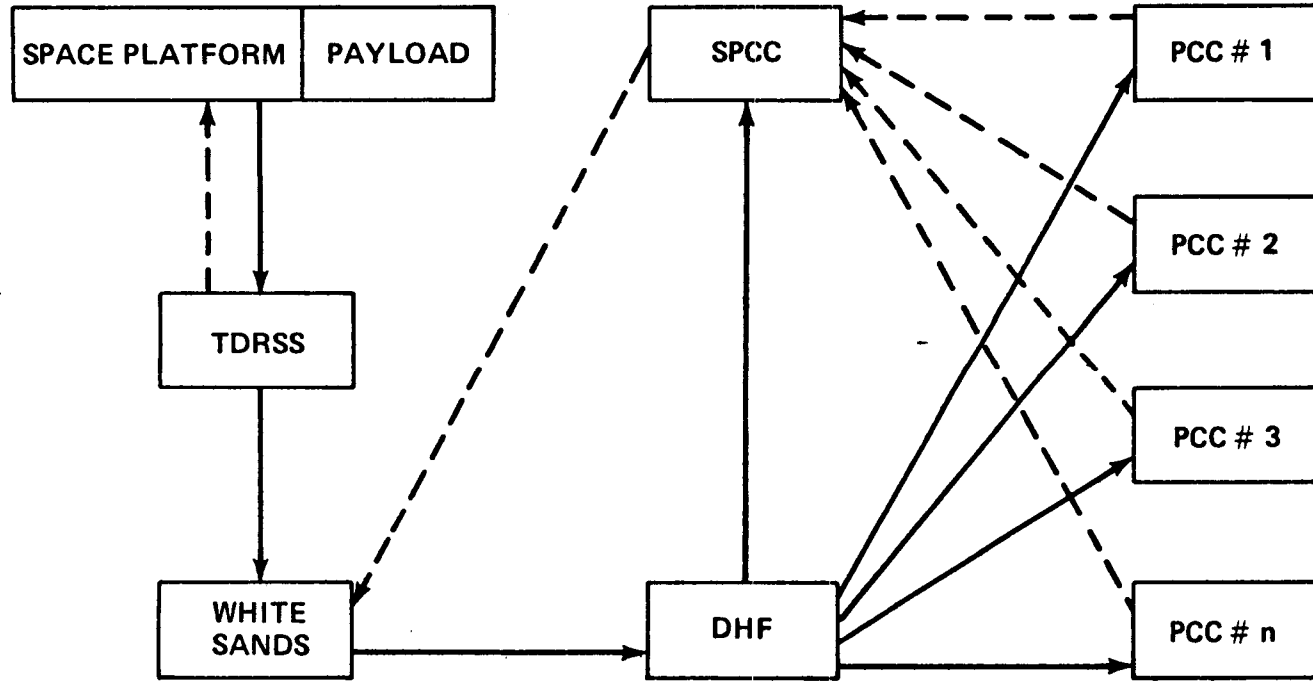


FIG. 2 SPACE PLATFORM FREE-FLYER OPERATIONS CONCEPT

- o RECEIVE, PROCESS, AND DISPLAY 50 KBPS TELEMETRY STREAM
- o MONITOR AND CONTROL SPACE PLATFORM SUBSYSTEMS OPERATION AND PERFORMANCE
- o STORE, RETRIEVE, AND PERFORM TREND ANALYSES ON HOUSEKEEPING DATA
- o GENERATE ORBIT ENVIRONMENT PREDICTION INFORMATION FOR SPACE PLATFORM
- o GENERATE AND TRANSMIT REAL TIME AND STORED COMMAND MESSAGES
- o COORDINATE NETWORK REQUIREMENTS AND SCHEDULES
- o MONITOR AND CONTROL RESOURCE USAGE BY EXPERIMENTS (AT PORT INTERFACE)
- o IMPLEMENT ONBOARD SOFTWARE FLIGHT PROGRAM CHANGES
- o MULTIPLEX SPACE PLATFORM AND EXPERIMENT COMMANDS AND EXERCISE SAFETY OVERVIEW FUNCTION
- o REBOOST TARGETING AND EXECUTION
- o SUBSYSTEM ANALYSIS

FIGURE 3 - FUNCTIONS PERFORMED IN SPCC

- RECEIVE, PROCESS, AND DISPLAY EXPERIMENT TELEMETRY STREAM
- MONITOR EXPERIMENT PERFORMANCE AND CONTROL EXPERIMENTS WITHIN PREDETERMINED RESOURCE ENVELOPES
- CAPTURE EXPERIMENT DATA, SCIENCE DATA ARCHIVING, PROCESSING, AND DISTRIBUTION
- PLAN AND SCHEDULE EXPERIMENT OPERATIONS
- COMMAND EXPERIMENTS
- FLIGHT GEOMETRY COMPUTATIONS
- HOUSEKEEPING DATA STORAGE AND TREND ANALYSES
- ONBOARD COMPUTER REPROGRAMMING

FIGURE 4 - FUNCTIONS PERFORMED IN THE PCC

- o RECEIVE AND MONITOR HIGH AND LOW RATE DOWNLINKS
- o SORT DOWNLINKS FOR TRANSMISSION TO PCC'S AND SPCC
- o PERFORM BUILT-IN SYSTEMS SELF-CHECK FUNCTIONS
 - PROVIDE RESULTS AND STATUS TO SPCC FOR MONITORING AND CONTROL FUNCTIONS
 - STATUS COULD BE PROVIDED TO PCC'S
- o RECEIVE RF LINK CONTROL/SETUP INFORMATION FROM SPCC
- o DISTRIBUTE GROUND COMPUTED EPHEMERIS DATA TO PCC'S

FIGURE 5 - FUNCTIONS TO BE PERFORMED IN THE DHF

OPERATIONS

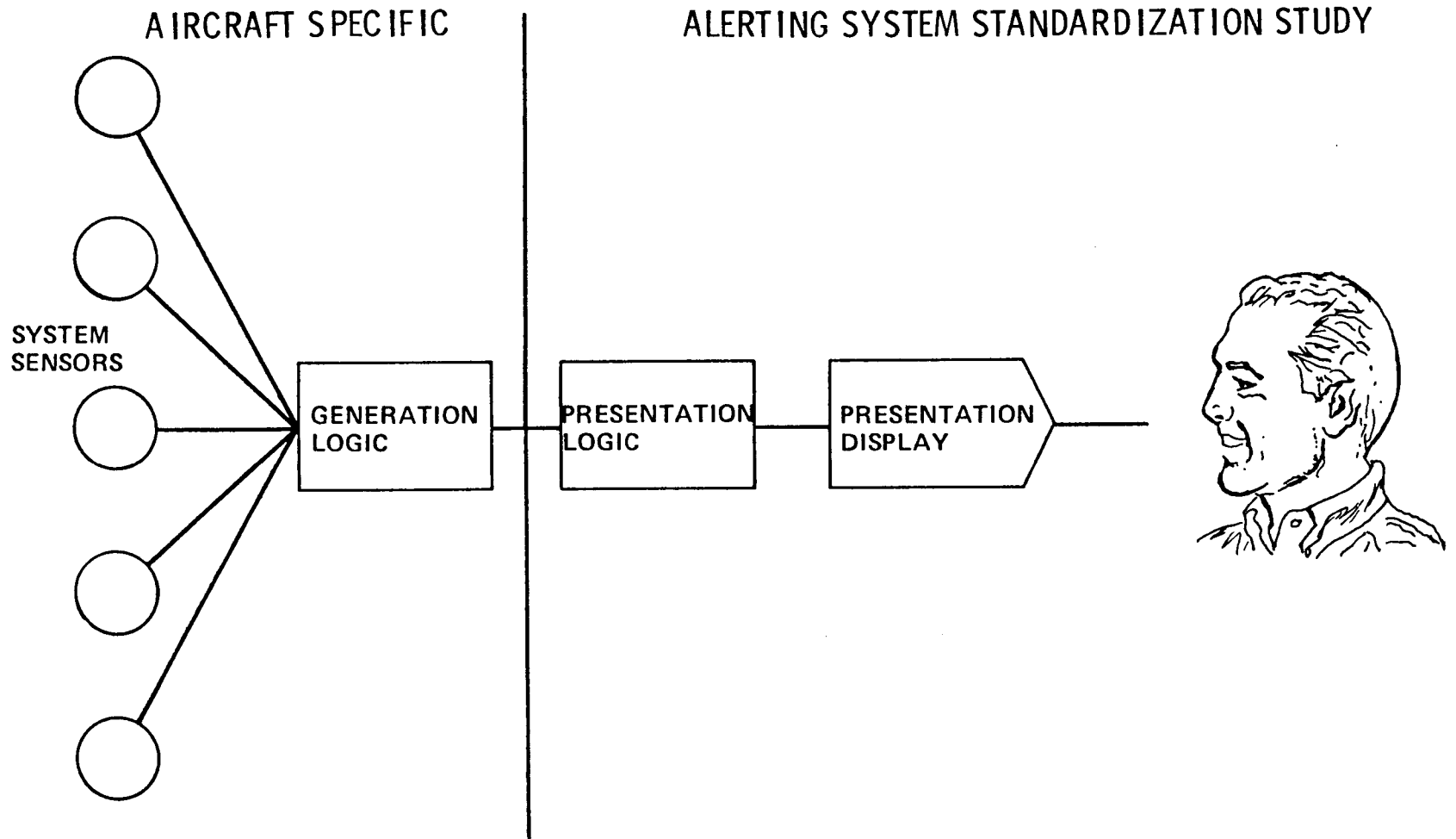
The consolidation team recommended that the crew operations functions be performed onboard. As noted earlier, to perform these functions it will be necessary to display all parameter outputs to the lowest replaceable unit on demand, perform automatic checkout and diagnostic functions on all systems continuously. Prediction trends will be generated which permit the study of any potential system degradation and failure. The system must display the current configuration of all systems with the capability to reprogram software and logic limits as required. For the purposes of this paper, this function will be examined in the light of current state-of-the-art technology in the aeronautic industry to determine if this technology is relevant to mission needs and objectives in the operational philosophy of the Space Platform, and additionally, to determine if it is feasible for the technology to be transferred to aerospace.

Over the past several years the Federal Aviation Administration (FAA) has conducted a comprehensive study of aircraft alerting systems. In the initial studies conducted in 1975, involving the development of an Independent Altitude Monitoring (IAM) concept in which sensor principles and control and display alerting methods for IAM systems were studied (Smith, 1975). The work evolved into a study of cockpit alerting systems problems. This program, a criteria study, included both an analytical review of the literature and also an experimental phase to build a stimuli response data base. The objectives of the first study included providing tabulation of the alerting methods and alerting requirements used on current commercial transport aircraft, developing a method for prioritizing alerting functions and providing recommendations for standardization of alerting functions/methods (Veitengrubes, J. E., et al., 1977 and Boricek, G. P., et al., 1977).

Figure 6 shows the Alert Information Flow beginning with system sensors which when activated feed into the generation logic. The generation logic performs the function of collecting the sensor data, analyzing it, and then feeding these inputs into the presentation logic. Depending on the criticality or priority of this input, the presentation logic determines in what form the information will be presented to the crew. The last step of the process is basically a human factors display problem. Previous studies (Cooper, 1977 and Veitengrubes et al., 1977) show that a discriminably unique audio, visual, or combination audio-visual presentation should be associated with each alert category. This is required so the crew can have rapid definition of a criticality/urgency of an alerting situation in order to take timely action.

A four level alerting system has become the standard in the aeronautical industry: warning - immediate corrective or compensatory crew action; caution - immediate crew awareness and subsequent crew action; advisory - crew awareness and subsequent or future crew action; and, information - flight deck indication, but not necessarily as part of the integrated alerting system. The system is clearly hierarchical, the higher the urgency level, the more alerting system components used to insure crew detection and appropriate response within required time limits (Berson, et al., 1981).

ALERT INFORMATION FLOW



XXXV-16

FIG. 6 FLOW OF ALERTING INFORMATION FROM SYSTEM SNESENSORS TO THE ATTENTION OF THE CREW

Warning alerts are the most critical, and as a result, all of the resources of the display system should be employed when such a condition exists. In a warning status condition, the crews' attention must be obtained and the display should inform them of the criticality, location, and nature of the problem. Research has shown that this requires the use of a red master visual alert, the alphanumeric message should be presented in red and located above the caution and advisory messages. A master aural sound should be used. If the warning is time critical the display should provide the crew appropriate guidance information. The visual and auditory display envelopes are critical for warning alerts and must be consistent with human factors findings regarding location, form, size, color, frequency range, loudness, etc. For example, intermittent, wavering sounds with low and high frequency components are labeled as warnings by line pilots (Boucek et al., 1980).

Caution alerts also involve master visual and aural alerts but specifically are programmed to be discriminably different from warnings. This can be accomplished by using different colored displays, aural cautions of different frequencies and intensities from warnings, and locating the cautions more to the periphery of the critical crew display envelope. Cautions are signaled by yellow color-coded displays and steady state midrange frequency sounds.

Alerting and informing functions for advisories are accomplished by means of an aural alert and visually displayed message. The message informs the crew of the nature and location of the alerting situation. Boucek, et al. (1980) found that a low frequency, single stroke sound was most often classified as an advisory alert by line pilots. Line pilots preferred use of a third color for alerts and did not want an aural component for this level even though they missed alerts without the aural component. The crews felt that master visual cautions and warnings and voice messages should be used only for situations requiring immediate crew awareness and are not required for advisory alerts.

The steps in the development of an alerting system for Space Platform would likely proceed along parallel lines to the development of new standards in the aeronautical field. The FAA program consisted of two major phases. Phase I objectives for the Aircraft Alerting Systems Criteria Study (Veitengrubes, et al., 1977 and Boucek, et al., 1977) were discussed above. Phase II (Boucek, et al., 1981 and Berson, et al., 1981) established aircraft alerting systems standards. Volume I presents results of a candidate system validation and a time-critical display evaluation. Volume II presents aircraft alerting systems design guidelines to promote standardization within the industry. These guidelines were substantiated by experimental as well as simulation data and reflect the views and opinions of commercial transport aircraft manufactures, certification authorities, airline operators, and pilots.

The approach taken by the FAA to update and improve the alerting systems was comprehensive, thorough, and permitted commercial transport manufacturers to incorporate the most recent developments in computer graphics in this alerting systems. This resulted in the development of more sophisticated alerting systems that are more reliable, have greater redundancy, consume less space and weight, are more versatile, and can be updated as technology continues to advance.

THE BOEING 757/767 FLIGHT MANAGEMENT SYSTEM (FMS)

The Boeing 757/767 FMS is of particular interest in evaluating the feasibility of Space Platform autonomy. Commercial transports fly with little reliance on ground control, and the 757/767 moves toward an even more efficient two-man crew eliminating the flight engineer. The design data and guidelines developed in the alerting system criteria and standardization studies are implemented in the FMS. Consequently, the Boeing FMS incorporates state-of-the-art digital technology, an automatic flight control system, and advanced electronic displays.

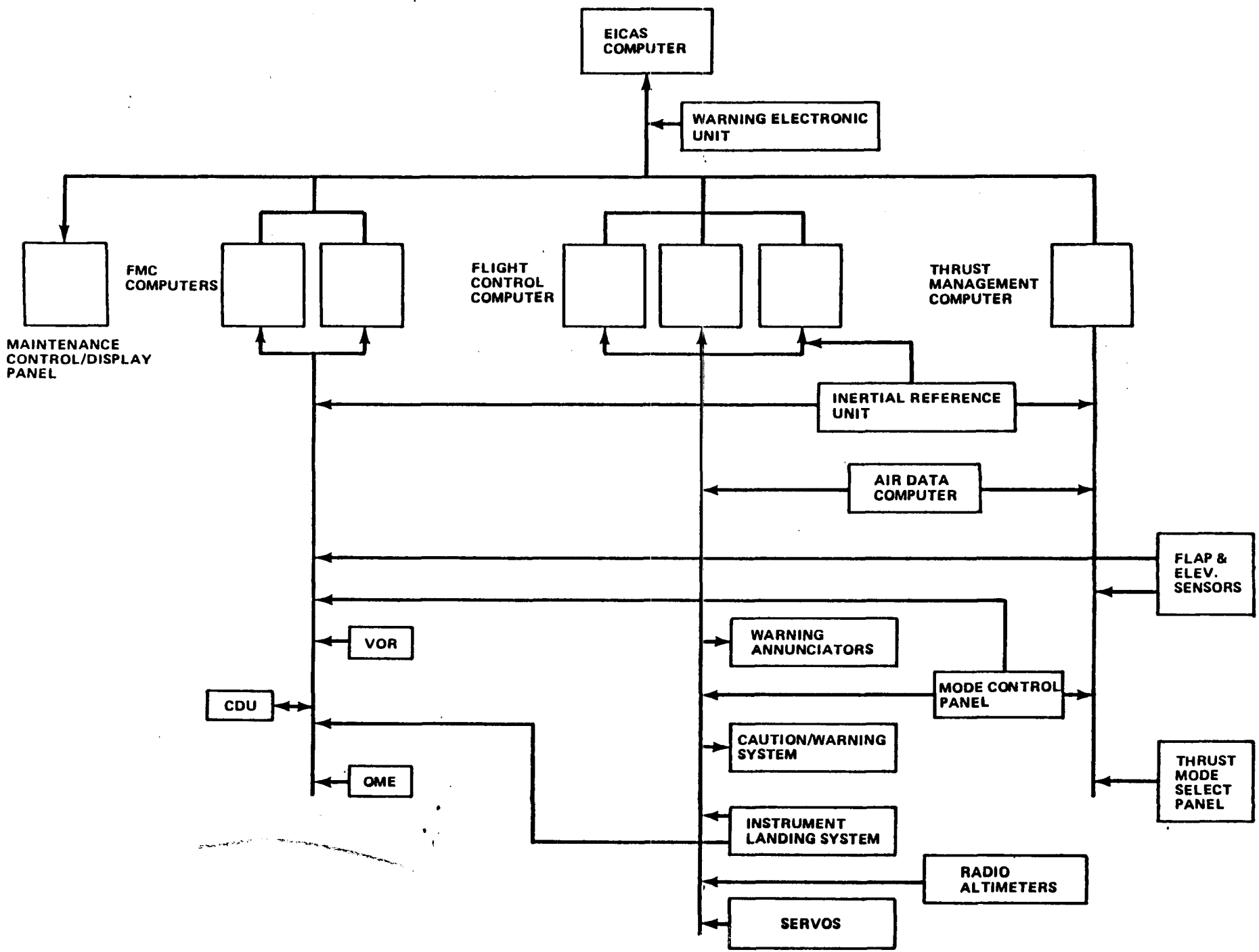
The 757/767 FMS, an integrated network of subsystems, i.e., digital technology, computers, microprocessors and electronic displays, perform four major functions: automatic flight control; performance management; navigation and guidance; advisory, caution and warning; and controls and displays. As noted in the Boeing document distributed to potential buyers of the 757/767:

The system assembles and stores the flight plan from crew generated flight progress, navigation, and performance data which are displayed to the pilot; issues guidance commands to the auto-pilot and/or flight director; issues control commands; and performs automatic fault detection, redundancy management, caution and warning annunciation, and maintenance data storage and display. The principal new capability provided by the FMS is continuous automatic navigation and inflight performance optimization (p. 22).

Digital technology advances have contributed substantially to the sophistication of the FMS. Digital systems afford a number of advantages over mechanical and analog systems. Maintenance costs are reduced by the greater reliability of the digital systems. Higher mean time between failures have been demonstrated in prototype systems. Built-in test equipment contributes to rapid fault isolation and replacement of line replaceable units. The FMS has reduced the crew workload affording the crew more time for in-flight planning and outside watch. The general configuration of the FMS can be seen in figure 7.

The FMS is the first operational application of the CRT displays as the primary flight instrument on a commercial airliner. Based on the FAA sponsored research, the displays present information to the crew for accurate and timely interpretation. Many of the data integration functions previously performed by the crew are now analyzed and integrated by a computer and presented to the crew in terms of the appropriate action to be taken.

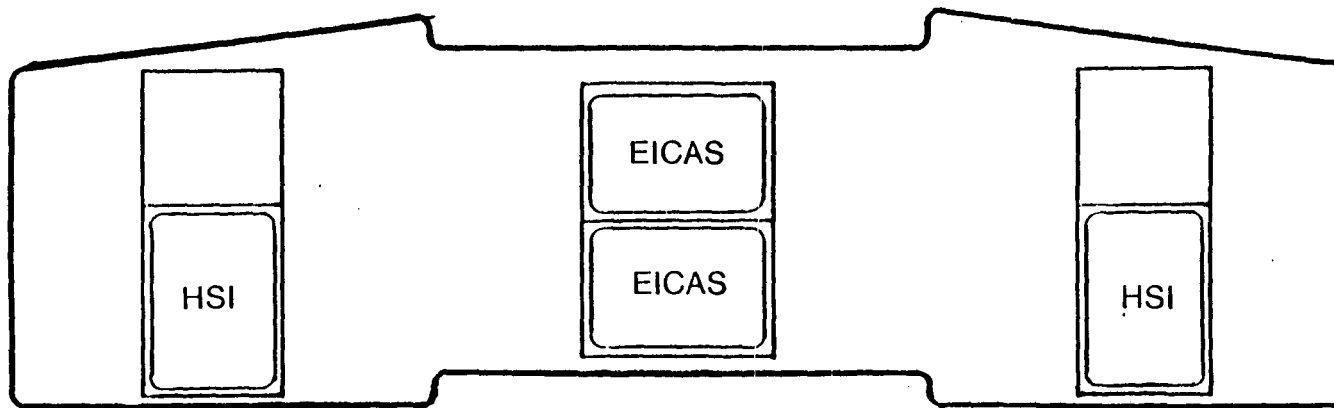
FIG. 7 CONFIGURATION OF THE FLIGHT MANAGEMENT SYSTEM FOR THE 757/767



XXXX-19

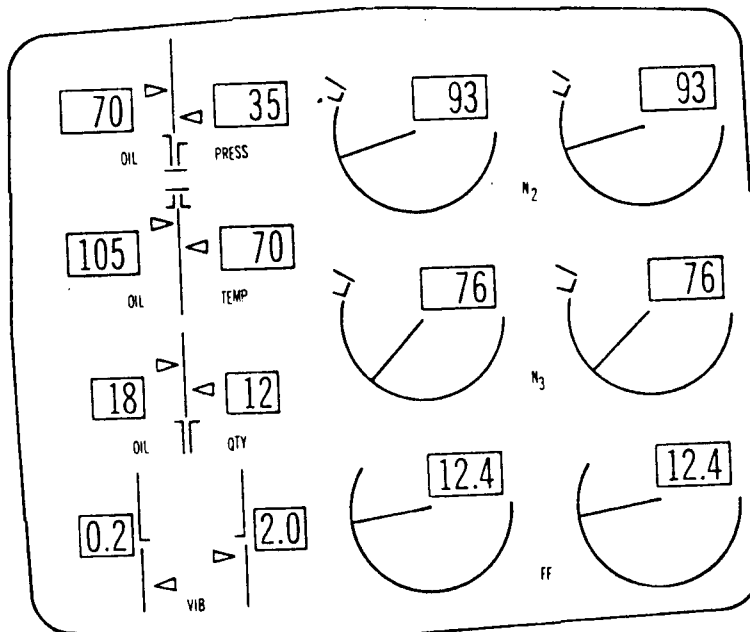
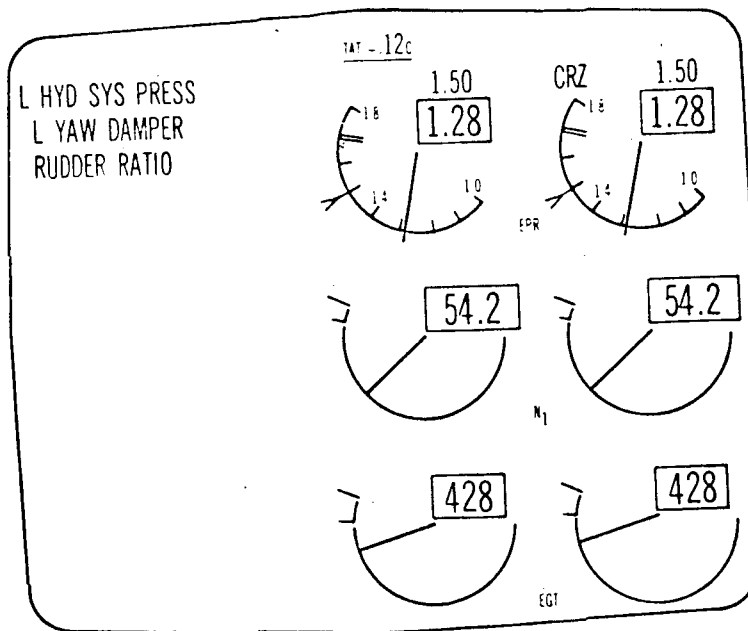
ENGINE INDICATION AND CREW ALERTING SYSTEM

Engine and system monitoring and the caution and warning functions are performed by the Engine Indication and Crew Alerting System (EICAS) which monitors 400 inputs and incorporates two color CRT displays to present graphic and alphanumeric indications and annunciations. The system is color coded and the CRT readout identifies the specific system fault and degree of urgency. Highest priority alerts are presented at the top with the most recent first. The EICAS continuously displays information needed for normal operation on the upper CRT. Out-of-tolerance systems are displayed in terms of their degree of urgency (i.e., warning, caution, or advisory) on a fixed area of one CRT. The system also has a status and maintenance mode (only operated on the ground). Figure 8 shows the location of the EICAS on the 767 display panel. Figure 9 shows the EICAS in full alert format with alert messages.



**EICAS uses HSI rotated 90°
(identical part number)**

Figure 8 - Locations of EICAS on Display Panel



**Full-Up Format
(With Alert Messages)**

Figure 9 - EICAS in Full Alert Format with Alert Messages

SPACE PLATFORM APPLICATIONS AND CONCLUSIONS

The goal of autonomous onboard crew operations appears to be attainable if a major high level commitment within the NASA organization is made. It is organizationally unreasonable to expect operations personnel to further this goal without a high level administrative directive since it represents a major change in operations philosophy. In all likelihood it will require an inter-center task team with line administrative authority to monitor the evolution of autonomous systems concept development and the systems development life cycle. Competition is very likely the driving force that resulted in Boeing implementing the most current state-of-the-art technology in their new generation aircraft. Clearly, the same momentum created in the Space Platform program would enhance utilization of current technological advances. The long term reduction in cost resulting from such a commitment would justify the task force and would be realized for years.

Advances in technology, i.e., digital systems, computer graphics, micro-processors, and electronic displays has provided the hardware and software capabilities to support development of autonomous operations concepts. In all likelihood, additional technological breakthroughs which occur prior to the Space Platform implementation will permit even more sophisticated onboard operations. The 757/767 experience has shown the validity of an approach in which human engineering studies were carefully and systematically conducted, utilizing existing research and filling the gaps where they existed to enhance crew performance. State-of-the-art technology was then integrated with the human engineering data to be compatible. Hardware was then moved through a program schedule leading to flight certification involving design, procurement/fabrication, and testing in 41 months. First certification of the FMS will occur in July 1982, on the 767.

- Adams, J.A., and Chambers, R.W., Response to Simultaneous Stimulation of Two Sense Modalities, Journal of Experimental Psychology, Volume 63, pp. 193-206, 1962.
- Adams, J.A., Humes, J.M., Stenson H.H., Monitoring of Complex Visual Displays: III Effects of Repeated Sessions of Human Vigilance, Human Factors, Volume 4 (3), pp. 149-158, 1962.
- Bate, A.J., Cockpit Warning Systems Comparative Study, Report No. AMRL-TR-68-193, Aeromedical Research Laboratory, Wright-Patterson AFB, Ohio, 1969.
- Berson, B.L., Po-Chedley, D.A., Boucek, G.P., Hanson, D.C., Leffer, M.F., and Wasson, R.L., Aircraft Alerting Systems Standardization Study, Volume II: Aircraft Alerting Systems Design Guidelines, DOT/FAA Report, FAA-RD-81/38/II, January, 1981.
- Boucek, G.P., Veitengruber, J.E., and Smith, W.D., Aircraft Alerting Systems Criteria Study, Volume II: Human Factors Guidelines and Aircraft Alerting Systems, FAA Report, FAA-RD-76-222, May, 1977.
- Boucek, G.P., Erickson, J.B., Berson, B.L., Hanson, D.C., Leffler, M.F., Po-Chedley, D.A., Aircraft Alerting Systems Standardization Study, Phase I Final Report, Report No. FAA-RD-80-68, February, 1980.
- Cooper, G.E., A Survey of the Status of and Philosophies Relating to Cockpit Warning Systems, Report No. NASA CR-152071. NASA Ames Research Center, Moffett Field, California, 1977.
- Crawford, A., The Perception of Light Signals: The Effect of the Number of Irrelevant Lights, Ergonomics, Volume 5, pp. 417-428, 1962.
- Crawford, A., The Perception of Light Signals: The Effect of Mixing Flashing and Steady Irrelevant Lights, Ergonomics, Volume 6, pp. 287-294, 1963.
- Davis, R.C., Motor Components of Responses to Auditory Stimuli: The Relation of Stimulus Intensity and Instructions to Respond, American Psychologist, Volume 2, pp. 308, 1947.

- Egan, J.P., Carterette, E.C., and Thwing, E.J., Some Factors Affecting Multi-Channel Listening, Journal of the Acoustical Society of America, Volume 26, pp. 774-782, 1954.
- Eike, D., Malone, T., and Fleger, F., Human Engineering Design Criteria for Modern Display Components and Standard Parts, Essex Corporation, Alexandria, Virginia, 1980.
- Eldred, K.M., Gannon, W.J. VonGierke, H., Criteria for Short Time Exposure of Personnel to High Intensity Jet Aircraft Noise, Report No. WADC-TN-55-355, Wright Air Development Center, Wright-Patterson AFB, Ohio, 1955.
- Erickson, J.B., Voice Warning Questionnaire Results, Internal McDonnell-Douglas Company AVI, December 1978.
- Federal Aviation Regulation 25.1322, Airworthiness Standards: Transport Category; Airplanes, Department of Transportation, Federal Aviation Administration, Washington, D.C., June 1974.
- FED-STD-595, Colors, Washington, D.C., March 1979.
- Fletcher, H., Munson, W.A., Loudness, Its Definition, Measurement, and Calculation, Journal of the Acoustical Society of America, Vol. 5, pp. 82-108, 1933.
- Fletcher, H., Speech and Hearing in Communications, D. Van Nostrand Company, Inc., Princeton, J.J., 1953.
- Gerathewohl, S.G., Conspicuity of Steady and Flashing Light Signals: Variation of Contrast, Journal of the Optical Society of America, Volume 43, pp. 567-571, 1953.
- Gopher, D., Kahneman, D., Individual Differences in Attention and the Prediction of Flight Criteria, Perceptual and Motor Skills, Vol, 33, pp. 1335-1342, 1971.
- Hart, S.A. and Simpson, C.A., Effects of Linguistic Redundancy on Synthesized Cockpit Warning Message Comprehension and Concurrent Time Estimation (NASA TMX-73, 170), 12th Annual Conference on Manual Control, University of Illinois at Champaign-Urbana, Illinois, May 1976.
- Hawkins, H.L., Stevens, S.S., The Masking of Pure-Tones and of Speech by White Noise, Journal of the Acoustical Society of America, Vol. 22, No. 6, 1950.
- Kemmerling, P., Geiselhart, R., Thorburn, D.E., Cronburg, J.G., A Comparison of Voice and Tone Warning Systems as a Function of Task Loading, Technical Report ASD-TR-69-104, Air Force Systems Command, Wright-Patterson AFB, Ohio, 1969.

- Kerce, E.W., Intelligibility Testing of Voice Model and Phoneme-Synthesized Voices for Aircraft Caution - Warning Systems, California State University, Long Beach, California, 1979.
- Kohfeld, D.L., Simple Reaction Time as a Function of Stimulus Intensity in Decibels of Light and Sound, Journal of Experimental Psychology, Volume 88(2), pp. 251-257, 1971.
- Licklider, J.C., Audio Warning Signals for Air Force Weapon Systems, USAF, WADD, Technical Report 60-814, March 1961.
- Luckiesk, M., Light, Vision and Seeing, Van Nostrand, New York, 1944.
- McCormick, E.J., Human Factors Engineering, McGraw-Hill Book Company, New York, 1970.
- Meister, D., and Sullivan, D.J., Guide to Human Engineering Design for Visual Displays, AD 693237, Office of Naval Research, Department of the Navy, Arlington, Virginia, 1969.
- Merriman, S.C., Operational Attention - Intrusion Effects Associated with Aircraft Warning Lights of Various Size, Report No. NADC-AC-6901, Department of the Navy, Naval Air Development Center, Aerospace-Crew Equipment Department, Warminster, Pennsylvania, 1969.
- Miller, G.A., The Magical Number Seven, Plus or Minus Two: Some Limits on Our Capacity for Processing Information, Psychological Review, Volume 63(2), pp. 81-96, 1956.
- Mills, A.W., On the Minimum Audible Angle, Journal of the Acoustical Society of America, Volume 30, pp. 237-246, 1958
- MIL-C-25050, Colors, Aeronautical Lights and Lighting Equipment, General Specification for, Department of Defense, 30 September 1971.
- MIL-M-18012B, Markings for Aircrew Station Displays, Design and Configuration of, Department of Defense, February 17, 1972.
- MIL-STD-411D, Aircrew Station Signals, Department of Defense, August 30, 1974.
- MIL-STD-1472B, Human Engineering Design Criteria for Military Systems, Equipment, and Facilities, Department of Defense, May 10, 1978.
- Morgan, C.T., Cook, J.S., Chapanis, A., Lund, M.W., Human Engineering Guide to Equipment Design, McGraw-Hill Book Company, New York, 1963.
- Mudd, S.A., The Scaling and Experimental Investigation of Four Dimensions of Pure-Tones and Their Use in an Audio-Visual Monitoring Problem, Ph.D. Thesis, Purdue University, Lafayette, Indiana, 1961.

Munson, W.A., The Growth of Auditory Sensitivity, Journal of the Acoustical Society of America, 1947.

Noise Lectures presented by Bonvallet at the Inservice Training Course on Acoustical Spectrum, February 5-8, 1952, Sponsored by the University of Michigan School of Public Health and Institute of Industrial Health, University of Michigan Press, Ann Arbor, Michigan.

Parks, D.L., Personal Communication Concerning Unpublished Test Results, 1979.

Peason, K., Effect of Tone/Noise Combination of Speech Intelligibility, Journal of the Acoustical Society of America, Vol. 61, No. 3, March 1977.

Po-Chedley, D.A., Burington, C.R., The Effects of Alert Prioritization and Inhibit Logic on Pilot Performance, Report No. MDC J9076, McDonnell Douglas Corporation, 1981.

Pollack, I., Ficks, L., Information of Multidimensional Auditory Displays, Journal of the Acoustical Society of America, Vol. 26, pp. 155-158, 1954.

Pollack, I., The Information of Elementary Auditory Displays, Journal of the Acoustical Society of America, 24, pp. 745-459, 1952.

Pollack, J.D., Teece, J., Speech Annunciator Warning Indicator System: Preliminary Evaluation, Journal of the Acoustical Society of America, Vol. 30, pp. 58-61, 1958

Raab, D., and Fehrer, E., The Effects of Stimulus Duration and Luminance on Visual Reaction Time, Journal of Experimental Psychology, Volume 64(3), pp. 326-327, 1962.

Randle, R.J., Larson, W.E., Williams, D.H., Some Human Factors Issues in the Development and Evaluation of Cockpit Alerting and Warning Systems, NASA, Ref. Publication 055, January, 1980.

Sheehan, D.J., Heads-Up Display Warning Requirements Research, Final Report NR 213-086, Office of Naval Research, Department of the Navy, Arlington, Virginia, 1972.

Shower, E.G., and Biddulph, R., Differential Pitch Sensitivity of the Ear, Journal of the Acoustical Society of America, 3, pp. 275-287, 1931.

Siegel, A.I., and Crain K., Experimental Investigations of Cautionary Signal Presentations, Ergonomics, Volume 3, pp. 339-356, 1960.

Simpson, C.A., Effects of Linguistic Redundancy on Pilot's Comprehension of Synthesize Speech, Proceedings of the Twelfth Annual Conference on Manual Control, NASA TMX-73, pp. 294-308, May 1976.

- Simpson, C.A., and Williams, D.H., Human Factors Research Problems in Electronic Voice Warning System Design, N75-33681, 11th Annual Conference on Manual Control, NASA Ames Research Center, Moffett Field, California, May, 1975.
- Simpson, C.A., and Hart, S.G., Required Attention for Synthesized Perception for Three Levels of Linguistic Redundancy, 93rd Meeting of the Acoustical Society of America, Pennsylvania State College, June, 1977.
- Simpson, C.A., and Williams, D.H., The Effects of an Alerting Tone and of Semantic Context on Pilot Response Time for Synthesized Speech Voice Warnings in a Simulated Air Transport Cockpit, MCI Report No. 78-001, NASA Ames Research Center, Moffett Field, California, 1978.
- Society of Automotive Engineers, Aerospace Recommended Practice: Flight Deck Visual, Audible and Tactile Signals (Draft ARP 450D), Society of Automotive Engineers, Inc., New York, September, 1979.
- Speith, W., Curtis, J.F., Webster, J.C., Responding to One of Two Simultaneous Messages, Journal of the Acoustical Society of America, Vol. 26, pp. 391-396, 1954.
- Steinman, A.R., Reaction Time to Change Compared with Other Psychophysical Methods, Archives of Psychology, New York, Volume 292, pp. 34-60, 1944.
- Steinman, A.R. and Venias, S., Simple Reaction Time to Change as a Substitute for the Disjunctive Reaction, Journal of Experimental Psychology, Volume 34, pp. 152-158, 1944.
- Stevens, S.S. and Davis, H., Hearing, Its Psychology and Physiology, John Wiley and Sons, New York, 1938.
- Stevens, S.S., Handbook of Experimental Psychology, John Wiley and Sons, Inc., New York, 1951.
- VanCott, H.P. and Kinkade, R.G., Human Engineering Guide to Equipment Design, United States Printing Office, Washington, D.C., 1972
- Vanderschraff, A., Problem Area: Warning Systems, Fokker, VFW Aircraft Proceedings from the 20th International Air Safety Seminar of the Flight Safety Foundation, Anaheim, California, October 25-29, 1976.
- Veitengruber, J.E., Design Criteria for Aircraft Warning, Caution and Advisory Alerting Systems, 77-1240 AIAA Aircraft Systems and Technology Meeting, Seattle, Washington, August, 1978.

- Veitengruber, J.E., Boucek, G.P. and Smith, W.D., Aircraft Alerting Systems Criteria Study, Volume I: Collation and Analysis of Aircraft Alerting Systems Data, FAA Report, FAA-RD-76-222, May, 1977.
- Tannas, L.E., Jr., and Goede, W.F., Flat Panel Displays, a Critique, I.E.E.E. Spectrum, pp. 26-32, July, 1978.
- Wegel, R.L. and Lane, C.E., The Auditory Masking of One Pure-Tone by Another and Its Probable Relation to the Dynamics of the Inner Ear, Psychological Review, Vol. 23, pp. 266-285, 1924.

1982

NASA/ASEE SUMMER FACULTY RESEARCH FELLOWSHIP PROGRAM

MARSHALL SPACE FLIGHT CENTER
THE UNIVERSITY OF ALABAMA

EXPERIMENTAL STUDY OF TIME-DEPENDENT FLOWS IN
LABORATORY ATMOSPHERIC FLOW MODELS

Prepared By: J. E. Rush

Academic Rank: Associate Professor

University and Department: The University of Alabama in Huntsville
Department of Physics

NASA/MSFC:
(Laboratory) Space Sciences
(Division) Atmospheric Sciences
(Branch) Fluid Dynamics

MSFC Conterpart: W. W. Fowlis

Date: August 6, 1982

Contract No.: NGT-01-02-099
(University of Alabama)

EXPERIMENTAL STUDY OF TIME-DEPENDENT FLOWS IN
LABORATORY ATMOSPHERIC FLOW MODELS

By

J. E. Rush, Ph.D.
Associate Professor of Physics
The University of Alabama in Huntsville
Huntsville, Alabama

ABSTRACT

The atmospheric General Circulation Experiment (AGCE) planned for Spacelab by NASA/MSFC is designed to model large-scale atmospheric flows using a liquid confined within a spherical shell. The spherical shell of liquid will be rotated in low g, with a radio gravity force simulated by the electrical force on a dielectric material, and with radial and lateral temperature gradients. A low-g environment is necessary because otherwise the electrical force would be insignificant compared to gravity.

Previous laboratory studies simulating large-scale atmospheric flows have been done with a rotating cylindrical annulus of liquid and a radial temperature gradient. While this model is less representative than the AGCE, it has led to much understanding of steady flows in the atmosphere. There are, however, unsteady atmospheric flows which are not well understood, with laboratory counterparts which have not been thoroughly studied.

We report here on studies of steady and unsteady flows with a rotating cylindrical annulus of liquid. For a better understanding of the results of the AGCE, those studies were conducted also at shallow depths, (10 cm to 1 cm) both with and without a rigid lid.

We find that flows with a rigid lid are basically the same as those with a free surface, except for a decrease in flow rate. At shallow depths we find steady flows in essentially the same form, but the incidence of unsteady flows is greatly diminished.

ACKNOWLEDGEMENTS

It is a pleasure to acknowledge the guidance and support of Dr. William W. Fowlis during the course of this work. Dr. Fowlis' knowledge and experience, coupled with his dedication to careful scientific work, were invaluable. The assistance of Mr. Benny Lott of MSFC in setting up and maintaining the apparatus, and of Ms. Edeltraud von Spakovsky of UAH in typing the manuscript, were also greatly appreciated, as was the hospitality provided by Dr. George H. Fichtl and Dr. William W. Vaughan of MSFC.

LIST OF FIGURES

<u>Figure No.</u>	<u>Title</u>	<u>Page</u>
1	Schematic drawing of the proposed AGCE apparatus	XXXVI-6
2	Typical regime diagram	XXXVI-8
3	Schematic diagram illustrating rotating fluid annulus	XXXVI-11
4	Examples of ranges of values of Ω for given wave numbers	XXXVI-15
5	Regime diagram showing results of this experiment	XXXVI-17

INTRODUCTION

A primary goal of dynamic meteorology is the interpretation of large-scale atmospheric motions in terms of physical laws. While much progress has been made toward this goal during the past three decades, there remains a great deal of fundamental work to be done before a clear understanding can be achieved - much less reliable predictability - because of the complexity of the system itself and of the basic physical equations which describe it.

The essence of the large-scale atmospheric system is represented by a rotating spherical shell of fluid acted upon by an unward-directed radial force (gravity), and having both radial and latitudinal temperature variations, which result in a state in which pressure and density gradients are not aligned (baroclinity). Such a system is difficult to reproduce in a laboratory at 1 g, because the gravitational force is uniformly directed downward, not radially inward. The radial force can be reproduced by an electrical force in a dielectric fluid, but the uniform gravitational force would still dominate the dynamics of the system. With the advent of orbiting laboratories, however, it is now possible to make the actual gravitational force insignificant to the behavior of such a system, and thus to study a good working model of large-scale atmospheric flow. This is precisely what the atmospheric General Circulation Experiment (AGCE), proposed by NASA/MSFC for Spacelab, is being designed to do (see Fig. 1). The work described herein was conducted in support of the AGCE project.

Since the late 1940's a substantial amount of experimental and theoretical effort has been devoted to the study of baroclinic flows in a rotating and differentially-heated cylindrical annulus of liquid. While much has been learned from these studies related to the large-scale motion of the atmosphere, there are unsteady flows (as described in the next section) which have a simple form but which have not been fully studied and explained. This research constitutes, in part, a systematic study of these fluctuating flows in a laboratory model as a function of rotation rate, depth of fluid, and nature of surface. Also important for the AGCE is a study of the general effects at shallow depths with a rigid lid, and such a study is also part of this research.

The fluctuations reported here are variations in the regular wave patterns which exist for certain ranges of rotation rate and temperature difference. These baroclinic waves are a combination of radial and azimuthal motion forming a continuous pattern in the annulus of liquid. As seen from a frame of reference rotating with the container, the pattern is one of an integer (usually 2 to 8) number of repeated wave shapes, not necessarily sinusoidal. The fluctuations are referred to in the literature as amplitude oscillations (or vacillations), tilted-through vacillations, and dispersion, and are regular and persistent variations in the shapes of the baroclinic waves, occurring at fixed rotation rates and fixed temperature differences. They are not to be confused with a change in shape which also occurs as the rotation rate and/or temperature difference are varied.

ORGANIZATION:

SPACE SCIENCES LABORATORY

MARSHALL SPACE FLIGHT CENTER

GEOPHYSICAL FLUID DYNAMICS GROUP

NAME:
WILLIAM W. FOWLIS

DATE:
APRIL, 1981

9-1AXXX

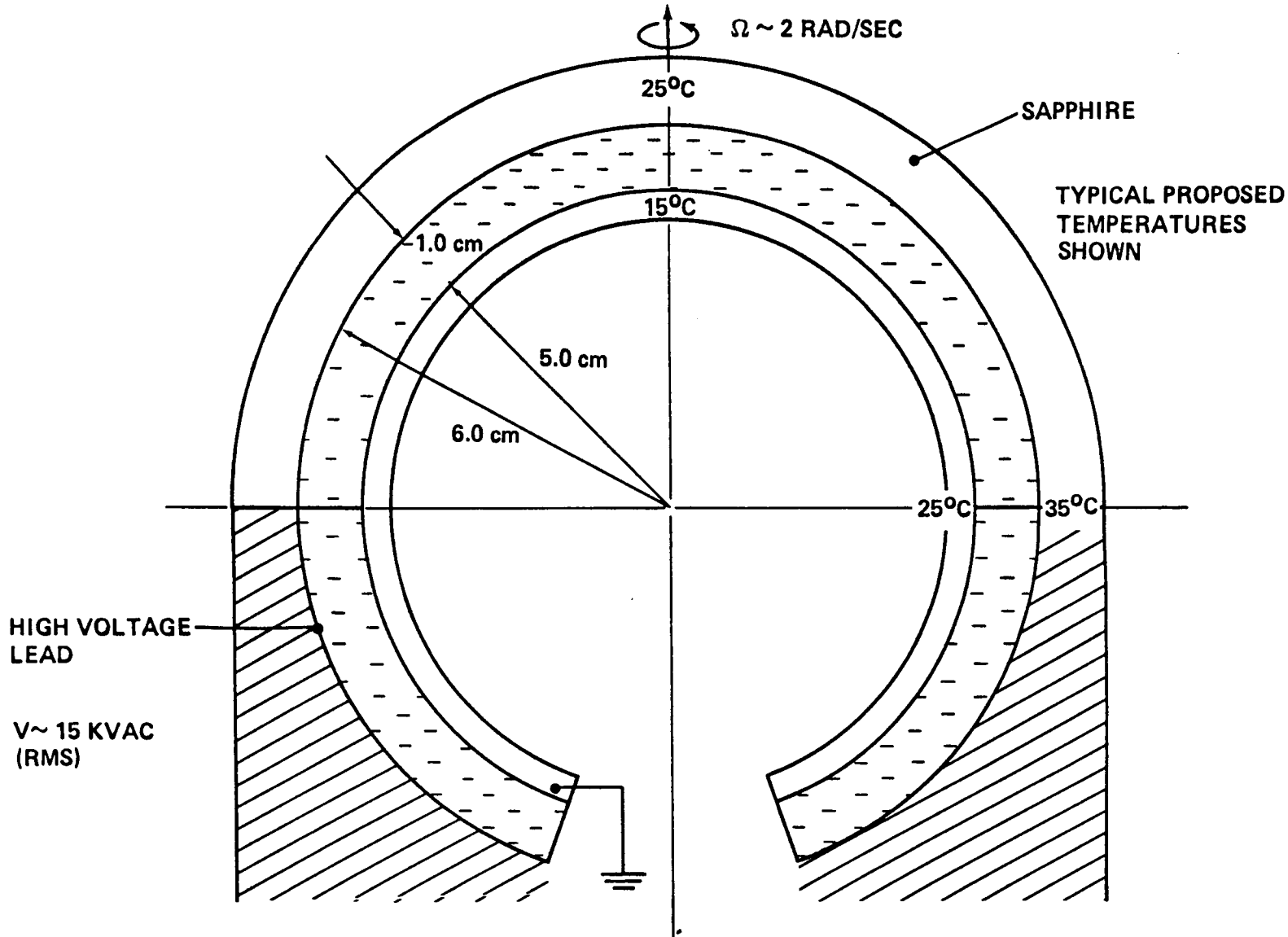


Figure 1. SCHEMATIC DRAWING OF THE PROPOSED AGCE APPARATUS

The results of this work, especially the comparison between open surface and rigid lid and the studies at shallow depths, will be used as an aid in the final design of the AGCE.

OBJECTIVES

The objectives of this research are to study baroclinic waves in a rotating, differentially-heated annulus of liquid in support of the AGCE, and to determine: (1) the nature of the flow at shallow depths, (2) the effect of a rigid lid vs. free surface, and (3) the nature of fluctuations in the waves as a function of rotation rate, depth, and type of surface.

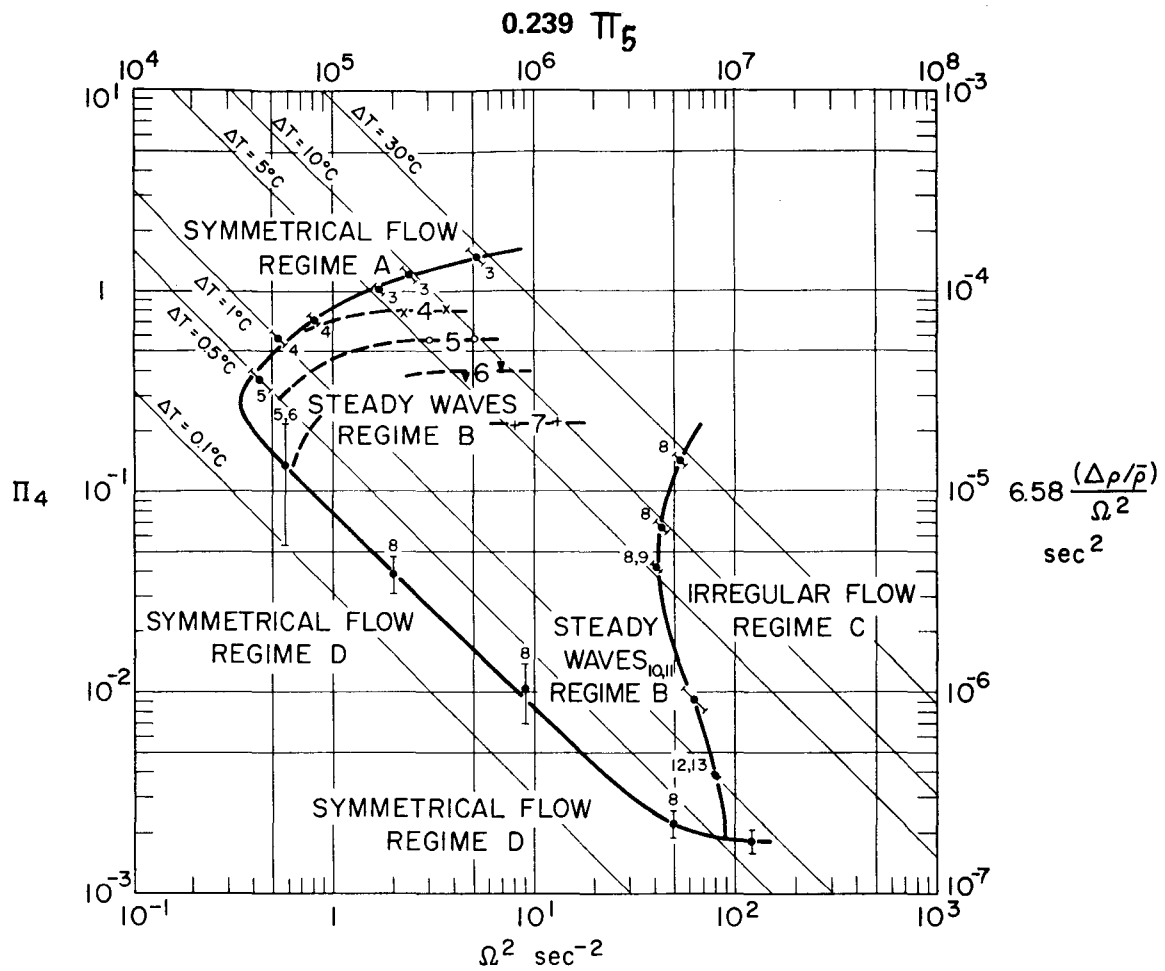
BACKGROUND

Studies of baroclinic flows in a rotating, differentially heated cylindrical annulus of liquid were initiated by Fultz (1) and Hide (2). A relatively recent (1975) review of experimental and theoretical work in this area was published by Hide and Mason (3). The experimental studies include a determination of the nature of the fluid flow as a function of the following variables:

- (1) Ω - rotation rate of system relative to laboratory
- (2) ΔT_r - temperature difference between cylindrical boundaries
- (3) a, b - radii of inner and outer cylindrical boundaries, respectively
- (4) d - depth of fluid
- (5) $\bar{\nu}$ - mean kinematic viscosity of fluid
- (6) \bar{k} - mean thermal conductivity of fluid
- (7) nature of fluid surface (open or closed)

Since $\Delta T_r \leq 30^\circ\text{C}$ in the studies done to date, ν and k were essentially uniform throughout the fluid.

Hide (2,4) determined that there are distinctly different types of flow in different regimes of parameter space. They are generally characterized (3) as axisymmetric flow (Ω small and/or ΔT_r small); regular flow or regular baroclinic waves ($\Delta T_r \geq 0.3^\circ\text{C}$); and irregular flow or irregular baroclinic waves ($\Omega \geq 6 \text{ rad/s}$). The values of Ω and ΔT_r in parentheses are for water. These results are shown clearly on a regime diagram as in Figure 2, which is taken from a paper by Fowles and Hide (5). The regular waves are in the form of a jetstream flow, with a combination of radial oscillation and azimuthal motion in the direction of rotation, resulting in a pattern that looks like a stationary wave shape at a given time, in the rotating frame. This type of flow is apparently an efficient mechanism for energy transfer from the hot surface to the cold one. The wave shape, which is basically described by the number of waves in the pattern, is not usually sinusoidal, and rotates slowly in the direction of rotation of the system. The number of waves increases with increasing Ω or decreasing ΔT_r , for $T_b > T_a$.



$$\Pi_4 = \frac{gd(\Delta\rho/\bar{\rho})}{\Omega^2(b-a)^2}, \quad \Pi_5 = \frac{4\Omega^2(b-a)^5}{\bar{\nu}2d}, \quad \Pi_6 = \frac{\bar{\nu}}{\kappa}.$$

Figure 2. Experimental results on the transitions between the flow regimes and wave numbers for a fixed depth of water in the annulus and for fixed radii of the cylinders, plotted in the Π_4 versus Ω^2 diagram. Experimental details: $a = 3.48$ cm, $b = 6.02$ cm, $d = 10.00$ cm, $\bar{T} = 20.0^\circ\text{C}$, $\bar{\nu} = 1.01 \times 10^{-2} \text{ cm}^2 \text{ sec}^{-1}$, $\bar{\rho} = 0.998 \text{ gm cm}^{-3}$, $\Pi_6 = 7.19$.

Hide also found that for fixed values of the external parameters other than Ω , a rapid spin up to a given value of Ω does not produce a unique wave number, although the statistical likelihood of given wave numbers could be estimated from repeated experiments. Fultz et al. (6) showed that transitions from one wave number to another, produced by slowly varying the external parameters, are subject to significant hysteresis effects (3). Koschmieder and White (7) made a careful study of these hysteresis effects for fixed Ω and slowly varying ΔT_r . They determined that the wave number transitions occur at rather well-defined values of ΔT_r , if ΔT_r is changed sufficiently slowly. However, the nature of the hysteresis effect in ΔT_r is such that the transition values for increasing ΔT_r are distinctly different from those for decreasing ΔT_r .

In the regular-wave regime, there are steady waves, showing no apparent change in shape over time, and a variety of systematic variations in steady-wave patterns, which Hide (3) terms vacillations. Four distinct types have been observed:

- (1) amplitude vacillations, in which the amplitude of the waves oscillates in a regular way;
- (2) tilted-trough vacillations (or shape vacillations), in which the shape of the waves changes periodically;
- (3) wave dispersion, in which an asymmetry in the wave pattern slowly propagates at an angular speed different from the pattern; and
- (4) wavenumber vacillation, in which the dominant wavenumber fluctuates periodically between two neighboring values.

All these effects occur near a point of transition from one wave number to another. They all appear to be stable, in the sense that they persist indefinitely, although one can say very little in a definitive way about wavenumber vacillation (3).

Tilted-trough vacillations were first reported in this context by Hide (2), and were compared by him to a similar phenomenon in the atmosphere. In Hide's words, "...there is a distinct leaning backward of the troughs [peaks in the radial direction] and a decrease of their width. This is followed by the troughs returning to N.-S. [radial] orientation and then leaning forward in preparation for the stage when the 'jet' stream is actually interrupted and intense cyclones are formed in the position of the wave troughs. The cyclones decay and the jet is re-established." This phenomenon was further studied by Hide (4) and by Fultz and Kaylor (8). The vacillations occur at large values of Ω and/or small values of ΔT_r in a region near the transition to a higher wave number.

Amplitude vacillations were, apparently, first seen by Pfeffer, et al. (9). These authors made a study of 4-wave amplitude vacillation. Later Pfeffer and Chiang (10) reported it as a new phenomenon. Fowles and Pfeffer (11) studied the characteristics of the vacillations. The vacillations increase in intensity as Ω is decreased, until eventually there is a transition to a lower wave number and no more vacillations occur. At fixed Ω , however, they persist indefinitely. Amplitude vacillations in a 3 wave have been studied for increasing ΔT_r at fixed Ω by

White and Koschmieder (12) who investigated the period of oscillation compared to the period of pattern rotation.

Wave dispersion was produced with a sloping bottom by Fultz and Kaylor (8), but was first reported for a flat bottom by Pfeffer and Fowles (13). They observed a pattern which appeared to be a superposition of a 4 wave and a 5 wave pattern. Pfeffer and Fowles gave evidence for this hypothesis in the form of calculated superposition patterns of 4-wave and 5-wave sinusoidal functions, propagating at different speeds, which closely resembled the patterns observed. They later (11) were able to give a more quantitative characterization of wave dispersion using temperature probes. The effect occurred at a rotation rate near the transition to a higher wave number. It is thus an effect which competes with tilted-trough vacillation, with the latter generally occurring in higher wave numbers and closer to the irregular flow regime.

Wave-number vacillations have only rarely been observed and are not well characterized at present.

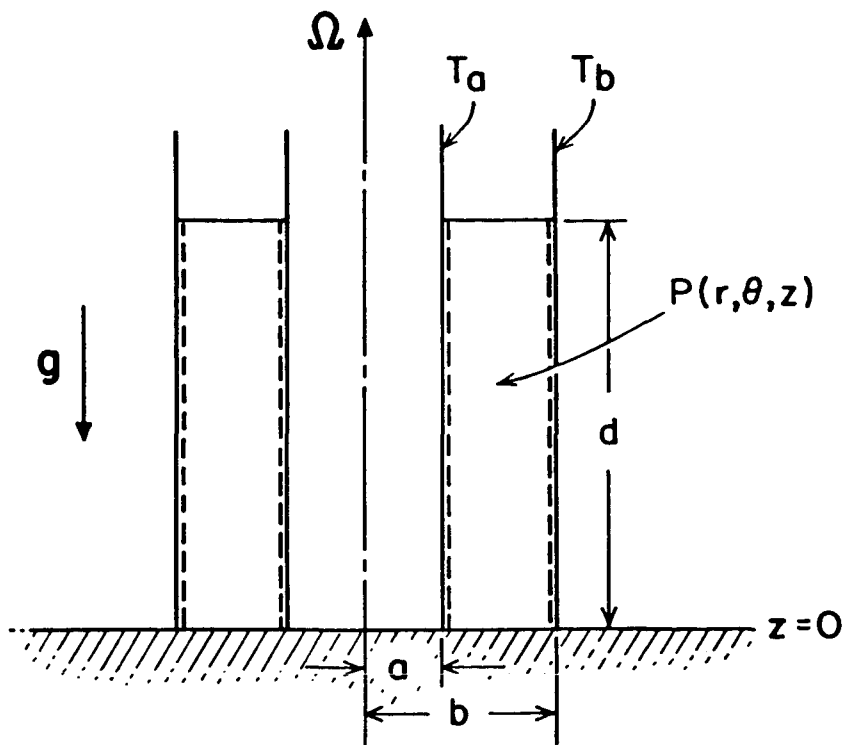
The work described above was done with fluid depths between 3.8 and 15 cm, mostly with open surfaces. The present work was undertaken in order to give an indication of the types of phenomena to expect at shallow depths (1 to 3 cm) and with a rigid surface bounding the fluid.

APPARATUS

The basic apparatus used in the experiments reported here is represented in Figure 3. The fluid to be studied is confined between two brass cylindrical shells with outer radius a (inner cylinder) and inner radius b (outer cylinder), mounted on a plexiglass base. A plexiglass cylindrical shell surrounds the outer brass cylinder and plexiglass caps cover the top surfaces of the inner and outer regions, A and B, which contain distilled water at temperatures T_a and T_b respectively. The entire apparatus is mounted on an electrically driven, variable speed turntable.

The temperature of the water in region A is maintained in a cooling reservoir from which the water is pumped to region A and returned. The water flows into the inner region from a vertical copper tube, with several small openings on each side, and out through an opening in the bottom of the plexiglass base. The water in the outer region is likewise heated in a second reservoir and pumped through the outer region by a similar arrangement, with the return opening on the opposite side of the large cylinder from the entrance tube. An arrangement of plexiglass sliprings in a teflon tube mounted on the axis of the turntable is used for transferring water from the fixed reservoirs to the apparatus.

The temperature of the water in the reservoirs was maintained at a fixed value with a variation of less than 0.1°C . We estimate the temperatures T_a and T_b of the brass cylinders to be within 0.1°C of the temperatures in the respective reservoirs. The period of rotation of the turntable is determined by an electronic counter with a pickup mounted near the rim of the turntable which is actuated by a small permanent magnet attached to the turntable rim. A mirror above the cylinder and a rotoscope



P - General point having cylindrical polar coordinates (r, θ, z) in frame rotating with the apparatus

$\Omega = (0, 0, \Omega)$ - rotation vector

$\mathbf{g} = (0, 0, -g)$ - acceleration of gravity

b, a, d - fluid occupies region

$$a < r < b, 0 < z < d \left[1 + \frac{\Omega^2}{2g} \left(r^2 - \frac{1}{2}(b^2 + a^2) \right) \right] \approx d$$

$T(r, \theta, z, t)$ - temperature at general point P and time t

T_a, T_b - $T(a, \theta, z, t); T(b, \theta, z, t)$ respectively

FIGURE 3. SCHEMATIC DIAGRAM ILLUSTRATING ROTATING FLUID ANNULUS

synchronized with the turntable drive allow visual observation in both rotating and fixed frames of reference.

EXPERIMENTAL PROCEDURE

Parameters maintained throughout the experiments were

$$\begin{aligned} T &= 19.0^{\circ}\text{C} \\ T^a &= 29.0^{\circ}\text{C} \\ a &= 2.40 \text{ cm} \\ b &= 5.08 \text{ cm} \end{aligned}$$

The fluid under study was distilled water with a small amount of tracer material. For observations of fluid motion with a rigid (plexiglass) lid, we used a rheoscopic concentrate (trade name Kalliroscope) at about a 1% concentration. For observations of surface motion without contact with a lid we used a small amount of aluminum powder with a few drops of detergent. To assure that the surface motion was not significantly different from the interior motion we also used the concentrate in conjunction with Al powder. A fluorescent light mounted below the plexiglass base of the apparatus, in combination with the polymer, gave a good representation of the interior motion of the fluid. While the lid was not in contact with the fluid during free-surface studies, it was kept in place above the fluid to prevent contamination, to shield the surface from air currents, and to deter evaporation.

The fluid depths which were used, both with and without a rigid lid, were 10.0, 5.0, 3.0, 2.0, and 1.0 cm. Rotation rates Ω ranged from 0.8 to 5 rad/s, but most of the work was in the range from 1 to 4 rad/s. In looking for fluctuating flows, the usual procedure was to select an approximate rotation rate and establish a wave pattern with a predetermined number of waves. We would then vary the rotation rate, either increasing or decreasing, slowly enough so as not to disrupt the wave pattern. The smallest variations of Ω were less than 5%. This variation would be continued, with typical relaxation times of 10 to 20 minutes, until we detected a stable fluctuation or until the fluid underwent a change to a different wave number. All observations of fluid flow were visual.

RESULTS

A. General Results

The qualitative results of our observations of the fluid with different depths d , with and without a rigid lid, are summarized in Tables I and II where we show the different wave numbers observed, and the types of vacillations seen and not seen. The symbols A, D, and T are self-explanatory.

Table I
Qualitative Results with Open Surface

d(cm)	Wave Number										
	1	2	3	4	5	6	7				
10.0	-	X,S	D	A	D	A	T	X	T,I	-	-
5.0			X	X	X	I	X	T,I	X	T,I	
3.0					X,S	T	X	X		R	
2.0		-		-	S		X,S				
1.0				(D)		R					

A = Amplitude Vacillations	I = Irregular-flow Regime
D = Dispersion	S = Symmetric-flow Regime
T = Tilted-trough Vacillations	X = No Vacillations Detected
R = Regular Waves	() = Tentative
- = No Regular Waves	

An X means that vacillations were sought in the appropriate region but not detected. A dash means that the corresponding wave number was sought but not detected. I (S) imply that the irregular-flow (symmetric-flow) regimes were reached with the corresponding wave number. R means that regular waves were observed. Parentheses imply that the results are tentative. It should be emphasized here that these results are not exhaustive, both because our methods of observation were not quantitative and because changes in rotation-rate Ω were not sufficiently slow to assure equilibrium (see Ref. 7).

Table II

Qualitative Results with Rigid Lid

d(cm)	Wave Number						
	1	2	3	4	5	6	7
10.0	X,S X	X D	A D	A T	X		
5.0			X X	X X	X X	R	
3.0				X X	(D)	X	X
2.0				X X		R	R
1.0						R	R

A = Amplitude Vacillations

D = Dispersion

T = Tilted-trough Vacillations

R = Regular Waves

- = No Regular Waves

I = Irregular-flow Regime

S = Symmetric-flow Regime

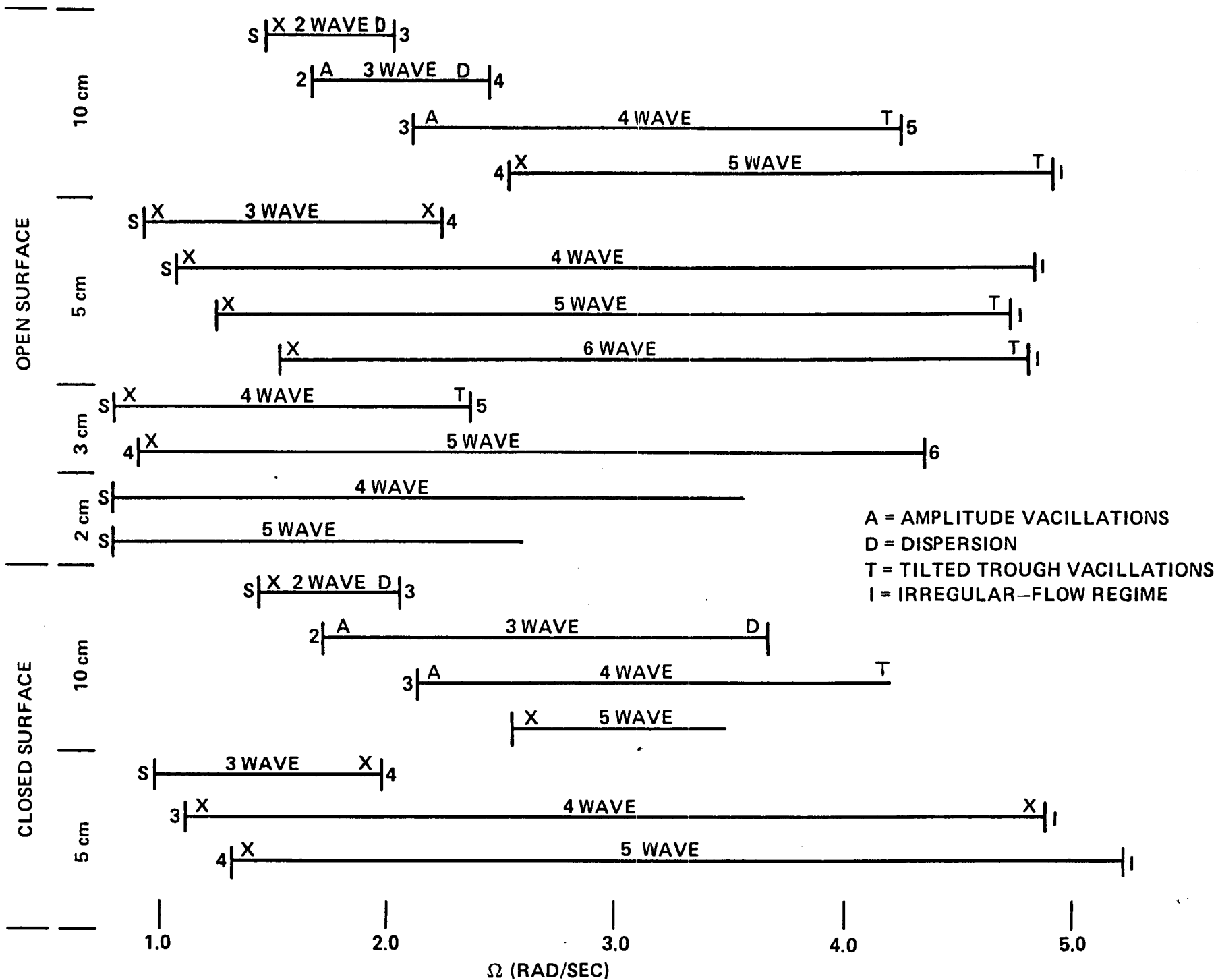
X = No Vacillations Detected

() = Tentative

We looked for vacillations by establishing a wave pattern at a given rotation rate, then slowly increasing or decreasing the rotation rate. If a transition to a given wave number occurred soon after a change, we repeated the process with smaller changes. Very large hysteresis effects in Ω were manifest, appearing as an overlap of two or more wave numbers in a given Ω range. Some examples of this effect are illustrated in Figure 4. A horizontal line in Figure 4 indicates a range of Ω values within which a given wave number persisted. Vertical lines indicate points of transition to higher or lower wave numbers, as indicated, or to irregular flow (I) or symmetric flow (S). Hysteresis is indicated by two or more parallel lines overlapping in Ω values for a given depth d . At points where a horizontal line terminates without a vertical line, observations were stopped before a change of wave number occurred.

The hysteresis effects which we observed are related to those studied by Koschmieder and White (7), but are in the variable Ω rather than ΔT_r . Likewise, the presentation in Figure 4 is somewhat different from that of Koschmieder and White, in that they plot results for continuously increasing ΔT_r and continuously decreasing ΔT_r separately. In fact, at depths of 5.0 cm or less, there are wave numbers which can be produced but which are not accessible by slowly and continuously increasing Ω from the symmetric-flow regime, or likewise decreasing Ω from the irregular flow regime. To achieve these wave numbers we had to make sudden starts at particular values of Ω . For example, one notes in Figure 4 that the 4-wave range is almost the entire range of Ω for regular waves at 5.0 cm. For decreasing Ω our wave-number transitions at 10.0 cm with the rigid lid occurred at larger values of Ω than the extrapolated results of Ref. 7. However, we do not consider the differences significant because of the differences in experimental technique used.

Figure 4. Examples of ranges of values of Ω for given wave numbers
 XXXVI-15



B. Vacillations

As noted in Section A, we observed amplitude vacillations, tilted-trough vacillations, and dispersion. All three types were readily produced at a depth of 10.0 cm, but rarely occurred at depths of 5.0 cm or less. At all depths there were transitions which occurred without vacillations, even though Ω was varied very slowly and a reasonable time was allowed for equilibrium to be established after each change in Ω .

The most significant effect of using a rigid lid vs. a free surface was an order of magnitude increase in the rotation rate of a given wave pattern relative to the cylinders, as noted by White and Koschmieder (12). Except as noted in the discussion below, vacillations occurred in essentially the same form at the same rotation rates. However, they were much more difficult to detect because they were slower, probably because they are related to the pattern rotation rate, which is also slower.

In Figure 5 we present the results on vacillations in a regime diagram similar to that of Fowlis and Hide (5). We have given a log-log plot in terms of two dimensionless parameters π_4 and π_5 given by Hide. Here

$$\pi_4 = [gd/\Omega^2(b-a)^2](\Delta\rho/\bar{\rho})$$

where g is the acceleration due to gravity; a , b , d , and Ω have been defined earlier, $\bar{\rho}$ is the mean density of the fluid, and

$$\Delta\rho = \rho(T_a) - \rho(T_b).$$

We have taken $g = 980 \text{ cm/s}^2$

$$\bar{\rho} = 0.997 \text{ g/cm}^3$$

and

$$\Delta\rho = 2.46 \times 10^{-3} \text{ g/cm}^3$$

so

$$\Delta\rho/\bar{\rho} = 2.47 \times 10^{-3} \text{ g/cm}^3.$$

The other dimensionless parameter is

$$\pi_5 = 4 \Omega^2 (b-a)^5 / v^2 d$$

where $\bar{\nu}$ is the mean viscosity of the fluid, taken as

$$\bar{\nu} = 9.17 \times 10^{-3} \text{ g/cm} \cdot \text{s (poise)}$$

Using the values given, we find

$$\pi_4 = 0.337 \text{ d}/\Omega^2$$
$$\pi_5 = 6.58 \times 10^6 \Omega^2/\text{d}$$

for d/Ω^2 in $\text{cm} \cdot \text{s}^2$. The parameters π_4 and π_5 are related to the thermal Rossby number Ro_T and the Taylor number Ta by

$$\pi_4 = \text{Ro}_T$$
$$\pi_5 = [(b - a)/\text{d}] \text{Ta}.$$

The data taken in this work fall on the diagonal line (slope -1), which falls about midway between the lines for $\Delta T = 10^\circ\text{C}$ and $\Delta T = 30^\circ\text{C}$ on the regime diagram of Fowlis and Hide (see Fig. 2). Our $\Delta T = 10^\circ\text{C}$ line differs from theirs because our (b-a) value is different. We find the boundary between symmetric and regular flow essentially the same as theirs at 10.0 cm and 5.0 cm, but it goes to higher points in our line at shallower depths, a trend indicated in their data.

The three types of vacillations, at the points or ranges of occurrence, are indicated on our line by A, D, and T, respectively. In parentheses are the wave numbers in which they occurred and the fluid depths d, respectively. Following the parentheses are O for open surface or C for closed surface. Note that the results are essentially the same. Note also that tilted-trough vacillations occur at higher rotation rates, while amplitude vacillation and dispersion occur at lower rotation rates.

The dotted-line rectangle shown in Fig. 5 represents the region of parameter space studied by Koschmieder and White (7, 12). It is clear why they observed amplitude vacillation (oscillation) and dispersion (which they call phase modulation) but not tilted trough vacillation.

The tilted-trough vacillations which we observed were of the same form as those which were first reported by Hide (2) and later by Fultz and Kaylor (8). They were slower and less pronounced with the rigid lid, but were clearly observable. At 5.0 cm we noted that they did not necessarily precede a transition to a higher wave number, but for 5 waves and 6 waves continued instead to the irregular-flow regime. At the boundary of the irregular flow regime they became sequential around the pattern rather than simultaneous, so that all phases of vacillation were visible at once.

We also observed amplitude vacillations, as first reported by Pfeffer, et al. (9). In agreement with White and Koschmieder (12), we found that they occurred only at the lower wave numbers in a transition to an even lower wave number. We did not observe amplitude vacillations in the transition from 2 wave to 1 wave at 10 cm. However, the amplitude at that rotation rate is small and the pattern is quite faint, so that we could have easily missed them. We also observed the increase in amplitude and decrease in rate of the amplitude vacillations as one approaches a transition to a lower wave number, as reported in Ref. 12. If amplitude oscillations occur at depths of 5.0 cm or less, they are much more difficult to detect than at 10.0 cm.

Finally we noted the dispersion effect first reported by Pfeffer and Fowlis (13), and called phase modulation by Koschmieder and White (12). We did not, however, observe the effect in a transition from 4 wave to 5 wave, as reported by Pfeffer and Fowlis, undoubtedly because our transition was in a different part of the regime diagram. Instead, we observed the effect predicted by them in a transition from 3 wave to 4 wave, in almost the same form as their predicted pattern, suggesting that their explanation of a superposition of two wave numbers has merit. The fact that we observed tilted-trough vacillations in the 4- to 5-wave transition, rather than dispersion, can be explained by the observation that our transition lay much closer to the irregular flow regime than theirs.

With a rigid lid at 10.0 cm, we observed an effect resembling wave dispersion in the 3 wave transition. However, the effect was manifest as an enlargement of one or two troughs, an effect which propagated slowly in the opposite direction to the pattern rotation, at about the same speed. We also noted that the transition to a 4 wave occurred at a much higher rotation rate than with an open surface, in contrast to results with other wave numbers.

The dispersion vacillations observed in the transition from 2- to 3-wave also have the appearance of a superposition of two patterns rotating at different speeds. However, the second pattern could not be a 3 wave, since the vacillations maintain a 180° rotational symmetry (not bilateral), and such a symmetry would be changed by an odd-number wave. The nature of the changing pattern is that of a rectangle with rounded corners, in which the corners on one diagonal are stretched. This stretching is then transmitted to the opposite set of corners, and the pattern again becomes a rectangle.

Tilted-trough vacillations, when observed for a given wave number at a given depth, persisted over a broad range of Ω values. In some cases it was possible to observe tilted-trough oscillations with decreasing Ω after a transition from a higher wave number. The vacillations would gradually diminish and disappear as Ω was decreased further. On the other hand, amplitude vacillations in a given wave number at a given depth continued over a much smaller range of Ω , while dispersion was only manifest in certain quite narrow ranges.

C. Shallow Depths

Observations at shallow depths are more difficult because motion of the fluid is slower, because tracer materials are more difficult to see, and because the materials reach the bottom sooner. We found aluminum powder to be much less suitable than Kalliroscope for these reasons.

One notes also that the symmetric-flow boundary lies at lower values of Ω , and that lower wave numbers do not appear. At 3.0 cm or less, the amplitude of a given wave decreases with decreasing Ω , the pattern getting fainter, until at $\Omega \sim 0.75$ rad/s it simply disappears.

No amplitude vacillations were observed at depths of 3.0 cm or less. This can be explained in part by the fact that the range of Ω values for a given wave number is much greater, so that transitions to another wave number, if they occurred, were generally at values of Ω near the symmetric-flow or the irregular flow regimes. On the other hand, we determined that regular waves are manifest at a depth of 1.0 cm, with or without a rigid lid, and that they are clearly observable.

At 3.0 cm depth, we observed clear tilted-trough vacillations in the 4 wave with an open surface, and a dispersion effect similar to that described in the previous section (enlarged troughs propagating) in the 5 wave with a rigid lid. There was also a strange type of dispersion at 1.0 cm in the 3 wave with an open surface. However, we need to take further care in eliminating any possible asymmetries in the apparatus before announcing these dispersion effects with complete confidence.

Finally, at 2.0 cm we noted a transition from a 6 wave to a 5 wave with increasing Ω . A simple explanation, of course, is that the 6 wave was never firmly established and would have undergone a spontaneous transition given sufficient time. We note it here only because it occurred both with and without a rigid lid.

CONCLUSIONS AND RECOMMENDATIONS

We have presented results of a systematic study of fluid flow in a rotating, differentially heated annulus of liquid. The fluid used was water, the temperature difference was 10.0°C, and the depths studied were 10.0, 5.0, 3.0, 2.0, and 1.0 cm, with and without a rigid lid.

We found that vacillations in regular waves occurred readily at 10.0 cm, but rarely at 5.0 cm or less. Amplitude oscillations and wave dispersion occurred at low rotation rates and tilted-trough vacillations at higher rotation rates. At each depth these were also transitions to a different wave number with no apparent vacillations.

The primary effect of a rigid lid was to reduce the rate of pattern rotation and vacillation considerably, and to change the appearance of vacillations somewhat. With few exceptions, we observed transitions at the same rotation rate with and without a rigid lid. The changed appearance of vacillations was primarily for wave dispersion. Dispersion with a rigid lid seems to be manifest as an enlargement of some troughs, with this enlargement propagating in the opposite

direction to pattern rotation, but this observation needs further study before it can be stated conclusively.

At shallower depths we found higher wave numbers occurring at lower rotation rates, with some lower wave numbers apparently excluded. At depths of 3.0 cm or less, a given wave number may span the entire regime of regular waves, so that transitions to other wave numbers are less likely.

REFERENCES

1. D. Fultz, "Experimental Analogies to Atmospheric Motions," Compendium of Meteorology (Boston, American Meteorological Society, 1951), pp. 1235-48.
2. R. Hide, "Some Experiments on Thermal Convection in a Rotating Liquid," Quart. J. Roy. Meteorol. Soc. 79, 161 (1953).
3. R. Hide and P. J. Mason, "Sloping Convection in a Rotating Fluid," Advances in Phys. 24, 47 (1975).
4. R. Hide, "An Experimental Study of Thermal Convection in a Rotating Liquid," Phil. Trans. R. Soc. A 250, 441 (1958).
5. W. W. Fowlis and R. Hide, "Thermal Convection in a Rotating Annulus of Liquid: Effect of Viscosity on the Transition between Axisymmetric and Non-Axisymmetric Flow Regimes," J. Atmos. Sci. 22, 541 (1965).
6. D. Fultz, R. R. Long, G. V. Owens, W. Bohan, R. Kaylor, and J. Weil, "Studies of Thermal Convection in a Rotating Cylinder with some Implications for Large-Scale Atmospheric Motions," Meteorological Monographs, Vol. 4, No. 21 (Boston, American Meteorological Society, 1959).
7. E. L. Koschmieder and H. D. White, "Convection in a Rotating, Laterally Heated Annulus. The Wave Number Transitions," Geophys. Astrophys. Fluid Dynamics 18, 279 (1981).
8. D. Fultz and R. Kaylor, "The Propagation of Frequency in Experimental Baroclinic Waves in a Rotating Annular Ring," in B. Bolin, ed., The Atmosphere and the Sea in Motion (Rossby Memorial Volume) (Oxford, New York, 1959), pp. 359-371.
9. R. L. Pfeffer, D. Mardon, P. Sterbenz, and W. W. Fowlis, "A New Concept of Available Potential Energy," Proc. Intern. Symp. Dynamics Large-Scale Processes (Moscow, USSR, 1965).
10. R. L. Pfeffer and Y. Chiang, "Two Kinds of Vacillation in Rotating Laboratory Experiments," Mon. Wea. Rev. 95, 75 (1967).
11. W. W. Fowlis and R. L. Pfeffer, "Characteristics of Amplitude Vacillation in a Rotating, Differentially Heated Fluid Determined by a Multiprobe Technique," J. Atmos. Sci. 26, 100 (1969).
12. H. D. White and E. L. Koschmieder, "Convection in a Rotating, Laterally Heated Annulus. Pattern Velocities and Amplitude Oscillations," Geophys. Astrophys. Fluid Dynamics 18, 301 (1981).
13. R. L. Pfeffer and W. W. Fowlis, "Wave Dispersion in a Rotating, Differentially Heated Cylindrical Annulus of Fluid," J. Atmos. Sci. 25, 361 (1968).

1982

NASA/ASEE SUMMER FACULTY RESEARCH FELLOWSHIP PROGRAM

MARSHALL SPACE FLIGHT CENTER
THE UNIVERSITY OF ALABAMA

A MARKOV CHAIN MODEL FOR RELIABILITY
GROWTH AND DECAY

Prepared By:	Kyle Siegrist, Ph.D.
Academic Rank:	Assistant Professor
University and Department:	University of Alabama in Huntsville Department of Mathematics
NASA/MSFC Laboratory:	Systems Dynamics
MSFC Counterpart:	Mario H. Rheinfurth
Date:	August 6, 1982
Contract No.:	NASA NGT-01-002-099

ACKNOWLEDGEMENT

I would like to thank my MSFC counterpart Mario H. Rheinfurth for introducing me to the subject of reliability theory and for many stimulating conversations during the summer.

A MARKOV CHAIN MODEL FOR RELIABILITY
GROWTH AND DECAY

Kyle Siegrist
Assistant Professor of Mathematics
University of Alabama in Huntsville
Huntsville, Alabama

ABSTRACT

A mathematical model is developed to describe a complex system undergoing a sequence of trials in which there is interaction between the internal states of the system and the outcomes of the trials. For example, the model might describe a system undergoing testing that is redesigned after each failure. The basic assumptions for the model are that the state of the system after a trial depends probabilistically only on the state before the trial and on the outcome of the trial and that the outcome of a trial depends probabilistically only on the state of the system before the trial.

It is shown that under these basic assumptions, the successive states form a Markov chain and the successive states and outcomes jointly form a Markov chain. General results are obtained for the transition probabilities, steady-state distributions, etc. The model is shown to generalize many other reliability growth models in the literature.

A special case studied in detail describes a system that has two possible states ("repaired" and "unrepaired") undergoing trials that have three possible outcomes ("inherent failure," "assignable-cause failure" and "success"). For this model, the reliability function is computed explicitly and an optimal repair policy is obtained.

INTRODUCTION

Over the last twenty years, the theory of reliability growth has been developed in an attempt to describe a system undergoing testing and improvement. The systems that have been modeled can be divided into two general categories according to the nature of the testing. A system undergoing discrete time testing (such as a missile system) is subjected to a sequence of trials of relatively short duration. After each trial the system may, based on the outcomes of past trials, be redesigned. For such systems, the object of interest is usually the sequence of success probabilities (the reliability function). On the other hand, a system undergoing continuous time testing is operated until it fails. The system may then, based on past performance, be redesigned and is again operated until failure. For these systems, the object of interest is typically the sequence of expected times between failure.

Much of the reliability growth literature has been concerned with postulating parametric forms for the reliability function or the mean time between failure and then using standard statistical methods to estimate the parameters. References [5], [6], [7], [11], [12], [14], and [19] fall into this category. Some authors however have developed more elaborate models, together with accompanying statistical methods, that make certain assumptions about the inner workings of the system, the possible types of outcomes of the tests, and the nature of the redesign efforts. References [3], [4], [8], [10], [17], and [20] fall into this category, References [1] and [9] survey the reliability growth literature.

In this paper, a general model is developed to describe systems undergoing discrete time testing. The model has several important features. First it allows wide latitude in the workings of the system, the types of outcomes of the trials, and the nature of the redesign efforts. The model generalizes most of the discrete time reliability growth models in the literature and allows new variations as well, such as reliability decay. Also, the structure of the model is rich enough to allow the formulation of new problems that have not previously been associated with reliability growth theory. For example, an optimization problem is formulated that weighs the cost of failure against the cost of redesign.

In Section 1, the model is developed as a bivariate stochastic process. One component describes the internal state of the system; the other component describes the outcomes of the trials. There are two basic assumptions. First, the state of the system after a trial depends probabilistically only on the state before the trial and on the outcome of the trial. Second, the outcome of a trial depends probabilistically only on the state of the system before the trial. Under these assumptions, it is shown that the state process is a Markov chain and also that the joint state-outcome process is a Markov chain. The remainder of Section 1 is devoted to a basic study of these Markov chains. Transition probabilities, communicating states, invariant distributions, and special cases are considered.

In Section 2, the general model is used to extend a simple model studied by Barr [4], Lloyd-Lipow [15], et. al. In this model the system has two states--a repaired state and an unrepaired state and the trials have three possible outcomes--inherent failure, assignable-cause failure, and success. It is assumed that after an assignable-cause failure, which is possible only in the unrepaired state, an attempt is made to repair the system. In addition, we allow the possibility of decay from the repaired state to the unrepaired state. For this model, the reliability function is computed explicitly, the distribution of the time required to enter the repaired state is found, and a simple optimization problem is solved.

1. THE MARKOV CHAIN MODEL

Consider a system or device whose internal states form a denumerable set E . The system undergoes a sequence of trials or tests. The possible outcomes of the trials (usually various modes of success and failure) form a denumerable set F . We assume that the state of the system can change only during the course of a trial. Thus, let X_n , $n = 1, 2, \dots$ denote the state of the system before the n 'th trial is performed and let Y_n , $n = 1, 2, \dots$ denote the outcome of the n 'th trial. Then $X = (X_n : n = 1, 2, \dots)$ and $Y = (Y_n : n = 1, 2, \dots)$ are stochastic processes defined on a common probability space (Ω, \mathcal{F}, P) ; X takes values in E and Y takes values in F . Let $Z_n = (X_n, Y_n)$ for $n = 1, 2, \dots$ so that Z_n represents the state before the n 'th trial and the outcome of the n 'th trial. Then $Z = (Z_n : n = 1, 2, \dots)$ is a stochastic process on (Ω, \mathcal{F}, P) taking values in the phase space $E \times F$.

Two assumptions are basic. First, the state of the system after a trial depends probabilistically only on the state before the trial and on the outcome of the trial. That is,

$$(1.1) \quad P(X_{n+1} = x \mid Z_1, \dots, Z_n) = P(X_{n+1} = x \mid Z_n)$$

for $x \in E$ and $n = 1, 2, \dots$. Also, the right hand side of (1.1) is independent of n . Thus we define

$$A_y(x, u) = P(X_{n+1} = u \mid X_n = x, Y_n = y)$$

for $x, u \in E$ and $y \in F$. For fixed y note that

$$A_y(x, u) \geq 0, \quad \sum_u A_y(x, u) = 1$$

so A_y is a transition probability kernel for a Markov chain on E . This chain would describe the evolution of the states if all outcomes were y .

Next we assume that the outcome of a trial depends probabilistically only on the state of the system before the trial. That is,

$$(1.2) \quad P(Y_n = y \mid Z_1, \dots, Z_{n-1}, X_n) = P(Y_n = y \mid X_n)$$

for $y \in F$, $n = 1, 2, \dots$. Also, the right side of (1.2) is independent of n . Thus we define

$$a_x(y) = P(Y_n = y \mid X_n = x)$$

for $x \in E, y \in F$. Note that for fixed x ,

$$a_x(y) \geq 0, \sum_y a_x(y) = 1$$

so that a_x is a probability function on F which describes the outcome of a trial when the state is x .

Let ν denote the distribution of X_1 , i.e., $\nu(x) = P(X_1 = x), x \in E$. The parameters A, a , and ν will be called the basic data of the system. It will be shown later that the basic data completely determine the probability law for the joint process Z . First however a number of interesting reliability problems can be easily formulated in terms of Z :

(a) Prediction. Given the basic data, compute reliability as a function of the trial number. That is, if $s \in F$ denotes "success," compute the function $r_n, n = 1, 2, \dots$ defined by

$$r_n = P(Y_n = s).$$

Note that in light of (1.2),

$$r_n = E(a_{X_n}(s)).$$

Hence this problem is solved once the distribution of X_n is known.

(b) Prediction. Given the basic data, find the distribution of the trial number at which a certain state is first entered. That is, find the distribution of

$$M_x = \min\{n: X_n = x\}.$$

For example, $x \in E$ might be an absorbing state that represents the system when completely repaired.

(c) Prediction. Given the basic data, find the distribution of the trial number at which a certain outcome occurs. That is, find the distribution of

$$N_y = \min\{n: Y_n = y\}.$$

For example, $y \in F$ might represent catastrophic failure.

(d) Optimization. Frequently the transition probability function A is partially determined by certain repair or maintenance policies. Let A denote the set of all admissible functions A that can arise from the repair policies. Let $c: E \times E \rightarrow [0, \infty)$ and suppose that $c(x, u)$ represents the cost of a transition from state x to state u (for example, a transition into a repaired state would usually entail a cost). Let $d: F \rightarrow [0, \infty)$ and suppose

that $d(y)$ represents the cost of outcome y (for example, failure would usually entail a cost). The expected average cost per trial for a transition function A (a and v are assumed fixed) resulting from a given repair policy is

$$v(A) = \lim_{n \rightarrow \infty} \frac{E(\sum_{i=1}^n c(X_i, X_{i+1}) + \sum_{i=1}^n d(Y_i))}{n}.$$

The problem here is to compute

$$\inf_{A \in \mathcal{A}} v(A)$$

and to find $A^* \in \mathcal{A}$ such that

$$v(A^*) = \inf_{A \in \mathcal{A}} v(A).$$

(e) Inference. In realistic situations some of the basic parameters will be unknown. A major problem is to estimate these parameters (or others derived from them) from data collected by observing the states and/or outcomes.

We will now prove some basic results about the stochastic processes X , Y , and Z .

(1.3) Theorem. Under assumptions (1.1) and (1.2), X is a Markov chain on E with transition probability kernel

$$B(x, u) = \sum_y a_x(y) A_y(x, u); \quad x, u \in E.$$

Proof. Let $n \in \{1, 2, \dots\}$ and let $x_1, \dots, x_n, x_{n+1} \in E$. Then

$$\begin{aligned} & P(X_{n+1} = x_{n+1} \mid X_1 = x_1, \dots, X_n = x_n) \\ = & \sum_y P(X_{n+1} = x_{n+1} \mid X_1 = x_1, \dots, X_n = x_n, Y_n = y) \cdot \\ & \quad \cdot P(Y_n = y \mid X_1 = x_1, \dots, X_n = x_n) \\ = & \sum_y P(X_{n+1} = x_{n+1} \mid X_n = x_n, Y_n = y) P(Y_n = y \mid X_n = x_n) \\ = & \sum_y A_y(x_n, x_{n+1}) a_{x_n}(y). \quad \square \end{aligned}$$

(1.4) Theorem. Under assumptions (1.1) and (1.2), Z is a Markov chain on $E \times F$ with transition probability kernel

$$C((x, y), (u, v)) = A_y(x, u) a_u(v); \quad (x, y), (u, v) \in E \times F.$$

Z has initial distribution $\mu(x, y) = v(x) a_x(y)$ where v is the initial distribution of X .

Proof. Let $n \in \{1, 2, \dots\}$ and let $z_1, \dots, z_n, z_{n+1} \in E \times F$ where $z_i = (x_i, y_i)$. Then

$$P(Z_{n+1} = z_{n+1} \mid Z_1 = z_1, \dots, Z_n = z_n)$$

$$\begin{aligned}
&= P(Y_{n+1} = y_{n+1} \mid Z_1 = z_1, \dots, Z_n = z_n, X_{n+1} = x_{n+1}) \cdot \\
&\quad \cdot P(X_{n+1} = x_{n+1} \mid Z_1 = z_1, \dots, Z_n = z_n) \\
&= a_{x_{n+1}}(y_{n+1}) A_{y_n}(x_n, x_{n+1}).
\end{aligned}$$

Also,

$$P(Z_1 = (x,y)) = P(Y_1 = y \mid X_1 = x)P(X_1 = x) = a_y(x)v(x). \quad \square$$

It is fairly easy to characterize those stochastic processes on $E \times F$ which satisfy assumptions (1.1) and (1.2). The following two results are stated without proof.

(1.5) Theorem. Let $Z = (Z_n: n = 1, 2, \dots)$ be a stochastic process on $E \times F$ where $Z_n = (X_n, Y_n)$. Assumptions (1.1) and (1.2) are equivalent to the following two conditions:

(a) Z is a Markov chain.

(b) $P(Y_n = y \mid Z_{n-1}, X_n) = P(Y_n = y \mid X_n)$ (independent of n) for $y \in F$.

(1.6) Corollary. Suppose that Z is a Markov chain on $E \times F$ with transition probability kernel C . For assumptions (1.1) and (1.2) to be satisfied, it is necessary and sufficient that

$$\frac{C((x,y), (u,v))}{\sum_{t \in F} C((x,y), (u,t))}$$

be independent of (x,y) for each $(u,v) \in E \times F$. In this case, A and a are given by

$$\begin{aligned}
A_y(x,u) &= \sum_{t \in F} C((x,y), (u,t)) \\
a_x(y) &= \frac{C((u,v), (x,y))}{\sum_{t \in F} C((u,v), (x,t))}.
\end{aligned}$$

We now consider some special cases.

(1.7) Theorem. Y_n is independent of X_n for $n = 1, 2, \dots$ if and only if $a_x(y)$ is independent of x for each y . In this case, Y is a sequence of independent, identically distributed random variables with probability function a .

Proof. The first claim follows directly from the definition of a :

$$a_x(y) = P(Y_n = y \mid X_n = x).$$

For the second claim, let $y_1, \dots, y_n, y_{n+1} \in F$. Then

$$P(Y_{n+1} = y_{n+1} \mid Y_1 = y_1, \dots, Y_n = y_n)$$

$$\begin{aligned}
&= \sum_{x_1, \dots, x_{n+1}} P(Y_{n+1} = y_{n+1} \mid X_1 = x_1, Y_1 = y_1, \dots, X_n = x_n, Y_n = y_n, X_{n+1} = x_{n+1}) \\
&\quad \cdot P(X_1 = x_1, \dots, X_{n+1} = x_{n+1} \mid Y_1 = y_1, \dots, Y_n = y_n) \\
&= \sum_{x_1, \dots, x_{n+1}} a_{x_{n+1}}(y_{n+1}) P(X_1 = x_1, \dots, X_{n+1} = x_{n+1} \mid Y_1 = y_1, \dots, Y_n = y_n) \\
&= a_{x_{n+1}}(y_{n+1}). \quad \square
\end{aligned}$$

(1.8) Corollary. Suppose that $F = \{0,1\}$ and that $a_x(y)$ is independent of x for each y . Then Y is a Bernoulli trials process.

(1.9) Theorem. Suppose that $A_y(x,u)$ is independent of x . That is, $A_y(x,u) = b_y(u)$ for $x, u \in E, y \in F$ where

$$b_y(u) \geq 0, \quad \sum_u b_y(u) = 1.$$

Then X is a Markov chain on E with transition probability kernel

$$B(x,u) = \sum_y a_x(y) b_y(u); \quad x, u \in E$$

and Y is a Markov chain on F with transition probability kernel

$$D(y,v) = \sum_x b_y(x) a_x(v); \quad y, v \in F.$$

Proof. The statement about X follows immediately from Theorem (1.3).

Thus let $y_1, \dots, y_n, y_{n+1} \in F$. Then as in the proof of Theorem (1.7),

$$\begin{aligned}
&P(Y_{n+1} = y_{n+1} \mid Y_1 = y_1, \dots, Y_n = y_n) \\
&= \sum_{x_1, \dots, x_{n+1}} a_{x_{n+1}}(y_{n+1}) P(X_1 = x_1, \dots, X_{n+1} = x_{n+1} \mid Y_1 = y_1, \dots, Y_n = y_n) \\
&= \sum_{x_1, \dots, x_{n+1}} a_{x_{n+1}}(y_{n+1}) P(X_{n+1} = x_{n+1} \mid Z_1 = z_1, \dots, Z_n = z_n) \\
&\quad \cdot P(X_1 = x_1, \dots, X_n = x_n \mid Y_1 = y_1, \dots, Y_n = y_n) \\
&= \sum_{x_1, \dots, x_{n+1}} a_{x_{n+1}}(y_{n+1}) b_{y_n}(x_{n+1}) P(X_1 = x_1, \dots, X_n = x_n \mid Y_1 = y_1, \dots, Y_n = y_n) \\
&= \sum_{x_{n+1}} a_{x_{n+1}}(y_{n+1}) b_{y_n}(x_{n+1}). \quad \square
\end{aligned}$$

The following theorem gives a simple sufficient condition for one state to lead to another.

(1.10) Theorem. Fix $y \in F$ and suppose that $a_x(y) > 0$ for $x \in E$. If $x, u \in E$ and $A_y^n(x,u) > 0$ then $B^n(x,u) > 0$. In particular, if A_y is irreducible, then so is B .

Proof. We prove the first statement by induction on n . The second

statement is then immediate. Let $x, u \in E$. If $A_y(x, u) > 0$ then

$$B(x, u) = \sum_v a_x(v) A_v(x, u) \geq a_x(y) A_y(x, u) > 0.$$

Assume the truth of the statement for $n = k$. Suppose $x, u \in E$ and $A_y^{k+1}(x, u) > 0$. Then there exists $s \in E$ such that $A_y^k(x, s) > 0$ and $A_y(s, u) > 0$. But then $B^k(x, s) > 0$ and $B(s, u) > 0$ so $B^{k+1}(x, u) > 0$. \square

The following theorem characterizes the absorbing states of X in terms of the basic data.

(1.11) Theorem. Let $x \in E$. Then x is absorbing for X if and only if x is absorbing for the chain governed by A_y for each y in the support of a_x .

Proof. Let $x \in E$ and let $S = \{y \in F: a_x(y) > 0\}$ denote the support of a_x . Suppose that x is absorbing for the A_y chain for each $y \in S$. Then

$$B(x, x) = \sum_{y \in F} a_x(y) A_y(x, x) = \sum_{y \in S} a_x(y) A_y(x, x) = \sum_{y \in S} a_x(y) = 1.$$

Conversely, suppose that x is absorbing for X . Suppose that for some $y_0 \in S$, $A_{y_0}(x, x) < 1$. Then

$$\begin{aligned} 1 = B(x, x) &= \sum_{y \in S} a_x(y) A_y(x, x) \\ &= a_x(y_0) A_{y_0}(x, x) + \sum_{y \in S - \{y_0\}} a_x(y) A_y(x, x) \\ &< a_x(y_0) + \sum_{y \in S - \{y_0\}} a_x(y) = 1 \end{aligned}$$

--a contradiction. Hence $A_y(x, x) = 1$ for each $y \in S$. \square

We close this section with several results that characterize the invariant measures of X and Z in terms of the basic data.

(1.12) Theorem. Suppose that ν is an invariant measure for X . Define π by

$$\pi(x, y) = \nu(x) a_x(y).$$

Then π is an invariant measure for Z .

Proof. Let $(u, v) \in E \times F$. Then

$$\begin{aligned} \sum_{x, y} \pi(x, y) C((x, y), (u, v)) &= \sum_{x, y} \nu(x) a_x(y) A_y(x, u) a_u(v) \\ &= a_u(v) \sum_x \nu(x) \sum_y a_x(y) A_y(x, u) \\ &= a_u(v) \sum_x \nu(x) B(x, u) \\ &= a_u(v) \nu(u) \\ &= \pi(u, v). \quad \square \end{aligned}$$

(1.13) Theorem. Suppose that $\pi: E \times F \rightarrow [0, \infty)$. Then π is an invariant

measure for Z if and only if the following two conditions are satisfied:

$$(a) \sum_{x,y} \pi(x,y)A_y(x,u) = \sum_v \pi(u,v) \text{ for } u \in E,$$

$$(b) a_x(y)\sum_v \pi(x,v) = \pi(x,y) \text{ for } x \in E \text{ and } y \in F.$$

Proof. Suppose that π is invariant for Z. For $(u,v) \in E \times F$,

$$\sum_{x,y} \pi(x,y)C((x,y),(u,v)) = \pi(u,v)$$

or

$$\sum_{x,y} \pi(x,y)A_y(x,u)a_u(v) = \pi(u,v).$$

Summing both sides over $v \in F$ we have

$$\sum_{x,y} \pi(x,y)A_y(x,u) = \sum_v \pi(u,v)$$

which is (a). Now recall from above that

$$\sum_{x,y} \pi(x,y)A_y(x,u)a_u(v) = \pi(u,v)$$

so

$$a_u(v)\sum_{x,y} \pi(x,y)A_y(x,u) = \pi(u,v)$$

and hence from (a) we get

$$a_u(v)\sum_t \pi(u,t) = \pi(u,v)$$

which is (b).

Conversely, suppose that (a) and (b) are satisfied. Let $(u,v) \in E \times F$.

Then

$$\begin{aligned} \sum_{x,y} \pi(x,y)C((x,y),(u,v)) &= \sum_{x,y} \pi(x,y)A_y(x,u)a_u(v) \\ &= a_u(v)\sum_{x,y} \pi(x,y)A_y(x,u) \\ &= a_u(v)\sum_t \pi(u,t) && \text{(from (a))} \\ &= \pi(u,v) && \text{(from (b))} \end{aligned}$$

so π is an invariant for Z. \square

(1.14) Corollary. Suppose that π is an invariant measure for Z. Define

$$\nu(x) = \sum_y \pi(x,y).$$

Then ν is an invariant measure for X.

Proof. Note first from Theorem (1.13) that ν is finite valued. Now let $u \in E$. Then

$$\begin{aligned} \sum_x \nu(x)B(x,u) &= \sum_x \nu(x)\sum_y a_x(y)A_y(x,u) \\ &= \sum_{x,y} \nu(x)a_x(y)A_y(x,u) \end{aligned}$$

$$\begin{aligned}
&= \sum_{\mathbf{x}, \mathbf{y}} \sum_{\mathbf{v}} \pi(\mathbf{x}, \mathbf{v}) a_{\mathbf{x}}(\mathbf{y}) A_{\mathbf{y}}(\mathbf{x}, \mathbf{u}) \\
&= \sum_{\mathbf{x}, \mathbf{y}} \pi(\mathbf{x}, \mathbf{y}) A_{\mathbf{y}}(\mathbf{x}, \mathbf{u}) && \text{(from (1.13)(a))} \\
&= \sum_{\mathbf{v}} \pi(\mathbf{u}, \mathbf{v}) && \text{(from (1.13)(b))} \\
&= v(\mathbf{u}). \quad \square
\end{aligned}$$

2. EXAMPLES

We first consider a device that can be in two states. Thus we let $E = \{0,1\}$ where 0 stands for "unrepaired" and 1 for "repaired." The device is subjected to a sequence of trials, each of which has three possible outcomes. We let $F = \{0,1,2\}$ where 0 stands for an "inherent" failure, 1 for an "assignable-cause" failure, and 2 for a success. An assignable-cause failure is one that is due to a design defect and thus can occur only in the unrepaired state. An inherent failure or a success can occur in either state.

In this section, if $c \in [0,1]$, then \bar{c} denotes $1 - c$.

We define A as follows:

$$(2.1) \quad \begin{aligned} A_y(0,0) &= 1, A_y(0,1) = 0 \text{ for } y = 0, 2, \\ A_1(0,0) &= \bar{p}, A_1(0,1) = p \text{ (where } p \in [0,1]), \\ A_y(1,0) &= b, A_y(1,1) = \bar{b} \text{ for } y = 0, 1, 2, \text{ (where } b \in [0,1]). \end{aligned}$$

We have the following interpretation: After an inherent failure or a success, the system if unrepaired remains unrepaired. After an assignable-cause failure, the unrepaired system has probability p of being repaired. Finally, after any outcome, if the system is repaired, it has probability b of degenerating back into the unrepaired state.

We define a as follows:

$$(2.2) \quad \begin{aligned} a_0(0) &= q_0, a_0(1) = q_1, a_0(2) = \overline{q_0 + q_1}, \\ a_1(0) &= q_0, a_1(1) = 0, a_1(2) = \overline{q_0}. \end{aligned}$$

where $q_0, q_1 > 0$ and $q_0 + q_1 < 1$. We have the following interpretation: An inherent failure is state independent and occurs with probability q_0 on each trial. In the unrepaired state, an assignable-cause failure occurs with probability q_1 ; in the repaired state, an assignable-cause failure is impossible.

To complete the basic data, let $\nu = (\theta, \bar{\theta})$ be the distribution of X_1 where $\theta \in [0,1]$.

From Theorem (1.3), we can easily compute the transition matrix B of X :

$$B = \begin{matrix} & \begin{matrix} 0 & 1 \end{matrix} \\ \begin{matrix} 0 \\ 1 \end{matrix} & \begin{bmatrix} \overline{q_1 p} & q_1 p \\ b & \bar{b} \end{bmatrix} \end{matrix}.$$

The distribution of X_n can now be computed by standard techniques (see, for example, [13]):

$$P(X_n = 0) = \frac{b}{q_1 p + b} + (1 - q_1 p - b)^{n-1} \left(\theta - \frac{b}{q_1 p + b} \right)$$

$$P(X_n = 1) = \frac{q_1 p}{q_1 p + b} + (1 - q_1 p - b)^{n-1} \left(1 - \theta - \frac{q_1 p}{q_1 p + b} \right).$$

Note that the limiting distribution of X is

$$\left(\frac{b}{q_1 p + b}, \frac{q_1 p}{q_1 p + b} \right)$$

which gives the long term probabilities of being in the unrepaired and repaired states, respectively. Note also that if $q_1 p + b = 1$, then

$$B = \begin{matrix} & 0 & 1 \\ 0 & \begin{bmatrix} b & \bar{b} \end{bmatrix} \\ 1 & \begin{bmatrix} b & \bar{b} \end{bmatrix} \end{matrix}$$

and $P(X_n = 0) = b$, $P(X_n = 1) = \bar{b}$ for $n = 2, 3, \dots$. In this case, X_n , $n = 2, 3, \dots$ are independent and identically distributed.

The following theorem gives a complete analysis of the reliability function r .

(2.3) Theorem. The reliability function r is given by

$$r_n = 1 - q_0 - \frac{q_1 b}{q_1 p + b} - q_1 \left(\theta - \frac{b}{q_1 p + b} \right) (1 - q_1 p - b)^{n-1}$$

for $n = 1, 2, \dots$. The limiting reliability is

$$r_\infty = 1 - q_0 - \frac{q_1 b}{q_1 p + b}.$$

Moreover,

- (a) If $q_1 p + b > 1$ but $\neq b/\theta$ then $r_n \rightarrow r_\infty$ in an oscillating manner.
- (b) If $b/\theta < q_1 p + b < 1$ then r_n increases to r_∞ (reliability growth).
- (c) If $q_1 p + b < \min\{1, b/\theta\}$ then r_n decreases to r_∞ (reliability decay).
- (d) If $q_1 p + b = 1$ or b/θ then $r_n = r_\infty$ for $n = 1, 2, \dots$.

Proof. The expression for r_n is easily obtained from the distribution of X_n by the formula $r_n = E(a_{X_n}(2))$. Note that r has the form

$$(2.4) \quad r_n = r_\infty - \alpha\beta^{n-1}, \quad n = 1, 2,$$

where

$$r_\infty = 1 - q_0 - \frac{q_1 b}{q_1 p + b},$$

$$\alpha = q_1 \left(\theta - \frac{b}{q_1 p + b} \right),$$

$$\beta = 1 - (q_1 p + b).$$

Note that $|\beta| < 1$ so $r_n \rightarrow r_\infty$ as $n \rightarrow \infty$. Also $r_\infty > 0$. The rest of the analysis follows easily: Under the conditions in (a), $\beta < 0$ and $\alpha \neq 0$ so $r_n \rightarrow r_\infty$ in an oscillating manner. Under the conditions in (b), $\beta > 0$ and $\alpha > 0$ so r_n increases to r_∞ . Under the conditions in (c), $\beta > 0$ and $\alpha < 0$ so r_n decreases to r_∞ . Under the conditions in (d), either $\alpha = 0$ or $\beta = 0$ so $r_n = r_\infty$ for $n = 2, 3, \dots$. \square

The parametric form (2.4) has been used by Bonis [5] and others to model reliability growth. However, these authors restrict α and β to be positive. This example shows that a more versatile parametric form is obtained by allowing α and β to be negative. Also, it is interesting to note that it is possible to have pure reliability growth even with a positive breakdown probability b .

In the special case $b = 0$ (no possibility of breakdown from the the repaired state to the unrepaired state), the reliability function r has been obtained by Barr [4] and Lloyd-Lipow [15]. In this case, another interesting statistic is

$$M_1 = \min\{n: X_n = 1\},$$

the trial number at which the system first enters the absorbing repaired state. The distribution of M_1 is easy to obtain:

$$P(M_1 = 1) = P(X_1 = 1) = 1 - \theta$$

and for $n = 2, 3, \dots$,

$$\begin{aligned} P(M_1 = n) &= P(X_1 = 0, \dots, X_{n-1} = 0, X_n = 1) \\ &= \theta(B(0,0))^{n-2} B(0,1) \\ &= \theta(1 - q_1 p)^{n-2} q_1 p. \end{aligned}$$

The expected trial number at which the system first enters the repaired state is

$$E(M_1) = 1 + \theta/q_1 p.$$

Finally, we consider an optimization problem in the setting of (2.1) and (2.2). Suppose that each repair costs \$c and that each failure costs \$d (c, d > 0). The long term expected average cost per trial is

$$v = \lim_{n \rightarrow \infty} \frac{E(c \sum_{i=1}^n 1_{(0,1)}(X_i, X_{i+1}) + d \sum_{i=1}^n 1_0(Y_i) + 1_1(Y_i))}{n}$$

$$= \lim_{n \rightarrow \infty} \frac{c \sum_{i=1}^n P(X_i = 0, X_{i+1} = 1) + d \sum_{i=1}^n P(Y_i = 0 \text{ or } 1)}{n}.$$

Using standard conditional probability arguments we can show that

$$P(X_i = 0, X_{i+1} = 1) = pq_1 P(X_i = 0),$$

$$P(Y_i = 0 \text{ or } 1) = q_0 + q_1 P(X_i = 0).$$

Hence,

$$v = dq_0 + (dq_1 + cpq_1) \lim_{n \rightarrow \infty} \frac{\sum_{i=1}^n P(X_i = 0)}{n}.$$

But $\frac{\sum_{i=1}^n P(X_i = 0)}{n}$ converges to $\frac{b}{q_1 p + b}$, the limiting distribution at 0, as $n \rightarrow \infty$. Therefore,

$$(2.5) \quad v = dq_0 + (dq_1 + cpq_1) \frac{b}{q_1 p + b}.$$

Now suppose that the failure probabilities q_0 and q_1 and the breakdown probability b are fixed but that the repair probability $p \in [0, 1]$ may be chosen arbitrarily (thus, p becomes a control parameter). Minimizing v in (2.5) with respect to p we obtain the following:

(2.6) Theorem. If $cb > dq_1$ then the minimum value of v is $dq_0 + dq_1$ and it occurs when $p = 0$ (i.e., we never repair). If $cb < dq_1$ then the minimum value of v is

$$dq_0 + (dq_1 + cq_1) \frac{b}{q_1 + b}$$

and it occurs when $p = 1$ (i.e., we repair with certainty after each assignable-cause failure).

We will close this section by mentioning several other reliability growth models in the literature that can be easily formulated in terms of the general model of Section 1.

(2.7) Suppose as above that the system has two states--the repaired state and the unrepaired state, and that the trials have three possible outcomes--inherent failure, assignable-cause failure, and success. Now, however, we suppose that the probability that the system is repaired after an assignable-cause failure depends on the total number of assignable-cause failures that have occurred. This model is due to Barr [4].

To cast this problem in the setting of Section 1, we let $E = \{\Delta, 0, 1, 2, \dots\}$ be the state space where Δ means that the system is repaired and where $x \in \{0, 1, 2, \dots\}$ means that the system is unrepaired and that x assignable-cause failures have occurred in the past. As before we let $F = \{0, 1, 2\}$ be the outcome space where 0 means an inherent failure, 1 means an assignable-cause failure, and 2 means success. Define $A_y(x,x) = 1$, $A_y(x,u) = 0$ for $x, u \in E$, $x \neq u$, and $y = 0, 2$ (i.e., after an inherent failure or a success, the state of the system does not change). Define $A_1(\Delta, \Delta) = 1$, $A_1(\Delta, u) = 0$ for $u \neq \Delta$, and for $x \neq \Delta$, define $A_1(x, \Delta) = p_{x+1}$, $A_1(x, x+1) = 1 - p_{x+1}$, $A_1(x, u) = 0$ otherwise (i.e., if an assignable-cause failure occurs and the system is in state x , then $x+1$ assignable-cause failures have occurred totally so the system is repaired with probability $p_{x+1} \in (0,1)$). Finally, define $a_x(0) = q_0$, $a_x(1) = q_1$, $a_x(2) = 1 - q_0 - q_1$ for $x \neq \Delta$ and $a_\Delta(0) = q_0$, $a_\Delta(1) = 0$, $a_\Delta(2) = 1 - q_0$.

For this problem, the reliability function can be computed explicitly and the distribution of the trial number at which the system first enters the absorbing repaired state can be found. Interestingly, we can show that if p_x decreases fast enough, the system may, with positive probability, never enter the repaired state.

(2.8) We suppose as before that the trials have three possible outcomes--inherent failure, assignable-cause failure, and success. Now however we suppose that an assignable-cause failure can come from any one of k distinct sources. Various forms of this problem have been considered by Barr [4], Wolman [21], et. al. We make the following assumptions:

- (a) On each trial, inherent failure, assignable-cause failure, and success are mutually exclusive and collectively exhaustive.
- (b) On each trial, the occurrence of an inherent failure is independent of the state of the system and has probability q_0 .
- (c) If n assignable-cause failure modes are unrepaired when a trial is conducted and if an inherent failure does not occur, then the number of

assignable-cause failures is binomially distributed with parameters n and q .

(d) Once an assignable-cause failure source has been repaired, it remains repaired.

To cast this problem in the setting of Section 1, we let $E = \{0, 1, 2, \dots\}$ be the state space where $x \in E$ means that x assignable-cause failure sources are repaired (and $k - x$ are unrepaired). We let $F = \{0, 1, 2\}$ be the outcome space, as before. Based on assumptions (a), (b), and (c), we can show that a should be defined as follows: $a_x(0) = q_0$, $a_x(1) = (1 - (1 - q)^{k-x})(1 - q_0)$, and $a_x(2) = 1 - a_x(0) - a_x(1)$ for $x \in E$. The definition of A of course depends on the repair policy. Barr [4] has considered the following policies:

(a) If on a trial at least one assignable-cause failure occurs, then exactly one assignable-cause failure source is repaired.

(b) If on a trial at least one assignable-cause failure occurs, then exactly one assignable-cause failure source is repaired with probability p .

(c) If n assignable-cause failures occur on a trial, then those n assignable-cause failure sources are repaired.

(d) If n assignable-cause failures occur on a trial, then those n assignable-cause failure sources are repaired independently of one another with probability p .

Each of these repair policies can be incorporated into our model. For example, for repair policy (d), which is the most complicated, we can show that A should be defined as follows: $A_y(x,x) = 1$, $A_y(x,u) = 0$ for $x, u \in E$ $x \neq u$, $A_1(k,k) = 1$, $A_1(k,u) = 0$ for $u \neq k$, and for $x \neq k$,

$$A_1(x,u) = \frac{\binom{k-x}{u-x} (pq)^{u-x} (1-pq)^{k-u}}{1 - (1-q)^{k-x}}, \quad u > x$$

$$A_1(x,x) = \frac{(1-pq)^k}{1 - (1-q)^{k-x}}.$$

CONCLUSIONS AND RECOMMENDATIONS

A general mathematical model has been developed to describe a system undergoing a sequence of trials in which there is interaction between the internal states of the system and the outcomes of the trials. The model generalizes many discrete time reliability growth models in the literature. In addition, it allows new variations such as reliability decay and allows the formulation of interesting new problems such as the optimization problem. Several general theorems have been proven for the Markov chains that describe the state and the joint state-outcome of the system. In particular, the transition probabilities are characterized, the invariant measures are characterized, and several special cases are pointed out. A simple two state, three outcome system has been studied in detail. In particular, the reliability function of this system has been analyzed and a simple optimization problem solved.

This model warrants further study. Some specific recommendations and comments follow:

(a) The class of Markov chains that are used to describe the state and joint state-outcome in the model need further study. It would be particularly interesting to have conditions on the basic data that are necessary and sufficient for the chains to be recurrent or transient.

(b) The important optimization problem formulated in Section 1 needs to be solved. A first step in this direction would be a thorough survey of the available Markov control and decision theory literature.

(c) Continuing work needs to be done on the problem of modeling. That is, reasonable assumptions need to be found concerning the internal states of the system, the possible outcomes of the trials, and the redesign policies. Such assumptions are crucial for defining the basic data correctly.

(d) A project similar to the one summarized in this report needs to be carried out for systems undergoing continuous time testing. In particular, it seems likely that a stochastic process could be formulated that would generalize and improve many of the continuous time reliability growth models in the literature.

REFERENCES

1. Balaban, H. S., "Reliability growth models," J. Environmental Sciences, 11 - 18, 1978.
2. Barlow, R. E. and F. Proschan, Mathematical Theory of Reliability, Wiley, New York, 1965.
3. Barlow, R. E. and E. M. Scheuer, "Reliability growth during a development testing program," Technometrics, Vol. 8, No. 1, 53 - 60, 1966.
4. Barr, D. R., "A class of general reliability growth prediction models," Operations Research, Vol. 18, No.1, 52 - 65, 1970.
5. Bonis, A. J., "Reliability growth for one shot devices," Proc. 1977 Annual Reliability and Maintainability Symp., 181 - 185, 1977.
6. Codier, E. O., "Reliability growth in real life," Proc. 1968 Annual Symp. on Reliability, 458 - 469, 1968.
7. Codier, E. O., "Reliability prediction--help or hoax?" Proc. 1969 Annual Symp. on Reliability, 383 - 390, 1969.
8. Corcoran, W. J., H. Weingarten, and P. W. Zehna, "Estimating reliability after corrective action," Management Science, Vol. 10, No. 4, 786 - 795, 1964.
9. Crow, L. H., "Reliability growth modeling," U. S. Army Materiel Systems Analysis Agency Technical Report No. 55, 1972.
10. Crow, L. H., "On the AMSAA reliability growth model," Proc. Inst. Environmental Sciences.
11. Duane, J. T., "Learning curve approach to reliability monitoring," IEEE Trans. on Aerospace, Vol. 2, No. 2, 563 - 565, 1964.
12. Fink, R. W., "Screening for reliability growth," Proc. 1971 Annual Symp. on Reliability, 316 - 320, 1971.
13. Hoel, P. G., S. C. Port, and C. J. Stone, Introduction to Stochastic Processes, Houghton Mifflin, Boston, 1972.
14. Kreuze, F. J., "Growth curves--a practical management tool," Proc. 1972 Annual Reliability and Maintainability Symp., 430 - 436, 1972.
15. Lloyd, D. K., and M. Lipow, Reliability: Management, Methods, and Mathematics, sec. ed., 1977.
16. MacFarland, W. J., "Use of Bayes theorem in its discrete formulation for reliability estimation purposes."

17. Pollock, S. M., "A Bayesian reliability growth model," IEEE Trans. on Reliability, Vol. R-17, No. 4, 187 - 198, 1968.
18. Ross, S. M., Applied Probability Models with Optimization Applications, Holden-Day, San Francisco, 1969.
19. Virene, E. P., "Reliability growth and its upper limit," Proc. 1968 Annual Symp. on Reliability, 265 - 270, 1968.
20. Weiss, H. K., "Estimation of reliability growth in a complex system with a Poisson-type failure," J. of Operations Research Soc. of Amer., Vol. 4, 532 - 545, 1956.
21. Wolman, W., "Problems in system reliability analysis," Statistical Theory of Reliability, Ed. M. Zelen, U. Wisconsin Press, 149 - 166, 1963.

1982

NASA/ASEE SUMMER FACULTY RESEARCH FELLOWSHIP PROGRAM

MARSHALL SPACE FLIGHT CENTER
THE UNIVERSITY OF ALABAMA

MAGNETOSPHERIC RAY TRACING STUDIES

Prepared By:	N. Frank Six
Academic Rank:	Professor
University and Department:	Western Kentucky University Department of Physics & Astronomy
NASA/MSFC:	Space Science Laboratory
Division:	Solar-Terrestrial
Branch:	Magnetospheric Physics
MSFC Counterpart:	James L. Green, ES53
Date:	October, 1982
Contract No.:	

MAGNETOSPHERIC RAY TRACING STUDIES

BY

N. Frank Six
Department of Physics & Astronomy
Western Kentucky University
Bowling Green, Kentucky

ABSTRACT

The radio emission from Jupiter in the decametric range (2-40 MHz) has been studied for three decades. It is known that this emission is correlated with particular longitude regions on the planet and with the position of the satellite Io. The Planetary Radio Astronomy experiment on the Voyager 1 and 2 spacecraft observed this emission, obtaining valuable new information.

Using a model of Jupiter's magnetized plasma environment, radiation raypaths have been calculated with a three-dimension ray tracing program. It is assumed that energetic particles produce the emission in the planet's auroral zone at frequencies just above the electron gyrofrequencies. This radiation is generated in narrow sheets defined by the angle of a ray with respect to the magnetic field line. By specifying the source position: latitude, longitude and radial distance from the planet, signatures in the spectrum of frequency versus time seen by Voyager 1 and 2 have been duplicated. The frequency range and the curvature of the decametric arcs in these dynamic spectra are the result of the geometry of the radiation sheets (imposed by the plasma and by the B-field) and illumination of Voyager 1 and 2 as the rotating magnetosphere mimics a pulsar.

ACKNOWLEDGEMENT

This project has been a joint effort by five co-investigators: Dr. James Green, NASA/MSFC; Dr. Douglas Menietti, Southwest Research Institute; Dr. Samuel Gulkis, Jet Propulsion Laboratory; Dr. Donald Gurnett, Department of Physics and Astronomy, University of Iowa; and the author. Dr. Green is responsible for the three-dimensional ray tracing program in its present format. The larger project, of which this effort is a part, is funded as "Ray Tracing of Jovian Low Frequency Radiation" under the Jupiter Data Analysis Program.

LIST OF FIGURES

<u>Figure</u>	<u>Title</u>	<u>Page</u>
1.	JOVIAN DECAMETRIC RADIATION SIGNATURES	4
2.	MODEL OF JUPITER'S MAGNETIC FIELD AND PLASMA	5
3.	RADIATION SHEETS OF DIFFERENT FREQUENCIES INTERSECTING THE 6R _J SHELL	7
4.	RADIATION SHEETS INTERSECTING THE 6R _J SHELL (top) AND THE 100R _J SHELL (bottom)	8
5.	RADIATION SHEETS INTERSECTING THE 100R _J SHELL	10
6.	RADIATION SHEETS FOR 2 MHz (top) AND 25 MHz (bottom) LAUNCHED AT DIFFERENT WAVE NORMAL ANGLES	11
7.	RADIATION SHEETS EMANATING FROM SOURCES LOCATED AT DIFFERENT LONGITUDES	12

INTRODUCTION

For nearly three decades, intense and variable decametric radio emissions from Jupiter have been observed from the earth over the frequency range 5 MHz to 40 MHz. Near-earth satellites have extended the low frequency limit set by the terrestrial ionosphere down to a frequency of 425 kHz. The radiation is characterized by a high degree of elliptical polarization, complex dynamic spectra, and an upper cutoff frequency of ~ 39.5 MHz. It's probability of occurrence, dynamic spectral characteristics, polarization, and intensity are related to the central meridian longitude of Jupiter and to the orbital phase of Io.

Pioneer and Voyager spacecraft have sampled the magnetized plasma environment of the giant planet and added immensely to our knowledge. The magnetosphere of Jupiter, if "visible", would appear from earth four to five times as large as the sun. This makes it the largest structure in the solar system, if we exclude the expanding solar corona. The plasma near Jupiter's bow shock has been measured at $300 - 400 \times 10^6$ °K, hottest in the solar system. Inside this magnetic cavity in the solar wind, the magnetic field of Jupiter, strongest of any planet, forces the trapped plasma to co-rotate with the planet. And, immersed in this complex system is a torus of plasma straddling the orbit of the inner Galilean satellite Io. Volcanic activity on Io provides the source for particles in the plasma torus, while the magnetic field lines threading the torus terminate in Jupiter's auroral zones.

Recently the Planetary Radio Astronomy Experiment (PRA) on the Voyager 1 and 2 spacecraft obtained dramatic new information about Jupiter both because of its proximity to Jupiter and because it was able to measure the radio emissions to much lower frequencies than has been possible from earth and near-earth observatories. The data reveal a nested family of arcs in the decametric spectral region and strong kilometric/hectometric emissions. Encounter observations show unique spectral characteristics due to the spacecraft's proximity to Jupiter.

OBJECTIVES

Using techniques which have proven successful in explaining the propagation of electromagnetic waves in the terrestrial magnetosphere, a model of Jupiter's magnetic environment has been formulated and tested for validity using the data accumulated by the Pioneer and the Voyager spacecraft. The objectives of this investigation are the following:

1. Using a three-dimensional ray tracing program which includes magnetic field and plasma models, calculate propagation paths for decametric wavelength radiation in Jupiter's magnetosphere.
2. Generate radiation sheets for various combinations of the parameters: frequency, source location, and wave normal angle (angle between a launched ray and the B-field).
3. Compare the model-dependent radiation sheets with the observations made by the Voyager Planetary Radio Astronomy (PRA) experiments.
4. Re-format the PRA data to produce spectrograms of Jovian radiation intensity as a function of Voyager longitude, with Io at fixed longitudes.
5. Learn the location of the decametric source regions and the wave normal angles at which the radiation is emitted.

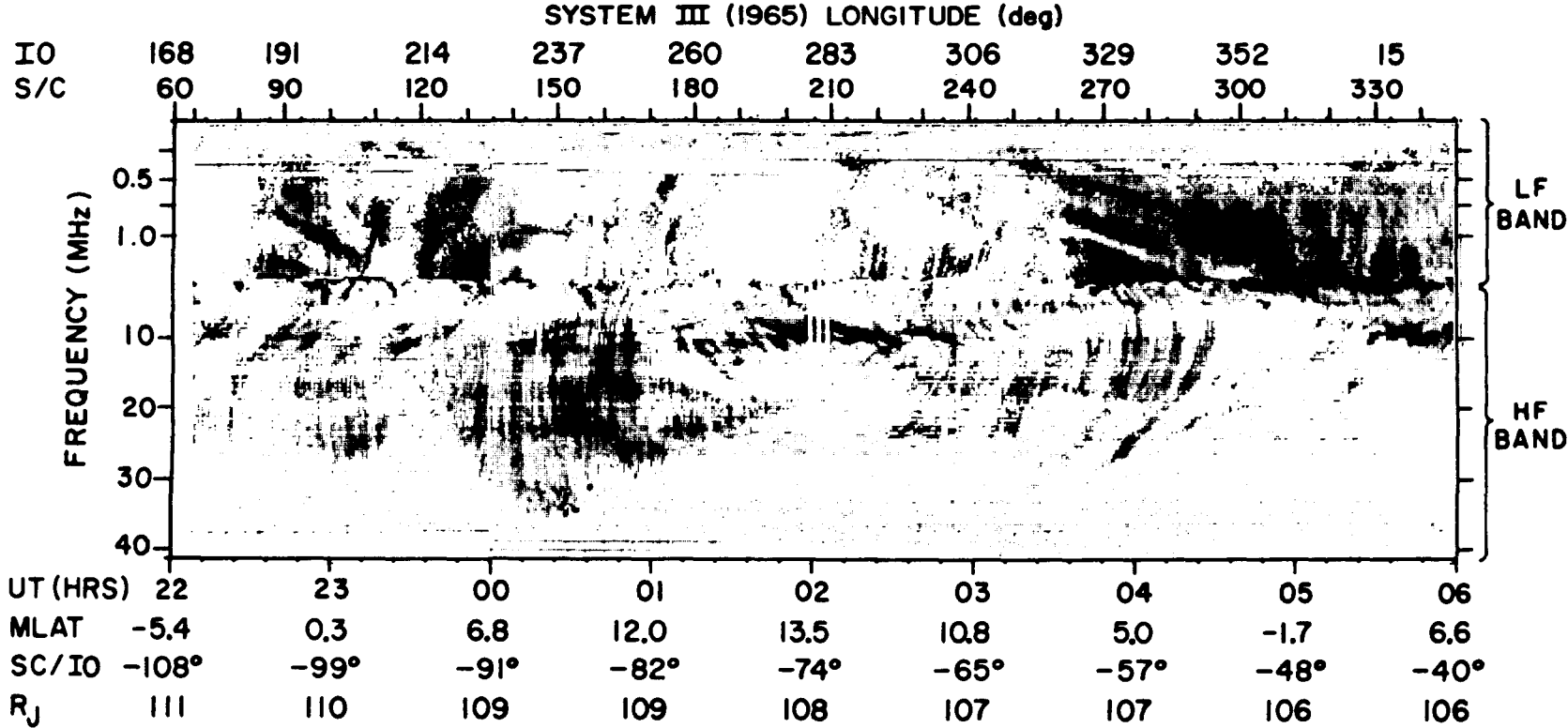
TECHNICAL APPROACH

Voyager PRA High Band Measurements. The Voyager observations of the decametric emissions from the giant planet are the most complete set of data available in the frequency range from 1.2 MHz to 40.5 MHz. We extend appreciation to the PRA experiment team for making this data available to us. Figure 1 is representative of the frequency-time spectra derived from the Voyager observations. Notice that frequency increases downward and time increases to the right. The most predominant features of such spectra are the "nested arcs" of both decreasing and increasing frequency with time. The curvature of a single "arc" might span as much as thirty minutes of time. Vertical features are also observed, i.e., a range of frequencies arriving at the detector simultaneously. These data were obtained in the stepping mode by the PRA instrument, sweeping through 198 frequency channels from 1.2 KHz to 40.5 MHz in six seconds, recording the total power and the polarization sense.

Ray Tracing Program. The soft-ware employed in this study is based on the Stix cold-plasma formulation of the index of refraction and Haselgrove's set of first order differential equations, amenable to numerical solution. The following inputs are chosen: a source position (radial distance from the center of Jupiter, latitude, and longitude-Sys.III'65), from which waves of a specified frequency are to be launched, at a specific wave normal angle (WNA) with respect to the magnetic field direction. At the origin of the ray, i.e., at the launch point, the program calculates an index of refraction surface for R-X mode waves, based on B-field and on background plasma parameters. Next, the program takes an incremental step in the direction perpendicular to the index of refraction surface, i.e., in the direction of the group velocity or energy flow, and then determines the coordinates of this new point on the raypath. Then, another index of refraction surface is calculated through this new point and the steps are repeated. The direction of the ray changes as it travels through the magnetized plasma. The raypath's behavior is determined by the initial conditions: the frequency of the wave, the wave normal angle (WNA), the coordinates of the source point, the propagation mode (R-X), and the magnetospheric model (plasma and B-field parameters). In practice, thirty-six rays are launched, one every 10° around B at the specified wave normal angle and frequency. It is necessary to specify the radial distance from the center of the planet to which the raypath is to be calculated. The output represents, in mercator projection, the intersection of the thirty-six raypaths with a chosen radial shell concentric with Jupiter. Run time for a single frequency, a single source location, a set of four WNA's, and raypaths traced to 150R_J (150 Jupiter radii) is four to thirty minutes, depending on the number of steps (bisections) necessary to achieve the desired accuracy.

B-field and Plasma Models. The raypaths calculated by the procedure described above are dependent on the magnetospheric model chosen. The description of the Jovian magnetic field utilized in these calculations is that published by Acuna and Ness (1976); the background plasma, Sentman and Goertz (1978); and the Io torus, Warwick, et al (1979). Figure 2 is an abbreviation of this combined "Jovian magnetosphere" showing contours of plasma frequency in the $200^\circ - 20^\circ$ meridian plane. Suspected source regions in the northern and southern hemispheres are shaded. A subroutine "MAGNET" uses a spherical harmonic analysis to calculate the magnitude of the field: B_0 , the components B_r , B_θ , and B_ϕ and their derivatives. Another subroutine "MODEL" calculates the plasma density along the raypath, and the spatial gradients.

VOYAGER I PRA EXPERIMENT FEBRUARY 26-27, 1979



XXXV 111-4

(FROM WARWICK et al., 1979)

Figure 1. JOVIAN DECAMETRIC RADIATION SIGNATURES

5-111AXXX

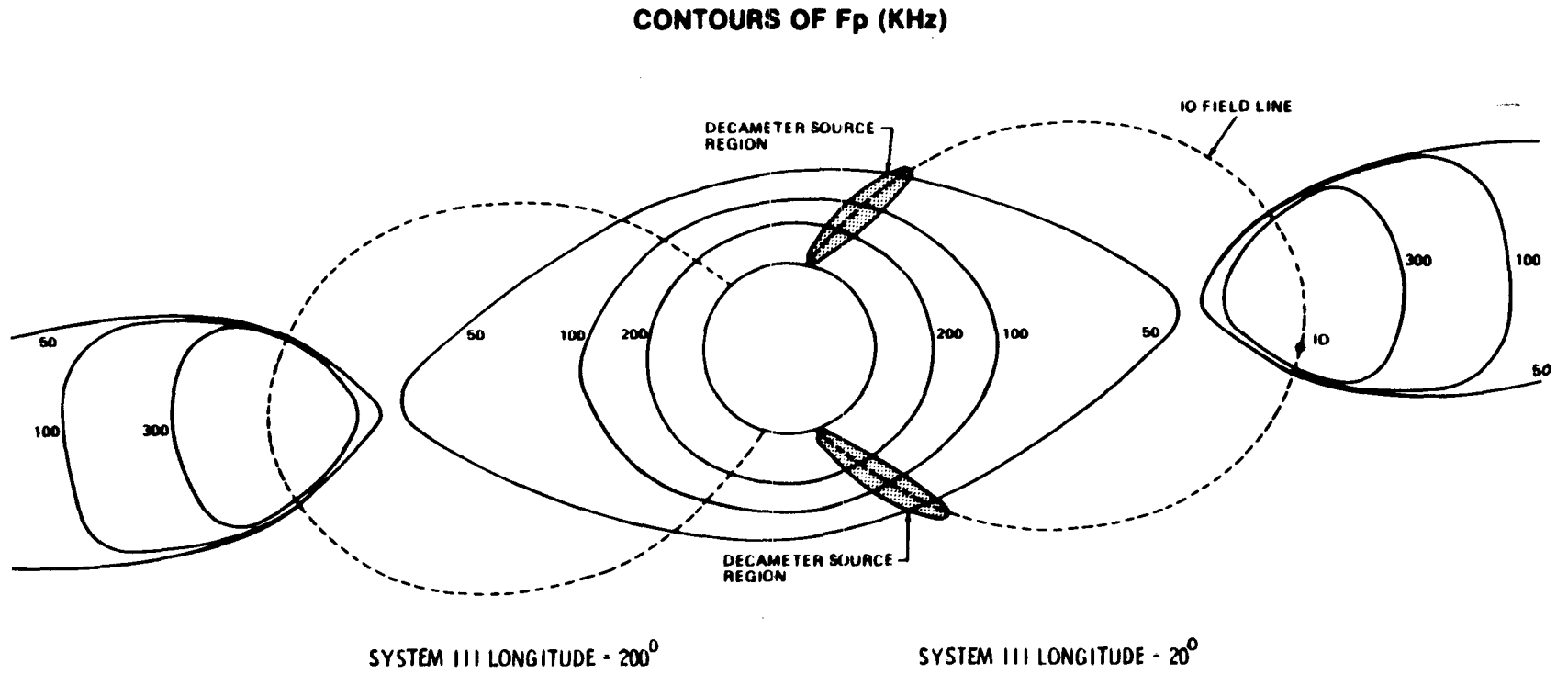


Figure 2. MODEL OF JUPITER'S MAGNETIC FIELD AND PLASMA

RESULTS

To calculate the raypaths, assumptions have been made regarding the initial conditions (input parameters): source coordinates, wave frequency and mode of the escaping wave. The source-points have been chosen to be on field lines through Io. These are likely locations for sources, since field aligned currents could provide the accelerating mechanism for particle beams. The wave frequency has been chosen to be 20% above the gyrofrequency. Once the field line through Io has been identified and the wave frequency assigned, the magnetic field program determines the coordinates of the launch (source) point. Polarization studies of the decametric emission and in situ measurements of the earth's auroral kilometric radiation indicate that the Jovian decametric radiation escapes in the R-X mode. A choice of sign in the index of refraction equation dictates the wave mode.

Radiation sheets of different frequencies are shown in Figures 3, 4, and 5. These figures present mercator projections of certain radial shells centered on Jupiter. The intersections of the calculated, model-dependent radiation sheets with these radial shells are labeled according to frequency. In Figure 3, the radial shell is at $6R_J$ and the Io torus is shown in shaded cross-section. Jovian latitude is indicated on the vertical axis and longitude System III '65, on the horizontal axis. Each point on the figure is the intersection of a raypath with the $6R_J$ shell. In three dimensions, the rays are symbolized as the bent ribs of an umbrella, while the fabric corresponds to the warped radiation sheet. All of the rays in Figure 3 were launched at a WNA = 90° . Sheets of two frequencies, 2 MHz and 20 MHz, originate from source points in the northern hemisphere labeled "X", and sheets of 2 MHz and 10 MHz radiation originate from source points in the southern hemisphere. At $6R_J$ parts of the radiation sheets are penetrating the Io plasma torus. We will see the effect of this penetration in the next figure. From close scrutiny of Figure 3, one notices the source points for different frequencies are displaced in longitude (horizontally), as well as in latitude. Since different frequencies are launched near the local gyrofrequency, one expects the source points to have different latitudes. The longitudinal separation of the source points for different frequencies is an indication of the azimuthal twist in the field line threading Io. This field line is shown dashed, as it is projected onto the $6R_J$ shell. Also, notice that the radiation sheets of differing frequencies can intersect. The consequences of this will be explained.

In Figure 4, the lower panel has been added to illustrate the evolution of the raypaths out to a distance of $100R_J$. The lower panel is the mercator projection of the $100R_J$ radial shell showing the intersections of the radiation sheets. The points represent the same rays seen in the top panel, but now traced to $100R_J$. Comparing the lower panel with the upper, it is easy to see that the sheets of radiation have spread out. Near longitude 230° , the radiation from the northern hemisphere sources reaches a southern latitude of -60° , while the radiation emanating from the southern hemisphere sources reaches a northern latitude of 45° . The radiation sheets at $100R_J$ (bottom panel) intersect the equator plane at different points (more widely separated) compared with the intersections of the same sheets with the equator plane at $6R_J$ (top panel). Notice that the radiation sheets in the bottom panel (at $100R_J$) are smooth and have the same gentle curvature as in the top panel (at $6R_J$). Since a portion of the radiation sheets traversed the Io plasma torus at $6R_J$, one might expect "kinks" to occur in the sheets, beyond the torus. No evidence

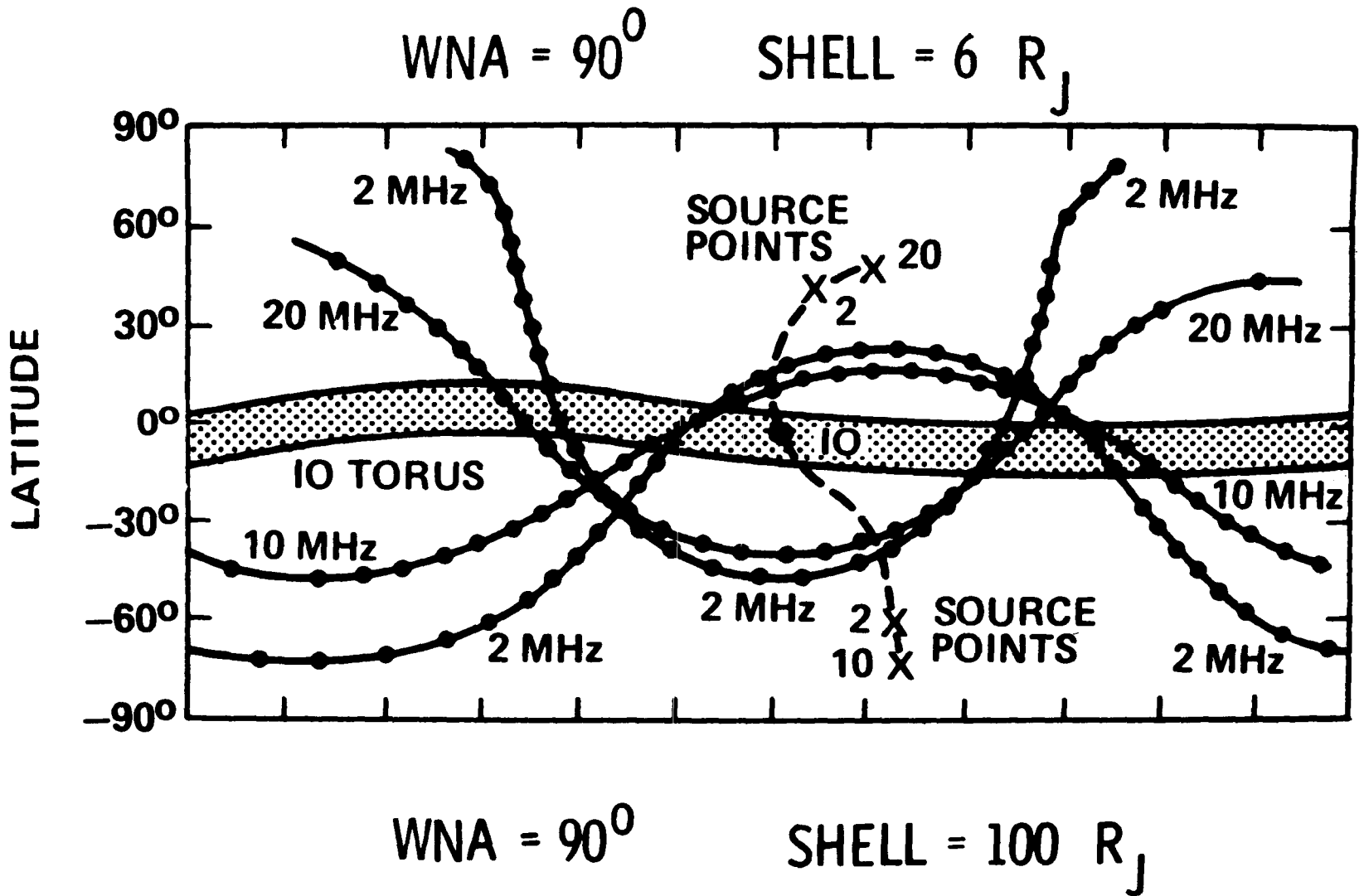


Figure 3. RADIATION SHEETS OF DIFFERENT FREQUENCIES INTERSECTING THE $6R_J$ SHELL

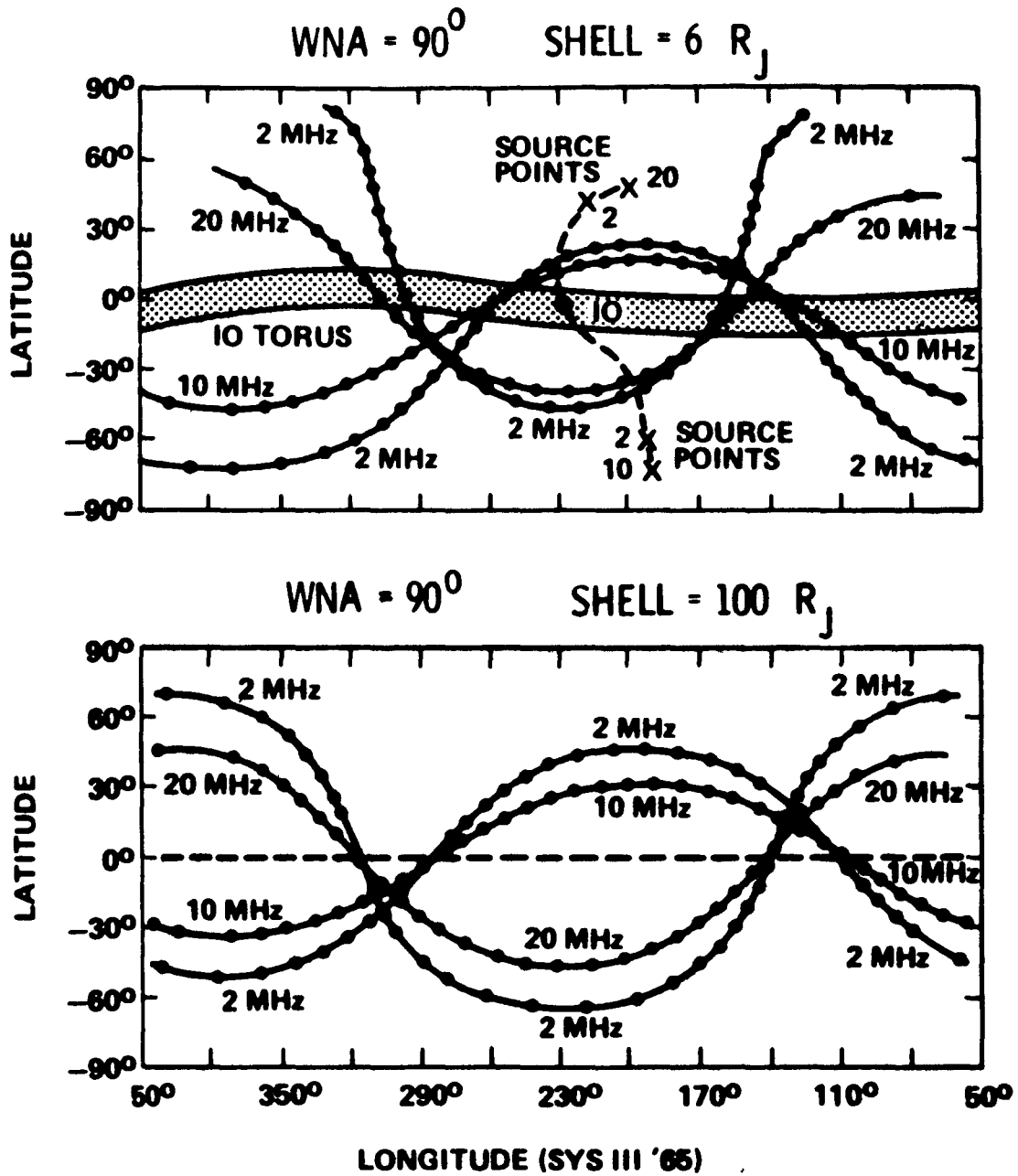


Figure 4. RADIATION SHEETS INTERSECTING THE $6R_J$ SHELL (top) AND THE $100R_J$ SHELL (bottom)

of diffraction effects, caused by the torus, are seen in the lower panel. We conclude that the torus has negligible effect even at 2 MHz, the lowest frequency traced, and leads us to surmise that propagation effects are confined to the region close to the planet.

Closer examination of the projection at $100R_J$, reproduced in Figure 5, reveals "crossings" of the radiation sheets of different frequencies. This should not be surprising since different frequencies are launched from different source points (assumption: radiation occurs near the local electron gyrofrequency). The twist in the field lines from one source point to the next produces intersections of the radiation sheets of different frequencies. The trajectory of Voyager 1 was slightly above the Jovian equator. As the magnetic field rotates, the radiation sheets sweep from left to right over the spacecraft (or, in the Jovian frame, the spacecraft flies from right to left, slightly above the equator). As the spacecraft intercepts these radiation sheets, the PRA experiment records frequencies which decrease or increase with time, depending on the nature of these intersections, i.e., the geometry of the radiation sheets. The latter is governed, in this model, by the plasma and magnetic field in and around the source region. It is probable that the Voyager decametric arcs are produced in this manner.

Radiation sheets produced by launching rays at different wave normal angles are shown in Figure 6. The top panel contains radiation sheets for 2 MHz and WNA's of 60° , 80° , 100° , and 120° . This mecatron projection was taken at the $100R_J$ radial shell. Note that the radiation sheets "open up" as the WNA increases from 60° to 100° , then the radiation emitted at WNA = 120° refracts upwards from the R-X cutoff. The bottom panel illustrates the same effect for radiation sheets of 25 MHz. Since the source of the 25 MHz radiation is closer to the pole, in this model, the sheets do not reach as far south. WNA is one parameter which shifts the intersection of the radiation sheets at the equator (and at the spacecraft) toward earlier or later longitudes.

Radiation sheets emanating from different source locations are shown in Figure 7. These 25 MHz radiation sheets, launched at WNA = 90° from adjacent source longitudes intersect the radial shell at $100R_J$. The projected source positions are located at the top of the frame. Should adjacent field lines host the emission of radiation at a given WNA, a family of "nested radiation sheets" of that particular frequency is produced. The warping of the radiation sheets from left to right across the frame is caused by the azimuthal asymmetry in the field, which is an integral part of this model. As the Jovian magnetic field rotates, the spacecraft is illuminated by this frequency as long as these radiation sheets intersect the spacecraft position. The spacecraft could "fly out of" this emission when sources are absent on adjacent field lines or when the geometry of the radiation sheets produces no illumination of the spacecraft.

01-1111XXXX

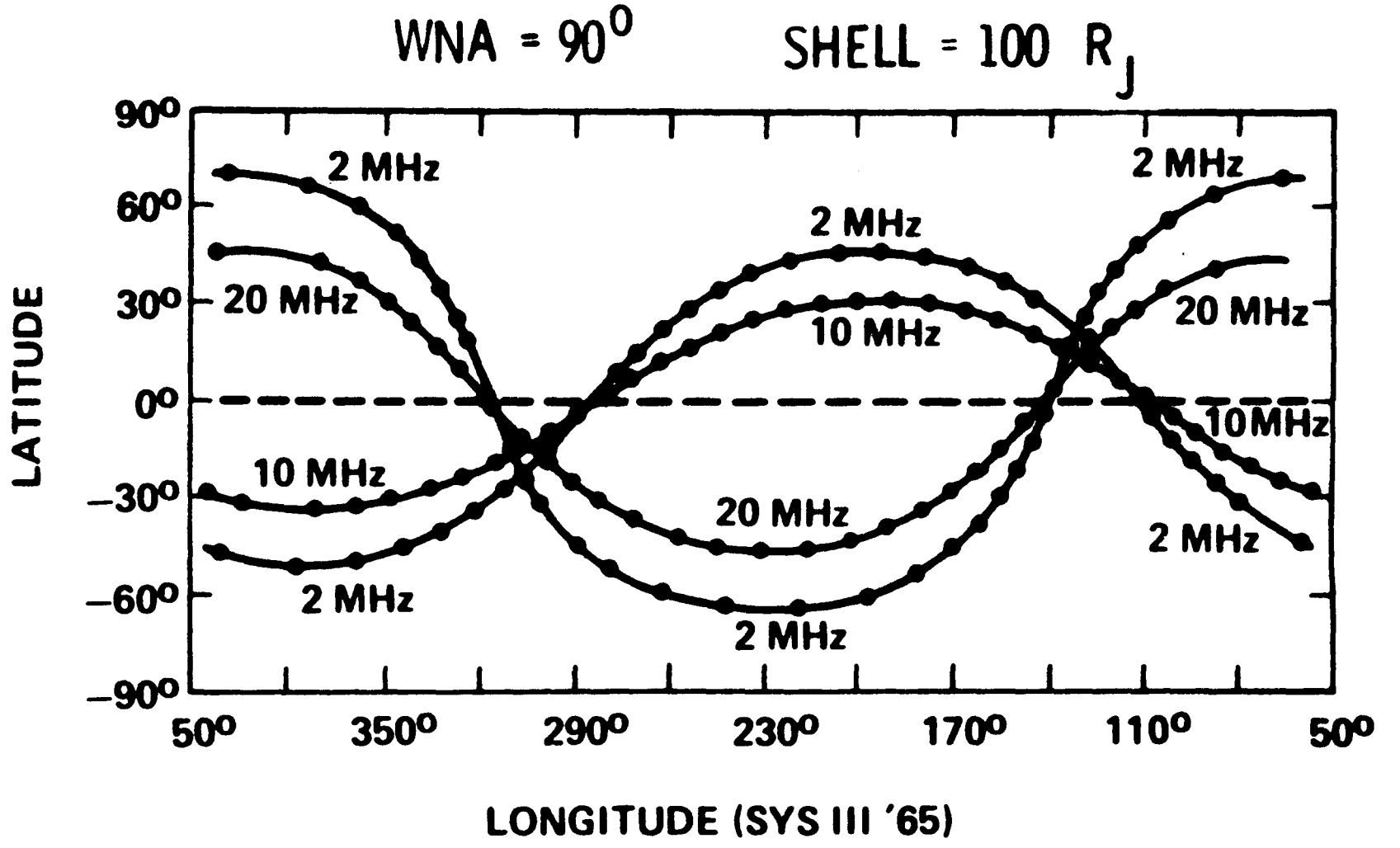


Figure 5. RADIATION SHEETS INTERSECTING THE $100R_J$ SHELL

EFFECT OF VARYING WAVE NORMAL ANGLE

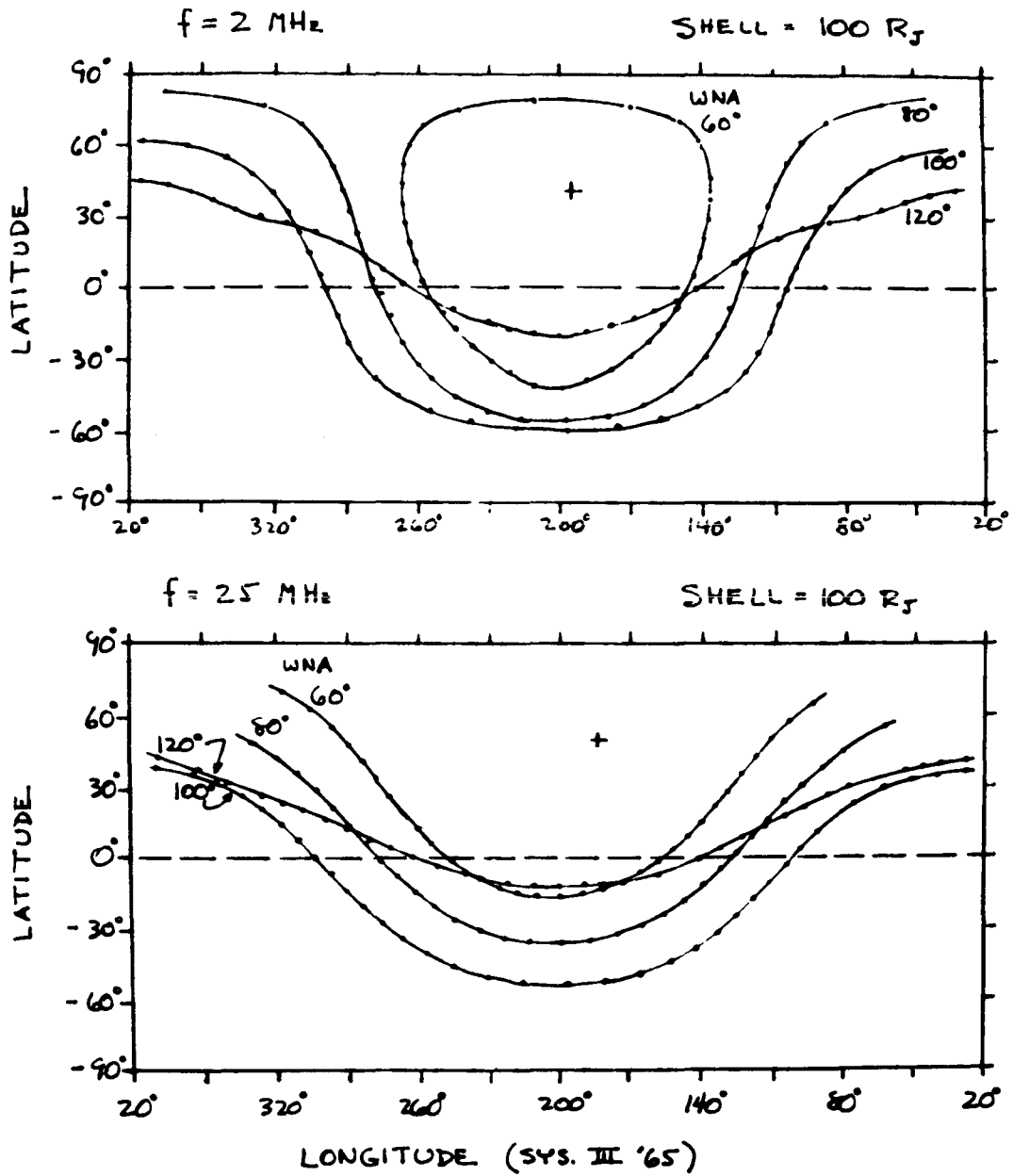


Figure 6. RADIATION SHEETS FOR 2 MHz (top) and 25 MHz (bottom) LAUNCHED AT DIFFERENT WAVE NORMAL ANGLES

XXXXVII-12

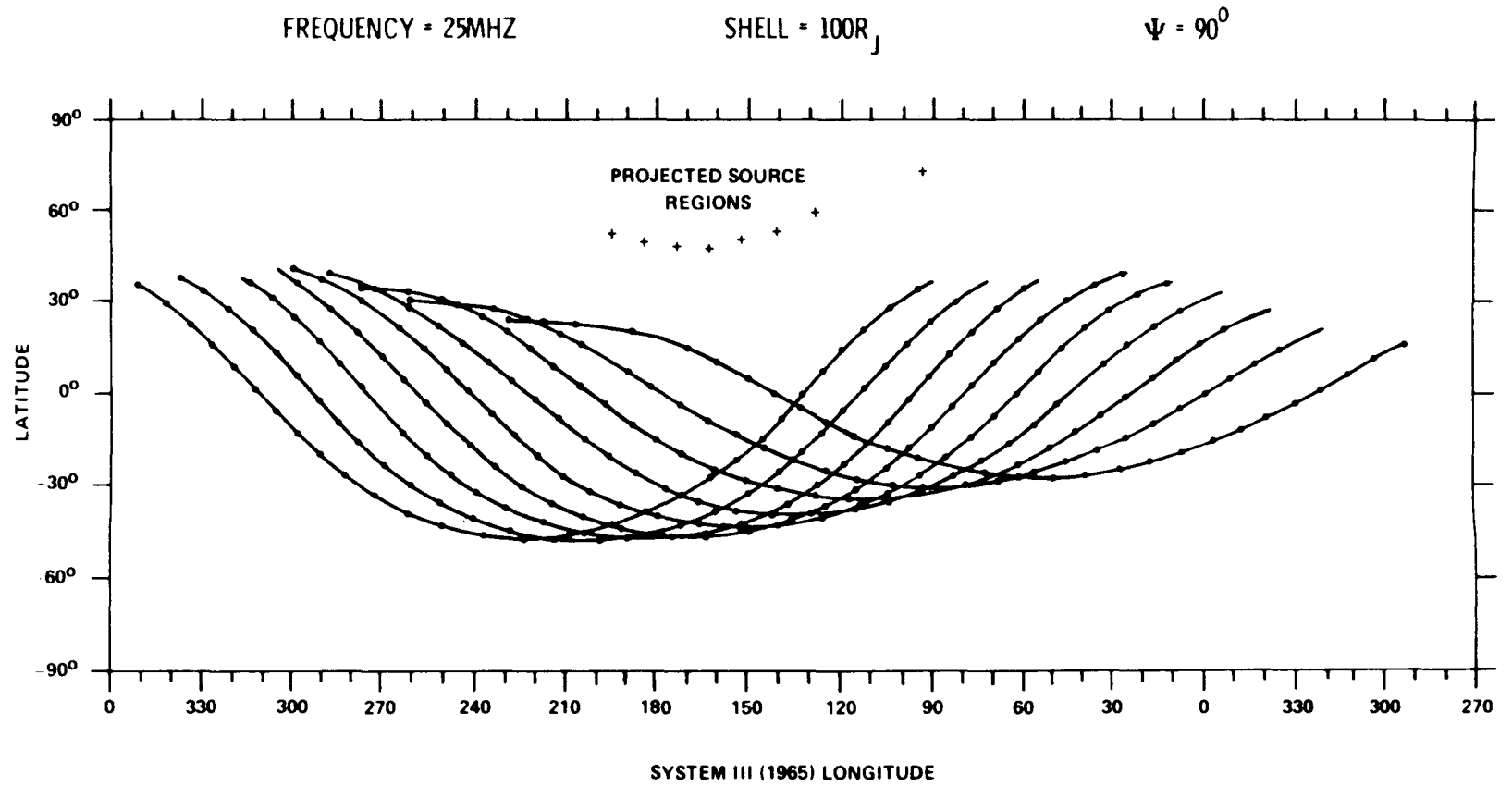


Figure 7. RADIATION SHEETS EMANATING FROM SOURCES LOCATED AT DIFFERENT LONGITUDES

CONCLUSIONS

Raypaths of radio frequency radiation have been generated in a model Jupiter magnetosphere using a three-dimensional code based on the Stix cold-plasma formulation of the index of refraction and Haselgrove's set of first order differential equations. The model magnetosphere incorporates a background ambient plasma, the 0-4 magnetic field description, and a plasma torus encompassing the orbit of Io. The raypaths which have been calculated are based on the following assumptions: 1) the radiation propagates in the R-X mode; 2) the source regions are located near the planet, at high latitudes, on field lines occupied by Io; 3) the radiation mechanism is Doppler-shifted gyro-emission; and 4) each frequency radiated is confined to a narrow sheet.

The decametric raypaths are refracted by the ambient plasma and the local B-field so that an observer is illuminated by radiation of different frequencies as the source regions co-rotate with the planet. Hence, the "on-off" nature of the emission, as observed at some point in space, is pulsar-like.

The growth-rate of the emission process causes the radiation to be confined to narrow sheets which are contoured by the plasma near Jupiter and by the azimuthal twist in the magnetic field, resulting in bends and ruffles like the familiar shapes of "auroral curtains", but on a grander scale. The intersection of these calculated sheets of radiation with the spacecraft produce arc-like signatures like those detected by Voyagers 1 and 2. Both the shape and the location (in longitude) of the low curvature arcs in the data are predicted by Doppler-shifted gyro-emission with all frequencies launched at a wave normal angle of approximately 90° . Decametric arcs of higher curvature appear to represent a different class of event. Initial studies imply that these higher curvature features are reproduced by allowing the wave normal angle to vary as a function of the wave frequency. It is suggested that these events could be produced by higher energy electrons whose gyro-emission is relativistically beamed closer to the B-field direction, i.e., launched with smaller wave normal angles.

There are still unexplained observations. Occasionally Voyager detected arcs of low curvature when the angle between the spacecraft and Io, with vertex at Jupiter, was greater than 90° . In order to reproduce those signatures, it may be necessary to postulate source regions outside of the Io flux tube. Those longitudes, which have been visited recently by Io, might be host to radiation sources, provided that energetic particle beams still reside there. Or, it may be necessary to incorporate a different B-field description, such as the Smith D-4 model, in order to duplicate those observations.

A continuing study is proposed to explain other structures in the Voyager dynamic spectra. There are aspects of Io's interaction which deserve closer scrutiny, such as, standing Alfvén waves in the plasma torus. Also, more attention will be devoted to source locations in the southern hemisphere. A re-formatting of the Voyager data, presently underway, should help immensely in the analysis. By sorting the radiation intensity, at various frequencies, with respect to Io position (in Jupiter's longitude system III), source regions should be revealed. The repetition of spectral features (nested arcs) are to be examined by the technique of power spectrum analysis of four individual frequencies, to provide clues to the "ringing" of the decametric source/s.

We have only scratched the surface regarding our ability to accurately describe the wave-particle interactions in Jupiter's magnetized plasma environment. Further analysis must be performed.

REFERENCES

1. Acuna, M. H. and N. F. Ness, "The Main Magnetic Field of Jupiter", J. Geophysical Research, 81, 2917, 1976.
2. Sentman, D. D. and C. K. Goertz, "Whistler Mode Noise in Jupiter's Inner Magnetosphere", J. Geophysical Research, 83, 3151, 1978.
3. Warwick, J. W., J. B. Pearce, A. C. Riddle, J. K. Alexander, M. D. Desch, M. L. Kaiser, J. R. Thieman, T. D. Carr, S. Gulkis, A. Boischot, C. C. Harvey and B. M. Pederson, "Voyager 1 Planetary Radio Astronomy Observations Near Jupiter", Science, 204, 995, 1979.

1982

NASA/ASEE SUMMER FACULTY RESEARCH FELLOWSHIP PROGRAM

MARSHALL SPACE FLIGHT CENTER
THE UNIVERSITY OF ALABAMA

MODIFICATION AND EVALUATION OF A BARNES-TYPE OBJECTIVE
ANALYSIS SCHEME FOR SURFACE METEOROLOGICAL DATA

Prepared by:	David R. Smith, Ph.D.
Academic Rank:	Assistant Professor
University and Department:	Purdue University Department of Geosciences
NASA/MSFC: (Laboratory) (Division) (Branch)	Space Sciences Atmospheric Sciences Fluid Dynamics
MSFC Counterpart:	Fred W. Leslie, Ph.D.
Date:	July 30, 1982
Contract No.:	NGT-01-002-099 (University of Alabama)

MODIFICATION AND EVALUATION OF A BARNES-TYPE OBJECTIVE
ANALYSIS SCHEME FOR SURFACE METEOROLOGICAL DATA

By

David R. Smith, Ph.D.
Assistant Professor of Atmospheric Sciences
Department of Geosciences
Purdue University
West Lafayette, Indiana

ABSTRACT

The Purdue Regional Objective Analysis of the Mesoscale (PROAM) is a Barnes-type scheme for the analysis of surface meteorological data. Modifications are introduced to the original version (Brady, 1982) in order to increase its flexibility and to permit greater ease of usage. The code has been rewritten for an interactive computer environment. Furthermore, a multiple iteration technique suggested by Barnes (1973) has been implemented for greater accuracy.

PROAM is then subjected to a series of experiments in order to evaluate its performance under a variety of analysis conditions. The tests include use of a known analytic temperature distribution in order to quantify error bounds for the scheme. Similar experiments were conducted using actual atmospheric data. Results indicate that the multiple iteration technique increases the accuracy of the analysis. Furthermore, the tests verify appropriate values for the analysis parameters in resolving meso- β scale phenomena.

ACKNOWLEDGMENTS

I would like to express my appreciation to the staff of the Atmospheric Sciences Division of the Space Sciences Laboratory at Marshall Space Flight Center for providing me the opportunity to conduct this investigation and the outstanding cooperation and support which they provided. I should especially acknowledge Ms. Glynda Meeks for typing the manuscript, Mr. Norman Reavis for his assistance with computer resources, and Dr. Gregory Wilson for his frequent input and interest in the study. Most importantly, I would like to express my sincerest gratitude to Dr. Fred W. Leslie who served as my counterpart at NASA/MSFC. Fred has been very active not only in the scientific aspects of this project but also in providing a stimulating and comfortable environment for conducting the research.

LIST OF FIGURES AND TABLES

<u>Figure No.</u>	<u>Title</u>	<u>Page</u>
1	Relationship of response function (R_f) to wavelength (λ) after one iteration for various choices of filter parameter (α).	XXXIX-8
2	Relationship of response function (R_f') to wavelength (λ) after two iterations for various choices of filter parameter (γ).	XXXIX-8
3	Data density map with cross-sectional axis and display area for analysis of surface temperatures (analytic and actual distributions).	XXXIX-12
4	Graph of cross-sectional values of an analytic temperature distribution and grid point analyses for one, two and three iteration schemes.	XXXIX-12
5	Same as Fig. 4 except for filter parameter, $\alpha = 0.2, 0.4$ and 0.8 (two iteration scheme only).	XXXIX-14
6	Same as Fig. 4 except for initial radius of influence, $R_{i,j} = 50, 200$ and 800 km (two iteration scheme only).	XXXIX-14
7	Analysis of temperature field ($^{\circ}\text{C}$) with isotropic weighting function, $\alpha = 0.4, R_{i,j} = 200$ km and two iteration scheme.	XXXIX-17
8	Same as Fig. 7, except with anisotropic weighting function.	XXXIX-17
9	Same as Fig. 7, except with one iteration.	XXXIX-18
10	Same as Fig. 7, except with three iterations.	XXXIX-18
11	Same as Fig. 7, except with $\alpha = 0.2$.	XXXIX-19
12	Same as Fig. 7, except with $\alpha = 0.8$.	XXXIX-19
13	Same as Fig. 7, except with $R_{i,j} = 50$ km.	XXXIX-20
14	Same as Fig. 7, except with $R_{i,j} = 800$ km.	XXXIX-20

<u>Table No.</u>	<u>Title</u>	<u>Page</u>
1	Average grid point errors in the objective analyses of the analytic distribution of temperature using different analysis parameters.	XXXIX-13

INTRODUCTION

Conventional weather observations fall into two categories: surface and upper air. The surface observations (temperature, pressure, winds, sky condition, etc.) are measurements made either manually or mechanically at ground level for stations that are irregularly distributed throughout continental areas. These observations provide a rather dense two-dimensional description of the atmosphere as seen at ground level. Upper air measurements, on the other hand, are made by balloon-mounted instrument packages, providing quasi-vertical distributions of temperature, relative humidity, pressure and winds. The upper air network consists of stations that are arranged in a more uniform and less dense fashion than the surface stations. Upper air observations are taken at 12 hourly intervals with a horizontal spacing of approximately 400 km, compared with the surface observations taken hourly (for many stations, at least during daylight hours) at a mean horizontal spacing of 70-100 km (depending upon the region of the country). While the upper air data does a reasonable job resolving synoptic scale features ($\lambda \sim 1000$ km), it is a bit coarse for analysis of many mesoscale phenomena such as the disturbances responsible for thunderstorms. However most of the forecasting techniques for predicting areas with the potential for the development of severe local storms rely heavily on the upper air data (Miller, 1972). Maddox and Doswell (1982) noted that while these techniques are effective for predicting severe convection in strongly baroclinic situations that occur in spring and early summer, they are inadequate for storms associated with weak synoptic scale forcing. Consequently, they have suggested application of the denser surface observations for identifying areas of development of severe local storms.

In order to assist in the analysis of surface measurements, especially for identifying areas of potential development of severe local storms, regional objective analysis schemes have been developed. The purpose of these schemes are to take the randomly distributed surface observations and interpolate values onto a spatially uniform grid. This has two advantages since gridded values permit computer graphics techniques to objectively analyze the field using computer drawn isopleths, as well as to perform calculations of derivative fields of the variables (e.g. convergence or vorticity). Ruthi and Kimpel (1977) describe two cases where they used objective analysis of hourly Airways Code (Service A) surface observations to identify areas of potential severe convection activity in Oklahoma as part of a tornado intercept project. Brady (1982) used a similar scheme for the study of severe convection in the Upper Midwest - Great Lakes region, employing surface data from the FAA 604 teletype circuit. This current study represents a refinement of the scheme employed by Brady in an attempt to improve upon the objective analysis of the surface features.

DESCRIPTION OF PROAM

The objective analysis scheme used by Brady (1982) is called PROAM (Purdue Regional Objective Analysis of the Mesoscale). PROAM is actually an adaptation of several schemes developed at the National Severe Storms Laboratory (NSSL) and Oklahoma University (OU), (Barnes 1964, 1973; Inman, 1970 and Ruthi, 1978), which has been reconfigured for use in the Upper Midwest - Great Lakes region.

PROAM performs an objective analysis of surface meteorological variables (temperature, dew point temperature, altimeter setting, wind speed and direction) that are routinely available on the FAA 604 teletype circuit. The data are collected from stations in a regional area of approximately 10^6 km² (containing perhaps 100-200 stations, depending upon the region), then analyzed using a Barnes-type scheme. Gridded values are then determined for a horizontally uniform 21 x 21 array and projected onto a polar stereographic map. The gridded data generated by PROAM includes analyses of observed data (e.g., temperature, altimeter setting, etc.) as well as derived quantities (equivalent potential temperature, vorticity, convergence of various quantities, etc.). Although this version was developed for a region centered over central Illinois, it can be used for any region where there is adequate surface data available.

The analysis scheme in PROAM uses a simplified version of the techniques developed by Barnes (1964, 1973). Grid point values, $Q_I(i,j)$, are interpolated from observed station values, $Q_O(k)$, using the following expression:

$$Q_I(i,j) = \frac{\sum_{k=1}^N w_{i,j,k} \cdot Q_O(k)}{\sum_{k=1}^N w_{i,j,k}} \quad (1)$$

The function $w_{i,j,k}$ assigns a weight to each station (k) that lies within a specified area of influence of the grid point (i,j). This weighting function is given by

$$w_{i,j,k} = \exp \left[\frac{-D_{i,j,k}^2}{(\alpha A_F)} \right] \quad (2)$$

where $D_{i,j,k}$ is the distance between the station (k) and the grid point (i,j), A_F is an anisotropic factor and α is an arbitrary filter parameter.

The area of influence is specified by a radius ($R_{i,j}$). Any station that lies within this radius of influence contributes to the value of the variable at the grid point. PROAM does require that at least 2 stations contribute to each grid point value. In a data sparse region where 2 stations are not within the area of influence, $R_{i,j}$ is expanded until the 2 station minimum criterion is met.

The anisotropic parameter A_F determines the shape of the area of influence. If $A_F = 1$ the area of influence is circular. Anisotropy can be introduced to the weighting function by permitting A_F to have values different than unity, thereby generating an area of influence which is elliptical. Inman (1970) describes a method whereby

$$A_F = (1 + \beta_k \cos^2 \phi_{i,j,k}) \quad (3)$$

in which $\phi_{i,j,k}$ is the angle between the vector from the grid point to the station and the reported wind vector at the station (k). The term β_k is the parameter controlling the degree of anisotropy given by

$$\beta_k = \frac{V_k}{0.5 V_{\max}} \quad , \quad (4)$$

where V_k is the station wind speed and V_{\max} is the maximum reported wind in the field. The effect of the anisotropic weighting factor is to simulate the advective nature of the atmosphere.

PROAM, as described by Brady, was a single iteration filtering process (i.e., it passes through the data one time only). Barnes (1973) has shown that for a single iteration with an isotropic weighting function, the response of the weighting function (i.e., the percentage of the amplitude of the disturbance for a given wavelength, λ , that is actually retained after the data has been filtered) is dependent upon the filter parameter, α , and the wavelength of interest, λ ,

$$R_f = \exp \left(\frac{-\alpha\pi^2}{\lambda^2} \right) \quad . \quad (5)$$

Fig. 1 gives a plot of several R_f vs. λ curves for various values of α . The effect of α thus determines the amount of smoothing performed by the weighting function.

Barnes (1973) has described a technique for improving the fit of the interpolated values to the observed data. This is accomplished by performing multiple corrective interactions through the data until there is desired convergence of the interpolated field to the observed values. This will be described in detail in a later section.

Consequently, there are four factors which contribute to the quality of the PROAM objective analysis scheme for a given data set and desired grid point spacing:

- 1) Radius of influence,
- 2) Anisotropy parameter,
- 3) Filter parameter, and
- 4) Number of iterations through the data.

OBJECTIVES OF PRESENT STUDY

There are four primary objectives of this study designed to improve the flexibility and performance of the scheme and to evaluate its performance under various conditions. These objectives are:

- 1) To rewrite the existing code to increase its flexibility and to permit its use in an interactive computing mode;
- 2) To incorporate the multiple (corrective) iteration technique described by Barnes (1973) for improving the fit to the observed data;

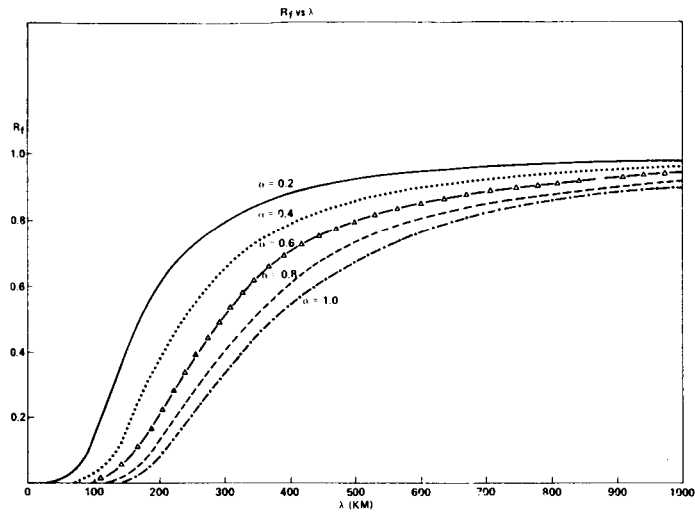


Figure 1. Relationship of response function (R_f) to wavelength (λ) after one iteration for various choices of filter parameter ($\alpha = 0.2, 0.4, 0.6, 0.8$ and 1.0 cm^2).

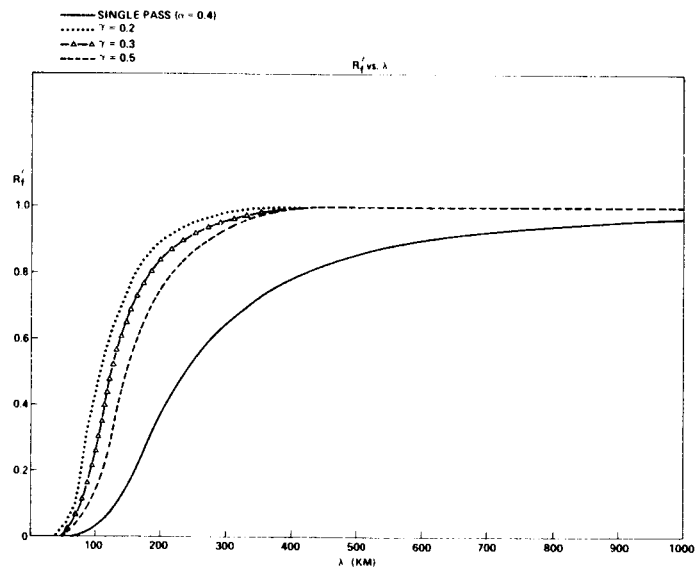


Figure 2. Relationship of response function (R_f') to wavelength (λ) after two iterations for various choices of filter parameter ($\gamma = 0.2, 0.3$ and 0.5) with $\alpha = 0.4 \text{ cm}^2$. (Response function for single iteration also displayed for comparison.)

3) To use a known analytic distribution for a variable in order to determine the accuracy of the scheme in reproducing this distribution; and

4) To use an actual data set under various conditions in order to evaluate the effect of those factors which contribute to the analysis (i.e. radius of influence, anisotropy parameter, filter parameter and number of iterations through the data).

METHODOLOGY

The following section is a description of the methods used to accomplish the stated objectives.

a) Increased flexibility/Interactive capability

This constitutes a relatively minor adjustment to the existing code requiring a determination of those parameters which affect the analysis (e.g., region of interest, desired grid point spacing, filter parameters, number of iterations, etc), then rearranging the code so these parameters can be input interactively. The parameters are:

STLAT, STLON - Latitude and longitude of the center grid point

DELTA - Grid point spacing (on the image plane)

ALFA, GAMMA - Filter parameters on the weighting function for first and successive iterations through the scheme

RADINF - Initial value for the radius of influence (on the image plane)

ISOTRP - Anisotropic weighting option

NXG, NYG - Number of grid points in x (north-south) and y (west-east) directions respectively

NPASS - Number of iterations through the Barnes scheme

The code now permits these values to be input interactively during execution of the code, thereby allowing greater flexibility for the user.

b) Multiple (corrective) iteration technique

Although the single pass version of PROAM (and its predecessor used at NSSL/OU) have proven to be an effective tool for objectively analyzing surface variables, especially for studying mesoscale phenomena, Barnes (1973) has shown that multiple iterations can significantly improve the detail of the analysis at only a limited increase in computational effort. The process requires correcting the grid point values $Q_T(i,j)$ as determined by eq. (1), by performing an analysis on a residual field using a weighting function slightly modified from that expressed in eq. (2).

The process involves producing an interpolated value $Q^*(k)$ at the location of each station k (bilinear interpolation of the four surrounding grid point values is used), then computing the residual value between this interpolated value and the actual observed value, expressed as $\Delta Q(k) = Q(k) - Q^*(k)$. A weighting function, $w'_{i,j,k} = \exp\left(-D^2_{i,j,k} / \alpha \gamma A_F\right)$, is then applied to the residual field, giving a correction to the first iteration grid point values,

$$Q'(i,j) = \frac{\sum_{k=1}^N w'_{i,j,k} \Delta Q(k)}{\sum_{k=1}^N w'_{i,j,k}} \quad (6)$$

This correction value is then added to the first pass value $Q(i,j) = Q(i,j) + Q'(i,j)$. Barnes (1973) has shown that the new response function, R'_f is given by

$$R'_f = R_f (1 + R_f^{\gamma-1} - R_f^\gamma), \quad (7)$$

where γ is a filter parameter that increases the convergence of the interpolated field toward the actual data when $0 < \gamma < 0.5$. Fig. 2 gives a plot of the response function for the two pass filter with various values of the parameter γ . One sees as γ approaches 0, the response curve tends to approximate a nearly vertical slope (i.e., a step function) at a specified wavelength. The advantage of such a filter is to retain maximum output near a wavelength of interest, in this study $\lambda \sim 100$ km, which corresponds well to meso- β scale phenomena (Orlanski, 1975). Koch, et al., (1981) provide a mathematical analysis of the effect of making additional iterations through the data, which indicates that no real benefit is gained by making more than a second pass through the data.

c) Test of PROAM using a known analytic distribution

Since actual meteorological data is rather irregular in nature, it is somewhat difficult to evaluate the performance of an analysis scheme using actual data. Consequently an analytic distribution similar to a realistic temperature field was chosen. The function used at each station k is given by

$$T(k) = 20^\circ + 4 \cdot \underbrace{\left(\frac{X(k) - X(1)}{5\Delta X} \right)}_A - \cos \underbrace{\left(\frac{2\pi Y(k)}{20\Delta y} \right)}_B \quad (8)$$

where $X(k)$ and $Y(k)$ are coordinates of station k , and ΔX and ΔY are grid spacings. Term A permits a linear temperature increase as one progresses from north to south. Term B permits a single sinusoidal wave pattern in the west to east direction. The actual distribution at each grid point is generated as the benchmark. The objective analysis scheme is run for one, two and three iterations. The results are presented in the next section.

d) Experiments with an actual data set

A series of experiments were conducted in order to compare results for different values of those factors which are known to affect the analysis. The experiments include:

(i) Varying the radius of influence:

$$R_{i,j} = 50, 200 \text{ and } 800 \text{ km} \\ (0.5, 2.0 \text{ and } 8.0 \text{ cm on the map plane}),$$

(ii) Varying the anisotropy parameter:

Anisotropy vs. isotropy,

(iii) Varying the filter parameter:

$$\alpha = 0.2, 0.4 \text{ and } 0.8 \text{ cm}^2,$$

(iv) Varying the number of iterations:

$$N = 1, 2 \text{ and } 3 .$$

Results of these experiments are presented in the next section.

RESULTS

This section describes the major findings associated with the testing of the features added to the PROAM scheme.

a) Tests with an analytic distribution of temperature

A known analytic distribution for temperature given by eq. (8) was used at the stations denoted by the solid circles and squares in Fig. 3. These station values were then run through the objective analysis scheme under a variety of conditions and compared with the exact analytic distribution of values at each grid point. Since the distribution consists of a family of identical sinusoidal waves, one needs to consider values only for a single horizontal (west to east) row of grid points to evaluate the ability of the scheme to reproduce this wave pattern.

In the first experiment the filter parameters ($\alpha = 0.4$, $\gamma = 0.3$) and the radius of influence (200 km) are held constant for the isotropic weighting function. The number of iterations through the data field was allowed to vary from one to three passes. The purpose of this test was to determine the optimum number of passes necessary to resolve the wave. Fig. 4 shows the exact solution and the analyzed fields along a cross-section through the center of the grid (note west to east cross-sectional axis through Fig. 3). Examination of the curves indicate that all three approximate the gross features of the analytic wave fairly accurately, although there is an overestimation of as much as 1°C to the left (east) of the major trough axis. The average grid point errors (summation of the absolute deviation from the exact value at each grid point, divided by the total number of grid points) are tabulated in Table 1. The

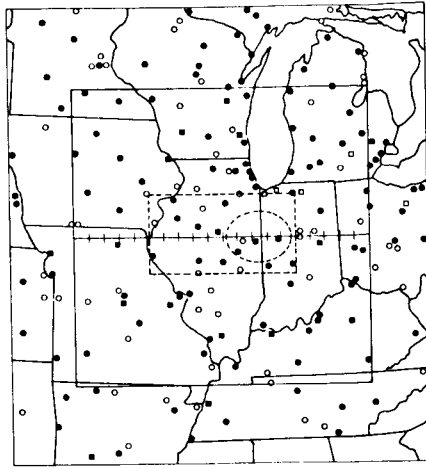


Figure 3. Data density map with cross-sectional axis (solid line with tick marks) and display area (dashed inner rectangle) for analysis of surface temperatures (analytic and actual distributions). Stations are marked with squares/circles with reported stations blackened.

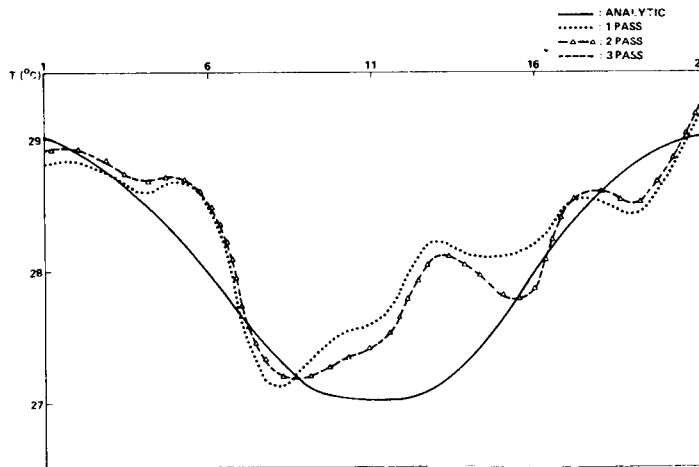


Figure 4. Graph of cross-sectional values of an analytic temperature ($^{\circ}\text{C}$) distribution (solid) and grid point analyses for one (dot), two (triangle) and three (dash) iteration schemes ($\alpha = 0.4$, $R_{i,j} = 200 \text{ km}$, and isotropic).

smallest error was associated with the three pass scheme, although there is not sufficient improvement over the two pass scheme to warrant the additional computations. This is consistent with the finding of Barnes (1973) who suggested that the scheme converges sufficiently after just two passes through the data.

Table 1. Average grid point errors in the objective analyses of the analytic distribution of temperature using different analysis parameters.

Exp 1: Variation of the number of iterations through the data ($\alpha = 0.4$; $R_{i,j} = 200$ km; Isotropic)

<u>Iterations</u>	<u>Average Error</u>
N = 1	0.478
N = 2	0.436
N = 3	0.435

Exp 2: Variations in the filter parameter (α)

<u>α</u>	<u>Average Error</u>
0.2	0.526
0.4	0.436
0.8	0.367

Exp 3: Variations in the initial radius of influence ($R_{i,j}$)

<u>$R_{i,j}$ (km)</u>	<u>Average Error</u>
50	0.474
200	0.436
800	0.436

There are probably two reasons for the obvious deviations from the exact solution. One is a result of the values of the filter parameters chosen ($\alpha = 0.4$, $\gamma = 0.3$). There appears to be five minor waves in each of the interpolated curves (Fig. 4) with $\lambda \sim 4\Delta X \sim 200$ km. Fig. 2 shows that for $\alpha = 0.4$ and $\gamma = 0.3$ approximately 90% of the amplitude is retained for $\lambda = 200$ km for the two pass scheme (somewhat higher for three passes). Consequently 200 km wave patterns should appear in the analyzed field. The 1°C deviation is very apparent in Fig. 4. This represents an error of approximately 3.5%, which is what one would expect according to the response function curve (Fig. 1) for a 1000 km wave with $\alpha = 0.4$. This error can be explained further by examining Fig. 3. Note that in the elliptical area outlined by the dashed marks (corresponding to the area of influence for the grid points along the cross-section) there are no stations north (above) of the cross-section line. Since the analytic function is one that represents temperature increasing in the x-direction (north-south), and those stations influencing the grid points are on the warm (south) side of the cross-section, these interpolated grid point values would experience a bias toward warmer temperatures. Also note that there appears to be a fairly uniform distribution of stations

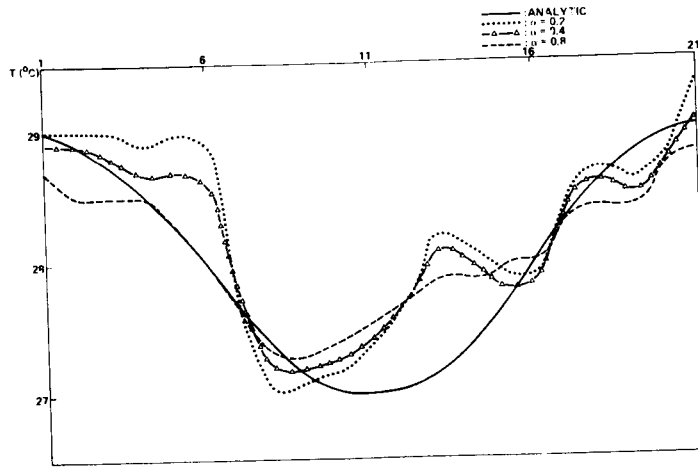


Figure 5. Same as Fig. 4, except for filter parameter $\alpha = 0.2$ (dot), 0.4 (triangle) and 0.8 (dash) cm^2 (two iteration scheme only).

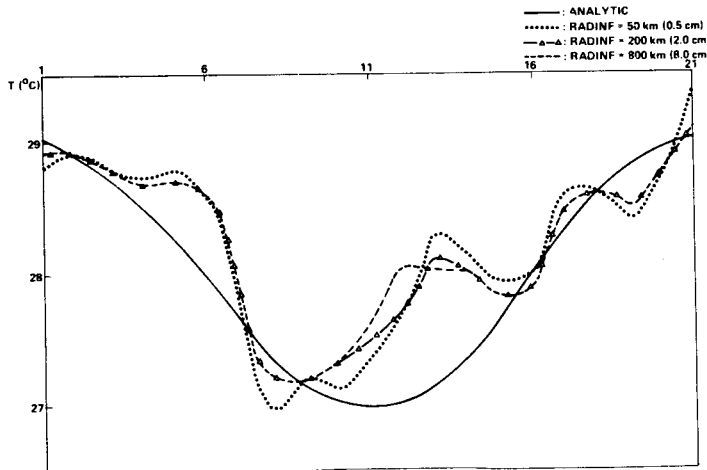


Figure 6. Same as Fig. 4, except for initial radius of influence, $R_{i,j} = 50$ (dot), 200 (triangle) and 800 (dash) km (two iteration scheme only).

everywhere else along the cross-section line, consequently this bias would not be evident elsewhere.

Therefore, increasing the number of passes through the data does increase the accuracy of the analysis scheme, although no additional benefit is derived beyond two passes. Furthermore, the scheme appears to generate the response as predicted by theory.

The second set of experiments with the analytic distribution involves variation of the filter parameter ($\alpha = 0.2, 0.4$ and 0.8). An examination of Fig. 1 reveals that more detail should be retained at shorter wavelengths for smaller values of α . Fig. 5 verifies this by showing larger amplitudes in the disturbances for $\alpha = 0.2$, and a smoother curve for $\alpha = 0.8$. Since the analytic function has a wavelength of 1000 km, one would anticipate the higher filter parameter would best capture this wave pattern. To test that the smaller filter parameter is indeed better for smaller wavelengths, one should perform a similar analysis using 100-200 km disturbances.

The third experiment involved variation of the radius of influence. Fig. 6 displays the analyzed fields using values for the initial radius of influence of 50, 200 and 800 km (0.5, 2.0 and 8.0 cm on the image plane). The initial radius of influence represents the distance from each grid point through which the program initially searches for a minimum of two stations which will influence the grid point value. (Recall that if the two station minimum criteria is not met, the radius is increased.) Table 1 shows that the average grid point error is reduced as the radius of influence increases. This is to be expected since for a smaller scanning radius a grid point could be greatly influence by a smaller number of stations. If one of these stations reflects a highly localized effect (e.g. lake breeze cooling) or an erroneous observation, it would tend to weigh more heavily on the surrounding grid points. There does appear to be a limit to the effectiveness of increasing the radius of influence for error reduction, since the magnitude of the error is essentially the same for scanning radius of both 200 and 800 km. This is due to the nature of the weighting function which is an exponential function of $-r^2$. Consequently, increasing the scanning radius will increase the number of stations (hence the computations) but with diminishing improvement in accuracy. For the desired objective analysis of meso- β scale phenomena, a radius of influence of approximately 200 km appears to be appropriate for PROAM.

b) Tests with an actual temperature distribution

Although an analytic distribution of a variable is instructive for evaluation purposes, atmospheric variable fields tend to be more complex. A set of experiments involving a data set of actual atmospheric temperatures were performed similarly to those for the analytic distribution. Unfortunately, exact solutions are not available for computing absolute errors, hence a portion of the analyzed field is presented, with the grid point and observed station values plotted in their appropriate locations.

Figs. 7-14 display the analyzed fields of temperature for the display area (denoted by the dashed inner rectangular area in Fig. 3). These charts depict the analyzed grid point values, the ten observations contained within this display area and manually drawn isotherms (2°C increments). The isopleth patterns are strikingly similar for all eight cases, which is to be expected since the data field is identical for all. Any deviations in the isopleths and the grid point values are a result of the variations in the analysis parameters. Fig. 7 should be considered as the control case since all other charts represent a variation of one of the analysis parameters used to produce Fig. 7 (i.e., 2 pass, $\alpha = 0.4$, $R_{i,j} = 200$ km, isotropic).

Fig. 8 shows the effect of including the anisotropic factor [$\beta \neq 0$ in eq. (3)]. A comparison with Fig. 7 (the isotropic case) indicates slightly warmer temperatures in the north central region enclosed by the 22°C isotherm and slightly cooler temperatures in the northeast corner. This reflects the advective nature of the anisotropic weighting functions. Stations near the warmer region have southwesterly winds, hence warm air advection is occurring. Stations near the cooler region lie just south of Lake Michigan and would be cooler due to the influence of the large water body.

Figs. 9 and 10 show results from one and three iterations respectively. A comparison of the one (Fig. 9) and two (Fig. 7) iteration analyses indicate that the second pass through the data adjusts the analysis, giving a close fit to the observations. This is shown best by noting that the four grid point values surrounding the 25.0°C observation (southwest of the center of both figures) are all less than the station value in the one iteration scheme. These same grid points in the two iteration scheme are higher and are consistent with the station observation. The three pass scheme (Fig. 10) is essentially the same as the two pass scheme.

Figs. 11 and 12 represent analyses with variations in the filter parameter ($\alpha = 0.2$ and 0.8 respectively). The lower filter parameter should allow greater detail of small scale features which is evident in the northeast corner of the display area (Fig. 11). Using the higher value produces a slightly smoother analysis (Fig. 12). There is much less smoothing apparent on the actual observations than displayed for the analytic distributions (Fig. 5). This is probably due to the fact that the gradients in the temperature field are smaller for the case using actual observations.

Figs. 13 and 14 display the effect of varying the initial radius of influence. Other than the absence of the 24°C (Fig. 13) isopleth in the southeast corner in the analysis of the smaller scanning radius, there are no distinguishing variations from that of the control case (Fig. 7).

Consequently, the experiments run with an actual set of observations indicate that the inclusion of the multiple iteration process offers improvement over the single pass scheme utilized in the original version of PROAM. There is evidence of smoothing associated with variations in the filter parameter, however, for the data set chosen, it does

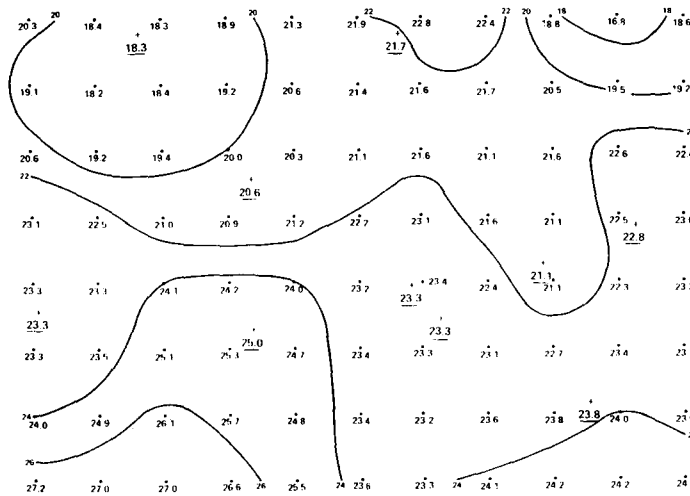


Figure 7. Analysis of temperature field ($^{\circ}\text{C}$) with isotropic weighting function, $\alpha = 0.4$, $R_{i,j} = 200$ km and two iteration scheme. (Grid point position noted by (.), stations by (+). Contour interval is 2°C .)

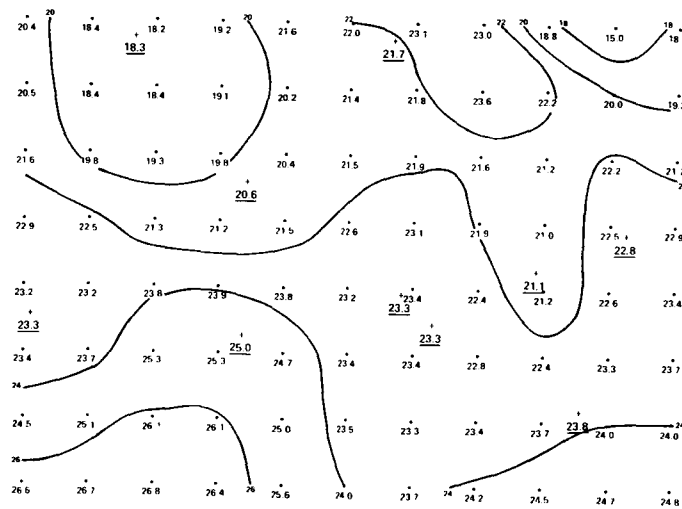


Figure 8. Same as Fig. 7, except with anisotropic weighting function.

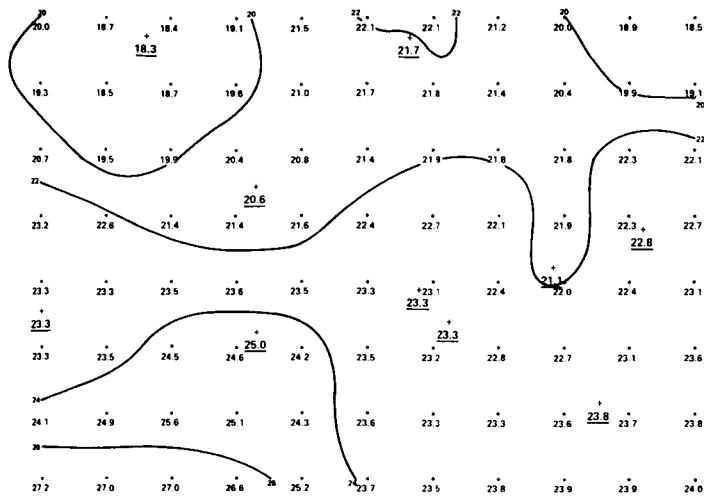


Figure 9. Same as Fig. 7, except with one iteration.

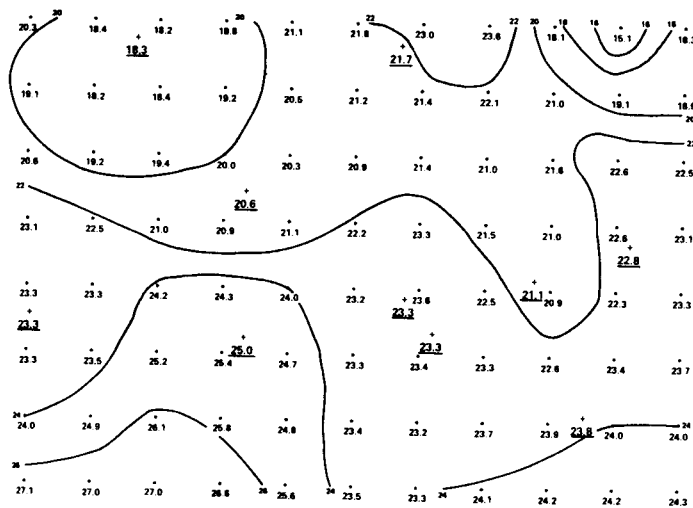


Figure 10. Same as Fig. 7, except with three iterations.

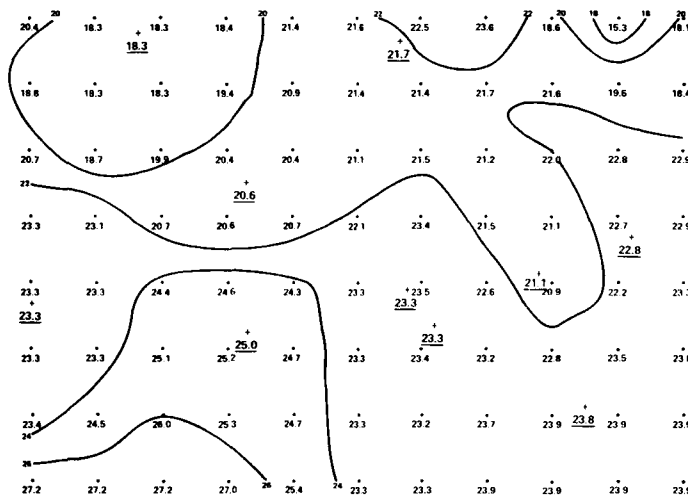


Figure 11. Same as Fig. 7, except with $\alpha = 0.2$.

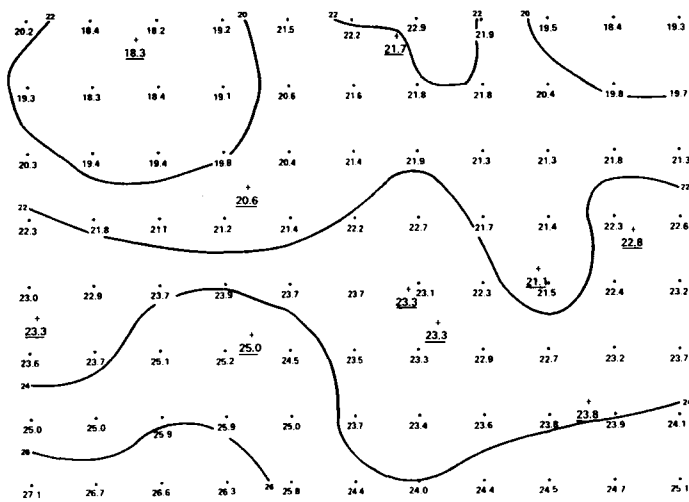


Figure 12. Same as Fig. 7, except with $\alpha = 0.8$.

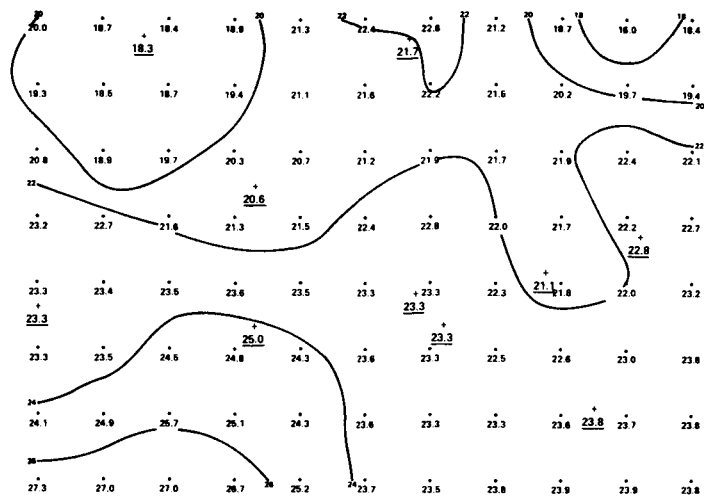


Figure 13. Same as Fig. 7, except with $R_{i,j} = 50$ km.

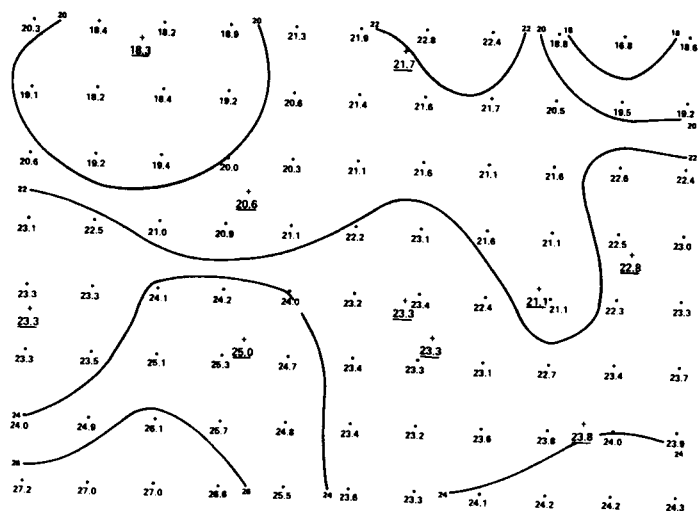


Figure 14. Same as Fig. 7, except with $R_{i,j} = 800$ km.

not appear to produce significant differences in the analysis. Variations in the initial radius of influence are essentially inconsequential as far as the analysis is concerned, although there should be economic computational advantages for using a smaller scanning radius.

CONCLUSIONS AND RECOMMENDATIONS

An objective analysis scheme (PROAM) used for hourly surface data has been modified. The major modifications include:

- 1) Rewriting the code so that it is interactive in nature, thereby increasing its flexibility and ease of usage; and
- 2) Incorporation of a multiple iteration correction scheme to improve the accuracy of the analysis in fitting actual observations.

PROAM was then subjected to a series of tests in order to evaluate its performance under a variety of conditions. Both an analytic distribution and actual observations were considered for various experiments involving:

- 1) Variations in the number of iterations through the data field;
- 2) Variations in the filter parameter;
- 3) Variations in the initial radius of influence; and
- 4) Variations in the isotropy of the weighting function.

Results indicate that the multiple iteration process improves the accuracy of the analyzed values when compared with the observations. However, there is little additional benefit in using more than two passes. The filter parameter acts to smooth the analysis for larger values of α , and retain greater small scale detail for smaller values. The initial radius of influence serves more to reduce the number of computations rather than improving the accuracy of the analysis. Finally the anisotropic weighting factor reflects the advective nature of atmospheric processes by allowing greater influence to observations either directly upwind or downwind of the grid point.

Future work with such an objective analysis scheme should include testing with different types of analytic distributions, particularly with wavelengths on the order of meso- β scale phenomena. Similar testing of analytic functions for desired quantities such as convergence and vorticity would also provide useful information for the use of the finite differencing techniques utilized. A further improvement would involve incorporation of temporal analysis as well as spatial analysis. This would be particularly helpful for utilization of the special observations that occur during highly variable weather situations (as would occur in convectively active situations). Barnes (1973) offers guidance for inclusion of data taken at different times. Finally, it is recommended that techniques be explored for handling large data-void areas. This would be most beneficial not only for surface analysis, but for more generalized objective analysis of any single atmospheric level of data.

For example the analysis of satellite measurements such as the VAS system which are unable to collect data over cloud covered areas could be greatly improve.

Obviously, objective analysis techniques will provide an important analysis tool for future meteorological studies. However, it is essential to thoroughly evaluate the performance of such schemes, as was done in this study, in order to have a confidence in the output of objective analysis schemes.

REFERENCES

- Barnes, S. L., 1964: A technique for maximizing detail in numerical weather map analysis. J. Appl. Meteor., 3, 396-409.
- Barnes, S. L., 1973: Mesoscale objective map analysis using weighted time-series observations. NOAA Tech. Memo. ERL NSSL-62, (NTIS COM-73-10781), 60 pp.
- Brady, III, R. H., 1982: The Purdue Regional Objective Analysis of the Mesoscale and its application to two severe weather events. M.S. Thesis, Purdue University, West Lafayette, IN, 104 pp.
- Inman, R. L., 1970: Papers on operational objective analysis schemes at the National Severe Storms Forecast Center, NOAA Tech. Memo. ERLTM-NSSL 51, (NTIS COM-71-00136), 91 pp.
- Koch, S. E., M. des Jardin and P. J. Kochin, 1981: The GEMPAK Barnes objective analysis scheme, NASA Tech. Memo. 83851, (NTIS COM-81-22161), 56 pp.
- Maddox, R. A. and L. A. Doswell, III, 1982: Forecasting severe thunderstorms: A brief evaluation of accepted techniques. Preprints 12th Conference on Severe Local Storms, San Antonio, TX, Amer. Meteor. Soc., Boston, MA, 92-95.
- Miller, R. C., 1972: Notes on analysis and severe storm forecasting procedures of the Air Force Global Weather Central. AWS Tech. Rep. 200 (Rev.) (NTIS-AD-744042), 108 pp.
- Orlanski, I., 1975: A rational subdivision of scales for atmospheric processes. Bull. Amer. Meteor. Soc., 56, 527-530.
- Ruthi, L. J., 1978: An evaluation of surface quantities in the short term prediction of the intensity of convective activity. M.S. Thesis, Univ. of Oklahoma, Norman, OK, 90 pp.
- Ruthi, L. J. and J. F. Kimpel, 1977: Objective analysis used in forecasting severe storms during a tornado intercept project. Preprints 10th Conference on Severe Local Storms, Omaha, NB, Amer. Meteor. Soc., Boston, MA, 390-394.

1982

NASA/ASEE SUMMER FACULTY RESEARCH
FELLOWSHIP PROGRAM

MARSHALL SPACE FLIGHT CENTER
THE UNIVERSITY OF ALABAMA

AN ANALYSIS OF NICKEL CADMIUM BATTERIES

Prepared By:	J. B. Turner, Jr.
Academic Rank:	Assistant Professor
University and Department:	Alabama A&M University Department of Engineering Technology (Electrical)
NASA/MSFC	
Organization:	Science & Engineering
Laboratory:	Information and Elec- tronic Systems
Division:	Electrical
Branch:	Electrical Power
MSFC Counterparts:	J. R. Lanier, Jr. L. J. George
Date:	August 6, 1982
Contract No:	NGT-01-002-099

AN ANALYSIS OF
NICKEL CADMIUM BATTERIES

BY

J. B. Turner, Jr.
Assistant Professor of Engineering Technology
Alabama A and M University
Normal, Alabama

ABSTRACT

The following study will present an investigation of work done in the area of Nickel-Cadmium batteries. The study will attempt to explore such areas as temperature effects, reconditioning, divergencies, capacity, charge rates, depth of discharge, and cell matching and their effects on battery life.

From the analysis of data on the above parameters, a more accurate determination of battery performance can be made. Such information can play an important role in design of batteries for future spacecraft power needs. Additional areas for further investigations are also presented.

ACKNOWLEDGEMENTS

I would like to express my appreciation to the NASA/ASEE Summer Faculty Fellowship program for the research opportunity it has provided. Thanks also are extended to Dr. Bob Barfield, Dr. Jim Dozier, and Mr. Marion Kent for their very capable administration of this program; special thanks to my counterparts, Mr. J. R. Lanier, Jr. and Mr. L. J. George. Appreciation is also expressed for the help of Mr. J. Bush, Jr. and Mr. Bob Kapustka for their assistance and to Mrs. Peggy Geddings for typing this report.

INTRODUCTION

For the past few years, research has been undertaken at the George C. Marshall Space Flight Center (MSFC) to develop an efficient and reliable means for characterizing Nickel Cadmium (Ni-Cd) batteries.

The aim of the program has been to devise a practical strategy for predicting battery life by subjecting cells to simulated cyclic operation under various parameter variations (such as temperature variation, cell capacity variation, etc.) and predicting how the cells will perform under normal conditions.

Thus, this study will explore cyclic parameters with a view toward making a better evaluation of the present program.

OBJECTIVE

The objective of this research is to devise a practical strategy for predicting battery life.

BATTERY ANALYSIS

Temperature

The preponderance of data indicates that the most important factor in extending life of Ni-Cd cells or batteries is temperature.

McDermott¹ concluded that of eight variables used in testing Ni-Cd batteries, temperature and depth of discharge were the most important parameters for use in predicting life.

In similar research Gross² states that the nickel-cadmium cell behavior is strongly temperature dependent and longest life is obtained at about 5° to 15°C. At low temperature cell wearout occurs very slowly, but low temperature charge can cause hydrogen generation, especially at high charge rates or if the prior discharges were at high temperature.

Capacity

The measured capacity of a cell is the output of the cell in ampere-hours to an end of discharge voltage of 1.000 volt.

Bauer³ states that if the battery is fully charged and is discharged at a higher current or a lower temperature than that of the capacity measurement standard, increased polarization causes the terminal voltage to reach the minimum acceptable level sooner. Bauer further states that the capacity available from a nickel-cadmium cell depends upon the method used for charge control. When the cells are undercharged the next cycle may completely discharge the cells. When overcharged, the cell will generate oxygen and hydrogen gases and cause a rapid degradation of the electrodes.

Divergency

The divergency problem occurs when cells in a series-connected battery are not properly matched.

Anomalies in the cell are due to different capacities of the cells or product variation.

Bauer³ states that if one cell reaches full charge or full discharge first and is not detected by the charge control sensors, the low-capacity cell is subjected to overcharge or underdischarge, and gas evolves. As the total number of series-connected cells increases the problem enlarges as a result of increasing probability of having one cell of divergent capacity and the decreasing sensitivity of detection.

Depth of Discharge

Depth of discharge (DOD) of nickel cadmium cells is one of the most important variables used in predicting life. High DOD causes excessive fatigue of the electrodes especially in low orbit application where there is a 36 minute (dark) discharge and a 60 minute (light) charge.

Figure 2 illustrates that at low temperature and low DOD the life (in cycles) of the cell or battery can be extended.

It appears that the most satisfactory range for DOD in low orbit cycling is between 20 and 30 percent at a temperature range of 0°C to 15°C.

Cell Matching

Miller⁴ in a test for the Air Force indicates that, "All cells manufactured from the same run using the same separator material were stored electrically shorted in a laboratory room environment until preparation for this experiment." All cells were electrically conditioned and matched with nearly identical charge voltage, resistance, and discharge capacities.

After reviewing chronological events of Skylab battery tests at Marshall Space Flight Center for between April 1972 and June 1972, I have concluded that these cells were individually tested and then matched in groups for batteries.

Reconditioning

It has been demonstrated both in the laboratory and on

operational spacecraft that periodic deep discharge of Ni-Cd batteries well beyond the operating level tend to restore their terminal voltage performance in long term cyclic service. This experimentally discovered phenomenon called reconditioning has been known in the battery industry for some time, but is not well understood in terms of electrochemical theory. Generally, it is attributed to the formation of large cadmium crystals in the negative plate.

When a Ni-Cd battery of series-connected cells is subjected to discharge beyond the normal, some of the cells are driven into reversal with attendant hydrogen generation and ultimate cell failure.

One approach to avoiding this problem is the use of a Battery Protection and Reconditioning Circuit (BPRC) that was designed and is currently being used in Marshall Space Flight Center's battery testing program (see Fig. 1). It involves a dc-to-dc converter, a current sensing device, and the capability of protecting individual cells against reversal. During the discharge of the battery if a cell voltage becomes low, the BPRC will hold that cell voltage up and allow it to continue to discharge on the system. When the cell is good, the voltage is above one volt and the BPRC diodes are reversed biased, and the current drawn out of the system then is very low.

If voltage drops on a cell to seven-tenths of a volt, the circuit starts picking up the load and helps hold the overall battery voltage up.

Lanier⁵ stated that repeated use of this device for reconditioning during a test of over 24,000 cycles resulted in restoring to nearly new capacity each time.

CONCLUSIONS

The results of this study indicate that the main factor for extending the life of any Ni-Cd is temperature. Providing a temperature range of 0° to 15°C, preferably 0°C, significantly increases its life span.

Another life time factor is the depth of discharge (DOD). High DOD causes electrode fatigue that shortens the life of the cells.

Reconditioning has proven to be a vital asset for restoring cell capacity. There is conclusive evidence that faster reconditioning occurs at higher temperature (20°C to 25°C).

The divergence problem can be solved or minimized by matching cells as closely as possible.

RECOMMENDATIONS

As a result of this study the following recommendations are made concerning the present test:

1. To analyze stored data and attempt to match cells through statistical analysis using standard deviation. Samples of individual cell voltages could be taken at intervals of 500 to 1000 cycles or to unscheduled test shut down.
2. To do more research on charge and discharge rates of batteries.
3. To do additional research with temperature and DOD especially with a temperature of 0°C.

REFERENCES

1. McDermott, P. P.; "Some Practical Observations on the Accelerated Testing of Nickel-Cadmium Cells", Energy Conversion Vol. 2, pp 1305-1309.
2. Gross, S.; "Unsolved Problems of Nickel Cadmium Batteries", Energy Conversion Vol. 1, pp 177-181.
3. Bauer, Paul; "Batteries for Space Systems", NASA SP-172, 1968.
4. Miller, G.; "Acceleration Life Tests for Nickel Cadmium Cells", 26th Power Sources Symposium, 1974.
5. Lanier, R.; "A Nickel Cadmium Battery Reconditioning Circuit", NASA TND-8508, Marshall Space Flight Center, April 1977.

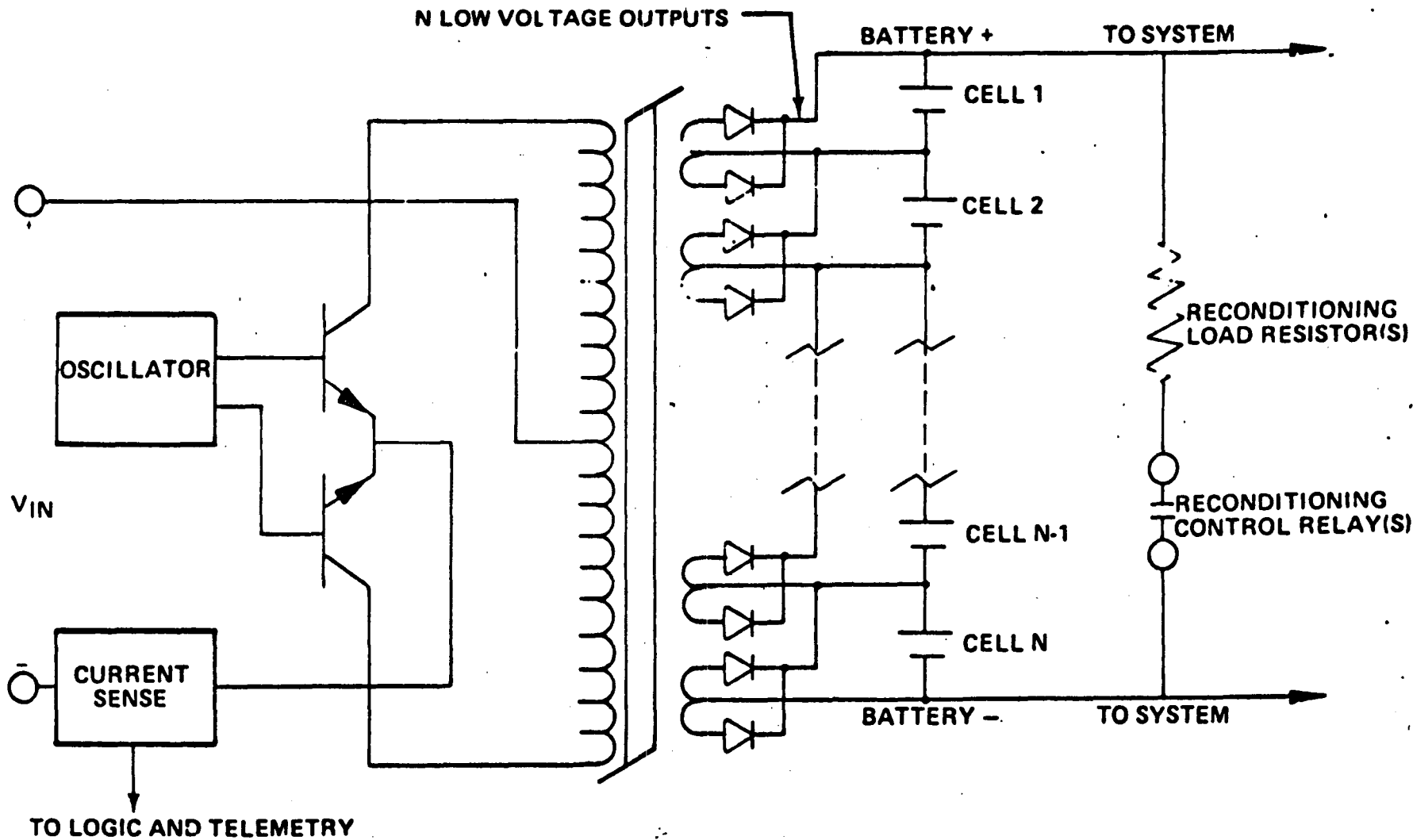
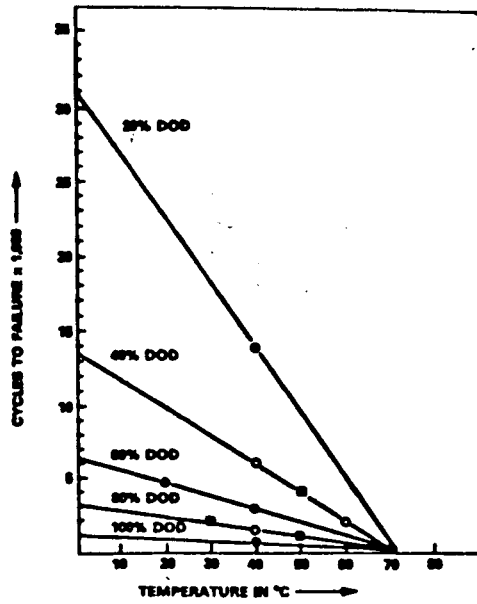


Figure 1: Simplified flight reconditioning circuit.

**CYCLES TO FAILURE VS.
TEMPERATURE (°C)
AT VARIOUS
DEPTHS-OF-DISCHARGE**



**FIG. 2 - FAILURE AS FUNCTION
OF TEMPERATURE**

1982

NASA/ASEE SUMMER FACULTY RESEARCH FELLOWSHIP PROGRAM

MARSHALL SPACE FLIGHT CENTER
THE UNIVERSITY OF ALABAMA

INVESTIGATION OF COMPOSITIONAL SEGREGATION
DURING UNIDIRECTIONAL SOLIDIFICATION OF SOLID
SOLUTION SEMICONDUCTING ALLOYS

Prepared By:	Jai-Ching Wang
Academic Rank:	Associate Professor
University and Department:	Alabama A&M University Department of Physics
NASA/MSFC:	
(Laboratory)	Space Science Laboratory
(Division)	Space Processing
(Branch)	Semiconductors and Devices
MSFC Counterparts:	S. L. Lehoczky, F. R. Sofran
Date:	August 5, 1982
Contract No.:	NGT-01-002-099 University of Alabama

XLI-1

INVESTIGATION OF COMPOSITIONAL SEGREGATION DURING UNIDIRECTIONAL
SOLIDIFICATION OF SOLID SOLUTION SEMICONDUCTING ALLOYS

By

Jai-Ching Wang, Ph.D.
Associate Professor of Physics
Alabama A&M University
Normal, Alabama

ABSTRACT

Compositional segregation of solid solution semiconducting alloys in the radial direction during unidirectional solidification is investigated by calculating the effect of a curved solid liquid interface on solute concentration at the interface on the solid. The formulation is similar to that given by Coriell, Boisvert, Rehm, and Sekerka except that we are working in a more realistic cylindrical coordinate system which is moving with the interface. Analytical results has been obtained for very small and very large values of β with $\beta = VR/D$, where V is the velocity of solidification, R the radius of the specimen and D the diffusivity of solute in the liquid. For both very small and very large β , the solute concentration at the interface in the solid C_{si} approaches C_0 (original solute concentration) i.e., the deviation is minimal. The maximum deviation of C_{si} from C_0 occurs for some intermediate value of β .

ACKNOWLEDGEMENTS

I would like to express my sincere appreciation to the NASA/ASEE Summer Faculty Program for providing me the opportunity to participate in this activity. Special thanks goes to my NASA counterparts: Drs. S. L. Lehoczky, and F. R. Szofran for their valuable time, suggestions and guidance. Appreciation also goes to Dr. Larry Holland and James Zwiener for their valuable discussions and Ms. Linda Burns for typing this report.

1. INTRODUCTION

Solid solution semiconducting alloys such as $\text{Hg}_{1-x}\text{Cd}_x\text{Te}$ produced under unidirectional solidification technique shows compositional segregation in both axial and radial directions⁽¹⁻³⁾. Since material properties such as energy band gap depend on alloy composition, it is important to understand the causes of such segregations so that one can develop a set of suitable parameters for producing compositionally homogeneous alloys.

It has been shown that compositional segregation in the axial direction is a consequence of diffusion limited growth⁽⁴⁻⁶⁾ which is unavoidable. However, under the proper growth rate, the composition in the steady state growth region can be quite homogeneous. But there is still compositional segregation in the radial direction. It has been determined⁽⁷⁾ and observed⁽⁸⁾ that the solid liquid interface is curved. The possible causes for radial compositional segregations are diffusion across a curved solid-liquid interface^(9,10) gravity driven solute flow⁽¹¹⁾, thermal effect⁽¹²⁾ as well as convection effect⁽¹³⁾. Thus, the main issue is to determine what is the dominant mechanism for compositional segregation in the radial direction.

In section 2, we give the objective of this study. Then we treat a two dimensional diffusion problem with curved solid liquid interface shape under unidirectional solidification with no convection in section 3. The formulation is similar to that given by Coriell, Boisvert, Rehm, and Sekerka except that we are working in a more realistic cylindrical coordinate system which is moving with the interface. In section 4, results of analytical approximation are obtained for very small and very large β with $\beta = VR/D$, where V is the velocity of solidification. R is the radius of the specimen and D is diffusion coefficient of solute in the liquid. The concentration of the solute in the solid at the interface C_{Si} is given in terms of parameters β , distribution coefficient K , and the interface shape $W(r)$. We find that for very small and very large β . C_{Si} approaches C_0 (original solute concentration) i.e. deviation is minimal, which is the same as given by Coriell etc. However, the interface shape dependence is different as expected. In section 5, we give conclusion and recommendations.

2. OBJECTIVES

The objectives of this study is to determine whether diffusion is the main mechanism for radial compositional segregation. The approach is to treat a two dimensional diffusion problem with curved solid-liquid interface shape under unidirectional solidification with no convection.

3. THEORY

Liquidus of a binary semiconducting alloy usually does not coincide with its solidus. This leads to a redistribution of solute at the solid-liquid interface when an alloy is solidified from a liquid state. The ratio of the solute concentration in the solid to that in the liquid at the solid-liquid interface denoted by "k" is called distribution coefficient. If $k < 1$, part of the solute will be "rejected" into the liquid during solidification, if $k > 1$ then part of the solvent will be rejected into the liquid. The rate of this rejection is measured by the advancing speed of the solid-liquid interface. The process of this rejection is balanced by diffusion process in the liquid which tends to spread the solute uniformly throughout the liquid.

Consider a cylindrical specimen which has radius R and is unidirectionally solidified at a constant speed V . Choose a cylindrical coordinate system (r', ϕ', z') which is fixed at and is moving with the solid-liquid interface. The solid-liquid interface shape is denoted by $z' = W'(r')$. This system is similar to the system treated by Coriell, Boisvert, Rehm, and Sekerka except that we are working on a physically more realistic cylindrical system.

We adapt the formulation given in reference 10. In the steady state solidification region, the solute concentration $C'(r', z')$ in the liquid satisfies the diffusion equation.

$$D \frac{\partial^2 C'(r', z')}{\partial r'^2} + \frac{1}{2} \frac{\partial C'(r', z')}{\partial r'} + \frac{\partial^2 C'(r', z')}{\partial z'^2} + V \frac{\partial C'(r', z')}{\partial z'} = 0 \quad (1)$$

With the following boundary conditions.

$$V C'_I(r', z') (k-1) = \frac{\partial C'(r', z')}{\partial z'} \Big|_I - \frac{\partial C'(r', z')}{\partial r'} \Big|_I \frac{\partial W'(r')}{\partial r'} \quad (2)$$

$$C'(r', z' \rightarrow \infty) = C'_0 \quad (3)$$

$$\frac{\partial C'(r', z')}{\partial r'} = 0 \quad \text{at } r' = R \quad (4)$$

The subscript I denotes that the value is evaluated at the solid-liquid interface.

After changing to dimensionless variables

$$r = \frac{r'}{R}, \quad z = \frac{z'}{R}, \quad W = \frac{W'}{R}, \quad C = \frac{C'}{C'_0}, \quad \beta = \frac{VR}{D}$$

We have

$$\frac{\partial^2 C(r, z)}{\partial r^2} + \frac{1}{r} \frac{\partial C(r, z)}{\partial r} + \frac{\partial^2 C(r, z)}{\partial z^2} + \beta \frac{\partial C(r, z)}{\partial z} = 0 \quad (5)$$

$$C_I(r, z) (k-1) = \frac{\partial C(r, z)}{\partial z} \Big|_I - \frac{\partial C(r, z)}{\partial r} \Big|_I \frac{\partial W}{\partial r} \quad (6)$$

$$C(r, z \rightarrow \infty) = 1 \quad (7)$$

$$\frac{\partial C(r, z)}{\partial r} = 0 \quad \text{at } r = 1 \quad (8)$$

From these equations, we see that C_1 depends on the dimensionless quantities β , k and the interface shape $z = W(r)$.

For $W(r)$ independent of r , i.e. $W(r) = W_0$, the solution for C_1 should be r independent. The equations which have to be satisfied under this condition are:

$$\frac{\partial^2 C(r,z)}{\partial z^2} + \beta \frac{\partial C(r,z)}{\partial z} = 0 \quad (9)$$

$$C_1(r,z) (k-1) = \frac{\partial C(r,z)}{\partial z} \quad (10)$$

$$C(r, z \rightarrow \infty) = 1 \quad (11)$$

$$\frac{\partial C(r,z)}{\partial r} = 0 \quad \text{at } r = 1 \quad (12)$$

The solution for these equations is

$$C(r,z) = 1 + \frac{1-k}{k} e^{-\beta (y - W_0)} \quad (13)$$

This shows that the solute will build up a diffusion layer right in front of the interface and then decay to its original concentration exponentially.

4. ANALYTICAL RESULTS

In the limits of very small and very large β , by making some approximations the set of equations (5) to (8) can be solved to obtain the solute concentration in the solid at the interface as function of $W(r)$, β , and k .

A. Very small β limit

This is the case that the diffusion layer is very thick. By using variable separating method, eq. (5) can be solved to give

$$C(r, z) = A J_0(\alpha r) e^{-\frac{\beta}{2} \left[1 + \sqrt{1 + \left(\frac{2\alpha}{\beta} \right)^2} \right] z} + A' \quad (14)$$

Where J_0 is zero order Bessel's function, α^2 is the variable separation constant. A and A' are constants to be determined.

From the boundary condition

$$C(r, z \rightarrow \rho) = 1, \text{ we have } A' = 1$$

From $\frac{\partial C(r, z)}{\partial r} = 0$ we have

$$\frac{\partial J_0(\alpha r)}{\partial r} = -\alpha J_1(\alpha r) = 0 \quad (15)$$

Let $\alpha = U_n$, $n = 0$ to be the values which satisfies condition (15).

Thus we have

$$C(r, z) = \sum_{n=1}^{\infty} A_n J_0(U_n r) e^{-\frac{\beta}{2} [1 + p(n)] z} + 1 \quad (16)$$

$$\text{with } p(n) = \left[1 + \left(\frac{2U_n}{\beta} \right)^2 \right]^{\frac{1}{2}} \quad (17)$$

The expression (16) should also satisfy the boundary condition eq. (7).

Let us assume that $W(r)$ and $dW(r)/dr$ are sufficiently small such that the second order terms in these quantities can be neglected.

We express $W(r)$ as Fourier-Bessel series.

$$W(r) = W_0 + \sum_{n=1}^{\infty} \delta(n) J_0(U_n r) \quad (18)$$

with $J_1(U_n) = 0$,

Substitute eq. (18) into eq. (6) we obtain

$$A_n = \frac{2\beta(1-k)\delta(n)}{2k + p(n) - 1} \quad (19)$$

and

$$C(r, z) = 1 + \frac{1-k}{k} e^{-\beta(z-W_0)} + \sum_{n=1}^{\infty} \frac{2\beta(1-k)\delta(n)}{2k + p(n) - 1} e^{-\frac{\beta}{2}[1 + p(n)] z} \quad (20)$$

The solute concentration in the liquid at the interface is obtained by

letting $z = W(r)$ which gives.

$$C_I(r, z) = \frac{1}{k} - \frac{\beta(1-k)}{k} \sum_{n=1}^{\infty} \frac{\delta(n) J_0(U_n r)}{1 + 2k/p(n) - 1} \quad (21)$$

The solute concentration in the solid at the solid liquid interface is

$$C_{si} = k C_I \quad \text{i.e.}$$

$$C_{si} = 1 - \beta (1-k) \sum_{n=1}^{\infty} \frac{\delta(n) J_0(Un r)}{1 + 2k/[p(n) - 1]} \quad (22)$$

Eq. (22) shows that the deviation of C_{si} in the steady state region is linearly proportional to β and $(1-k)$ which agrees with that obtained in reference 10. However, the result shows that the interface shape is more properly expressed by Bessel function than by a cosine function that is, the interface shape has larger deviation from the planarity.

If $2k/[p(n) - 1] \ll 1$ then eq. (22) has a simple expression.

$$C_{si} \approx 1 - \beta(1-k) [W(r) - W_0] \quad (23)$$

i.e., The deviation of C_{si} is proportional to β , $(1-k)$, and the deviation of interface shape from planarity.

B. Very Large β Limit

For $\beta \gg 1$, i.e. the diffusion layer is very thin cases, we introduce new coordinates (ξ, η) such that $\xi = r$, $\eta = \beta [z - W(r)]$. Then the diffusion equation and the boundary equations can be written as

$$\frac{\partial^2 C}{\partial \eta^2} \left[1 + \frac{\partial W}{\partial \xi^2} \right] + \frac{\partial C}{\partial \eta} - \left\{ 2 \frac{\partial^2 C}{\partial \xi \partial \eta} \left(\frac{\partial W}{\partial \xi} \right) + \frac{\partial C}{\partial \eta} \cdot \left[\frac{\partial^2 W}{\partial \xi^2} + \frac{1}{\xi} \frac{\partial W}{\partial \xi} \right] \right\} / \beta + \left[\frac{\partial^2 C}{\partial \xi^2} + \frac{1}{\xi} \frac{\partial C}{\partial \xi} \right] / \beta^2 = 0 \quad (24)$$

$$(k-1) C_I = \frac{\partial C}{\partial \eta} \left[1 + \left(\frac{\partial W}{\partial \xi} \right)^2 \right] - \frac{\partial C}{\partial \xi} \frac{\partial W}{\partial \xi} / \beta \quad (25)$$

$$C(\xi, \eta \rightarrow \infty) = 1 \quad (26)$$

$$\frac{\partial C}{\partial \xi} - \beta \frac{\partial C}{\partial \eta} \frac{\partial W}{\partial \xi} = 0 \quad \text{at} \quad \xi = 1 \quad (27)$$

We proceed to expand C as power series in β^{-1} , that is let

$$C(\xi, \eta) = C_0(\xi, \eta) + C_1(\xi, \eta) \beta^{-1} + C_2(\xi, \eta) \beta^{-2} \quad (28)$$

Substitute of (28) into eq. (24) and equate the coefficients of β^{-n} to $n = 2$. We have

$$\frac{\partial^2 C_0}{\partial \eta^2} \left[1 + \left(\frac{\partial W}{\partial \xi} \right)^2 \right] + \frac{\partial C_0}{\partial \eta} = 0 \quad (29)$$

$$\frac{\partial^2 C_1}{\partial \eta^2} \left[1 + \left(\frac{\partial W}{\partial \xi} \right)^2 \right] \frac{\partial C_1}{\partial \eta} - 2 \frac{\partial^2 C_0}{\partial \xi \partial \eta} \left(\frac{\partial W}{\partial \xi} \right) - \left[\frac{\partial^2 W}{\partial \xi^2} + \frac{1}{\xi} \frac{\partial W}{\partial \xi} \right] \frac{\partial C_0}{\partial \eta} = 0 \quad (30)$$

$$\begin{aligned} \frac{\partial^2 C_2}{\partial \eta^2} \left[1 + \left(\frac{\partial W}{\partial \xi} \right)^2 \right] + \frac{\partial C_2}{\partial \eta} - 2 \frac{\partial^2 C_1}{\partial \xi \partial \eta} \left(\frac{\partial W}{\partial \xi} \right) - \left[\frac{\partial^2 W}{\partial \eta^2} + \frac{1}{\xi} \frac{\partial W}{\partial \xi} \right] \frac{\partial C_1}{\partial \eta} \\ + \frac{\partial^2 C_0}{\partial \xi^2} + \frac{1}{\xi} \frac{\partial^2 C_0}{\partial \xi} = 0 \end{aligned} \quad (31)$$

Substitute eq. (28) into eq. (25) and equate the coefficient of

β^{-n} to $n = 2$. We have

$$(k-1) C_{0I} = \frac{\partial C_0}{\partial \eta} \Big|_1 \left[1 + \left(\frac{\partial W}{\partial \xi} \right)^2 \right] \quad (32)$$

$$(k-1) C_{1I} = \frac{\partial C_1}{\partial \eta} \Big|_1 \left[1 + \left(\frac{\partial W}{\partial \xi} \right)^2 \right] - \frac{\partial C_0}{\partial \xi} \Big|_1 \frac{\partial W}{\partial \xi} \quad (33)$$

$$(k-1) C_{2I} = \frac{\partial C_2}{\partial \eta} \Big|_1 \left[1 + \left(\frac{\partial W}{\partial \xi} \right)^2 \right] - \frac{\partial C_1}{\partial \xi} \Big|_1 \frac{\partial W}{\partial \xi} \quad (34)$$

Do the same thing for eq. (26) and (27) we have

$$C_0 (\xi \eta \rightarrow \infty) = 1 \quad (35)$$

$$C_1 (\xi \eta \rightarrow \infty) = 0 \quad (36)$$

$$C_2 (\xi \eta \rightarrow \infty) = 0 \quad (37)$$

$$\frac{\partial C_0}{\partial \xi} - \frac{\partial W}{\partial \xi} = 0 \quad \text{at } \xi = 1 \quad (38)$$

$$\frac{\partial C_0}{\partial \xi} - \frac{\partial C_1}{\partial \eta} - \frac{\partial W}{\partial \xi} = 0 \quad \text{at } \xi = 1 \quad (39)$$

$$\frac{\partial C_1}{\partial \xi} - \frac{\partial C_2}{\partial \eta} - \frac{\partial W}{\partial \xi} = 0 \quad \text{at } \xi = 1 \quad (40)$$

$$\frac{\partial C_2}{\partial \xi} = 0 \quad \text{at } \xi = 1 \quad (41)$$

Solving eqs. (29) and (30) with boundary conditions (35) to (41) we obtain

$$C_0 (\xi \eta) = \frac{1-k}{k} e^{-\frac{\eta}{1 + \frac{\partial W}{\partial \xi}^2}} + 1 \quad (42)$$

$$C_1 (\xi \eta) = \frac{1-k}{k} \frac{2 \left(\frac{\partial W}{\partial \xi} \right)^2 \frac{d^2 W}{d \xi^2}}{1 + \frac{\partial W^2}{\partial \xi}} \eta^2 + \frac{\left[\frac{\partial^2 W}{\partial \xi^2} + \frac{1}{\xi} \frac{\partial W}{\partial \xi} \right]}{1 + \frac{\partial W^2}{\partial \xi}} \eta + \frac{1}{k} \left[\frac{\partial^2 W}{\partial \xi^2} - \frac{1}{\xi} \frac{\partial W}{\partial \xi} \right] \quad (43)$$

$$\times e^{-\frac{1}{1 + \frac{\partial W}{\partial \xi}^2} \eta}$$

We have substituted eqs. (42) and (43) into eq. (31) to solve for $C_2(\xi, \eta)$. However, the equation becomes too complicated, we have not obtained a result for $C_2(\xi, \eta)$ yet, however, $C_0(\xi, \eta)$ and $C_1(\xi, \eta)$ will give us the important features of $C(\xi, \eta)$.

$$\text{i.e. } C_1 = \frac{1}{k} + \frac{1-k}{k^2} \left[\frac{\partial^2 W}{\partial \xi^2} + \frac{1}{\xi} \frac{\partial W}{\partial \xi} \right] \frac{1}{\beta} \quad (44)$$

$$\text{and } C_{si} = 1 + (1-k) \left[\frac{\partial^2 W}{\partial \xi^2} + \frac{1}{\xi} \frac{\partial W}{\partial \xi} \right] / (k\beta) \quad (45)$$

This shows that $C_{si} \rightarrow 1$ as $\beta \rightarrow \infty$

According to eq. (22) $C_{si} \rightarrow 1$ as $\beta \gg 0$. Thus, we see that the maximum deviation of C_{si} from 1 occurs for some intermediate value of

In order to better compare eq. (22) to eq. (45), we take $W(r) = \delta J_0(u, r)$. From eq. (45), we have

$$\begin{aligned} C_{si} &= 1 + (1-k) \left[\frac{\partial^2}{\partial \xi^2} + \frac{1}{\xi} \frac{\partial}{\partial \xi} \right] J_0(u, \xi) / k\beta \\ &= 1 - \frac{(1-k)}{k} \delta u_1^2 J_0(u, \xi) \end{aligned} \quad (46)$$

From eq. (22), we have

$$\begin{aligned} C_{si} &= 1 - \beta(1-k) \frac{J_0(u_1, \xi)}{1 + 2k / [p(1) - 1]} \\ p(1) - 1 &= \left[1 + \left(\frac{2u}{\beta} \right)^2 \right]^{\frac{1}{2}} - 1 \approx \frac{2u_1^2}{\beta^2} \\ C_{si} &= 1 - \beta(1-k) \frac{\delta J_0(u, \eta)}{1 + k^2 / u_1^2} \\ &\approx 1 - \frac{1-k}{k\beta} \delta u_1^2 J_0(u, \xi) \end{aligned} \quad (47)$$

That is, for $\beta^2 \gg \frac{u_1^2}{k}$ eq. (22) agree with eq. (45), with the linear term in δ . Thus demonstrating a common region of validity of these analytical approximation.

CONCLUSIONS AND RECOMMENDATIONS

We have treated a two dimensional cylindrical symmytric diffusion problem with curved solid liquid interface under unidirectional solidification with no convection. Analytical approximation for lateral compositional segregation at solid liquid interface in the limits of very small and very large β have been obtained. The solute concentration in the solid at the interface C_{si} have the same β and k dependence as that obtained in reference 10. The dependence in these two liquid interface shape on C_{si} in these studies are different due to the fact that in reference 10, the diffusion process is along a curved interface line while in our study the diffusion process taking place along a curved interface surface. For both $\beta \ll 1$ and $\beta \gg 1$ limits, that is for both very thick diffusion layer and very thin diffusion layer limits, the deviation of the solute concentration C_{si} from original concentration is minimal, that is maximum deviation of C_{si} occurs for intermediate value of β . It is recommended that a numerical calculation should be performed to find lateral compositional segregation for whole range of β . Then compare with the results obtained in reference 10 and the existing experimental data.

For doing numerical calculations, we should consider for the variation in interface temperature, distribution coefficient, and the growth velocity with composition. A one dimensional mode developed for treating compositional

segregation in directional solidified HgCd Te by J. C. Clayton etc.⁽¹⁴⁾
can be modified and expanded for calculating our two dimensional diffusion
problem.

REFERENCES

1. Lehoczky, S.L. and F. R. Szofran, "Directional Solidification and Characterization of $\text{Hg}_{1-x}\text{Cd}_x\text{Te}$ Alloys", in Materials Research Society Symposium Proceedings -- Materials Processing in the Reduced Gravity Environment of Space, ed., Guy E. Rindone (Elsevier, New York), 409, 1983.
2. Lehoczky, S.L. and F.R. Szofran, "Advanced Methods for Preparation and Characterization of Infrared Detector Materials", NAS8-33107, September 1981.
3. Lehoczky, S.L., F.R. Szofran and B. G. Marton, "Advanced Methods for Preparation and Characterization of Infrared Detector Materials", NASA NAS8-33107 (July 1980).
4. Tiller, W.A., K. A. Jackson, J. W. Rutter, and R. Chalmers, "The Redistribution of Solute Atoms During the Solidification of Metals", ACTA METALLURGICA, Vol. 1, 428, 1953.
5. Smith, V.G., W. A. Tiller and J. W. Rutter, "A Mathematical Analysis of Solute Redistribution During Solidification", Canadian Journal of Physics, Vol. 33, 723, 1953.
6. Clayton, J.C., "Transient and Diffusion Analysis of Hg Cd, Te", NAS8-33698 May, 1982.
7. Gillies, D.C. and J.C. Clayton, "Indirect Determination of the Interface in Solid Solution Crystals", to be published.
8. Szofran, F.R., private conversation.
9. Coriell, S.R. and R.F. Sekerka, "Lateral Solute Segregation During Unidirectional Solidification of a Binary Alloy with a Curved Solid-Liquid Interface", Journal of Crystal Growth 46, 479, 1979.
10. Coriell, S.R., R.F. Boisvert, R.G. Rehm, and R.F. Sekerka, "Lateral Solute Segregation During Unidirectional Solidification of a Binary Alloy with a Curved Solid-Liquid Interface", Journal of Crystal Growth 54, 167, 1981.
11. Burden, M.H. D.J. Helditch and J.D. Hunt, "Macroscopic Stability of a Planar Cellular or Dendritic Interface During Directional Freezing", Journal of Crystal Growth 20, 121, 1973.
12. Holmes, D.E. and H.C. Gatos, "Convective Interference and 'Effective' Diffusion - Controlled Segregation During Directional Solidification Under Stabilizing Vertical Thermal Gradients Ge", J. Electrochem Soc. Solidstate Science and Technology, Vol. 128, no. 2, 429, 1981.

13. Bartlett, B.E., P. Capper, J.E. Harris and M.J.T. Queich, "The Effects of Growth Speed on the Compositional Variations in Crystals of Cadmium Mercury Telluride", Journal of Crystal Growth 46, 623, 1979.
14. Clayton, J.C., M.C. Davidson, D.C. Gillies, S.L. Lehoczky, "One Dimensional Analysis of Segregation in Directional Solidified HgCd Te", to be published.

1982

NASA/ASEE SUMMER FACULTY RESEARCH FELLOWSHIP PROGRAM

Marshall Space Flight Center
The University of Alabama

The Study of X-Ray Scattering
To Determine Surface Topography
of Smooth Surfaces

Prepared By:	Alton C. Williams
Academic Rank:	Assistant Professor
University and Department:	Alabama A & M University Department of Physics
NASA/MSFC:	
(Laboratory)	Space Sciences
(Division)	Astrophysics
(Branch)	X-Ray Astronomy
MSFC Counterpart:	Martin Weisskopf, Ph.D.
Date:	August 6, 1982
Contract No.:	NGT-01-002-099 (University of Alabama)

ACKNOWLEDGEMENTS

I wish to acknowledge the kind and most useful help of my NASA counterpart, Dr. Martin Weisskopf, in providing the basic insight in X-ray scattering techniques. Also, the help of NASA's J. Reilly is very much appreciated for his assistance in collecting data. Acknowledgement also go to a graduate assistant, Vernon Smith, who helped in many ways.

LIST OF FIGURES

<u>Figure No.</u>	<u>Title</u>	<u>Page</u>
1	The Experimental Geometry	XLII-13
2	A Direct Slit Image for 2.99 KeV X-rays	XLII-14
3	A Direct Slit Image for 6.4 KeV X-rays	XLII-15
4	A Direct Slit Image for 8.06 KeV X-rays	XLII-16
5	25' Reflected Image for 2.99 KeV X-rays	XLII-17
6	25' Reflected Image for 6.4 KeV X-rays	XLII-18
7	25' Reflected Image for 8.06 KeV X-rays	XLII-19
8	39' Reflected Image for 2.99 KeV X-rays	XLII-20
9	51' Reflected Image for 2.99 KeV X-rays	XLII-21
10	25' Image for Bad Figure Surface for 2.99 KeV Image	XLII-22
11	Point Spread Function for $R = 200$ Km, $\theta = 25'$	XLII-23
12	Point Spread Function for $R = -10$ Km, $\theta = 25'$	XLII-24

THE STUDY OF X-RAY SCATTERING
TO DETERMINE SURFACE TOPOGRAPHY
OF SMOOTH SURFACES

By

Alton C. Williams, Ph.D.
Assistant Professor of Physics
Alabama A & M University
Huntsville, Alabama

ABSTRACT

The amount of power enclosed in a given resolution element of an X-ray reflecting telescope is determined primarily by the surface microtopography of the reflecting surfaces. A perfectly smooth surface is one in which there are no roughness components present. Although, the state-of-the-art of mirror polishing and finishing can reduce the roughness to below the 10 angstroms RMS level, it can by no means eliminate the roughness completely.

The roughness components in the surface cause X-rays to be scattered out of a resolution element. An experimental program is presently underway at Marshall Space Flight Center to study the scattering of X-rays from state-of-the-art smooth surfaces. The experimental set-up allows information to be obtained with subarcsecond resolution. A sample of data obtained is present along with a possible theoretical model for its interpretation.

INTRODUCTION

There is presently an extensive experimental program underway which has as its goal to test the state-of-the art in smooth optical surfaces. The motivations for such a program is the Advanced X-ray Astrophysics Facility (AXAF)¹ which is to be a national X-ray observatory in space. Because of the demanding goals of this X-ray facility of 0.5 arcsecond resolution and an encircled energy of 60% within a 1.0 arcsecond diameter circle at 2.5 KeV, the microtopography of the reflecting surfaces becomes an important factor.

In fact, the scattering of X-rays out of the specularly reflected beam because of surface roughness as small as 20 angstroms in height is the main threat to not being able to achieve the goals of AXAF. In this paper, some results of the experimental program are presented and partially analyzed for the scattering of X-rays from smooth flat surfaces.

OBJECTIVES

The objectives of the overall experimental program are several. These include 1) experimental justification for the selection of a mirror substrate, 2) determination of the optimum technique for surface generation, figuring and polishing, 3) measurement and alignment procedures, and 4) optical design.

The particular objectives that are addressed in this paper are 1) to describe the theoretical relationship between surface roughness and X-ray scattering and 2) to show examples of the tests to demonstrate the feasibility of the AXAF program with present state-of-the-art surface finishing techniques.

DESCRIPTION OF EXPERIMENTAL SETUP

The experimental arrangement is shown in Fig. 1. It consists of an X-ray generator at one end of a 312 meter long evacuated tube. Inside the tube at a distance of 130 meters from the X-ray source is the assembly which houses the mirrors from which the X-rays scatter. This assembly consists of a collimating long narrow slit and two mirror surfaces in a periscope geometry. This geometry is used in order to take advantage of the long tube for making measurements in the sub-arcsecond region.

The mirror assembly can be remotely positioned at four separate locations. One of these is a position where the X-rays go through the slit without striking the mirrors. The other three locations are for X-rays passing through the slit and subsequently striking the surfaces at grazing angles of incidence of 25, 39, and 51 arcminutes.

After reflecting on scattering from the mirrors, the X-rays travel the other 182 meters down the tube to a vacuum chamber where a position-sensitive detector is located. The results in this paper are for those taken by a one dimensional proportional counter.

EXPERIMENTAL RESULTS

Some experimental results are illustrated in Figs. 2-10. The incident X-rays included the Ag L_{α} , Fe K_{α} and Cu K_{α} lines which have energies of 2.99 KeV, 6.4 KeV, and 8.06 KeV, respectively. The corresponding wavelengths are 4.15, 1.94, and 1.54 angstroms. Figures 2, 3 and 4 show the images of the direct slit (no reflection) pattern for each of these energies. These illustrate that for the experimental geometry and energies that were used, there is essentially no difference between the direct slit images due to a difference in energies.

Figs. 5-9 illustrate typical reflecting and/or scattering patterns that results when the X-rays are allowed to strike the mirror surfaces. The mirror illustrated here has a fuse silica substrate and coated with platinum. It was manufactured by Perkin-Elmer. These images demonstrate, conclusively, that mirrors roughness can be controlled during finishing to such a degree as to minimize the scattering of X-rays. In fact, these images all have 50% of their energy well within 1 arcsecond and 90% of it within 2 arcseconds.

Because of the experiment's ability to measure within the arcsecond region, the distortion of the reflected image due to local non-flatness of the surface (i.e. finite radius of curvature on the local level) could be seen clearly when it existed. Fig. 10 illustrates the degradation of an image due to this effect.

THEORETICAL DESCRIPTION OF SCATTERING

If $Z(x)$ represents the surface roughness height as a function of the distance x along the mirror surface, then it can be expressed in terms of a Fourier series

$$Z(x) = \sum_{n=-\infty}^{+\infty} \left[a_n \cos \left(n \pi \frac{x}{L} + \phi_n \right) \right]$$

Where L is the illuminated length of the surface. The root-mean-square roughness is then related to the Fourier amplitudes via the relation

$$\sigma_{\text{RMS}} = \langle Z^2 \rangle = \sum_{n=-\infty}^{+\infty} \langle a_n^2 \rangle .$$

Given the Fourier amplitudes, the intensity of the reflected and scattered image is given by (2)

$$I(\theta) = k C \left[\left\{ 1 - (2k \sin \theta_i)^2 + \sum_{n=-\infty}^{+\infty} \langle a_n^2 \rangle \right\} F(\theta) + (2k \sin \theta_i)^2 + \sum_{n=-\infty}^{+\infty} \langle a_n^2 \rangle F\left(\theta + \frac{n \lambda}{2W}\right) \right]$$

where C is a constant, $k = 2\pi/\lambda$, θ_i is the angle of incidence and $F(\theta)$ is the point spread function of the system. $F(\theta)$ is given by

$$F(\theta) = \left| \frac{1}{2W} \int_{-W}^{+W} dy \exp [i k (\alpha y + \beta y^2)] \right|^2$$

Where $2W$ is the width of the collimating slit and

$$\beta = \frac{1}{2} \left(\frac{1}{D_1} + \frac{1}{D_2} \right) - \frac{2}{r \sin \theta_i}$$

with D_1 being the distance from the X-ray source the slit; D_2 being the distance from the slit to the detector, and r being the radius of curvature of the reflecting surface.

The point spread function essentially describes what will happen to the X-rays even if there were no scattering. Figs. 11 and 12 illustrate this point spread function for two radii of curvature.

An analysis of the collected data would include the fitting of the results to this model to determine a set of Fourier amplitudes which could in turn determine a root-mean-square surface roughness and other surface microtopographical features.

CONCLUSIONS AND RECOMMENDATIONS

From the results collected so far, it can be confidently concluded that the fabrication of smooth surfaces, which could minimize the scattering of X-rays in order to make AXAF possible, is definitely within the state-of-the-art. Furthermore, it can be concluded that local slope deviations in the surface present the main obstacle in manufacturing optimum reflecting mirrors for X-ray telescopes.

Further analysis of this data in terms of theoretical models is in progress and will be published in a forthcoming paper.

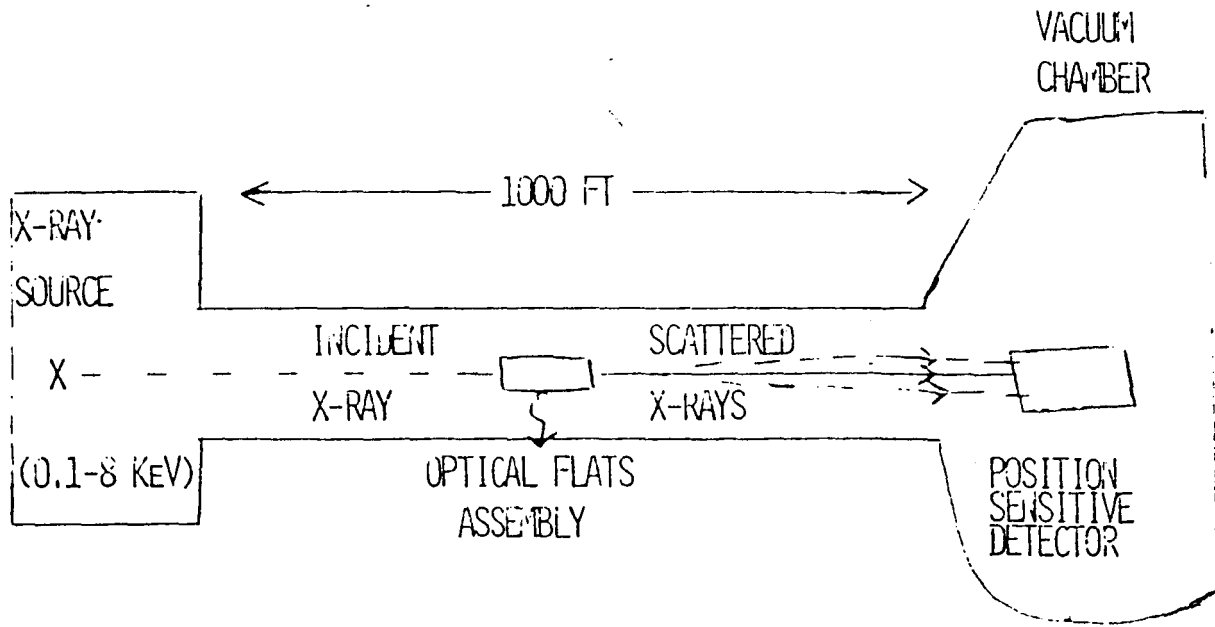
REFERENCES

1. M. V. Zombeck, C. W. Wyman, M. C. Weisskopf, "High Resolution X-ray Scattering Measurements for the Advanced X-ray Astrophysics Facility (AXAF)", Opt. Eng. Jan/Feb. 1982 Vol. 21 No. 1, pgs. 63-72.
2. E. L. Church, "Interpretation of High-Resolution X-ray Scattering Measurements" proceeding of the SPIE (1981).

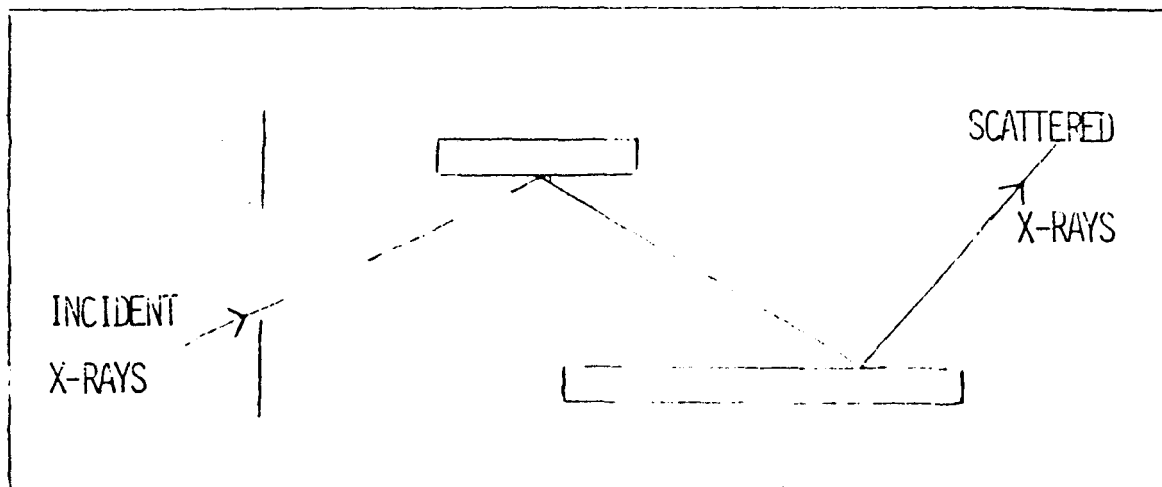
FIG. 1.

X-RAY SCATTERING FROM SMOOTH SURFACES

I. EXPERIMENTAL SET UP



BLOW-UP OF
OPTICAL FLATS ASSEMBLY



XLII-14

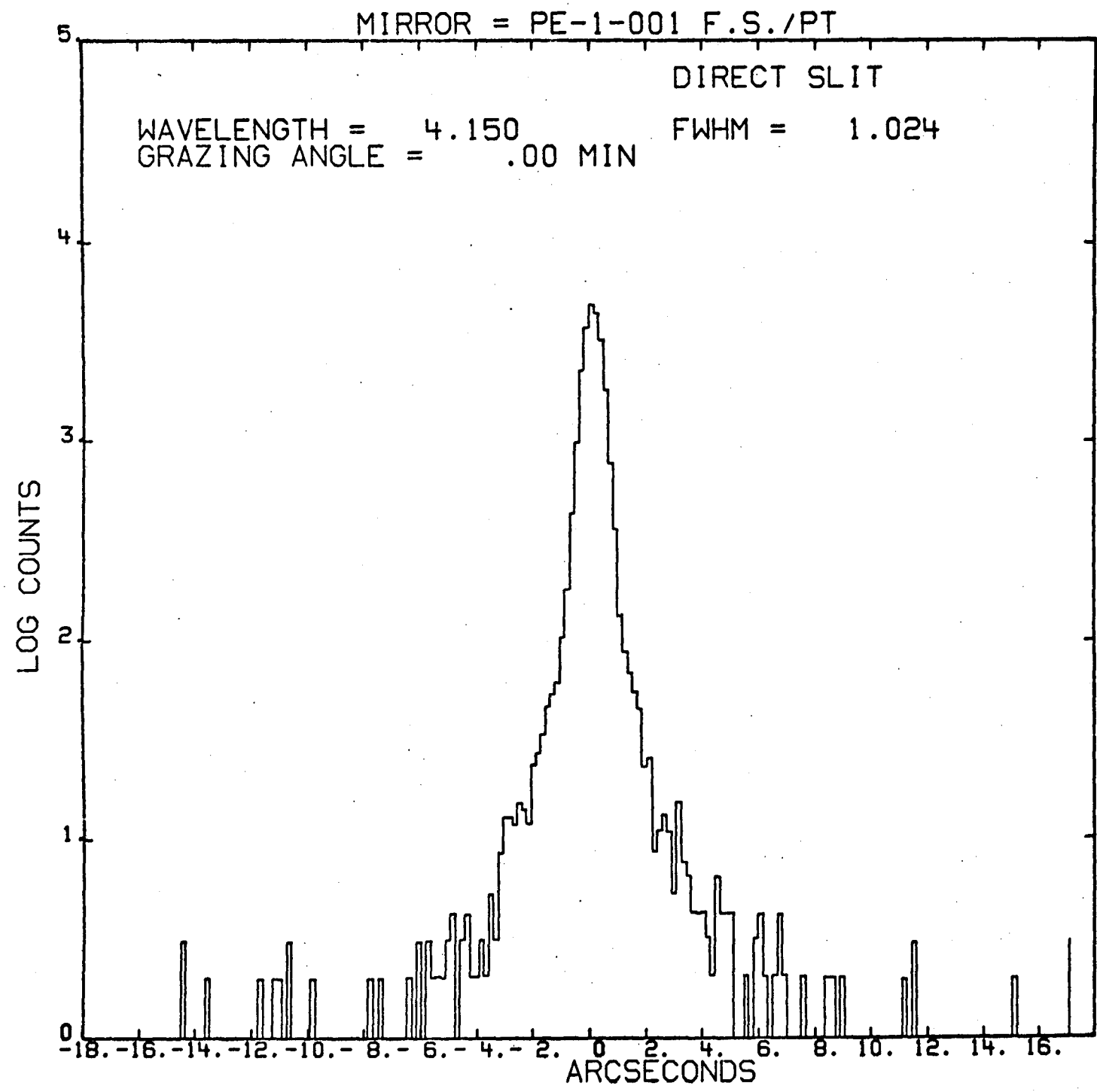


FIG. 2.

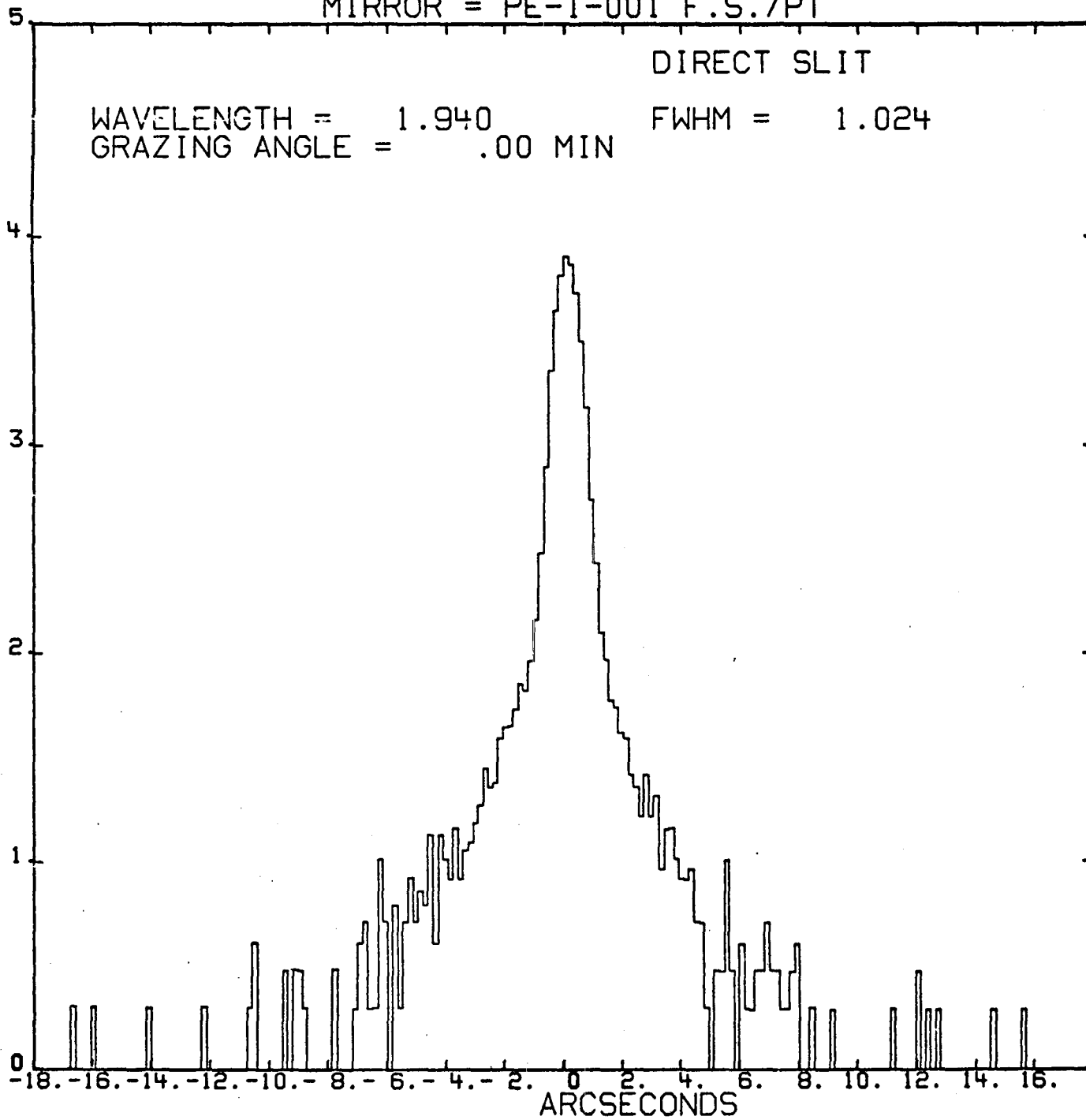
MIRROR = PE-1-001 F.S./PT

DIRECT SLIT

WAVELENGTH = 1.940
GRAZING ANGLE = .00 MIN

FWHM = 1.024

LOG COUNTS



XLII-15

FIG. 3

91-111X

LOG COUNTS

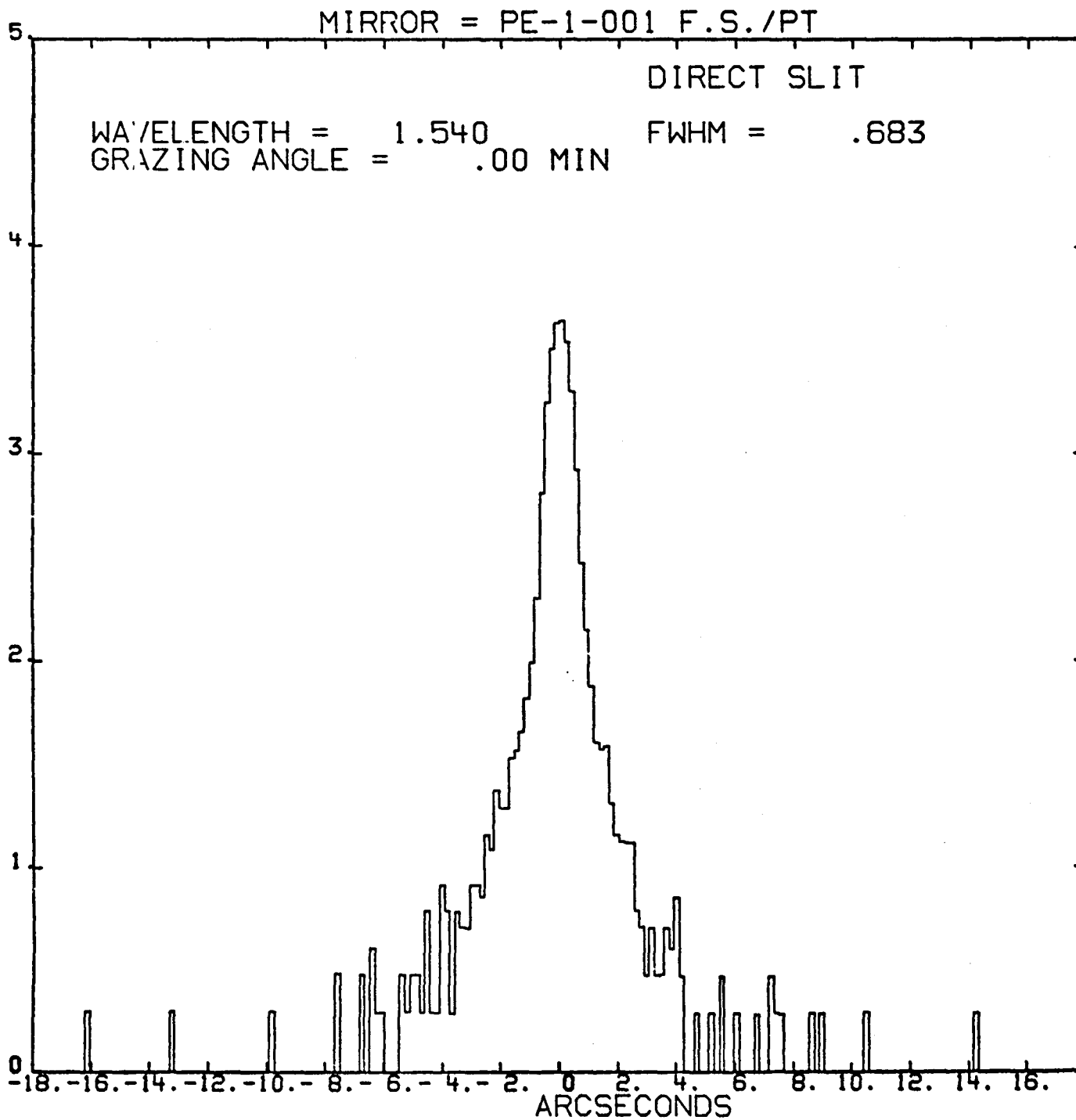


FIG. 4

XLII-17

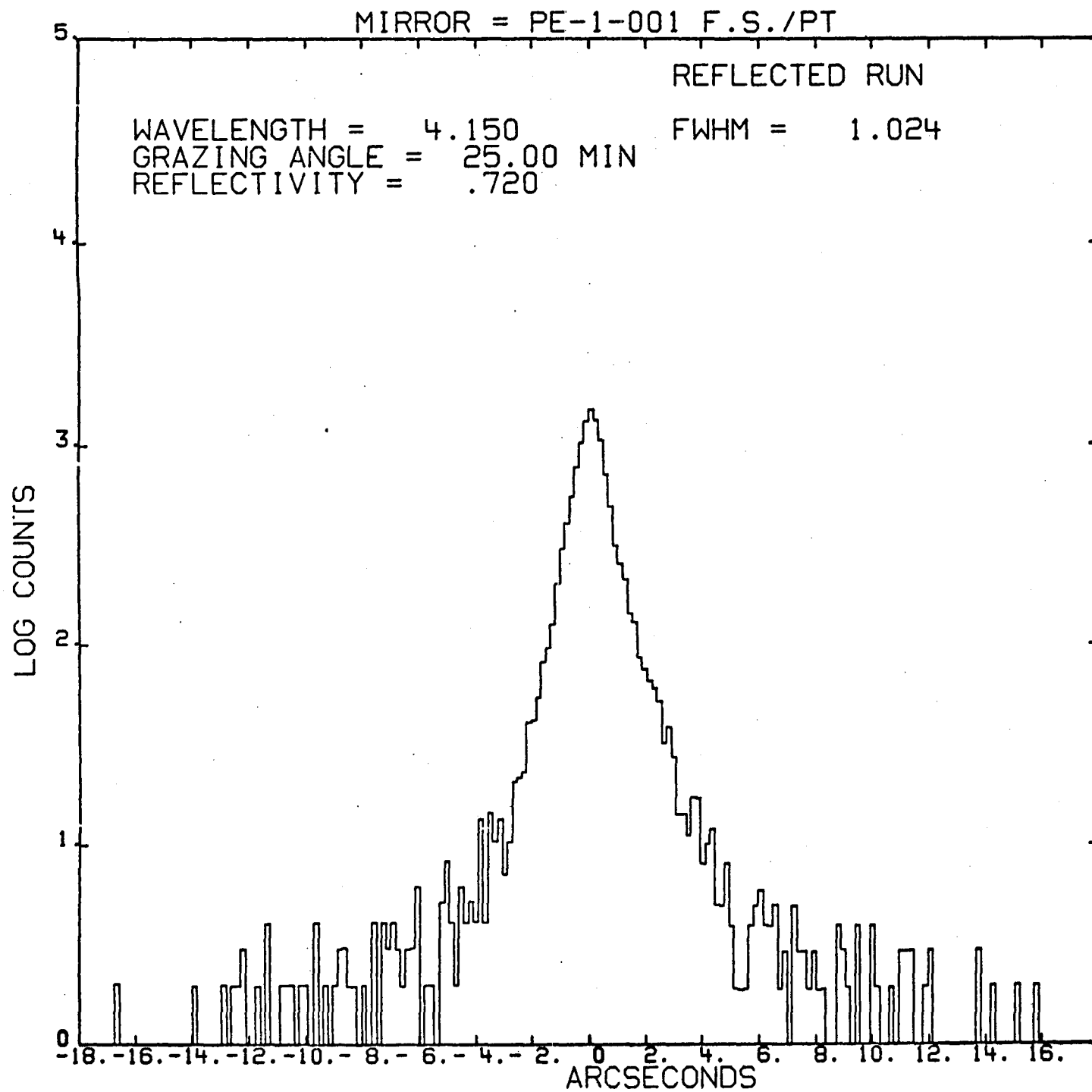


FIG. 5

MIRROR = PE-1-001 F.S./PT

REFLECTED RUN

WAVELENGTH = 1.940
GRAZING ANGLE = 25.00 MIN
REFLECTIVITY = .752

FWHM = 1.706

81-117X

LOG COUNTS

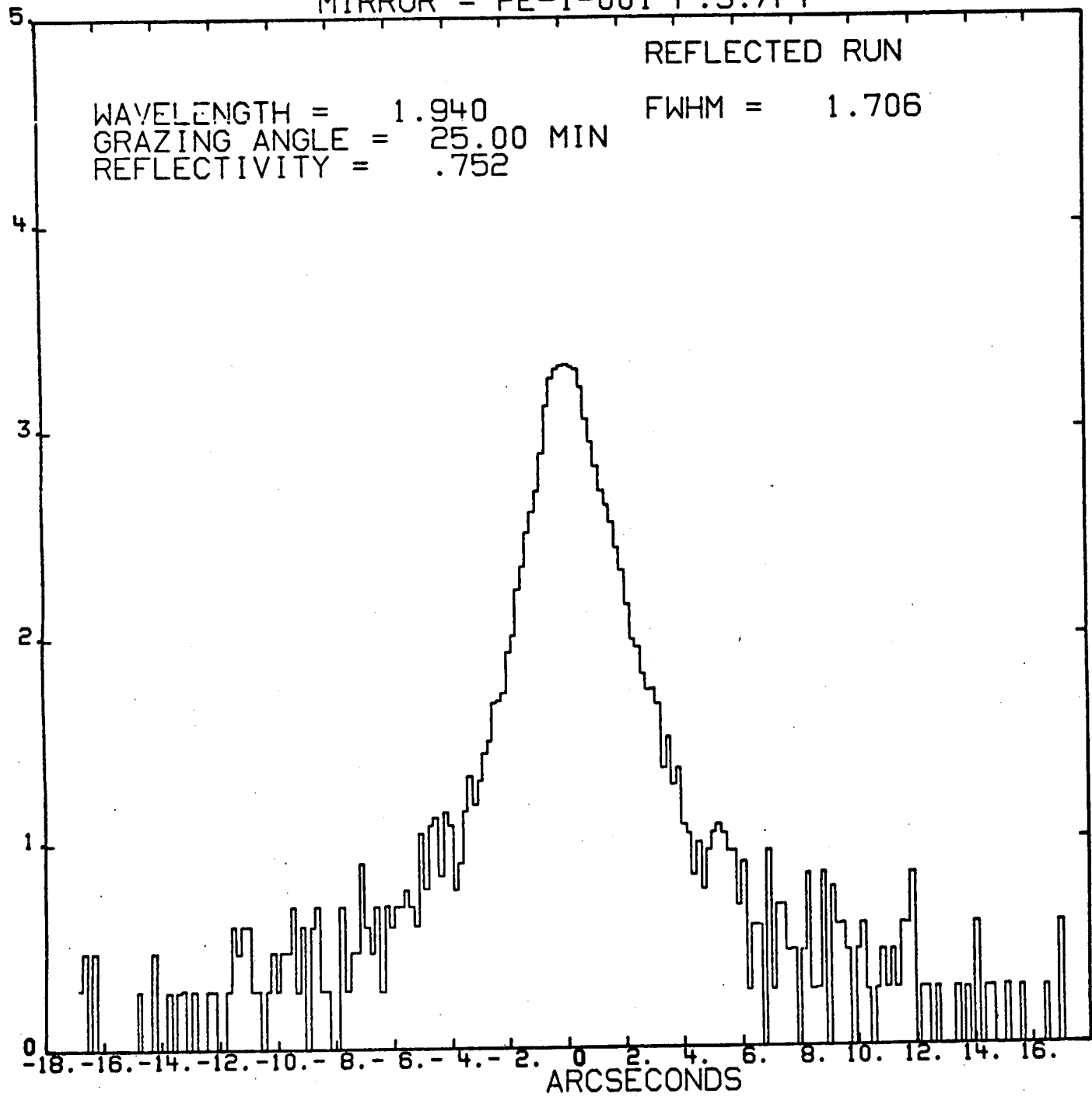


FIG. 6

MIRROR = PE-1-001 F.S./PT

REFLECTED RUN

WAVELENGTH = 1.540
GRAZING ANGLE = 25.00 MIN
REFLECTIVITY = .725

FWHM = 2.389

6111-19

LOG COUNTS

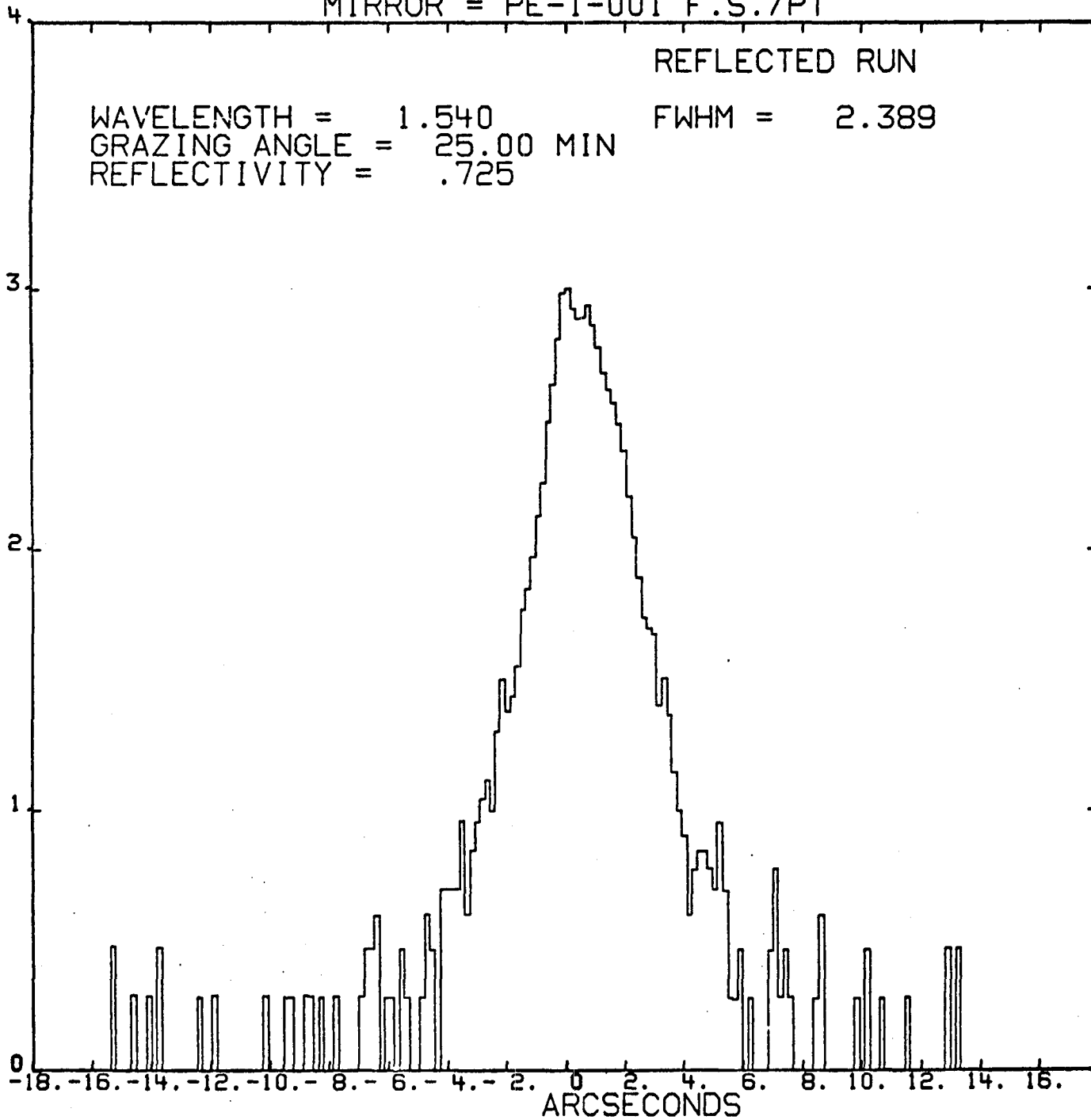


FIG. 7

XLII-20

LOG COUNTS

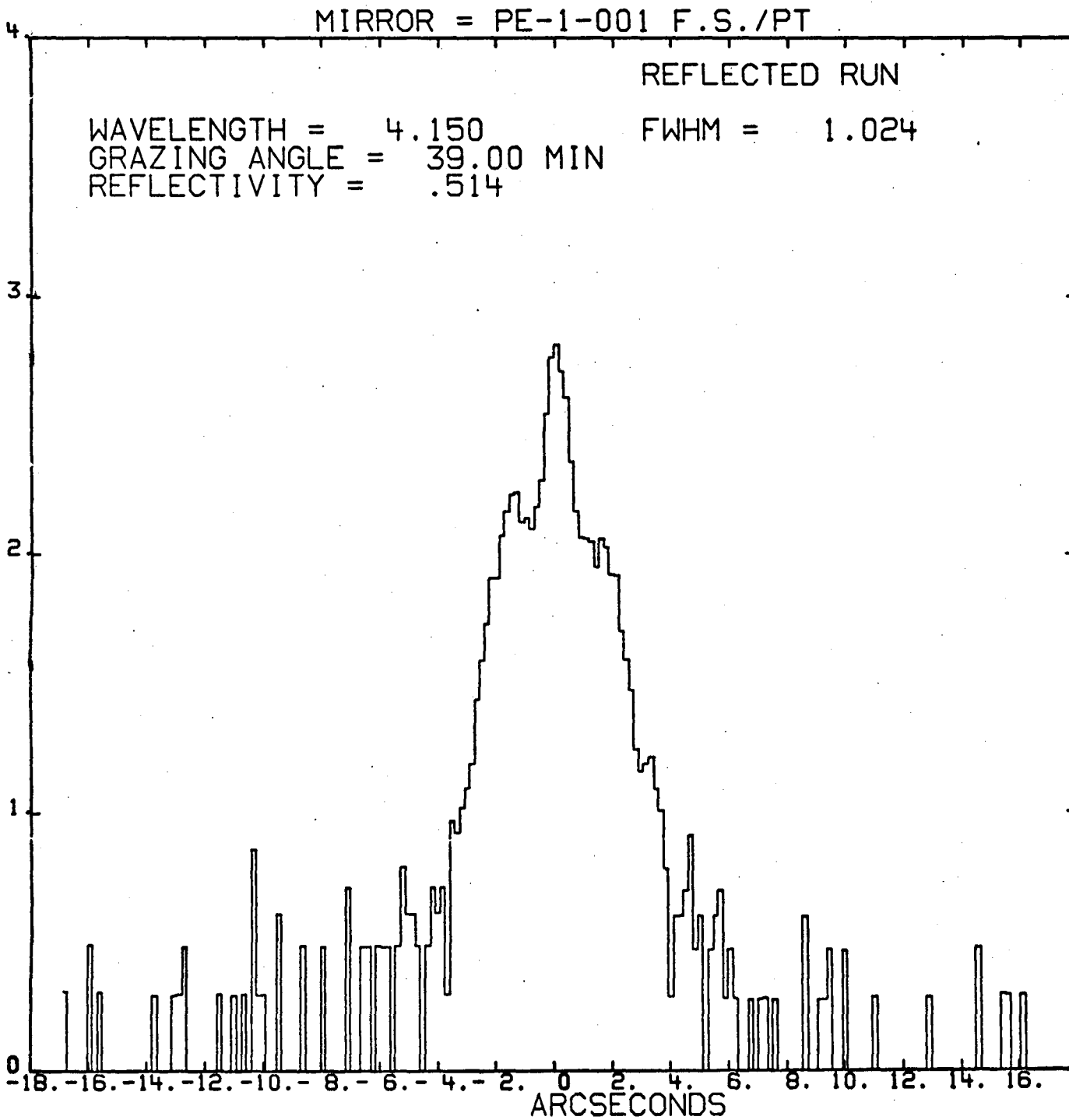


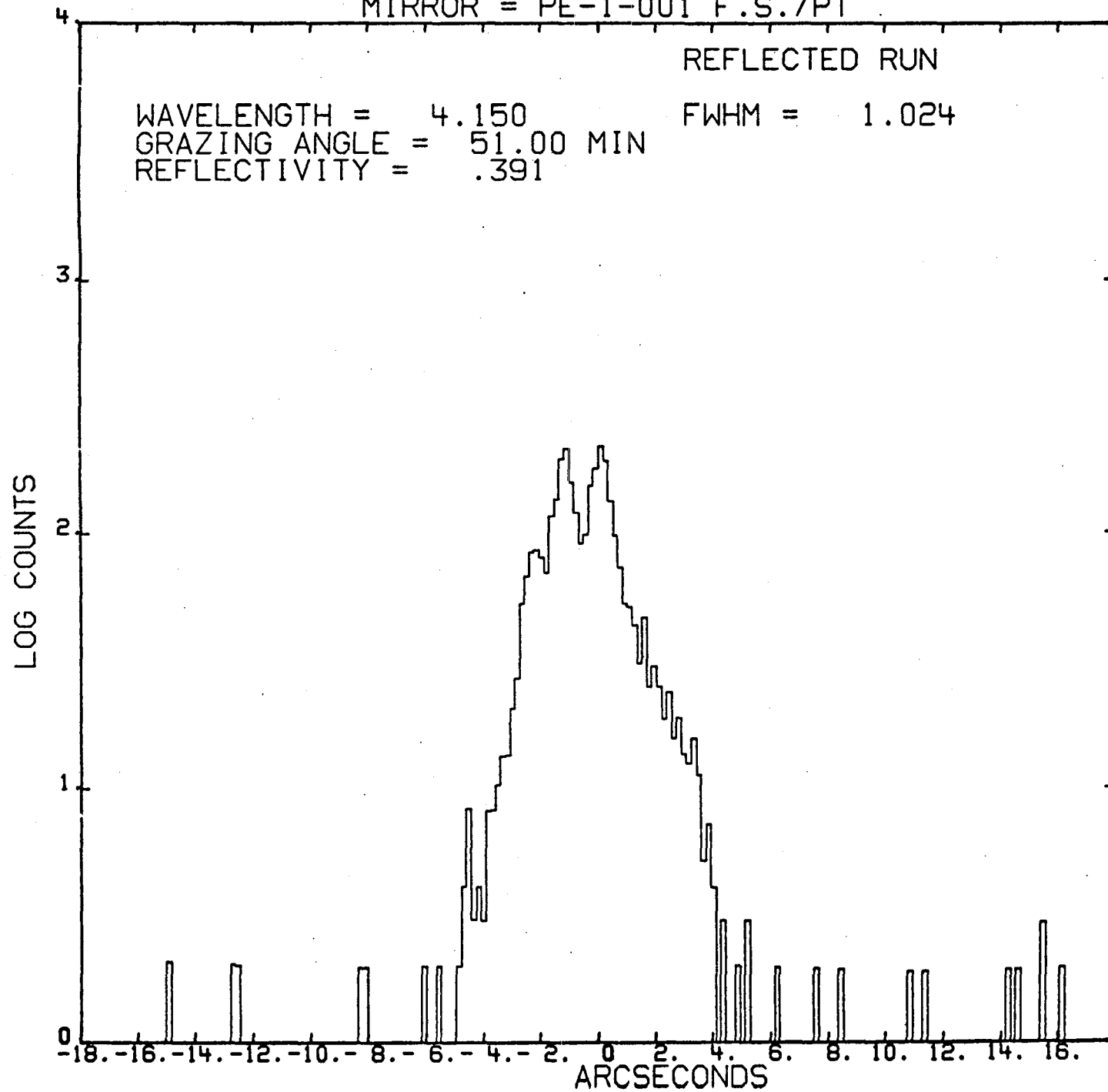
FIG. 8

MIRROR = PE-1-001 F.S./PT

REFLECTED RUN

WAVELENGTH = 4.150
GRAZING ANGLE = 51.00 MIN
REFLECTIVITY = .391

FWHM = 1.024



XLII-21

FIG. 9

XLII-22

LOG COUNTS

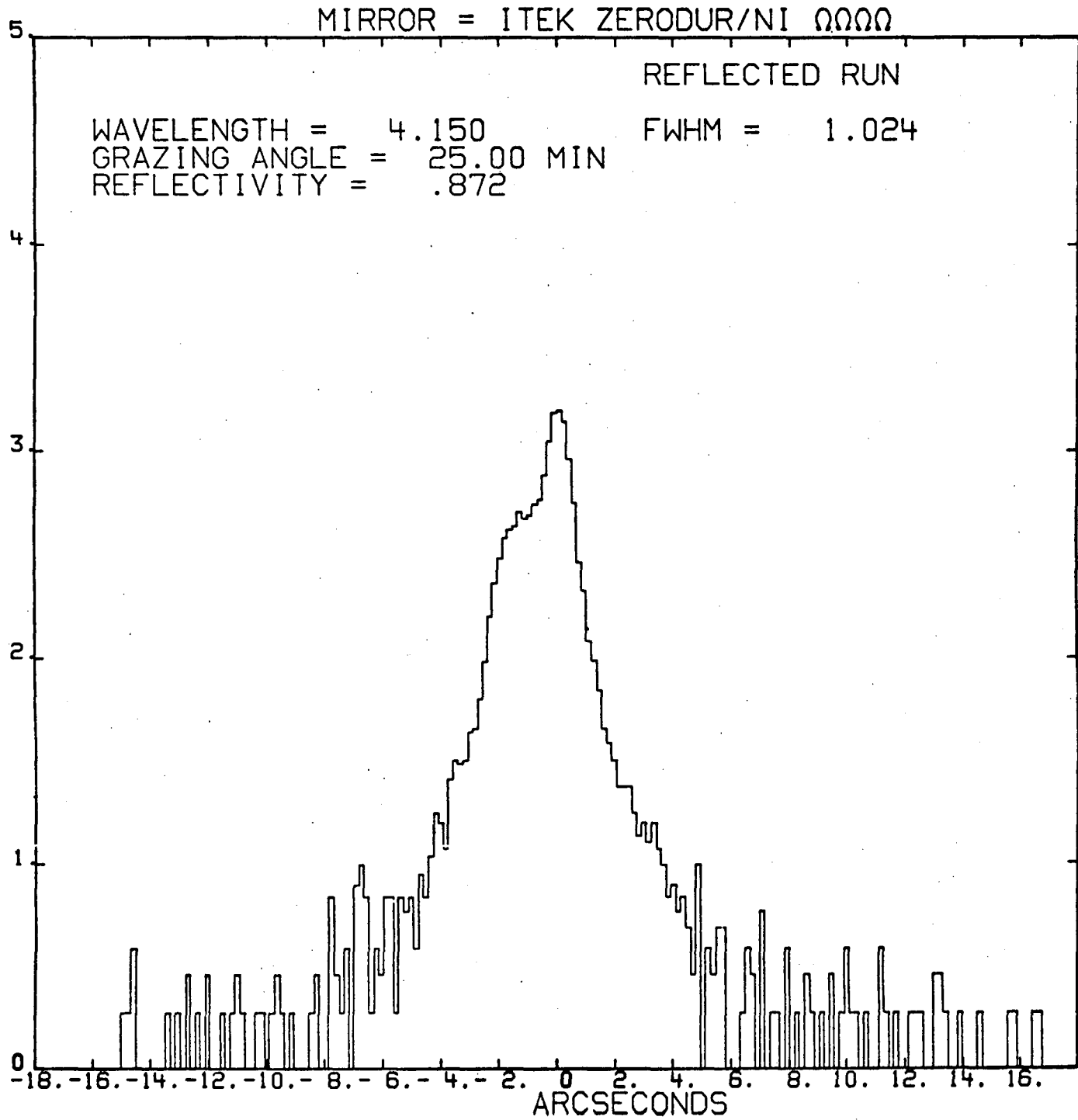


FIG. 10

XLI-23

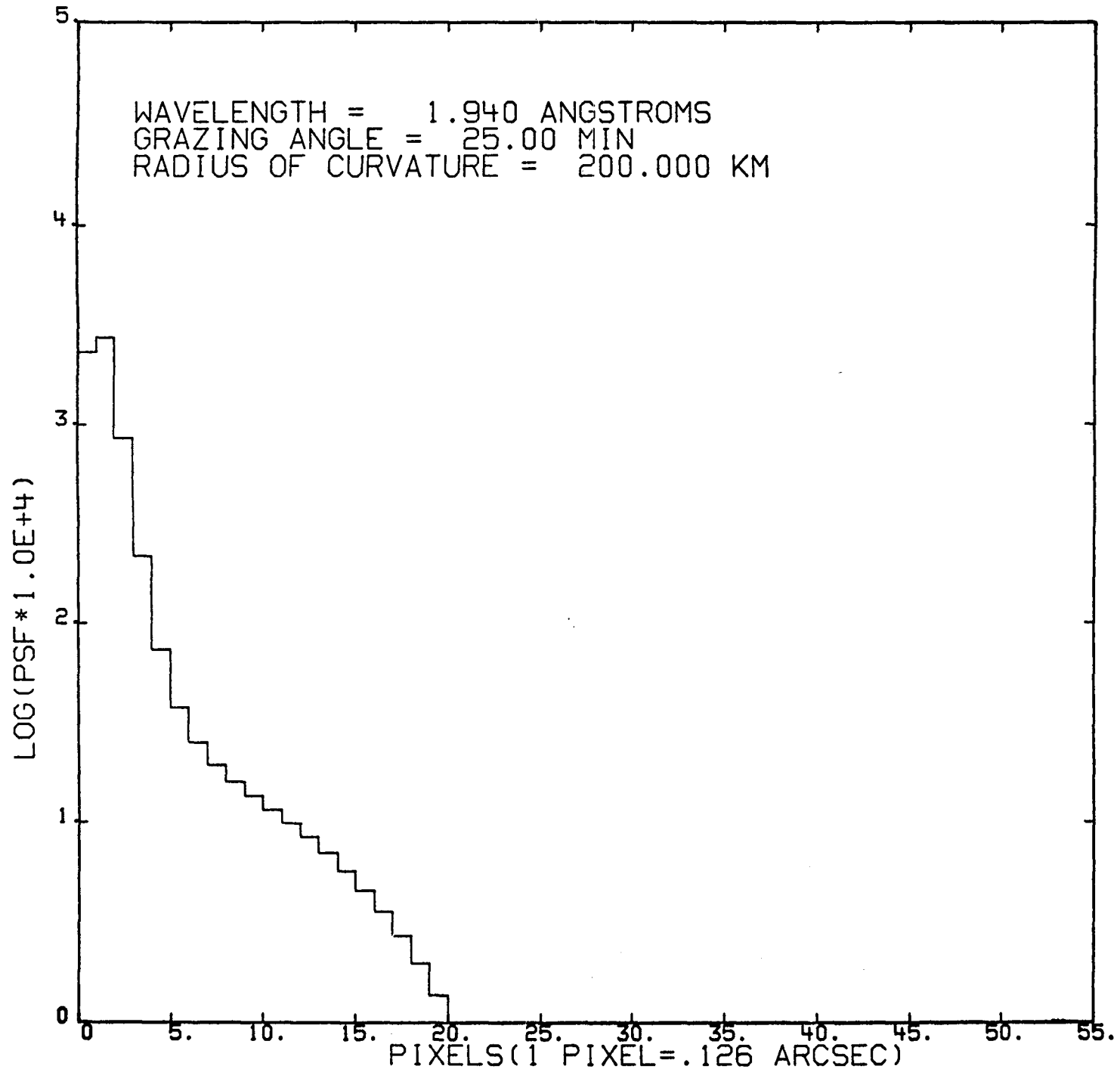


FIG. 11

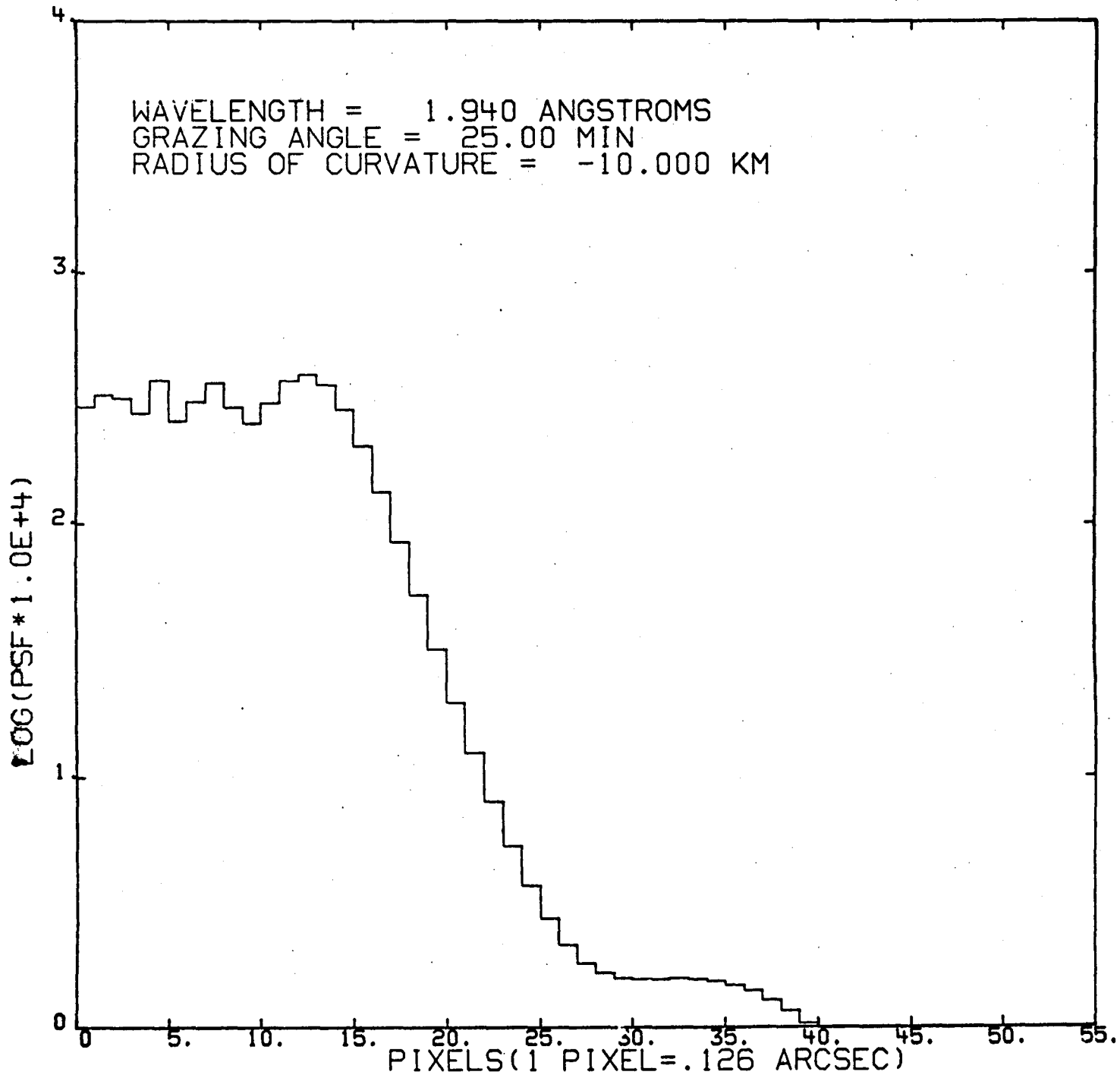


FIG. 12

1982

NASA/ASEE SUMMER FACULTY RESEARCH FELLOWSHIP PROGRAM

MARSHALL SPACE FLIGHT CENTER
THE UNIVERSITY OF ALABAMA

STUDIES WITH SAMPLE CONDUCTIVITY, INSERTION RATES, AND PARTICLE
DEFLECTION IN A CONTINUOUS FLOW ELECTROPHORESIS SYSTEM

Prepared By: Mr. George Williams, Jr.
Academic Rank: Chairman, Dept. of Science
Academic Institution: Calhoun State Community College
Decatur, AL 35602

NASA/MSFC:
(Laboratory) Space Science Laboratory
(Division) Space Processing
(Branch) Separation Processes

MSFC Counterpart: Dr. Robert S. Snyder

Date: August 6, 1982

Contract No.: NGT-01-002-099
University of Alabama

STUDIES WITH SAMPLE CONDUCTIVITY, INSERTION RATES, AND
PARTICLE DEFLECTION IN A CONTINUOUS FLOW ELECTROPHORESIS SYSTEM

By

George Williams, Jr.
Department of Natural Sciences
Calhoun Community College
Decatur, Alabama

ABSTRACT

The continuous flow electrophoresis system makes electrophoresis possible in a free-flowing film of aqueous electrolyte medium. The sample continuously enters the electrolyte at the top of the chamber and is subjected to the action of a lateral DC field. This divides the sample into fractions since each component has a distinctive electrophoretic mobility. Tests were made using monodisperse polystyrene latex microspheres to determine optimum sample conductivity, insertion rates and optimum electric field applications as baseline data for future STS flight experiments. Photographic documentation of particle stream characteristics was also an important phase of the research.

Optimum sample flow rates for the selected samples were determined to be approximately 26 $\mu\text{l}/\text{min}$. Experiments with samples in deionized water yielded best results and voltages in the 20 V/cm to 30 V/cm range were optimum.

Deflections of formaldehyde fixed turkey and bovine erythrocytes were determined using the continuous flow electrophoresis system. Evaluation of the effects of particle interactions on sample resolution and migration in the chamber was also a portion of the research. These cells were tested alone and in combination with the other species at varying concentrations.

ACKNOWLEDGEMENTS

I wish to express appreciation to the following individuals who have provided assistance in this research. Dr. Robert Snyder, Chief, Separation Processes Branch, Space Processing Division, who served as my NASA counterpart and co-investigator in these studies. Ms. Teresa Miller who provided the experimental design, expertise with the CPE system and served as co-investigator. Mr. Darby Mason for providing technical assistance with the photographic aspects of the project and treatment of data. Ms. Jewell Reynolds for typing the final report.

Appreciation is also expressed to the staff of the NASA Photo Lab for photographic services. Thanks also to members of the Graphics Services Lab for preparation of the graphs for this report.

I would also like to thank Mr. Marion Kent, Dr. B. F. Barfield, Dr. James Dozier and Dr. Gerald Karr for administration of the NASA/ASEE Summer Research Fellowship Program.

LIST OF FIGURES

<u>Figure No.</u>	<u>Title</u>	<u>Page</u>
1	Photo of Beckman Continuous Particle Electrophoresis system	XLII-8
2	Photo of syringe pump with injection tubing attached to injection tip	XLII-9
3	Photo of 33 mm camera with macro lens mounted on a tripod in front of viewing chamber	XLII-11
4	Photos of the formation of the crescent in CPE using PSL microspheres	XLII-15
5	Photos of PSL particle stream at zero field, 20 V/cm and 30 V/cm in deionized H ₂ O	XLII-16
6	Photos of PSL particle stream at zero field, 20 V/cm and 30 V/cm in 1/10x dilute R-1 buffer	XLII-17
7	Voltage deflection in CPE for cow and turkey erythrocytes	XLII-19
8	CPE studies - Voltage deflection for cow and turkey RBC's	XLII-22

LIST OF TABLES

	<u>Page</u>
Table 1. Results of tests with sample conductivity and insertion rates on particle stream shape and thickness	XLII-12
Table 2. Deflection of fixed cow and turkey red blood cells in the CPE system	XLII-18
Table 3. Deflection of fixed cow and turkey red blood cells in the CPE system using lower concentrations of cells	XLII-21
Table 4. Band widths in mm of RBC's with electrophoresis in the CPE system	XLII-23

I. Introduction

Projects included on recent Space Shuttle flights lend evidence to the priority which NASA has placed on studies in electrophoresis. Snyder (1981) discussed in detail several facets of the ground-based studies which have been conducted at MSFC. In the Space Sciences Laboratory, Separation Processes Branch, electrophoresis investigations have been conducted using a variety of particles, cells, instrumentation, buffers, measurements, collection techniques and procedures. Many of the methods employed have specific advantages and disadvantages. The fact that the continuous flow electrophoresis system will be included in a future STS flight requires information regarding introduction of the sample into the specific electrophoresis chamber selected for the experiment.

The following research project was undertaken to provide information upon which recommendations could be made to the Principal Investigators in these future STS experiments.

II. Objectives

A. Monodisperse Polystyrene Latex (PSL) microspheres were used to meet the following objectives:

1. To investigate the factors which result in sample spread in the thickness of the chamber, i.e., sample flow vs. curtain flow, sample conductivity relative to curtain conductivity, and optimum voltages.
2. To provide baseline photographic documentation of the particle stream shape at the viewing chamber.
3. To provide photographic documentation of possible artifacts, wall effects, effects of voltage on stream shape and the "crescent phenomenon" as observed at the viewing chamber.

B. A second portion of the project included studies with fixed red blood cells of selected vertebrates in the continuous particle electrophoresis system. The objectives of these experiments include:

1. To determine voltage deflection for fixed red blood cells of selected vertebrates separately and in combination with the cells of other species.

2. To determine the effects of the concentration of red blood cells in the sample on band width and deflection after the electric field application.

III. Methods and Materials

A. Methods for determining optimum flow rates, conductivities and voltages using PSL microspheres.

In order to determine the effects of sample flow rates on particle stream shape a Beckman Continuous Particle Electrophoresis (CPE) system was used (see Figure 1). The CPE system makes electrophoresis possible in a free-flowing film of aqueous electrolyte medium. The chamber is 1.5 mm thick, 45 mm wide and 500 mm long. The electrodes are 300 mm long and are housed on each side of the chamber within cellulose acetate membranes in order to separate the electrode chamber from the electrophoresis chamber. The sample, which continuously enters the electrolyte at the top of the chamber, is subjected to the action of a lateral DC field. This divides the sample into fractions since each has a distinctive electrophoretic mobility based upon differences in surface charge density or zeta potential (Beckman Instruments, 1967).

A syringe pump (Sage Instruments, Model 355) was employed to introduce the sample by syringe into the sample injection tip (see Figure 2). Three different flow rates for each of three concentrations of R-1 buffer (Seaman, unpublished, 1977) as well as deionized water were selected. The phosphate buffer developed for ground and space electrophoresis experiments include: Na_2HPO_4 , 1.76 mM; KH_2PO_4 , 0.367 mM and $\text{Na}_2\text{EDTA} \cdot 2 \text{H}_2\text{O}$, 0.336 mM in deionized water. The sample included monodisperse polystyrene latex (PSC) microspheres 0.369 μm in diameter, obtained from Dow Chemical Corporation, mixed in the suspending solutions resulting in final concentrations of 0.1 percent solids. Observations and photographs were made and notations were recorded



Figure 1. Beckman Continuous Particle Electrophoresis System (NASA Photo)

XLIII-8



Figure 2. Syringe pump with injection tubing attached to injection tip (NASA Photo)

concerning the percentage of the chamber relative to its walls in which the sample flowed at zero field and at each of the applied voltages. The buffer curtain was carefully controlled at 15 cc/min. and the electric fields of 10 V/cm, 20 V/cm and 30 V/cm were applied. Following any change in the electric field, the sample was allowed to stabilize before observations and photographs were attempted.

In order to obtain the best possible photographs, two distinct approaches were employed. First, the microscope attachment (see Figure 1) designed to enhance viewing of resolution and deflection was mounted on the front of the CPE. An Olympus on-mount photomicro adapter was coupled to the existing observation tube and the 10x eyepiece replaced by a 2.5x eyepiece with an adapter of the proper focal length to correct for the removal of the 10x eyepiece. An Olympus OM-2N, 35 mm camera body was attached to the camera adapter. The light source was a cross-section illuminator (CSI) described by Strickler (1970) mounted in the back of the CPE at the rear of the viewing chamber. The camera was mounted on a tripod for support and elimination of vibrations from the peristaltic buffer pumps. Shutter speeds from twenty to 1/60 sec. were used. Photos were made with Kodak Tri-X

film and processed with D-76 developer.

The second approach to the photographic portion of the experiment involved the use of a macro lens positioned in front of the viewing chamber (see Figure 3). A Canon F-1 35 mm body with a Vivitar 70-210 mm telephoto/macro lens was mounted on a tripod. By turning off all laboratory lights and using the rear-positioned CSI, it was possible to focus on the particle stream and at the same time have slight illumination of the rear and front walls of the chamber. Again, several shutter speeds in combination with selected apertures were used to determine the best results.

B. Methods and materials used in red blood cell studies:

Formaldehyde fixed turkey and bovine red blood cells with mobilities of 2.93 and 2.0 $\mu\text{cm}/\text{V sec}$ respectively, were centrifuged, washed three times, and diluted in R-1 buffer. Cell concentrations were determined with a Coulter Counter, Model ZBI, Coulter Electronics, Inc. A 3 cc syringe and needle with a small magnetic stirring bar was attached via plastic tubing to the injection tip and placed in the Sage syringe pump. The sample was stirred constantly during each experiment using a Tri-R magnetic stirrer, Model MS-7, Tri-R Instruments, Inc., and introduced into the CPE curtain. A flow rate of 8 ± 0.5 cc/min was selected and the samples were introduced by the syringe pump. The front plate of the CPE was cooled by pumping water through at a constant temperature of $17 \pm 2^\circ\text{C}$. The storage tanks of curtain and electrode buffer solutions were both placed in the same constant temperature bath in order to provide cooling of the entire fluid system.

Voltage deflections were measured for the cells at each of the voltages and mobilities determined by these distances compared to stream position at zero field. Cells at each concentration were tested at 20 V/cm, 30 V/cm, 40 V/cm and 50 V/cm separately and mixed with cells of the other species. The concentration of cow cells was approximately twice that of turkey cells providing better viewing and photography due to their smaller size. Data were collected by measurement of deflections and band width on the scale at the bottom of the viewing chamber. Photographs of the results were obtained by using the macro lens as described above.

IV. Results and Discussion

The results of the studies with sample conductivity and insertion rates are shown in Table 1. Photographs were taken at each of the insertion rates, each dilution, and at each of the applied voltages. A discussion of some of the

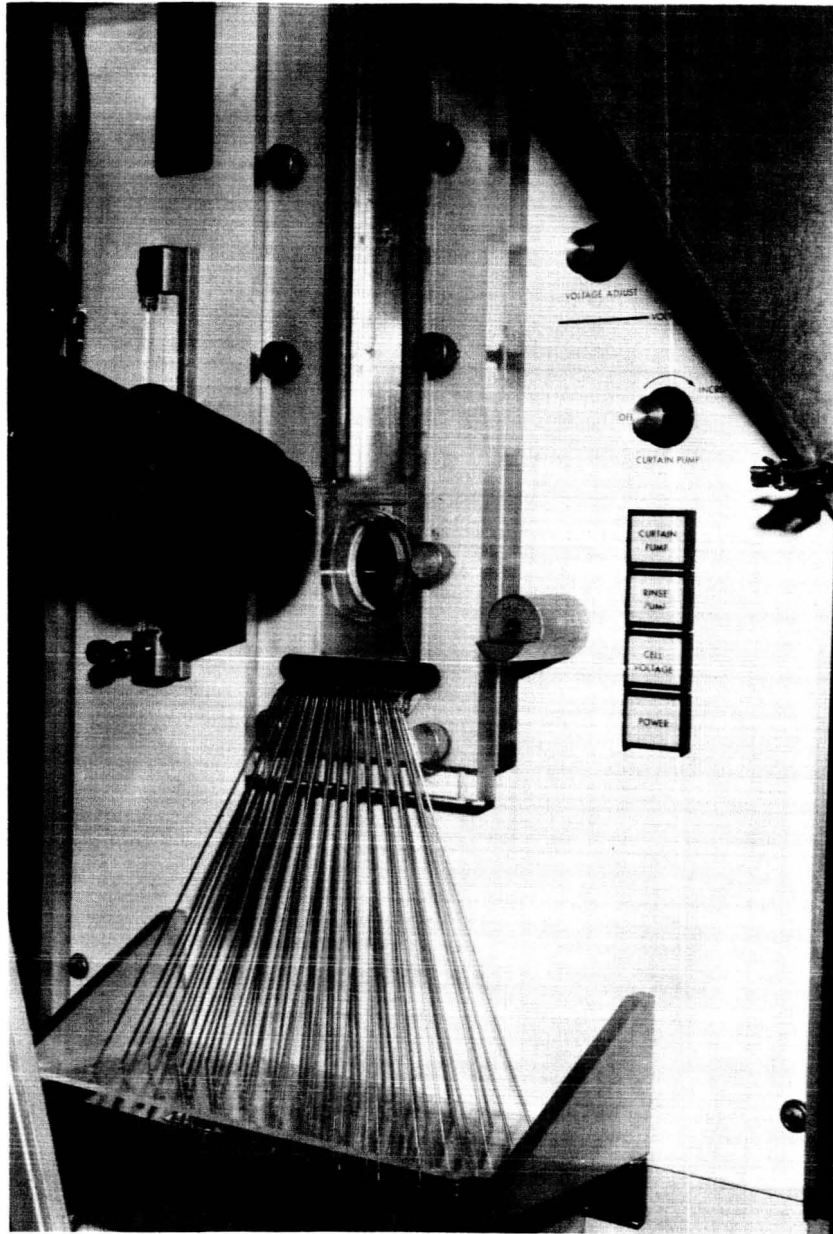


Figure 3. 33 mm Camera with macro lens mounted on a tripod in front of viewing chamber (NASA photo). Note: Vertical particle stream may be seen in viewing chamber in the zero field position.

Dilution	Sample Insertion Rate	Estimated Sample Stream Thickness Relative to Chamber Thickness			
		0 V/cm	10 v/cm	20 V/cm	30 V/cm
.1 x dilute R-1	26 μ l/min	25%	75%	85%	*NE
	51 μ l/min	50%	80%	95%	80%
	80 μ l/min	50%	80%	90%	75%
.05 x dilute R-1	26 μ l/min	50%	60%	60%	60%
	51 μ l/min	40%	70%	80%	70%
	80 μ l/min	60%	60%	80%	80%
.2 x dilute R-1	26 μ l/min	40%	50%	60%	60%
	51 μ l/min	40%	50%	85%	80%
	80 μ l/min	75%	60%	85%	80%
DI H ₂ O	26 μ l/min	30%	30%	50%	40%
	51 μ l/min	30%	40%	50%	60%
	80 μ l/min	40%	60%	80%	70%

Table 1. Results of tests with sample conductivity and insertion rates on particle stream shape and thickness.

*No Estimate due to movement of sample at viewing chamber

photographs will follow. First, we will consider the results in Table 1. Based upon observations and photographs, the particle stream may be studied best when the PSL microspheres are diluted with deionized water. Our results also indicated that the sample in 2/10x dilute R-1 give the second best results with 1/20x dilute R-1 and 1/10x dilute R-1 following in that order. However, the photographs lend additional evidence. Our findings generally agree with Strickler's (1970) who noted that tolerance to lower-than-curtain conductivity in the sample is usually greater than that to higher-than-curtain conductivity. Further, that suspension of sample in distilled water is feasible for some samples at flow rates up to 50 $\mu\text{l}/\text{min}$. We observed greater depth spread with particles in the 1/10x R-1 buffer than at either the 1/20x R-1 or 2/10x R-1. This apparent discrepancy shown in the 2x buffer is consistent with that reported by Strickler. He noted that sample conductivity up to three times that of the curtain buffer does not necessarily adversely affect particle stream shape.

The optimum sample insertion rate could depend upon three variables. The size of the particles and percent solids in the diluted sample. We used 0.1 percent solids and particles 0.369 μ in diameter. If the cross section illuminator is used, as in these experiments, the shape of the particle stream may be readily observed, photographed and deflections determined. In addition, the shape of the particle stream could be affected by an increase or decrease in the curtain buffer flow rate. At slower rates than the 15 cc/min used in these investigations, wall effects, meandering of sample, and other abnormal sample spreading may occur. At curtain flow rates faster than 15 cc/min the higher insertion rate of 80 $\mu\text{l}/\text{min}$ could be used. Therefore, the best results were those observed using flow rates of 26 $\mu\text{l}/\text{min}$ and 51 $\mu\text{l}/\text{min}$.

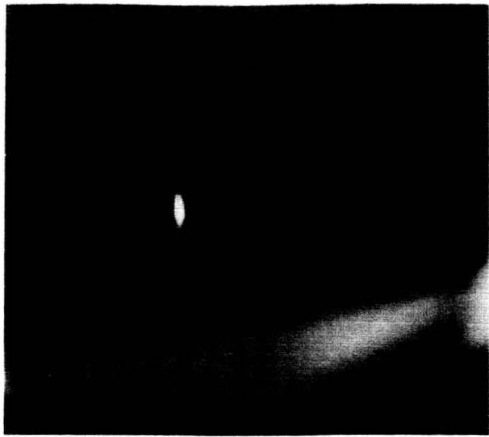
Optimum electric fields applied to the samples were found to be in the 20-30 V/cm range. At 30 V/cm more lateral band spreading was observed. Meandering of the crescent occurred more often at the higher voltages also.

Photographs taken with the photomicrographic equipment as described in Section III were acceptable. However, due to the required exposure time (5 secs to 20 secs) it was possible for the particle stream to take on new shapes, spread, and form apparent artifacts. This method certainly has merit when one considers the magnification possible. For best results when photos of the particle stream are desired, we recommend the use of the macro lens.

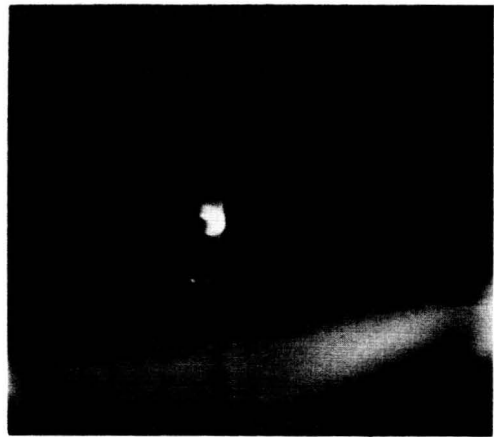
Figure 4 gives a photographic representation of the formation and movement of the "crescent phenomenon" as described by Strickler, 1970. The sequence was made using Kodak Tri-x film push processed at ASA 800. A medium aperture setting of F-5.6 and shutter speed of 1/15 sec provides excellent results. Photo # 1 was made with the stream at zero field. When the electric field is applied at approximately 60 V/cm the particle stream will begin to move toward the anode (at right) and the clearly formed crescent may be photographed. Photo Nos. 2 and 3 show the crescents forming and Photo No. 4 is a perfectly shaped crescent. In Nos. 5 and 6, abnormal horizontal in-depth distribution of the particles may be seen. Exposure at 1/30 sec would provide enough light for the crescent to be photographed; however, it is advantageous to know where the front and rear chamber walls occur relative to the sample. Both walls can be seen in these photographs and for this reason we recommend these camera settings.

Figure 5 includes photos of PSL particle stream at zero field, 20 V/cm and 30 V/cm in deionized water. The sample flow rate was 26 μ l/min and curtain flow was 15 cc/min. This sequence represents the best results of our studies regarding sample insertion, conductivity and particle stream stability. For comparison see Figure 6 with photos of PSL streams at zero field, 20 V/cm and 30 V/cm with the sample flow at 80 μ l/min and curtain flow at 15 cc/min. Note that the band spread is deeper through the chamber in these photos and a crescent can be observed at 20 V/cm. The maximum in-depth stream spread occurred at 20 V/cm. At higher voltages the crescent arms elongated and moved farther from the apex. This elongation, evident at 30 V/cm, resulted in more lateral band spreading.

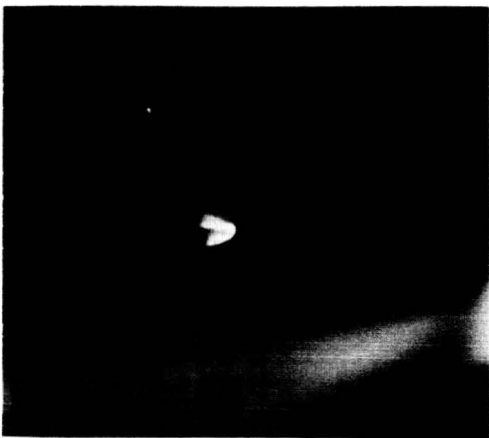
Results of CPE studies with fixed cow and turkey erythrocytes at selected concentrations are shown in Table 2. This information is also shown graphically in Figure 7. It can be noted that at these concentrations, deflection of the cow RBC's was greater when combined with turkey cells than when electrophoresized separately at the lower voltages. At 40 V/cm and 50 V/cm deflection of the cow cells was not as great in combination as when they were measured separately. However, a close look at the standard deviations would show that these mean distances could be nearly identical. The turkey cells apparently migrated faster when combined than they did when electrophoresized separately. Again, when the standard deviations are taken into account these values are almost identical. Therefore, the apparent differences in the distances as shown in Figure 7 may not exist. McGuire and Snyder (unpublished report, 1980) found that both turkey and cow RBC's did exhibit greater mobilities when in combination. The concentration of cells used in these studies were in the 1×10^8 range. Further,



1.



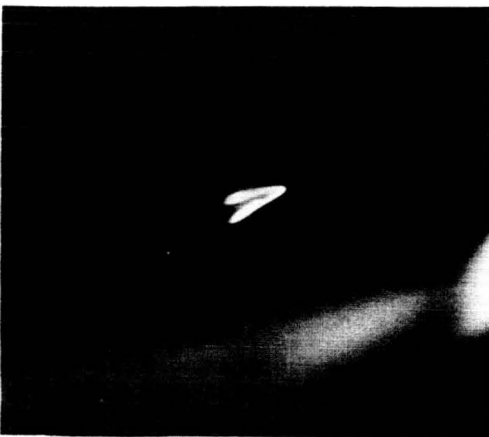
2.



3.



4.



5.



6.

Figure 4. Formation of crescent in a continuous flow electrophoresis system using polystyrene latex microspheres.

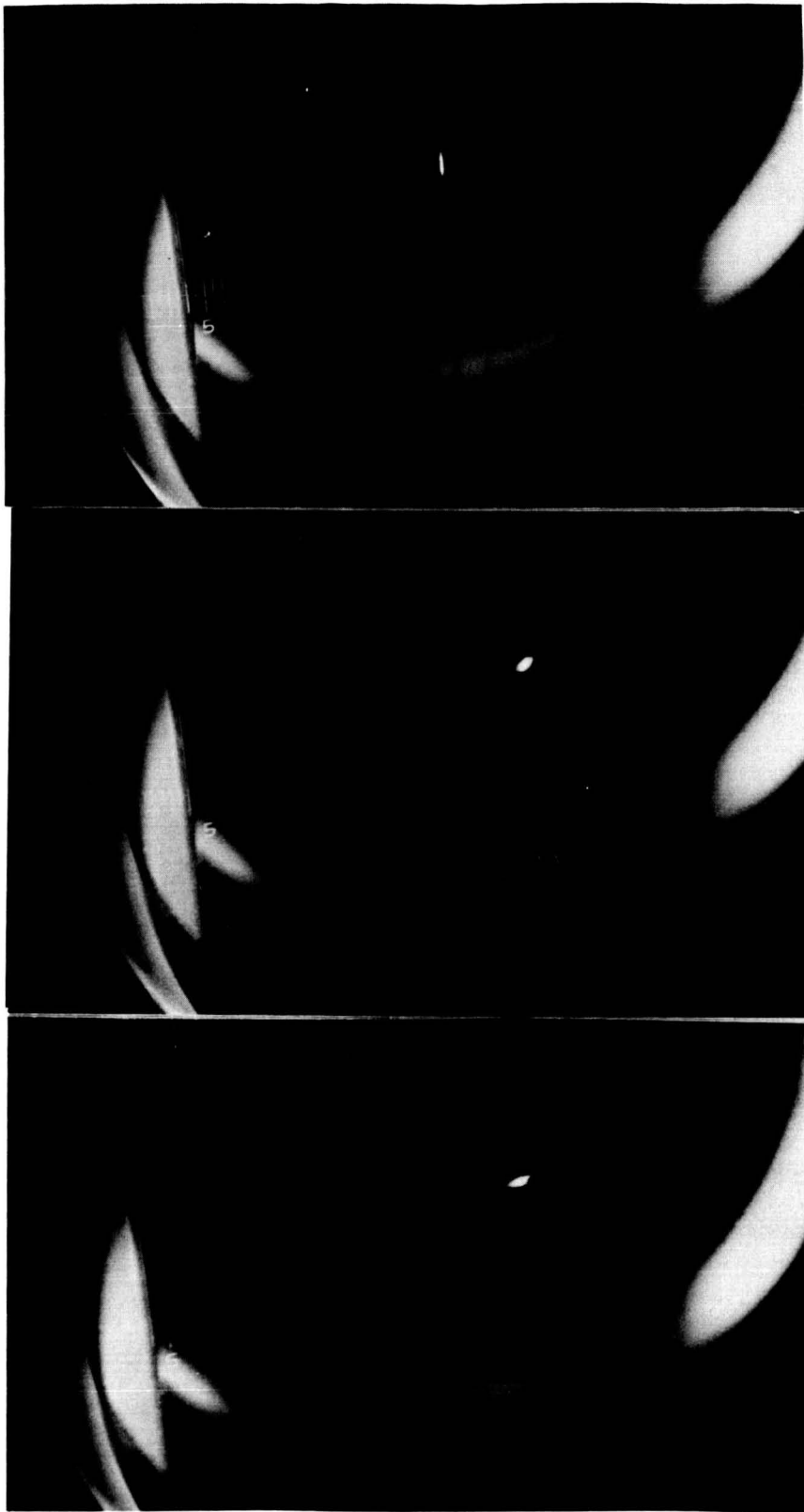


Figure 5. Photos of PSL particle stream at zero field (top), 20 V/cm (middle) and 30 V/cm (bottom) in deionized H₂O. Sample flow = 26 μ l/min, curtain flow = 15 cc/min

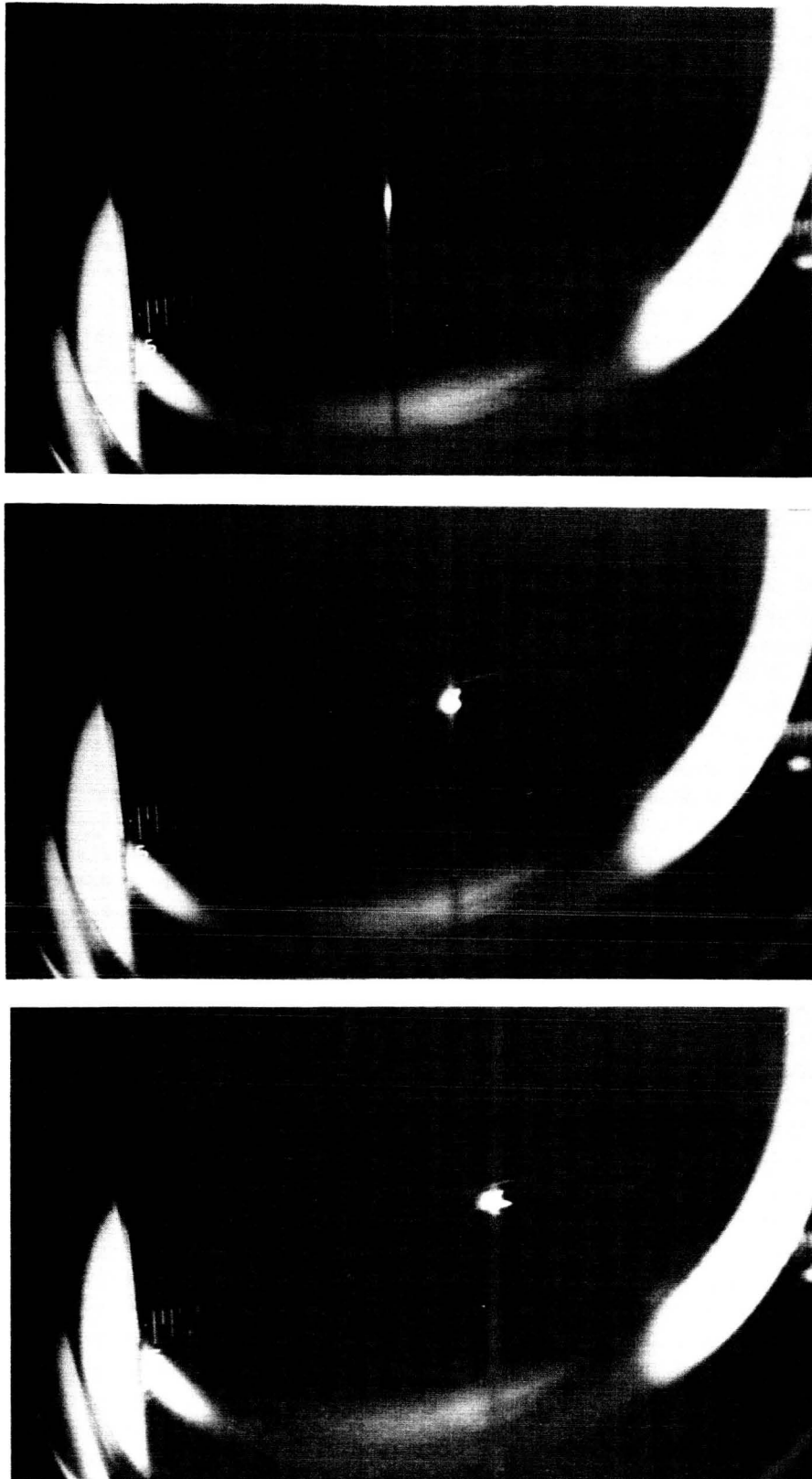


Figure 6. Photos of PSL particle stream at zero field (top), 20 V/cm (middle) and 30 V/cm (bottom) in 1/10x dilute R-1 buffer. Sample flow = 80 μ l/min, curtain flow = 15 cc/min.

20 V/cm	30 V/cm	40 V/cm	50 V/cm
Cow RBC's $\bar{X} = 8.8 \text{ mm SD} = .5$	$\bar{X} = 11.9 \text{ mm SD} = .3$	$\bar{X} = 13.5 \text{ mm SD} = .3$	$\bar{X} = 14.9 \text{ mm SD} = .5$
Cow mixed with Turkey RBC's $\bar{X} = 9.3 \text{ mm SD} = .7$	$\bar{X} = 12.1 \text{ mm SD} = .5$	$\bar{X} = 13.0 \text{ mm SD} = .6$	$\bar{X} = 14.7 \text{ mm SD} = 1.1$
Turkey RBC's $\bar{X} = 10.4 \text{ mm SD} = .4$	$\bar{X} = 14.0 \text{ mm SD} = .6$	$\bar{X} = 15.1 \text{ mm SD} = .3$	$\bar{X} = 16.6 \text{ mm SD} = .6$
Turkey mixed with Cow RBC's $\bar{X} = 10.9 \text{ mm SD} = .7$	$\bar{X} = 14.1 \text{ mm SD} = .6$	$\bar{X} = 15.2 \text{ mm SD} = .6$	$\bar{X} = 16.8 \text{ mm SD} = .8$

Table 2. Deflection in mm of fixed cow and turkey red blood cells in the CPE system.

\bar{X} = mean, SD = Standard Deviation (N = 5)

Concentration of cow RBC's = 5.58×10^7 /ml

Concentration of turkey RBC's = 2.63×10^7 /ml

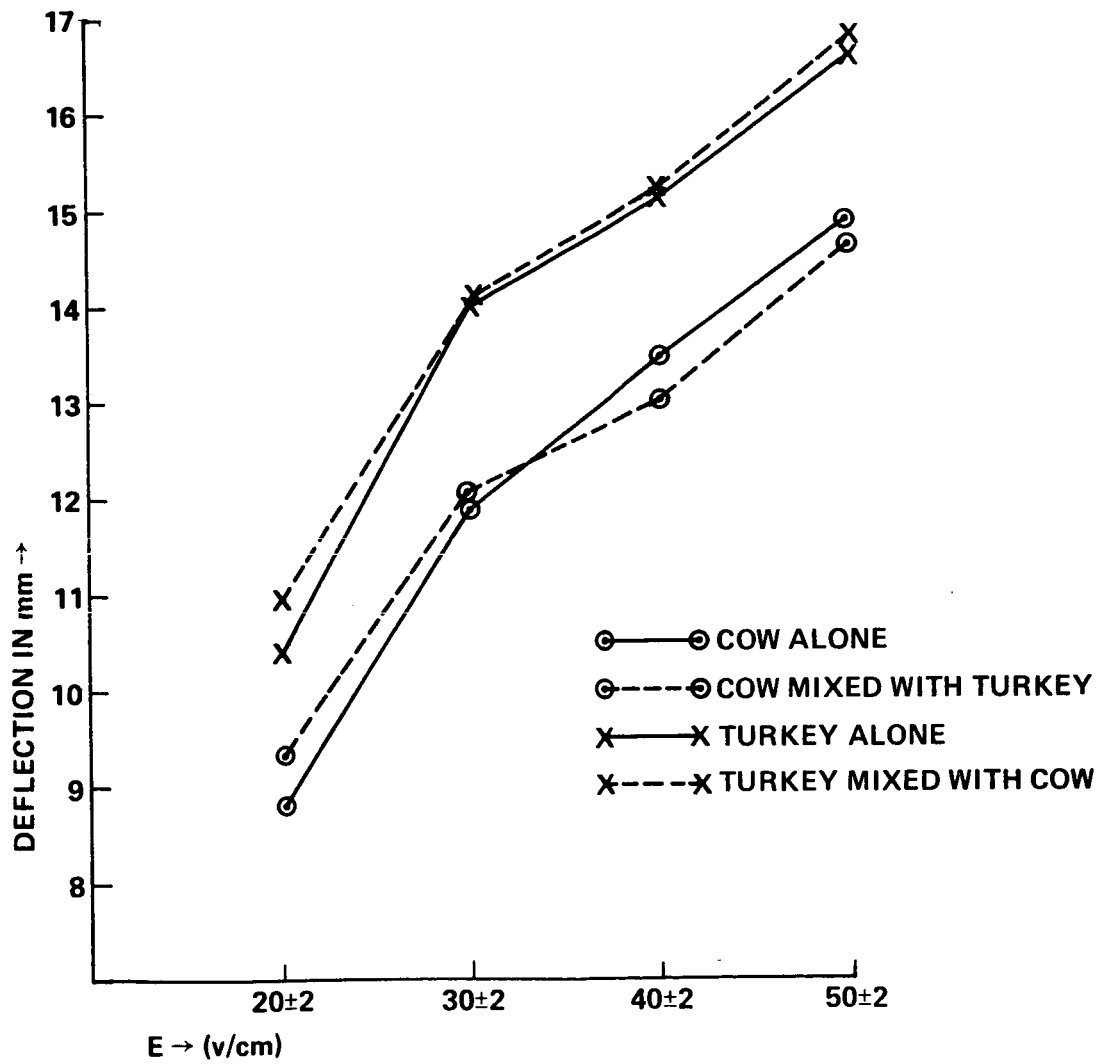


Figure 7. Voltage deflection in CPE for cow and turkey erythrocytes.

based upon the experiments by McGuire and Snyder, we expected the electrophoretic mobilities relative to the voltage gradient to be linear. Results of a series of experiments using lower concentrations of RBC's of the same species are shown in Table 3 and Figure 8. In these studies, cow cells alone at the selected concentrations had greater mobilities than when combined with turkey cells. This was not the case with turkey erythrocytes. A comparison of the mean voltage deflections shows the turkey cells move slower when mixed with cow cells in the CPE system (see Figure 8). Again, when standard deviations are considered this may only be an apparent difference.

The concentration of the mixture of cells in Table 3 is approximately twice that of the cells when tested individually. This concentration difference could be responsible for the difference in the measured mobilities of the cow/turkey mixture as shown in Figures 7 and 8. There is sufficient evidence presented here to merit additional studies with these cells at various concentrations.

Table 4 gives the average band widths of the red blood cells of cow and turkey in continuous flow electrophoresis. As predicted, band widths increased at the higher voltages. These averages provide excellent baseline data for comparison in future experiments. McGuire and Snyder (unpublished report, 1980) found band widths much smaller in cow and turkey cells at similar voltages in the CPE. They reported most widths in the .125 - .5 cm range. However, the curtain flow rate employed was approximately 25 cc/min. In our experiments, band widths were smaller when the cell concentrations were smaller. This also complicated the determination of resolution when the cross section illuminator was used. For this reason, the dark field illuminator is more satisfactory in blood cell mobility studies with the CPE system.

V. Conclusions and Recommendations

If PSL microspheres are used in continuous flow electrophoresis studies, sample flow rates of 26 - 50 μ l/min are optimum with moderate (15 cc/min) curtain flow rates. Conductivity of the sample can be much less than that of the curtain buffer. We recommend using deionized water in studies similar to those discussed in this paper. For best results, voltages in the 20 V/cm to 30 V/cm range are optimum. Details of photographic documentation with recommendations were described earlier (see Section IV).

Sufficient data were collected to provide baseline mobility determinations with the CPE system. More research is needed using varying red blood cell concentrations for

	20 V/cm	30 V/cm	40 V/cm	50 V/cm
Cow RBC's $\bar{X} = 9.0$ mm SD = .4		$\bar{X} = 12.0$ mm SD = .2	$\bar{X} = 13.7$ mm SD = .6	$\bar{X} = 14.6$ mm SD = .7
Cow mixed with Turkey RBC's (No separation)		$\bar{X} = 12.0$ mm SD = 1.3	$\bar{X} = 13.5$ mm SD = 1.0	$\bar{X} = 13.9$ mm SD = .8
Turkey RBC's $\bar{X} = 10.1$ mm SD = .4		$\bar{X} = 14.0$ mm SD = .4	$\bar{X} = 15.8$ mm SD = .3	$\bar{X} = 16.3$ mm SD = .4
Turkey mixed with Cow RBC's $\bar{X} = 10.9$ mm SD = .1		$\bar{X} = 13.8$ mm SD = 1.2	$\bar{X} = 15.0$ mm SD = 1.2	$\bar{X} = 15.6$ mm SD = 1.3

Table 3. Deflection in mm of fixed cow and turkey red blood cells in the CPE system using lower concentrations of cells

\bar{X} = mean
SD = standard deviation
(N = 5)

Concentration of Cow RBC's = 6.042×10^6 /ml

Concentration of Turkey RBC's = 3.78×10^6 /ml

Concentration of Cow/Turkey RBC's mixed = 1.14×10^7 /ml

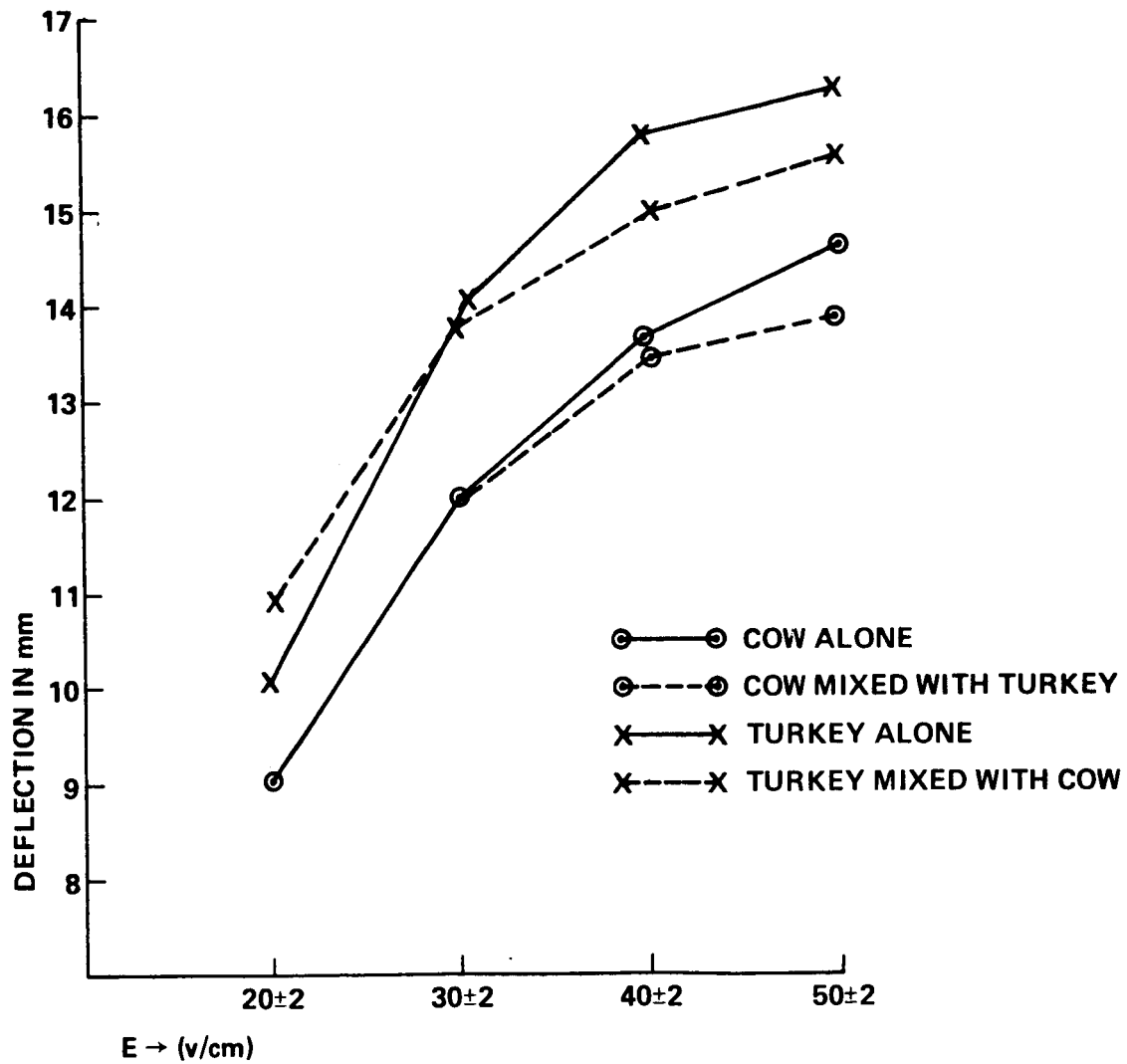


Figure 8. CPE studies - Voltage deflection for cow and turkey RBC's.

	0 V/cm	20 V/cm	30 V/cm	40 V/cm	50 V/cm
Cow RBC's @ 5.58×10^7 /ml	.5	2.0	3.2	3.8	5.0
Cow RBC's @ 6.042×10^6	.5	2.7	2.8	2.2	2.6
Turkey RBC's ₇ @ 2.63×10^7 /ml	.5	3.3	4.1	4.2	4.2
Turkey RBC's ₆ @ 3.78×10^6 /ml	.5	2.3	2.5	3.0	2.6

Table 4. Band Widths in mm of RBC's with electrophoresis in the CPE system
(N = 5) buffer curtain flow rate - $8.0 \pm .5$ cc/min

the vertebrate species which may be selected for STS flight studies.

During these investigations we were able to learn about the complexities of continuous flow electrophoresis. The techniques employed, problems encountered, and data collected will be of value to NASA and the investigator in future studies.

References

1. Beckman Instruments. 1967. CPE System for Continuous Particle Electrophoresis. Bulletin 7096-B.
2. McGuire, J. K. and Snyder, R. S., 1980. Characterization of Continuous Flow Electrophoresis for Improvement of Resolution and Throughput. NASA - Marshall Space Flight Center, AL. Unpublished report.
3. Seaman, G. V. F., 1977. Electrophoretic Separator Experiments - Composition and Properties of the Candidate Buffer R-1. Univ. of Oregon Health Sciences Center. Unpublished results.
4. Snyder, R. S., 1981. Review of the NASA Electrophoresis Program. Published in Electrophoresis '81. Walter de Gruyter and Co., New York, p. 883-897.
5. Strickler, A., 1970. Optimizing CPE Performance: Crescents, Artifacts, and Conductivity Effects. CPE Exchange No. 4.